THE UNIVERSITY OF CHICAGO

GEOCHEMISTRY AND COSMOCHEMISTRY OF URANIUM STABLE ISOTOPES

A DISSERTATION SUBMITTED TO
THE FACULTY OF THE DIVISION OF THE PHYSICAL SCIENCES
IN CANDIDACY FOR THE DEGREE OF
DOCTOR OF PHILOSOPHY

DEPARTMENT OF THE GEOPHYSICAL SCIENCES

BY
FRANÇOIS L. H. TISSOT

CHICAGO, ILLINOIS
DECEMBER 2015

To my loved ones,

Denis, Catherine et Géraldine,

Parrain,

Ariella, and the blueberry.

"La santé, l'argent et l'amour nous procurent des plaisirs et nous assurent le bonheur — mais les plus grandes joies de la vie nous sont données par le travail."

Sacha Guitry, *Jusqu'à nouvel ordre...*

"Boxer worked harder than ever. [...] The others said, 'Boxer will pick up when the spring grass comes on'; but the spring came and Boxer grew no fatter. Sometimes on the slope leading to the top of the quarry, when he braced his muscles against the weight of some vast boulder, it seemed that nothing kept him on his feet except the will to continue. At such times his lips were seen to form the words, 'I will work harder'; he had no voice left."

George Orwell, *The Animal Farm*

TABLE OF CONTENTS

LIST OF FIGURES

LIST OF TABLES

ACKNOWLEDGMENTS

This thesis was a six-year long endeavor shaped by important interactions with many people. Here I would like to take the time (and space) to thank these people.

- My advisor, Nicolas Dauphas, for giving me the opportunity to pursue a Ph.D under his supervision, for all I learned from him, and for his friendship.
- The members of my committee: Fred Ciesla, Andrew Davis, Lawrence Grossman and Frank Richter, for their guidance and complementary pickiness, which undoubtedly improved the quality of this work.
- The Origins Lab postdocs: Tom Ireland, Paul Craddock, Marc-Alban Millet, Chris Burkhardt and Nick Greber, for their generous help and friendship along the way.
- My fellow students: Haolan Tang, Reto Trappitsch, Levke Kööp, Corliss Sio, Nicole Nie, and Cindy Chen for their precious support and shared moments of cheer no matter the time of the day or night.
- The undergrads who worked with me on the carbonate project: Matt Go, Magdalena Naziemiec, Garrett Healy and Leonard Shaw, for their work, friendship, and for the things I learned chaperoning them.
- The staff trio: Brian Lynch, James Eason and Katie Casey, for making it easier to focus on science.
- My parents, Denis and Catherine Tissot, and my sister, Géraldine Tissot, for their unconditional love and support during this extreme adventure.
- My wife, Ariella, for braving with me the ups and downs of the daily scientific pursuit.
- My friends: Josh, Sam, Andy, Maria, Julia, Andrew, James, Claire, Paul, Tuttle and Buttle, for their support during all, or part of, this journey, which made this experience worthwhile beyond the scientific results.

- Last but not least, my younger self, for his resilience in pulling through what seemed at times unbearable, and for never loosing sight of the element of happiness behind the curtain of pain this thesis drew on him.

ABSTRACT

In the late 2000s, an assumption three-quarters of a century old was overthrown when sub-permil variations were discovered in the ratio of "stable" U isotopes. This dissertation is part of the subsequent effort that turned the $^{238}U/^{235}U$ ratio from a constant value into a crucial variable of Pb-Pb dating and a promising paleoredox tracer.

Herein, the reader will find the analytical details on how to achieve routine high-precision U isotope analysis with double spike technique, while properly estimating the uncertainties via Monte-Carlo simulations (Chapter 2).

Measurement of many igneous rocks will be used to (i) assess the U isotopic composition of Earth's crust, and (ii) demonstrate the absence of Soret diffusion in Lachlan Fold Belt granitoids. Measurements of seawater samples and data compilation will also be used to (i) show that the ocean is homogeneous with regards to U isotopes, (ii) constrain the extent of modern oceanic anoxia, (iii) confirm that the U oceanic budget is in steady-state, and (iv) validate the assumption that the ratio of U "stable" isotopes tracks the global oceanic redox conditions. Two case studies applying the U proxy on ancient sediments will be presented (Chapter 3).

Analysis of a series of angrite samples will allow the revision of their Pb-Pb ages, thus reducing the discrepancies between absolute Pb-Pb ages and relative Al-Mg ages in early Solar System materials. Finally, the discovery of a large ^{235}U excess in a fine-grained group II CAI, will bring definitive evidence that ^{247}Cm was alive when the Solar System formed, thereby putting to rest a four-decade long controversy. The initial Solar System abundance of Curium-247 derived will be shown to be incompatible with the existence of an actinide-specific *r*-process site and instead suggests that a single *r*-process nucleosynthetic environment is relevant to the long-term evolution of the Galaxy, with the last *r*-process production event occurring ~ 100 Myr before Solar System formation (Chapter 4).

Of interest to both geo- and cosmochemists, a Pneumatic-Fluoropolymer HPLC system will also be introduced, as a mean of bringing HPLC systems up to the resistance and

separation standards of isotope chemistry (Chapter 2).

CHAPTER 1

INTRODUCTION

To the newborn, the world seems immobile, unchangeable, eternal. Stars come with every dusk and go with every dawn, oceans and mountains appear immutable, seasons return in a clockwise fashion. This stillness is nothing but a mask which the newborn learns to peel away through the exercise of reason, as he asks repeatedly "Why?" *As he grows, the ever expanding knowledge of his own kind is transmitted to him and with it will come a partial understanding of the world he lives in. The reassurance brought by this understanding allows the newborn to affirm the grasp of his reason on the world that surrounds him, and, fed by an overwhelming sea of answers, his curiosity might eventually be quenched. He will have, by then, become an adult. If, despite everything, his questioning hasn't ceased, he will have become a scientist.*

As two of the countless fields of science that have emerged since the introduction of the scientific method, Isotope Geo- and Cosmochemistry are quite peculiar. They are concerned with the processes that shaped the observable universe and essentially aim to understand the transformations that the physical world went through. Yet they focus on minute differences in the abundances of some of the smallest building blocks of matter. As a whole, isotope geochemistry, is the study of the relative abundances of isotopes of various elements in rock, air, and water bodies in order to constrain the ages and origins of those bodies, as well as the processes of interaction between them. The lack of correlation between the scale of the objects studied (the isotopes of a given element) and the scale of the processes to be constrained (*e.g.*, the formation of the Solar System) is probably the most counter-intuitive feature of this field. Yet, since the foundations of isotope chemistry were first laid out in 1947 by Harold Urey [442] and Bigeleisen & Mayer [42], the premise of the field has stood up to the test of the scientific method and many isotope systematics have been developed, thereby providing a plethora of tools to the isotope chemist wishing to study the Earth and the Universe. Each of these systematics brings specific information about the sample under scrutiny, such as, for instance: absolute ages (*e.g.*, Pb-Pb, U-Pb, U-Th, ^{14}C dating), relative ages (*e.g.*, ^{26}Al-^{26}Mg, ^{53}Mn-^{53}Cr, ^{182}Hf-^{182}W, ^{60}Fe-^{60}Ni), closure times of various

minerals from which the cooling history can be inferred (*e.g.*, U-Th-Pb geochronology), redox conditions prevailing during the formation of the sample (*e.g.*, oxidation state of Ti and Fe, depletion in Mo, W or Ce abundances in meteoritic inclusions), genetic relationship (*e.g.*, O isotopes, nucleosynthetic anomalies), details on planetary accretion and differentiation (*e.g.*, ^{182}Hf-^{182}W, correlated nucleosynthetic anomalies in Mo-Ru, highly siderophile element patterns), or even past climate, diets or body temperatures (*e.g.*, H, O, C, N isotopes), to name only a few.

Clearly, no one isotopic system can provide all the answers sought after, and it is only by combining the unique properties of different systematics that a robust picture of the processes that shaped the sample can be painted. With the advancement of analytical capabilities, new systematics can be explored and, therefore, new tools of isotope chemistry can be forged.

Uranium (Z=92) is a lithophile, refractory element of the actinide group in the periodic classification of elements. It is one of three so-called *primordial actinides* (*i.e.*, which have not been produced by natural processes since the formation of the Solar System, Th, U, Pu) and the second heaviest primordial nuclide after ^{244}Pu, which is now quasi-extinct. Uranium can exist in various valence states (+2, +3, +4, +5, and +6), but is mostly present in natural environments in either the soluble U^{VI} (oxidized) form or the insoluble U^{IV} (reduced) form. This element has only three naturally occurring isotopes: ^{238}U ($t_{1/2} = 4.468 \times 10^9$ yr) and ^{235}U ($t_{1/2} = 703.8 \times 10^6$ yr) which are both long-lived radioactive isotopes produced by the *rapid* neutron capture process (r-process); and ^{234}U ($t_{1/2} = 245,620 \pm 260$ yr, [107]), which is part of the decay series of ^{238}U. Because both long-lived isotopes decay with very different half-lives, the ^{238}U/^{235}U ratio dramatically changed over time (Fig. 1.1), evolving from a value of about 3.113 at the time of formation of the Solar System (4.567 Gyr ago) to its present value of about 137.794 [177] (only ~ 1 % of the initial ^{235}U and ~ 49 % of the initial ^{238}U remains today). This temporal variability is, however, not accompanied by a spatial variability, and the ^{238}U/^{235}U ratio was long considered constant, at any given time, throughout all Solar System material [100, 103]. Because of the importance of the exact

value of this ratio for Pb-Pb dating, the scientific community decided on a value to use for all dating purposes, the so-called *consensus value* of 137.88 [409].

The introduction of Multi-Collector Inductively Coupled Plasma Mass Spectrometers (or MC-ICP-MS) at the turn of the century improved the analytical precision achievable in the measurement of the $^{238}U/^{235}U$ ratio by two orders of magnitude, reducing the uncertainties from $\pm$ 5 ‰ to $\pm$ 0.05 ‰. With such powerful instrumentation, it only took a couple of years before sub-permil (Fig. 1.2) variations in the $^{238}U/^{235}U$ ratio of natural samples were identified [412, 460]. This discovery immediately changed the *status quo* and the "stable" U isotope systematics became the subject of a sustained research effort aimed at understanding the causes and implications of the natural variability of the $^{238}U/^{235}U$ ratio.

This dissertation is part of the exploratory effort that focuses on the ratio of "stable" U isotopes, effectively transforming a constant – consensus – value, into a crucial variable of Pb-Pb dating and a promising paleoredox tracer. The rest of Chapter 1 will briefly introduce notations, some basics of isotopic fractionation and isotopic anomalies, along with some generalities about U isotope systematics and the potential implications that stem from the natural variability of the $^{238}U/^{235}U$ ratio. Chapter 2 will describe the analytical developments undertaken to establish a robust high-precision U isotope analysis protocol. This method will be applied in Chapter 3 on an array of crustal rocks, carbonates, sediments and seawater samples. The results will first be used to show that the "stable" U isotopes are indeed tracers of the global redox conditions in the modern ocean, thereby validating the use of the U proxy to reconstruct the redox state of the ancient ocean. The results obtained on ancient sediments (both black shales and carbonates) will be used to constrain the redox state of the past ocean in the second half of Chapter 3. In Chapter 4, the methodology will be applied first to some targeted angrite meteorites in order to revise their Pb-Pb ages. The second part of Chapter 4 will then focus on the measurements performed on a series of specific Calcium, Aluminum-rich inclusions (CAIs), which are thought to be the first solids to condense in the Solar System, and show how the discovery of a 59 ‰ excess of ^{235}U in

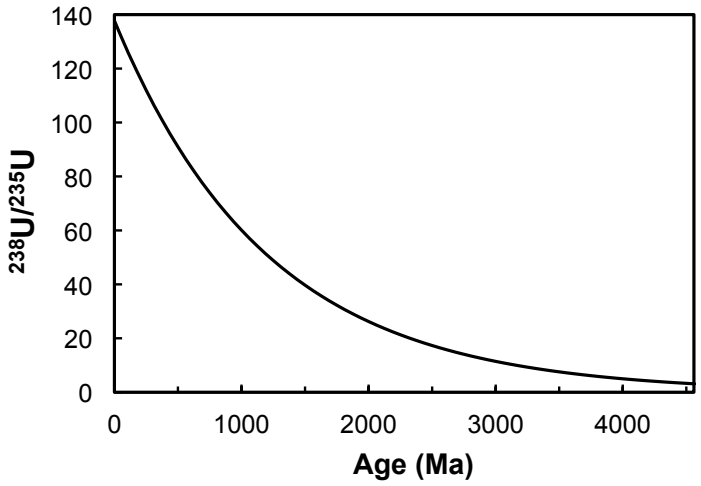

Figure 1.1: Evolution of the $^{238}U/^{235}U$ ratio over the lifetime of the Solar System.

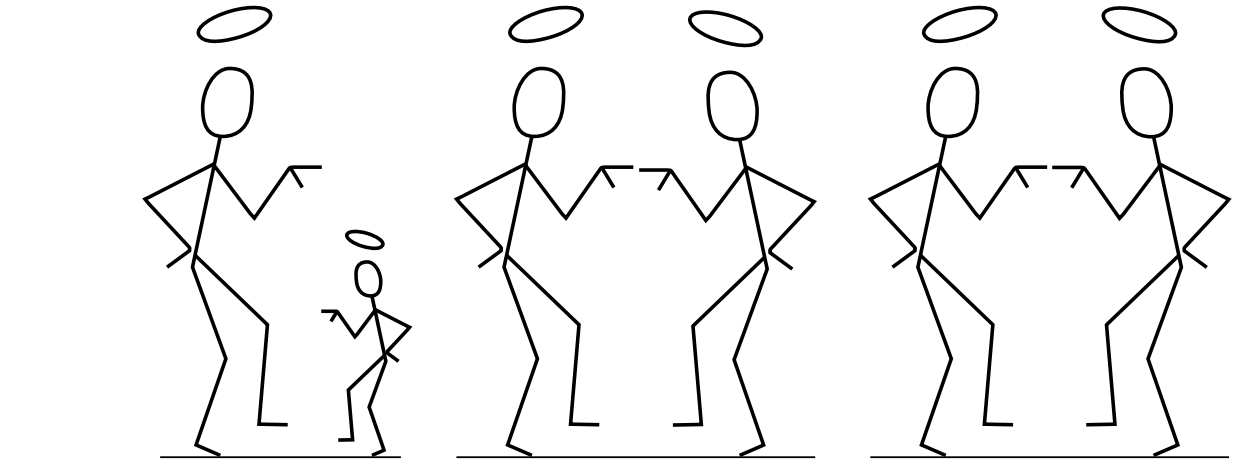

Figure 1.2: To illustrate how minute the isotopic differences quantified in isotope geochemistry are, three pairs of characters are drawn. In each pair, the character on the right is smaller than the one of the left by a given percentage (50 %, 1 % and 0.1 % = 1 ‰, left to right). With modern instrumentation, variations in the $^{238}U/^{235}U$ ratio as small as 0.1 ‰ can be unambiguously identified. That is equivalent to telling apart a person 2.0000 m tall from another one 1.9998 m tall, solely based on their height. This is a 200 μm difference: about three human hairs side to side.

one inclusion brings definitive evidence for live ^{247}Cm in the Early Solar System (ESS). The implications for models of Solar System (SS) formation and Galactic Chemical Evolution (GCE) are discussed. Finally, Chapter 5 will summarize the main results of this dissertation and outline some future directions of research where U isotopes could prove useful.

1.1 Notations

There are several ways to express the difference of isotopic composition between two phases. A common practice consists of considering the ratio of isotope ratios between two phases; this value is called the *fractionation factor*, and noted α. Taking the example of the ^{238}U/^{235}U ratios in two phases A and B, the fractionation factor is:

$$\alpha_{\text{A-B}} = \frac{\left(^{238}\text{U}/^{235}\text{U}\right)_{\text{A}}}{\left(^{238}\text{U}/^{235}\text{U}\right)_{\text{B}}} \tag{1.1}$$

Since the scale of the variations observed in the ^{238}U/^{235}U ratios of natural samples is small (Fig. 1.2), α is often very close to unity. It is therefore easier to consider the residue of $\alpha - 1$, which is where the delta notation (permil unit, ‰) becomes useful:

$$\delta^{238}\text{U} = \left[\frac{\left(^{238}\text{U}/^{235}\text{U}\right)_{\text{Sample}}}{\left(^{238}\text{U}/^{235}\text{U}\right)_{\text{Standard}}} - 1\right] \times 1000 \tag{1.2}$$

The delta notation allows for easy comparison of two numbers which differ only on the fourth or fifth significant figure. For instance, if a sample and the standard to which it is compared are characterized by a ^{238}U/^{235}U ratio of 137.894 and 137.88, respectively, then the fractionation factor is $\alpha = 1.0001$, while the delta value of the sample is $\delta^{238}\text{U} = +0.1$ ‰. In such a case, the sample is said to be 0.1 permil heavier than the standard. The difference of delta values between two samples is often reported as $\Delta_{\text{A-B}} = \delta_{\text{A}} - \delta_{\text{B}}$.

The relationship between $\alpha_{\text{A-B}}$ and $\Delta_{\text{A-B}}$ can be established by introducing δ_{A} and δ_{B}

in Eq. (1.1):

$$\alpha_{\text{A-B}} = \frac{(\delta_{\text{A}}/1000 + 1)}{(\delta_{\text{B}}/1000 + 1)} = \frac{\delta_{\text{A}} + 1000}{\delta_{\text{B}} + 1000} \tag{1.3}$$

Now subtracting one on each side of Eq. (1.3) gives:

$$\alpha_{\text{A-B}} - 1 = \frac{\delta_{\text{A}} - \delta_{\text{B}}}{\delta_{\text{B}} + 1000} \approx \frac{\delta_{\text{A}} - \delta_{\text{B}}}{1000} \tag{1.4}$$

Replacing the numerator on the RHS of Eq. (1.4) by $\Delta_{\text{A-B}}$ leads to the commonly used approximation:

$$\Delta_{\text{A-B}} \approx (\alpha_{\text{A-B}} - 1) \times 10^3 \tag{1.5}$$

For small isotopic fractionations, $\alpha_{\text{A-B}}$ is close to unity, and therefore $\ln \alpha_{\text{A-B}} \approx \alpha_{\text{A-B}} - 1$, which means that Eq. (1.5) is equivalent to

$$\Delta_{\text{A-B}} \approx 10^3 \ln \alpha_{\text{A-B}} \tag{1.6}$$

In this work, all results are reported using the delta notation (Eq. 1.2) relative to the U metal standard CRM-112a (also named SRM-960 or NBL-112a; CRM-145 for the solution form). All literature data used herein have been renormalized to the CRM-112a standard.

Beside its simplicity, another advantage of the delta notation is that the isotopic composition of a sample, once expressed as a δ^{238}U value, is independent of the age of the sample. This is true whether one, or both, of the isotopes of the ratio of interest are radioactive (as long as they are still alive). In other words, even though the absolute $^{238}\text{U}/^{235}\text{U}$ ratio of a sample changes with time (Fig. 1.1), if this sample is characterized today by a δ^{238}U value of x ‰ relative to a standard, it will be characterized, at any time, by the same value of x ‰ relative to the same standard. Though this might seem counter-intuitive, it is particularly handy when comparing materials (*e.g.*, minerals, meteoritic inclusions) of different ages.

A slightly different delta notation is used to express the $^{234}U/^{238}U$ ratios:

$$\delta[^{234}U/^{238}U] = \left[\frac{\left(^{234}U/^{238}U\right)_{\text{Sample}}}{\left(^{234}U/^{238}U\right)_{\text{Sec.}}} - 1\right] \times 1000 \tag{1.7}$$

where $\left(^{234}U/^{238}U\right)_{\text{Sec.}}$ is the atomic ratio at secular equilibrium and is equal to the ratio of the decay constants of ^{238}U and ^{234}U, $\lambda_{238}/\lambda_{234} = \left(1.5513 \times 10^{-10}\right) / \left(2.8220 \times 10^{-6}\right) = 5.497 \times 10^{-5}$ [107]. The rationale for this notation comes from the fact that ^{234}U is part of the decay chain of ^{238}U, and, for a system which has been not exchanging with its surroundings for a long enough time, the $^{234}U/^{238}U$ ratio reaches a steady-state value, known as the *secular equilibrium* value and equal to $\lambda_{238}/\lambda_{234}$. Using Eq. (1.7), a sample at secular equilibrium will be characterized by a $\delta[^{234}U/^{238}U]$ value of 0. Any disturbance (*i.e.*, loss/gain of either ^{234}U or ^{238}U), will drive the $^{234}U/^{238}U$ ratio away from the secular equilibrium value and the $\delta[^{234}U/^{238}U]$ value of the system will not be equal to 0 anymore, making the $^{234}U/^{238}U$ ratio a valuable tracer of closed-system behavior. After re-isolation, the system will return to within 1 % of secular equilibrium on a timescale of $\sim$ six half-lives, or 1.5 Myr [54].

1.2 Isotopic fractionation and isotopic anomalies

Natural isotopic variations can be the expression of either (1) processes that fractionate isotopes from one another – in which case one speaks of *isotopic fractionation* – or (2) the existence of an excess/deficit abundance in one or more isotopes – in which case one speaks of *isotopic anomalies*. The section below briefly presents the different types of isotope fractionations and isotopic anomalies, with a special attention being brought to the processes relevant to U "stable" isotope systematics.

1.2.1 Mass-dependent equilibrium fractionation

It was long thought that the electronic structure of an atom was the only characteristic dictating its chemical properties. Two atoms with the same electronic structure, *i.e.*, two

atoms of the same element, were thought to be identical twins, and predicted to behave in identical ways. The discovery of *isotopes* – variants of an element with the same number of protons, and therefore electrons, but different number of neutrons – did not initially change this view. The chemical and physical properties of two isotopes of an element were expected to remain identical, except for those properties directly related to mass (such as density, or diffusion rates, for instance). In 1947, however, two seminal studies [442, 42] showed that isotopes and isotopic compounds in fact differ in their thermodynamic properties, because the small, yet non-negligible, mass difference between two isotopes actually affects their vibrational, translational and rotational properties when bound to another atom. Therefore, two identical molecules which differ only in their isotopic composition (or *isotopologues*), will be characterized by different chemical bond strengths, and different accessible energy levels. The isotopologue containing the heavier isotope will have a lower zero point energy, and therefore will be characterized by stronger bonds.

From a quantitative point of view [1], consider a simple isotope exchange reaction between a molecule and an ideal atomic gas, such as:

$$a\mathrm{AX} + b\mathrm{A}' = a\mathrm{A}'\mathrm{X} + b\mathrm{A} \tag{1.8}$$

where a and b are stoichiometric coefficients, A and A$'$ are, respectively, the light and heavy isotopes of element A, and X represents either a monoatomic or a polyatomic group. Any more complex exchange reaction (for instance between two diatomic molecules) can be decomposed into a series of simple exchange reactions between a molecule and an isolated atomic species as written in Eq. (1.8). For such a reaction, the equilibrium constant can be written as:

$$\mathrm{K} = \frac{[\mathrm{A}'\mathrm{X}]^a \times [\mathrm{A}]^b}{[\mathrm{AX}]^a \times [\mathrm{A}']^b} \tag{1.9}$$

where the square bracket denotes activities. From statistical mechanics, the same equilibrium

1. For more details, see [442, 42, 284, 124, 383, 392, 463].

constant can also be written as:

$$\mathrm{K} = \frac{\prod (\mathrm{Q}_i)^{ni}\ \text{products}}{\prod (\mathrm{Q}_i)^{ni}\ \text{reactants}} = \frac{\left(\mathrm{Q}_{\mathrm{A'X}}\right)^a (\mathrm{Q}_{\mathrm{A}})^b}{(\mathrm{Q}_{\mathrm{AX}})^a \left(\mathrm{Q}_{\mathrm{A'}}\right)^b} = \left(\frac{\mathrm{Q}_{\mathrm{A'X}}}{\mathrm{Q}_{\mathrm{AX}}}\right)^a \left(\frac{\mathrm{Q}_{\mathrm{A}}}{\mathrm{Q}_{\mathrm{A'}}}\right)^b \tag{1.10}$$

where Q is called the *partition function*, and represents the sum of the energy distribution over all quantum states accessible to the system considered (here, a given isotopologue). The interest of the partition function is that it can be calculated from quantum mechanics. Since there are three main modes of motion available to gaseous molecules, the total partition function can be written as the product of the partition functions of each mode:

$$\mathrm{Q}_{\mathrm{total}} = \mathrm{Q}_{\mathrm{vib}}\mathrm{Q}_{\mathrm{trans}}\mathrm{Q}_{\mathrm{rot}} \tag{1.11}$$

where "vib," "trans" and "rot" stand for "vibrational," "translational" and "rotational," respectively. The vibrational motion is, by far, the most important contributor to isotopic fractionation (*e.g.*, [383]). In the approximation of a diatomic harmonic oscillator, the vibrational energy of the molecule at a given energy level (relative to the bottom of the potential-energy well) is given by:

$$E_{vib} = \left(n + \frac{1}{2}\right) h\nu, \tag{1.12}$$

where h is Planck's constant, n is the energy level (and is an integer: 0, 1, 2, ...) and ν is the frequency of vibration of the diatomic oscillator. This last parameter is linked to the mass of the isotopes constituting the molecule by:

$$\nu = \frac{1}{2\pi}\sqrt{\frac{k}{\mu}} \tag{1.13}$$

where k is the spring constant of the harmonic oscillator and characterizes the stiffness of

the chemical bond, and μ is the reduced mass of the diatomic molecule, equal to:

$$\mu = \frac{m_1\ m_2}{m_1 + m_2}, \tag{1.14}$$

with m_i the mass of atom i. Assuming that the population of the various energy levels follows a Boltzmann distribution (*i.e.*, the probability for a molecule to populate a given energy level decreases exponentially as the energy of that level increases), the vibrational partition function for a diatomic molecule is defined as:

$$\mathrm{Q_{vib}} = \sum_i e^{-E_{vib,i}/\mathrm{k}T} \tag{1.15}$$

where k is Bolztmann's constant and T is the temperature. Replacing the vibrational energy $E_{vib,i}$ by its expression (Eq. 1.12) yields:

$$\mathrm{Q_{vib}} = \sum_{n=0}^{\infty} e^{-\left(n+\frac{1}{2}\right)h\nu/\mathrm{k}T} = e^{-h\nu/2\mathrm{k}T} \sum_{n=0}^{\infty} e^{-nh\nu/\mathrm{k}T} \tag{1.16}$$

The second term on the RHS of Eq. (1.16) is a geometric series of the form $\sum_{n=0}^{\infty} x^n = \frac{1}{1-x}$ (for $0 < x < 1$). Equation (1.16) can therefore be rewritten:

$$\mathrm{Q_{vib}} = \frac{e^{-h\nu/2\mathrm{k}T}}{1 - e^{-h\nu/2\mathrm{k}T}} \tag{1.17}$$

This last equation (Eq. 1.17) is valid for a diatomic molecule under the harmonic oscillator approximation, and assuming that the energy levels are populated according to a Boltzmann distribution. The term on the numerator arises from the zero point energy of the molecule, while the denominator depends on the spacing of the vibrational energy levels. The mass dependency of the vibrational partition function is contained in the frequency of vibration ν (Eq. 1.13). The above result can be generalized to polyatomic molecules by recognizing that these molecules have multiple frequencies of vibration, which can be expressed as a set

of independent harmonic oscillators (using normal coordinates). The vibrational partition function is then written as [284]:

$$\mathrm{Q_{vib}} = \prod_{j=1}^{3N-6} \frac{e^{-h\nu_j/2\mathrm{k}T}}{1 - e^{-h\nu_j/2\mathrm{k}T}} \tag{1.18}$$

where N is the number of atoms of the molecule, $3N-6$ is the number of vibrational modes available ($3N-5$ in the case of a linear polyatomic molecules), and ν_j is the vibrational frequency associated with the jth normal mode of vibration.

Similarly, rotational and translational motions are also quantized and mass-dependent. For a diatomic molecule, the rotational motion can be approximated to the one of a dumbbell rotating about the center of mass (*i.e.*, rigid rotator approximation), and the translational motion can described by a molecule moving freely in a box. The partition functions of both modes of motion are then written:

$$\mathrm{Q_{rot}} = \frac{8\pi^2 I\mathrm{k}T}{\sigma h^2} \tag{1.19}$$

and

$$\mathrm{Q_{trans}} = \frac{(2\pi M\mathrm{k}T)^{3/2}}{h^3}V \tag{1.20}$$

where I is the moment of inertia of the molecule and is equal to the product of the reduced mass and the square of the interatomic distance ($I = \mu r^2$), σ is the symmetry factor of the molecule (equal to 1 for heteronuclear – non-symmetric – molecules such as ^{16}O-^{18}O, and 2 for homonuclear – symmetric – molecules such as ^{16}O-^{16}O), M is the mass of the molecule and V is the volume of the box within which the molecule moves. For a polyatomic molecule, the translational partition function is unchanged, but the rotational partition function takes the more complex expression [284]:

$$\mathrm{Q_{rot}} = \frac{8\pi^2\sqrt{ABC}\,(\mathrm{k}T)^{3/2}}{\sigma h^3} \tag{1.21}$$

where A, B and C are the three principal moments of inertia.

Using Eq. (1.17), (1.19) and (1.20) yields the following expression of the total partition

function for a diatomic molecule under the harmonic oscillator and rigid rotator assumptions:

$$\mathrm{Q_{tot}} = \frac{8\pi^2 I \mathrm{k}T}{\sigma h^2} \frac{(2\pi M \mathrm{k}T)^{3/2}}{h^3} V \frac{e^{-h\nu/2\mathrm{k}T}}{1 - e^{-h\nu/2\mathrm{k}T}} \tag{1.22}$$

Going back to the equilibrium constant of the isotope exchange reaction, Eq. (1.10), it is the ratio of partition functions of two isotopologues (*e.g.*, AX and A′X) that is needed. Many terms coming from the rotational and translational partition functions will cancel out when taking the ratio of partition functions as written in Eq. (1.22). Considering, the $\mathrm{Q_{A'X}}/\mathrm{Q_{AX}}$ ratio, one obtains:

$$\frac{\mathrm{Q_{A'X}}}{\mathrm{Q_{AX}}} = \frac{I_{\mathrm{A'X}}\ \sigma_{\mathrm{AX}}}{I_{\mathrm{AX}}\ \sigma_{\mathrm{A'X}}} \left(\frac{M_{\mathrm{A'X}}}{M_{\mathrm{AX}}}\right)^{3/2} \left(\frac{e^{-h\nu_{\mathrm{A'X}}/2\mathrm{k}T}}{1 - e^{-h\nu_{\mathrm{A'X}}/2\mathrm{k}T}}\right) \left(\frac{1 - e^{-h\nu_{\mathrm{AX}}/2\mathrm{k}T}}{e^{-h\nu_{\mathrm{AX}}/2\mathrm{k}T}}\right) \tag{1.23}$$

The last step is to apply the Teller-Redlich product rule, which relates the masses (M_i), frequencies of vibration (ν_i) and moments of inertia (I_i) of each isotopologues to the masses of the substituted isotopes (m_i) [442]:

$$\frac{\nu_1}{\nu_2} = \left(\frac{m_2}{m_1}\right)^{3/2} \frac{I_1}{I_2} \left(\frac{M_1}{M_2}\right)^{3/2} \tag{1.24}$$

Equation (1.23) therefore becomes:

$$\frac{\mathrm{Q_{A'X}}}{\mathrm{Q_{AX}}} = \frac{\nu_{\mathrm{A'X}}\ \sigma_{\mathrm{AX}}}{\nu_{\mathrm{AX}}\ \sigma_{\mathrm{A'X}}} \left(\frac{m_{\mathrm{A'}}}{m_{\mathrm{A}}}\right)^{3/2} \left(\frac{e^{-h\nu_{\mathrm{A'X}}/2\mathrm{k}T}}{1 - e^{-h\nu_{\mathrm{A'X}}/2\mathrm{k}T}}\right) \left(\frac{1 - e^{-h\nu_{\mathrm{AX}}/2\mathrm{k}T}}{e^{-h\nu_{\mathrm{AX}}/2\mathrm{k}T}}\right) \tag{1.25}$$

This ratio is often called the *reduced partition function*. Calculation of the ratio of partition functions for the isolated isotopes A and A′ is simple, as the total partition function of each species is equal to the translational partition function alone (no vibrational nor rotational component for isolated atoms), which gives:

$$\frac{\mathrm{Q_{A'}}}{\mathrm{Q_{A}}} = \left(\frac{m_{\mathrm{A'}}}{m_{\mathrm{A}}}\right)^{3/2} \tag{1.26}$$

By injecting the reduced partition functions $Q_{A'X}/Q_{AX}$ and $Q_{A'}/Q_{A}$, into Eq. (1.10), it is possible to calculate the equilibrium constant of the isotope exchange reaction (Eq. 1.8) at any given temperature as:

$$K = \left[\frac{\nu_{A'X}\ \sigma_{AX}}{\nu_{AX}\ \sigma_{A'X}}\left(\frac{e^{-h\nu_{A'X}/2kT}}{1-e^{-h\nu_{A'X}/2kT}}\right)\left(\frac{1-e^{-h\nu_{AX}/2kT}}{e^{-h\nu_{AX}/2kT}}\right)\right]^{a}\ \left(\frac{m_{A'}}{m_{A}}\right)^{\frac{3(a-b)}{2}} \tag{1.27}$$

Note that the isotope exchange reaction (Eq. 1.8) can always be written in a way so that $a = b$, and the last term on the RHS of Eq. (1.27) is equal to unity.

The degree of isotopic fractionation can, in turn, be quantified by calculating the fractionation factor, $\alpha_{AX\text{-}A}$, which is the ratio of isotope ratio in the two phases, AX and the ideal gas, and is related to the equilibrium constant as follows:

$$\alpha_{AX\text{-}A} = \frac{\left(\frac{A'}{A}\right)_{AX}}{\left(\frac{A'}{A}\right)_{A}} = \left(\frac{K}{K_{\infty}}\right)^{1/n} \tag{1.28}$$

where n is the maximum number of atoms exchanged in any one molecule under consideration (here $n = 1$) and K_{∞} is the equilibrium constant at infinite temperature. The $1/n$ exponent accounts for multiple substitution in molecules containing more than one atom of A. The equilibrium constant at infinite temperature only depends on the symmetry factors and is equal to [124, 463]:

$$K_{\infty} = \left(\frac{\sigma_{AX}}{\sigma_{A'X}}\right)^{a} \tag{1.29}$$

The fractionation factor, $\alpha_{AX\text{-}A}$, for an isotopic exchange reaction between diatomic molecules ($n = 1$) and an ideal atomic gas (Eq. 1.8) under the harmonic oscillator and rigid rotator assumptions is thus:

$$\alpha_{AX\text{-}A} = \left[\frac{\nu_{A'X}}{\nu_{AX}}\left(\frac{e^{-h\nu_{A'X}/2kT}}{1-e^{-h\nu_{A'X}/2kT}}\right)\left(\frac{1-e^{-h\nu_{AX}/2kT}}{e^{-h\nu_{AX}/2kT}}\right)\right]^{a} \tag{1.30}$$

From the above equation, one can see that the extent of isotopic fractionation is (1) mass-

dependent (through the vibrational frequency dependency), and (2) temperature dependent, but only through the vibrational mode of motion, as other temperature terms canceled out. The temperature dependency of mass-dependent isotopic fractionation is therefore a consequence of the vibrational properties of the isotopologues alone.

A more general equation can be derived, which is applicable to diatomic molecules as well as larger molecules [383]:

$$\alpha_{\text{AX-A}} = \left[\prod_{j=1}^{3N-6} \frac{\nu_{\text{A}'\text{X},j}}{\nu_{\text{AX},j}} \left(\frac{e^{-h\nu_{\text{A}'\text{X},j}/2\text{k}T}}{1 - e^{-h\nu_{\text{A}'\text{X},j}/2\text{k}T}} \right) \left(\frac{1 - e^{-h\nu_{\text{AX},j}/2\text{k}T}}{e^{-h\nu_{\text{AX},j}/2\text{k}T}} \right) \right]^{a/n} \tag{1.31}$$

where a is the stochiometric coefficient in Eq. (1.8), AX and A$'$X are two isotopologues (light and heavy, respectively) containing n atoms of element A and N total atoms, and $\nu_{X,j}$ is the vibrational frequency associated with the jth normal mode of vibration in compound X. In the case of a linear polyatomic molecule, the product is done over only $3N - 5$ degrees of freedom since a linear molecule has one less rotational mode compared to a non-linear molecule. (For more details on the derivation of Eq. (1.31) for polyatomic molecules, see [154, 284, 124, 383]).

Looking back at the isotope exchange reaction written in Eq. (1.8), only a few key parameters and input data are needed to predict the isotopic fractionation expected between the two compounds ($\alpha_{\text{AX-AY}} = \alpha_{\text{AX-A}}/\alpha_{\text{AY-A}}$), namely: the vibrational frequencies of the isotopologues, the masses of the isotopes of which they are made, and the temperature at which the equilibration is taking place.

Though the above considerations apply to all elements, mass-dependent isotopic fractionation will be especially pronounced only in elements (i) of low atomic mass, (ii) that have large relative mass difference between their isotopes, (iii) that exist in more than one oxidation state, and (iv) that tend to form highly covalent bonds. The last two points, not discussed in the above section, influence the bond strength, which determine the force constant of the bond and affects the vibrational properties of the isotopologues. For heavy el-

ements, such as uranium, only very minor effects are expected from mass-dependent isotopic fractionation (Fig. 1.3, panel b).

1.2.2 Mass-independent equilibrium fractionation

The theory of mass-dependent isotopic fractionation considers only the effect of the mass and the electronic structure (*i.e.*, number of electrons) of the nucleus. The shape and volume of the nucleus are not taken into account, as they are not expected to have a significant influence on the degree of isotopic fractionation.

From 1976 to 1978, three studies reported uranium isotope shift measurements [170, 171, 172]. They discovered that, for isotopes of uranium with odd mass number (^{233}U, ^{235}U), the isotope shift was non mass-dependent (Fig. 1.3, panel a), a phenomenon known as *odd-even staggering*. Already at that time, the authors interpreted this result as being a consequence of the nuclear field shift effect (NFS, also named field effect, volume effect, nuclear volume effect or even nuclear size and shape effect), which is *a displacement of the ground electronic energy of an atom or molecule due to the differences in nuclear sizes and shapes of the isotopes* [41]. Two decades later, a series of experiments investigating the isotope exchange reaction of uranium between different oxidation states (U^{IV}-U^{VI}) [168, 169, 167, 423, 148, 313] found a similar odd-even staggering effect in the form of enhancement of ^{233}U and ^{235}U above the mass-dependent fractionation line. These results prompted new developments in the theory of equilibrium fractionation [41] which are summarized below.

Considering an isotope exchange reaction such as, $AX + A'Y = A'X + AY$, where X and Y are polyatomic groups, and A and A' the light and heavy isotope of element A, respectively, the fractionation factor, $\alpha_{X\text{-}Y}$, can be written as:

$$\alpha_{X\text{-}Y} = \alpha_0 \times K_{anh} \times K_{BOELE} \times K_{ns} \times K_{NFS} \tag{1.32}$$

In Eq. (1.32), the term α_0 is the fractionation factor as determined under the harmonic

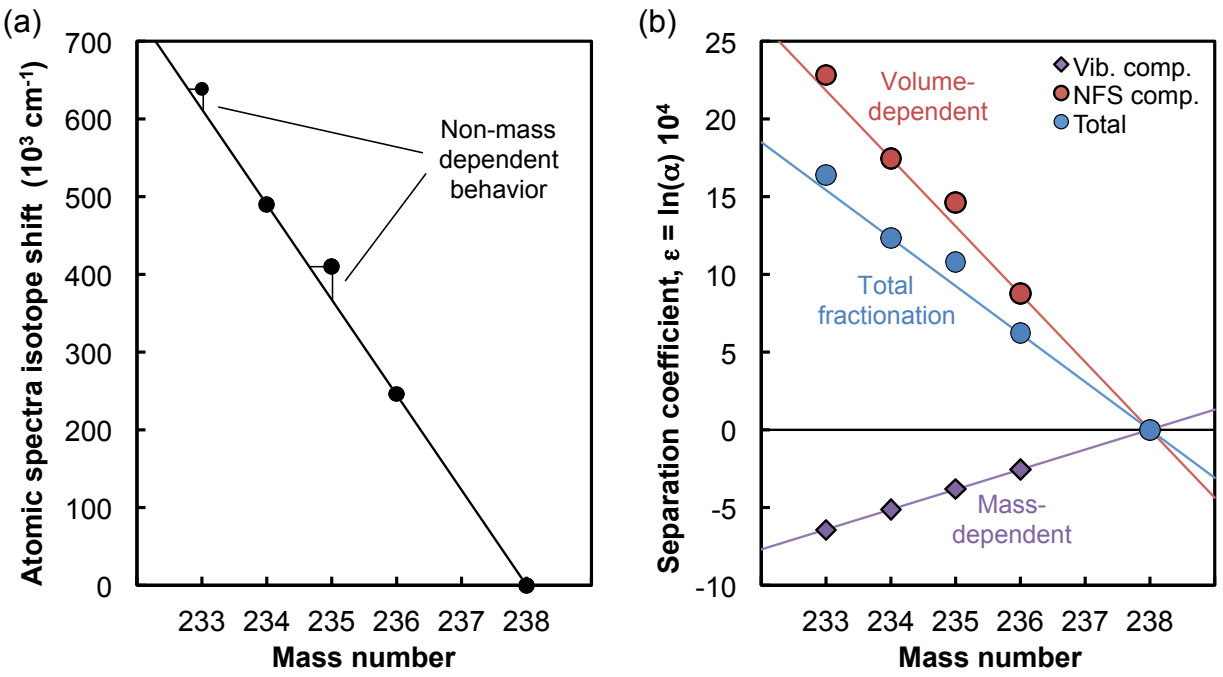

Figure 1.3: Uranium atomic spectra isotope shift (a) and theoretical separation coefficient for the U^{IV}-U^{VI} exchange reaction at 433 K (b). The isotope shift was the first indication that for heavy elements, the mass-dependent effect was small and that the nuclear volume effect was the main contributor to isotopic effects (data from [170, 171, 172, 313]). Using the theoretical framework for the NFS effect from [41], the relative contribution of the vibrational effects (*i.e.*mass-dependent) and the NFS effects (*i.e.*, volume-dependent) to the total separation coefficient are plotted.

oscillator and rigid rotator assumptions (see Section 1.2.1), while the other terms on the RHS of Eq. (1.32) account for previously neglected effects: (K_{anh}) is the anharmonic vibration correction term, K_{BOELE} is the Born-Oppenheimer approximation and isotope mass shift correction, K_{ns} is the nuclear spin effect term, and K_{NFS} is the nuclear field shift effect term. Bigeleisen [41] showed that, for heavy elements, and in particular for uranium, these correction terms were negligible with the exception of the NFS effect, which is significant (Fig. 1.3, panel b). In the simplified framework where only the vibrational effect and the NFS effect contribute to the isotopic fractionation, the fractionation factor of the exchange reaction can then be approximated by:

$$\alpha_{\text{X-Y}} = \left(\frac{hc}{\text{k}T}\right) |\Psi(0)|^2 \delta\langle r_i^2\rangle \times a + \left(\frac{1}{24}\right)\left(\frac{h}{2\pi \text{k}T}\right)^2 \left(\frac{1}{m_1} - \frac{1}{m_2}\right) \times b \qquad (1.33)$$

where $|\Psi(0)|^2$ is the electron density of the nucleus, $\delta\langle r_i^2\rangle$ is the isotopic change in mean-squared nuclear charge radius, m_1 and m_2 are the mass of the light and heavy isotope, respectively, c is the velocity of light, and a and b are scaling factors for the field shift effect and the mass-dependent effect, respectively, which can be calculated using the isotope shift values from [170, 171, 172, 313], the absolute separation coefficients ($\epsilon = \ln\alpha\ 10^4$) for ^{235}U [163], and the experimental ratio of the separation coefficient for ^{234}U and ^{235}U at 433 K [168, 313]. As can be seen in Fig 1.4, the addition of the NFS effect to the stable isotopic fractionation theory is sufficient to explain the mass-independent behavior observed in U redox experiments. Nowadays, the isotopic fractionation effects can be predicted using so-called *ab initio* calculations which are based on first-principles vibrational frequency and the electronic structure of the isotopes involved in the reaction (*e.g.*, [384, 1]).

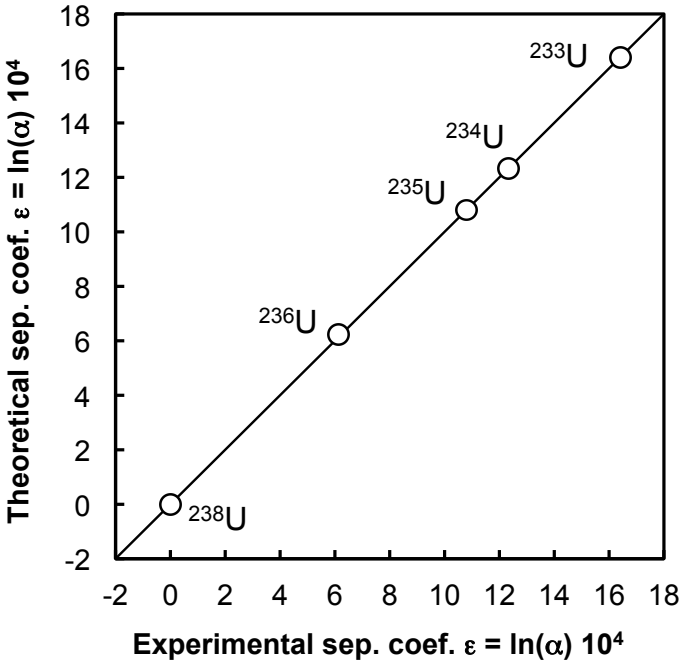

Figure 1.4: Comparison of theoretical and experimental separation coefficients ($\epsilon = \ln\alpha\ 10^4$) for the U^{IV}-U^{VI} exchange reaction at 433 K. The theoretical values are from [41] and the experimental values from [163, 168, 313]. Addition of the NFS effect to the mass-dependent effect can explain the "odd-even staggering" observed in experiments.

From Eq. (1.33), it can be seen that the direction and magnitude of the NFS effect

are directly related to the electron density of the nucleus ($|\Psi(0)|^2$) and the isotopic change in mean-squared nuclear charge radius ($\delta\langle r^2\rangle$) [41, 384]. The proportionality of the NFS to $\delta\langle r^2\rangle$ explains the "odd-even staggering" in the separation coefficients of U isotopes observed during exchange reaction experiments. Indeed, isotopes with an odd number of neutrons tend to have smaller root mean squared charge radii than expected from a trend line through even-numbered isotopes, thereby leading to a strong nonlinearity in the NFS effect as function of isotopic mass [384].

For a given isotopic system, the lowest energy is achieved when the larger (*i.e.*, heavier) isotope is incorporated in the chemical species with the smallest electron density at the nucleus (*i.e.*, with the smallest number of s electrons in the bonding or valence orbital). If the redox transition involves a change in the number of s electrons, the NFS effect will be large and usually in the same direction as the mass-dependent effect, as is the case for Hg and Tl where the heavy isotopes get enriched in the oxidized phase (Hg^0–$[Xe]4f^{14}5d^{10}6s^2$ *vs.* Hg^{2+}–$[Xe]4f^{14}5d^{10}6s^0$, and Tl^0–$[Xe]4f^{14}5d^{10}6s^26p^1$ *vs.* Tl^{3+}–$[Xe]4f^{14}5d^{10}6s^06p^0$). Interestingly, if the redox transition involves a change in the number of p, d or f electrons, the NFS effect will be smaller than in the case where s electrons are involved, and of direction opposite to the mass-dependent effect, as is the case for U (U^{4+}–$[Rn]5f^2$ *vs.* U^{6+}–$[Rn]5f^0$). Though elements other than uranium have transitions which involve the p, d or f electrons (*e.g.*, Te, Ce, Eu, Pt), uranium is unique in that the magnitude of the NFS effect largely overwhelms the mass-dependent effect, leading to a *global* isotopic fractionation of direction opposite to the mass-dependent fractionation, allowing for the discrimination between the two effects in natural settings (Fig. 1.3, panel b). It is this very characteristic that makes the "stable" U isotope ratio a promising paleoredox tracer.

Note that in the above discussion, it is not the reduction of U that leads to the isotopic fractionation, but the exchange of U isotopes between the oxidized and the reduced phase. The importance of the distinction will become apparent in the next section.

1.2.3 Kinetic fractionation

In contrast to equilibrium fractionation, kinetic fractionation is associated with processes that are rapid, incomplete and/or unidirectional such as evaporation/condensation, diffusion, dissociation reactions or biologically-mediated reactions. But like equilibrium fractionation, kinetic fractionation is still a consequence of the mass difference between the two isotopes considered. Either directly, as in the case of diffusion, where the lighter isotope diffuses faster than the heavier isotope, or indirectly, as in the case of chemical reactions, where the weaker bonds of the species with the light isotopes are more easily broken. In general, when reactions do not reach equilibrium, the lighter isotopes will be enriched in the reaction products (*e.g.*, the lighter isotope evaporates faster during evaporation, condenses faster during condensation, dissociates faster during dissociation reactions, etc...).

Consider first a chemical reaction. From a quantitative point of view, this reaction is characterized by a reaction rate constant, k, which is given by the Arrhenius equation:

$$k = Ae^{-Ea/\mathrm{k}T} \tag{1.34}$$

where k is the Boltzmann constant, T the temperature (in Kelvin), Ea the activation energy (or barrier energy) needed for the reaction to occur, and A is a factor, independent of isotopic composition, that quantifies the total number of atomic collisions per second (often called the *frequency factor*). The mass difference between two isotopes will show in the value of the activation energy term. Because species involving the heavier isotope have lower zero point energy, the value of Ea for the heavy isotopologue will be larger than for the light isotopologue, leading to $\alpha_{\mathrm{Reaction}} = k_{\mathrm{light}}/k_{\mathrm{heavy}} > 1$: the reaction will proceed faster (more easily) for the light isotopologue. This difference in reaction rate will be mainly significant for low mass elements, and drops rapidly as the mass increases.

Whether or not such kinetic effects can be resolved for U isotopes is still an open question. Most biologically-mediated U reduction experiments [52, 35, 418, 413] found similar

fractionation factors equivalent to $\Delta_{U^{Red}\text{-}U^{Ox}} \sim +0.6 - 0.8‰$, which was suggested to be the result of a kinetic fractionation driven by an NFS effect, or a "reverse" vibrational zero-point energy term [52, 35, 413]. This interpretation is hard to reconcile with other observations that show (i) the lack of isotopic fractionation during U abiotic reduction by zerovalent iron (Fe^0) and zerovalent zinc (Zn^0) [351, 412], (ii) the lack of isotopic fractionation for abiotic sulfide- or organic-mediated U reduction [418], (iii) the fact that kinetic fractionation should favor the light isotope in the reduced species (*i.e.*, $\Delta_{U^{Red}\text{-}U^{Ox}}$ should be negative), and (iv) the observation that the abiotic reduction of U by divalent iron (Fe^{II}) leads to enrichment of ^{235}U in the reduction product, as expected for a kinetic effect [418]. A careful study by Stylo et al. (2015) [418] proposed that in biologically-mediated U reduction, any kinetic fractionation is overwritten by the equilibrium NFS effect during rapid U^{VI}-U^{IV} exchange in the vicinity of the enzyme. They further suggest that the lack of isotopic fractionation during abiotic Fe^0, Zn^0, sulfide- or organic-mediated U reduction is the consequence of direct two-electron transfer to U^{VI}, resulting in the sequestration of U^{IV} without significant fractionation. In such a framework, kinetic fractionations of U are observed only during the reduction of U by divalent iron (Fe^{II}). Confirmation of such hypotheses will require further investigation.

Consider now an evaporation/condensation reaction whereby a liquid or solid is evaporating into/condensing from a gas. The net condensation or evaporation flux J_i (in moles per unit area per unit time) of a chemical species i, is given by the Hertz-Knudsen equation:

$$J_i = \frac{n_i \gamma_i \left(P_{i,sat} - P_i\right)}{\sqrt{2\pi m_i RT}} \tag{1.35}$$

where R is the gas constant, T the temperature, n_i is the number of atoms of i in the gas species molecule, m_i the molecular weight of the gas species containing i, γ_i is the evaporation/condensation coefficient, and P_i and $P_{i,sat}$ are the partial and saturation vapor pressure of i at the evaporating surface, respectively (a net flux from the condensed phase

to the gas is counted positively). The coefficient γ_i (also called *sticking coefficient*) accounts for the fact that only a fraction of the atoms impacting the liquid/solid surface are actually incorporated in the liquid/solid phase. In the case of two isotopes i and j, the ratio of fluxes is [363, 365]:

$$\frac{J_i}{J_j} = \frac{\gamma_i}{\gamma_j}\sqrt{\frac{m_j}{m_i}}\frac{P_{i,sat} - P_i}{P_{j,sat} - P_j} \tag{1.36}$$

The kinetic fractionation factor, α_{Kin}, quantifies the difference in evaporation/condensation speed of the two isotopes, and is therefore simply defined as:

$$\alpha_{\text{Kin}} = \frac{\gamma_j}{\gamma_i}\sqrt{\frac{m_i}{m_j}} \tag{1.37}$$

In an idealized case, the sticking coefficients are the same for both species and the two species evaporating/condensing are mono atomic molecules in a low pressure gas (*i.e.*, infrequent collisions between molecules), and m_i and m_j are the molar masses of the isotopes themselves. In such a case, the maximum isotopic fractionation expected for the "stable" isotopes of U would be:

$$\Delta_{\text{Kin}} \approx 10^3\left(\alpha_{\text{Kin}} - 1\right) = 10^3\left(\sqrt{\frac{238}{235}} - 1\right) \approx 6.3\ ‰ \tag{1.38}$$

If the above assumptions can be applied to either (i) the condensation of solid matter in the early solar nebula, or (ii) the incomplete evaporation of a portion of the solar nebula, then U isotopic fractionation of up to 6.3 ‰ could be recorded in early condensates.

The above case is, obviously, a worst case scenario, as two factors will likely limit the amount of kinetic fractionation: (i) the pressure in the early solar nebula is thought to be high enough (10^{-5}-10^{-3} atm) that frequent collision of the condensing species with H_2 molecules must have happened, and (ii) based on the thermodynamic properties of U species and on condensation calculations (*e.g.*, [184, 189, 140]), U in the early solar nebula was likely present as UO_2(g) (see Fig. 1.5). In such a case, the masses to consider are the reduced

masses of the UO_2(g) and H_2 species, which gives:

$$\Delta_{\text{Kin}} \approx 10^3 \left(\sqrt{\frac{1.985294}{1.985130}} - 1 \right) \approx 0.04 \text{ ‰} \tag{1.39}$$

resulting in essentially no isotopic fractionation.

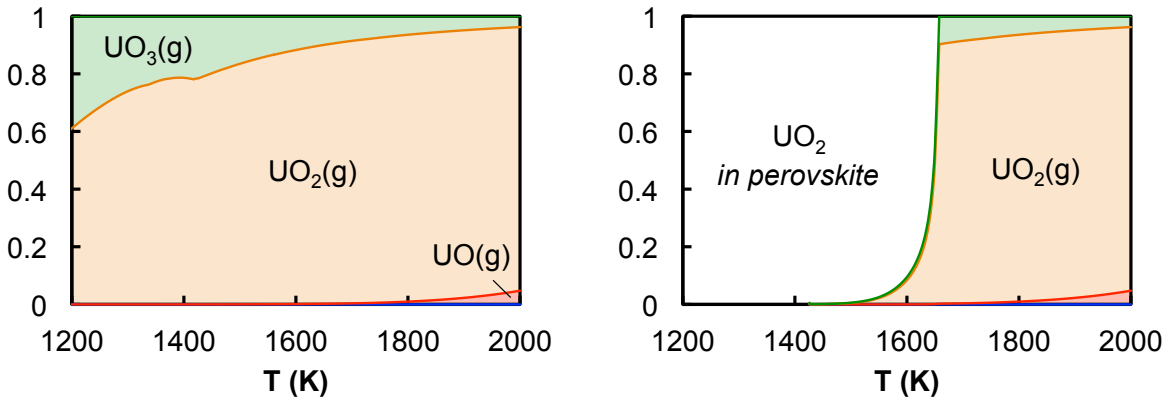

Figure 1.5: (Left) Fraction of U species in the solar nebula, and (right) same with U condensing into perovskite: the main host phase of actinides in fine-grained CAIs ([306], see Chapter 4 for details on CAIs). The condensation calculations were provided by Lawrence Grossman (*e.g.*, [140, 184]) for a gas of solar composition [17], with $P(H_2) = 10^{-3}$ atm. The thermodynamic data (*i.e.*, enthalpy and entropy of formation) are from [2].

The two scenarios outlined above (evaporation/condensation of U isotopes *vs.* evaporation/condensation of UO_2 in an H_2 rich gas) are at both extremes of the range of possibilities. The actual extent of kinetic fractionation during evaporation/condensation in the early solar nebula is probably somewhere in between. Such intermediate isotopic fractionations were actually observed for calcium isotopes in some CAIs [218]. In these early Solar System inclusions, mass-dependent fractionation between ^{40}Ca and ^{44}Ca covered a range of $\sim$ 6 ‰, which is lower than the maximum kinetic fractionation expected during evaporation/condensation of atomic Ca in a low pressure gas is $10^3 \left(\sqrt{\frac{44}{40}} - 1 \right) \approx 49$ ‰, but greater than the maxium effect expected from evaporation/condensation of CaO(g) in an H_2 rich gas is $10^3 \left(\sqrt{\frac{1.93548}{1.93103}} - 1 \right) \approx 1.15$ ‰. In this work, and in order to be conservative, it will be considered that evaporation/condensation processes in the early solar nebula can lead to a maximum isotopic fractionation of 6.3 ‰ between ^{235}U and ^{238}U (*i.e.*, evapora-

tion/condensation of atomic U in a low pressure gas).

The kinetic fractionation factor given in Eq. (1.37) quantifies the degree of fractionation between a reservoir and the flux of atoms from this reservoir to another. To describe the isotopic evolution of the two reservoirs themselves, a different formalism is needed. Two situations can be envisioned. In the first case, the two reservoirs stay in close proximity and can exchange with one another, potentially erasing any kinetic fractionation. In the second case, the two reservoirs might be segregated as the reaction proceeds. This second situation is commonly described by the so-called *Rayleigh distillation* (or fractionation) whereby the product of the reaction is removed from the system as the reaction proceeds. Because this sequestration of the reaction product suppresses the possibility for re-equilibration, processes described by a Rayleigh distillation can lead to very large isotopic effects. Consider an element in a gas, with isotopic composition $R_{\text{gas}} = N_j/N_i$, where i and j are two isotopes (see Fig. 1.6). During condensation (without re-evaporation), the change of abundance of each isotope is:

$$\mathrm{d}N_i = -J_i A \mathrm{d}t \tag{1.40}$$

$$\mathrm{d}N_j = -J_j A \mathrm{d}t \tag{1.41}$$

where A is the surface area through which the flux is considered. Combining Eq. (1.40) and Eq. (1.41), gives:

$$\mathrm{d}N_j = \frac{J_j}{J_i}\mathrm{d}N_i \tag{1.42}$$

The kinetic fractionation during the condensation process, α_{Cond}, relates the composition of the gas to the composition of the flux from the gas to the solid, $\alpha_{\text{Cond}} = (N_i/N_j)/(J_i/J_j)$. Eq. (1.42) can therefore be rewritten:

$$\frac{\mathrm{d}N_j}{N_j} = \alpha_{\text{Cond}}\frac{\mathrm{d}N_i}{N_i} \tag{1.43}$$

After integration Eq. (1.43) becomes:

$$\ln\left(\frac{N_j}{N_{j,0}}\right) = \alpha_{\rm Cond}\,\ln\left(\frac{N_i}{N_{i,0}}\right) \tag{1.44}$$

where $N_{i,0}$ and $N_{j,0}$ is the amount of isotope i and j initially present in the gas. Using the fact that $a\,\ln x = \ln(x^a)$, Eq. (1.44) can be rewritten as,

$$\left(\frac{N_j}{N_{j,0}}\right) = \left(\frac{N_i}{N_{i,0}}\right)^{\alpha_{\rm Cond}-1}\left(\frac{N_i}{N_{i,0}}\right) \tag{1.45}$$

which it is convenient to rearrange into the following equation,

$$\frac{\left(N_j/N_i\right)}{\left(N_{j,0}/N_{i,0}\right)} = \left(\frac{N_i}{N_{i,0}}\right)^{\alpha_{\rm Cond}-1} \tag{1.46}$$

The numerator and denominator on the LHS of Eq. (1.46) are simply the isotopic ratios in the remaining gas and initial gas, respectively. Denoting f, the fraction of isotope i remaining in the gas, Eq. (1.46) becomes:

$$\frac{R_{\rm gas}}{R_{\rm gas,0}} = f^{\alpha_{\rm Cond}-1} \tag{1.47}$$

Note that, if the kinetic fractionation during the condensation process is small (*i.e.*, $\alpha_{\rm Cond}$ close to unity), the ratio $N_i/N_{i,0}$ is approximately equal to the ratio N/N_0, the fraction of the element remaining in the gas. Eq. (1.47) describes the evolution of the isotopic composition of the gas, $R_{\rm gas}$, as the condensation proceeds. At each instant, the composition of the instantaneous solid condensing, $R_{\rm inst\ solid}$, can be calculated by recognizing that $\alpha_{\rm Cond} = (N_i/N_j)/(J_i/J_j) = R_{\rm inst\ solid}/R_{\rm gas}$, which gives:

$$\frac{R_{\rm inst\ solid}}{R_{\rm gas,0}} = \alpha_{\rm Cond} \times f^{\alpha_{\rm Cond}-1} \tag{1.48}$$

The isotopic composition of the cumulative solid, $R_{\rm cumul\ solid}$, is calculated by simple mass

balance, as:

$$\frac{R_{\text{cumul solid}}}{R_{\text{gas},0}} = \frac{(1 - f^{\alpha_{\text{Cond}}})}{1 - f} \tag{1.49}$$

Figure (1.6) shows the time integrated evolution of the isotopic composition of the gas, and the instantaneous and cumulative solids, assuming that uranium isotopes are condensing from the solar nebula as mono atomic gaseous species (*i.e.*, $\alpha_{\text{Cond}} = 1.0063$). Under such conditions, extreme enrichment in ^{238}U in instantaneous solids is possible, while enrichment in ^{235}U in both the instantaneous and cumulative solids is limited to a maximum of ~ 6 ‰. This result will be important later in this work (see Section 1.4).

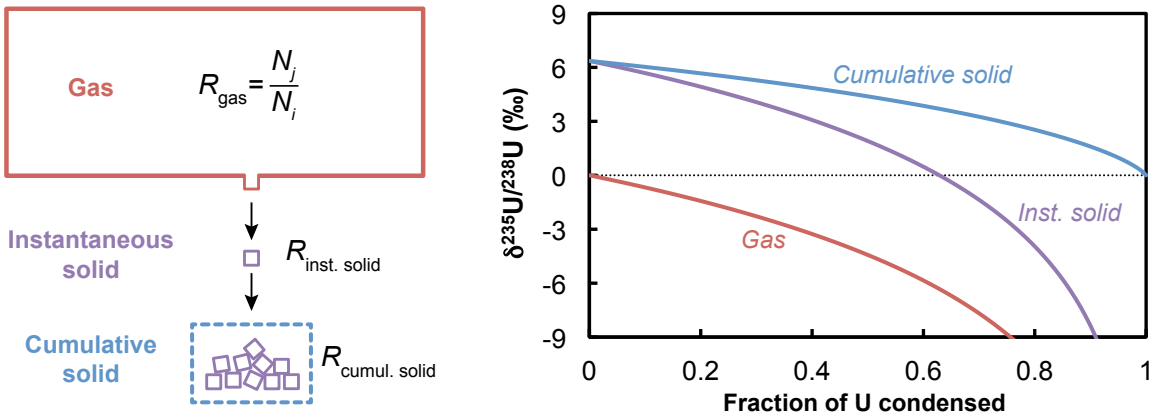

Figure 1.6: (Left) Schematic representation of a Rayleigh distillation, and (right) evolution of the isotopic composition of the gas, instantaneous solid and cumulative solid, as a function of the fraction of U condensed, $\alpha_{\text{Cond}} = \sqrt{238/235} = 1.0063$. Figure submitted in [432].

1.2.4 Isotopic anomalies

When the excess/deficit in the abundance of an isotope can be explained by neither equilibrium nor kinetic processes, the nuclide is said to display an anomaly. These anomalies can have three main origins:

- If the anomaly is an excess, it might be because the nuclide considered is the end product of a decay scheme (*e.g.*, ^{26}Mg, ^{60}Ni, ^{53}Cr, ^{182}W). In this case, the father-daughter nuclide system forms a chronometer, and the anomaly holds information

about the closure time of the sample (this date should only be called the *age* of the sample if it can be shown that the closure date and the formation date of the sample are the same [9]).

- The nuclide considered might be affected by cosmogenic effects, resulting from neutron capture of galactic or solar cosmic rays as the meteorite traveled from its parent body to the Earth. Both isotopic excesses and deficits can be produced, depending on whether the isotope considered is the target nuclide (characterized by a large thermal neutron cross section, σ_γ; its burning will produce a deficit anomaly) or the product of neutron capture (the nuclide will display an excess anomaly). Cosmogenic anomalies are useful, as the magnitude of the anomaly will be a function of the depth of burial and duration of exposure to the cosmic rays, therefore bringing information on the time since disruption of the meteorite parent body.

- Finally, the anomaly can be of nucleosynthetic origin. Three main nucleosynthetic processes are responsible for the production of elements with atomic masses heavier than ~ 70 amu: the *s*-process (*slow* neutron capture), the *r*-process (*rapid* neutron capture) and the *p*-process (*proton* process, also called the γ-process). Based on the overall isotopic pattern of the element after internal normalization, the nucleosynthetic nature of the anomaly can be identified and its origin ascribed to an excess and/or deficit in the product of one or more stellar processes. Since individual presolar grains are the carriers of nucleosynthetic anomalies, the identification of extremely large anomalies at the micron scale is to be expected. The survival of such anomalies at the meteoritic and planetary scale is, however, puzzling and three hypothesis have been put forward to explain the isotopic variability observed in chondrites: (i) the heterogeneity was directly inherited from the interstellar medium [132] (ii) thermal processing of dust fractionated carriers of isotopic anomalies from average SS material and subsequent gas-dust separation created large planetary reservoirs with isotopic anomalies [132, 438, 75], or

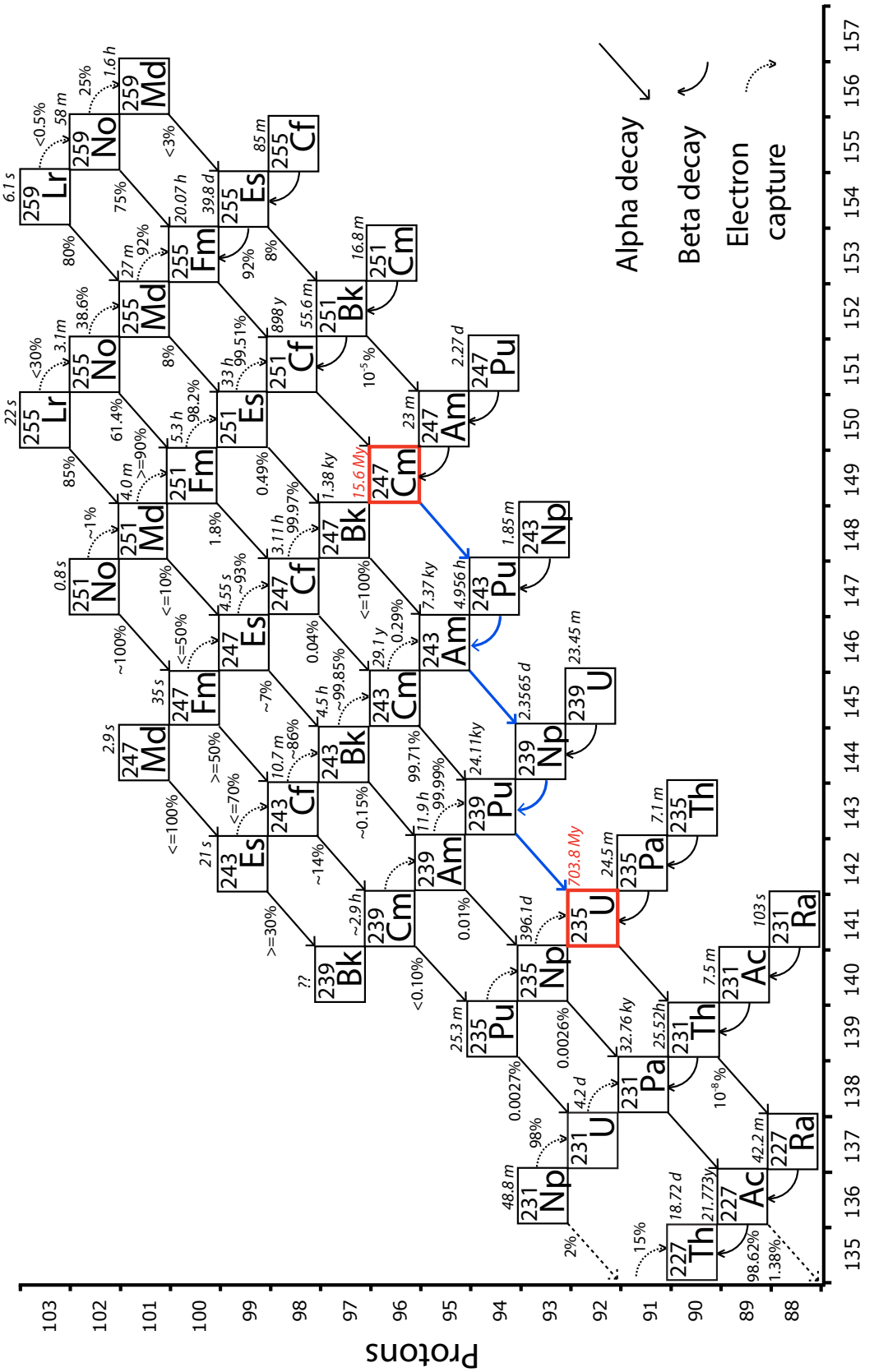

Figure 1.7: Extract of the nuclide table showing ^{235}U and elements of higher masses which could potentially decay into ^{235}U. Half-lives are in italic while percentages apply to the decay branches. Red squares highlight elements with half-lives ≥ 1 Myr. ^{247}Cm is the only possible parent-nuclide for ^{235}U that could result in anomalies in the ^{238}U/^{235}U ratio of ESS materials.

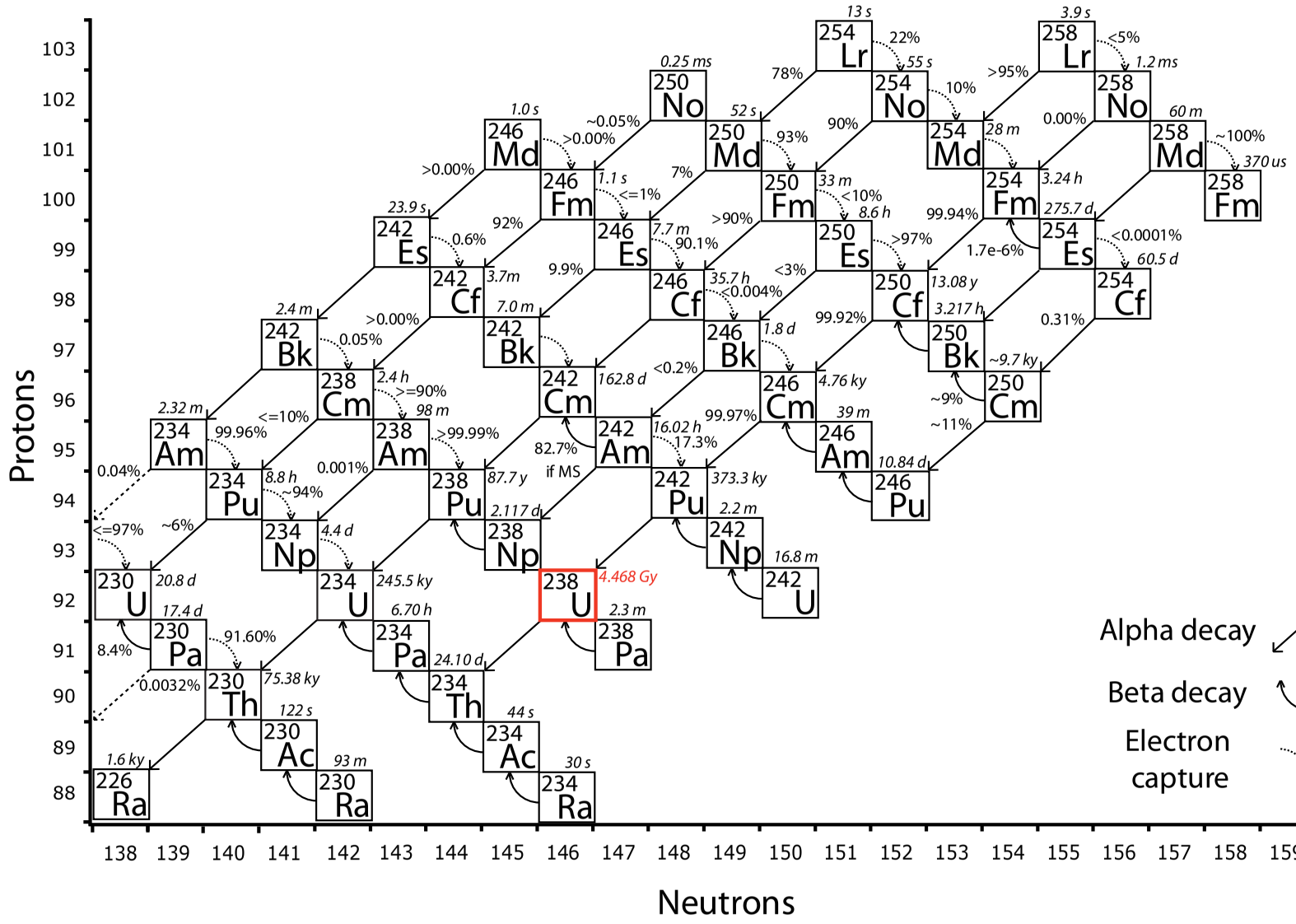

Figure 1.8: Extract of the nuclide table showing ^{238}U and elements of higher masses which could potentially decay into ^{238}U. Half-lives are in italic while percentages apply to the decay branches. Red squares highlight elements with half-lives ≥ 1 Myr. There is no parent nuclide for ^{238}U which could result in anomalies in the ^{238}U/^{235}U ratio of ESS materials.

(iii) grain-size sorting separated fine presolar carriers of isotopic anomalies from coarser SS material [136]. The origin of planetary scale isotopic anomalies remains one of the outstanding questions of isotope cosmochemistry.

Though other sources of isotopic fractionation might exist, there is, as of today, no isotopic variability that cannot be explained by any one of the processes discussed above.

In the case of U, no cosmogenic anomaly is expected due to the small thermal cross-sections of the uranium isotopes. Similarly, because the carriers of nucleosynthetic anomalies are small (nm to μm sized), it is unlikely that large anomalies in the $^{238}U/^{235}U$ ratio of centimeter-sized objects could be caused by nucleosynthetic anomalies. The only potential source of anomalies in the ratio of U "stable" isotopes is the decay of ^{247}Cm into ^{235}U. As can be seen on Fig. (1.7) and Fig. (1.8), curium-247 is the only parent isotope of either ^{235}U or ^{238}U with a long enough half-life that it wouldn't have completely decayed during the time between nucleosynthesis and formation of the SS. Therefore, large excess of ^{235}U in ESS material would be the smoking gun that ^{247}Cm was alive in the ESS (see Section 1.4).

1.3 U geochemistry

Uranium is part of a family of elements, along with V, Cr, Ni, Cu, Zn, Mo, Ru, Cd or Re, which are called *redox-sensitive*, as their oxidation state and solubility are a function of the environmental redox conditions. Because redox-sensitive trace metals tend to be more soluble under oxidizing conditions and less soluble under reducing conditions, they can be useful paleoredox proxies (*e.g.*, [126, 436]). Used individually, or in combination, these elements can provide information about the depositional environment of the samples, the extent of oxidative weathering on the continent, or the average global seawater oxidation state at the time of sample formation (*e.g.*, [153, 78, 301, 435]). The geochemistry of U has, therefore, been extensively studied, both in terms of its concentration and distribution in the ocean (*e.g.*, [444, 245, 33, 153, 244, 114, 301, 149, 195]) and in the context of the

U-series (*e.g.*, [55] and references therein). Here, the main geochemical features of uranium are presented.

In terrestrial surface environments, uranium exists mostly in two oxidation states : oxidized hexavalent U (noted U^{6+}, or U^{VI}), which is soluble in seawater, and reduced tetravalent U (noted U^{4+}, or U^{IV}), which is insoluble [248]. In ocean water, U has a uniform concentration of ~ 3.3 ppb [245, 99], and behaves conservatively (*i.e.*, U concentration correlates linearly with water salinity [245, 320]). Soluble U in ocean water is mostly present in the form of chemically unreactive uranyl carbonate complexes, $UO_2(CO_3)_3^{4-}$, [248, 244, 78]. The reactivity of an element in ocean water can be quantified by its *mean residence time*, τ, in the oceans, which is equal to:

$$\tau_X = \frac{\text{Total amount of element X in the oceans}}{\text{(Rate of supply) } or \text{ (Rate of removal)}} \tag{1.50}$$

The residence time of U in the ocean is ~ 400 kyr [245], a value much larger than the global mixing time of the ocean (determined as $\sim 1-2$ kyr by ^{14}C reservoir ages [245, 99]). The long residence time and uniform distribution of U in the ocean are consistent with the lack of reactivity of the uranyl carbonate complexes.

Since U is not sourced from hydrothermal systems [176], the main input of U to the ocean is the riverine influx: $\sim 40-46$ Mmol/yr [149]. This influx is balanced by incorporation of uranium into several sinks, including suboxic sediments, anoxic/euxinic sediments, carbonates, and altered oceanic crust, salt marshes and Fe-Mn nodules [33, 301, 149, 195].

Because of the contrasting behaviors of the two oxidation states of uranium, mobilization of soluble U can only be achieved through oxidative weathering of the continental crust. Furthermore, accumulation of U into the ocean is only possible in an oxic ocean. This implies that the concentration of U in the ocean is determined by the redox state of both the atmosphere and the ocean and explains why the disappearance of detrital uraninite after the Archean marks the rise of oxygen in Earth's atmosphere/hydrosphere [352, 183, 353, 166].

Knowledge of the concentration of U in the ocean through time can only be gained indirectly, by studying the rock record. Compilations of U concentrations in black shales and iron formations of various ages, spanning most of Earth's history, have recently brought significant insight into the major steps of oceanic oxygenation and the average oceanic redox conditions through time [323, 324]. Isotopes can bring an increased level of detail by providing information, not only on the average redox state of the ocean, but also on the *actual amount* of anoxia in the ocean through time. Indeed, because different isotopic fractionation factors, $\Delta_{\text{Sink-SW}}$, are associated with incorporation of U in different sedimentary sinks, the U isotopic composition of seawater itself is a function of the relative size of these U sinks in the ocean (see Fig. 1.9, and Chapter 3 for more details).

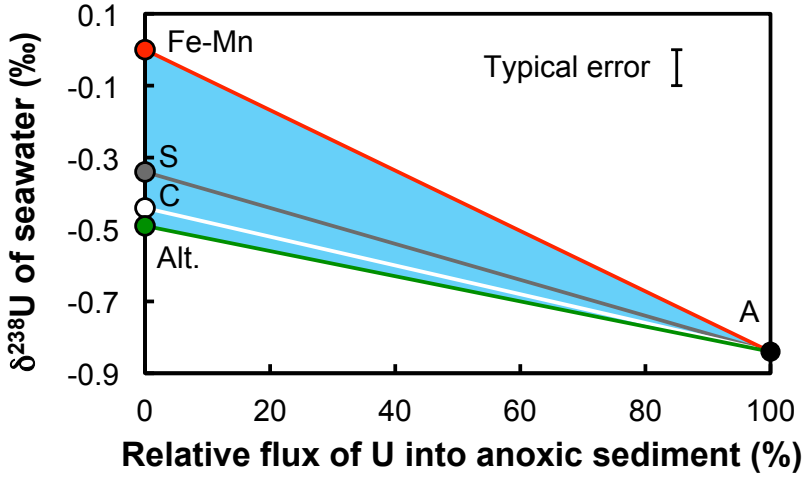

Figure 1.9: Expected $\delta^{238}U_{\text{Seawater}}$ plotted as a function of the flux of U into anoxic sediments, relative to the total U flux out of the ocean. The sinks considered are: anoxic sediment (A), manganese nodules and metalliferous sediments (Fe-Mn), suboxic sediments (S), carbonates (C), and altered oceanic crust (Alt.). Lines between the endmembers represent the evolution of the $\delta^{238}U_{\text{Seawater}}$ assuming that U is only incorporated in the two endmembers considered, and that the oceanic U budget is at steady-state. Details on the modeling and fractionation factors can be found in Chapter 3.

In this dissertation, significant effort was devoted to validating the status of the U "stable" isotope ratio as a paleoredox proxy by (i) constraining the fractionation factors associated with the various U sinks in the ocean, (ii) testing the U redox proxy on the modern ocean,

(iii) investigating the effects of early diagenesis on the U isotopic composition of carbonates, and (iv) applying this proxy to ancient sediments (blacks shales and carbonates). These points are the focus of Chapter 3.

1.4 U cosmochemistry

The two "stable" isotopes of uranium have a particular place in the realm of cosmochemistry, as they are at the heart of one of the most important isotopic dating methods that exist. Each of the two long-lived U nuclides is the source of a decay series (^{238}U-^{206}Pb, $t_{1/2} = 4.468 \times 10^9$ yr, and ^{235}U-^{207}Pb, $t_{1/2} = 703.8 \times 10^6$ yr) at the basis of a powerful chronometer allowing the dating of events ranging from a few million years old (Pliocene) to 4.567 billion years old (the age of the SS; *e.g.*, [59, 14]). Taken together, both parent and daughter isotopes form yet another chronometer, the Pb-Pb clock, whose precision actually increases with the age of the sample, thereby allowing the determination of ages for objects as old as the SS with an unmatched precision (*e.g.*, ± 0.2 Myr, [9]).

One of the fundamental assumptions of the Pb-Pb dating method as it has been used until recently, however, is that all SS materials have the same ^{238}U/^{235}U ratio. The existence of variations in the ratio of U "stable" isotopes implies that this assumption is no longer valid, which means that accurate and precise Pb-Pb ages can only be obtained through the determination of the isotopic composition of both Pb and U in the same sample. In Chapter 3, the implications of the natural variability of the ^{238}U/^{235}U ratio for Pb-Pb and U-Pb ages will be discussed in more detail and in more quantitative terms while, below, focus is brought to the potential sources of U anomalies in ESS materials and the implications the existence of such anomalies would have (other than dating).

As for terrestrial samples, redox processes can potentially lead to U isotopic fractionation in meteoritic samples. Such redox processes could have occurred either on the parent body of the meteoritic sample or on Earth between the time of fall and the time of finding of the meteorite. Beside redox processes, there are three potential sources of U anomalies in ESS

materials at the centimeter scale:

• First, there is the existence of nucleosynthetic anomalies in U isotopes. As pointed out at the end of Section 1.2.4, such anomalies, if they exist, are unlikely to be responsible for large variations in the $^{238}U/^{235}U$ ratio of centimeter- to meter-sized objects because the carriers of nucleosynthetic anomalies are small and rare (nm to μm sized).

• Then, there is the possibility of fractionation during evaporation/condensation processes. Depending on the nature of the U species which are condensing during the cooling of the solar nebula, kinetic fractionation (as exemplified by Rayleigh distillation in Section 1.2.3) could lead to ^{235}U enrichments in ESS materials of up to 6.3 ‰. In this case, the direction and magnitude of the U isotopic anomaly would hold information about the extent of evaporation/condensation that the sample experienced.

• Last, there is the existence of live ^{247}Cm in the ESS, which would have far-reaching implications for models of stellar nucleosynthesis and GCE. Indeed, the site and number of different *r*-processes is still a matter of debate [453, 294, 224, 129, 220], and current models talk of up to three different *r*-processes: one producing the lighter *r*-nuclides (A<140), another the heavier *r*-nuclides (A>140) and yet another the actinides (*e.g.*, ^{244}Pu). This framework results from the comparison of (i) the ESS abundances of three short-lived *r*-nuclides (^{129}I, ^{182}Hf, ^{244}Pu), and (ii) the abundances of these nuclides as predicted by GCE models. Taken at face value, there are, at present, as many different *r*-processes as short-lived *r*-nuclides investigated. ^{244}Pu is, however, ill-equipped to constrain the nucleosynthetic environment of the ESS, owing to its long half-life ($t_{1/2} = 79.3 \times 10^6$ yr) and the large uncertainties on its production ratio relative to ^{238}U or ^{232}Th [312]. In contrast, ^{247}Cm ($t_{1/2} = 15.6 \times 10^6$ yr) would be particularly well suited for the task, provided its existence in the ESS can be demonstrated, and its abundance constrained.

For the longest time, ^{247}Cm eluded detection [100, 103, 414, 415], which led to the famous saying that "*^{247}Cm occurred abundantly in a journal called Nature, but did not occur in nature*" – Gerald J. Wasserburg [452]. Recently, however, ^{235}U excesses of up to

3.5 ‰ were found in four fine-grained CAIs [71] (Fig. 1.10). Such excesses are within the range of isotopic fractionation allowed by kinetic fractionation (see Fig. 1.6) and could therefore be the results of evaporation/condensation processes in the early solar nebula. In this case, the "pseudochron" shown in Fig. (1.10) could very well represent a mixing line between average Solar System material and early condensates characterized by low U content and fractionated U isotopic composition. Definitive evidence of live ^{247}Cm is therefore still awaiting the discovery of an ESS material with a ^{235}U anomaly outside of the ± 6.3 ‰ range allowed by fractionation during evaporation/condensation. A primary goal of the work presented in this dissertation was to find such a phase.

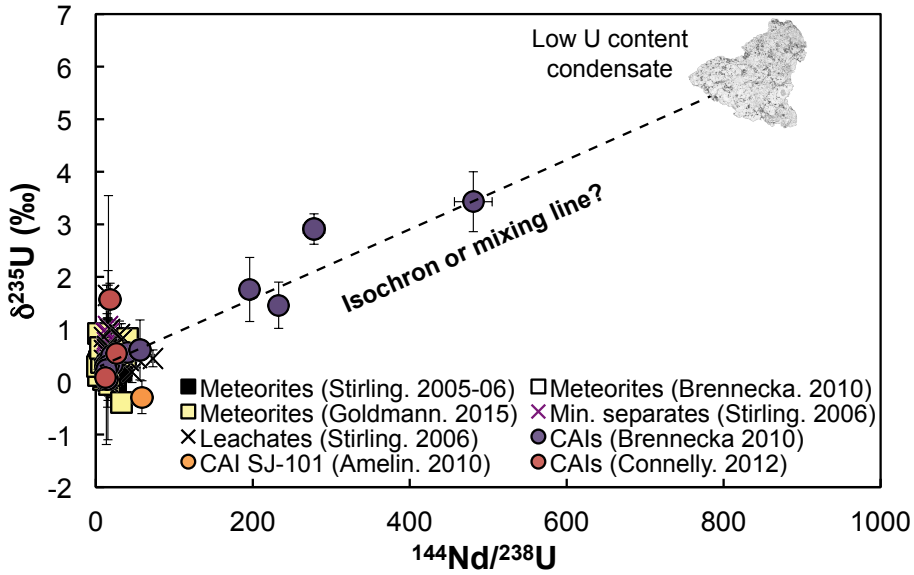

Figure 1.10: U isotopic composition of meteorites and CAIs plotted as a function of the ^{144}Nd/^{238}U ratio. From meteoritic measurements an average SS value is calculated as $\delta^{235}U_{SS} = +0.32 \pm 0.20$‰ (relative to CRM-112a) [177]. Departures from this range are observed in some CAIs which seem to align on a pseudochron, as expected from decay of ^{247}Cm [71]. As, however, fractionation during evaporation/condensation could create anomalies of up to 6.3 ‰, this correlation might also be a mixing line between average SS materials and early SS condensates with fractionated U [14, 119, 270].

After introducing the specifics of the ^{247}Cm-^{235}U chronometer, Chapter 4 will detail the methodological approach taken to find an ESS phase with large U anomaly, how this approach led to the discovery of an excess anomaly in ^{235}U of 59 ‰, and what the implications of this discovery are.

CHAPTER 2

METHODS OF ISOTOPE GEOCHEMISTRY

"Hâtez-vous lentement, et sans perdre courage,
Vingt fois sur le métier remettez votre ouvrage."
Nicolas Boileau – *L'Art Poétique*

Part of this chapter is based on:

• [222]: Ireland T.J., Tissot F.L.H, Yokochi R., Dauphas N. (2013) Teflon-HPCL: A novel chromatographic system for application to isotope geochemistry and other industries. *Chemical Geology* **357**, 203-214.

• [341]: Pourmand A., Tissot F.L.H, Arienzo M., Sharifi A. (2014) Introducing a comprehensive data reduction and uncertainty propagation algorithm for U-Th geochronometry with extraction chromatography and isotope dilution MC-ICP-MS, *Geostandards and Geoanalytical Research* **38-2**, 129-148.

• [431]: Tissot F.L.H., Dauphas N. (2015) Uranium isotopic compositions of the crust and ocean: Constraints on the U budget and global extent of modern anoxia, *Geochimica et Cosmochimica Acta*, **167**, 113-143.

2.1 Introduction

At the root of many methods of isotope geo- and cosmochemistry are two major assumptions: (i) the element to be investigated can be perfectly extracted from all the other elements making up the sample, and (ii) the isotopic composition of this purified fraction can be determined with high precision and accuracy. Given the technological advances that the last two centuries have witnessed, it would be reasonable to assume that the elemental purification is a trivial preliminary step compared to the difficult task of measuring the abundance of isotopic species. Yet, a tremendous amount of effort and time is spent on this purification step, which often represents as much of a challenge as the isotopic measurement itself.

The first part of this chapter will present the sample preparation and chromatographic methods commonly used to go from a rock/water sample to a purified elemental fraction. This will allow the opportunity to review the limitations of the current chromatographic methods and introduce some developments that have been accomplished, as part of this thesis, to overcome these limitations. This will be followed by the presentation of the chemical purification protocol for U. The third part of this chapter will provide the details of the high-precision U isotope analysis protocol developed for the present work, while the last part of this chapter will focus on the specifics of the data reduction scheme adopted.

2.2 Sample Preparation and Elemental Purification

Most analysis techniques of isotope chemistry require partial to complete destruction of the sample under study. When the isotopic variations to measure are large enough, *in situ* methods such as Laser-Ablation (LA-ICPMS) or Secondary Ion Mass-Spectrometry (SIMS) can be used to estimate the composition of individual phases or minerals. When high-precision is needed, however, (as is the case for U isotopes) analysis by Thermal Ionization Mass-Spectrometry(TIMS) and/or Multi-Collector Inductively Coupled Plasma Mass-

Spectrometry (MC-ICPMS) require complete destruction of the sample and a high degree of elemental purification. These destructive techniques are often based on an initial mechanical homogenization step (such as crushing of a whole rock sample into a fine powder), followed by a chemical digestion step (often using acid attacks). Altogether, these techniques transform a geological sample (*e.g.*, mineral, inclusion, whole rock) into a solution where the nonvolatile elements constituting the sample are present only as dissolved species. Those dissolved species are then separated from one another (using, for instance, column chemistry methods), before analysis on the mass spectrometer can be done.

2.2.1 Sampling, crushing and spiking

Rock samples were obtained either directly in powder form, or in whole rock form. In the latter case, the sample was crushed manually, in an agate mortar precleaned by crushing fine silica grains followed by rinsing with Milli-Q water (MQ water) and methanol. This cleaning procedure was carried out three times before the crushing of a sample. Two separate mortars were available, the first one was used to crush terrestrial samples only, while the second one was used exclusively for meteoritic samples.

Seawater, lake and river samples were filtered in the field at the time of collection using 0.45 μm polycarbonate Nuclepore filters (Whatman) and a Nalgene inline filter holders (Thermo Scientific). The filtered samples were collected in amber Nalgene bottles to prevent further exposure to light and were acidified to a pH of ~ 2 with concentrated HCl, within three days of sampling.

Unless the sample mass was the limiting factor, enough sample was processed to recover about 200 to 300 ng of U to ensure that high-precision analysis could be performed. The mass of rock samples digested varied from 3 mg to 1.6 g, while the mass of water sample used ranged from 80 to 320 g, depending on the U concentrations of the samples analyzed.

All samples were double-spiked using IRMM-3636 spike, which is made of 50.45 % of ^{233}U and 49.51 % of ^{236}U (^{238}U/^{235}U $= 5.1629 \pm 0.0118$; [447]). Spiking was most often done

prior to digestion, but in some cases, when the U concentration of the sample was unknown, digestion and U concentration measurement on a small sample aliquot were carried out first and spiking was only done prior to column chemistry. Spiking after digestion, but before column chemistry, was found to have no effect on the results as shown by a test on geostandard BCR-2 (Basalt Columbia River) and the agreement of our results with literature values, where spiking was not always done prior to digestion [460]. The amount of spike added was such that the U_{Spike}/U_{Sample} ratio was ~ 3 % for each sample.

2.2.2 Sample digestion

The samples investigated in this work ranged from seawater to ESS condensates. Faced with such a variety of sample matrices, a general digestion protocol was established, which could be adapted to the particularities of each sample type. All digestion and sample drying steps were carried out in Teflon labware (*i.e.*, PFA vials and beakers from Savillex) precleaned with boiling aqua regia (3:1 mixture of HCl:HNO_3) three times, followed by boiling MQ water. Some reagents and elution cuts were temporarily stored in polypropylene centrifuge tubes (Corning). Before being used, all centrifuge tubes were rinsed three times with MQ water and/or leached with 50 % HCl overnight before being rinsed with MQ water.

The general digestion protocol was based on four consecutive acid attacks lasting between one day to one week each. The first two steps consist of acid attacks in $HF/HNO_3/HClO_4$ (3:1: several drops), while the last two steps consist of acid attacks in HCl/HNO_3 (3:1). All steps were carried out on hot plates at 160°C. After the fourth acid attack, and provided the sample were fully digested (*i.e.*, no residues visible to the naked eye, even after centrifugation), the samples were dried completely, taken back into solution in concentrated HNO_3 and put back on hot plates for 24 h. The samples were then diluted to 3 M HNO_3, and placed back on hot plates for 24 h. If the sample solution obtained at this stage was clear and non-sticky (*i.e.*, the solution wet the Teflon like pure 3 M HNO_3), and if no residues were visible, then the sample was considered ready for column chromatography. In the case

where particles were still present, additional acid attacks were carried out until full sample digestion was achieved.

Slight modifications of this protocol were done for some specific samples:

- For all granites and geostandards susceptible to hosting chemically resistant phases (*e.g.*, zircons), an additional step was inserted between the second HF/HNO_3 attack and the first HCl/HNO_3 attack. Between these two steps, the samples were placed in Parr bombs for 5 days in HF/HNO_3 (3:1) at 180°C, to ensure complete dissolution of refractory phases, and thus that the U isotope measurements are representative of the bulk rocks.

- For samples with high organic matter content (*i.e.*, the black shale samples studied in [28]), an additional step was added before the first acid attack. In this step, samples were placed in individual aluminum foil envelopes and ashed at $\sim$ 500°C overnight in a Barnstead Thermolyne 47900 furnace, in order to burn off the organic matter. Comparison of isotopic measurement of ashed and nonashed sample replicates showed no difference in U isotopic composition.

- For angrites and CAIs, each acid attack lasted a full week (or more) in order for refractory phases to be fully digested. During each acid attack, the beakers were placed in a sonicator for $\sim$ 1 h. After the four acid attacks, the samples were reconstituted in concentrated HNO_3 and put back on hot plates for 4 days, before dilution to 3 M HNO_3. All samples were transferred into cleaned centrifuge tubes and centrifuged for 5 min at $\sim$ 1500 rpm. No residue was visible.

- For water samples, the digestion protocol was greatly simplified. The samples were evaporated completely and taken back into concentrated HNO_3, before dilution to 3 M HNO_3. In rare cases where particles were visible after this single step process, evaporation and reconstitution in concentrated HNO_3 was repeated until full digestion of the solids was achieved.

2.2.3 Extraction chromatography

Once the sample has been turned into an analyte solution (where all elements exist as dissolved species), the challenging task of isolating the element(s) of interest begins. Many techniques exist that play on the various physical and chemical properties of the elements, such as volatility, density or a change of state during a reaction (*e.g.*, solid to gas, for instance). For non-volatile elements, *liquid-liquid extraction* (also called *solvent extraction*), and *solid-liquid extraction* (also called *solid-phase extraction*, or *extraction chromatography*) are the most commonly used methods. Liquid-liquid extraction, uses the solubility difference of the analyte between two immiscible liquids (such as water and an organic solvent), to concentrate the analyte into one liquid phase or the other. In solid-phase extraction, however, dissolved compounds carried in a mobile phase (*e.g.*, water, acids, bases) are passed through a solid, stationary phase, and separated based on their relative affinity for the mobile and stationary phases, respectively.

Extraction chromatography is especially used in isotope chemistry because it combines the selectivity of solvent extraction with the ease of operation of chromatographic methods [216]. Many subcategories of extraction chromatography exist depending on the exact separation mechanism involved. For instance, in *normal-phase chromatography*, the retention is based on the interaction of polar functional groups of the analytes with polar functional groups on the surface of the stationary phase (such as ≡Si-OH or ≡Al-OH). In contrast, during *reversed-phase chromatography*, the stationary phase is nonpolar (such as a long-chain hydrocarbon bound on a silica base) and the mobile phase is polar (*e.g.*, mixture of water with a polar solvent such as methanol) The retention is therefore a function of hydrophobicity, and the larger the hydrophobic part of the analyte, the longer the retention. Reversed-phase chromatography is used in $\sim$ 90 % of the analytical separations of low-molecular-weight compounds [309].

In isotope chemistry, a third type of chromatography is used, which allows the separation of individual ions: *ion-exchange chromatography*. In ion-exchange chromatography, an ion

(or a charged functional group) is covalently fixed onto a stationary phase. To ensure the electroneutrality of the ensemble, a counterion is bound to the ion. When the mobile phase is passed through the stationary phase, the counterions can be exchanged by analyte ions of the same charge. The difference in affinity of the analyte ions for the ion covalently fixed to the stationary phase is the basis for the ion-exchange separation.

2.2.4 The "Theory of Plates"

In 1941, Martin & Synge [272] developed a successful theory of chromatography (a work for which they were awarded the Nobel Prize in Chemistry, 1952). The so-called *Theory of Plates* states that a chromatographic column can be divided into a finite number of theoretical plates of defined height (noted HETP, for *Height Equivalent to a Theoretical Plate*). Within each plate, and at any point in time, equilibrium between the liquid (mobile) phase and the solid (stationary) phase is achieved. Using this theory, it is possible to model the behavior of elements onto a resin and test various elution schemes to optimize the separation of the elements of interest.

Consider C_s and C_l the concentration of the element in the solid phase (in mol/g) and the liquid phase (in mol/mL), respectively. The affinity of a resin for a particular element is given by the partition coefficient, K_d (unit mL/g), which is defined as:

$$K_d = \frac{C_s}{C_l} \tag{2.1}$$

As the liquid moves down the column from theoretical plate to theoretical plate, it equilibrates with the solid in the next plate. When the liquid in plate $i-1$ moves down to plate i, the distribution of the element contained in the liquid (from plate $i-1$) and in the solid (from plate i) is not at equilibrium anymore (*i.e.*, $K_d \neq C_s/C_l$). The distribution of the element between the liquid and the solid phase changes according to the K_d value imposed by the reagent type and molarity. The following mass balance equation can be written to

describe this process:

$$m_s^i + m_l^{i-1} = m_{s_{eq}}^i + m_{l_{eq}}^i \tag{2.2}$$

where the exponents refer to the plate position, m_s and m_l to the mass of element in the solid phase and the liquid phase, respectively, and the subscript eq to values after equilibrium has been reached (*i.e.*, $K_d = C_s/C_l$). This equation can be rewritten as:

$$C_s^i dV_s^i + C_l^{i-1} V_l^{i-1} = C_{s_{eq}}^i dV_s^i + C_{l_{eq}}^i V_l^i \tag{2.3}$$

where d refers to the density of extractant-loaded beads (*i.e.*, density of the resin, in g/mL), and V_l and V_s, respectively, to the volume of liquid and solid in the plate (in mL). The volumes of liquid and solid are the same in each plate, and can be expressed as a function of the porosity of the resin (ϕ) and the volume of the plate V^i, as:

$$V_l^i = V^i \times \phi \tag{2.4}$$ and $$V_s^i = V^i \times (1-\phi) \tag{2.5}$$

By substituting Eqs. (2.1), (2.4) and (2.5) into Eq. (2.3), one can calculate the equilibrium concentration of the element in the liquid moving down into the column in each plate as:

$$C_{l_{eq}}^i = \frac{(1-\phi)dC_s^i + \phi C_l^{i-1}}{(1-\phi)dK_d + \phi} \tag{2.6}$$

and the corresponding equilibrium concentration of the element in the solid becomes:

$$C_{s_{eq}}^i = K_d \times C_{l_{eq}}^i \tag{2.7}$$

Using Eqs. (2.6) and (2.7), a chromatography simulation code was developed in Mathematica language to predict the elution behaviors of elements in a given resin (the code is available in [222], or on request for an updated, faster running version). The architecture of the code is extremely simple (see Table 2.1) and allows the user to rapidly simulate complex

elution schemes. Only a few input parameters are required: (i) the column length and the parameters needed to calculate the volume of resin in each theoretical plate (*i.e.*, column radius, porosity, and the HETP), (ii) the volume of each elution step, (iii) the density of the extractant-loaded beads and (iv) the partition coefficient of the element(s) for the resin during each elution step (*i.e.*, K_d corresponding to the reagent type and molarity). For a given column configuration and a given element, the HETP defines the peak width, while the K_d values set the position of the elution peak. One parameter often unknown is the HETP of the resin. This value can be easily estimated by using published K_d values and by adjusting the HETP value until the simulated elution fits published elution curves obtained on the resin of interest.

Architecture of the chromatography simulation code developed
Set collection volume.
Import resin characteristics : HETP (cm),
Column height (cm),
Column radius (cm),
Resin porosity,
Density of extractant-loaded beads (g/mL).
Import elution details : Number of elution steps,
Volume of each elution step (mL),
Element concentration in each elution step (mol/mL),
K_d of elements in each elution step (mL/g).
Elution simulation loop
For each elution step:
The characteristics of the liquid volume to inject are updated,
The liquid in the last plate is eluted,
The liquid in each plate above the last one is moved down one plate,
The liquid to inject is added to the first plate,
Liquid-solid equilibrium is calculated in each plate using Eqs. (2.6) and (2.7).
End of the loop
Plot the simulated elution curve (% recovery *vs.* volume). Two graphs are plotted, in the first one, the volume step is the plate volume, in the second one it is the collection volume specified by the user.
Export the results as xls or xlsx file.

Table 2.1: Architecture of the chromatography simulation code. Code published in [222].

2.2.5 Quantification of the chromatographic separation: resolution

The "goodness" of a chromatographic separation is readily visible on a Recovery *vs.* Volume Eluted plot, as the two compounds of interest will define two distinct peaks. One way to quantify the extent of separation is to assess the *resolution*, R, of successive pairs of bands. The resolution is defined as the distance between two successive peaks, divided by the sum of the width of the peaks, and, if the elution peaks are approximated by Gaussian curves (as expected from theory in the limit of a large enough number of plates, see [272]), can be written as:

$$R = \frac{V_2 - V_1}{2\sigma_2 + 2\sigma_1} \tag{2.8}$$

where V_i is the volume at the peak maximum of element i, and $2\sigma_i$ is the band width at a height $e^{-1/2}$ times the peak height of element i [80]. A separation will be considered good if $R > 1$, meaning that the distance between two successive peaks is greater than the widths of the peaks. In other words, the two curves overlap at a distance 2σ away from their respective means. If the resolution is equal to 1.5, the two peaks will overlap at a distance 3σ away from their respective mean, and for any value of R, the two peaks will overlap at a distance $R \times 2\sigma$ away from their respective mean. Quantitatively, the amount of overlap can therefore be calculated using the separation resolution and the cumulative distribution function (CDF) of a Gaussian curve of mean μ and standard deviation σ:

$$\text{Overlap}(R) = 1 - \text{CDF}(\mu, \sigma; \mu + R \times 2\sigma) = 1 - \frac{1}{2}\text{erf}\left[\frac{-2R}{\sqrt{2}}\right] \tag{2.9}$$

where erf is the error function. A good separation, characterized by a resolution of $R = 1$, will therefore have ~ 2.5 % of element 1 overlapping with element 2, and vice-versa. If, instead, $R = 1.5$, the overlap is only 0.13 %. Although Eqs. (2.8) and (2.9) assume Gaussian elution peaks, they can still be reasonably applied to peaks that are only near-Gaussian or slightly asymmetrical (as is the case in this work).

2.2.6 Strengths and weaknesses of open-column chromatography

Thanks to the development of (i) a theory of column chromatography [272], and (ii) a series of highly specific resins by several companies (*e.g.*, BioRad, Eichrom), open-system, gravity-driven column chromatography has established itself as an essential step in many isotope geochemistry methods where high purity separations of the elements of interest from matrix elements are required. If a particular separation scheme requires the use of large acid volumes, open columns can even be placed on the top of a vacuum-box, whereby the flow rate is increased and controlled by the pressure difference between the atmosphere (where the top of the column is) and the inside of the box (where the bottom of the column is).

These well-established traditional column techniques are undoubtedly useful, yet they suffer from significant limitations pertaining to the overall column length, resin size, lack of temperature control and diffusion effects, which can severely compromise separation efficiencies. The application of open-column techniques to new, challenging problems of isotope geochemistry is therefore limited, and some fine-scale separations still require complicated multi-step and time-consuming protocols (*e.g.*, Ni-Mg separation [425]).

Commercially available high-performance liquid chromatography (HPLC) systems, while overcoming many of these limitations (*e.g.*, closed-system setups; pressurized systems, hence longer columns and better separation; semi-automated set-up), suffer from several shortcomings that have hampered their adoption in isotope geochemistry. Mainly, (i) the liquid flow path often contains glass and/or metal parts which are easily corroded/dissolved by concentrated acids or organic solvents, leading to contamination of the samples, and (ii) the electronic controls and housing are often spatially associated with the HPLC unit, drastically shortening the lifespan of the apparatus as the metallic parts rapidly corrode in these harsh chemical environments (*e.g.*, [401]). Table 2.2 presents a side-by-side comparisons of the advantages and limitations of open columns and HPLC systems.

To push the boundaries of the field of isotope chemistry will require combining the advantages of open-column setups with those of current HPLC systems, thereby bringing HPLC

systems up to the resistance and separation standards of isotope chemistry. A list of requirements that such a novel system should meet is presented in Table 2.3.

	Current HPLC systems	Open-columns
Corrosion resistant (to strong, hot acid)	✗	✓
Low blanks / no contamination	✗	✓
Electronics close to flow path	!	N.A.
Separation reproducibility	✓	✓
Automated	✓	✗
Controlled set-up (e.g. T, flow rate)	✓	≈

Table 2.2: Comparison of the strengths and weaknesses of current HPLC systems and open-columns chromatography setups

Enhanced elemental separation for complex separation requires:	System
Long and narrow columns → **Driving force for liquid flow (Pressure)** The ability to perform fine step (gradient) elution → **Computer control of the reagents mixing** Enhanced peak separation → **Thermally controlled and uniform system**	HPLC
The use of strong acids/bases or organic reagents → **Chemically resistant, inert liquid path (Fluoropolymer)** A durable system → **Isolation of electronics and pneumatic actuation**	PF-HPLC

Table 2.3: Requirements and proposed improvements to bring HPLC systems up to the resistance and separation standards of isotope chemistry.

2.2.7 Development of a Pneumatic-Fluoropolymer HPLC system

Significant effort was devoted, as part of this thesis, to the development of a durable HPLC system capable of handling the harsh reagents commonly used in isotope chemistry. These efforts resulted in the creation of the first Pneumatic-Fluoropolymer HPLC (or PF-HPLC), whose main features respond to the requirements listed in Table 2.3 (see [222]).

These features include: (i) a flow path entirely made of chemically resistant and inert fluoropolymer (*e.g.*, Teflon, PTFE, PFA); (ii) pneumatic actuation of all components of the system, (iii) isolation of the electronics in a positively pressurized enclosure preventing any contact with acid fumes; (iv) a custom-designed Teflon mixing chamber for reagent mixing (Fig. 2.1); (v) a modular and adjustable chromatographic column setup (both in diameter and length); (vi) control over the thermal state of the entire system (up to 80°C); (vii) a HPLC injection loop (Fig. 2.2) entirely made out of chemically resistant plastics (Fig. 2.3); (viii) an all plastic X-Y stage at the bottom of the column to automatically collect up to 16 different elution cuts (Fig. 2.4); and (ix) complete automation using LabView software and a specifically designed code.

The above description applies to the latest iteration of the system (see Fig. 2.5b). In the development process, two other versions were tried. In the first version of the system (largely the work of Thomas Ireland, see [222] and Fig. 2.5a), no pneumatic actuation was implemented and the electronics were not isolated from the acid fumes. Though this early iteration provided very satisfactory results in terms of elemental separation (all tests presented here were performed with this first prototype and the results were published in [222]), its short lifespan was a major drawback. In the second iteration, pneumatic actuation was implemented and the electronics were isolated from the flow path. Extensive resistance tests were conducted on this prototype, which sustained without any apparent damage, prolonged functioning using concentrated nitric acid (HNO_3) and hydrochloric acid (HCl) heated to 70°C. This version of the system, however, suffered from dead volume issues in both the sample injection component and the manifold supposed to automatically separate the various elution cuts at the bottom of the column. These problems rendered both the calibration of gradient elution schemes and the collection of clean elution cuts essentially impossible. These issues are addressed in the latest version (Fig. 2.5b) of the PF-HPLC system which features a typical HPLC injection loop system and a mobile X-Y stage below the column, for automated elution cut collection. The uniqueness of both components resides

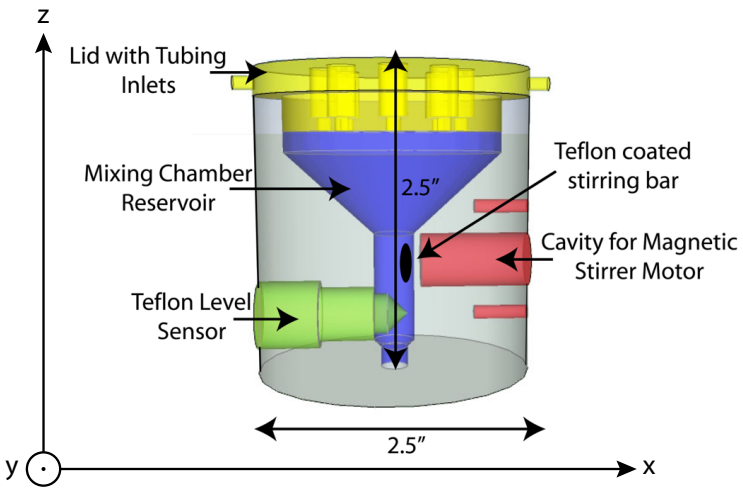

Figure 2.1: 3D diagram showing the main features of the Teflon mixing chamber designed for the PF-HPLC system. The z-axis is the vertical axis.

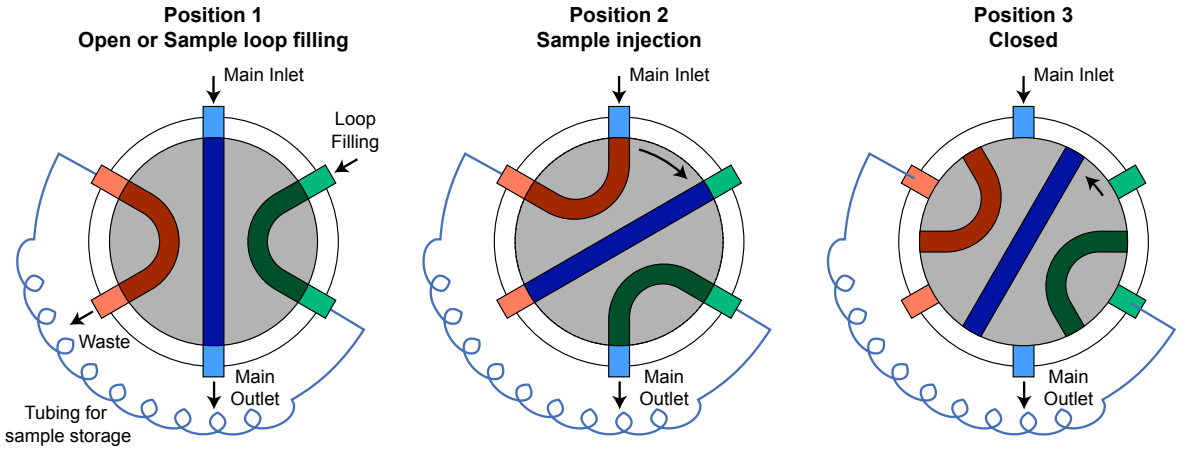

Figure 2.2: Diagram showing the typical functioning of an HPLC injection loop.

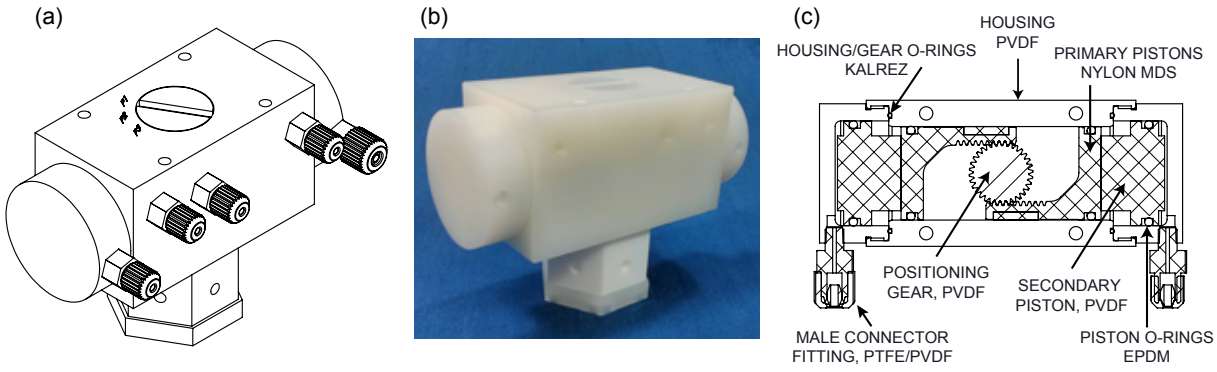

Figure 2.3: Custom-made, all plastic, pneumatically actuated HPLC sample injection loop. (a) Concept diagram, (b) picture of finished product, and (c) cross-section through the actuation part. Individual figures courtesy of International Polymer Solutions (IPS).

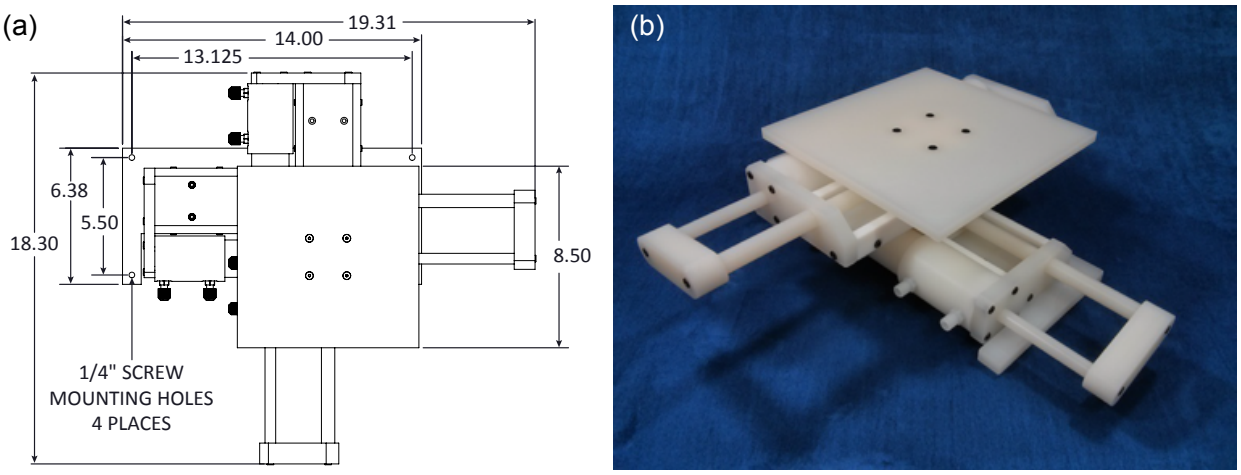

Figure 2.4: Custom-made, all plastic, pneumatically actuated 16-position X-Y stage. (a) Concept diagram, (b) picture of finished product. Individual figures courtesy of IPS.

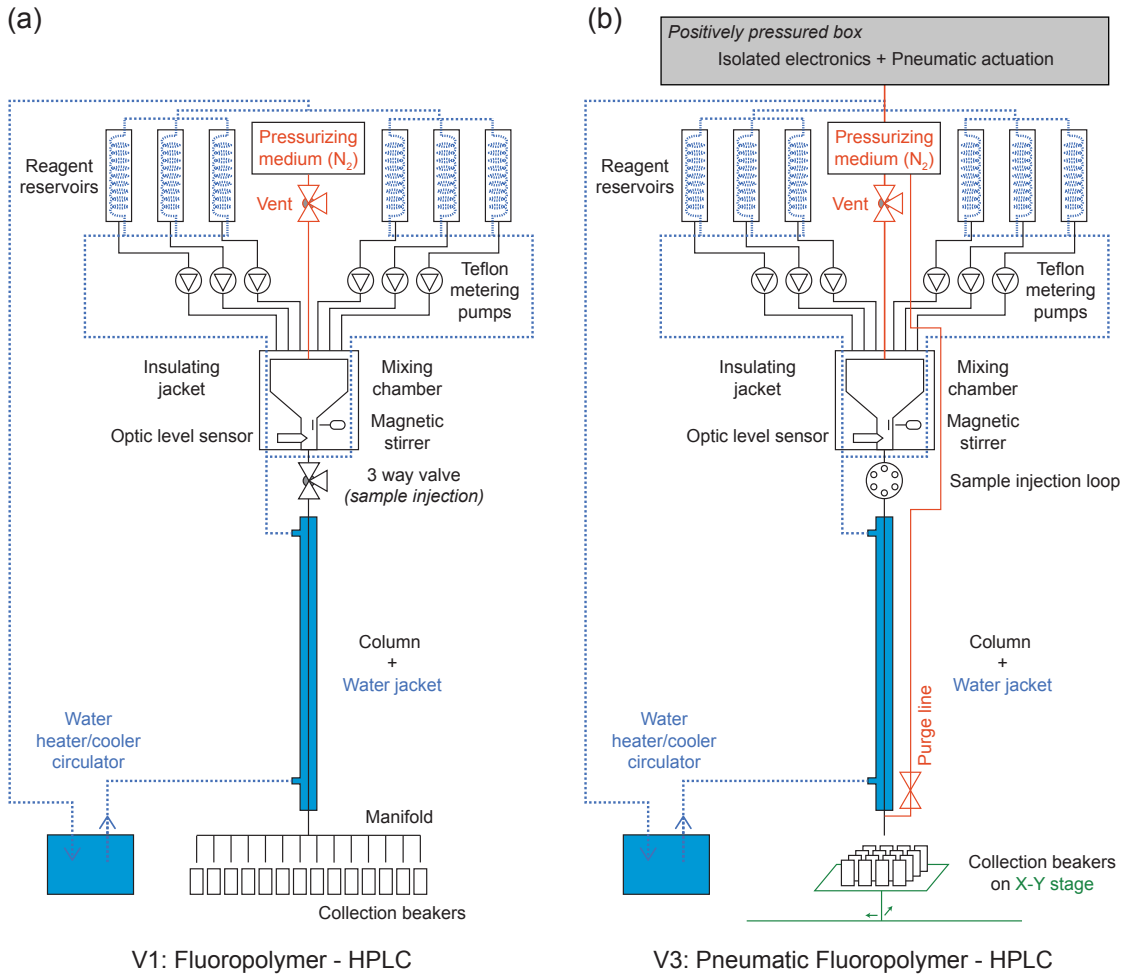

Figure 2.5: Schematic diagram of the first (a) and third (b) versions of the HPLC system developed to try and combine the advantages of HPLC systems and open-column setups.

in their being entirely made out of chemically resistant plastic (*i.e.*, absence of metal, or other easily corroded parts), such as Teflon (PTFE/PFA), PVDF, EPDM or Kalrez. This was made possible by technological transfers from the semiconductor industry and the availability of Teflon-manufactured parts. The injection loop, X-Y stage and many of the fluoropolymer fittings used in the PF-HPLC were designed and/or custom-made by International Polymer Solutions Inc. (IPS).

Below, the performances of the PF-HPLC system are compared to those of traditional chromatography setups.

2.2.8 PF-HPLC performances: Ni-Mg separation

The separation of Ni and Mg was the first test to which the initial version of the PF-HPLC was subjected. The study of Ni isotopic anomalies and Ni stable isotope variations by TIMS and MC-ICP-MS has been a very active area of research in cosmochemistry and isotope geochemistry [44, 395, 397, 348, 131, 356, 350, 349, 408, 425]. In particular, the ESS abundance of ^{60}Fe (an extinct radionuclide that decays to ^{60}Ni, $t_{1/2}$ = 2.62 Myr; [378]), has been a matter of intense debate, with estimates varying by up to two orders of magnitude [395, 422, 302, 190, 425, 297, 298, 426]. Since, the ^{60}Fe/^{56}Fe ratio in the ESS has significant bearing on the astrophysical context of Solar System birth, properly constraining its value is key for models of SS formation. A major difficulty faced by analysts is to separate Ni from Mg in silicate rocks (where the Mg/Ni ratio is high). A high degree of separation is required, owing to (i) the presence of an argide interference produced from ^{24}Mg (^{24}Mg^{40}Ar), which can interfere with the low abundance isotope ^{64}Ni, and (ii) the decrease in the measurement precision of the other Ni isotopes (^{58}Ni, ^{60}Ni, ^{61}Ni and ^{62}Ni) with increasing matrix concentration in the measured solution. To ensure a negligible matrix effect, a ratio of $C_{\mathrm{matrix}}/C_{\mathrm{Ni}} < 0.5$ is required.

To tackle the question, Tang and Dauphas (2012) [425] developed a 3-step column chromatography process for the purification of Ni from matrix elements. The second step of this

procedure represents a significant time impediment to the overall process, and was the focus of the PF-HPLC test. Using a 40 cm long (0.3 cm ID) Teflon column filled with Bio-Rad AG50-X12 (200-400 mesh) hydrogen-form cation exchange resin, a vacuum box to facilitate the elution, and a mixture of 10 M HCl and acetone (20:80), 5 column passes were needed to reach the Ni-Mg separation required for high-precision analysis. Each column pass took $\sim$ 14 hours, and, because the HCl-acetone mixture becomes unstable over the course of an elution as acetone evaporates, the reagents had to be freshly mixed every half-hour.

Figure (2.6) shows the two tests conducted using the PF-HPLC. The first test (panel a) essentially reproduces the elution conditions used by [425]. The poor separation between Ni and Mg is readily seen as the two peaks are broad and clearly overlap. Assuming the Mg peak is symmetrical, the resolution of this separation is $\sim$ 0.96. In the second test, the unique capabilities of the PF-HPLC were used: the column length was increased to 80 cm and the temperature of the system set to 65°C. The separation of Ni from Mg at these conditions is excellent: the two peaks are well separated, and the Ni-Mg resolution is $\sim$ 2.1. Furthermore, the entire procedure took only 10 hours. A single column pass on PF-HPLC is therefore sufficient to properly separate Ni from Mg, turning a 5×14 h human effort into a single 10 h automated protocol.

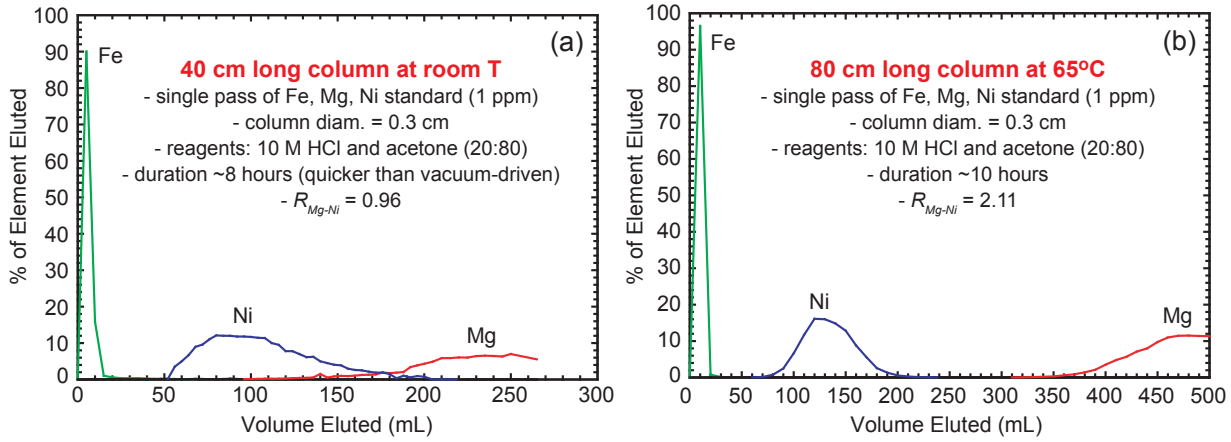

Figure 2.6: Ni-Mg separation using the PF-HPLC system. In panel (a) the setup reproduces the open-column chemistry from [425], while in (b) an optimized elution was performed using the PF-HPLC abilities. Modified from [222].

2.2.9 PF-HPLC performances: REE separation

For the second test of the PF-HPLC, the aim was to realize in a single column pass the separation of all Rare Earth Elements (REEs) from each other. The REEs (also called Lanthanides) are a series of 14 elements (from Lanthanum to Lutetium) of particular interest in geo- and cosmochemistry, but which are notoriously difficult to separate from each other at the level required for isotope geochemistry work. This stems from the fact that (i) the REEs are chemically very similar and (ii) most of these metal ions exist only in the trivalent oxidation state. For this reason the separation and quantitation of the individual members of the REE series has been called "*one of the greatest challenges in the separation of metal ions*" [308].

Several well-established methods have been employed for the bulk separation of REEs for geochemical applications by traditional column chemistry (*e.g.*, [174, 417, 213, 449, 125, 196, 32, 31, 340]) or by HPLC (see review by [448]). These methods are effective for obtaining bulk concentration data and chondrite-normalized REE patterns, but are not suitable for high-precision isotopic analyses of the individual REEs, where the levels of isobaric, oxide and molecular interferences that may be present during ICP-MS analysis need to be minimized. Attempts at separating individual REEs by HPLC have been met with moderate success [400, 80, 276, 466, 90, 287, 401, 191, 448], and these analytical developments have not yet transitioned into isotope geochemistry due to the lack of suitable HPLC systems meeting the stringent standards of this field.

Over the past several years, it has become increasingly important in geo- and cosmochemistry to address various questions involving REE isotope systematics (*e.g.*, [86, 61, 24, 25, 38, 85, 317, 429, 173, 3]). For instance, in the geologic community, much attention has been centered on separating Nd and Sm from the rest of the REEs because of two commonly used radiogenic isotope systems (^{147}Sm $\rightarrow^{143}$Nd, $t_{1/2}$ = 106 Gyr; ^{146}Sm $\rightarrow^{142}$Nd, $t_{1/2}$ = 68 Myr), and chromatographic techniques for these two elements are fairly well established [263, 143, 454, 226, 357, 61, 87, 142, 88]. Methods of separating the individual REEs

using α-HIBA (alpha-hydroxyisobutyric acid; *e.g.*, [197, 287, 85]) or Ln-resin (a Lanthanide-specific resin that uses HDEHP as the extractant phase; *e.g.*, [357, 331, 216, 58, 201]) have also been refined over time, but these studies have mainly focused on a small subset of the REEs or have not provided enough resolution between REEs to allow for high-precision isotopic analysis.

The ability to measure the isotopic compositions of all the REEs from a single sample digestion and column procedure could be a significant leap forward in terms of how these elements are analyzed, with implications for nucleosynthetic processes [278, 279, 24, 25, 85, 173, 347], neutron capture and cosmic-ray exposure effects on meteorites [156, 155, 76, 261, 379, 48, 199, 198, 200, 201] and mass fractionation effects [3]. Although the Ln-resin is a powerful method for separating REEs, α-HIBA has been favored in HPLC systems because the HDEHP chemistry requires the use of high molarity and corrosive acids that cannot be handled by commercial HPLC systems. This is most clearly expressed by Sivaraman et al. (2002) [401] who considered the feasibility of using an HDEHP coated column in an HPLC system, but decided against this approach because of concern that the high molarity acids would damage the system.

Below is a comparison of the REE separation using α-HIBA and Ln-Spec resin in combination with the PF-HPLC system.

2.2.9.1 Attempt at REE separation using cation exchange resin and α-HIBA eluent

The α-HIBA chemistry is an ion-exchange chemistry using the alpha-hydroxyisobutyric acid, $(CH_3)_2$-COH-COOH, as the eluent, and an ion exchange resin as the stationary phase. In this work, the AG50W-X8 (200-400 mesh) NH_4^+ resin was used. It is a strong cation exchange resin of Analytical Grade (AG), composed of sulfonic acid functional groups attached to a styrene divinylbenzene copolymer lattice (type 50), with 8 % polymerization of the divinylbenzene lattice (cross-linkage X8), where the particle diameter is between 38 and

75 μm (mesh size 200-400), and conditioned to the ammonium form (the counterion is NH_4^+). The medium crosslinkage of the resin limits the bead pore size and, with it, the molecular weight of the compounds that the resin can exchange (X8 is used for separations of amino acids, cations and metals). The particle size, on the other hand, affects the flow rate and the separation resolution: the attainable resolution increases with decreasing particle size and narrower size distribution range. The 200-400 mesh size corresponds to the smallest particle size, and therefore, the best achievable separation using this resin.

The resin was cleaned in a large Teflon column ($\sim$ 1 L) accordingly to the following procedure:

- MQ water rinse (3 column volume, cv),
- 6 M HCl rinse (3 cv),
- MQ water rinse (3 cv),
- Transfer of the resin to triple cleaned Teflon bottle,
- Soaking of the resin in 1 M NH_4OH (ammonium hydroxyde), for 1 h,
- MQ water rinse (2 cv),
- Soaking of the resin in MQ water.

At this point the pH should be neutral, and the resin converted to ammonium form.

The α-HIBA solution was prepared in glassware precleaned by a quick rinse in 10 % (volume) HCl, followed by an overnight immersion in 6 M HCl on a hot plate. The acid was bought from Alfa Aesar, as 2-Hydroxyisobutyric acid, 99 % (dry wt.) (Lot# 10158384, molar mass 104.11 g/mol). About 208.30 g of the acid was dissolved in $\sim$ 650 ml of MQ water, and left to react for 2 h, after which the solution was filtered to remove any non-dissolved acid particles. Filtration took $\sim$ 6 h and was done with a PTFE-faced funnel and base glass filter holder and 0.45 μm Fluoropore hydrophobic PTFE membranes (Millipore), pre-wetted with alcohol. The pH of the filtered solution ($\sim$ 650 mL) was adjusted to 4.5 by addition of $\sim$ 95 mL of ammonium hydroxide (NH_4OH). The pH adjusted solution ($\sim$ 718.48 g) was transferred into a triple cleaned Teflon bottle and diluted with MQ water to a final weight

of 1000.04 g, corresponding to an α-HIBA concentration in the final solution of $\sim$ 2 mol/L.

From the above protocol, it is evident that one of the main drawbacks in using α-HIBA as the eluent is that the actual molarity of the solution is never precisely known. Since the pH adjustment with ammonium hydroxide prevents any titration of the molarity of the acid solution, the calibrations of the separation protocols are only valid for the resin and acid batch used for the calibration. Upon remaking of the 2 M HIBA solution, one has to recalibrate all separation schemes, which is a major time impediment.

All elution tests were carried out using a multi-element REE solution containing $\sim$ 10 μg/g of each REE, as well as Sc and Y (which behave similarly to the REEs). In each test, $\sim$ 1 μg of each REE was loaded onto the AG50W-X8 resin in ammonium form, and the chromatographic separation was conducted at room temperature, using 21 cm long quartz columns, with internal diameters of 1.9 mm.

To optimize the REE separation achievable with the HIBA chemistry, elution simulations were run using the chromatography simulation code I developed as part of this thesis and published in [222]. Knowledge of the partition coefficients (K_d) of the REEs for the AG50W-X8 (200-400 mesh) NH_4^+ resin under a range of acid molarities is a prerequisite to any elution simulation. The K_d values were therefore estimated for a range of α-HIBA molarities from 0.01 to 2 mol/L [251], and are presented in Table (2.4) and Fig. (2.7). The experimental protocol is identical to the one used to measure the partition coefficients of the U/Teva resin (see Section 2.3.1), except that here $\sim$ 2 g of dry resin were equilibrated with 6 ml of a 100 ppb standard solution. As in the case of the Ln-Spec resin, there is a linear relationship between the K_d values and the molarity of the acid, and Table (2.5) gives the linear regression statistics for each curve (slope and intercept). The spread of K_d observed on AG50W-X8 using α-HIBA is smaller than the one observed on Ln-Spec with both HNO_3 and HCl as the eluent phase [330, 214, 222], which means that the best separation of REEs theoretically achievable will use the Ln-Spec resin, rather than the α-HIBA chemistry.

Using the newly obtained K_d values, the height of plate (HETP) of the ion exchange

Distribution coefficients (*Kd*) of REEs on AG50W-X8 200-400 resin as a function of the molarity of α-HIBA acid.

Molarity	Sr	Y	Ba	La	Ce	Pr	Nd	Sm	Eu	Gd	Tb	Dy	Ho	Er	Tm	Yb	Lu	Ta	Th	U
0.010	10142	44430	>10^5	>10^5	>10^5	>10^5	>10^5	>10^5	>10^5	>10^5	>10^5	>10^5	>10^5	>10^5	>10^5	>10^5	>10^5	481	32512	8976
0.016	8773	38675	18912	>10^5	>10^5	>10^5	>10^5	>10^5	>10^5	>10^5	>10^5	>10^5	>10^5	>10^5	>10^5	>10^5	>10^5	186	20746	3209
0.026	7905	19518	15362	>10^5	>10^5	>10^5	>10^5	>10^5	>10^5	>10^5	>10^5	63054	35617	21845	13422	7938	5754	3035	2736	497
0.041	6629	4707	13846	>10^5	>10^5	>10^5	>10^5	53146	44051	31263	12154	6290	3760	2059	1248	744	517	89	206	116
0.063	4616	420	9875	84935	44084	28856	19437	7007	3701	3769	994	488	285	158	92	54	36	128	19	27
0.082	2990	62	7518	22218	9982	5741	3774	1144	601	612	148	71	41	22	13	7.5	4.9	389	3.5	8.6
0.107	2705	23	7423	10096	4116	2346	1518	433	222	226	53	26	15	8.7	5.4	3.7	2.8	62	<√10	6.5
0.135	2384	9.1	6716	3995	1555	895	577	159	81	85	20	10	6.5	4.3	<√10	<√10	<√10	76	<√10	4.7
0.159	1733	<√10	4789	1406	540	313	202	55	28	31	7.3	4.1	2.9	2.1	<√10	<√10	<√10	21	<√10	<√10
0.186	1219	<√10	3447	570	217	126	81	22	11	13	<√10	<√10	<√10	<√10	<√10	<√10	<√10	<√10	<√10	<√10
0.212	1152	<√10	2974	256	99	56	36	11	6.1	8.3	<√10	<√10	<√10	<√10	<√10	<√10	<√10	13	<√10	<√10
0.240	1033	<√10	2755	214	82	47	30	8.5	4.8	6.8	<√10	<√10	<√10	<√10	<√10	<√10	<√10	12	<√10	<√10
0.265	780	<√10	650	114	44	25	16	4.6	2.7	4.3	<√10	<√10	<√10	<√10	<√10	<√10	<√10	<√10	<√10	<√10
0.290	668	<√10	1658	79	31	18	11	3.3	<√10	3.4	<√10	<√10	<√10	<√10	<√10	<√10	<√10	5.9	<√10	<√10
0.318	502	<√10	1153	38	15	9	5.8	<√10	<√10	<√10	<√10	<√10	<√10	<√10	<√10	<√10	<√10	<√10	<√10	<√10
0.345	576	<√10	1330	37	16	10	6.9	<√10	<√10	<√10	<√10	<√10	<√10	<√10	<√10	<√10	<√10	28	<√10	<√10
0.371	312	<√10	729	15	6.0	3.4	<√10	<√10	<√10	<√10	<√10	<√10	<√10	<√10	<√10	<√10	<√10	<√10	<√10	<√10
0.398	345	<√10	768	14	6.3	4.0	<√10	<√10	<√10	<√10	<√10	<√10	<√10	<√10	<√10	<√10	<√10	3.6	<√10	<√10
0.420	259	<√10	584	8.4	3.6	<√10	<√10	<√10	<√10	<√10	<√10	<√10	<√10	<√10	<√10	<√10	<√10	7.4	<√10	<√10
0.525	164	<√10	393	3.5	<√10	<√10	<√10	<√10	<√10	<√10	<√10	<√10	<√10	<√10	<√10	<√10	<√10	<√10	<√10	<√10
0.677	101	<√10	275	<√10	<√10	<√10	<√10	<√10	<√10	<√10	<√10	<√10	<√10	<√10	<√10	<√10	<√10	<√10	<√10	<√10
0.828	52	<√10	156	<√10	<√10	<√10	<√10	<√10	<√10	<√10	<√10	<√10	<√10	<√10	<√10	<√10	<√10	<√10	<√10	<√10
1.032	32	<√10	106	<√10	<√10	<√10	<√10	<√10	<√10	<√10	<√10	<√10	<√10	<√10	<√10	<√10	<√10	<√10	<√10	<√10
2.000	<√10	<√10	22	<√10	<√10	<√10	<√10	<√10	<√10	<√10	<√10	<√10	<√10	<√10	<√10	<√10	<√10	<√10	<√10	<√10

Table 2.4: Distribution coefficients (K_d) of REEs on AG50W-X8 (200-400 mesh) resin as a function of the molarity of α-HIBA eluent.

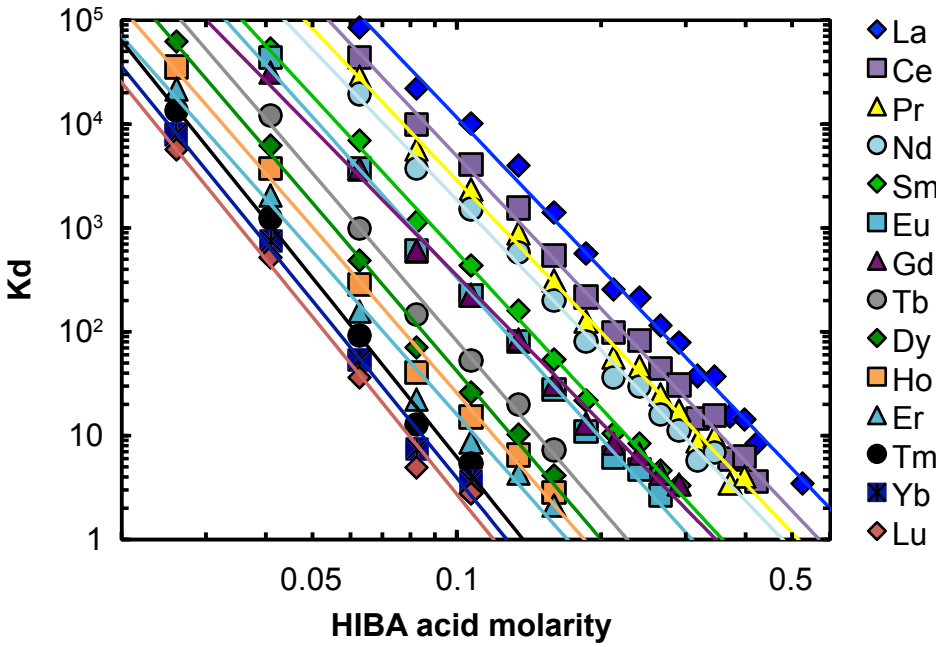

Figure 2.7: Distribution coefficients (K_d) of REEs on AG50W-X8 (200-400 mesh) resin as a function of the molarity of α-HIBA eluent. The solid curves are fits through the data.

Element	Equation (log form)	Slope	Err slope	y-int	Err y-int	r^2
La	y= -4.838 x log(x) -0.776	-4.838	0.095	-0.776	0.067	0.995
Ce	y= -4.885 x log(x) -1.195	-4.885	0.094	-1.195	0.068	0.995
Pr	y= -4.856 x log(x) -1.398	-4.856	0.104	-1.398	0.077	0.995
Nd	y= -4.812 x log(x) -1.543	-4.812	0.117	-1.543	0.092	0.994
Sm	y= -4.992 x log(x) -2.228	-4.992	0.090	-2.228	0.081	0.997
Eu	y= -5.142 x log(x) -2.623	-5.142	0.127	-2.623	0.117	0.995
Gd	y= -4.703 x log(x) -2.163	-4.703	0.138	-2.163	0.124	0.992
Tb	y= -5.373 x log(x) -3.465	-5.373	0.233	-3.465	0.250	0.993
Dy	y= -5.383 x log(x) -3.763	-5.383	0.176	-3.763	0.204	0.995
Ho	y= -5.308 x log(x) -3.899	-5.308	0.204	-3.899	0.237	0.993
Er	y= -5.214 x log(x) -4.013	-5.214	0.256	-4.013	0.296	0.988
Tm	y= -5.738 x log(x) -4.946	-5.738	0.253	-4.946	0.321	0.994
Yb	y= -5.672 x log(x) -5.081	-5.672	0.298	-5.081	0.377	0.992
Lu	y= -5.676 x log(x) -5.241	-5.676	0.344	-5.241	0.435	0.989

Table 2.5: Linear regression statistics for determination of REE K_d's as a function of α-HIBA molarity at room temperature.

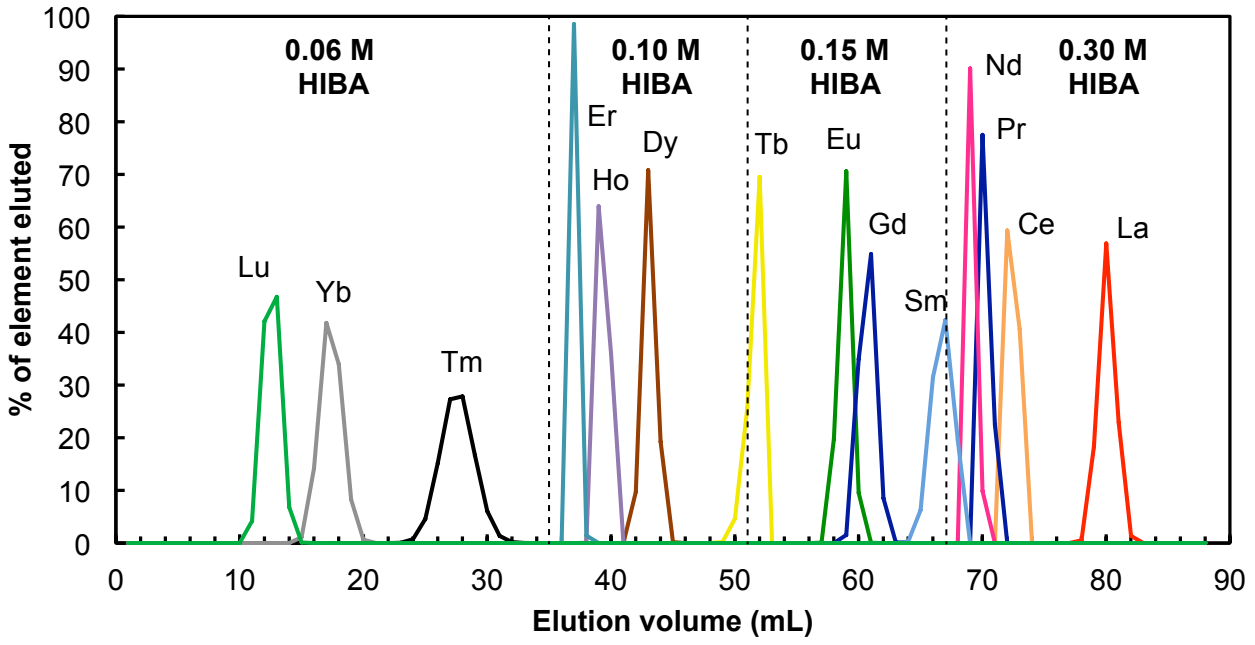

Figure 2.8: Results of simulated elution of the REEs on AG50W-X8 (200-400 mesh) cation exchange resin with α-HIBA as the eluent, and a simple step elution.

resin used in combination with HIBA was determined by adjusting the value of the HETP to fit elution profiles. The $\mathrm{HETP}_{\mathrm{HIBA}}$ value was found to be ~ 0.5 mm, in agreement with the value of 1 mm or less found by [80]. Elution simulations were then carried out to try to optimize the REE separation. Figure (2.8) shows an example of a simple step elution where most REEs are separated from one another.

Though the elution presented in Fig. (2.8) is relatively short (only 85 mL), three complicating factors make such an elution a real challenge: (i) the α-HIBA eluent tends to stick to Teflon, and the HIBA chemistry is therefore typically carried out in glass columns, which are fragile, (ii) when the chromatography is gravity-driven, the flow rate is extremely slow ($\sim$ 1 ml per hour), which means that the elution on Fig. (2.8) would require 85 hours to complete, and (iii) any air bubble passing through the column would preclude the separation, as parts of the resin will not rewet upon new addition of acid. This last point prevents the use of any vacuum system to accelerate the elution (as the suction can partially dry off the resin), leaving pressurization as the only option. After several failed attempts during which the glass columns broke because the walls of the columns were too thin to stand the pressure (1.7 mm), custom-designed columns were ordered. These columns have thicker walls (3 mm), and a plastic screwing cap on the top of the column that also plays the role of tube fitting, allowing for easy attachment of a nitrogen gas line and pressurization of the system. Application of a small pressure ($\sim$ 15 psi) increased the flow rate by a factor 30 ($\sim$ 1 ml per 2 min). A typical elution obtained using a pressurized glass column is presented in Fig. (2.9b), together with the corresponding elution simulation (Fig. 2.9a). The Lu peak elutes at the right position, but the Lu and Yb peaks are 3 times broader than expected. Furthermore, though both peaks are roughly Gaussian in shape, some unexpected second order oscillations are present, which most likely testify to non-equilibrium behavior within the column. Some more tests using lower pressure levels were carried out. At $\sim$ 5 psi, no oscillations are present, but the flow rate is still very low ($\sim$ 1 ml per 12 ml), and the elution presented on Fig. (2.8) would still require 17 hours to complete.

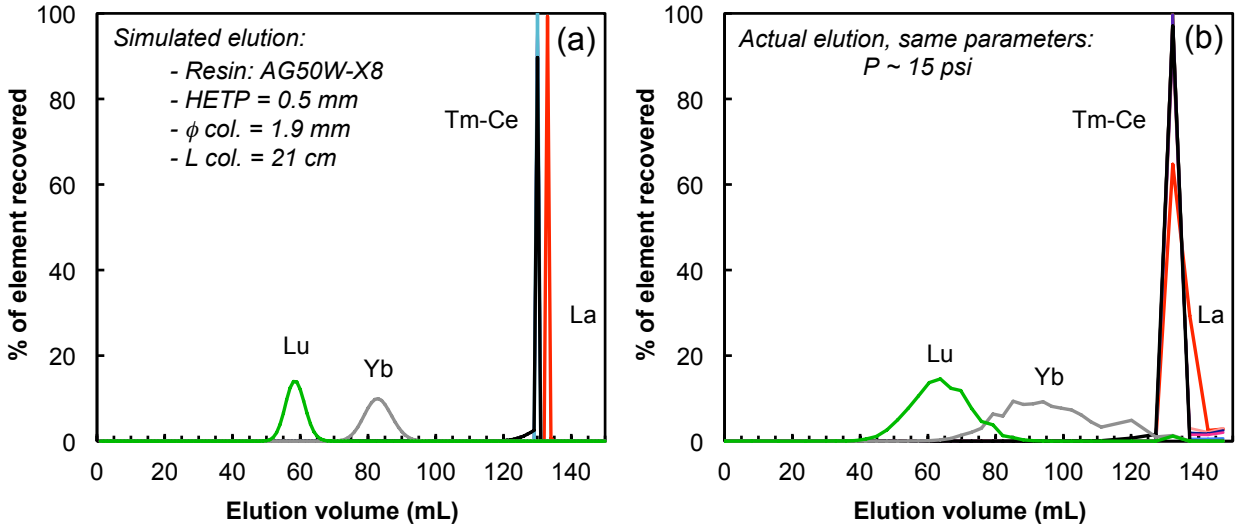

Figure 2.9: Simulated (left) and actual elution (right) of REEs on AG50W-X8 resin, using 130 mL of 0.060 M HIBA followed by a 20 mL rinsing step with 0.3 M HIBA. The quartz columns used were 21 cm long, with internal diameter of 1.9 mm. In the actual elution, the column was pressurized to $\sim$ 15 psi using N_2.

Even though 17 h is a *reasonable* time for a non-automated chromatography, the impossibility to precisely estimate the molarity of the HIBA solution makes the calibration work extremely arduous. In Fig. (2.8), the 0.060 M HIBA step can theoretically separate Lu from Yb with less than 1 % of the Lu in the Yb cut. However, if the molarity of the acid is 10 % higher (0.065 M HIBA), the amount of Lu in the Yb cut will jump to $\sim$ 25 %. Four HIBA solutions of expected concentrations ranging from 0.060 M to 0.075 M HIBA (by 0.005 M increment step) were prepared and used to calibrate the first step of the elution scheme presented in Fig. (2.8). The results of these tests are shown in Fig. (2.10). Very good separation was obtained for a minimal elution volume with the 0.065 M solution (Fig. 2.10b), resulting in less than 0.1 % of the Lu eluting in the Yb cut (resolution $R = 1.14$).

Despite the good separation obtained for Lu and Yb in this calibration, attempts at separating the full spectrum of REEs from one another using AG50W-X8 and α-HIBA solution was not pushed further, and for several reasons: (i) the theoretical optimal separation achievable with HIBA is not as good as the one using Ln-Spec resin, (ii) the calibration work is extremely time consuming (as can be seen above), (iii) the chromatography procedure

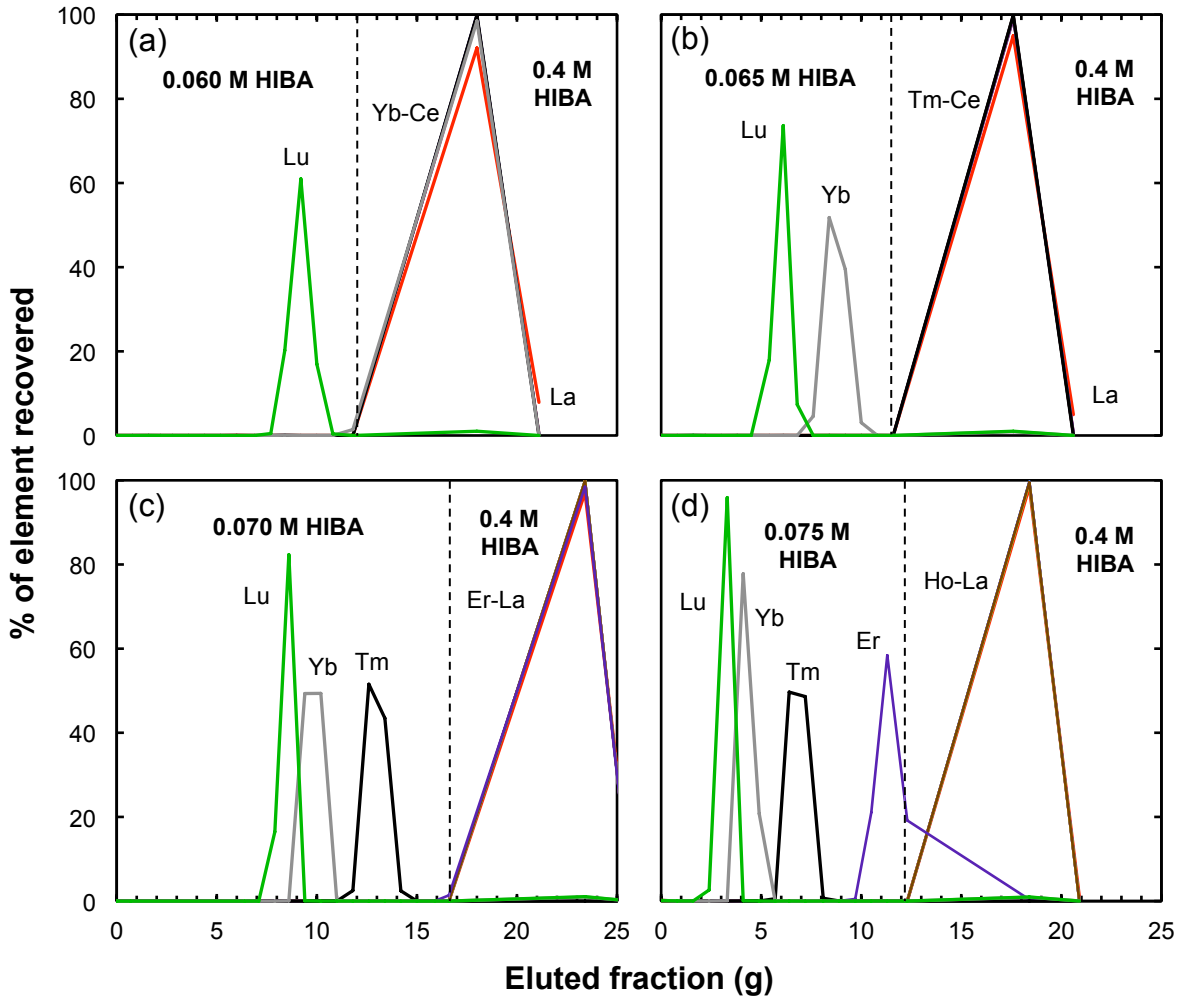

Figure 2.10: Gravity-driven REE elution on AG50W-X8 resin, using 0.060 M (a), 0.065 M (b), 0.070 M (c) and 0.075 M (d) HIBA followed by rinsing with 0.4 M HIBA. Small molarity differences lead to widely different separations. Same quartz columns as in Fig. (2.9).

remains very time consuming, with or without pressurized columns, and (iv) when applying the Lu-Yb separation protocol to a few geostandards, it was found that the effectiveness of the separation is sensitive to very slight variations (less than 10 %) in the diameter of the glass columns as well as the amount of residual matrix elements in the loading solution, leading to variations in the recovery yield of Yb from 99 % down to 6 %. In the face of these observations, it was decided to focus on the development of the PF-HPLC system.

2.2.9.2 REE separation using Ln-spec resin and the PF-HPLC system

The lanthanide-specific resin (Ln-Spec) from Eichrom, is a cation exchange resin which uses the di (2-ethylhexyl) orthophosphoric acid (or HDEHP), of formula $(CH_3\text{-}(CH_2)_3\text{-}CH\text{-}(C_2H_5)\text{-}CH_2O)_2$ POOH, as the extractant bound to the stationary phase. To enhance the separation, the smallest bead size available was used ($25 - 50$ μm). The resin was initially cleaned using 50 mL of 10 M HCl and then conditioned with 30 mL of 0.05 M HCl. To test the performances of the PF-HPLC, a multi-element REE solution was prepared, containing 10 μg/g of each REE, as well as Sc and Y (which behave similarly to the REEs).

The chromatography simulation program was used to optimize the separation. Determination of the HETP for Ln-resin ($\sim 2.0 \pm 0.5$ mm) was done using the K_d values measured by [222], and by adjusting the HETP value until simulated elution patterns fit published elution curves obtained on Ln-resin [339, 6]. This value is in good agreement with earlier studies reporting estimates between 2 to 4 mm [93, 406]. Using the above value of HETP, the K_d values of the REEs, a resin density of 1.15 g/mL, and a porosity of 67 % (also called FCV – free column volume – and equal to the free volume in mL per mL of packed resin, [216]), elution patterns of the REEs were simulated for various ramps of HCl molarity (Fig. 2.11).

The molarity ramps are calculated using the following arbitrary function:

$$D(v) = M_r \times \left[1 - \frac{\frac{1}{e^{\left([v/v_f]^p\right)}} - 1/e}{1 - 1/e} \right] + M_i \tag{2.10}$$

where v_f is the total elution volume, M_r the range of molarity spanned during the elution, M_i the initial molarity of the ramp, and v the eluted volume. p is a curvature parameter that can vary from 0 to ∞. A small value of p (below 0.5) leads to a very rapid molarity increase at the beginning of the elution while a large value of p (above 3) leads to a slow molarity increase at the beginning of the elution (Fig. 2.11). A p value of ~ 1.4 corresponds to an

essentially linear molarity increase with elution volume. Figure (2.11) shows a set of molarity ramps (left panels) and their corresponding simulated elution of the 14 REEs + Yttrium (right panels). As can be seen, when separating the REEs, the elution scheme (*i.e.*, shape of the ramp) is a crucial parameter to optimize in order to obtain the best separation of the elements in the minimum volume of elution. The bottom panels show the best optimized elution ramp and separation pattern, obtained for $M_i = 0.1$, $M_r = 10$, $v_f = 700$ mL and $p = 4$.

This best optimized elution ramp, starting at 0.1 M HCl and increasing to 10 M HCl, was implemented into the LabView program, which controls the PF-HPLC, as a series of 176 steps of 4 mL each. A 70 cm long column (diameter of 3 mm) was filled with Ln-resin with $25 - 50$ μm resin bead size. The experiment was conducted at 70°C with the pressure in the mixing chamber adjusted to provide a flow rate of ~ 0.5 mL/min. The whole elution scheme was automated. Each mixing step involved a total of 4 mL of reagents, and the eluted solution was collected in either 2 mL or 4 mL increments, depending on when elements were predicted to elute. In total, 680 mL of solution were collected over a period of 15 h. These solutions were subsequently evaporated to near-dryness and then picked up in 0.46 M nitric acid for analysis on the Neptune MC-ICP-MS.

Figure (2.12) shows a plot of the desired molarity ramp as defined by Eq. (2.10), along with the molarity of the elution steps as calculated by the LabView program and several intervals where titration of the eluted solution was carried out to check the solution molarity. This figure demonstrates that the PF-HPLC system is very effective and accurate at controlling reagent mixing and molarities.

The results of the elution itself are plotted in Fig. (2.13). There is some overlap of mono-isotopic REEs with neighboring multi-isotopic REEs (*e.g.*, Pr overlaps with Nd), but this is not a big concern since there are no isobaric interferences between these isotopes. In addition, there is some dissimilarity between the elution curve from Fig. (2.13) and the simulated elution curve from Fig. (2.11), although the broad shapes of each curve, and the

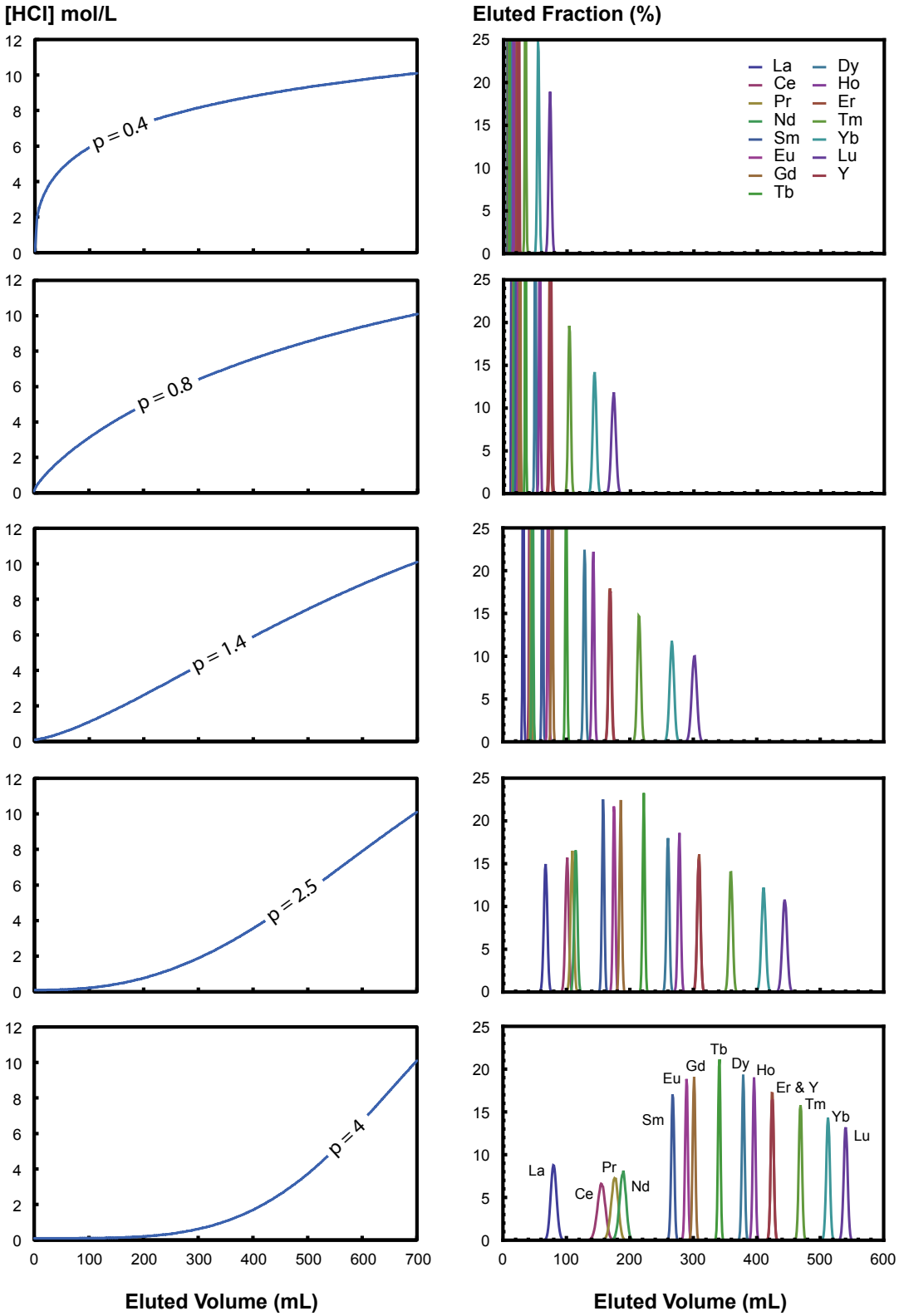

Figure 2.11: Results of simulated elution of the REEs on Ln-Spec resin obtained using various ramps of HCl molarity. See text for details. Figure published in [222].

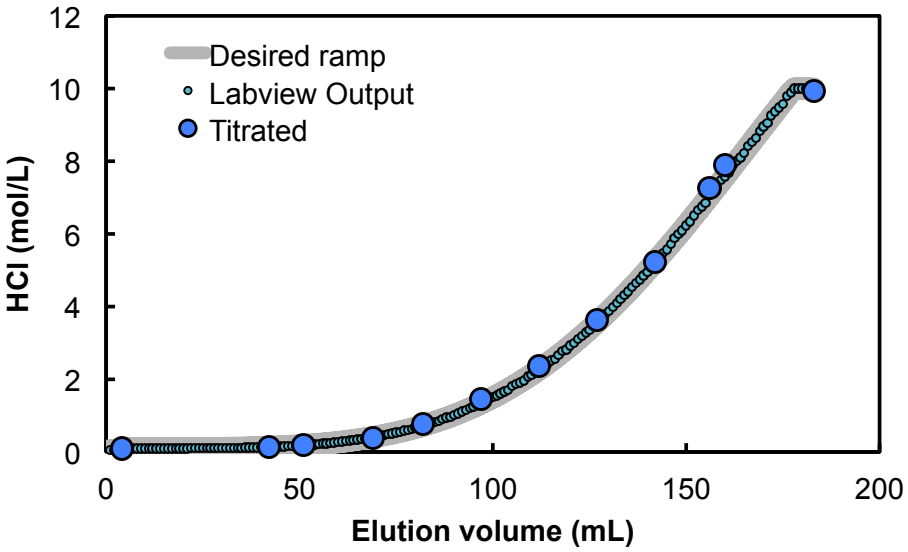

Figure 2.12: Comparison of the desired elution ramp (gray line), as modeled by the elution simulation, and molarity of the elution steps as calculated by the LabView program which controls the PF-HPLC (small blue dots). Several elution steps were titrated during the experiment to test the accuracy of the PF-HPLC system. The excellent agreement between these curves illustrates the effectiveness and reliability of the acid pumping and mixing system. Figure published in [222].

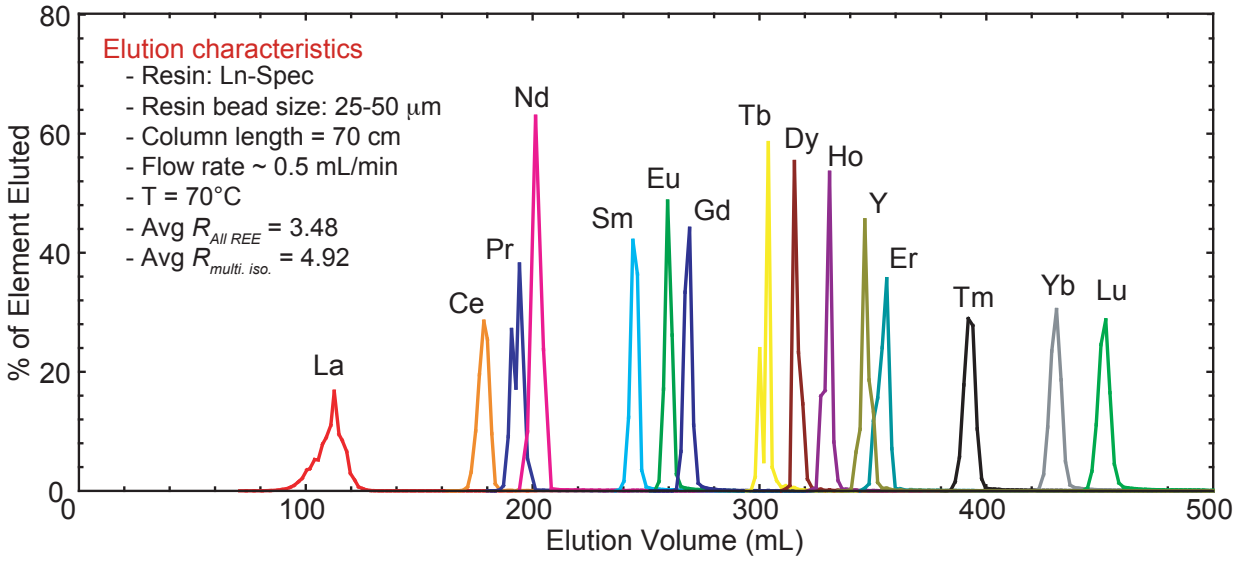

Figure 2.13: Elution curve for the separation of the REE as a function of the volume eluted. There is very good to excellent separation of all the multi-isotopic REE (La, Ce, Nd, Sm, Eu, Gd, Dy, Er, Yb, and Lu) from one other, demonstrating the effectiveness of the first version of the PF-HPLC system. The column was 70 cm long (0.3 cm diameter) and utilized Ln-resin at $25-50$ mesh size, at a temperature of 70°C. Figure published in [222].

relative placement of the elution peaks, are consistent with each other. The slight discrepancy may be attributed to uncertainties in the experimentally determined K_d values and/or to the fact that the K_d values used in the simulation were determined at room temperature, while the PF-HPLC experiment was run at 70°C. Conversion factors for the differences between the Kd at 70°C versus those at room temperature are given in [222], and range from 1.38 for La to ~ 0.83 for Dy to Lu.

Most importantly, however, the PF-HPLC system achieved excellent separation of the multi-isotopic REEs (La, Ce, Nd, Sm, Eu, Gd, Dy, Er, Yb and Lu) from each other – a result that is difficult to obtain with current techniques. Of particular interest, there is strong separation of Nd from both Ce and Sm, which is a key factor for studies concerned with the Sm-Nd isotopic systems. The resolution factor R for each elemental couple is shown in Table 2.6. The average resolution for all REEs is 3.48, while resolution for the multi-isotopic REEs is 4.92. For comparison, the best average resolutions obtained by previous studies are 2.6 and 3.04, respectively [329, 330, 93, 406, 80, 276, 401]. Furthermore, the individual and average resolutions obtained experimentally are in very good agreement with the theoretical expectations from simulated elution, which shows that the estimate of the HETP value determined for the Ln-Spec resin is robust, and constant throughout the entire elution. Admittedly, fifteen hours is a long amount of time for a single column; however, most of the procedure is done automatically. From the above results, it is clear that the PF-HPLC system constitutes a vast improvement relative to current techniques, as it allows for superior separation of the elements, while meeting the chemical resistance standards of isotope chemistry.

2.2.10 PF-HPLC blank, tailing and future improvements

A major concern with any new geochemical method, especially those that require large volumes of reagents, is the analytical blank. There are two main potential sources of blank contamination in an HPLC setup, the first from the reagents being used and the second from

Comparison of the resolution factors for adjacent REEs using various resins, eluents, column configurations and HPLC systems.

Study	P&P 1962	Pierce et al. 1963	Cerrai et al. 1963	S&S 1964		Campbell 1973		Matsui et al. 1981	Sivaraman et al. 2002	This work 2013	
Column material	Pyrex	Pyrex	Pyrex	?		Glass		Glass	?	PTFE	
Pressure	?	?	?	?		Up to 800 psi		#N/A	#N/A		60 psi
Stationnary phase	HDEHP	HDEHP	HDEHP	HDEHP		AG50W-X8		Cation exch.	HDEHP	HDEHP	HDEHP
Eluent	HClO4	HClO4	HCl	HCl	HNO3	HIBA		HIBA	HIBA	HCl	HCl
Temperature	60°C	60°C	85°C	?		80°C		60°C	?	Room T	70°C
Column height (mm)	120	120	140	100		330		300	250	700	700
Column ID (mm)	5	5	3	3		9		3	4	3.175	3.175
Resin density (g/mL)										1.15	1.15
HETP (cm)										0.20	
REE pair										*Simulation*	*Experiment*
La-Ce	1.39	4.7		2.8	2.7	2.36	2.36	4.06	1.83	4.06	7.23
Ce-Pr	1.14	1.3		1.5		2.21	1.68	2.68	1.25	1.02	1.51
Pr-Nd	1.02	1.4		1.3		1.63	1.65	1.76	1.57	0.73	0.72
Nd-Sm	3.36	~4.7		~5.9	~4.8	4.38	4.10	3.94	1.29	6.10	5.38
Sm-Eu	1.27	1.8	1.83	2.2	2.1	1.72	1.53	1.56	1.50	2.83	2.20
Eu-Gd	1.07	1.5	0.90	1.5	1.7	1.23	0.71	1.12	1.63	1.41	1.49
Gd-Tb	1.74	5.2	3.55	5.0	5.5	2.33	1.85	1.91	3.18	5.69	6.53
Tb-Dy	1.40	1.9	2.00	2.6	3.0	1.22	0.53	1.59	3.00	5.38	2.73
Dy-Ho	1.27	1.8	1.19	2.1	2.2	1.84	3.04	1.36	2.75	2.30	3.41
Ho-Er	1.23	2.7	1.68	2.8	2.7	1.43	1.45	1.85	2.41	3.91	4.13
Er-Tm	1.96	3.3	2.44	3.4	3.5	1.90	0.71	1.54	1.89	5.36	3.96
Tm-Yb	1.85	2.2	1.81	2.8	3.1	1.82	1.16	1.43	1.30	4.63	3.79
Yb-Lu	1.00	1.8	0.98	1.9	1.9	1.58	0.70	1.00	0.96	2.56	2.17
All REEs avg.	**1.51**	**2.6**	**1.82**	**2.8**	**3.0**	**1.97**	**1.65**	**1.99**	**1.89**	**3.54**	**3.48**
Ce-Nd	2.31				1.55	4.41	3.32	4.69	2.60	1.75	2.46
Nd-Sm	3.36					4.38	4.10	3.94	1.29	6.10	5.38
Gd-Dy	3.10		5.33			3.56	2.34	3.97	6.00	10.17	8.10
Dy-Er	2.34		2.90			4.15	3.33	3.28	4.99	5.97	6.69
Er-Yb	3.58		4.39			3.96	1.70	3.08	3.00	10.06	8.58
Multi-isotopic avg.	**2.16**		**2.72**			**3.04**	**2.23**	**2.97**	**2.64**	**4.99**	**4.92**

NB: Values preceded by a "~" sign are calculated using the resolution of the Nd-Pm and Pm-Sm couples, and assuming that the Nd, Pm and Sm peaks have similar widths.

Table 2.6: Comparison of the resolution factors for adjacent Rare Earth Elements using various resins, eluents, column configurations and HPLC systems.

the resin. To minimize the blank from reagents, only acid distilled multiple times through quartz and Teflon stills was used. Additionally, purified water from a Milli-Q system, with a resistivity of 18.2 MΩ/cm, was used as the diluent. This careful preparation of reagents, as well as the internal monitoring of blank levels over time, can help ensure that there is a minimal contribution from these sources.

To address the potential blank contribution from the resin, a couple of cleaning steps were implemented prior to the column chemistry. First, loose resin ($\sim$ 25 to 50 g) was poured into a 1 L precleaned PFA bottle, containing 6 M HCl. This solution was shaken vigorously throughout the day, and allowed to settle overnight. The following morning, the acid was decanted, the resin was rinsed with MQ water, and the process was repeated. After this

step, the resin was stored in MQ and ready for use. After loading the resin into a column, an additional cleaning step was employed, as 50 mL of 10 M HCl were eluted through the system. This should remove any REE that may still be present because the K_d of the REEs on Ln-resin at high HCl molarities is very low.

A complete system blank was evaluated by running the elution scheme outlined in Fig. (2.12) through the PF-HPLC system, without a loading step. In this manner, a total of 670 mL of solution was collected, and was subsequently evaporated to near-dryness and picked up in 0.46 M HNO3 for analysis on the ICP-MS. Table 2.7 shows the concentrations of REE blanks measured on the PF-HPLC system, and a comparison of this blank with REE levels in CI chondrites [340]. The measured system blanks range from 100 pg for Nd up to a high of 1481 pg for Ce, although blanks for individual elution steps would be reduced. Improvements on this value can easily be made in the future by (i) cleaning further the reagents and (ii) decreasing the diameter of the column to reduce the volume of acids and resin used. If 1 g of an average CI chondrite is dissolved and run through the PF-HPLC system, this system blank would represent less than 0.5 % for most of the REE.

A noted concern with utilizing Ln-resin is a tailing effect of elution peaks that can often be observed as acid molarity is increased [357, 331, 269, 205]. The small-step gradient ramp employed with the PF-HPLC system reduced this tailing significantly, compared to previous attempts using an open system column with broad molarity steps, but did not eliminate it. When the elution percent axis is viewed on a log scale, this tailing effect is readily apparent. The last $\sim$ 0.25 to 0.75 % of each REE has a long drawn-out tail that intersects the elution peaks of the other REE (Fig. 2.14). Such tails could have fractionated isotopic composition. Whether this is a problem during isotopic analysis remains to be tested.

The results presented above were obtained using a $1/8^{\text{th}}$ inch ID column and the first iteration of the PF-HPLC (before pneumatic actuation was implemented, Fig. 2.5a). Improvements have been made to the system since then. Notably, finer columns can be mounted onto the system. In the third iteration of the PF-HPLC system, columns of ID down to

	CI chondrite concentration[a] (ng/g)	Total system blank (pg)	Blank % of sample[b]
La	246.9	783	0.32
Ce	632.1	1481	0.23
Pr	95.9	149	0.16
Nd	485.4	116	0.02
Sm	155.6	330	0.21
Eu	59.9	617	1.03
Gd	209.3	882	0.42
Tb	37.8	495	1.31
Dy	257.7	514	0.20
Ho	55.4	368	0.66
Er	166.7	357	0.21
Tm	26.1	238	0.91
Yb	169.4	286	0.17
Lu	25.6	169	0.66

[a] Data from [340].
[b] For 1 g of CI chondrite sample.

Table 2.7: Evaluation of PF-HPLC system blank. Table published in [222].

$1/16^{\text{th}}$ inch can be used. As the diameter of the column is reduced, the flow decreases (for a constant flow driving pressure), leading to little change in elution time. This factor 2 reduction in the ID of the column, however, will lead to a factor 4 reduction in the elution volume for a given chromatographic separation. In the case of the REE (Fig. 2.13), the total volume needed will decrease from 680 mL to 170 mL. This will greatly help in reducing the system blank. The introduction of an all-plastic sample injection loop (Fig. 2.3) and X-Y-stage (Fig. 2.4) will also help in keeping the blanks lower than in the original version of the system, where metal and electronics were still in close proximity to the flow path at these two key places.

Overall the development of the PF-HPLC represents a major step forward for isotope chemistry as the effectiveness and the robustness of the system enable even the most difficult of column chromatography separations.

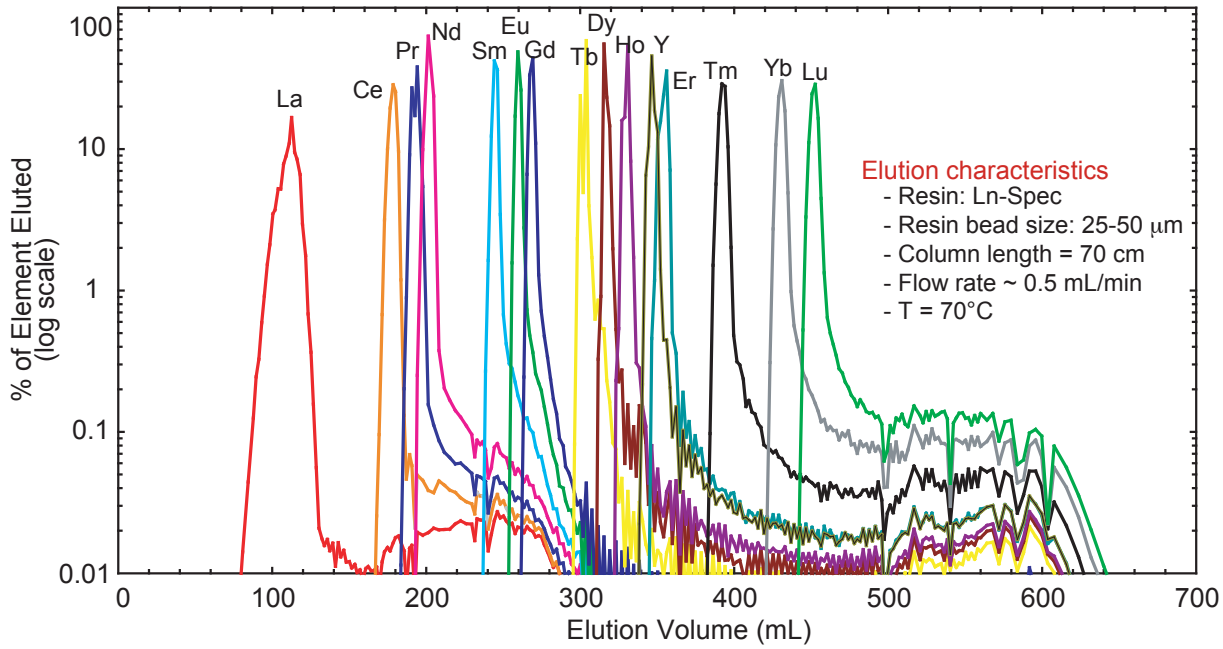

Figure 2.14: Elution curve from Fig. 2.13 with the y-axis on a logarithmic scale. Note the long tails of each REE, which intercept the elution curves of the other REE. This tailing accounts for 0.25 to 0.75 % of each element. Figure published in [222].

2.3 Purification protocol of U on U/Teva resin

Unlike the separation of REEs, the elemental purification of U can be easily performed using traditional open-column techniques, in combination with a vacuum box. This is due to the existence of a series of actinide specific resins such as the Diphonix resin, Tru resin, Teva resin or U/Teva resin (from Eichrom). In this work, the "Uranium and Tetravalent Actinide specific" resin, named U/Teva [215], was used. It is an extraction chromatographic resin that uses the diamyl, amylphosphonate, $C_{15}H_{33}O_3P$, (DAAP) as the extractant coating the inert polymeric stationary phase. The DAAP forms nitrato complexes with the actinide elements, and the formation of these complexes is driven by the concentration of nitrate in the sample solution (*i.e.*, the uptake of the actinides increases with increasing nitric acid concentration).

Below, the behavior of major and minor elements on the U/Teva resin is presented, followed by the details of the elution scheme used to purify the U fraction before mass

spectrometric analysis (Section 2.3.1 and 2.3.2). All Teflon labware used was precleaned with boiling aqua regia (3:1 mixture of HCl:HNO_3) three times, followed by boiling MQ water. Single element ICP-MS standard solutions (Spex CertiPrep) at concentrations of 1000 ± 5 μg/mL were used for all concentration measurements. Pre-packed, 2 mL cartridges containing U/Teva resin (particle size $50 - 100$ μm) were purchased from Eichrom.

2.3.1 Distribution coefficients of elements on U/Teva resin

To optimize the chemical separation on U/Teva resin, the partition coefficients for U and fifteen other elements (Na, Mg, Al, Ca, Sc, Ti, Fe, Ni, Y, Zr, Sn, La, Yb, Hf, Th) were measured in HNO_3, HCl and HCl + 0.1 M oxalic acid (Table 2.8 and Fig. 2.15). Calibration of the elution curve was done using the same set of elements, plus K and Gd (Table 2.9 and Fig. 2.16). As the age and repeated use of the resin are known to affect the partition coefficients [250], all tests were done on unused resin less than a year old (maximum duration for which the partition coefficients are certified by Eichrom).

As already explained in Section 2.2.4, the distribution coefficient (K_d) quantifies the partition of an element between the acid solution (mobile phase) and the extractant (stationary phase), and is defined as:

$$K_d = \frac{C_{\text{solid}}}{C_{\text{solution}}} \tag{2.11}$$

where C_{solid} is the concentration of element bound to the resin, in micrograms per gram of dry U/Teva resin, and C_{solution} is the concentration of ions, in micrograms per mL of solution, which remains in solution after equilibration is established between the acid and the resin.

Single element standards are commercially available in combinations of dilute HF, H_2O_2, HCl, HNO_3 and $C_4H_6O_6$ (tartaric acid) solutions. Potential modification of the partition behavior of elements in U/Teva resin could occur if these acids were present in the mobile phase during the resin-solution equilibration. In order to avoid this problem, aliquots (5 mL

Distribution coefficients[a] (K_d) on U/Teva resin as a function of acid molarity for HNO_3, HCl and HCl + Oxalic acid 0.1 mol/L.

Element	Molarity HNO_3 (M)																		
	0.10	0.20	0.40	0.66	1.03	1.53	2.00	3.09		4.11		5.23	6.18	7.31	8.23	9.5	12.23	15.45	
Sc	<15	<15	<15	<15	<15	<15	<15	15.7	17.3	18.8	19.2	<15	<15	<15	<15	22.5	103	589	611
Ti	<15	17.7	<15	<15	<15	<15	<15	<15	<15	<15	<15	<15	<15	<15	<15	<15	26.6	110	117
Y	<15	<15	<15	<15	<15	<15	<15	<15	<15	<15	<15	<15	<15	<15	<15	<15	<15	41.1	42.6
Zr	23.4	37.6	<15	<15	<15	<15	16.4	20	21.6	58	58	121	358	851	2210	4872	3394	575	574
Yb	<15	<15	<15	<15	<15	<15	<15	<15	<15	15.1	15.5	<15	<15	<15	<15	<15	26.1	75	78
Hf	40.1	71	<15	<15	<15	<15	<15	<15	<15	24.8	24.1	23.5	72	210	605	1710	792	113	120
Th	<15	<15	<15	15.6	36.8	66	136	229	243	388	383	385	562	555	521	544	392	192	213
U	<15	15.9	85	119	191	243	402	559	606	829	827	710	749	607	385	332	263	200	223
Fe	<15	<15	<15	<15	<15	<15	<15	<15	<15	<15	<15	<15	<15	<15	<15	<15	31.9	2039	470
Sn	94	72.2	<15	<15	<15	<15	<15	<15	<15	<15	<15	<15	<15	<15	<15	<15	23.2	78	32.6

Elements with $K_d < 15$ for most molarites: Na, Mg, Al, Ca, Ni and La

Element	Molarity HCl (M)														
	0.10	0.20	0.40	0.64	1.02	1.50	2.01	3.02	4.13	5.03	6.05	7.08	8.13	9.13	11.38
Sc	<15	<15	<15	<15	<15	<15	<15	<15	<15	17.3	86	1090	7137	>10^4	>10^4
Ti	<15	<15	<15	<15	<15	<15	<15	<15	<15	<15	<15	<15	51	130	602
Zr	68	83	34.2	59	55	30.5	64	45.3	27.4	49.1	235	2692	>10^4	>10^4	>10^4
Hf	82	220	64	109	64	33.2	70	47.8	29.3	50	160	1168	>10^4	>10^4	>10^4
Th	<15	<15	<15	<15	<15	<15	<15	<15	<15	<15	<15	33.2	134	470	602
U	<15	<15	<15	<15	<15	<15	19.5	69	162	304	415	409	307	195	65
Fe	<15	<15	<15	<15	<15	<15	65	894	7291	>10^4	>10^4	>10^4	>10^4	>10^4	>10^4
Sn	<15	<15	61	148	312	830	1810	>10^4	8179	>10^4	>10^4	8641	752	522	61

Elements with $K_d < 15$ for most molarites: Na, Mg, Al, Ca, Ni, Y, La and Yb

Element	Molarity HCl M + Oxalic acid 0.1 M																	
	0.11	0.13	0.16	0.19	0.30	0.49	0.75	1.11	1.59	2.10	3.10	4.20	5.19	6.10	7.10	7.95	8.80	10.85
Sc	<15	<15	<15	<15	<15	<15	<15	<15	<15	<15	<15	<15	<15	57	817	3772	6686	>10^4
Ti	<15	<15	<15	<15	<15	<15	<15	<15	<15	<15	<15	<15	<15	<15	<15	23.0	55	535
Zr	<15	<15	<15	<15	<15	<15	<15	<15	<15	<15	<15	<15	<15	<15	<15	194	4701	>10^4
Hf	<15	<15	<15	<15	<15	<15	<15	<15	<15	<15	<15	<15	<15	<15	15.9	134	1971	>10^4
Th	<15	<15	<15	<15	<15	<15	<15	<15	<15	<15	<15	<15	<15	<15	<15	54	153	417
U	<15	<15	<15	<15	<15	<15	<15	<15	<15	19.4	45.9	107	223	316	342	331	241	62
Fe	<15	<15	<15	<15	<15	<15	<15	<15	<15	<15	125	2849	>10^4	>10^4	>10^4	>10^4	>10^4	>10^4
Sn	<15	<15	<15	<15	<15	26.4	65	133	267	435	1308	2524	4442	6515	2725	1859	584	79

Elements with $K_d < 15$ for most molarites: Na, Mg, Al, Ca, Ni, Y, La and Yb

[a] NB: Only values between 15 and 10^4 are reported because of limitations with the experimental set up.

Table 2.8: Distribution coefficients (K_d) on U/Teva resin as a function of acid molarity for HNO_3, HCl and HCl + Oxalic acid 0.1 mol/L. Table published in [431].

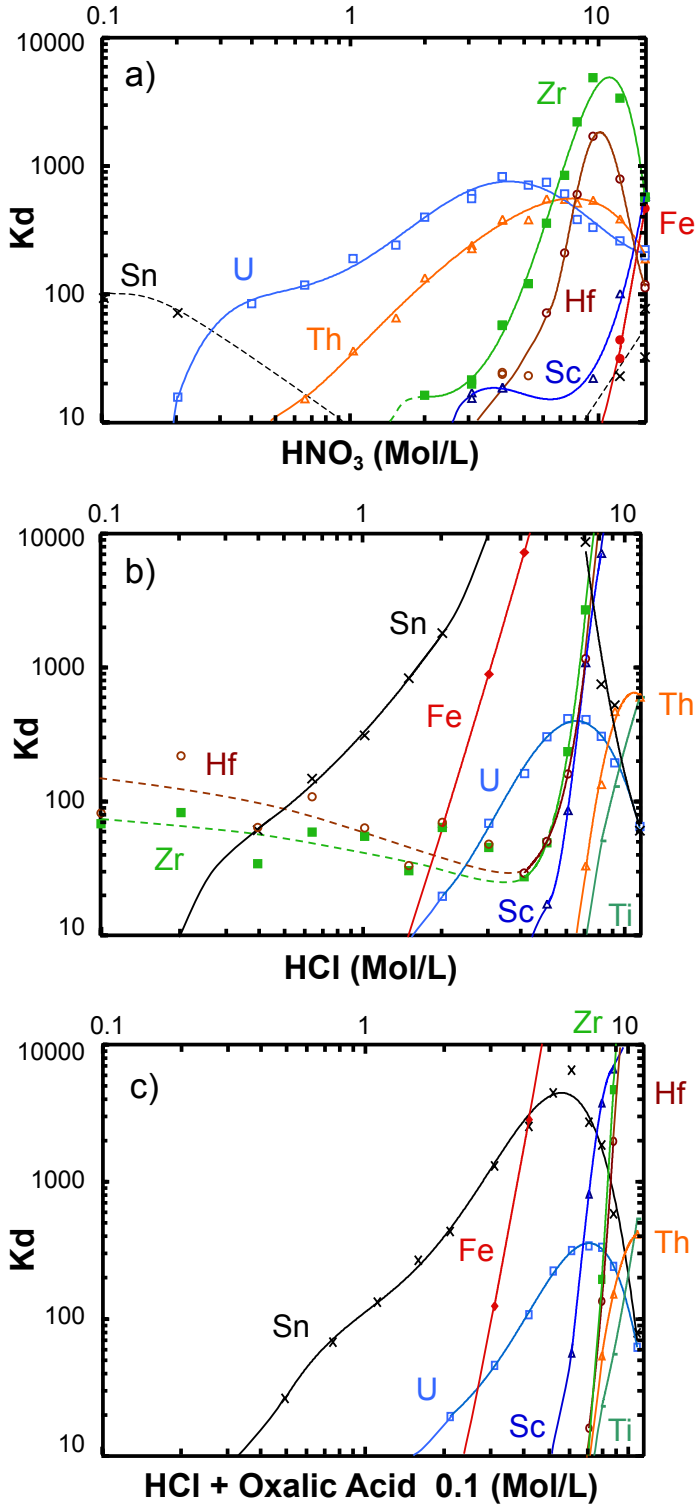

Figure 2.15: Distribution coefficients (K_d) of selected elements on U/Teva resin as a function of acid molarity in (a) HNO_3, (b) HCl and (c) HCl + Oxalic acid 0.1 M. The solid curves are polynomial fits to the data. Figure published in [431].

for major elements Na, Mg, Al, Ca, Ti, Fe, Ni, and 0.5 mL for minor elements Y, Sc, Zr, Sn, La, Gd, Yb, Hf, Th, U) of commercially manufactured standard solutions (1000 μg/mL) were transferred to a precleaned, 35 mL Savillex Teflon-PFA beaker and the mixture was evaporated to dryness. Right before complete evaporation, the residual droplet was taken back into 2 mL of 1 M HNO_3. The process was repeated three times to ensure complete removal of other acids. In the last step, 50 mL of 1 M HNO_3 was added to the beaker and transferred to a centrifuge tube. Particles visible to the naked eye were present in the solution, which were removed by centrifugation. Energy-dispersive microanalysis done with a scanning electron microscope (SEM-EDX) showed that the residue was made of Ti, Fe, Sn and Hf. An aliquot of the solution remaining after particle removal was analyzed by MC-ICPMS. All elements added to the standard, except Gd (not reported), were detected at levels at least one order of magnitude above blank solutions (1 M HNO_3). One third of the standard solution investigated was then sampled and saved for batch experiments in HNO_3 acid (50 ppm and 5 ppm for major and minor elements, respectively), and the remaining two thirds was dried down and taken back in 1 M HCl three times before final dissolution in 33 mL of 1 M HCl (50 ppm and 5 ppm for major and minor elements, respectively).

A fixed amount of the standard solution containing the 16 elements investigated was dried down into Teflon beakers, taken back into 2 mL of acid at a given molarity (from 0.1 to 15 mol/L for HNO_3; from 0.1 to 11 mol/L for HCl; and from 0.2 to 11.1 mol/L for HCl + 0.1 M oxalic acid, hereafter HCl + 0.1 M Ox), dried again and taken back into 6 mL of the same acid. A 1 mL aliquot was taken and saved for each sample, providing a standard for normalization. The remaining 5 mL were then equilibrated with 166 ± 1.8 mg (about 0.5 mL) of dry U/Teva resin (particle size $50 - 100$ μm). The element to resin ratio was 300 μg per g of resin for major elements (Na, Mg, Al, Ca, Ti, Fe, Ni) and 30 μg per g of resin for minor elements (Y, Sc, Zr, Sn, La, Yb, Hf, Th, U). The resin and the acid-standard solutions were stirred by placing the vials on a Thermoline Vortex shaker (1000 rpm) for $5 - 10$ min every 2 h. After 8 h of equilibration, the mixture was filtered using precleaned 10 mL Bio-Rad

Poly-Prep chromatography columns, to separate the resin from the mobile phase. The acid solutions were collected in centrifuge tubes and transferred back into cleaned Teflon beakers. Molarities of the equilibrated solutions (samples) and the unequilibrated aliquots (standards) were adjusted to $\sim$ 1 M HNO_3. The volume was adjusted so the standards contained $\sim$ 1 ppm and 0.1 ppm of the major and minor elements, respectively. A similar dilution was done on the samples (*i.e.*, if the resin has no affinity for an element, its concentration will be the same in the equilibrated sample and in the standard). Samples (and standards) in HCl and HCl + 0.1 M Ox were dried down, taken back into 2 mL of 1 M HNO_3, dried once more and finally taken back into 1 M HNO_3, while the molarity and concentration of the samples (and standards) in HNO_3 were adjusted to reach a final molarity of 1 M HNO_3 by adding directly one or several of the following: concentrated HNO_3, 1 M HNO_3 and Milli-Q water.

Concentration measurements were performed on a ThermoFinnigan Neptune MC-ICP-MS at the Origins Lab of the University of Chicago. The 1 M HNO_3 solutions were introduced into the Neptune using a 100 μL/min PFA Teflon self-aspirating nebulizer. A combined quartz cyclonic and Scott-type spray chamber (Stable Introduction System from ESI) was used for measuring all distribution coefficients. Measured isotopes were selected with preference given to higher relative abundances and absence of isobaric interferences. Instrumental drift was corrected for by bracketing every batch of three samples with a multi-element standard solution (std-smp-smp-smp-std). The procedural blank and acid contributions (generally below 1 %) were subtracted from each analysis. The following equation was used to calculate the distribution coefficients for each element (*e.g.*, μg of an element per g of resin divided by μg of an element per mL of solution):

$$K_d = \frac{(C_b/C_a - 1) \times V}{w} \tag{2.12}$$

where C_b and C_a are the elemental concentrations in micrograms per mL of solution before and after equilibration, respectively, w is the weight of dry U/Teva resin in grams and V is

the volume of acid solution in milliliters. Table 2.8 and Fig (2.15 a-c) show the partition coefficients (logarithmic scale) on U/Teva as a function of HNO_3, HCl and HCl + 0.1 M Ox concentrations. For a given concentration, a high K_d value means that the element is preferentially retained on the resin, while a low K_d indicates the release of the element to the mobile phase (acid solution).

Previously, Horwitz et al. (1992) [215] studied some of the properties of U/Teva extraction chromatography resin in slurry-packed gravity columns. This study graphically represented the number of free column volumes to peak maximum, k', also called *resin capacity factor* ($K_d = 1.7 \times k'$, see Appendix A in [431]), of five elements (Pu, U, Th, Np and Am) in HNO_3 and three (U, Th, and Np) in HCl solutions. Here, we report K_d values for 16 elements in HNO_3, HCl and HCl + 0.1 M Ox solutions. This last acid type was used by [215] to elute Np while keeping U bound to the resin, and the HCl + 0.1 M Ox experiment was performed to make sure that the change in K_d of U is indeed negligible when oxalic acid is present. The partition behaviors of U and Th on U/Teva resin are comparable between this study and that of [215] (Fig. 2.17). The small differences might be due to the fact that the earlier study used multi-element stock solutions directly, while in the present study all standards were converted to HNO_3, HCl or HCl + 0.1 M Ox prior to use. The distribution coefficients from this study presented in Table 2.8 and Figs. 2.15 and 2.17 do not show values of K_d outside of the range $15 < K_d < 10^4$ because below 15, insufficient changes in the solution concentrations occur, while above 10^4, the solution concentrations approach the limits of detection of the instrument.

2.3.2 Column chemistry

Based on the established K_d values and earlier work by [460], an elution was performed using a U/Teva prepacked cartridge (2 mL, 1.14 cm diameter, 2.56 cm length, $50 - 100$ μm particle size) and a vacuum box (Table 2.10). The flow rate was kept between 0.5 and 2 mL per minute. The results are given in Fig. (2.16) and Table 2.9. More than 99 % of the U

Elution behaviors of 16 elements on U/Teva. Values are percent eluted in each step.[a]

Elution step	Loading	Rinse				Conversion	Th + Np rinse		Oxalic Rinse	U rinse		
Reagents	3 M HNO_3	3 M HNO_3				11 M HCl	5 M HCl + 0.1 M Oxalic		5 M HCl	0.5 M HCl		
Number of column volume (2 mL)	1–5	6–10	11–15	16–20	21–25	26–28	29–33	34–38	39–43	44–48	49–53	54–58
Element												
Na	**91.49**	**8.32**	b.d.l.	b.d.l.	b.d.l.	b.d.l.	b.d.l.	0.14	0.05	<0.01	b.d.l.	<0.01
Mg	**90.76**	**8.62**	0.09	0.05	0.04	0.14	0.08	0.04	0.05	0.10	0.03	<0.01
Al	**91.22**	**8.59**	0.01	b.d.l.	b.d.l.	0.04	0.01	<0.01	0.02	0.09	<0.01	<0.01
Ca	**89.73**	**8.46**	b.d.l.	b.d.l.	b.d.l.	0.29	0.53	0.71	0.07	0.17	<0.01	0.04
Sc	**72.92**	**27.03**	0.05	b.d.l.	b.d.l.	b.d.l.	b.d.l.	<0.01	<0.01	b.d.l.	b.d.l.	b.d.l.
Ti	**89.03**	**8.43**	0.09	0.04	0.03	0.06	0.98	1.02	0.24	0.08	<0.01	0.01
Fe	**90.81**	**8.57**	0.05	0.01	<0.01	0.03	0.03	0.01	<0.01	0.39	0.05	0.04
Ni	**91.17**	**8.75**	0.04	0.01	<0.01	<0.01	<0.01	b.d.l.	b.d.l.	0.01	b.d.l.	<0.01
Y	**87.51**	**12.44**	0.05	<0.01	<0.01	<0.01	b.d.l.	b.d.l.	b.d.l.	b.d.l.	b.d.l.	b.d.l.
Zr	**59.88**	**27.83**	**10.37**	**1.44**	0.21	0.13	b.d.l.	0.01	0.02	0.05	0.05	<0.01
Sn	**90.89**	**8.55**	0.12	0.08	0.06	0.06	0.05	0.04	b.d.l.	0.14	b.d.l.	b.d.l.
La	**90.28**	**9.65**	0.04	<0.01	<0.01	b.d.l.	b.d.l.	b.d.l.	b.d.l.	0.02	b.d.l.	b.d.l.
Yb	**87.35**	**12.58**	0.04	<0.01	b.d.l.	b.d.l.	b.d.l.	b.d.l.	b.d.l.	0.02	0.01	b.d.l.
Hf	**85.28**	**14.30**	0.02	b.d.l.	b.d.l.	b.d.l.	b.d.l.	0.03	0.13	0.12	0.10	0.02
Th	0.03	<0.01	<0.01	0.03	0.11	0.06	**99.15**	0.17	0.40	0.04	<0.01	<0.01
U	<0.01	<0.01	<0.01	<0.01	<0.01	0.05	0.08	0.22	0.46	**98.91**	0.18	0.09

For each element, values in bold represent where most of the element (98%) was eluted.

[a] For each element, collected values are normalized to the fraction collected from loading to the end of the elution. The collected fraction is typically more than 97% of the calculated fraction passed onto the column.

Table 2.9: Elution behaviors of 16 elements on U/Teva. Values are percent eluted in each step. Table published in [431].

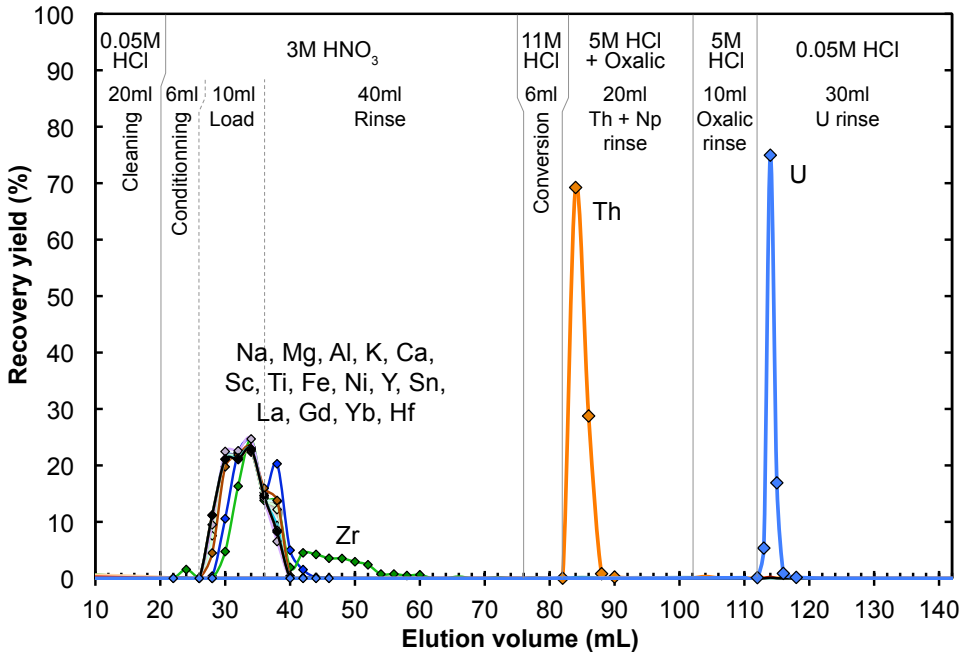

Figure 2.16: Elution curves for 18 elements on a 2 mL cartridge (1.14 cm diameter, 2.56 cm length) of U/Teva resin ($50 - 100$ μm particle size). Except for Th and Np, all matrix elements are removed during the load, followed by rinsing in 3 M HNO_3. Th and Np are removed in 5 M HCl + oxalic acid. Figure published in [431].

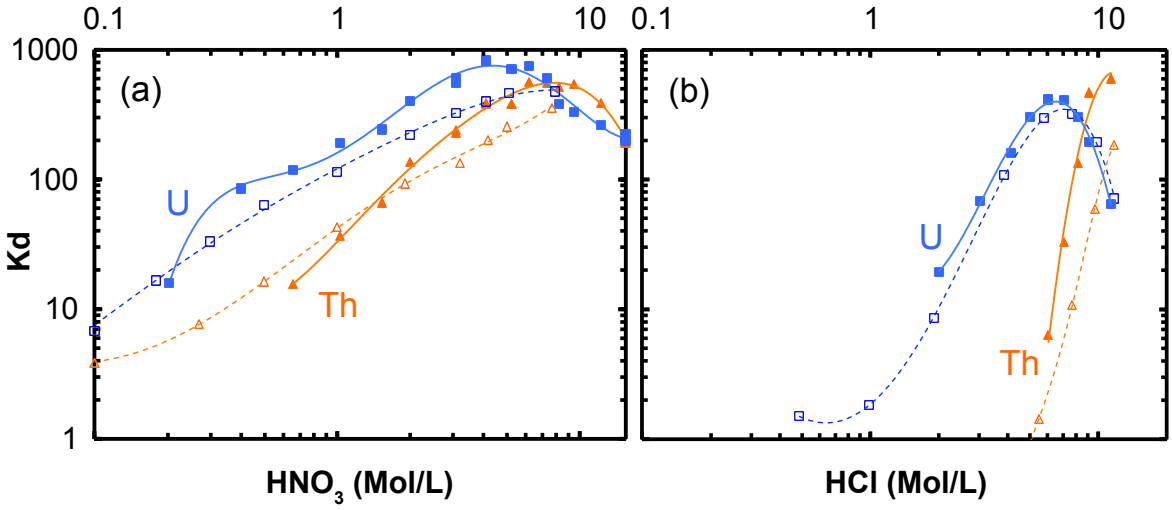

Figure 2.17: Comparison with Horwitz et al. (1992) of the distribution coefficients (Kd) on U/Teva resin of U and Th in (a) HNO_3 and (b) HCl. The curves are polynomial fits to the data. Filled symbol and solid curves are data from this work (see Fig. 2.15) while open symbols and dashed curves are from [215]. Figure published in [431].

is released during the U elution step (using 0.05 M HCl) after elution of all other elements. Less than 0.4 % of the matrix elements are released during the U elution step. This elution can be reproduced using the chromatography simulation code [222] for $HETP_{U/Teva} \sim 0.5$ mm. This value can be used in future studies to predict elution curves for U/Teva column chemistries using the same mesh size resin and elution rate as in this work.

After double spiking and digestion (see Section 2.2.1 and 2.2.2), all samples went through

Step	Acid type	Volume	Comment
Cleaning	0.05 M HCl	20 mL	
Conditioning	3 M HNO_3	6 mL	
Sample loading	3 M HNO_3	10 mL	
Matrix rinse	3 M HNO_3	40 mL	Matrix elution, except U, Th, Np
HCl conversion	10 M HCl	6 mL	
Th rinse	5 M HCl + 0.1 M oxalic	20 mL	Th and Np elution
Oxalic acid rinse	5 M HCl	10 mL	
Elution	0.05 M HCl	25 mL	U is recovered

Table 2.10: Chromatographic extraction protocol of U on U/TEVA. Column volume (cv) = 2 mL. Modified from [460]. Table published in [431].

the separation protocol outlined in Table 2.10. The loading volume varied from sample to sample, depending on the mass of sample being processed. Typically, the loading volumes for sample masses around 150, 600 and 1200 mg were 5, 25 and 50 mL of 3 M HNO_3, respectively. To ensure complete purification of uranium, the separation procedure was done one to three times, depending on the U content of the sample and the mass of sample processed (see also Section 2.5.5).

After chemistry, the U cut was collected in cleaned centrifuge tubes, and transferred to triple cleaned Teflon beakers, before being dried down completely. The elution of organic compounds from the resin, concomitantly with U, can lead to isobaric interferences during the isotopic analyses. The removal of organics from the resin was therefore done by the taking back and drying of the samples in 0.2 mL of HNO_3/H_2O_2 (1:1) [370, 179, 305, 18, 177]. After this hydrogen peroxide treatment, the size of the residue left in the beaker was considerably decreased (*i.e.*, going from a $1-2$ mm diameter dark circle to a barely visible spot). This small fraction of purified U was then dissolved in 1 mL of concentrated HNO_3, evaporated to near dryness, and taken back in a small volume of 0.3 M HNO_3. At this stage, the sample is essentially ready for isotopic analysis, and the only thing left to do is adjust the volume of the solution so as to optimize the U concentration, and thus the intensity of the signal during the isotopic measurement.

2.4 Mass spectrometry

2.4.1 Principle of mass spectrometry

The quantification of the relative amount of the isotopes of a given element in a sample relies on the possibility of separating those isotopes from one another. This is realized in practice using mass spectrometers, in which the isotopes are ionized and accelerated in an electrostatic field (noted $\vec{E}$), before entering a magnetic sector with a constant magnetic field (denoted B) oriented perpendicular to the plane containing the ions. For an ion of mass m,

the radius of curvature, R, which describes the trajectory of the ion in the magnetic field, can be written as:

$$\mathrm{R} = \sqrt{\frac{2\mathrm{U}}{\mathrm{B}^2}\frac{m}{q}} \tag{2.13}$$

where U is the potential of the electrostatic field $\vec{E}$ used to accelerate the ions, and q is the charge of the ion. From Eq. (2.13) it is clear that the radius of curvature depends on the ratio of the ion's mass considered to its charge (m/q). Therefore, two ions of identical charge entering the magnetic field at the same place, will exit the magnetic field at a location which is directly proportional to their mass. Heavier atoms will tend to have a larger radius than lighter atoms, and multiply charged atoms will move along a trajectory of smaller radius than singly charge atoms. This result implies that doubly charged species can interfere with singly charged species of half their mass (*e.g.*, W, Os, Pt or Hg can interfere on Mo), and underlines once more the need for proper elemental purification in order to achieve high-precision isotopic measurements.

Two main types of mass-spectrometers are used in isotope geo- and cosmochemistry, which differ mainly in the way the elements are ionized. In TIMS (Thermal Ionization Mass Spectrometer), an electric current is circulated through a filament (typically Pt, Re, Ta or W), and the ionization of the sample placed on the filament is done by the heating of the filament. The samples are generally loaded in an inorganic acid (such as HCl, HBr, HNO_3), and the filament/sample ensemble is placed in a source chamber, in which vacuum conditions are established. As the sample evaporates, mass-dependent fractionation occurs, which has to be corrected for. A major advantage of the TIMS, however, is that the instrumental mass bias is small, meaning that the isotopic ratios measured are very close to the true isotopic ratios of the sample being introduced. A disadvantage is that some elements have very low ionization efficiencies in TIMS, and sample throughput is limited.

In MC-ICPMS (Multi-Collector Inductively Coupled Plasma Mass-Spectrometer), the ionization is done in an argon plasma, at $\sim$ 8000 K, which ionizes most of the elements very efficiently. The sample is most commonly introduced into the plasma in the liquid form

in dilute acid, by aspiration through a nebulizer that yields an aerosol, and the finer the aerosol droplets, the more efficient the ionization. Introduction of the sample in the solid form (as is the case in Laser Ablation) or even gas form, are possible. The transition from atmospheric pressure in the plasma to vacuum conditions in the mass-spectrometer ($< 10^{-8}$ mbar) is realized with a series of cones which separate zones of decreasing pressure. During this transition, most of the analyte ions are lost, and the heavier isotopes are preferentially transmitted compared to the lighter isotopes. The MC-ICPMS therefore combines a large ionization efficiency with rapid sample throughput and data acquisition, but suffers from two main drawbacks: (i) the instrumental mass bias is large and needs to be corrected for using techniques such as internal normalization, standard bracketing or double spiking (see Section 2.5.1), and (ii) due to high ionization efficiency, isobaric interferences can be a significant concern (*e.g.*, $^{40}Ar^{16}O^{+}$ interferences on $^{56}Fe^{+}$) and have to be carefully resolved. In some cases, interferences simply cannot be resolved: *e.g.*, ^{40}Ca is lost in the ^{40}Ar signal.

Clearly, TIMS and MC-ICPMS are complementary in that some elements are better measured on one instrument type or the other. In this work, uranium isotopes were measured on MC-ICPMS, taking advantage of the strong ionization efficiency and the large sample throughput of the instrument.

2.4.2 Mass spectrometry for U isotopic analyses

The measurements were performed at the Origins Lab of the University of Chicago on a ThermoFinnigan Neptune MC-ICP-MS upgraded with an OnToolBooster 150 jet pump (Pfeiffer) and using Jet sample cones and X-skimmer cones. An Aridus II desolvating nebulizer was used for sample introduction. When the signal was found to be too unstable, enhanced signal stability was achieved by placing a spray chamber between the Aridus II and the MC-ICPMS. All measurements were done using the static cup configuration shown in Table 2.11, and in low resolution mode. A typical peak scan is shown in Fig. (2.18), where the peaks of the various U isotopes have been rescaled so that their respective plateaus are

Faraday collector configurations and method specifications for U isotopic measurements by MC-ICPMS at low resolution

	Configuration										
	L2	L1	Axial	H1	H2	H3					
Resistor (Ω)	10^{11}	10^{11}	SEM	10^{11}	10^{11}	10^{11}	Focus	Dispersion	Uptake Time	Acquisition Time	Rinse Time
Main[a]	-	^{233}U	^{234}U	^{235}U	^{236}U	^{238}U	-1.5 V	0 V	90 s	210 s	> 210 s
SEM/F calibration[b]	-	-	^{236}U	^{238}U	-	-	-1.5 V	0 V	90 s	210 s	> 210 s

[a] The "main" sequence is used to measure the samples and the bracketing standards.

[b] The "SEM/F calibration" sequence was used weekly to determine the conversion factor from counts per second (cps) to volts on the SEM.

Table 2.11: Faraday collector configuration and method specification for U isotopic measurements by MC-ICPMS at low resolution. Table published in [431].

superimposed. Even in low resolution mode, the peak plateau is clearly defined, and the center of the plateau is easily identified. All measurements are done at this peak center. The peak for ^{234}U shows large oscillations owing to the very low abundance of this isotope in natural materials (^{234}U is $\sim 18,000$ times less abundant than ^{238}U) and the difficulty of accurately measuring the signal on a Faraday Cup. For this reason, ^{234}U is measured on the Secondary Ion Multiplier (SEM) during the actual isotopic measurement. Indeed, in the SEM detector, it is the number of atoms per second colliding with the detector that is being measured (65,000 counts per second are equivalent to about 1 mV using a Faraday cup). This allows for much higher precision in the measurements of the ^{234}U/^{238}U ratios, with 2σ uncertainties from counting statistics dropping to $\pm$ 0.2 ‰ from $\pm$ 6 ‰ for geostandard BCR-2 (Table 3.2, Chapter 3).

In order to lower the uncertainties due to counting statistics, measurements consisted of 50 to 60 cycles of 4.194 s integration time. The rinsing time was adjusted to make sure that the background had decreased to a low and stable value between each sample/standard measurement, and was typically 210 s or more (Fig. 2.19). For each sample solution, typically nine measurements were performed, except when the mass of sample available was the limiting factor. Measurements were done using 25 ppb solutions, corresponding to a signal of $\sim$ 25 V on ^{238}U (*i.e.*, a transfer efficiency between atoms introduced into the mass spectrometer and ions analyzed of $\sim$ 1 %), signals of 400 mV on ^{233}U and ^{236}U, 175 mV on ^{235}U and 1.4 mV on ^{234}U (or 90,000 cps when using the SEM). Baseline measurement and gain calibration of the amplifiers was done at least daily. Estimation of the cps to volt

conversion factor was done once a week (see Table 2.11). The errors were calculated as:

$$2\sigma_{Sample} = \frac{2\sigma_{Standard}}{\sqrt{n}} \tag{2.14}$$

with $2\sigma_{Standard}$ the daily external reproducibility of measurements of standard CRM-112a bracketed by itself, and n the number of sample solution measurements (typically nine).

Quantification and correction of mass fractionation during chemical separation and mass spectrometry was done using a $^{233}U/^{236}U$ double spike (IRMM-3636). Each sample measurement was bracketed by standards spiked to the same level as the sample. The U procedural blanks after removal of organics from the resin by drying in 0.2 mL of HNO_3/H_2O_2 (1:1) [370, 179, 305, 18, 177] varied from 4 to 13 pg. This typically represents 0.02-0.05 ‰ of the signal measured. Sample measurements made early in this thesis (data presented in Tables 3.1, 3.2, 3.5, 3.8 and 4.2, Chapter 3 and 4) were not dried in HNO_3/H_2O_2 (1:1) and isobaric interferences from organics represent the equivalent of 50-160 pg of U based on the signal measured at mass 238. The rest of the samples analyzed in this work (modern and ancient carbonates, and data in Tables 4.7, 4.9, 4.10, and 4.11, Chapter 3 and 4) were subjected to an organic removal step in HNO_3/H_2O_2 before mass spectrometry.

A series of corrections need to be applied to the raw data acquired during a measurement. These corrections are presented in the order in which they are applied.

- A standard On Peak Zero (OPZ) correction is applied, to subtract from the sample signal the contribution of the dilute acid (0.3 M HNO_3) in which the sample has been diluted. The OPZ correction also allows correction for a potential increase in background intensity if, despite the long rinsing time, U accumulates in the introduction system (capillary or desolvating nebulizer). To do this, the 0.3 M nitric acid solution is regularly measured along with the samples (usually every five sample measurements).

- Abundance sensitivity and hydride formation are then corrected for in a single step. The abundance sensitivity correction accounts for the fact that the tail of the ma-

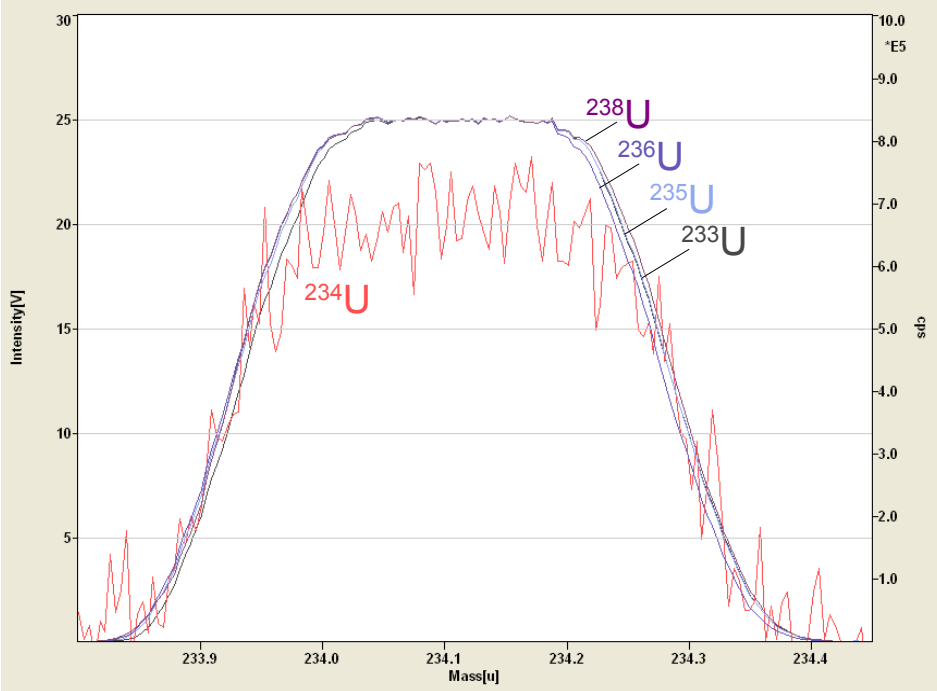

Figure 2.18: Typical shape and alignment of the peaks for the various uranium isotopes, obtained with a 26 ppb U solution spiked with IRMM-3636 (U_{Spike}/U_{Sample} = 3 %). The y-axis is the signal intensity (V), and the x-axis is the atomic mass.

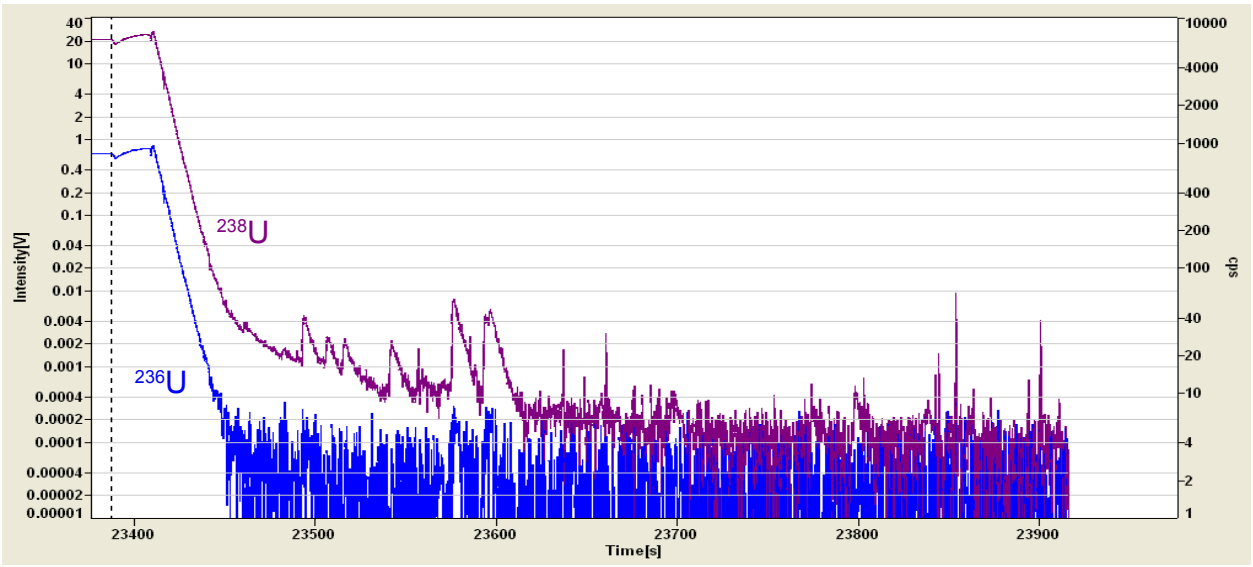

Figure 2.19: Signal intensity of ^{238}U and ^{236}U (log scale) as a function of rinsing time (in seconds). The vertical dotted line marks the time when the probe was sent from the sample to the acid rinse solution. After an initial signal increase due to free aspiration (*i.e.*, the length of the liquid column decreases, which accelerates the aspiration), the signal drops as the acid rinse is being aspired. Leaching of the U from the capillary takes a non-negligible amount of time. Only after $\sim 200 - 300$ s is the signal back to background levels.

jor ^{238}U beam affects the neighboring isotopes (Fig. 2.20), as the instrument is not equipped with a Retarding Potential Quadrupole, RPQ, filter. Tailing of the ^{238}U beam onto ^{236}U, ^{235}U and ^{234}U was estimated to be, respectively, 0.6×10^{-6}, 0.25×10^{-6} and 0.1×10^{-6} of the ^{238}U signal (the contribution on ^{233}U is completely negligible). For a single, non-bracketed measurement, tailing corrections were found to be significant on all isotopes, but when looking at deviations from a bracketing standard (δ values), the tailing correction was only important for ^{234}U (*i.e.*, above 0.01 ‰). The formation of hydride (compounds of the type UH^+) can also potentially affect the relative abundances of the various isotopes of U and were corrected for. Formation of hydride was estimated by measuring the intensity at mass 239 ($^{238}UH^+$) in a CRM-112a U standard solution. The ratio $^{238}UH^+/^{238}U$, was found to be 7.3×10^{-7}, a value slightly larger than 3×10^{-7}, found by [460] who assessed the hydride level by measuring $^{235}UH^+$. Noting h, the hydride formation ratio ($h = ^{238}UH^+/^{238}U$), and t^i, the tailing factor from the ^{238}U beam at mass i, the measured intensity I^i and the corrected intensity I^i_{corr} of isotope i, are related by:

$$I^i_{corr} = I^i\,(1+h) - I^{i-1}h - t^i I^{238} \tag{2.15}$$

The first, second and third terms on the RHS of Eq. (2.15), account for the loss of signal at mass i due to hydride formation at mass i, the gain in signal at mass i due to hydride formation at mass $i-1$, and the gain in signal at mass i due to tailing of the ^{238}U peak, respectively. The hydride correction was found to have no influence on the results.

- A correction is also applied to the certified isotopic ratios of the spike to account for the decays of ^{233}U and ^{236}U in the spike between the certification date of the spike and the measurement date.

Despite the low influence on the results of some of these effects, corrections for OPZ,

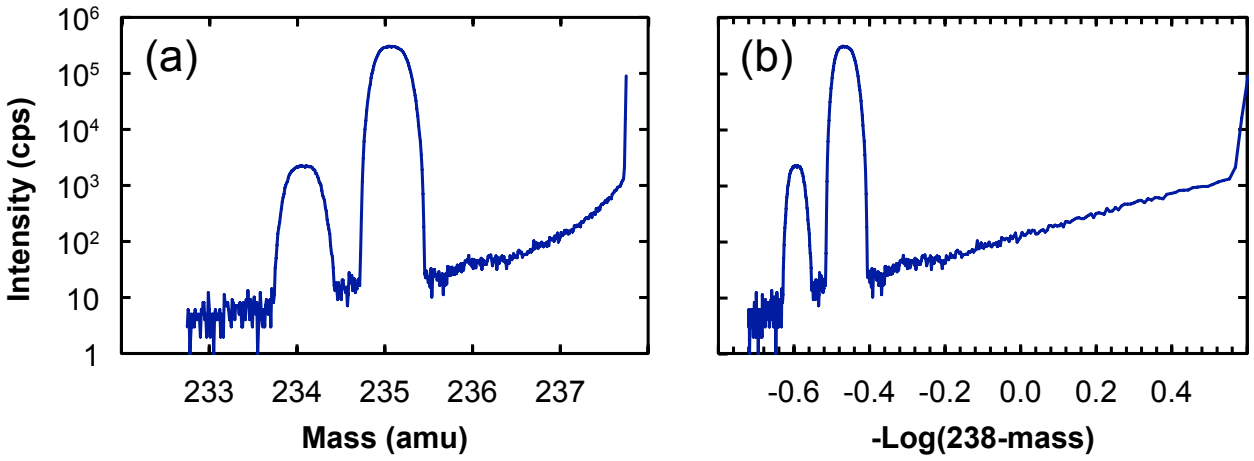

Figure 2.20: Counts per seconds (log scale) as a function of (a) atomic mass and (b) -log(238-mass). This mass scan was acquired on the MC-ICPMS with a solution of U standard CRM-112a, non-spiked, and shows the tailing of the major ^{238}U beam onto the minor isotopes of U. The linear relationship between mass 236.5 and 237.6 (panel b) implies a power law relationship between the tailing of the major U peak and the distance from the peak, as previously observed by [202].

abundance sensitivity, hydride formation, and decay of spiked isotopes were applied to all samples, for the purpose of consistency.

There are several places between the aspiration of the sample and the detection of the ions on the collectors where physical and electronic components can influence the accuracy of the isotopic analysis. Moving from the sample solution inward inside the mass spectrometer, these places are: (i) the injection system, *i.e.*, the nebulizer, desolvating nebulizer and/or spray chamber which determine the particle size of the aerosol being injected into the plasma, (ii) the shape and composition of the cones, which influence the transmission of the ions into the instrument, (iii) the choice of the resolution slit (*i.e.*, low, medium or high resolution), which is crucial in resolving isobaric interferences, (iv) the cup configuration (*i.e.*, the position of the collectors and the beam dispersion, as will be shown below), and (v) the calibration of the amplifiers connected to the Faraday cups, which can lead to systematic errors if the relative gain of the amplifiers is not properly assessed.

Uranium, being a trace element in most natural materials, requires high sensitivity in order to maximize the amount of data obtained from a single sample preparation. Further-

more, because the dynamic range of the measurement is large (the ^{235}U signal is $\sim$ 137 times lower than the ^{238}U), high-precision measurements can only be achieved if the concentration of the sample solution allows for high counting statistics of the ^{235}U signal. For these reasons, in this work, an Aridus II desolvating nebulizer (dry plasma) was used in combination with Jet sample cones and X-skimmer cones, and the instrument was equipped with a jet pump (Pfeiffer). With this setup, the sensitivity is improved by a factor of 60 compared to a typical spray chamber, general cones and standard pump setup. Individually, the jet pump leads to a factor of 2 increase, the Aridus II to a factor of 5 increase, and the cones to a factor of 4 increase in sensitivity. Because precision is nothing without accuracy, tests were conducted to assess (i) the influence of the cone shape on the isotopic analysis, (ii) the influence of the cup configuration on the measurement, and (iii) whether enhanced accuracy could be achieved by rotating the amplifiers to avoid systematic gain bias.

Results of the test concerned with the influence of the chosen set of cones and cup configuration are shown in Fig. (2.21). New baseline and gain calibrations were done after aligning the cups and changing the cones. It was found that using different cup configurations, (*i.e.*, using different isotopes in the axial Faraday cup), as well as different cones, led to different estimates of the absolute U isotopic composition of the measured sample. For instance, measurements done with Jet cones (*i.e.*, Jet Sample cones and X-skimmer cones) led to ^{238}U/^{235}U ratios that were offset by 0.08 ‰ to 0.21 ‰ compared to measurements done with general cones and the same cup configuration. Difference between the cones comes from their shape, which in turn influences the ion transmission and can result in fractionation of the isotopes following different mass fractionation laws depending on the type of cones used. To investigate this effect, the data was treated using the generalized power law [271, 5], which relates the true isotopic ratio, R, to the measured isotopic ratio, r, in the following way:

$$\mathrm{r} = \mathrm{R}\ g^{\left(M_2^n - M_1^n\right)} \tag{2.16}$$

where M_1 and M_2 are the masses of the denominator and numerator isotopes, respectively,

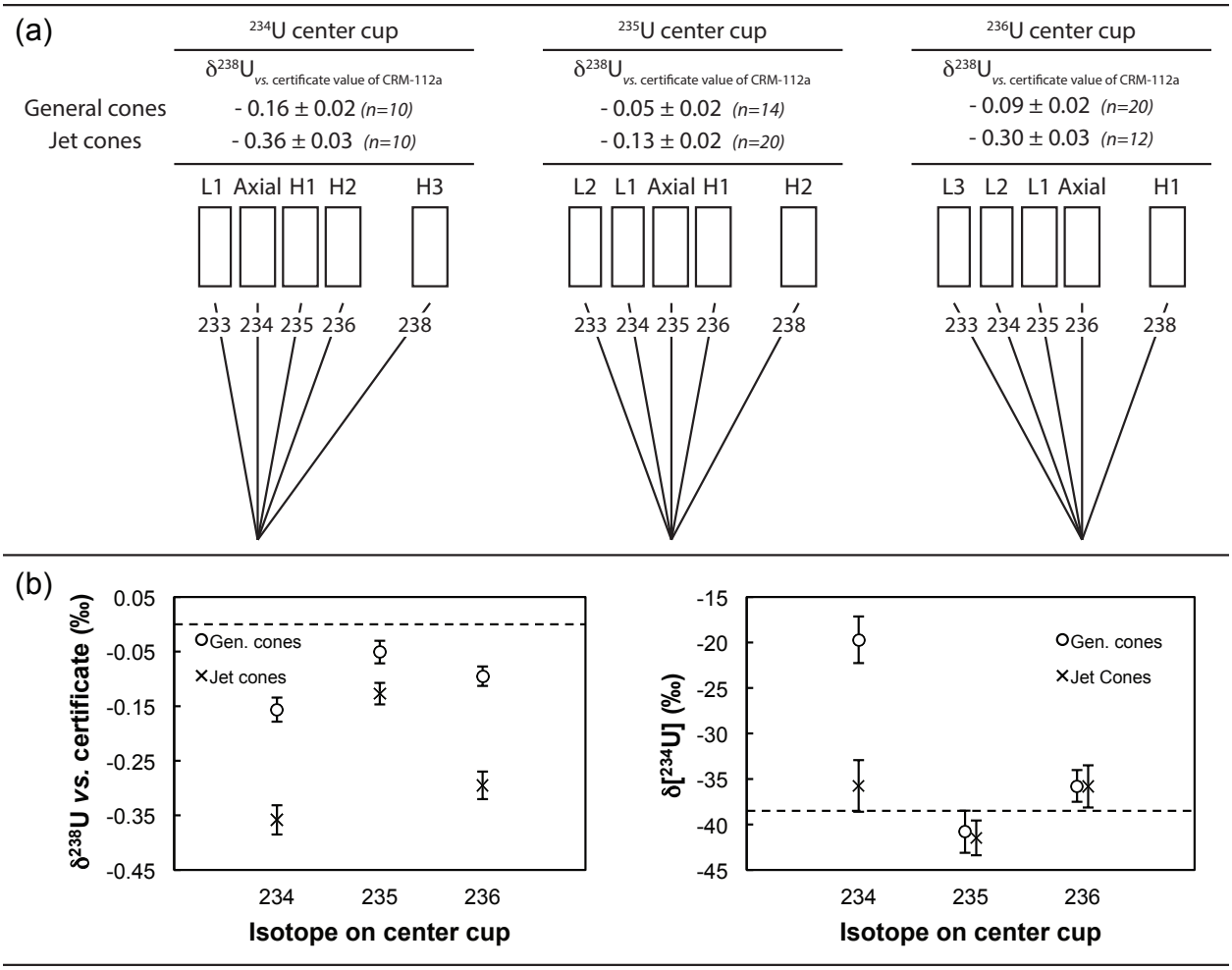

Figure 2.21: (a) Schematic representations of test measurements done to assess the effect of the cup configuration on U isotopic composition measurement, with δ^{238}U reported relative to the CRM-112a certificate value. The incident angles of the ion beams are exaggerated for the purpose of clarity. The uranium isotopic compositions using either general cones or jet cones (*i.e.*, Jet sample cones and X-skimmer cones) are given. (b) δ^{238}U/^{235}U (left) and $\delta[^{234}\text{U}/^{238}\text{U}]$ (right) of CRM-112a plotted as a function of the isotope measured in the axial collector: ^{234}U, ^{235}U or ^{236}U. δ^{238}U is reported relative to the CRM-112a certificate value (dotted line), while $\delta[^{234}\text{U}]$ is relative to secular equilibrium, using the half-lives from [107] (dotted line shows the CRM-112a value measured by [107]). It can be seen that the choice of the center isotope has a large impact on the determined absolute U isotopic composition of the measured solution. U isotopic analyses using the most symmetrical cup configuration (^{235}U in the axial cup) and regular cones gives isotopic ratios that are not biased relative to values reported previously using other techniques (TIMS) [367, 118]. This effect should be investigated for other systems, and kept in mind when assessing absolute ratios. Figure published in [431].

g the fractionation factor and n the fractionation law (*e.g.*, $n = 1$ for the power law, $n \to 0$ for the exponential law, etc). The value of n was changed until the measured $^{238}U/^{235}U$ ratio after spike correction was found to be identical to the standard value (137.837, from [367]). From this test, it appears that the fractionation induced by the general cones is best described by $n = 0.199$ (close but not identical to $n = 0$, the exponential law), while the fractionation induced by the jet cones is best described by $n = -0.425$ (close to the inverse square root law, $n = -0.5$).

The exact knowledge of the mass fractionation law is, however, not necessary to process the data as long as the same mass fractionation law is being applied to the sample and the bracketing standards. In this work, the exponential fractionation law was used. This law – which can be obtained as the limit of the generalized power law (Eq. 2.16) when n tends towards zero [271] – relates the true isotopic ratio of the sample, $R = N_j/N_i$, to the measured isotopic ratio, r, in the following way:

$$r = R \left(\frac{M_j}{M_i} \right)^{\beta} \tag{2.17}$$

where β is the exponential mass fractionation factor. It was recently shown [4] that for heavy elements, which tend to have higher transmissions, τ, β is a function of the transmission of the mass-spectrometer for the nuclide of interest:

$$\beta = C \; ln(\tau) \tag{2.18}$$

where C is a constant whose value depends on the nuclide being measured. The typical transmission on the MC-ICPMS in the work presented here was between 0.8 and 1.6 %, and the exponential mass fractionation factor of the instrument varied between 0.7 and 1.1, leading to a value of C between -0.15 and -0.27 (the range of values is large as the exact sensitivity of each measurement was not recorded). This is in general agreement with [4], who found $C \sim -0.23$ for U using MC-ICPMS.

The choice of the cup configuration was also found to affect the isotopic measurement. Using cup configurations that were strongly asymmetrical (*e.g.*, ^{234}U or ^{236}U on the center cup) offset the ^{238}U/^{235}U ratio measured by 0.04 ‰ to 0.23 ‰ relative to a more symmetrical configuration (*i.e.*, ^{235}U on the center cup) (Fig. 2.21). A possible explanation is that when the beam is asymmetric, it arrives at an angle onto the outermost cups and hits the wall of the cups, creating secondary ions, which are not corrected for and thus alter the measurement. This would imply that the cups have an "optimal" spatial configuration and that asymmetrical beams do not hit the "sweet spot" of each cup. At any rate, when measurements were performed with ^{235}U in the axial cup, which corresponds to the most symmetric cup configuration of those tested, and with general cones, good agreement with literature data was found for both $^{238}\mathrm{U}/^{235}\mathrm{U} = 137.842 \pm 0.003$ (95 CI) (against literature value, 137.837 ± 0.015, [367]) and $\delta[^{234}\mathrm{U}/^{238}\mathrm{U}] = 40.8 \pm 2.3$ ‰ (95 CI) (against literature value, 38.5 ± 0.3 ‰, [107]). This is not the case for the other configurations that put other isotopes in the central cup. Because of this bias, and even though a double spike was used to correct for instrumental mass fractionation, it is important to bracket sample measurements by standard measurements to obtain reliable absolute isotopic ratios. In fact, it is recommended that the isotopic composition of a sample always be determined and reported relative to a given standard (δ values), whose isotopic composition can then be used to convert the data into absolute ratios. This became particularly important at the turn of the 2010 decade, when a series of revisions was made to the absolute U isotopic ratios of some uranium standards (*e.g.*, [118, 367, 275]). A thorough data compilation work was done as part of this thesis, in which all high-precision U isotopic measurements published to date have been expressed back in terms of δ^{238}U notations relative to CRM-112a (see supplementary material in [431]). This compilation allows for easy and proper comparison of the data reported by different research groups.

A final test was performed to assess the relevance of implementing amplifier rotation (Virtual Amplifier) during the isotopic measurement. The amplifier rotation sequentially

connects the Faraday Cup 1 to the amplifier 1, then the amplifier 2, and so on and so forth, until each amplifier in the Virtual Amplifier has been used to measure the isotopic signal. In practice, this means that the measurements must be made up of as many blocks as there are ion beams being measured (in the case of U, 5 blocks). This procedure is supposed to cancel out the uncertainties in gain calibration of the various amplifiers. Measurements made using the Virtual Amplifier showed systematic bias after transition between two amplifiers, leading to erroneous estimation of isotopic ratios (Fig. 2.22). The use of the Virtual Amplifier was therefore not considered further.

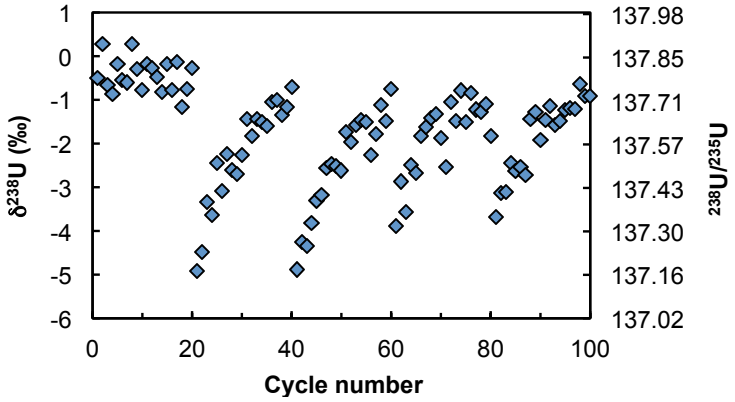

Figure 2.22: Double-spike corrected U isotopic composition of individual cycles while using the Virtual Amplifier on the MC-ICPMS (*i.e.*, amplifier rotation). Systematic bias after each amplifier transition (every 20 cycles) led to erroneous estimation of isotopic ratios, and the Virtual Amplifier was not used in this work beyond this test.

2.5 U data reduction, error propagation, and quality control

2.5.1 Double spike data reduction

For any element that has four isotopes or more, double spiking is a well-adapted technique to achieve high precision measurements. Double spiking allows for correction of instrumental mass bias (Fig. 2.23) as well as fractionation occurring during chemical separation (provided spiking of the sample is done before chemistry). Initially described by Dodson (1963) [147], the method has since then been applied to a large number of elements (*e.g.*, Ca, Ti, Fe, Sr, Mo, Ba, Pb, U, first developed by, respectively, [206, 310, 228, 325, 459, 157, 116, 145]). By

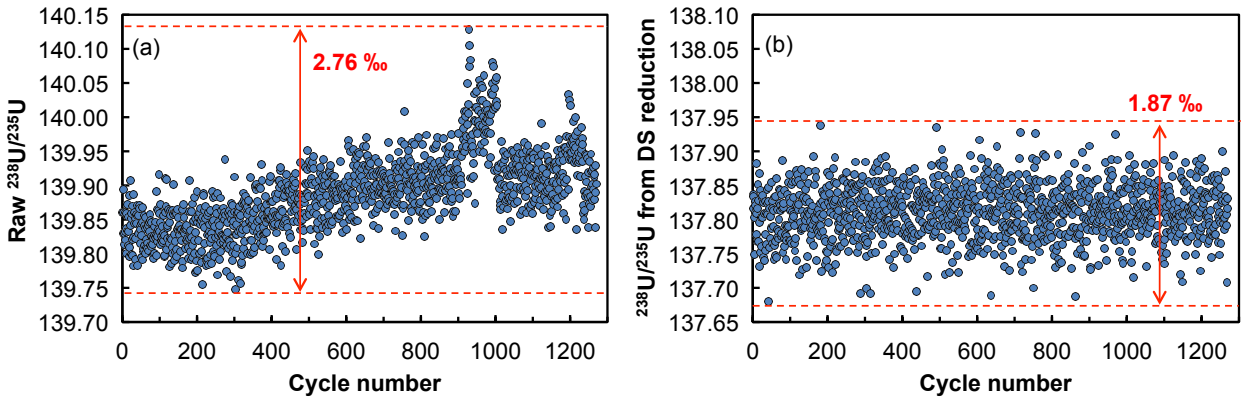

Figure 2.23: $^{238}U/^{235}U$ ratio of the CRM-112a standard as measured (a) and the same data after double spike reduction (b). Each point represents an individual cycle (4.194 s integration time, 3 s idle time). The measurement was performed over a 2.5 h time period. Despite a long term shift and short term spikes in the measured ratio, the double spike reduced data are uniform, showing the efficiency of the instrumental bias correction offered by the double spike method. Red dashed lines show the maximum variability of the data.

decomposing the measured signal into proportions coming from the spike and sample (Eq. 2.19), it is possible to extract the isotopic composition of the sample from measurement of the spike-sample mixture. A data reduction method (applicable to any double spike) is presented below that is both comprehensive in the way the errors are propagated and simple to implement. The reduction scheme uses Newton methods for system resolution (thus avoiding risky trial-and-error two nested iterations, [398]) and Monte-Carlo simulations to propagate analytical errors [342, 253, 341, 296, 431].

When using the double spike technique, various sources of errors have to be taken into account, namely: (i) the error on the measurement itself (counting statistics), (ii) the error introduced by conversion from counts per second (cps) to volts of the signal when measuring an isotope on the secondary electron multiplier (SEM), (iii) the error on the mass of spike added to the sample and on the mass of sample digested (for concentration calculations). In addition, correlations between isotope ratio errors must be taken into account when a common normalizing isotope is involved. The raw data are therefore reduced as follows:

1. The measured ratios are corrected for OPZ contribution, abundance sensitivity of the minor U isotopes to the dominant ^{238}U isotope, hydride contribution and decay of the

spiked isotopes since the certificate was issued (see Section 2.4.2).

2. For each measured ratio of two isotopes i1 and i2, denoted $\mathrm{R}^{\mathrm{i1/i2}}_{\mathrm{Measured}}$, the following equation can be written,

$$\mathrm{R}^{\mathrm{i1/i2}}_{\mathrm{Measured}} = \left[p\ \mathrm{R}^{\mathrm{i1/i2}}_{\mathrm{Spike}} + (1-p)\ \mathrm{R}^{\mathrm{i1/i2}}_{\mathrm{Sample}}\right] \left(\frac{\mathrm{M_{i1}}}{\mathrm{M_{i2}}}\right)^{\beta} \tag{2.19}$$

where p is the ratio of abundance of isotope i2 in the spike to that of i2 in the spike-sample mix, $\mathrm{R}^{\mathrm{i1/i2}}_{\mathrm{Spike}}$ and $\mathrm{R}^{\mathrm{i1/i2}}_{\mathrm{Sample}}$ are the isotopic ratios of i1 to i2 in the spike and the sample, respectively, $\mathrm{M_i}$ is the molar mass of isotope i, and β is the instrumental + chromatographic mass fractionation factor assuming that isotopic fractionations in the instrument and during column chromatography follow the exponential law. As pointed out in Section 2.4.2, other fractionation laws, such as the generalized power law [271] can be used just as well but do not affect the results significantly because samples are bracketed by double-spiked standards, which eliminates the influence of instrumental mass-fractionation. By convention, we write that the isotopic ratios in the sample are related to those in the standard following the exponential mass-fractionation law,

$$\mathrm{R}^{\mathrm{i1/i2}}_{\mathrm{Sample}} = \mathrm{R}^{\mathrm{i1/i2}}_{\mathrm{Standard}} \left(\frac{\mathrm{M_{i1}}}{\mathrm{M_{i2}}}\right)^{\alpha} \tag{2.20}$$

where α is the fractionation factor between the standard and the sample (natural fractionation). Though uranium isotopic fractionation is known to be driven by nuclear field shift effects (see Section 1.2.2, [41, 384, 1]), which are not mass-dependent, the convention of using Eq. (2.20) for reporting uranium isotopic composition has no consequence for the double-spike inversion because uranium has only two naturally-occurring long-lived isotopes. Combining equations Eq. (2.19) and Eq. (2.20) gives:

$$\mathrm{R}^{\mathrm{i1/i2}}_{\mathrm{Measured}} = \left[p\ \mathrm{R}^{\mathrm{i1/i2}}_{\mathrm{Spike}} + (1-p)\ \mathrm{R}^{\mathrm{i1/i2}}_{\mathrm{Standard}} \left(\frac{\mathrm{M_{i1}}}{\mathrm{M_{i2}}}\right)^{\alpha}\right] \left(\frac{\mathrm{M_{i1}}}{\mathrm{M_{i2}}}\right)^{\beta} \tag{2.21}$$

Equation (2.21) simply expresses the fact that every isotopic ratio measured is a mixture of the isotopic ratio of the spike and a fractionated standard, which has been fractionated by the instrument and the chromatography. The equation has three unknowns: proportion of spike (p), natural fractionation (α) and instrumental + chromatographic fractionation (β). To solve the system at least four isotopes are needed (*i.e.*, three isotopic ratios). In the data reduction scheme adopted herein, the system of three equations given by $R_{Measured}^{^{233}U/^{238}U}$, $R_{Measured}^{^{235}U/^{238}U}$ and $R_{Measured}^{^{236}U/^{238}U}$ is solved exactly using the Newton method. The reason why $R_{Measured}^{^{234}U/^{238}U}$ is not used to solve the system is that ^{234}U is a decay product of ^{238}U and, as such, the variations in this ratio are not expected to follow mass-fractionation. The ratio $R_{Sample}^{^{234}U/^{238}U}$ is calculated after the system of equations has been solved by rearranging Eq. (2.19) into

$$R_{Sample}^{^{234}U/^{238}U} = \frac{R_{Measured}^{^{234}U/^{238}U} / \left(\frac{M_{^{234}U}}{M_{^{238}U}}\right)^{\beta} - p\, R_{Spike}^{^{234}U/^{238}U}}{1-p} \tag{2.22}$$

Note that for isotopic systems where four (or more) ratios are available and are affected by the same mass fractionation law, the system would be over-constrained (4 equations, or more, in 3 unknowns) and an exact solution would not exist. In such a case, a solution can be obtained using a least squares approach.

3. The last step in the data reduction is the propagation of errors via a Monte-Carlo simulation, which is detailed in the next section (2.5.2).

A point worth noting concerns the choice of the normalizing isotope during double spike data reduction. As emphasized in Rudge et al. (2009) [376], the normalizing isotope should not be one that is of minor abundance to "avoid the numerical problems of dividing by small quantities". In the U system the choice of ^{238}U is obvious as any other isotope is minor compared to ^{238}U. Tests conducted to check the validity of this choice showed that data reduction done with ^{238}U or ^{235}U as the normalizing isotopes led to close but non-identical

results in the $^{234}U/^{238}U$ ratio estimation (difference on the order of 1.5 ‰). In particular, when ^{235}U was used as the normalizing isotope on a sample measured several times, it was observed that,

$$\text{Mean}\left(\frac{^{234}U/^{235}U}{^{238}U/^{235}U}\right) \neq \frac{\text{Mean}\left(^{234}U/^{235}U\right)}{\text{Mean}\left(^{238}U/^{235}U\right)} \tag{2.23}$$

This difference could be as high as 3 ‰. This was not observed when the most abundant isotope, ^{238}U, was used as the normalizing isotope; instead, both values were identical to within 0.05 ‰.

2.5.2 Error propagation

The propagation of errors was done using Monte-Carlo simulation [342, 253, 341, 296, 431]. For each variable, a large number n (1000) of random values is generated. This provides n sets of randomly generated simulated data (in the present case the set comprises the $^{233}U/^{238}U$, $^{234}U/^{238}U$, $^{235}U/^{238}U$ and $^{236}U/^{238}U$ ratios). The mean, standard deviations, and underlying structure of the real data are used to generate the synthetic data. In particular, the covariant character of the four isotopic ratios is taken into account by using the covariance matrix of the mean ratios, noted S_m, which is the covariance matrix of the ratios divided by the number of cycles in the measurement. Denoting U, V, W and X the isotopic ratios of $^{233}U/^{238}U$, $^{234}U/^{238}U$, $^{235}U/^{238}U$ and $^{236}U/^{238}$, respectively, S_m is thus written:

$$S_m = \begin{pmatrix} \text{Var[U]} & \text{Cov[U,V]} & \text{Cov[U,W]} & \text{Cov[U,X]} \\ \text{Cov[U,V]} & \text{Var[V]} & \text{Cov[V,W]} & \text{Cov[V,X]} \\ \text{Cov[U,W]} & \text{Cov[V,W]} & \text{Var[W]} & \text{Cov[W,X]} \\ \text{Cov[U,X]} & \text{Cov[V,X]} & \text{Cov[W,X]} & \text{Var[X]} \end{pmatrix} / \text{Number of cycles} \tag{2.24}$$

For each synthetic datum, a solution to the double spike system of equations is calculated (in the present case p, α and β). Other sources of error (SEM to Faraday conversion, mass of spike added, mass of sample digested, concentration of the spike) are propagated in the

double-spike data reduction using the same Monte-Carlo approach.

One of the advantages of the Monte-Carlo treatment is that it allows one to easily propagate errors whose influence on the final result would otherwise be difficult to estimate. For instance, the calculation of U-Th ages relies on the solving of the following system of equation (Eqs. (1) and (2) in [152]),

$$\begin{cases} \left[\frac{^{230}\mathrm{Th}}{^{238}\mathrm{U}}\right]_{\mathrm{m}} = 1 - e^{-\lambda_{230}t} + \frac{\delta^{234}\mathrm{U_m}}{1000}\left(\frac{\lambda_{230}}{\lambda_{230}-\lambda_{234}}\right)\left(1 - e^{(\lambda_{234}-\lambda_{230})t}\right) & (2.25) \\ \delta^{234}\mathrm{U_m} = \delta^{234}\mathrm{U_i}\ e^{-\lambda_{234}t} & (2.26) \end{cases}$$

where the square brackets denote activity ratios (*i.e.*, the product of the atomic ratio and the ratio of decay constants of the two isotopes considered), λ_{i} is the decay constant of isotope i, $\delta^{234}\mathrm{U}$ is the deviation in parts per thousand of the $^{234}\mathrm{U}/^{238}\mathrm{U}$ ratio from secular equilibrium ($\delta^{234}\mathrm{U} = \left(\left[^{234}\mathrm{U}/^{238}\mathrm{U}\right] - 1\right) \times 1000$), t is the age of closure of the system, and the subscripts m and i stand for "measured" and "initial" respectively. These equations are nonlinear with respect to time, and there are no analytical solutions to this system. Numerical (or graphical) methods must be used to solve for t. The problem remains when trying to propagate the uncertainties of the various input parameters on the final age. Using Monte-Carlo simulation, a code was developed in Mathematica language to alleviate this problem and published in [341]. An important result of this paper was to clearly identify the sources of uncertainty and their relative contributions onto the total U-Th age uncertainty (Table 2.12). Obtaining such a breakdown of the sources of error is crucial to readily identify which part of the analytical protocol can be improved to achieve better precision.

Another benefit of the Monte-Carlo simulation is that it allows one to examine the distribution of errors resulting from the propagation rather than assuming an a priori Gaussian distribution. The final errors are estimated by looking at the statistical dispersion of the solutions of a large enough number of simulated data (n $\geq$ 1000, [20]). In this thesis, all samples had nearly Gaussian distributions and the uncertainties on the double-spike inversion are therefore reported as the 95 % confidence interval; *i.e.*, (97.5 percentile-2.5 percentile)/2.

CCSTND-01	Corrected age (year)	±		Contribution to total error (%)
		95% CI (year)	‰	
Counting statistics	21555	19	0.89	6
U/Th ratio of the spike	21556	45	2.07	35
Decay constants	21556	48	2.22	40
Initial Th	21555	16	0.76	5
Calibrator bracketing	21556	28	1.31	14
Total uncertainty (quadratic sum)		76	3.52	100

Spike and sample mass uncertainties are not included as they do not affect the uncertainty on the age.

Table 2.12: Contribution of systematic and random uncertainties to U-Th age uncertainty for a speleothem standard (CCSTND-01). Errors are calculated by Monte-Carlo Simulation, using a code specifically developed for U-Th dating. Table published in [341].

2.5.3 Sample-standard bracketing

Once the data have been subjected to the double spike data treatment, the final correction to apply is the sample-standard bracketing. As pointed out several times in Section 2.4.2, bracketing sample measurements by standard measurements allows correction for effects which even the double spike cannot account for, such as the influence of the set of cones, or the cup configuration used to perform the analysis. Consider a succession of measurements such as depicted in Table 2.13, where STD and Smp stand for "Standard" and "Sample", respectively.

STD	Smp	STD	Smp	STD	Smp	STD	Smp	STD	Smp	STD
i-5	i-4	i-3	i-2	i-1	i	i+1	i+2	i+3	i+4	i+5

Table 2.13: Hypothetical measurement sequence.

In the simplest approach, only the standards immediately to the left (i-1) and to the right (i+1) of sample i are used for bracketing, and the δ^{238}U value of the bracketing standard is calculated using a simple linear interpolation between the standards:

$$\delta^{238}\mathrm{U}_{\mathrm{Bracketed,i}} = \delta^{238}\mathrm{U}_{\mathrm{Smp,i}} - \frac{\delta^{238}\mathrm{U}_{\mathrm{STD,i\text{-}1}} + \delta^{238}\mathrm{U}_{\mathrm{STD,i+1}}}{2} \tag{2.27}$$

Considering that the structure to the fluctuations responsible for the variations of the standard values measured are not necessarily linear, it might be beneficial to use more than

one standard on each side of the sample. An easy way to do this is to use a polynomial (Lagrangian) interpolation, which is an exact interpolation as it passes through every point of the data set. The Lagrangian interpolation is written as

$$L(x) = \sum_{j=0}^{k} y_j l_j(x) \tag{2.28}$$

with the lagrange basis polynomial given by,

$$l_j(x) = \sum_{\substack{0 \le m \le k \\ m \ne j}} \frac{x - x_m}{x_j - x_m} \tag{2.29}$$

Each measurement is characterized by a couple of coordinates (x,y), where, in the present case, x is the position of the measurement in the sequence and y is the isotopic ratio measured. Using the measurement sequence shown in Table 2.13, and considering two standards on each side of the sample measurement, the Lagrangian interpolation takes the form,

$$L(x_i) = y_{i-3} l_{i-3}(x) + y_{i-1} l_{i-1}(x) + y_{i+1} l_{i+1}(x) + y_{i+3} l_{i+3}(x) \tag{2.30}$$

with

$$\begin{cases} l_{i-3}(x) = \frac{x_i - x_{i-1}}{x_{i-3} - x_{i-1}} \frac{x_i - x_{i+1}}{x_{i-3} - x_{i+1}} \frac{x_i - x_{i+3}}{x_{i-3} - x_{i+3}} = \frac{0-(-1)}{-3-(-1)} \frac{0-1}{-3-1} \frac{0-3}{-3-3} = -\frac{1}{16} \\ l_{i-1}(x) = \frac{x_i - x_{i-3}}{x_{i-1} - x_{i-3}} \frac{x_i - x_{i+1}}{x_{i-1} - x_{i+1}} \frac{x_i - x_{i+3}}{x_{i-1} - x_{i+3}} = \frac{0-(-3)}{-1-(-3)} \frac{0-1}{-1-1} \frac{0-3}{-1-3} = +\frac{9}{16} \\ l_{i+1}(x) = \frac{x_i - x_{i-3}}{x_{i+1} - x_{i-3}} \frac{x_i - x_{i-1}}{x_{i+1} - x_{i-1}} \frac{x_i - x_{i+3}}{x_{i+1} - x_{i+3}} = \frac{0-(-3)}{1-(-3)} \frac{0-(-1)}{1-(-1)} \frac{0-3}{1-3} = +\frac{9}{16} \\ l_{i+3}(x) = \frac{x_i - x_{i-3}}{x_{i+3} - x_{i-3}} \frac{x_i - x_{i-1}}{x_{i+3} - x_{i-1}} \frac{x_i - x_{i+1}}{x_{i+3} - x_{i+1}} = \frac{0-(-3)}{3-(-3)} \frac{0-(-1)}{3-(-1)} \frac{0-1}{3-1} = -\frac{1}{16} \end{cases}$$

The value of the standard at the point x_i is thus simply

$$L(x_i) = -\frac{1}{16} y_{i-3} + \frac{9}{16} y_{i-1} + \frac{9}{16} y_{i+1} - \frac{1}{16} y_{i+3} \tag{2.31}$$

and the bracketed value of the sample is

$$\delta^{238}\mathrm{U}_{\mathrm{Bracketed,i}} = \delta^{238}\mathrm{U}_{\mathrm{Smp,i}} - L(x_i) \tag{2.32}$$

The data acquired in this thesis was treated once using the simple standard-bracketing (Eq. 2.27) and once with a 4-point polynomial interpolation (3rd order Lagrangian interpolation, Eq. 2.32). Both methods yielded identical $\delta^{238}\mathrm{U}_{\mathrm{Bracketed,i}}$ values.

The external reproducibility of the measurements can be obtained by bracketing the standard by itself. In the case of the simple standard-bracketing, calculation of the bracketed standard value still uses Eq. (2.27), as the relative distance between a sample and its neighboring standards is the same as between a standard and its neighboring standards (Table 2.13). For the Lagrangian interpolation, however, the relative spacing is different, and a new value of $L(x_i)$ needs to be calculated as

$$L(x_i) = y_{i-2}l_{i-2}(x) + y_{i-1}l_{i-1}(x) + y_{i+1}l_{i+1}(x) + y_{i+2}l_{i+2}(x) \tag{2.33}$$

which yields an interpolated standard value of

$$L(x_i) = -\frac{1}{6}y_{i-2} + \frac{4}{6}y_{i-1} + \frac{4}{6}y_{i+1} - \frac{1}{6}y_{i+2} \tag{2.34}$$

Comparison of the external reproducibility assessed with both methods showed that uncertainty values derived from Lagrangian interpolation are typically 15 % (up to 30 %) larger than the ones derived from simple standard-bracketing. The only difference between the two approaches is that the Lagrangian interpolation considers the structure of the standard data on a time range twice larger than the simple standard-bracketing. The larger uncertainties obtained with the polynomial interpolation tend to indicate that the structure of the standard data does not extend in time as far as the Lagrangian interpolation. This is to say, that the variations in the standard values measured represent only short term fluctuations,

and that there is some virtue to the simple standard-bracketing as written in Eq. (2.27).

Consequently, throughout this work, sample measurements were bracketed by only two standard measurements (one on each side of the sample), spiked to the same level as the sample (*i.e.*, ~ 3 %).

2.5.4 Accuracy and precision of $^{234}U/^{238}U$ ratios

For each sample analyzed in this work, both the $^{238}U/^{235}U$ and the $^{234}U/^{238}U$ ratios are reported. Though the focus of this dissertation is on the information enclosed in the $\delta^{238}U$ values, important insight about the closed-system or open-system behavior of the samples can be gained by looking at the $\delta[^{234}U/^{238}U]$ values (see Section 1.1). Given the very large dynamic range of the $^{234}U/^{238}U$ ratio measurement (^{238}U is $\sim 18,000$ times more abundant than ^{234}U in natural samples), assessing the accuracy and precision of the technique developed above is non-trivial. With this in mind, the absolute $^{234}U/^{238}U$ ratios and $\delta[^{234}U/^{238}U]$ values from this work are compared with literature data in Table 2.14. Despite the small number of geostandards available for inter-laboratory comparison, the $\delta[^{234}U/^{238}U]$ values of these samples range from ~ -40 ‰ (CRM-112a U standard) to $\sim +145$ ‰ (typical open ocean water), providing a good spectrum to test both accuracy and precision of the data.

As can be seen in Table 2.14 the measurements reported in this work are in very good agreement with the data obtained by other laboratories. Only one sample, NOD-A-1 (manganese nodule standard) was not measured at the same value as published in the literature: +85 ‰ in this work *vs.* +125 ‰ in [179]. The reason for this disagreement is unknown, but could be due to the fact that NOD-A-1 was one of the very first samples measured during the development of the analytical protocol. At the time, removal of the organics coming from the column chemistry was not implemented, and interferences from organics could be responsible for the 40 ‰ difference observed in the $\delta[^{234}U/^{238}U]$ value of NOD-A-1. Samples measured later during this thesis (BCR-2, BHVO-2, the seawater samples), and after

Sample info	Sample	Study	$^{234}U/^{238}U$	±*	$\delta^{234}U$ (‰)[a]	±*
U standard	**CRM-112a**	**This work**	**5.273E-05**	**1.2E-07**	**-40.8**	**2.3**
		Hiess et al. (2012)	5.287E-05	5.1E-08	-38.2	1.0
		Cheng et al. (2013)	5.285E-05	1.5E-08	-38.5	0.3
		Certificate value (NBL)	5.284E-05	8.2E-08	-38.7	1.6
		Richter et al. (2010)	5.285E-05	1.6E-08	-38.5	0.3
Basalt	**BCR-2**	**This study**	**5.525E-05**	**3.6E-07**	**5.0**	**6.5**
		This study	**5.524E-05**	**3.0E-07**	**4.8**	**5.5**
		This study	**5.492E-05**	**6.2E-07**	**-0.9**	**11.2**
		This study	**5.495E-05**	**1.2E-08**	**-0.3**	**0.2**
		This study	**5.498E-05**	**1.2E-08**	**0.1**	**0.2**
		This study	**5.501E-05**	**3.6E-08**	**0.8**	**0.7**
		This study	**5.502E-05**	**2.6E-08**	**1.0**	**0.5**
		Cheng et al. (2013)	5.503E-05	3.0E-08	1.0	0.5
		Andersen et al. (2015)	5.503E-05	5.5E-08	1.1	1.0
	BHVO-2	**This study**	**5.489E-05**	**3.2E-07**	**-1.5**	**5.8**
		Andersen et al. (2014)	5.503E-05	4.4E-07	1.0	8.0
		Andersen et al. (2015)	5.502E-05	3.3E-08	0.9	0.6
Mn-Nodule	**NOD-A-1**	**This study**	**5.967E-05**	**3.6E-07**	**85.5**	**6.1**
		Goto et al. (2014)	6.189E-05	1.9E-07	125.9	3.1
		Goto et al. (2014)	6.196E-05	3.5E-07	127.1	5.7
		Goto et al. (2014)	6.214E-05	5.5E-07	130.4	8.8
		Goto et al. (2014)	6.188E-05	3.3E-07	125.7	5.4
SW Atlantic	**Arguin, France**	**This study**	**6.291E-05**	**3.2E-08**	**144.5**	**0.5**
	Miami, FL	**This study**	**6.290E-05**	**3.5E-07**	**144.2**	**5.5**
	SW Gulf of Mexico	**This study**	**6.357E-05**	**3.8E-07**	**156.4**	**5.9**
	SW Gulf of Mexico	**This study**	**6.356E-05**	**1.3E-08**	**156.3**	**0.2**
	SW Gulf of Mexico	**This study**	**6.356E-05**	**1.6E-08**	**156.2**	**0.2**
	SW Gulf of Mexico	**This study**	**6.369E-05**	**4.0E-08**	**158.6**	**0.6**
	Seawater	Stirling et al. (2007)	6.296E-05		145	
	Seawater	Stirling et al. (2007)	6.296E-05		145	
	Seawater	Stirling et al. (2007)	6.296E-05		145	
SW Pacific	**Dive 4463 EPR**	**This study**	**6.294E-05**	**1.4E-07**	**145.0**	**2.3**
	Dive 3961 EPR	**This study**	**6.300E-05**	**2.5E-07**	**146.1**	**4.0**
	Pacific Ocean	**This study**	**6.301E-05**	**3.0E-08**	**146.3**	**0.5**
	SF, CA, USA	**This study**	**6.304E-05**	**2.6E-08**	**146.8**	**0.4**
	SF, CA, USA	**This study**	**6.302E-05**	**2.6E-08**	**146.4**	**0.4**
	SF, CA, USA	**This study**	**6.299E-05**	**3.6E-08**	**145.8**	**0.6**
	SF, CA, USA	**This study**	**6.295E-05**	**3.0E-08**	**145.2**	**0.5**
	SF, CA, USA	**This study**	**6.289E-05**	**2.4E-08**	**144.0**	**0.4**
	Guaymas, Mexico	**This study**	**6.329E-05**	**4.1E-07**	**151.3**	**6.5**
	Seawater	Stirling et al. (2007)	6.299E-05	5.7E-08	145.8	0.9
	Seawater	Stirling et al. (2007)	6.297E-05	1.9E-08	145.4	0.3
	Pacific/Atlantic	Andersen et al. (2014)	6.294E-05	5.0E-07	145.0	8.0
	Pacific/Atlantic	Andersen et al. (2014)	6.300E-05	1.3E-07	146.0	2.0
	SW Pacific/Atlantic	Andersen et al. (2015)	6.298E-05	3.3E-08	145.7	0.5

* Uncertainties as reported in the original studies (2SD, 2SE or 95 % CI depending on the study).

[a] $\delta^{234}U = [(^{234}U/^{238}U)smp / (^{234}U/^{238}U)eq -1]*1000$ where $(^{234}U/^{238}U)eq$ is the atomic ratio at secular equilibrium and is equal to $\lambda_{238U}/\lambda_{234U}$= 5.497e-5 (Cheng et al. 2013).

Table 2.14: Comparison of absolute $^{234}U/^{238}U$ ratios and $\delta[^{234}U/^{238}U]$ values from this work, with literature data. References: Stirling et al. (2007), [412]; Richter et al. (2010), [367]; Hiess et al. (2012), [202]; Cheng et al. (2013), [107]; Goto et al. (2014), [179]; Andersen et al. (2014), [19]; Andersen et al. (2015), [18].

removal of the organics from the resin, all agree with published values within less than a permil, which speaks for the reliability of the data reported herein.

2.5.5 Quality control

To conclude this chapter, and demonstrate the robustness of the analytical protocol developed to achieve high-precision U isotopic analysis, a quality control for double spike measurements is presented below.

This quality control is graphically presented in Fig. (2.24) as a plot of the $\delta^{238}U_{DS+SSB}$ values obtained from the double spike data reduction (Section 2.5.1) as a function of the $\delta^{238}U_{SSB}$ values obtained from the raw $^{238}U/^{235}U$ ratios (corrected only for OPZ, hydride formation and abundance sensitivity) bracketed by standard measurements but without double spike correction (SSB). Each point in the figure represents a different sample analyzed in the course of this thesis. As the spike isotopes (^{233}U and ^{236}U) are different from the naturally occurring isotopes (^{235}U and ^{238}U), the data reduction using the double spike is sensitive to artifacts such as isobaric interferences on any of the four isotopes, while the ratio obtained by SSB is sensitive to fractionation during sample digestion and purification, and artifacts affecting only ^{235}U and ^{238}U. As can be seen on Fig. (2.24a), the data for double-spike and SSB agree with each other, which is a strong internal validation of the quality of the measurements. This test can be applied to all double spikes where at least two naturally occurring isotopes have small contributions from the spike. As can be readily seen on Fig. (2.24a), the double spike approach offers much better precision than the SSB approach. Agreement is also found between DS+SSB and SSB for $\delta[^{234}U/^{238}U]$ values (Fig. 2.24b).

A few samples yielded different $\delta^{238}U$ and $\delta[^{234}U/^{238}U]$ values by double spike from those by standard-bracketing. There are two main reasons for the observed discrepancies:

1. The U_{Spike}/U_{Sample} ratio in the sample is far above the optimal 3 % value (red points in Fig. 2.24), and therefore the level of spike in the sample is different from the one in the bracketing standard. As the amount of spike in the sample increases, the $^{238}U/^{235}U$ ratio of the *sample + spike* mixture evolves along a mixing line between the natural $^{238}U/^{235}U$ ratio of ~ 137.837 and the spike $^{238}U/^{235}U$ ratio of ~ 5.163 (Fig. 2.24c).

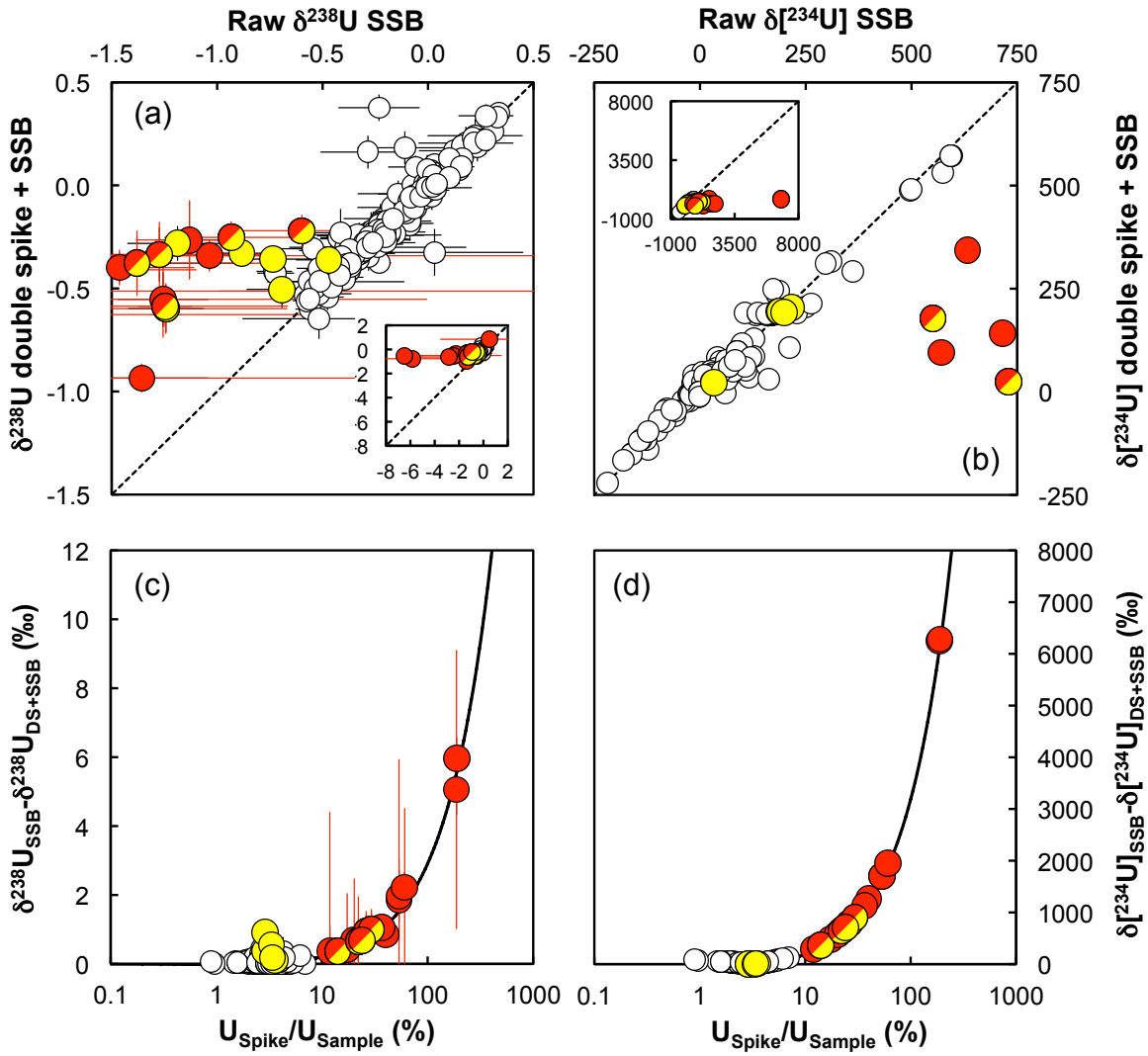

Figure 2.24: (a) δ^{238}U obtained from double spike data reduction plotted against the raw δ^{238}U measured; all values are standard bracketed (SSB). (b) Same plot as (a) but for $\delta[^{234}U/^{238}U]$. Despite being subject to different artifacts (see main text) most samples plot on a line of slope one, which is an internal validation of the quality of the results. Deviation from the 1:1 line (dotted line) can be explained if the $\delta^{238}U_{SSB}$ was affected by one of the following: (1) the U_{Spike}/U_{Sample} ratio was far above the optimal 3 % (red symbols), or (2) the mass of sample digested was high (> 1 g) and some matrix elements eluted together with U during column chemistry (yellow symbols). Samples showing both overspiking and high sample mass are shown in red and yellow symbols. (c) Difference between the δ^{238}U values obtained by double spike and by SSB as a function of the U_{Spike}/U_{Sample} ratio. (d) Same plot as (c) but for $\delta[^{234}U/^{238}U]$. The solid black curves represent mixing lines between the sample composition and the spike composition. The overspiked samples plot exactly on the mixing line, showing clearly that the excess of spike in the sample relative to the bracketing standard is responsible for the apparent discrepancy in δ^{238}U values obtained from DS + SSB and SSB only. This is also true for $\delta[^{234}U/^{238}U]$ values. Figure published in [431].

A similar mixing relationship is found for $\delta[^{234}U/^{238}U]$ values (Fig. 2.24d).

2. A large mass of sample was digested and passed through column chemistry (yellow points in Fig. 2.24). Even though the resin has a much stronger affinity for U than for matrix elements (K_d of U higher by at least 1 order of magnitude), matrix elements can stick to the column in a sufficient amount so as to be partially released at the same time as U and affect the measurement, and/or matrix elements can saturate the binding sites of the resin and prevent U from being fully retained on the resin, leading to isotopic fractionation on the column, which would not affect the DS+SSB result but would affect the SSB result.

To test the second hypothesis, $\sim$ 120 g of a seawater sample (Moulleau, Bassin d'Arcachon, Atlantic coast, France) was spiked and run through column chemistry three times. An aliquot was sampled after each column step. The three cuts show little difference in their values of $\delta^{238}U$ obtained from double spike (Table 3.5, Chapter 3), but the values obtained from raw intensities start far off the expected value (at -0.88 ‰ instead of -0.35 ‰) and get closer with the number of column passes (-0.42 ‰after two). Isotopic fractionation on the column thus seems unlikely, as there would be no reason for the situation to improve with more passes through the column, and we conclude that matrix effects during isotopic measurement are the most likely cause of the isotopic fractionation observed after the first column pass for this sample. In a second test, $\sim$ 400 g of a seawater sample (San Francisco) was spiked and split into 5 different beakers ($\sim$ 80 g of seawater each). The first split was passed through column chemistry only once, the second split twice, and so on until the fifth split. At this matrix level, we did not observe the same deviation of the raw $^{238}U/^{235}U$ ratio, possibly because there is insufficient matrix to saturate the column (80 g seawater for the San Francisco samples *vs.* 120 g for Moulleau). We recommend that no more than $\sim$ 1 g of matrix be loaded on 2 mL U/Teva cartridges to avoid elution of matrix elements in the U cut.

2.6 Conclusions

In this chapter, general methods of isotope chemistry were presented, with emphasis placed on extraction chromatography. A detailed description of some analytical developments in chromatographic techniques that resulted in the creation of the first Pneumatic-Fluoropolymer HPLC system was given, and should be of general interest for isotope geo- and cosmochemists. The analytical protocol developed during this project for U elemental purification on U/Teva resin was then introduced, along with the mass spectrometric and data reduction methods. As part of this effort, two programs were developed in Mathematica language to help standardize the data reduction of U-Th age calculations and high-precision U isotopic analyses. Finally, a quality control for double spike measurement was introduced.

CHAPTER 3

U IN THE CRUST AND THE OCEAN

"Les géographies, dit le géographe, sont les livres les plus précieux de tous les livres. Elles ne se démodent jamais. Il est très rare qu'une montagne change de place. Il est très rare qu'un océan se vide de son eau. Nous écrivons des choses éternelles."

Antoine de Saint-Exupéry – *Le Petit Prince*

Part of this chapter is based on:

• [428]: Telus M., Dauphas N., Moynier F., Tissot F.L.H., Teng F.-Z., Nabelek P.I., Craddock P.R., Groat L.A. (2012) Iron, magnesium, zinc and uranium isotopic fractionation during continental crust differentiation: The tale from migmatites, granites, and pegmatites. *Geochimica et Cosmochimica Acta* **97**, 247-265.

• [433]: Tissot F.L.H., Dauphas N., Reinhard C., Lyons T., Asael D., Rouxel O. (2012) Mo and U Geochemistry and Isotopes. Chapter 7.10.6 In *Reading the Archive of Earth's Oxygenation* (Melezhik, V.A. et al., Eds.), *Volume 3: Global Events in the Fennoscandian Arctic Russia - Drilling Early Earth Project*, 1500-1506.

• [28]: Asael D., Tissot F.L.H., Reinhard C.T., Rouxel O., Dauphas N., Lyons T.W., Ponzevera E., Liorzou C., Chéron S. (2013) Coupled molybdenum, iron and uranium stable isotopes as oceanic paleoredox proxies during the Paleoproterozoic Shunga Event. *Chemical Geology* **362**, 193-210.

• [431]: Tissot F.L.H., Dauphas N. (2015) Uranium isotopic compositions of the crust and ocean: Constraints on the U budget and global extent of modern anoxia, *Geochimica et Cosmochimica Acta*, **167**, 113-143.

3.1 Introduction

A variety of proxies are commonly used to reconstruct paleoredox conditions in Earth's atmosphere and ocean. Some proxies simply rely on the existence/absence of redox sensitive minerals. As such, the survival of detrital uraninite in the Archean requires that the atmospheric oxygen level at the time was low enough that oxidative weathering of uraninite did not occur ($P_{O_2} < 10^{-2} - 10^{-6}$ PAL (present atmospheric level), [183, 353]), and that the ocean itself was anoxic enough to preserve the detrital mineral from oxidation. Other proxies use the elemental and isotopic variations of redox sensitive elements (such as Mo, Re, U, etc...) in the rock record. For instance, in the ocean and under euxinic conditions (lack of oxygen, O_2, and significant amount of hydrogen sulfide, H_2S), Mo is completely scavenged from the water-column lying over the sediment, and the isotopic composition of Mo in the seawater is quantitatively transferred to the forming sediment. Using mass-balance models, this value can be interpreted in terms of global extent of anoxia in the ocean. These reconstructions, however, often rely on the assumption that a redox sensitive element precipitating *locally* in a sediment records the *global* redox conditions of the ocean. In the case of U, this assumption has not yet been validated. This chapter is concerned with the validation and use of the U paleoredox proxy.

A prerequisite to testing the U proxy is the characterization of a series of geological bodies acting either as sources or sinks in the U cycle. This will be the focus of the second part of this chapter, in which the determination of the isotopic composition of an array of igneous rocks will allow to define the average composition of Earth's crust. In a third part, the isotopic composition of the ocean and the various sinks of U in the ocean will be detailed, allowing for proper testing of the U proxy on the modern ocean. The fourth part of this chapter will focus on a case study of ancient shales (2.05 Gyr ago), while the last part will be concerned with the possibility of using carbonates as a better rock record to reconstruct paleoredox conditions. The first part of this chapter will be a preamble relevant to both geochemistry (Chapter 3) and cosmochemistry (Chapter 4), which will discuss the need for

age corrections stemming from the existence of small variations in the $^{238}U/^{235}U$ ratio.

3.2 Pb-Pb and U-Pb age corrections

The most immediate consequence of the natural variability of the ratio of "stable" U isotopes is that the Pb-Pb and U-Pb ages that assume the U composition of the samples being dated, instead of measuring it, have a greater uncertainty than reported, and need to be corrected for the difference between the assumed and actual U isotopic composition [460, 202]. Though this point is not the focus of this dissertation, development of three analytical equations was done during this project, which provide an easy way to calculate the age correction to apply to a sample of any age and any isotopic composition. When the composition of the sample is unknown, these formulae can be used to assess whether age corrections should be a concern for the sample, and to estimate a reasonable age uncertainty based on the typical isotopic variability of the rock type being dated. These developments are presented below.

3.2.1 ^{207}Pb—^{206}Pb age corrections

The U-Pb [49] and Pb-Pb [327, 326] dating methods are based on the decay schemes of the long-lived isotopes of U: ^{238}U decays into ^{206}Pb with a half-life of 4468 Myr ($\lambda_{238} = 1.551 \times 10^{-10}$) and ^{235}U decays into ^{207}Pb with a half-life of 704 Myr ($\lambda_{235} = 8.846 \times 10^{-10}$). As in any dating system based on a radioactive decay scheme (*e.g.*, Rb-Sr, K-Ar), the notion of "closure" is key to the meaning of an age. Before closure, that is, at high enough temperature, the diffusion rate of the daughter isotopes is fast enough that they do not accumulate in the system (for instance, a forming mineral). After closure, at low temperature, the diffusion rate is low enough that the daughter isotopes are essentially trapped in the system and accumulate in it. The transition temperature below which the daughter isotopes start to accumulate in the system is called the *closure temperature* (usually denoted T_c), and the time

at which the system goes through closure therefore defines the "age" of the system. The value of the closure temperature (and thus the calculated "age") will depend on the cooling history of the system, which is how rapidly the system goes through the closure temperature (see the seminal paper of Dodson (1973) [146]). Because the age of the system is dependent on the relative amount of the parent and daughter isotopes, a loss/gain of either types of isotope after closure of the system will lead to erroneous "age" estimates.

In the specific case of Pb-Pb and U-Pb dating, and for a sample where no loss/gain of either Pb or U occurred, the radiogenic component of lead is directly related to (i) the time since "closure" of the system and (ii) the U isotopic composition of the sample. Below, the impact of the natural variability of the ratio of "stable" U isotopes on the Pb-Pb and U-Pb ages is investigated.

Consider first the Pb-Pb ages. The Pb-Pb dating equation is written as follows:

$$\frac{^{207}\mathrm{Pb}^*}{^{206}\mathrm{Pb}^*} = \left(\frac{^{235}\mathrm{U}}{^{238}\mathrm{U}}\right) \frac{e^{\lambda_{235}t} - 1}{e^{\lambda_{238}t} - 1} \tag{3.1}$$

where the star denotes the radiogenic component, and t the time since closure of the system. If the actual $^{238}\mathrm{U}/^{235}\mathrm{U}$ ratio (noted $\mathrm{R_U}$ in the following equations) is different from the assumed ratio, an age correction is needed. The magnitude and direction of the age correction is a function of the age of the sample and its U isotopic composition. Because the variations on $\mathrm{R_U}$ (the $^{238}\mathrm{U}/^{235}\mathrm{U}$ ratio) are small, the age correction (Δt) will be small compared to the age of the sample, and it can be assumed that at this scale, the function $\mathrm{R_U} = f(t)$, is linear (see Fig. 1.1). The following relationship can thus be written:

$$\Delta t = \Delta \mathrm{R_U} \, \frac{\partial t}{\partial \mathrm{R_U}(t)} = \frac{\Delta \mathrm{R_U}}{\partial \mathrm{R_U}(t)/\partial t} \tag{3.2}$$

From Eq. (3.1), $R_U(t)$ is obtained, which is derived to obtain the following:

$$\Delta t = \frac{\Delta U \left(e^{\lambda_{238} t} - 1\right) \left(e^{\lambda_{235} t} - 1\right)}{1000 \left(\lambda_{238}\, e^{\lambda_{238} t} - \lambda_{235}\, e^{\lambda_{235} t} + (\lambda_{235} - \lambda_{238})\, e^{(\lambda_{238} + \lambda_{235}) t}\right)} \tag{3.3}$$

where ΔU is the difference between the actual and assumed U isotopic composition of the sample (in delta notation, ‰), t is the Pb-Pb age of the sample obtained using an "assumed" U isotopic composition, and Δt is the age correction to apply to the sample age. Figure (3.1) shows the age correction required for various ΔU values as a function of the age of the sample. The various curves are obtained using Eq. (3.3).

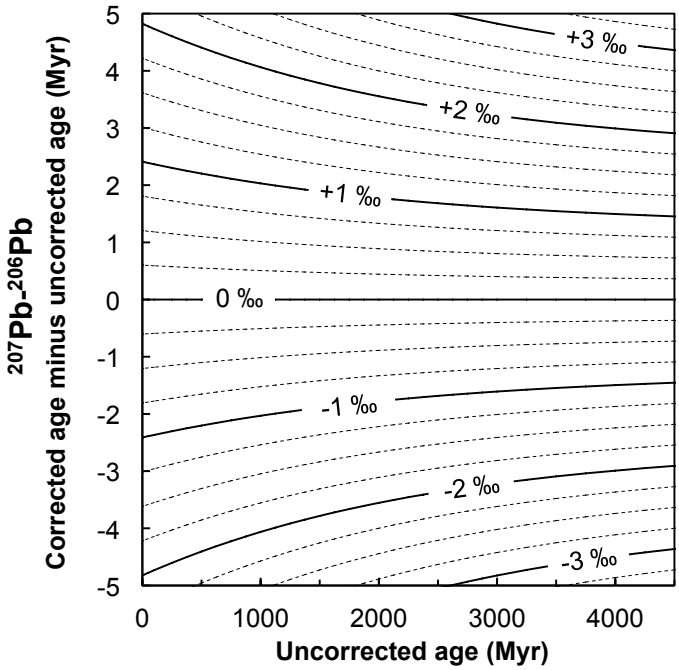

Figure 3.1: Age correction for various ΔU values as a function of the age of the sample, using the ^{207}Pb-^{206}Pb chronometer. If the age of a sample was calculated with an assumed $^{238}U/^{235}U$ ratio, which is different from the actual $^{238}U/^{235}U$ ratio in the sample ($\Delta U = \left[\left(^{238}U/^{235}U_{\text{Sample}}\right) / \left(^{238}U/^{235}U_{\text{Assumed}}\right) - 1\right] \times 1000$), then an age correction is likely needed. Lines of equal ΔU are 0.25 ‰ apart and were calculated using Eq. (3.3). Figure published in [431].

3.2.2 ^{206}Pb–^{238}U and ^{207}Pb–^{235}U age corrections

It is possible, in theory, to measure the abundances of ^{235}U, ^{238}U, ^{206}Pb and ^{207}Pb without making any assumption about the ^{238}U/^{235}U ratio of the sample, which would mean that no age correction need be applied to U-Pb ages. In practice, however, the ^{238}U/^{235}U ratio of the sample is rarely estimated and the "consensus" value (137.88, [409]) is often assumed to represent the sample value [386, 283], thus calling for an age correction of both ^{207}Pb-^{235}U and ^{206}Pb-^{238}U ages.

Consider the example of U-Pb ages calculated using the "consensus" value assumption, and the popular EARTHTIME distributed 'ET535 tracer' (a mixed ^{205}Pb-^{233}U-^{235}U tracer). The first place where the "consensus" value assumption will play a role is in the determination of the degree of isotopic fractionation (instrumental and introduced during chemical separation), in ‰/amu of the measured ratio relative to the true ratio. This parameter, the so-called *linear uranium fractionation factor*, is noted FU. Following the common U-Pb methodology used with the ET535 tracer [386, 283], and making the assumption that the ^{235}U blank is negligible (a valid assumption if the U blank is minimized), two equations can be written in which FU intervenes (Eq. 33 and 34 in [386], with addition of the ^{238}U blank term):

$$\mathrm{R85c} = \mathrm{R85m}\,(3\ \mathrm{FU} + 1) = \frac{^{238}\mathrm{U_s}\ +\ ^{238}\mathrm{U_t}\ +\ ^{238}\mathrm{U_b}}{^{235}\mathrm{U_s}\ +\ ^{235}\mathrm{U_t}} \tag{3.4}$$

$$\mathrm{R35c} = \mathrm{R35m}\,(1 - 2\ \mathrm{FU}) = \frac{^{233}\mathrm{U_t}}{^{235}\mathrm{U_s}\ +\ ^{235}\mathrm{U_t}} \tag{3.5}$$

where Rij is the ratio of uranium isotope ^{i}U/^{j}U, s, t and b stand for "sample", "tracer" and "blank", and m and c refer to the ratios "measured" and "corrected" for instrumental mass fractionation, respectively. As there are two equations in three unknowns (FU, ^{238}U$_s$ and ^{235}U$_s$), a third equation is added by recognizing that:

$$^{235}\mathrm{U_s} = \frac{1}{\mathrm{R_U}}\ ^{238}\mathrm{U_s} \tag{3.6}$$

where R_U denotes the $^{238}U/^{235}U$ ratio of the sample, which is not known but assumed to be equal to the "consensus value". Using Eqs. (3.4), (3.5) and (3.6), the linear uranium fractionation factor FU can thus be expressed as Eq. 38 in [386], with addition of the ^{238}U blank term:

$$FU = \frac{R35t\,(R_U - R85m) + R35m\left(R85t - R_U + {}^{238}U_b/^{235}U_t\right)}{2\ R35m\left(R85t - R_U + {}^{238}U_b/^{235}U_t\right) + 3\ R35t\ R85m} \tag{3.7}$$

Equation (3.7) shows clearly that FU depends on the assumed $^{238}U/^{235}U$ ratio (R_U). As FU is being used to correct all measured U isotopic ratios, the quantity of ^{238}U in the sample is going to depend on FU, and therefore to depend on the assumed $^{238}U/^{235}U$ ratio. Once the quantity of ^{238}U in the sample is known, the quantity of ^{235}U in the sample is calculated using Eq. (3.6), once again using the "consensus value" assumption. It is thus clear that the estimates of both ^{235}U and ^{238}U in the sample are dependent on the assumed $^{238}U/^{235}U$ ratio (R_U), and so are the U-Pb ages. The circularity introduced by the use of the $^{238}U/^{235}U$ ratio in the determination of the amount of both ^{238}U and ^{235}U in the sample will be discussed later (Section 3.2.2.3).

3.2.2.1 $^{206}Pb-^{238}U$ age corrections

Consider first the impact of the "consensus value" assumption on the ^{206}Pb-^{238}U ages. The amount of ^{238}U in the sample is written as (Eq. 48 in [386]):

$${}^{238}U_s = \frac{{}^{235}U_t\ R85m\,(1 + 3\ FU) - \left(R85t\ {}^{235}U_t\right) - {}^{238}\ U_b}{1 - \frac{1}{R_U}\ R85m\,(1 + 3\ FU)} \tag{3.8}$$

where s, t and m still stand for "sample", "tracer" and "measured", respectively, and b stands for "blank". The age of the sample is calculated using the following equation:

$$\frac{{}^{206}Pb^*}{{}^{238}U_s} = \left(e^{\lambda_{238} t8} - 1\right) \tag{3.9}$$

where the star denotes the radiogenic component, and $t8$ is the time since closure of the system as calculated from ^{206}Pb-^{238}U systematics. Because the variations on R_U (the $^{238}U/^{235}U$ ratio) are small, the age correction will be small compared to the age of the sample, and the following equation can be written:

$$\Delta t8 = \frac{\Delta R_U}{\partial R_U(t8)/\partial t8} \tag{3.10}$$

By substituting Eqs. (3.7) and (3.8) into (3.9), an expression for $R_U(t8)$ is obtained, which is used to derive the following:

$$\Delta t8 = -\frac{\left(1 - e^{-\lambda_{238} t8}\right) \text{R85m}}{1000\ \text{R85m} - 400\ R_U}\ \frac{\Delta U}{\lambda_{238}}, \tag{3.11}$$

where ΔU is the difference between the actual and assumed U isotopic composition of the sample (in delta notation, ‰), $t8$ is the ^{206}Pb-^{238}U age of the sample obtained using an "assumed" U isotopic composition, and $\Delta t8$ is the age correction to apply to the sample age. If the consensus value of $R_U = 137.88$ were used in place of the $^{238}U/^{235}U$ ratio of the sample, and a typical value of R85m = 1 ($^{238}U/^{235}U$ measured, $\sim$ equivalent to the sample/tracer $^{238}U/^{235}U$ ratio) were used, Eq. (3.11) simplifies to:

$$\Delta t8 = \left(18.467 \times 10^{-3}\right)\ \frac{\Delta U \left(1 - e^{-\lambda_{238} t8}\right)}{1000\ \lambda_{238}} \tag{3.12}$$

Figure (3.2b) shows the age correction required for ^{206}Pb-^{238}U ages at various ΔU values as a function of the age of the sample.

3.2.2.2 ^{207}Pb−^{235}U age corrections

Using the same approach and for the ^{207}Pb−^{235}U ages, the following equation is used

$$\frac{^{207}\mathrm{Pb}^*}{^{235}\mathrm{U_s}} = \left(e^{\lambda_{235} t5} - 1\right), \tag{3.13}$$

where the star denotes the radiogenic component, s denotes the sample and $t5$ is the time since closure of the system as calculated from ^{207}Pb-^{235}U systematics. Knowledge of the amount of ^{235}U in the sample is necessary, and this value is obtained by multiplying the amount of ^{238}U in the sample by the ^{238}U/^{235}U ratio (assumed) (Eq 3.6). Under this assumption, Eq. (3.13) thus becomes

$$\frac{^{207}\mathrm{Pb}^*}{^{238}\mathrm{U_s}} = \frac{1}{\mathrm{R_U}} \left(e^{\lambda_{235} t5} - 1\right) \tag{3.14}$$

Because the variations on $\mathrm{R_U}$ (the ^{238}U/^{235}U ratio) are small, the age correction will be small compared to the age of the sample, and the following equation can be written:

$$\Delta t5 = \frac{\Delta \mathrm{R_U}}{\partial \mathrm{R_U}(t5)/\partial t5} + \frac{\Delta ^{238}\mathrm{U_s}}{\partial ^{238}\mathrm{U_s}(t5)/\partial t5} \tag{3.15}$$

For a sample where no gain/loss of either Pb or U occurred, the ages $t5$ and $t8$ obtained from the ^{207}Pb-^{235}U and ^{206}Pb-^{238}U systematics, respectively, should be identical. The second term on the RHS of Eq. (3.15) thus becomes $\frac{\Delta ^{238}\mathrm{U_s}}{\partial ^{238}\mathrm{U_s}(t8)/\partial t8}$, which is nothing else than $\Delta t8$ (whose value is calculated using Eq. 3.12), and Eq. (3.15) thus becomes

$$\Delta t5 = \frac{\Delta \mathrm{R_U}}{\partial \mathrm{R_U}(t5)/\partial t5} + \Delta t8 \tag{3.16}$$

By rearranging Eq. (3.14), an expression of $\mathrm{R_U}(t5)$ is obtained, which is used to derive the following:

$$\Delta t5 = \frac{\Delta \mathrm{U}\left(1 - e^{-\lambda_{235} t5}\right)}{1000\ \lambda_{235}} + \Delta t8 \tag{3.17}$$

where ΔU, $t5$ and $\Delta t5$ are defined as in Eq. (3.11). Figure (3.2a) shows the age correction required for ^{207}Pb-^{235}U ages at various ΔU values as a function of the age of the sample.

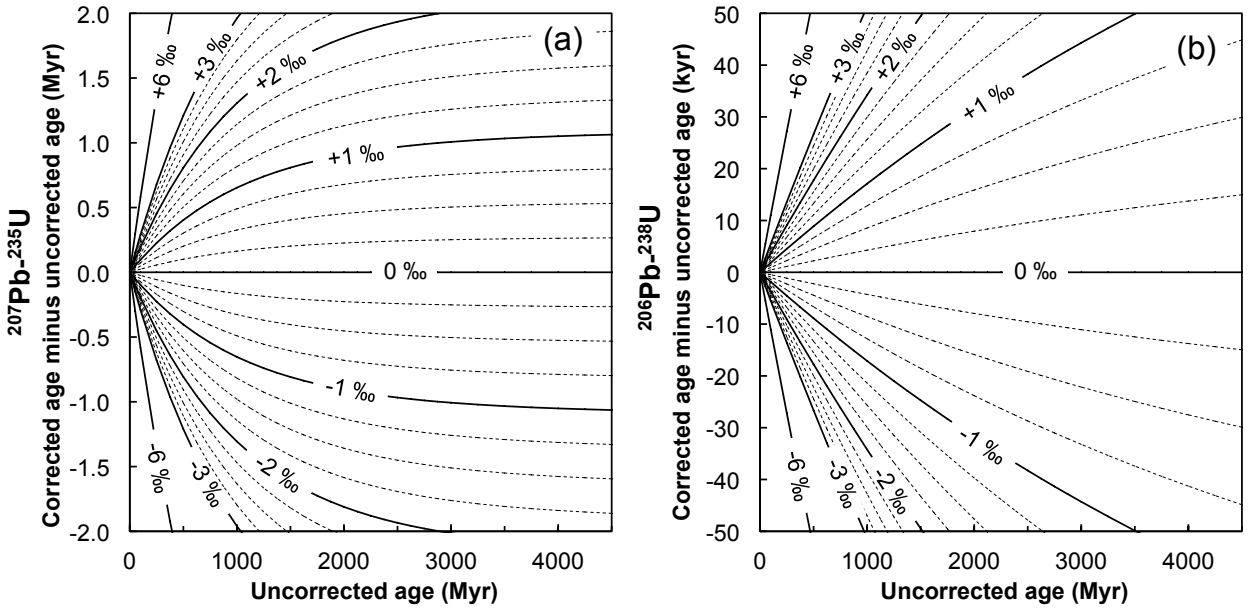

Figure 3.2: Age correction for various ΔU values as a function of the age of the sample, using (a) the ^{207}Pb-^{235}U and (b) the ^{206}Pb-^{238}U chronometers. Lines of equal ΔU are 0.25 ‰ apart and were calculated using Eqs. (3.12) and (3.17). Figure published in [431].

3.2.2.3 Circularity in calculation of U-Pb ages

As noted earlier, a circularity exists in the common U–Pb data reduction. Indeed, the ^{238}U/^{235}U ratio of the sample (R_U) is used to determine the amount of ^{238}U in the sample, which is then used to calculate the amount of ^{235}U in the sample as $^{235}U_s = {}^{238}U_s/R_U$. This situation is a result of the use of ^{235}U in the tracer (single or double spike) used to correct for instrumental mass fractionation. Such circular reasoning could be avoided by using a ^{233}U-^{236}U double spike, as the simultaneous determination of (i) the instrumental mass fractionation and (ii) the ^{238}U/^{235}U ratio of the sample would then be possible. Of course, the error on the ^{238}U/^{235}U ratio of the sample would need to be propagated to properly estimate the uncertainties on the ^{207}Pb-^{235}U and ^{206}Pb-^{238}U ages, but those ages would not require any further age correction.

3.2.3 Importance of age corrections

The importance of these age corrections is better understood when comparing them to the current precisions of Pb-Pb and U-Pb ages. With modern instrumentation, uncertainties on Pb-Pb ages of early Solar System materials can be as low as 0.2 Myr (*e.g.*, [12]), which is equivalent to a difference of 0.15 ‰ between the actual and assumed U isotopic composition of the sample. The typical spread of δ^{238}U values in coarse-grained CAIs (Calcium, Aluminum-rich inclusions) is $\sim$ 1 ‰ (*e.g.*, [71, 14, 119], see Fig. 1.10), which could mean an age difference of up to 1.5 Myr between two CAIs thought to be of equal age under the "consensus value" assumption. Because CAIs are thought to have formed within the first 1-2 Myr of the Solar System, determination of their U isotopic composition is required for proper dating using the Pb-Pb technique.

In geochronology, U-Pb is one of the most important isotopic dating methods (due to its high precision over a large age spectrum) and can be applied to bulk rocks as well as individual minerals: predominantly zircons, and in recent years, more and more to monazite, apatite, xenotime, titanite, rutile, baddeleyite, allanite, and perovskite (see [387] and references therein). With the exception of a few minerals (titanite, zircon) with δ^{238}U values up to 5 ‰, both igneous rocks and minerals show a roughly similar range of variation in their U isotopic compositions of $\pm$0.30 ‰ (Fig. 3.4; [202, 431]). Though the age corrections on ^{206}Pb-^{238}U ages for such isotopic variability are small compared to the uncertainties on the ages (on the order of 1 % of the error on the age before age correction), the effect on ^{207}Pb-^{235}U ages can be significant. For instance, for a 1 Gyr sample (and using typical analytical parameters from [386]), a 0.6 ‰ deviation from the "consensus" value in the ^{238}U/^{235}U ratio of the sample will translate into an age correction of 1.2 Myr (80 % of the error on the age before age correction). Considering an arbitrary maximum variability of 5 ‰ between individual zircons [202], the age corrections needed will range from 7 to 12 Myr for Pb-Pb ages and 0 to 5 Myr for ^{207}Pb-^{235}U ages, depending on the age of the sample. Clearly the characterization of the U isotopic composition of individual minerals is a necessary step in

order to obtain both accurate and precise ages using the Pb-Pb and U-Pb dating methods.

3.3 $^{238}U/^{235}U$ ratios in igneous rocks and the crust

3.3.1 U in granites

3.3.1.1 Motivation, sample description and methods

One of the early projects conducted as part of this dissertation aimed at characterizing the U isotopic composition of granitic rocks. The main motivation for this work was to assess whether the U isotopic compositions of granites (and by extension zircons, which carry a large fraction of the U in granitic rocks) could be related to the nature of the protolith rock (*i.e.*, sedimentary vs. igneous). If U isotopes did track the nature of the source material, the potential application to Hadean zircons was an exciting perspective as these samples provide the only record of Earth's evolution during that eon.

To determine whether the U isotopic compositions of granites depend on their source material, granitic rocks from the Silurian-Devonian Lachlan Fold Belt (LFB, Southeastern Australia) and Proterozoic Harney Peak Granite (Black Hills, South Dakota) were analyzed. These samples have been well characterized [204, 94, 307, 98, 391] and are divided into three groups according to their source rock [95, 257]. I-type granites (samples I1 to I9) are derived from partial melting of infracrustal meta-igneous rocks. They are hornblende-bearing (high grade regional metamorphism) and metaluminous [$Al_2O_3/(Na_2O+K_2O+CaO)< 1$]. S-type granites (samples S1 to S9) are derived from partial melting of supracrustal sedimentary source material that has been exposed to chemical weathering. They are generally more felsic (SiO_2-rich) and younger than I-types, and peraluminous ([$Al_2O_3/(Na_2O+K_2O+CaO)> 1$], due to aqueous removal of Ca and Na during weathering of feldspars into clay minerals [97]). S-type granites generally have lower $Fe^{3+}/ (Fe^{3+}+Fe^{2+})$ ratios (0.16) than I-types (0.30) [461]. The sedimentary sources of S-type granites are generally rich in graphite [162], which explains the more reducing conditions of their formation [165]. Classification of A-

type granite (samples A1 and A2) is more complex as it also involves considerations of the tectonic setting [257]. Several studies [462, 151, 50] provide detailed descriptions of the chemical and petrographic characteristics of A-type granites. They form in anorogenic environments, often in tensional regimes, are mildly alkaline, and their parental magmas are inferred to have been relatively water-poor. There is considerable uncertainty regarding their origin and a unique petrogenetic model may not be appropriate. Some of the major models that have been proposed include melting of relatively water-poor granulitic meta-igneous restite left from a prior episode of melt extraction [115, 112, 462], melting of granulitic crust metasomatized by mantle-derived alkaline fluids [273], derivation from basaltic magma by magmatic differentiation [257, 441], and partial melting of crustal tonalitic-granodioritic rocks [21, 123]. The chemical compositions of most samples studied here are available in the literature [204, 94, 96, 307, 98, 240, 391]. When not available (samples I4, I6, I7 and S7), however, the chemical compositions were measured at Service d'Analyse des Roches et des Minéraux (SARM), Nancy, France, using established protocols [84]. The SiO_2 concentrations of bulk samples range from 56 to 77 wt.%.

Samples were digested using the regular procedure outlined in Section 2.2.2, with addition of a 5 days digestion step in HF/HNO_3 2:1 at 180°C in Parr bombs to digest all refractory phases. The U purification (Section 2.3.2) was done twice to remove any matrix interferences. Isotopic measurements followed the protocol detailed in Section 2.4.2 and the data reduction outlined in Section 2.5. Enhanced signal stability was achieved by placing a spray chamber between the Aridus II and the MC-ICPMS. The procedural blank was estimated to be 0.02-0.05 ng U (0.01 % of sample uranium).

3.3.1.2 Results and the absence of Soret diffusion

The uranium isotopic compositions of 22 granitoids (I-, S-, and A-type) are reported in Table 3.1. The typical uncertainty for measurements of granitic rocks is ±0.05 ‰ (95 % confidence interval). For the most part granitoids show little isotopic variation, with $\delta^{238}U$

in most samples between -0.40 ‰ and -0.20‰.

			Double spike data reduction							Sample-standard bracketing			
Name	Rock Type	Mass (mg)	δ^{238}U (‰)	± (95CI)	δ [^{234}U/^{238}U] (‰)	± (95CI)	Conc (ppm)	± (95CI)	Usp/ Usmp	δ^{238}U (‰)	± (95CI)	δ [^{234}U/^{238}U] (‰)	± (95CI)
A1	Granite	45.06	-0.33	0.06	9.1	0.5	5.91	0.05	3.38%	-0.32	0.17	17.1	0.6
A2	Granite	52.83	-0.36	0.06	-455.5	0.5	7.21	0.06	2.36%	-0.41	0.17	-473.3	0.6
I1	Tonalite	122.88	-0.34	0.04	11.4	1.8	1.52	0.01	4.80%	-0.34	0.14	66.0	1.8
I2	Granodiorite	62.52	-0.21	0.04	-8.6	1.8	2.06	0.01	6.98%	-0.22	0.14	117.6	1.8
I3	Granodiorite	83.12	-0.22	0.04	-24.8	1.8	2.53	0.02	4.27%	-0.24	0.14	13.0	1.8
I4	Adamellite	34.92	-0.24	0.06	10.5	0.5	7.11	0.06	3.61%	-0.19	0.17	26.0	0.6
I5	Tonalite	240.54	-0.22	0.03	-131.9	0.2	1.5304	0.01	2.44%	-0.19	0.12	-156.9	0.2
I6	Qtz. Diorite	120.91	-0.26	0.04	-0.3	0.3	2.08	0.01	3.60%	-0.24	0.15	10.0	0.4
I7	Adamellite	83.28	-0.50	0.05	33.9	0.2	3.73	0.03	2.89%	-0.50	0.13	20.8	0.2
I8		41.87	-0.38	0.05	-11.1	0.2	7.60	0.06	2.84%	-0.41	0.13	-25.2	0.2
I9	Dacite	82.01	-0.32	0.05	5.3	0.2	3.94	0.03	2.79%	-0.31	0.13	-10.6	0.2
S1	Granodiorite	64.4	-0.23	0.06	-10.6	0.5	3.46	0.03	4.04%	-0.18	0.17	19.2	0.6
S1*	Granodiorite	63.5	-0.25	0.04	-14.8	1.8	3.50	0.03	4.12%	-0.28	0.14	18.0	1.8
S2	Granodiorite	62.66	-0.28	0.04	-42.2	1.8	2.91	0.02	4.99%	-0.27	0.14	19.4	1.8
S3	Granodiorite	63.64	-0.28	0.06	-8.7	0.5	3.43	0.02	4.14%	-0.23	0.17	24.5	0.6
S4	Adamellite	84.29	-0.28	0.04	-9.6	0.3	3.34	0.02	3.21%	-0.30	0.15	-11.6	0.4
S5	Granodiorite	83.1	-0.22	0.04	-48.9	0.3	3.01	0.02	3.57%	-0.21	0.15	-38.5	0.4
S6	Adamellite	46.05	-0.39	0.05	43.2	0.2	4.27	0.03	4.55%	-0.43	0.13	84.1	0.2
S7		30.26	-0.34	0.05	9.8	0.2	7.31	0.07	4.10%	-0.35	0.13	36.4	0.2
S8	Granite	41.97	-0.29	0.05	-1.0	0.2	7.53	0.06	2.87%	-0.25	0.13	-14.4	0.2
S9	Dacite	65.86	-0.27	0.05	21.5	0.2	3.88	0.03	3.51%	-0.29	0.13	28.9	0.2

* Denotes replicate on a newly digested sample.

Table 3.1: Sample name, type, mass, uranium concentrations and isotope compositions of granitoids (relative to CRM-112a standard). Data published in [428].

I-, S- and A-type granites have different protoliths and different modes of formation; however, there is no significant difference in δ^{238}U between these three granite types. Individual granitic rocks show variations in δ^{238}U. In particular, one I-type rock (I7) has a very low δ^{238}U value of -0.50 ± 0.05 ‰. The average δ^{238}U of all the granitoids is -0.31 ± 0.14 ‰ (2SD). These isotopic compositions agree well with previously documented U isotopic compositions of igneous rocks, including basalts [460, 430, 431]. There is no correlation between U isotopic variations and proxies for felsic magma evolution, such as SiO_2 content (see data in [428]), which is to say that U isotope variations in granites are not related to the nature of the protolith rock.

The original idea to be tested was proven false. Despite that, the data set in Table 3.1 can still be useful in testing one specific formation model for granites, by [264], in which granites form by a top-down thermal migration process. The model predicts that non-traditional stable isotope systems such as Fe, Mg and U should show signatures of thermal diffusion, also known as *Soret diffusion*, whereby the colder part (top) of the magma chamber is enriched

in heavy isotopes relative to the hotter part (bottom) of the magma chamber. The major problem of any model advocating for Soret effect is to sustain a large temperature gradient in the magma chamber on a long enough timescale for elemental and isotopic diffusion to occur. Indeed, it was shown as early as 1921 by Bowen that "*the time required to produce a significant amount of concentration of material by diffusion is enormously greater than that required for the mass to cool off*" [60]. The model of [264] proposes that continuous underplating of new magma at the base of the magma chamber can balance the heat loss at the top of the chamber and sustain a near steady-state temperature gradient (though nothing is said about convection in such a system). The main advantage of the model proposed by [264], is that it is testable. Magnesium, U and Fe isotopes in such a system should show strong and correlated mass-dependent fractionation as they do in experiments of thermal diffusion in silicate melts [366, 364, 217, 247], and therefore provide a straightforward means of identifying the Soret effect in geological processes [139].

The data set presented in Table 3.1 can thus be used in combination with the Mg and Fe isotopic data [428]. The Lachlan Fold Belt granitoids measured in this work are a good sample set to look for evidence of Soret diffusion as they are fresh samples and their Fe, Mg and U isotopic compositions were not affected by weathering. The isotopic fractionations observed in Mg and Fe are plotted against the variations in U isotopes in Fig. (3.3). Also plotted are expected correlations between isotope effects of different elements (dashed lines) based on theoretical and experimental considerations [364, 247]. If Soret diffusion were the driving mechanism of isotopic fractionation in the Lachlan Fold Belt granites, the samples should follow these trends.

As can be seen, there is no correlation in the sample set that would suggest that Soret diffusion was present. If anything, the variations would define a trend that is orthogonal to the trend predicted for Soret diffusion. Though these results do not rule out the possibility that Soret diffusion might be at play in some magmatic systems, it most definitely indicates that the granitoids investigated here (I-, S-, and A-type granitoids from the Lachlan Fold

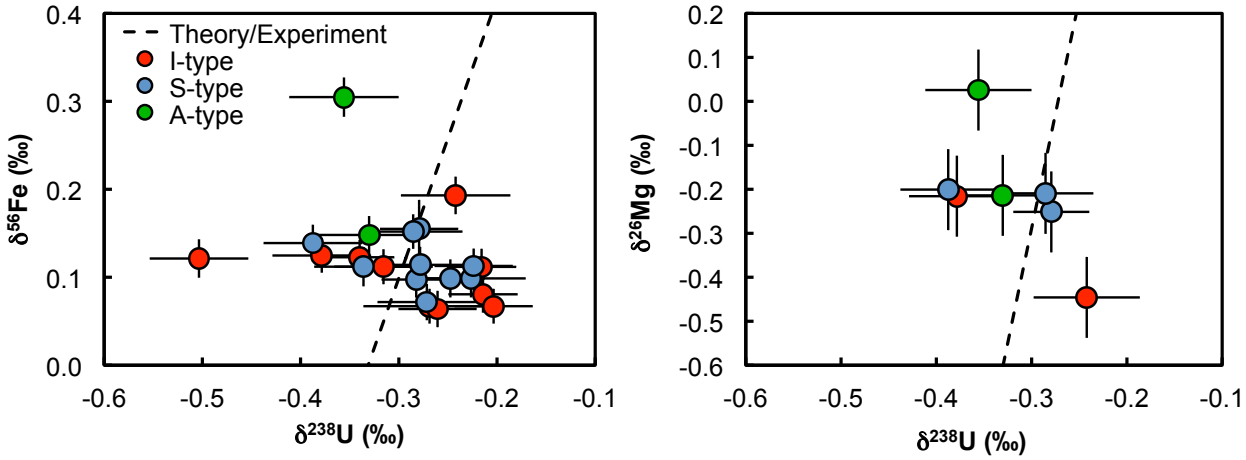

Figure 3.3: Expected isotopic fractionation of δ^{56}Fe-δ^{238}U (left), and δ^{26}Mg-δ^{238}U (right) produced by thermal (Soret) diffusion in a silicate melt (dashed lines: $\delta^{56}\text{Fe} = 3.18 \times \delta^{238}\text{U}$, and $\delta^{26}\text{Mg} = 10.41 \times \delta^{238}\text{U}$; [364, 247]). Soret diffusion has been proposed as a possible mechanism for fractionating iron isotopes (and other non-traditional stable isotopes) in felsic rocks [264]. The data do not follow the correlations expected for Soret diffusion. Modified from [428].

Belt) were not influenced by the Soret effect.

Together with other evidence presented in [428], this result suggests that fluid exsolution and fractional crystallization are the primary mechanisms for the δ^{56}Fe variations of felsic rocks.

3.3.2 U in Earth's crust

Riverine input is the dominant source of U into the ocean, and as such, its isotopic composition is a key parameter in oceanic mass-balance models. U from the crust is delivered to the ocean via oxidative weathering and transport by rivers. Understanding whether fractionation of U isotopes occurs during these processes requires knowledge of the isotopic composition of the starting material: Earth's crust. In this section, the isotopic composition of the crust is carefully evaluated.

3.3.2.1 U in geostandards

Table 3.2 reports the isotopic compositions of 41 geostandards (from USGS, GIT-IWG, ANRT and GSJ) covering commonly encountered rock types. In agreement with previously published values [412, 460, 428, 177], basalts show an average δ^{238}U of -0.29 ± 0.04 ‰, and the four granitic geostandards measured are at -0.23 ± 0.10 ‰. When combined with the larger granite data set previously measured (Table 3.1), the average δ^{238}U of granites is -0.32 ± 0.05 ‰. Consistent with limited U isotopic fractionation in rocks affected by terrestrial weathering [451], one soil sample (SoNE-1) and one bauxite sample (BX-N, a product of high weathering and good drainage), show δ^{238}U values close to basalts and granites. Most magmatic rocks have δ^{238}U values close to granites and basalts with the notable exception of two igneous rocks of intermediate compositions (andesite AGV-1 and AGV-2; and granodiorites GSP-1 and GSP-2) that display heavier isotopic compositions ($+0.16 \pm 0.04$ ‰, $+0.18 \pm 0.06$ ‰, -0.04 ± 0.04 ‰ and $+0.17 \pm 0.05$ ‰, respectively). These are outliers, as a larger granodiorite data set previously obtained (Table 3.1, [428]) gave an average δ^{238}U value for granodiorites of -0.22 ± 0.09 ‰, which is well within error of all other crustal rocks.

The shales measured here generally display heavier isotopic compositions than other crustal rocks (-0.26 ‰ to -0.17 ‰). SDO-1, a Devonian Black Shale deposited under euxinic conditions, shows a δ^{238}U of -0.08 ± 0.03 ‰, a value $+0.31$ ‰ higher than seawater.

Individual minerals show a small spread of isotopic compositions, with albite, biotite, kyanite and quartz having ^{238}U/^{235}U ratios identical to basalts and granites (-0.25 ‰), while glauconite, phologopite and zinnwaldite show lighter isotopic compositions, from -0.38 to -0.50 ‰ (see Section 3.2 for implications on Pb-Pb and U-Pb dating of individual minerals).

Summary of U isotopic compositions and concentrations of geostandards measured in this study.

Sample	Material			Resin #	Mass digested (mg)	*n*	From double spike data reduction									From sample-standard bracketing not using the double spike						Recommended		
							$\delta^{238}U/^{235}U$	95 CI	$\delta^{234}U/^{235}U$	95 CI	$\delta[^{234}U/^{238}U]$	95 CI	Conc. (ug/g)	2 SD	Usp/ Usmp	$\delta^{238}U/^{235}U$	95 CI	$\delta^{234}U/^{235}U$	95 CI	$\delta[^{234}U/^{238}U]$	95 CI	Conc. (ug/g)	±[b]	Source[c]
Rocks																								
AGV-1	Andesite	***	SEM	[1]	2	126.63	9	−0.16	0.05	29.2	0.3	−10.6	0.3	1.89	0.01	3.3%	−0.21	0.19	36.9	0.3	−3.5	0.4	1.92	0.15	(1)
AGV-2	Andesite	***	Far.	[1]	2	128.5	9	−0.18	0.09	31.9	8.7	−7.9	8.3	1.87	0.01	3.3%	−0.23	0.08	39.4	8.6	−1.0	8.2	1.88	0.16	(1)
Arhco-1	Basalt	***	SEM		2	174.4	9	−0.27	0.04	39.0	0.5	−1.0	0.5	1.39	0.01	3.3%	−0.22	0.13	41.5	0.5	0.4	0.6	1.4	*0.07*	(2)
BCR-1	Basalt	***	SEM		2	138.45	9	−0.26	0.05	39.0	0.3	−1.1	0.3	1.68	0.01	3.4%	−0.33	0.19	50.2	0.3	9.3	0.4	1.75	*0.09*	(3)
BCR-2	Basalt	*	Far.		2	302.03	9	−0.23	0.05	45.3	6.7	5.0	6.5	1.64	0.01	3.4%	−0.21	0.10	43.8	6.7	3.0	6.3	1.69	0.19	(1)
BCR-2 rep.	Basalt	**	Far.		2	150.3	9	−0.24	0.06	45.1	5.7	4.8	5.5	1.68	0.01	3.0%	−0.30	0.05	41.8	5.7	1.3	5.4	1.69	0.19	(1)
BCR-2 rep.	Basalt	***	Far.		2	142.68	3	−0.24	0.11	39.2	11.6	−0.9	11.2	1.67	0.01	3.2%	−0.27	0.33	43.4	11.6	2.9	11.2	1.69	0.19	(1)
BCR-2 rep. bef.[a]	Basalt	***	SEM		2	144.05	9	−0.26	0.05	39.7	0.2	−0.3	0.2	1.67	0.01	3.3%	−0.31	0.06	47.3	0.2	6.6	0.2	1.69	0.19	(1)
BCR-2 rep. aft.	Basalt	***	SEM		2	144.27	9	−0.26	0.05	40.2	0.2	0.1	0.2	1.66	0.01	3.4%	−0.30	0.06	48.5	0.2	7.7	0.2	1.69	0.19	(1)
BCR-2 rep.	Basalt	***	SEM		2	143.2	9	−0.26	0.03	40.9	0.7	0.8	0.7	1.66	0.01	3.4%	−0.23	0.12	49.1	0.7	8.1	0.7	1.69	0.19	(1)
BCR-2 rep.	Basalt	***	SEM		2	144.4	9	−0.26	0.04	41.1	0.5	1.0	0.5	1.70	0.01	3.3%	−0.32	0.09	47.5	2.6	6.7	2.5	1.69	0.19	(1)
BE-N	Basalt	*	Far.		2	98.13	9	−0.30	0.04	38.8	3.9	−1.2	3.8	2.41	0.01	1.8%	−0.26	0.07	−16.1	3.9	−53.8	3.7	2.4	0.18	(3)
BE-N rep.	Basalt	***	SEM		2	102.2	9	−0.33	0.05	37.9	0.5	−2.0	0.5	2.47	0.02	3.1%	−0.32	0.07	33.1	0.5	−7.0	0.4	2.4	0.18	(3)
BHVO-2	Basalt	**	Far.		2	571.8	9	−0.32	0.06	38.5	6.1	−1.5	5.8	0.404	0.002	3.6%	−0.34	0.08	54.5	6.0	13.4	5.8	0.42	*0.02*	(3)
BX-N	Bauxite	***	SEM		2	30.7	9	−0.34	0.05	44.9	0.3	4.8	0.3	9.15	0.06	3.1%	−0.32	0.12	44.6	0.3	4.0	0.3	8.8	*0.44*	(3)
BX-N rep.	Bauxite	***	SEM		2	28.8	9	−0.30	0.04	46.1	0.3	5.8	0.3	9.04	0.07	3.0%	−0.32	0.13	40.5	0.3	0.6	0.4	8.8	*0.44*	(3)
BSK-1	Bottom Sed.	***	SEM		2	81.39	9	−0.18	0.06	96.1	0.3	53.9	0.3	2.63	0.02	3.7%	−0.14	0.17	116.7	0.3	72.6	0.4	3	*0.15*	(4)
COQ-1	Carbonatite	**	Far.		2	24.8	9	−0.35	0.06	20.4	5.7	−18.8	5.5	9.07	0.10	3.7%	−0.37	0.05	41.5	5.7	1.0	5.4	11	0.60	(1)
COQ-1 rep.	Carbonatite	***	SEM		2	28.2	9	−0.31	0.05	26.4	0.5	−13.1	0.5	12.04	0.13	2.3%	−0.29	0.07	−5.6	0.5	−43.8	0.4	11	0.60	(1)
CLB-1	Coal	**	Far.		2	409.2	9	−0.32	0.06	53.7	6.1	13.2	5.8	0.497	0.003	3.7%	−0.35	0.08	72.0	6.0	30.1	5.8	0.55	*0.03*	(1)
CWE-1	Coal	***	Far.		2	801.1	7	−0.26	0.10	42.2	9.8	2.0	9.4	0.751	0.002	2.5%	−0.24	0.09	20.8	9.8	−18.8	9.3			
W-2	Diabase	***	Far.		2	453.58	9	−0.34	0.09	42.4	8.7	2.3	8.3	0.491	0.003	3.5%	−0.37	0.08	57.5	8.6	16.4	8.2	0.53	*0.03*	(1)
DR-N	Diorite	***	SEM		2	162.9	9	−0.32	0.06	41.3	5.0	1.2	4.8	1.56	0.01	3.2%	−0.41	0.20	38.4	5.0	−2.0	4.7	1.53	0.13	(5)
WS-E	Dolerite	***	Far.		2	370.17	9	−0.22	0.09	45.0	8.7	4.7	8.3	0.621	0.004	3.4%	−0.26	0.08	56.9	8.6	15.8	8.2	0.65	*0.03*	(3)
AC-E	Granite	*	Far.	[1]	2	109	9	−0.25	0.05	−7.2	6.7	−45.5	6.5	4.41	0.02	3.2%	−0.38	0.10	−12.8	6.7	−50.6	6.3	4.6	*0.23*	(3)
GA	Granite	*	Far.	[1]	2	100.28	9	−0.25	0.06	−13.7	4.8	−51.8	4.6	4.58	0.02	3.7%	−0.42	0.09	−3.1	4.8	−41.3	4.6	5	0.50	(3)
GS-N	Granite	***	Far.	[1]	2	34.5	9	−0.33	0.07	8.4	6.3	−30.5	6.0	7.73	0.07	3.0%	−0.30	0.06	4.5	6.3	−34.3	6.0	7.5	*0.38*	(3)
G-2	Granite	***	SEM	[1]	2	137.36	9	−0.11	0.10	33.4	0.3	−6.6	0.3	1.86	0.01	3.1%	−0.17	0.17	34.2	0.3	−6.1	0.4	1.76	*0.09*	(3)
G-3	Granite	***	Far.	[1]	2	136.9	9	−0.19	0.07	47.0	10.1	6.5	9.7	3.08	0.02	1.9%	−0.09	0.06	5.2	10.0	−33.8	9.6	2.3	0.30	(6)
GSP-1	Granodiorite	***	SEM	[1]	2	97.52	8	−0.04	0.05	15.0	0.3	−24.3	0.3	2.37	0.01	3.5%	−0.11	0.13	27.3	0.3	−12.6	0.3	2.54	*0.13*	(3)
GSP-2	Granodiorite	***	SEM	[1]	2	101.05	9	0.17	0.06	18.6	0.3	−21.1	0.3	2.44	0.02	3.3%	0.12	0.17	23.4	0.3	−16.7	0.4	2.4	0.19	(1)
JG-1	Granodiorite	***	SEM	[1]	2	63.63	8	−0.29	0.05	24.1	0.3	−15.3	0.3	4.00	0.02	3.2%	−0.28	0.13	25.9	0.3	−13.7	0.3	3.93	0.07	(7)
SDC-1	Mica-Schist	***	Far.	[1]	2	78.4	9	−0.30	0.09	34.7	8.7	−5.2	8.3	2.85	0.02	3.6%	−0.32	0.08	51.0	8.6	10.2	8.2	2.43	0.14	(8)
SDC-1 rep.	Mica-Schist	***	SEM		2	42.8	9	−0.26	0.04	36.3	0.5	−3.7	0.5			3.8%	−0.20	0.06	53.7	0.5	12.5	0.5	2.43	0.14	(8)
NOD-A-1	Mn-Nodule	**	Far.		2	34.6	9	−0.53	0.07	128.5	6.3	85.5	6.1	6.93	0.07	3.1%	−0.59	0.07	128.0	6.3	83.6	6.0	7	0.07	(9)
NKT-1	Nephelinite	***	SEM		2	107	9	−0.29	0.08	40.0	0.7	0.0	0.6	2.15	0.02	3.4%	−0.32	0.09	45.6	0.7	4.8	0.5	2.275	0.003	(10)
RGM-2	Rhyolite	***	Far.	[1]	2	46.5	9	−0.31	0.09	43.8	8.7	3.6	8.3	5.61	0.05	3.0%	−0.33	0.08	41.4	8.6	1.1	8.2	5.8	0.50	RGM-1 USGS
SBC-1	Shale	***	SEM		2	49	8	−0.26	0.05	35.6	0.7	−4.3	0.6	5.63	0.03	5.5%	−0.35	0.07	117.5	1.5	73.5	1.4	5.7	*0.29*	(11)
SBC-1 rep.	Shale	***	SEM		2	11.5	5	−0.25	0.06	24.4	0.4	−15.1	0.4	5.51	0.11	24.0%	−0.93	0.06	736.1	2.2	663.1	2.1	5.7	*0.29*	(11)
SDO-1	Shale	***	SEM		2	6.5	9	−0.07	0.05	40.6	0.2	0.3	0.2	43.58	1.50	3.3%	−0.12	0.08	49.6	1.6	8.6	1.5	48.8	6.50	(1)
SDO-1 rep.	Shale	***	SEM		2	5.4	9	−0.06	0.04	41.0	0.6	0.7	0.6	43.90	1.83	3.3%	−0.09	0.07	49.6	0.8	8.6	0.8	48.8	6.50	(1)
SDO-1 rep.	Shale	***	SEM		2	5	8	−0.11	0.05	40.8	0.6	0.5	0.6	41.61	1.86	4.0%	−0.06	0.05	73.3	3.5	30.9	3.3	48.8	6.50	(1)
SGR-1	Shale	*	Far.		2	92.99	9	−0.17	0.05	44.8	6.7	4.5	6.5	5.24	0.02	3.4%	−0.08	0.10	43.8	6.7	2.9	6.3	5.4	0.40	(1)
SGR-1 rep.	Shale	**	Far.		2	53.1	9	−0.22	0.07	36.7	6.3	−3.3	6.1	5.03	0.04	3.2%	−0.25	0.07	37.8	6.3	−2.6	6.0	5.4	0.40	(1)
SGR-1 rep.	Shale	**	Far.		2	48.9	9	−0.18	0.07	42.8	6.3	2.5	6.1	4.76	0.04	3.5%	−0.22	0.07	55.5	6.3	14.2	6.0	5.4	0.40	(1)
SoNE-1	Soil	***	SEM		2	118.8	9	−0.32	0.06	−40.7	0.3	−77.7	0.3	3.34	0.02	2.0%	−0.34	0.17	−78.3	0.3	−113.1	0.4			
STM-2	Syenite	***	SEM		2	27.8	9	−0.34	0.06	38.8	5.0	−1.2	4.8	8.06	0.09	3.6%	−0.39	0.20	48.9	5.0	8.0	4.7	9.06	*0.45*	(3)
ISH-G	Trachyte	***	SEM		2	30.9	9	−0.27	0.08	39.8	0.7	−0.2	0.6	9.11	0.09	2.8%	−0.31	0.09	24.7	0.7	−15.1	0.5	8.8	*0.44*	(3)
MDO-G	Trachyte	***	SEM		2	40.1	9	−0.34	0.05	34.3	4.5	−5.4	4.3	6.27	0.04	3.1%	−0.39	0.18	30.4	4.5	−9.6	4.2	6.3	*0.32*	(12)

Minerals																					
AL-I	Albite	***	SEM	2	43.4	9	−0.25	0.06	−58.0	5.0	−94.4	4.8	5.77	0.05	3.2%	−0.33	0.20	−60.3	5.0	−95.8	4.7	5.8	*0.29*	(3)
DT-N	Disthène	***	SEM	2	108.8	9	−0.26	0.04	24.3	0.6	−15.2	0.6	2.21	0.02	3.3%	−0.27	0.07	33.0	0.8	−7.1	0.8	2.3	0.43	(3)
GL-O	Glauconite	***	Far.	2	297.46	9	−0.38	0.07	63.0	6.3	22.2	6.0	0.81	0.01	3.3%	−0.39	0.06	68.6	6.3	27.1	6.0	0.80	*0.04*	(3)
Mica_Mg	Mica (phlogopite)	***	SEM	2	1615.88	9	−0.50	0.06	22.2	0.3	−17.0	0.3	0.140	0.001	3.4%	−0.69	0.17	32.4	0.3	−7.3	0.4	0.15	*0.01*	(3)
Mica_Fe	Mica (biotite)	***	SEM	2	3.48	9	−0.30	0.05	62.0	0.3	21.2	0.3	87.88	3.95	2.6%	−0.35	0.12	44.5	0.3	4.0	0.3	80	8	(12)
QLO-1	Quartz	***	SEM	2	128.6	9	−0.28	0.08	39.8	0.7	−0.2	0.6	1.84	0.01	3.4%	−0.32	0.09	43.5	0.7	2.8	0.5	1.9	0.1	(1)
ZW-C	Zinwaldite	**	Far.	2	12.7	5	−0.45	0.05	29.4	4.9	−10.1	4.8	19.36	0.26	3.2%	−0.42	0.06	31.6	4.9	−8.3	4.7	20	2.80	(3)

Far. Cup configuration for 233/234/235/236/238U is L3/L2/L1/C/H2.

SEM Cup configuration for 233/234/235/236/238U is L1/SEM/H1/H2/H3.

[a] Bef. and aft. denote, respectively, spiking before and after column chemistry.

[b] When no value is available for the uncertainty of the recommended concentration, a value of 5% was assumed (noted in italic).

[c] Tailing from ^{238}U on ^{236}U, ^{235}U and ^{234}U was taken as, respectively, 0.6 ppm, 0.25 ppm and 0.1 ppm. Hydride formation was corrected using the value $^{238}UH/^{238}U = 7.3e{-}7$.

[d] Activity ratio $[^{234}U/^{238}U]$ of the sample relative to secular equilibrium (in‰). $\delta\,[^{234}U/^{238}U] = \{(^{234}U/^{238}U)smp/(^{234}U/^{238}U)eq - 1\} * 1000$ where $(^{234}U/^{238}U)eq$ is the atomic ratio at secular equilibrium and is equal to $\lambda^{238}U/\lambda^{234}U = 5.497 * e{-}5$ (Cheng et al., 2013).

[e] References: (1) USGS certificate, (2) Burger and Krahenbuhl (1991), (3) Govindaraju (1994), (4) Lichte (1995), (5) Carignan et al. (2001), (6) Cotta and Enzweiler (2012), (7) Weyer et al. (2008), (8) Gouveia and Prudencio (2000), (9) Axelsson et al. (2002), (10) Matthews et al. (2011), (11) Webb et al. (2011), (12) Govindaraju (1995).

[*] Aridus I + Jet Cones.

[**] Aridus II + Jet Cones.

[***] Aridus II + Spray Chamber + Jet Cones.

[1] Sample was subjected to one step of digestion in Parr Bomb to dissolve refractory phases.

Table 3.2: Summary of U isotopic compositions and concentrations of geostandards measured in this study. References: Cheng et al. (2013), [107]; Burger & Krahenbuhl (1991), [73] ; Govindaraju (1994), [181]; Lichte (1995), [254] ; Carignan et al. (2001), [84]; Cotta and Enzweiler (2012), [121]; Weyer et al. (2008), [460]; Gouveia and Prudencio (2000), [180]; Axelsson et al. (2002), [29]; Matthews et al. (2011), [277]; Webb et al. (2011), [456]; Govindaraju (1995), [182]. Table published in [431].

3.3.2.2 Complementing with data compilation

The large number of measurements on geostandards (Table 3.2) and seawater samples (Section 3.6.1, Table 3.5) were supplemented by a thorough data compilation of 1297 isotopic measurements on 1140 samples from 32 studies. All $^{238}U/^{235}U$ ratios were converted back to $\delta^{238}U$ values and renormalized to the CRM-112a standard. This compilation is available as Table S2 in the Supplementary Material of [431] and is graphically represented in Fig. (3.4) and (4.1) (see figure captions for references).

The top panel of Fig. (3.4) represents the modern U isotope taxonomy. The horizontal blue line represents the seawater average of -0.392 ± 0.005 ‰ (see Section 3.6.1). Most crustal rocks and detrital sediments show isotopic compositions between -0.40 ‰ and -0.20 ‰ (*i.e.*, andesites, basalts, alkali basalts, rhyolites, trachytes, diorites, granites, granodiorites, syenite, mica-schist, soils, coals, arc lavas, ocean island basalts [OIB], and mid ocean ridge basalts [MORB]), while altered oceanic crust and 1 dunite show heavier compositions (up to +0.20 ‰). Large rivers have a $\delta^{238}U$ of -0.24 ‰, while the one lake measured in this study has a composition indistinguishable from seawater. Also very close to seawater are the 2 pelagic clays, 5 seafloor volcaniclastic sediments and modern corals. Fossil corals, oysters and speleothems show a large spread of $\delta^{238}U$ values, centered on the seawater value. Samples in which U is mostly adsorbed (a Ca-dolomite chimney from a hypersaline lagoon, evaporites and Fe-Mn crusts) have a distinctly light isotopic composition (-0.52 to -0.83 ‰), while samples incorporating U under euxinic or anoxic conditions have isotopic compositions on average heavier than seawater ($\delta^{238}U$ up to +0.40 ‰).

The bottom panel of Fig. (3.4) presents the U isotope systematics in individual minerals, ore deposits, past sediments and meteoritic bodies/inclusions. Note the change of scale relative to the top panel. Minerals show a somewhat larger range of isotopic composition than crustal rocks (from -0.68 to +0.52 ‰ with a few minerals up to +4.8 ‰), and Hiess et al. (2012) [202] proposed that these variations are due to crystal-chemical processes during crystallization. U in ore deposits shows large variations (from -4.13 to +2.10 ‰), while

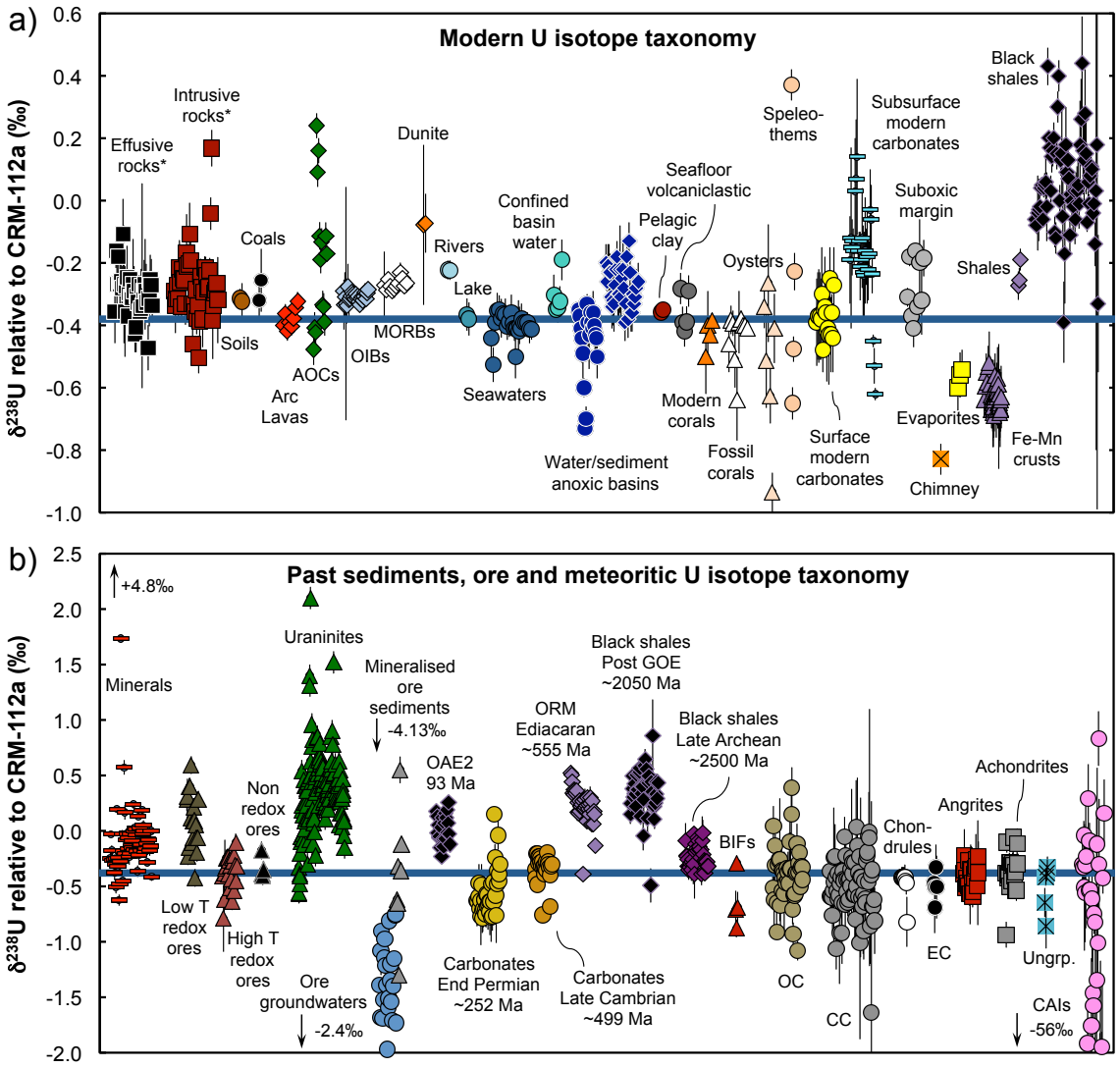

Figure 3.4: Compilation of the δ^{238}U values obtained from this work and literature data [414, 415, 412, 460, 51, 14, 71, 67, 300, 57, 68, 249, 69, 119, 202, 428, 28, 107, 231, 236, 370, 19, 127, 179, 221, 305, 443, 18, 177, 238, 314]) (see Table S2 in the Supplementary Material of [431] for actual values). The top panel shows the modern U taxonomy while the bottom panel shows the data for individual minerals, ore deposits, past sediments and meteoritic bodies and inclusions. Note the different scale on the two panels. See main text for details on the composition of Earth's crust, the modern oceanic budget and the U isotopic composition of the Solar System. AOC stands for altered oceanic crust, OAE for oceanic anoxic event, ORM for organic-rich mudrocks, BIF for banded iron formations, OC for ordinary chondrites, CC for carbonaceous chondrites, and EC for enstatite chondrites. Subsurface modern carbonates include carbonates down to 40 cm below the water/sediment interface. Minerals include albite, apatite, baddeleyite, glauconite, biotite, phologopite, monazite, quartz, titanite, xenotime, zinnwaldite, zircon. Effusive rocks* encompass andesites, basalts, alkali basalts, rhyolites and trachytes. Intrusive rocks* encompass diorites, granites, granodiorites, syenite, and mica-schist. Achondrites encompass howardites, eucrites, aubrite, and acapulcoite. Details of meteoritic samples are shown in Fig. (4.1). Published in [431].

the groundwaters in ore deposits display systematically light isotopic compositions (from -0.75 to -2.39 ‰). Both observations are thought to reflect NFS effects and depend on the efficiency of U reduction/oxidation processes and the composition of the source material [51, 67, 305, 443]. Of particular interest for paleoredox applications is the fact that ancient anoxic/euxinic sediments have compositions close to modern black shales (median δ^{238}U value of $+0.29$ ‰), with the exceptions of Archean black shales, which are much closer to modern crustal rocks (median δ^{238}U value of -0.26 ‰). The shift from crustal-like values to modern black shale-like values tracks the onset of oxidative weathering during the Great Oxidation Event, between 2.50 and 2.05 Gyr ago [300, 236, 28, 238]. In contrast, smaller scale variations in the δ^{238}U values of End Permian carbonates (decrease from $+0.15$ to -0.79 ‰) and Late Cambrian carbonates (excursion from -0.20 down to -0.76 ‰) are thought to reflect increases of oceanic anoxia at the time of sample deposition [68, 127]. Four BIFs show compositions similar to or lighter than the modern crust (from -0.88 to -0.29 ‰).

The compilation shown in Fig. (3.4) has several virtues: (i) it is an excellent pedagogic tool when trying to grasp the scale of the natural variability of the ratio of U "stable" isotopes, (ii) it allows the reader to develop a feel for the magnitude and direction of the isotopic fractionation between any two U reservoirs, and (iii) it provides reliable average compositions and associated uncertainties of most of the U reservoirs in the U cycle. Armed with this tool, it is now time to consider the crustal U isotopic composition.

3.3.2.3 The U isotopic composition of the continental and oceanic crust

U is a highly lithophile element. As such, it is mostly present in the crust and the mantle of the Earth, and is not expected to partition into the core [280]. A recent study [464], invoking sulfide-silicate equilibration under extremely reduced conditions, suggested that the core could contain up to 8 ppb of U. Even under this hypothesis, the core would contain only a minor fraction of the U of the Earth (< 17 %), and therefore in the following discussion, it is assumed that the crust and mantle are the only two U reservoirs of the

Earth. Constraining the isotopic composition of the continental crust is an important first step in trying to constrain the U isotopic composition of the Earth. Knowledge of the isotopic composition of both the continental crust and the mantle will, in turn, provide insights into (i) whether or not the bulk Earth is chondritic, (ii) whether or not any isotopic fractionation accompanied crustal extraction, or (iii) what the effect of crustal recycling is on "stable" uranium isotopes (this last point has been extensively discussed by [18]).

The fractions of various rock types in the continental and oceanic crust are used to calculate the concentrations and isotopic compositions of uranium in both types of crust. Two studies [335, 371] based on isostatic equilibrium suggested a two-layer model of the continental crust in which a granodioritic upper crust is overlaying a basaltic lower crust. Both models provide a breakdown of the whole (continental + oceanic) crust by mass and volume of the main rock types. Though more recent estimates of the composition of the crust are available, they are either mostly based on these two studies [457] or only report chemical compositions and not the details of the rock types present ([377] and references therein).

Table 3.3 shows the abundances, masses, U concentrations and isotopic compositions of the main types of rocks in the continental crust, the oceanic crust and the whole crust. The U concentrations are taken from [369], while the isotopic compositions are from this work (see Table S3 in Supplementary Material of [431]). Andersen et al. (2015) [18] showed that, because of incorporation of fractionated U in the oceanic crust during low-T hydrothermal circulation, the upper layer (top 500 m) of the altered oceanic crust (AOC) has a distinctly higher δ^{238}U than MORBs and OIBs (-0.17 ± 0.03 ‰ *vs.* -0.29 ± 0.01 ‰). In the present assessment of the composition of the oceanic crust, therefore, the value of -0.17 ± 0.03 ‰ was used for the top 500 m of the AOC ([U] = 400 ppb), and a basalt-like value of -0.29 ± 0.01 ‰ for the remaining 5500 m of oceanic crust ([U] = 50 ppb).

The two crustal models [335, 371] lead to similar average U concentrations and yield identical U isotopic compositions for both the continental and oceanic crust. The total

Poldervaart (1955)							Ronov and Yaroshevsky (1969)						
Rock type	% volume	Mass (10^{24} g)	U conc.[a] (ppm)	δ^{238}U (‰)	± (‰)	*n*	Rock type	% volume	Mass (10^{24} g)	U conc.[a] (ppm)	δ^{238}U (‰)	±[c] (‰)	*n*
Continental crust													
Sediments[*]	0.8	0.12	3	−0.30	0.05	4	Sediments[*]	1.7	0.35	3	−0.30	0.05	4
Clays[**]	0.7	0.10	3	−0.35	0.05	7	Clays[**]	2.8	0.56	3	−0.35	0.05	7
Shales	1.6	0.24	4	−0.24	0.11	3	Shales	2.5	0.51	4	−0.24	0.11	3
Granite/ Rhyolite	41.7	6.03	4	−0.34	0.04	17	Granites	14.2	3.07	4	−0.33	0.05	15
							Syenites, nepheline syenites	0.1	0.03	4	−0.31	0.03	6
							Gneisses	29.0	6.29	3.5	−0.26	0.04	1
Granodiorites	19.2	2.83	3	−0.21	0.09	8	Granodiorites, diorites	15.0	3.25	3	−0.25	0.05	16
Diorites/ Andesites	8.1	1.24	3	−0.28	0.04	10							
							Basalts, gabbros, amphibolites, eclogites	29.9	7.05	0.56	−0.29	0.01	43
Basalts	27.8	4.24	0.56	−0.29	0.01	43							
							Dunites, peridotites	0.0	0.01	0.01	−0.08	0.26	1
							Crystalline schists	4.1	0.88	2	−0.26	0.04	2
							Marbles	0.7	0.15	0.2	?		
Continental Crust	*100.0*	*14.80*	*2.7*	*−0.30*	*0.04*		*Continental Crust*	*100.0*	*22.14*	*2.5*	*−0.28*	*0.03*	
			$^{238}U/^{235}U$ ratio[b]	137.796	0.005					$^{238}U/^{235}U$ ratio[b]	137.799	0.004	
Modern oceanic crust													
Sediments[*]	2.2	0.18	3	−0.30	0.05	4	Sediments[*]	0.9	0.05	3	−0.30	0.05	4
Clays[**]	12.8	1.05	3	−0.35	0.05	7	Clays[**]	11.5	0.57	3	−0.35	0.05	7
Diorites	12.3	1.06	3	−0.28	0.04	8							
Basalts[§]							Basalts[§]						
Upper AOC	6.1	0.55	0.4	−0.17	0.03		Upper AOC	7.3	0.49	0.4	−0.17	0.03	
Lower crust	66.6	6.03	0.05	−0.29	0.01	43	Lower crust	80.3	5.37	0.05	−0.29	0.01	43
Oceanic crust	*100.0*	*8.86*	*0.83*	*−0.31*	*0.03*		*Oceanic crust*	*100.0*	*6.46*	*0.36*	*−0.33*	*0.04*	
			$^{238}U/^{235}U$ ratio[b]	137.794	0.004					$^{238}U/^{235}U$ ratio[b]	137.792	0.005	
Whole (continental + oceanic) crust													
Sediments[*]	1.3	0.30	3	−0.30	0.05	4	Sediments[*]	1.6	0.40	3	−0.30	0.05	4
Clays[**]	5.1	1.14	3	−0.35	0.05	7	Clays[**]	4.7	1.13	3	−0.35	0.05	7
Shales	1.0	0.24	4	−0.24	0.11	3	Shales	1.9	0.51	4	−0.24	0.11	3
Granite/ Rhyolite	26.7	6.0	4.0	−0.34	0.04	17	Granites	11.0	3.07	4	−0.33	0.05	15
							Syenites, nepheline syenites	0.1	0.03	4	−0.31	0.03	6
							Gneisses	22.4	6.29	3.5	−0.26	0.04	1
Granodiorites	12.3	2.83	3	−0.21	0.09	8	Granodiorites, diorites	11.6	3.25	3	−0.25	0.05	16
Diorites/ Andesites	9.6	2.30	3	−0.28	0.04	10							
							Basalts	42.9	12.90	0.34	−0.29	0.01	43
Basalts	44.0	10.82	0.27	−0.29	0.01	43							
							Dunites, peridotites	0.0	0.01	0.01	−0.08	0.26	1
							Crystalline schists	3.2	0.88	2	−0.26	0.04	2
							Marbles	0.5	0.15	0.2	?		
Whole crust	*100.0*	*23.66*	*2.0*	*−0.30*	*0.03*		*Whole crust*	*100.0*	*28.61*	*2.0*	*−0.28*	*0.03*	
			$^{238}U/^{235}U$ ratio[b]	137.795	0.005					$^{238}U/^{235}U$ ratio[b]	137.798	0.004	

[*] "Sediments" encompasses calcareous sands, siliceous oozes, sandstone and graywacke.

[**] "Clays and shales" encompasses red clay, carbonates, limestone, shelf sediments and hemipelagic sediments.

[§] The structure of the basaltic layer in the modern oceanic crust is taken from Andersen et al. (2015). The crust is assumed to be 6 km deep, with only the top 500 m being strongly altered by low temperature hydrothermal circulation ([U] = 0.4 ppm and high $\delta^{238}U = -0.17$‰) and the remaining 5500 m being MORB like ([U] = 0.05 ppm and $\delta^{238}U = -0.29$‰).

[a] Unless indicated otherwise, concentrations are taken from Rogers and Adams (1969).

[b] Absolute ratios are calculated using the $^{238}U/^{235}U$ ratio from Richter et al. (2010) of 137.837.

[c] Errors on the crust isotopic composition take into account the 2SD of the isotopic composition of each lithology, and assume a 25% uncertainty on concentration and masses of each lithology. The error on the isotopic composition dominates by almost a factor of 5.

Table 3.3: Abundances, masses, U concentrations and isotopic compositions of the main types of rocks in the modern continental crust, the modern oceanic crust and the modern whole crust. Table published in [431].

average δ^{238}U of the crust is calculated as -0.29 ± 0.03 ‰ (Table 3.3). This value takes into account the errors on the isotopic compositions of each lithology as well as a conservative 25 % uncertainty on their masses and uranium concentrations.

This estimate of the crustal value is in agreement with the values proposed by Kaltenbach (2013) [231], -0.30 ± 0.06 ‰, and Goldmann et al. (2015) [177], -0.30 ± 0.05 ‰. Those earlier estimates are, however, not well constrained. The former estimate is based on repeat measurements of only 6 volcanic and 6 plutonic rocks and the latter estimate is solely based on basalt analyses ($n = 14$). The approach followed herein, based on abundance estimates of the major rock types in the crust ($n = 101$) and taking into account the uncertainty on the isotopic compositions of the various rock types, is more robust. Using the CRM-112a ^{238}U/^{235}U ratio of 137.837 from Richter et al. (2010) [367], the absolute ^{238}U/^{235}U ratio of the crust is 137.797 ± 0.005, which can be used in U-Pb or Pb-Pb dating of crustal rocks when the ^{238}U/^{235}U ratio is not otherwise available.

3.3.2.4 Is the bulk Earth chondritic?

Having defined the isotopic composition of the crust, consider now the question of the δ^{238}U of the bulk Earth. For the bulk Earth, the following mass balance equation must be satisfied (assuming the amount of U in the core is negligible, and/or not heavily fractionated),

$$\delta^{238}\mathrm{U}_{\text{Bulk Earth}} \times \mathrm{U}_{\text{Bulk Earth}} = \delta^{238}\mathrm{U}_{\text{Crust}} \times \mathrm{U}_{\text{Crust}} + \delta^{238}\mathrm{U}_{\text{Mantle}} \times \mathrm{U}_{\text{Mantle}} \quad (3.18)$$

where U is the quantity of uranium (g) and δ^{238}U the isotopic composition of each reservoir. The bulk uranium concentration of the Earth is estimated to be 15 ppb [281, 7, 280], which, combined with the mass of the Earth of 5.97×10^{27} g, gives $\mathrm{U}_{\text{Bulk Earth}} = 8.96 \times 10^{19}$ g of U. The mass of the crust is taken as 24×10^{24} g [335] which, using a U concentration of 2 ppm (Table 3.3, in agreement with [207, 377]), gives $\mathrm{U}_{\text{Crust}} = 4.8 \times 10^{19}$ g of U, leaving 4.2×10^{19} g of U in the mantle ($\mathrm{U}_{\text{Mantle}}$). The continental crust U isotope composition

determined in this work is used ($\delta^{238}U_{Crust} = -0.29 \pm 0.03$ ‰), and previously reported U isotopic compositions of MORBs and OIBs are used as proxies for the mantle composition ($\delta^{238}U_{Mantle} = -0.29 \pm 0.02$ ‰; [414, 460, 231, 177, 18]). The similarity between the crust and mantle composition suggest that no isotopic fractionation occurs during crustal extraction. With these data, a $\delta^{238}U_{Bulk\ Earth}$ value of -0.29 ± 0.02 ‰ is calculated. The error takes into account the uncertainty on the crust and mantle composition.

The range of composition observed in meteorites is very large [-1.14 to $+0.39$ ‰, Figs. (3.4b) and (4.1)], and uncertainties remain concerning the actual average Solar System value. Nevertheless, the $\delta^{238}U_{Bulk\ Earth}$ value calculated above agrees with the two estimates of the average U isotopic composition of the Solar System (see Section 4.2.1), meaning that, to first order, the Earth has a chondritic U isotopic composition. The average Solar System value is, however, not very well constrained, and more work is needed to improve this estimate (see Section 4.2.1).

3.4 Validation of the U proxy in the modern ocean

3.4.1 U elemental and isotopic mass-balance in the ocean

To first order, paleoredox reconstructions rely on simple mass-balance considerations whereby the U input to the ocean is assumed to be constant and the ocean itself is at steady-state (*i.e.*, the amount of U being precipitated out of the ocean is the same as the amount being delivered from rivers). Within such a framework, the elemental abundance (*e.g.*, [323, 324]) and isotopic composition [300, 68, 238, 28, 19, 127, 238] of authigenic uranium in ancient sediments has recently been used to reconstruct paleoredox conditions in the oceans. The rationale is that, at steady-state, the uranium isotopic composition of seawater should be influenced by the proportions of sediments formed under different conditions because the extent of uranium isotopic fractionation differs in anoxic, euxinic, suboxic, and oxic sediments.

Such approaches rely on one major assumption, the fact that the ocean is at steady-state with regards to U mass-balance, and a series of key ingredients, the fractionation factors between the seawater and the various U sinks in the ocean, noted $\Delta_{\text{sedimentary sink - SW}}$, and defined as

$$\Delta_{\text{sedimentary sink - SW}} = \delta^{238}\text{U}_{\text{sedimentary sink}} - \delta^{238}\text{U}_{\text{SW}} \tag{3.19}$$

The first problem is that, even for a system as well characterized as the modern ocean, the various U budgets published in the literature are not necessarily in agreement with each other, nor are they necessarily at steady-state. If we cannot constrain the modern ocean, how can we reasonably hope to constrain past oceans? The second problem rests in the determination of the isotopic fractionation factors, $\Delta_{\text{sink - SW}}$. Undeniably, work has been done over the past several years to assess the characteristic fractionation factors of sediments formed under various conditions [351, 412, 460, 52, 70, 370, 393, 19, 179, 35, 305, 314, 451, 413]. Yet, in all cases, these fractionation factors are derived from local case studies, and it is unknown to what extent these are representative of the diverse conditions encountered in the oceans, where accumulation rate, organic matter burial rate, and mineral mode can vary.

Looking at the question of the U budget first, a typical budget is depicted in Fig. (3.5) (based mostly on the estimates from Dunk et al. (2002) [149]). There are two pieces of mass-balance information contained in the U oceanic budget: the flux mass-balance and the isotopic mass-balance. The flux mass-balance can be written as,

$$\frac{d\text{U}_{\text{SW}}(t)}{dt} = \sum_{Sources} F_i - \sum_{Sinks} F_j \tag{3.20}$$

where $\text{U}_{\text{SW}}(t)$ is the amount of U in the ocean at time t, and F_i and F_j are the fluxes of U coming in (sources) or out (sinks) of the ocean, respectively. At steady-state, the amount of U in the ocean is constant, and the LHS of Eq. (3.20) is null, giving

$$\sum_{Sources} F_i = \sum_{Sinks} F_j \tag{3.21}$$

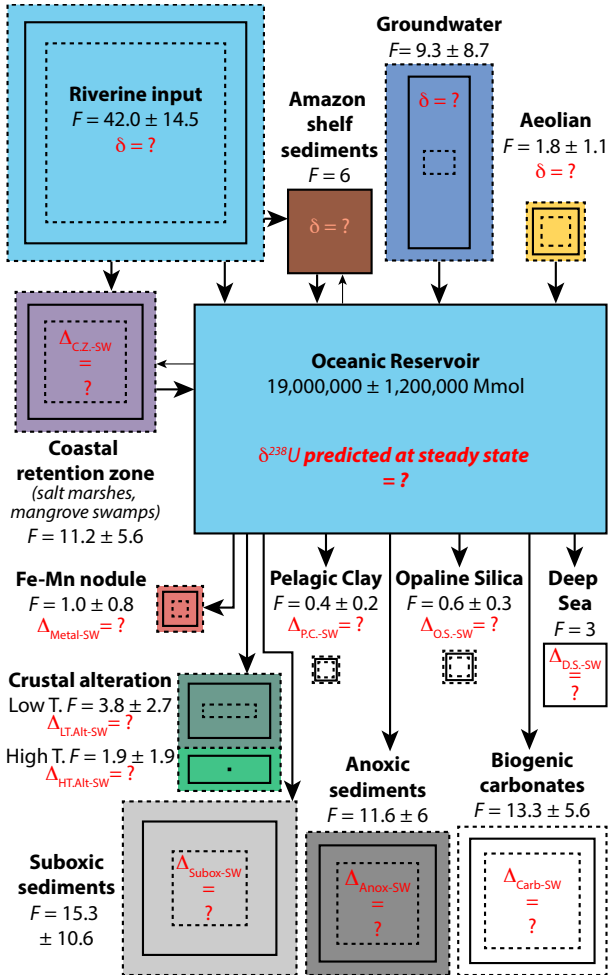

Figure 3.5: Schematic representation of the sources, sinks and fluxes of U in the modern ocean, based on the budget of [149]. Fluxes are in Mmol/yr. Except for the ocean, the surface area of the boxes is proportional to the U flux.

In the steady-state case, and assuming that the riverine input is the only input of U to the ocean, the isotopic mass-balance is written as:

$$\delta^{238}\mathrm{U}_{\mathrm{river}} F_{\mathrm{river}} = \sum_{Sinks} \delta^{238}\mathrm{U}_j F_j \tag{3.22}$$

Introducing the fractionation factor from Eq. (3.19) as $\delta^{238}\mathrm{U}_j = \Delta_{\text{sink-SW}} + \delta^{238}\mathrm{U}_{\mathrm{SW}}$, and dividing by F_{river}, gives

$$\delta^{238}\mathrm{U}_{\mathrm{river}} = \sum_{Sinks} \left(\Delta_{\text{sink-SW}} \times f_j\right) + \delta^{238}\mathrm{U}_{\mathrm{SW}} \sum_{Sinks} f_j \tag{3.23}$$

where f_j is the proportion of U incorporated in sink j, and the sum of all f_j terms is equal to 1. Eq. (3.23) can be rearranged to obtain the isotopic composition of the seawater as

$$\delta^{238}\mathrm{U_{SW}} = \delta^{238}\mathrm{U_{river}} - \sum_{Sinks} \left(\Delta_{\text{sink-SW}} \times f_j\right) \tag{3.24}$$

For a given oceanic U budget, the steady-state assumption can thus be tested on both the elemental and the isotopic level. Given that several U budgets have been proposed [33, 301, 149, 195], comparison of the $\delta^{238}\mathrm{U_{SW}}$ predicted by the various budgets, using the present best estimates isotopic fractionation factors, can help gain insight into (i) the validity of the steady-state assumption, (ii) the robustness of the fractionation factor estimates, and (iii) the validity of using U "stable" isotopes as a tracer of paleoredox conditions. Such a test requires the characterization of the isotopic composition of the seawater itself, and of the various sources and sinks of U.

3.4.2 The U isotopic composition of river water, lake water, evaporites and the ocean

Details on the water samples analyzed in this work are given in Table 3.4, while Table 3.5 reports the U isotopic compositions and U concentrations of several samples of seawater, river water, lake water, oysters, evaporites and coral samples (Fig. 3.4a).

The Atlantic ocean, the Pacific ocean, the Mediterranean sea, the Gulf of Mexico and the English Channel have identical isotopic compositions within error bars that agree with previously published values [412, 460, 19, 18]. The samples measured here define an average seawater δ^{238}U value of -0.38 ± 0.01 ‰ ($n = 13$). When combined with literature data ($n = 9$), the average seawater δ^{238}U value is calculated as -0.392 ± 0.005 ‰. This is the current best estimate of the modern ocean seawater U isotopic composition. The Persian Gulf and the Bassin d'Arcachon (Atlantic coast, France) show slightly heavier isotopic compositions at -0.33 ± 0.03 ‰ and -0.33 ± 0.05 ‰, respectively. The Bassin d'Arcachon is a partially

Sample	Material/Location	Date	Depth	Latitude	Longitude	Water (before filtration)	Filter changed every	Filter delay (h)	Acid delay (h)	HCl (g)	pH
Garonne river	France	8/9/11	0.10m	44°39'26.93N	0°21'28.89W	Turbide	30 ml		250	0.53	2.00
Garonne river	France	1/2/12	0.10m	44°39'26.93N	0°21'28.89W	Slightly turbide		54	57	0.47	1.97
Lake Michigan	Indiana Dunes, USA	7/9/11	0.30m	41°40'47.118N	87°00'58.175W	Many particles	250 ml		32	0.6	1.94
Lake Michigan	Chicago, USA	7/9/11	0.15m	41°47'4.062N	87°34'3.309W	No particle	250 ml		1	0.6	1.94
Arguin, France	Atlantic Ocean	8/16/11	0.20m	44°13'41N	1°15'15W	No particle	250 ml		82	0.53	2.00
Miami, FL	Atlantic Ocean	12/31/10	0.30m	25°46'06N	80°07'49W	Sand in suspension	250 ml		23	0.54	2.02
Dive 4463 EPR	Pacific Ocean	10/27/08	2500m	10°19'41.9514"N	103°33'28.62" W						
Dive 3961 EPR	Pacific Ocean	#N/A	2000m	9° 50' 20" N	104° 17' 28" W						
San Francisco,CA	Pacific Ocean	7/23/11	0.15m	37°45'36.712N	122°30'40.95W	Sand + Particles	120 ml		70.5	0.54	1.99
Cadaqués, Spain	Mediterranean Sea	8/5/11	0.20m	42°17'24.71N	3°18'9.02E	No particles	120 ml	27	346	0.53	2.00
Faedra, Crete	Mediterranean Sea	8/3/12	0.10m	35°09'58.84''N	25°42'40.0386''E	No particule	250 ml		57	0.51	2.01
Juan-les-Pins, France	Mediterranean Sea	9/6/10	2m	43°33'52N	7°06'51E	Very few particles	250 ml		62	0.54	1.99
Santorin, Greece	Mediterranean Sea	8/2/12	0.10m	36°23'54.96''N	25°22'48.3882''E	Many particles	180 ml		81	0.51	2.01
Galveston, TX	Gulf of Mexico	3/10/11	0.50m	29°17'56N	94°46'38W	Sand in suspension	No filter		54.5	0.29	2.26
Galveston, TX	Gulf of Mexico	3/22/12	0.10m	29°16'49.81''N	94°48'3.38''W	Sand in suspension	60 ml		34.5	0.46	2.01
Abu Dhabi, UAE	Persian Gulf	12/29/11	0.10m	24°28'42.8N	54°19'58.9E	No particles	250 ml	3.5	136	0.52	2.01
Dubaï, UAE	Persian Gulf	12/28/11	0.20m	25°08'45N	55°11'33E	Sand in suspension	250 ml	7	156.5	0.54	1.99
Arcachon, France	Arcachon Bassin	9/6/10	2m	44°40'20N	1°08'30W	Many particles	250 ml		55.5	0.53	2.00
Moulleau, France	Arcachon Bassin	9/6/10	0.30m	44°38'30.17N	1°12'16.29W	Many particles	250 ml		54	0.52	2.01
Moulleau, France	Arcachon Bassin	8/18/11	0.15m	44°38'30.17N	1°12'16.29W	Many particles	250 ml	0.25	28	0.53	2.00
Graveline, France	English channel	5/27/12		51°01'2.9814''N	02°06'52.2894''E	Many particles	250 ml		255	0.51	2.01
Guaymas, Mexico	Gulf of California	#N/A	2500m	27° 00' N	111° 24' W						
Tiki Island, TX	Jones Bay, USA	3/10/11	0.15m	29°18'25N	94°54'18W	Many particles	100 ml		44	0.64	1.94

Table 3.4: Details of the seawater samples analyzed in this work.

confined gulf in which spatial gradients driven by tidal hydrodynamics have been observed for water temperature, salinity and both N and C isotopes [53, 128]. Similar gradients might exist for U isotopes and could explain the slightly higher δ^{238}U value measured. This hypothesis could also explain the value measured on the south coast of the Persian Gulf: another partially confined gulf where strong temperature and salinity gradients have been observed [361]. Alternatively, and even though U behaves mostly conservatively in estuaries [89, 381], various uptake and release processes can take place in those areas such as flocculation of colloidal U or adsorption and/or reduction of U associated with organic matter, which might also influence the isotopic composition of the U remaining in solution (for more details see references in [149]).

Two samples from the Garonne river (France), taken a year apart, gave identical δ^{238}U of -0.22 ± 0.03 ‰, in excellent agreement with other major rivers [412, 315]. Two samples from Lake Michigan, taken on the same day 30 miles apart, yielded identical results at -0.37 ± 0.04 ‰. Oysters were more difficult to measure due to their low U concentrations (20 ng/g). Their isotopic compositions are typically within error of seawater. A modern coral measured twice shows a δ^{238}U indistinguishable from seawater within ±0.02 ‰, in agreement with earlier yet less precise measurements (±0.10 ‰, [412, 460]). Finally, three modern evaporite samples were measured: their U concentrations range from 6 to 13 ng/g, and their isotopic compositions average -0.57 ± 0.03 ‰.

3.4.3 U input to the ocean and isotopic fractionation factors

In all modern uranium budgets [33, 301, 149, 195], the main source of U in the ocean is the riverine input, which displays an average $\delta^{238}U_{river} = -0.24$ ‰ [412, 315]. The uncertainty on this value is not known precisely, but from published data it seems to be no larger than ±0.05 ‰. In particular, Noordmann et al. (2011) measured the isotopic composition of a large number of rivers and found all major rivers to average −0.24 ‰, with only small rivers showing departure from this value, most likely due to variations in the lithologies of

Summary of U isotopic compositions and concentrations of seawaters, lake, rivers, coral, oysters and evaporites measured in this study.

Sample	Material/ Location			Resin #	Mass digested (g)	*n*	From double spike data reduction									From sample standard bracketing not using the double spike						Recommended		
							$\delta^{238}U/^{235}U$	95 CI	$\delta^{234}U/^{235}U$	95 CI	$\delta[^{234}U/^{238}U]$	95 CI	Conc. (ng/g)	2 SD	Usp/ Usmp	$\delta^{238}U/^{235}U$	95 CI	$\delta^{234}U/^{235}U$	95 CI	$\delta[^{234}U/^{238}U]$	95 CI	Conc. (ng/g)	±	Source[b]
River																								
Garonne river 2011	France	***	SEM	3	81.366	8	−0.21	0.05	186.9	0.7	141.4	0.6	6.231	0.046	1.6%	−0.19	0.07	131.8	1.5	89.9	1.4	0.69	0.10	(1)
Garonne river 2011 rep.	France	***	SEM	3	320.590	5	−0.22	0.06	177.9	0.8	132.7	0.8	0.075	0.001	14.1%	−0.60	0.06	554.1	4.4	492.2	4.2	0.69	0.10	(1)
Garonne river 2012	France	***	SEM	3	326.130	8	−0.24	0.05	236.6	0.7	189.3	0.6	0.602	0.011	1.5%	−0.16	0.07	181.0	1.5	136.7	1.4	0.69	0.10	(1)
				Garonne river average			−0.22	0.03								−0.32	0.04							
Lake																								
Lake Michigan 1	Chicago, USA	***	SEM	2	80.350	3	−0.38	0.13	311.8	0.6	261.9	0.5	0.339	0.002	29.4%	−1.38	0.47	1213.5	0.7	1123.9	1.1	0.30	*0.02*	(2)
Lake Michigan 1 rep.	Chicago, USA	***	SEM	3	322.460	6	−0.36	0.06	315.3	0.7	265.2	0.6	0.330	0.006	3.1%	−0.38	0.06	311.6	2.0	261.2	1.8	0.30	*0.02*	(2)
Lake Michigan 2	Indiana dunes, USA	***	SEM	2	80.780	3	−0.34	0.13	309.2	0.6	259.3	0.5	0.352	0.003	26.2%	−1.27	0.47	1100.7	0.7	1016.0	1.1	0.30	*0.02*	(2)
Lake Michigan 2 rep.	Indiana dunes, USA	***	SEM	3	321.330	6	−0.39	0.06	309.8	0.8	260.0	0.7	0.345	0.006	2.8%	−0.46	0.08	297.9	1.7	248.6	1.6	0.30	*0.02*	(2)
				Lake Michigan average			−0.37	0.04								−0.43	0.05							
Evaporites																								
Salt_Gypsum	Santioco	***	SEM	3	3.6758	4	−0.60	0.07	244.4	0.9	197.2	0.9	13.8	1.0	1.5%	−0.56	0.07	187.0	4.9	142.7	4.7			
Salt_Halite	Santioco	***	SEM	3	9.448	4	−0.56	0.07	248.2	0.9	200.8	0.9	6.0	0.6	1.0%	−0.57	0.07	172.8	4.9	129.2	4.7	11	6	(3)
Guerande salt	France	***	SEM	3	8.3506	5	−0.54	0.06	190.1	0.8	144.8	0.8	10.0	0.8	0.9%	−0.48	0.08	105.8	3.4	65.3	3.3	11	6	(3)
				Evaporite average			−0.56	0.04								−0.54	0.04							
Coral																								
Modern coral	Florida, USA	***	SEM	1	0.19837	9	−0.38	0.03	188.2	0.5	142.8	0.5	1.96	0.01	2.5%	−0.37	0.06	163.8	4.3	120.5	4.1			
Modern coral rep.	Florida, USA	***	SEM	1	0.20019	9	−0.39	0.03	188.0	0.4	142.6	0.4	2.00	0.01	2.4%	−0.44	0.05	157.0	3.7	114.1	3.5			
				Coral average			−0.39	0.02								−0.41	0.04							
Oysters																								
Oyster_Arguin	Arguin, France	***	SEM	2	2.13899	5	−0.34	0.07	141.9	8.0	98.2	7.7	40.70	0.14	20.2%	−1.04	0.34	721.0	7.9	650.9	7.4			
Oyster_Gillardot	Gillardot France	***	SEM	2	2.16178	3	−0.63	0.09	166.1	10.3	121.8	9.9	13.02	0.05	60.7%	−2.85	0.44	2130.5	10.2	1995.7	9.6			
Oyster_Quiberon_7V	Quiberon, France	***	SEM	2	2.10936	3	−0.41	0.11	159.4	8.7	115.1	8.4	15.30	0.05	53.7%	−2.27	0.34	1885.7	8.6	1760.1	8.1			
Oyster_Quiberon	Oyster	***	SEM	2	2.10936	1	−0.51	0.15	162.8	17.9	118.5	17.2	15.30	0.05	53.7%	−2.48	0.77	1889.2	17.7	1766.0	16.6			
Oyster_PeconicBay	Peconic Bay, USA	***	SEM	2	2.0496	6	−0.93	0.06	94.5	7.3	53.2	7.0	46.68	0.16	17.3%	−1.36	0.31	574.4	7.2	512.0	6.8			
Tiki_Oyster	Carbonate	***	Far.	2	1.2536	2	−0.26	0.19	−9.3	18.4	−47.5	17.7	30.976	0.000	40.0%	−1.13	0.17	1255.9	18.3	1165.6	17.4			
Seawaters																								
Arguin, France	Atlantic Ocean	***	SEM	3	321.020	9	−0.39	0.04	189.9	0.5	144.5	0.5	3.15	0.01	3.0%	−0.39	0.06	179.5	0.5	135.5	0.5	3.22	0.06	(4)
Miami, FL	Atlantic Ocean	**	Far.	2	80.270	9	−0.35	0.06	189.6	5.7	144.2	5.5	2.81	0.02	4.4%	−0.43	0.05	229.7	5.7	183.2	5.4	3.22	0.06	(4)
				Atlantic Ocean average			−0.38	0.03	189.9	0.5	144.5	0.5				−0.41	0.04	180.0	0.5	136.0	0.5			
Dive 4463 EPR	Pacific Ocean	***	Far.	2	80.140	9	−0.39	0.03	190.5	2.4	145.0	2.3	3.12	0.02	3.0%	−0.40	0.06	185.9	2.4	141.7	2.3	3.22	0.06	(4)
Dive 3961 EPR	Pacific Ocean	***	Far.	2	80.250	9	−0.41	0.05	191.5	4.1	146.1	4.0	3.17	0.02	3.0%	−0.37	0.04	185.2	4.1	141.3	3.9	3.22	0.06	(4)
San Francisco, CA	Pacific Ocean	***	SEM	2	80.280	9	−0.45	0.04	191.7	0.5	146.3	0.5	2.95	0.02	3.3%	−0.40	0.09	191.9	0.5	146.9	0.5	3.22	0.06	(4)
San Francisco, CA rep.	Pacific Ocean	***	SEM	1	80.172	9	−0.38	0.05	192.3	0.4	146.8	0.4	3.03	0.02	3.1%	−0.42	0.08	189.8	3.2	145.4	3.0	3.22	0.06	(4)
San Francisco, CA rep.	Pacific Ocean	***	SEM	2	80.172	9	−0.36	0.05	191.9	0.4	146.4	0.4	3.03	0.02	3.1%	−0.41	0.06	190.9	2.4	146.3	2.2	3.22	0.06	(4)

San Francisco, CA rep.	Pacific Ocean	***	SEM	3	80.172	9	−0.36	0.04	191.3	0.6	145.8	0.6	3.03	0.02	3.1%	−0.36	0.07	189.6	0.8	145.3	0.8	3.22	0.06	(4)
San Francisco, CA rep.	Pacific Ocean	***	SEM	4	80.172	8	−0.41	0.07	190.6	0.5	145.2	0.5	3.03	0.02	3.1%	−0.39	0.07	189.0	0.7	144.7	0.6	3.22	0.06	(4)
San Francisco, CA rep.	Pacific Ocean	***	SEM	5	80.172	9	−0.34	0.04	189.5	0.4	144.0	0.4	3.03	0.02	3.1%	−0.33	0.07	183.6	3.4	139.1	3.2	3.22	0.06	(4)
				Pacific Ocean average			−0.40	0.02	191.4	0.3	145.9	0.3				−0.38	0.03	191.4	0.5	146.4	0.5			
Cadaques, Spain	Mediterranean Sea	***	SEM	2	80.230	9	−0.40	0.04	192.8	0.6	147.3	0.6	3.43	0.02	2.9%	−0.45	0.13	177.7	0.6	133.4	0.7	3.22	0.06	(4)
Faedra, Crete	Mediterranean Sea	***	SEM	3	160.710	9	−0.39	0.05	197.1	0.6	151.4	0.6	3.48	0.01	2.8%	−0.38	0.06	181.5	1.4	137.4	1.3	3.22	0.06	(4)
Juan-les-Pins, France	Mediterranean Sea	**	Far.	2	80.150	9	−0.36	0.06	187.3	5.7	141.9	5.5	3.16	0.02	3.6%	−0.42	0.05	201.5	5.7	156.3	5.4	3.22	0.06	(4)
Santorini, Greece	Mediterranean Sea	***	SEM	3	159.970	9	−0.39	0.04	189.2	0.5	143.8	0.5	3.42	0.01	2.8%	−0.38	0.06	170.6	0.5	126.9	0.5	3.22	0.06	(4)
				Mediterranean Sea average			−0.39	0.02	192.6	0.3	147.1	0.3				−0.40	0.03	174.5	0.4	130.4	0.4			
Galveston 2011, TX	Gulf of Mexico	***	Far.	2	80.320	9	−0.38	0.07	202.3	6.2	156.4	5.9	2.89	0.02	3.3%	−0.38	0.06	206.9	6.1	162.0	5.9	3.22	0.06	(4)
Galveston 2011, TX rep.	Gulf of Mexico	***	SEM	2	81.530	9	−0.35	0.05	202.2	0.2	156.3	0.2	2.85	0.01	3.4%	−0.42	0.06	210.7	0.2	165.3	0.2	3.22	0.06	(4)
Galveston 2011, TX rep.	Gulf of Mexico	***	SEM	2	80.050	9	−0.36	0.05	202.1	0.3	156.2	0.2	2.80	0.01	3.6%	−0.46	0.17	215.3	0.3	169.7	0.4	3.22	0.06	(4)
Galveston 2012, TX	Gulf of Mexico	***	SEM	3	160.430	8	−0.37	0.05	204.6	0.6	158.6	0.6	2.13	0.01	4.5%	−0.36	0.05	249.7	3.5	202.1	3.3	3.22	0.06	(4)
				Gulf of Mexico average			−0.36	0.03	202.3	0.2	156.4	0.2				−0.39	0.03	212.5	0.2	166.6	0.2			
Abu Dhabi, UAE	Persian Gulf	***	SEM	2	160.610	9	−0.34	0.05	187.2	0.5	141.8	0.5	3.93	0.02	2.4%	−0.34	0.07	155.8	0.5	112.8	0.4	3.22	0.06	(4)
Dubai, UAE	Persian Gulf	***	SEM	2	160.270	9	−0.32	0.05	186.2	0.5	140.8	0.5	3.82	0.01	2.5%	−0.29	0.07	157.3	0.5	114.2	0.4	3.22	0.06	(4)
				Persian Gulf average			−0.33	0.03	186.7	0.3	141.3	0.3				−0.32	0.05	156.5	0.3	113.5	0.3			
Arcachon, France	Arcachon Bassin	***	Far.	2	80.030	9	−0.30	0.06	195.1	6.7	149.4	6.5	2.98	0.02	3.0%	−0.39	0.19	189.0	6.7	145.4	6.5	3.22	0.06	(4)
Moulleau, France	Arcachon Bassin	***	Far.	1	120.540	8	−0.33	0.06	191.9	8.9	146.3	8.6	3.12	0.01	3.3%	−0.88	0.14	198.1	8.8	154.3	8.5	3.22	0.06	(4)
Moulleau, France	Arcachon Bassin	***	Far.	2	120.540	8	−0.35	0.07	192.9	7.2	147.3	6.9	3.12	0.01	3.3%	−0.42	0.07	199.1	7.2	154.6	6.9	3.22	0.06	(4)
Moulleau, France	Arcachon Bassin	***	Far.	3	120.540	8	−0.37	0.07	187.9	8.1	142.5	7.8	3.12	0.01	3.3%	−0.40	0.06	194.2	8.1	149.9	7.7	3.22	0.06	(4)
				Arcachon Bassin average			−0.33	0.05	193.5	4.3	148.3	4.1				−0.58	0.07	190.5	4.3	146.4	4.1			
Gravelines, France	English channel	***	SEM	3	160.390	9	−0.35	0.05	191.5	0.5	145.9	0.5	3.14	0.01	3.1%	−0.38	0.05	188.4	1.6	143.8	1.5	3.22	0.06	(4)
Guaymas, Mexico	Gulf of California	***	Far.	2	80.600	9	−0.38	0.06	197.0	6.7	151.3	6.5	3.12	0.02	3.0%	−0.41	0.07	191.4	6.7	148.2	6.3	3.22	0.06	(4)
Tiki Island, TX	Jones Bay, USA	***	Far.	2	80.040	9	−0.19	0.07	213.6	8.0	167.0	7.7	2.01	0.01	4.6%	−0.23	0.05	263.2	7.9	215.6	7.6	3.22	0.06	(4)

[a] Symbols and notations as in Table 5.

[b] References: (1) Saari et al. (2008), (2) Kennedy et al. (1977), (3) Stewart (1963), (4) Chen et al. (1986a).

Table 3.5: Summary of U isotopic compositions and concentrations of seawaters, lake, rivers, coral, oysters and evaporites measured in this study. Symbols and notations as in Table 3.2. References: Saari et al. (2008), [381]; Kennedy et al. (1977), [239]; Stewart (1963), [410], Chen et al. (1986a), [99]. Table published in [431].

their watersheds. The small difference between the isotopic composition of the upper crust (-0.29 ± 0.04 ‰) and that of the riverine flux suggests that little to no isotopic fractionation occurs during oxidative weathering. This hypothesis is supported by (i) the measurements of bauxite and soil samples which have δ^{238}U values identical to basalts and granites [431], and (ii) a recent experiment of uranium oxidation of solid tetravalent U [451], where only weak fractionation was observed, probably due to a "rind effect", where the surface layer of U(IV) must be completely oxidized before the next layer can be exposed to the oxidant.

Other U sources to the ocean are negligible and/or very poorly characterized. The aeolian input represents only a minor source of U (4 % of the riverine input), and likely has the same isotopic composition as the upper continental crust; $\delta^{238}U_{aeolian} = -0.29$ ‰. U released from shelf sediments could represent up to 15 % of the riverine input, as a study of the Amazon shelf sediments suggested [282], and submarine groundwater discharge could represent from 1 to 34 % of the riverine input [149]. The actual U fluxes from these sources are difficult to assess and their isotopic compositions are unknown. In the following discussion, it is considered that the δ^{238}U of the rivers represent the isotopic composition of the entire U input to the ocean (*i.e.*, including release from shelf sediments and submarine groundwater discharge). The uncertainty introduced by not knowing the magnitude and isotopic composition of the other sources is not considered.

In the following paragraphs, the different $\Delta_{sink\text{ - }SW}$ values used in the mass-balance model are defined and discussed, with more emphasis being placed on the environments for which these factors are not well constrained.

To first order, anoxic/euxinic sediments (anoxic: $[O_2]$ and $[H_2S] \sim 0$ μmol/L; euxinic: $[O_2] \sim 0$ μmol/L and $[H_2S] \geq 11$ μmol/L; [39, 411]) display a much heavier isotopic composition than seawater. In detail, the data show a large spread of isotopic compositions [460, 300, 19] equivalent to $0 \leq \Delta_{Anoxic/Euxinic\text{-}SW} \leq +0.83$ ‰. This is because *in situ* reductive authigenic U accumulation in anoxic/euxinic sediments occurs via coupled U diffusion and reduction in the porewater. Therefore, the fractionation expressed in the sed-

iment depends on the depositional setting of the sediment (*e.g.*, restricted basin or open setting; full or incomplete U extraction from pore water; oxic or anoxic overlaying water; [19]). For the present purpose, the average fractionation in anoxic/euxinic sediments of $\Delta_{\text{Anoxic/Euxinic-SW}} = +0.6$ ‰ is used [19]. This value is only half the fractionation obtained from first principles calculations in the case of pure U reduction [41, 384, 1], and is in good agreement with values derived from several case studies (+0.4 ‰, [305]; +0.7 ‰, [314]) and biologically-mediated U reduction experiments (+0.46 ‰, [52]; $+0.68 - 0.99$ ‰, [35]; +0.85 ‰, [418]; +0.77 ‰, [413]). One experiment of U reduction by anaerobic bacteria observed a negative fractionation (-0.3 ‰, [351]), and the same group later suggested that their original finding may have been the result of adsorption of UO_2Cl_2 onto microbial cells. Interestingly, abiotic reduction experiments have, to date, only produced U isotopic fractionation in the direction opposite to that imparted by biotic processes [418], or no measurable isotopic fractionation at all (with Zn^0: [412]; with Fe^0: [351]; with S^{2-} or organics, [418]).

To reconcile these apparently contradictory observations, Stylo et al. (2015) [418] proposed that in biologically-mediated U reduction, rapid U^{VI}-U^{IV} exchange in the vicinity of the enzyme makes equilibrium NFS effects the principal source of isotopic fractionation (*i.e.*, any isotopic fractionation associated with the U reduction itself is overwritten by the equilibrium fractionation). This makes sense as, in the NFS theory, it is not the reduction itself that leads to ^{238}U enrichment in the reduced phase, but the exchange of isotopic species between the oxidized and reduced phase. The lack of isotopic fractionation during abiotic Fe^0-, Zn^0-, sulfide- or organic-mediated U reduction would then be the result of U^{IV} sequestration without significant fractionation (due to direct two-electron transfer to U^{VI}), while the light U isotopic composition observed during reduction of U by divalent iron (Fe^{II}) would reflect kinetic effects (see [418] for details).

Whether or not the interpretation of [418] is correct does not change the observation that only biologically-mediated U reduction leads to ^{238}U enrichment in the reduced phase. The systematic shift to heavier isotopic composition of reduced sediments thus suggests

that, in the modern ocean, U reduction is principally the product of biologically-mediated reduction. This interpretation is in good agreement with earlier studies which found that inorganic U reduction did not occur at *in situ* concentrations of U and H_2S, or only extremely slowly [22, 258, 34, 436]. If the preferential incorporation of ^{238}U in reduced sediments is only achieved in the presence of specific micro-organisms, it also means that the ratio of U "stable" isotope in the rock record is sensitive to the extent of anoxic environments in which redox processes are biologically catalyzed. In this regard, the $^{238}U/^{235}U$ ratio is more of a bioredox proxy, than a redox proxy [418].

Similarly to anoxic/euxinic sediments, the average fractionation expressed in suboxic sediments ($[O_2] \leq 10$ μmol/L and $[H_2S] \leq 10$ μmol/L; [39, 411]) depends on the conditions of deposition, but unlike anoxic/euxinic sediments, the authigenic enrichment in suboxic sediments is small (for more details see [19]). Little literature data are available for such samples and we use the average fractionation of $\Delta_{\text{Suboxic-SW}} = +0.1$ ‰ [460].

Biogenic carbonates, a sink representing between 10 and 30 % of the U output from the modern ocean, seem to record the isotopic composition of the seawater from which they formed with a small, and well constrained, fractionation: $\Delta_{\text{Biogenic Carbonates-SW}} = +0.2$ ‰ [412, 460, 370, 19]. This value includes the effect of early diagenesis under euxinic conditions, in the first 40 cm below the water/sediment interface [370].

Mn nodules and metalliferous sediments have a fractionation factor of $\Delta_{\text{Metalliferous-SW}} = -0.24$ ‰, well constrained by both natural samples [412, 460, 179, 431] and adsorption experiments [70].

Another important sink of U is described as the "coastal retention zone" in Dunk et al. (2002) [149] and encompasses salt mashes, swamps and mangroves. In these estuarine settings, the salinity is low (< 12 psu, practical salinity unit) and, when the colloid fraction dominates, U behaves non-conservatively (*e.g.*, [89, 108, 336, 420, 23, 334]). U removal occurs initially through sorption of U onto Fe-oxyhydroxides/ organic colloids (in surface salt marshes 65 % of the U exists in adsorbed or complexed form, [108]). The colloids are then scavenged

and buried in sediments on a short timescale before U reduction occurs at depth within the sediment [419]. Because of the lack of measurement of salt marshes or mangrove sediments, the observation is made that phases with adsorbed/complexed U have similar isotopic composition (evaporites, Fe-Mn nodules, [412, 460, 179, 431]) and the hypothesis made that the same adsorption-complexation mechanism is at play in these samples and in coastal retention zones, leading to a similar isotopic fractionation. A $\Delta_{\text{Coastal Retention Zone-SW}} = -0.24$ ‰ is thus used, but further work is needed to ascertain this value.

The last important sink of U in the modern ocean is linked to hydrothermal circulation and seafloor alteration at high ($> 100°$C) and low ($< 100°$C) temperatures. High temperature hydrothermal circulation occurs at depth in the oceanic crust (> 1000 m), close to the spreading ridge axis, and U removal in this environment is thought to be nearly quantitative [295, 106]. It is therefore assumed that no fractionation occurs and $\Delta_{\text{HT Alteration-SW}} = 0$ ‰ is used. Since the HT hydrothermal flux is 2 to 10 times smaller than the LT hydrothermal flux, this assumption has no bearing on the exercise. Low-temperature alteration occurs at ridge flanks through percolation of relatively low-temperature seawater (all the way down to $60 - 70°$C, [303]; and even at temperatures as low as $20 - 30°$C, [164, 416]) and only affects the top $500 - 1000$ m of the oceanic crust. Basalts affected by low-temperature hydrothermal circulation have high U concentrations (up to $500 - 1000$ ppb, [149]) and display δ^{238}U values significantly higher than fresh MORBs (up to +0.16 ‰, [18]). To quantify the fractionation associated with low-temperature alteration, $\Delta_{\text{LT Alteration-SW}} = \delta^{238}\text{U}_{\text{LT Alteration}} - \delta^{238}\text{U}_{\text{Seawater}}$, the following mass-balance is considered:

$$\delta^{238}\text{U}_{\text{Altered}} = f \times \delta^{238}\text{U}_{\text{Fresh}} + (1 - f) \times \delta^{238}\text{U}_{\text{LT Alteration}} \tag{3.25}$$

where $\delta^{238}\text{U}_{\text{Altered}}$ and $\delta^{238}\text{U}_{\text{Fresh}}$ are the isotopic composition of the altered and fresh basalts, respectively, and f is the fraction of U of the altered basalt that was present before

alteration. The average U concentrations in non-altered and altered basalts are, respectively, 78 ppb and 390 ppb [194, 149, 234, 407], yielding $f = 78/(390-78) = 25$ %. The $\delta^{238}U_{Fresh}$ value of fresh basalt is -0.29 ‰ [431], and the $\delta^{238}U_{Altered}$ value of basalts altered by low-T hydrothermal circulation was recently estimated to be -0.17 ± 0.03 ‰ [18], using the "Super" composite sample from ODP Site 801 whose composition represents a weighted average of the top 420 m of altered oceanic crust [235, 8, 234]. With these input values, the isotopic composition of U incorporated during low-T hydrothermal circulation, $\delta^{238}U_{LT\ Alteration}$, is calculated to be -0.14 ‰, equivalent to $\Delta_{LT\ Alteration\text{-}SW} = +0.25$ ‰.

A minor sink noted as "Deep Sea" encompasses pelagic red clays, siliceous and calcareous deep-sea sediments. Only two pelagic clays have been measured thus far [18], and these samples have virtually the same $\delta^{238}U$ value as seawater: $\Delta_{Pelagic\ Clays\text{-}SW} = +0.04$ ‰. With the exceptions of pelagic clays, there are no other constraints on the U isotopic fractionation associated with the "Deep Sea" sink, which represents at most 10 % of the U budget and can therefore be neglected. No data exist for biogenic/opaline silica but this U sink represents only about 1 % of the total flux out, so it has negligible influence on the mass-balance.

3.4.4 Putting the U budgets to the test

The isotopic fractionation factors and fluxes relevant to the modern oceanic uranium budget are summarized in Fig. (3.6) and Table 3.6. Several studies ([33, 301, 149, 195]) have given estimates of uranium fluxes in the oceanic budget that differ in both the relative size of the U sinks and even in the sinks themselves. For each oceanic budget, the modern seawater isotopic composition is predicted using the simple mass-balance model outlined in Section 3.4.1. Steady-state is assumed and the riverine input is the only source of U to the ocean. For these conditions, the isotopic composition of seawater is calculated using Eq. (3.24).

The most recent budget by Henderson and Anderson (2003) [195] fails to reproduce the actual seawater composition and predicts a lighter isotopic composition (-0.502 ‰). The other three budgets (Barnes and Cochran, 1990; Morford and Emerson, 1999; Dunk et

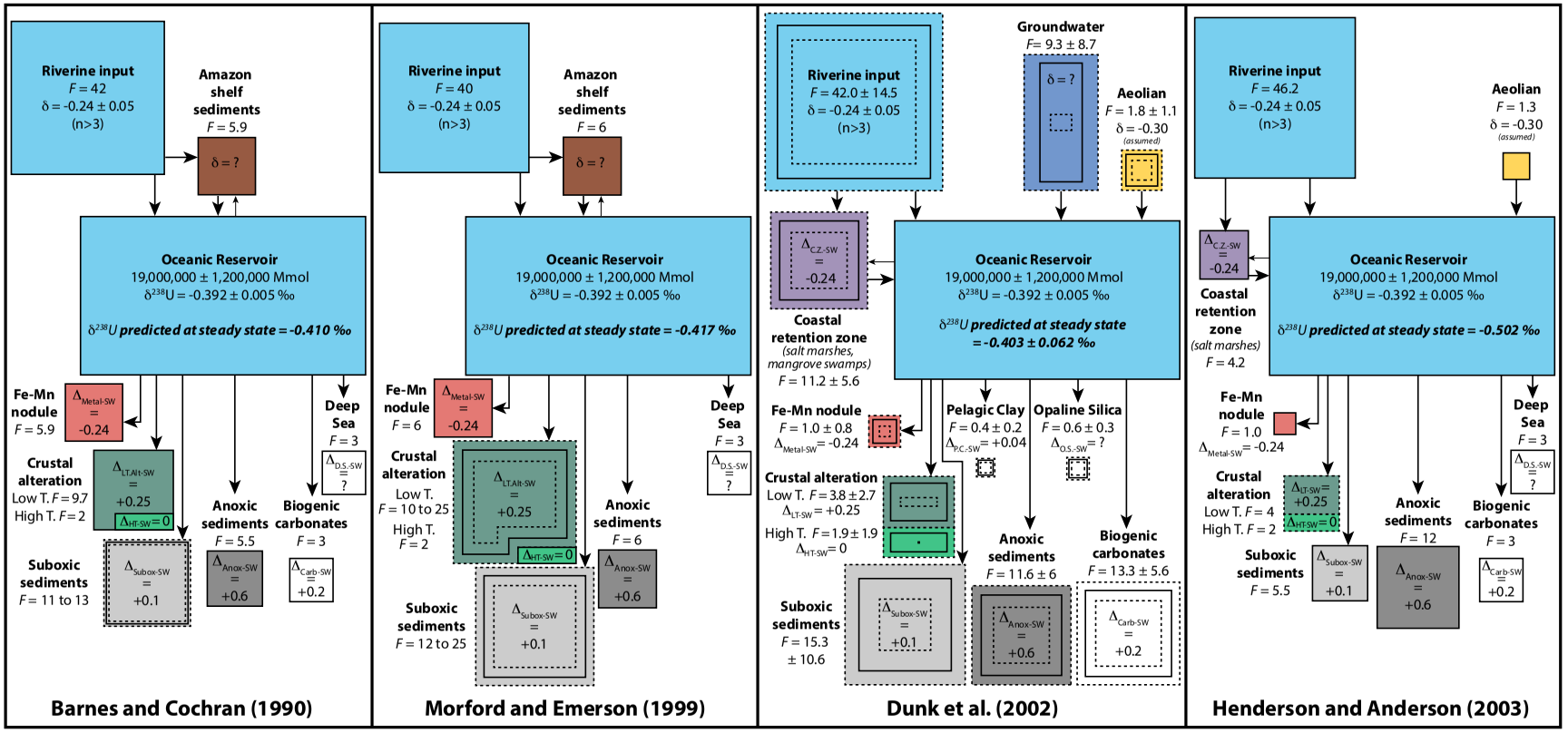

Figure 3.6: Schematic representation of the sources, sinks and fluxes of U in the modern ocean along with their isotopic composition (sources) or associated isotopic fractionation (sinks). Fluxes are in Mmol/yr, and isotopic compositions and fractionation factors are in permil (‰). Except for the ocean, the surface area of the boxes is proportional to the U flux. The four most recent oceanic budgets are compared (from left to right: [33], [301], [149], [195]). For each budget, the predicted isotopic composition of the seawater is compared to the modern seawater value of $\delta^{238}U_{SW} = -0.392 \pm 0.005$ ‰ (this work). The most recent budget of Henderson and Anderson (2003) fails to reproduce the actual seawater composition (-0.502 ‰ predicted *vs.* -0.392 ‰ measured). The other three budgets show very good agreement with the measured oceanic U isotopic composition. Figure published in [431].

Sources	$\delta^{238}U$ (‰)	Fluxes (Mmol/yr) B&C	M&E	Dunk et al.	H&A
Riverine input	$-0.24^{1,5,3}$	42	40	42.0 ± 14.5	46.2
Amazon shelf sediments	?	5.9	6		
Dust (aeolian input)	-0.29^{*}			1.8 ± 1.1	1.3
Submarine groundwater discharge	?			9.3 ± 8.7	
Total		*47.9*	*46*	*53.1 ± 16.9*	*47.5*
Sinks	$\Delta_{Reservoir\text{-}SW}$ (‰)				
Suboxic sediments (continental margin)	$0.1^{2,3}$	11–13	12–25	15.3 ± 10.6	5.5
Anoxic/euxinic sediments (organic-rich)	0.6^{7}	5.5	6	11.6 ± 6.0	12
Oxix sediments:					
Deep sea (pelagic red clay, siliceous and calcareous deep sea sediments)	?	3	3		3
Pelagic red clay	0.04^{9}			0.4 ± 0.2	
Biogenic carbonates	$0.2^{1,2,6,7,3}$	3		13.3 ± 5.6	3
Opaline silica (Biogenic silica)	?			0.6 ± 0.3	
Mn nodules and metalliferous sediments	$-0.24^{1,2,4,8,3}$	5.9	6	1.0 ± 0.8	1
Crustal alteration – high T	$0^{5,9}$	2	2	1.9 ± 1.9	2
Crustal alteration – low T	$0.25^{5,9}$	9.7	10–25	3.8 ± 2.7	4
Coastal zone retention[***]	-0.24^{3} [**]			11.2 ± 5.6	4.2
Total		*40–43*	*39–67*	*59.1 ± 14.9*	*34*
Predicted $\delta^{238}U$ of modern Seawater					
Assuming steady state in the modern ocean		−0.412– −0.408	−0.413– −0.422	-0.403 ± 0.062	−0.502

[*]Crustal composition ssumed (see Table 7).

[a]U oceanic budgets from: Barnes and Cochran (1990) (B&C); Morford and Emerson (1999) (M&E); Dunk et al., 2002; Henderson and Anderson, 2003 (H&A).

[b]References: (1) Stirling et al., 2007; (2) Weyer et al., 2008; (3) This study, (4) Brennecka et al., 2011b; (5) Noordmann et al., 2011; (6) Romaniello et al., 2013; (7) Andersen et al., 2014; (8) Goto et al., 2014; (9) Andersen et al., 2015.

[c]Note that for the anoxic/euxinic and suboxic reservoirs, the $\Delta_{Reservoir\text{-}SW}$ value is the averaged fractionation expressed in the sediment, which is different from the expected fractionation of ~1.2‰ obtained by *ab initio* calculations (Bigeleisen, 1996; Abe et al., 2008) due to coupled U diffusion and reduction below the sediment water interface. (See Andersen et al., 2014 for more details).

[**] The main removal process in the coastal zones is adsorption–complexation of U onto Fe-oxyhydroxides/organic colloids, followed by scavenging and burial on short timescales before U reduction occurs at depth within the sediment (Church et al., 1996; Swarzenski et al., 2004). We make the observation that phases with adsorbed/complexed U have similar isotopic composition (chimney, evaporites, Fe–Mn nodules, Stirling et al., 2007; Weyer et al., 2008; Goto et al., 2014; this study) and hypothesize that the same adsorption–complexation mecanism is at play in these samples and in coastal retention zones, leading to a similar isotopic fractionation.

[***] Salt marshes and mangrove swamps.

Table 3.6: Fluxes and isotopic constraints on the modern U budget of the oceans. References: Barnes & Cochran (1990), [33]; Morford & Emerson (1999), [301]; Dunk et al. (2002), [149]; Henderson & Anderson (2003) [195]; Stirling et al. (2007), [412]; Weyer et al. (2008), [460]; Brennecka et al. (2011b), [70]; Noordmann et al. (2011), [315]; Romaniello et al. (2013), [370]; Andersen et al. (2014), [19]; Goto et al. (2014), [179]; Andersen et al. (2015), [18]; Bigeleisen (1996), [41]; Abe et al. (2008), [1]; Church et al. (1996), [108]; Swarzenski et al. (2004), [419]. Table published in [431].

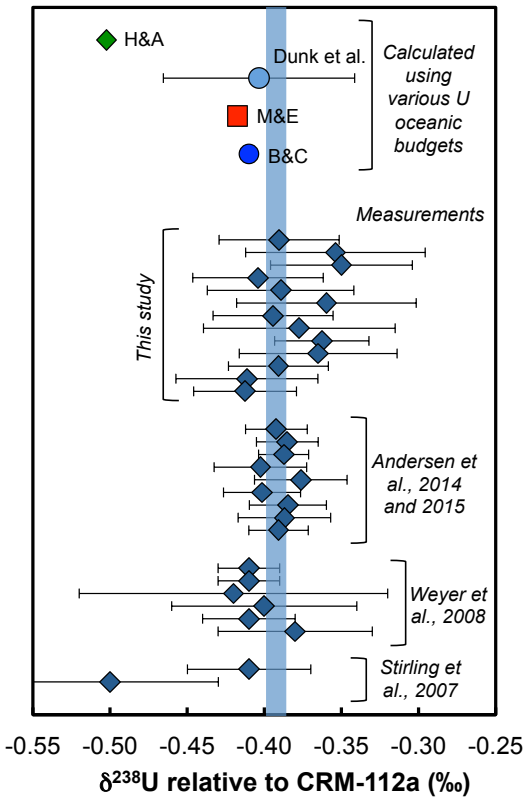

Figure 3.7: Uranium isotopic compositions predicted by the four most recent oceanic budgets (B&C; M&E; Dunk et al.; H&A, respectively, [33, 301, 149, 195]) and measurements of open ocean water samples (Atlantic ocean, Pacific ocean, Mediterranean sea, English Channel, Gulf of California and Gulf of Mexico) from this study (Table 3.5) and the literature [412, 460, 19, 18]. The blue bar shows the weighted average of the modern open seawater value at $\delta^{238}U_{SW} = -0.392 \pm 0.005$ ‰ (this study). Figure published in [431].

al., 2002) [33, 301, 149] show very good agreement with the measured oceanic U isotopic composition of $\delta^{238}U_{SW} = -0.392 \pm 0.005$ ‰ (Figs. 3.6 and 3.7). The budget of Dunk et al. (2002) [149] is the only one to include uncertainties on the fluxes and predicts a $\delta^{238}U_{SW}$ value of -0.403 ± 0.062 ‰, indistinguishable from the actual open ocean value measured in this work. $^{238}U/^{235}U$ systematics therefore points to a modern oceanic U budget in steady-state, as was suggested by the estimation of the U fluxes in and out of the ocean.

3.4.5 Global extent of modern oceanic anoxia

In addition to testing the steady-state assumption and isotopic fractionation factors, the budget comparison in Fig. (3.6) and Table 3.6 allows a constraint on the magnitude of

the flux of U into anoxic/euxinic sediments ($F_{Anoxic/euxinic}$) in the modern ocean. Indeed, because the uptake of U into anoxic/euxinic reservoirs is accompanied by a large isotopic fractionation compared to other sinks ($\Delta_{Anoxic/Euxinic\text{-}SW} = +0.6$ ‰, while other Δ values are between -0.24 and $+0.25$ ‰), the size of the anoxic/euxinic sink has a major influence on the predicted $\delta^{238}U_{SW}$ value. While keeping all other fluxes constants, the value of $F_{Anoxic/euxinic}$ in each one of the four budgets considered [33, 301, 149, 195] was adjusted until the $\delta^{238}U_{SW}$ predicted by the model matched the value measured in the open ocean (at -0.392 ± 0.005 ‰). The results are presented in Table 3.7 and give a value for $F_{Anoxic/euxinic}$ of 7.0 ± 3.1 Mmol/yr. Using an accumulation rate of U into anoxic/euxinic sediments of 9.2 μmol/m^2/yr [149] and a total surface of ocean floor of 3600×10^{11} m^2 [440], this value translates into a percent of ocean floor covered by anoxic/euxinic sediments of 0.21 ± 0.09 ‰. This value is in good agreement with values derived from mass-balance considerations of U and Mo (two redox-sensitive elements), 0.35 ± 0.05 % (U, [444]), 0.23 % (Mo, [40]), and 0.30 ± 0.18 (Mo and U, [153]).

From this test it can also be seen that the model of Henderson and Anderson (2003) [195] fails to predict the correct seawater isotopic composition because it overestimates the flux of U into anoxic/euxinic sediments relative to the total U flux out of the ocean, using a value of 35 % [195], when the maximum flux consistent with the isotopic composition of the modern seawater is 14 ± 3 % (second line in Table 3.7).

Based on the above work, the modern U budget of the ocean is presented in Fig. (3.8). The isotopic composition of each U reservoir can be read on the x-axis, and is derived from the compilation of data from 19 studies (including this work, see Table S3 in [431]). For the sinks, the area of the boxes is proportional to the U flux out of the ocean (fluxes from [149]). Fig. (3.8) represents the current best estimate of the modern U oceanic budget.

The above work demonstrates that the "stable" isotopes of U can trace the extent of anoxia in the modern global ocean, and thereby validates the application of U isotope measurements to paleoredox reconstructions.

	B&C	M&E	Dunk et al.	H&A
F anoxic/euxinic adjusted (Mmol/yr)	3.9	4.3	10.1	4.1
% of U in anoxic/euxinic sediments	11%	13%	18%	18%
Ocean floor surface (m^2)[c]	3.6E+14			
Acc. rate of U in anoxic/euxinic sediments ($\mu mol/m^2/yr$)[d]	9.2			
Surface covered by anoxic/euxinic sediments (10^{11} m^2)	4.2	4.7	11.0	4.5
% of ocean floor covered by anoxic/euxinic sediments	*0.12%*	*0.13%*	*0.30%*	*0.12%*

[a]U oceanic budgets from: Barnes and Cochran (1990) (B&C), Morford and Emerson (1999) (M&E), Dunk et al. (2002), Henderson and Anderson (2003) (H&A).
[b]Keeping all other fluxes constant, the flux of U into anoxic/euxinic sediments is adjusted so that the isotopic composition predicted by the model matches the one of the open ocean at -0.392 ± 0.005.
[c] Turekian (1969).
[d] Dunk et al. (2002).

Table 3.7: Isotopic constraints on the amount of anoxia in the modern ocean. References: Turekian (1969), [440], for the other references, see caption of Table 3.6. Table published in [431].

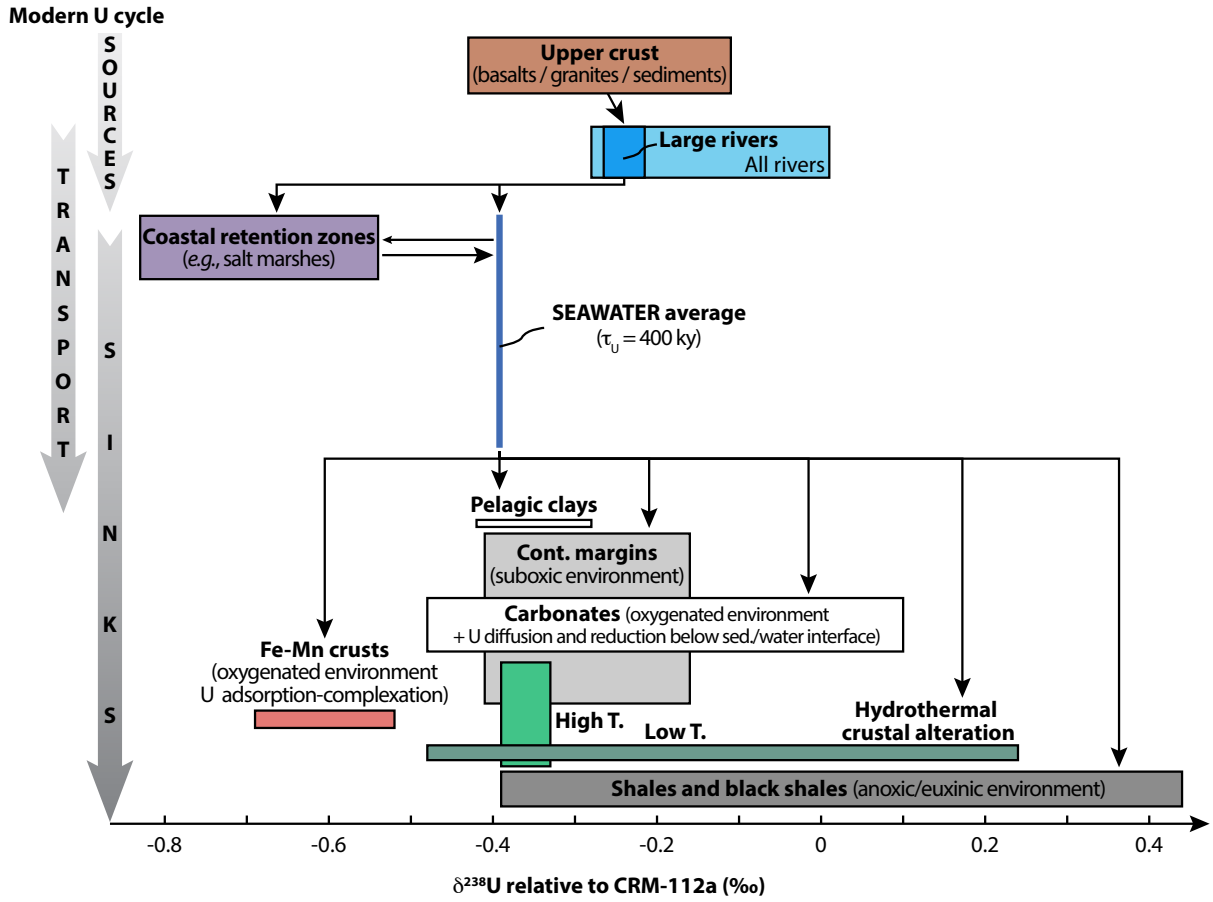

Figure 3.8: Schematic representation of the modern U oceanic budget. The isotopic composition of each U reservoir can be read on the x-axis. For the sinks, the area of the boxes is proportional to the U flux out of the ocean (fluxes from [149]). δ^{238}U values from this study (Tables 3.1, 3.2 and 3.5) and the literature [414, 412, 460, 14, 300, 249, 69, 231, 107, 370, 19, 127, 179, 221, 18, 177, 314]. Figure published in [431].

3.5 The U proxy in the wake of the Great Oxidation Event

The "Great Oxidation Event" (GOE) in the Paleoproterozoic (2.5 to 1.6 Gyr ago) was one of the most significant events in Earth history [210], which triggered the onset of oxidative weathering, shifts in ocean chemistry and a boosting of redox gradients and thus microbial metabolism on a global scale. During the GOE, atmospheric oxygen levels rose from Archean values of $\sim 10^{-5}$ PAL to mid-late Proterozoic values of $\sim 10^{-2}$ to 10^{-1} PAL [328]. The recognition that substantial Mass Independent Fractionation (MIF) of sulfur isotopes is restricted to the time interval before $\sim$ 2.3 Ga indeed argues for an anoxic atmosphere at that time [158, 328, 299, 318, 36, 160], as does the survival of minerals stable only in anoxic conditions such as detrital uraninite (UO_2), pyrite (FeS_2) and siderite ($FeCO_3$) [352, 183] and the existence of banded iron formations (BIFs) and Mn-oxides [210]. False-starts in biospheric oxygenation, referred to as whiffs of atmospheric oxygen [16], may have occurred one or more times during the latest Archean, although the evidence is currently disputed [241]. These presumably transient increases in oxygen are reflected in enrichments in the redox-sensitive elements Mo and Re in marine shales and a reduction in the extent of MIF precisely coincident with the peak in Mo and FeS_2 enrichment [16, 232, 359, 237].

The period between the end of the Archean at $\sim$ 2.5 Ga and the disappearance of BIFs at $\sim$ 1.8 Ga saw the progressive oxygenation of the atmosphere. Multiple lines of geological and geochemical evidence point towards an increase in atmospheric O_2 during this time: (i) the disappearance of the indicators of low atmospheric and oceanic O_2 cited above, consistent with the onset of an oxidative weathering environment [209, 159], (ii) the appearance of red beds at 2.3 Ga, which imply that oxidized Fe^{3+} became an important component of soils, (iii) positive $\delta^{13}C$ excursions in marine carbonate, indicating a net burial of organic matter and a corresponding net production of O_2 that was released into the atmosphere, and (iv) the increase in biologically-induced, mass-dependent fractionation of ^{34}S at $\sim$ 2.4 Ga. (see [81] and references therein). Furthermore, BIFs, whose existence requires soluble Fe, (*i.e.*, anoxic water conditions) were frequent and voluminous in the Archean but largely

disappeared during the early Paleoproterozoic ($2.3 - 2.0$ Ga), despite later reappearance at ~ 1.9 Ga due to enhanced global volcanism [117, 354].

The oxygenation of the atmosphere and the ocean might, however, not have been a simple unidirectional process. A significant increase in mass-dependent S isotope fractionation and decrease in Fe isotope fractionation in sedimentary pyrite after ~ 2.32 Ga [36, 83, 374] likely reflect an increase in seawater sulfate concentrations by that time. Yet the disappearance of shallow-marine sulfate evaporites after ~ 2.1 Ga suggests a rise and fall of the size of the marine sulfate reservoir [390]. This is consistent with S isotope evidence of carbonate-associated sulfate [332], and a positive excursion in the U content of shales [323].

Such observations of a rise and fall of oxygenation in the ocean post-GOE go against the accepted view of a unidirectional or stepwise increase in the oxygen content of the Proterozoic atmosphere-ocean system (*e.g.*, [113, 91, 210, 304]) and suggest oscillating redox conditions post-GOE. In particular, the redox state of the ocean in the aftermath of the rise of atmospheric oxygen remains poorly constrained and various models ranging from oxic [208], to euxinic [82], and to suboxic [402] have been proposed. Recent works hypothesized a redox structure characterized by pervasive anoxia within the deep sea and dynamic regions of euxinia along productive ocean margins (*e.g.*, [338, 333, 358]).

Some of the work done during this thesis project was part of a collaborative effort to understand the response of the global Paleoproterozoic ocean in the wake of the GOE. The study used a multi-proxy approach and combined Mo, Fe and U isotope measurements in the same samples with the specific aim of evaluating if (i) the evolution of the oceanic sulfur cycle through the Paleoproterozoic was such that by ~ 2.0 Ga it could support exceptionally widespread euxinic conditions in the marine realm, and (ii) oxidative continental weathering was important in setting up the sulfate and metal oxyanion inventories of seawater (*e.g.*, U and Mo) in the aftermath of the GOE. In the sections below, focus is brought only to the U part of this collaboration, but the curious reader is referred to Asael et al. (2013), [28], for the full conclusions of the study.

3.5.1 The Lomagundi and Shunga event

The Lomagundi-Jatuli Event – the largest carbon isotope excursion in Earth's history ($2.3 - 2.1$ Ga) (Fig. 3.9) – is associated with global burial of organic matter and release of oxygen to the atmosphere [288, 290]. Bekker et al. (2008) [37] showed that in contrast to the Late Neoproterozoic and Phanerozoic, mechanisms of carbon isotope fractionation were different in the Paleoproterozoic redox-stratified ocean, and the signal of primary productivity below the redoxcline was overprinted. This relationship complicates the reconstruction of spatial patterns and secular trends in the δ^{13}C values of dissolved inorganic carbon in Paleoproterozoic seawater.

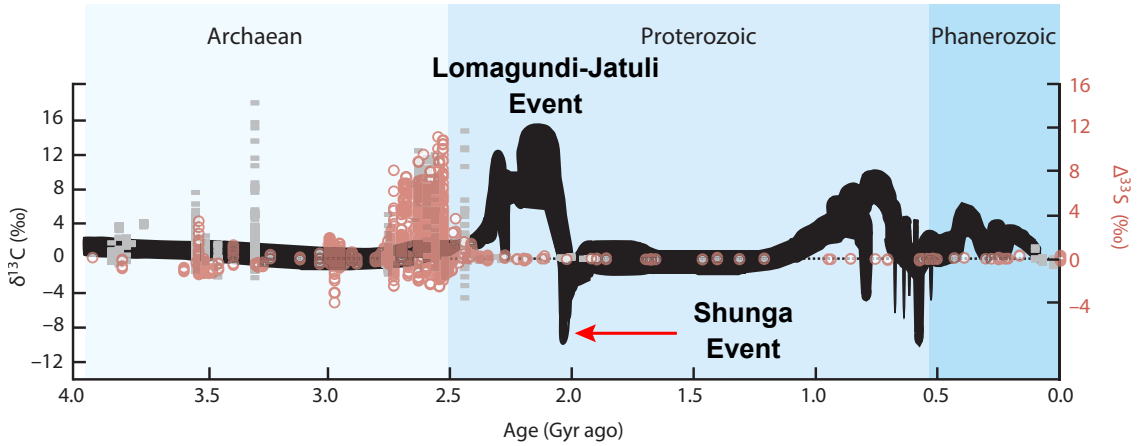

Figure 3.9: Summary of carbon (black) and sulfur (red and grey) isotope data through Earth's history. Data are shown as δ^{13}C (left axis) and Δ^{33}S ($= \delta^{33}\text{S} - 0.515\delta^{34}\text{S}$; right axis). Grey sulfur data were generated by SIMS; red circles designate all other data – bulk and small sample (micro-drilled and laser) analyses. Notable features include the large range of Δ^{33}S values during Archaean time, the large δ^{13}C excursion during the early Proterozoic, relative stasis in δ^{13}C during the mid- Proterozoic, and the large negative δ^{13}C excursions during the late Proterozoic. Figure modified from [266].

The study conducted as part of this thesis focused on the Shunga Event sequence from the Onega Basin, which directly follows the Lomagundi-Jatuli Event and, somewhat paradoxically in the face of decreasing δ^{13}C values, shows remarkable organic carbon accumulation and the first sedimentary phosphorite accumulation [289]. The Shunga Event is part of the stratigraphic section of the Onega Basin which was deposited as a regional platformal se-

quence, and similar sediments are found also in the Francevillian Group in Gabon (*e.g.*, [291] and references within). Together, these observations suggest that the studied section of the Shunga Event can provide insight into the open Paleoproterozoic ocean and associated global phenomena. The Shunga Event, well-known for its huge volume of Paleoproterozoic C_{org}-rich sediments (up to 99 % C), represents a giant petrified oil field, including petroleum source rock, joint-trapped metamorphosed oil, veins of migrated petroleum, redeposited subaerial oil spills and organo-siliceous substances that formed diapirs [291]. The Zaonega Formation from the Onega Basin is composed mainly of organic-rich shale, organo-siliceous rocks and mafic lavas and gabbro sills, and it also contains a petrified oil reservoir. Kump et al. (2011) [246] observed a negative δ^{13} excursion during the Shunga Event, which was considered to represent intense oxidative weathering of rocks as the result of the initial establishment of an oxygen-rich atmosphere. The age of the Zaonega Formation was constrained to be $\sim$ 2.06 Ga [319, 344, 345].

3.5.2 FAR-DEEP Samples

The samples studied here are sulfidic shales from drillcore Hole 13A from the Fennoscandian Shield, recovered as part of the FAR-DEEP project. The FAR-DEEP project (Fennoscandian Arctic Russia – Drilling Early Earth Project) was initiated in the frame of the International Continental Drilling Program (ICDP) [293]. About 3650 m of drill core were recovered and logged from the early Paleoproterozoic of Arctic Russia during the summer and fall of 2007 and represent a critical window into the tempo and mode of early Earth oxygenation. Water was the only drilling fluid to avoid potential contamination from drilling oils.

Hole 13A intersects the upper part of the Zaonega Formation, which, together with the overlaying Suisari Formation, records the Shunga Event in the Onega Basin in Karelia (Fig. 3.10), Russia (Eastern Fennoscandian Shield). The Shunga Event is defined by the oldest known significant accumulation of organic-carbon-rich sediments (termed shungite in the Onega Basin) and petroleum generation [285]. Sedimentary rocks of the Onega Basin were

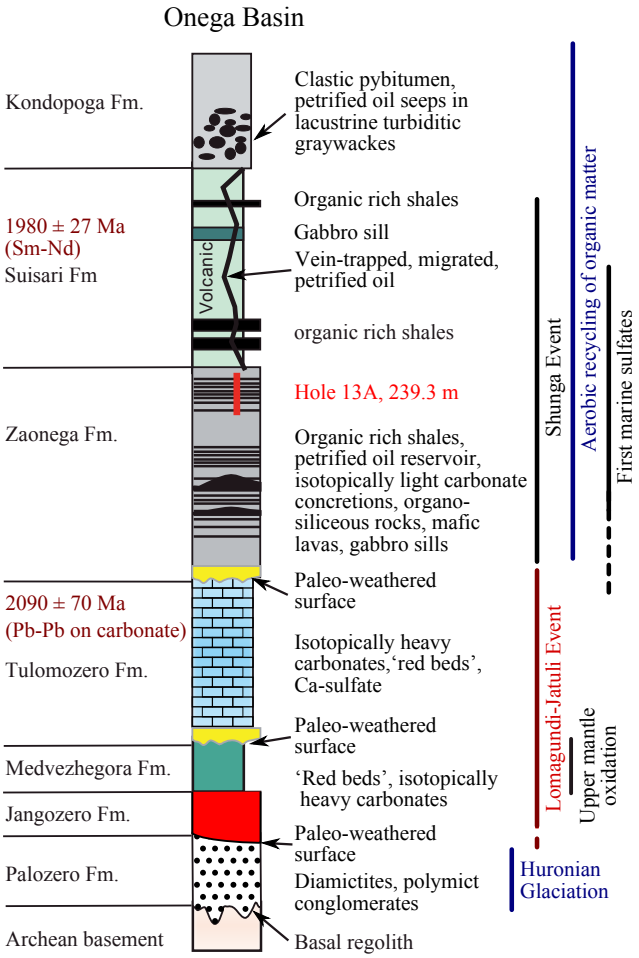

Figure 3.10: Composite ($\sim$ 5000 m thick) and simplified section of the Onega Basin linked to major paleoenvironmental events, modified from [292]. Radiometric dates from bottom to top are taken from [346, 319]. Vertical red line shows the position of drill hole 13A studied in this work. Figure from [28].

deposited in a marine basin within a rifted active continental margin (*e.g.*, [288, 290, 246]). Samples of fine-grained laminated and massive siliciclastic rocks, with occasional turbidite intervals, were selected for this study. Sporadic macroscopic and obviously secondary textures and features were avoided, with the aim of providing insight into the depositional redox characteristics of the Onega Basin during typical background sedimentation.

Samples were digested using the regular procedure outlined in Section 2.2.2. Before the first acid attack, the samples were placed in individual aluminum foil envelopes and ashed

at $\sim 500°$C overnight in a Barnstead Thermolyne 47900 furnace, in order to burn off the organic matter. The U purification (Section 2.3.2) was done twice to remove any matrix interference. Isotopic measurements followed the protocol detailed in Section 2.4.2 and the data reduction outlined in Section 2.5. Enhanced signal stability was achieved by placing a spray chamber between the Aridus II and the MC-ICPMS. The procedural blank was estimated to be ~ 0.07 ng U (0.05 % of sample uranium).

3.5.3 Results and detrital contamination

Results of U isotopic analyses of the FAR-DEEP samples are reported in Table 3.8. The δ^{238}U values range from -0.33 to $+0.39$ ‰ and average $+0.07 \pm 0.18$ ‰ ($n = 45$). There is no identifiable trend with depth.

To check that the ashing step did not affect the results, replicates of five core samples with U concentrations ranging from 0.45 ppm to 6.45 ppm were prepared following an identical procedure but with no ashing step (last five samples in Table 3.8). Comparison of ashed and non-ashed samples showed no difference in U isotopic composition.

Despite a high carbon content, XRD data [28] show a high detrital content in all the samples. A significant, negative correlation is observed between δ^{238}U and Al/U ratios (Fig. 3.11). These observations indicate that the bulk rock U isotope compositions of the samples are mainly a result of a mixing relationship between a low δ^{238}U detrital endmember and a high δ^{238}U authigenic endmember. Therefore, before interpreting the data in terms of global ocean redox conditions, the detrital signature needs to be corrected for.

3.5.4 Detrital correction and the U signal

One of the main contributions of the work carried out on U isotopes in the FAR-DEEP samples is the introduction of a correction for the detrital component in the samples: a practice now adopted by the community [19, 314] (though not always with proper referencing to this work). The detrital correction was made by extrapolating the isotopic composition

Sample	Depth (m)	Material			Resin #	Blk (ng)	Mass digested (mg)	n	From double spike data reduction							From sample-standard bracketing			
									$\delta^{238}U/^{235}U$	95 CI	$\delta\,[^{234}U/^{238}U]$	95 CI	Conc. (ug/g)	2 SD	Usp/Usmp	$\delta^{238}U/^{235}U$	95 CI	$\delta\,[^{234}U/^{238}U]$	95 CI
3109562	129.91	Carbonate-Silt	***	Far.	2	0.07	63.3	9	**-0.04**	0.06	**-60.9**	6.5	**4.06**	0.03	**3.1%**	-0.14	0.19	-61.8	6.5
3109566	131.40	Siltstone	***	Far.	2	0.07	96.9	9	**-0.01**	0.06	**-43.9**	6.5	**3.13**	0.02	**2.6%**	0.02	0.19	-61.2	6.5
3109640	134.23	Siltstone	***	Far.	2	0.07	21.2	9	**0.38**	0.06	**-252.5**	6.5	**11.77**	0.15	**3.2%**	-0.23	0.19	-248.4	6.5
3109576	134.97	Siltstone	***	Far.	2	0.07	25.5	9	**0.24**	0.08	**-182.1**	7.4	**11.06**	0.12	**2.8%**	0.22	0.22	-192.4	7.3
3109578	135.20	Siltstone	***	Far.	2	0.07	22.6	9	**0.18**	0.08	**-172.6**	7.4	**9.84**	0.12	**3.6%**	-0.11	0.22	-156.2	7.3
3109580	135.56	Siltstone	***	Far.	2	0.07	45.4	9	**0.21**	0.08	**-46.1**	7.4	**6.51**	0.06	**2.7%**	0.18	0.22	-60.2	7.3
3109582	136.06	Carbonate-Silt	***	Far.	2	0.07	76.5	9	**0.00**	0.04	**-149.1**	7.7	**3.91**	0.03	**2.6%**	-0.07	0.06	-162.9	7.6
3109594	137.01	Siltstone	***	Far.	2	0.07	55.9	9	**0.05**	0.04	**-130.2**	7.7	**4.65**	0.04	**2.9%**	0.04	0.06	-137.0	7.6
3109596	137.33	Limestone	***	Far.	2	0.07	74.0	9	**0.10**	0.04	**-150.2**	7.7	**3.89**	0.03	**2.7%**	0.03	0.06	-161.4	7.6
3109598	137.77	Limestone	***	Far.	2	0.07	61.3	8	**0.22**	0.05	**-184.9**	8.2	**4.67**	0.04	**2.8%**	0.25	0.07	-194.4	8.1
3109600	137.97	Limestone	***	Far.	2	0.07	35.6	9	**0.18**	0.04	**-43.3**	7.7	**7.30**	0.07	**3.0%**	0.18	0.06	-46.5	7.6
3109602	138.12	Limestone	***	Far.	2	0.07	30.3	9	**0.26**	0.05	**-36.1**	4.6	**10.10**	0.10	**2.6%**	0.31	0.05	-54.1	4.5
3109604	138.71	Limestone	***	Far.	2	0.07	27.5	9	**0.35**	0.05	**-63.8**	4.6	**10.03**	0.11	**2.8%**	0.33	0.05	-72.5	4.5
3109606	139.10	Limestone	***	Far.	2	0.07	32.6	9	**0.33**	0.05	**-108.0**	4.6	**8.64**	0.09	**2.8%**	0.33	0.05	-118.7	4.5
3109608	139.23	Siltstone	***	Far.	2	0.07	35.4	9	**0.34**	0.06	**-197.8**	8.1	**8.61**	0.08	**2.6%**	0.27	0.13	-213.5	8.0
3109612	140.03	Siltstone	***	Far.	2	0.07	76.3	9	**0.00**	0.06	**-149.5**	8.1	**4.42**	0.03	**2.3%**	0.01	0.13	-173.3	8.0
3109614	140.29	Siltstone	***	Far.	2	0.07	72.8	9	**0.09**	0.06	**-17.7**	8.1	**4.11**	0.03	**2.6%**	-0.06	0.13	-33.5	8.0
3109620	141.62	Siltstone	***	Far.	2	0.07	90.0	9	**0.01**	0.06	**-60.9**	6.5	**3.41**	0.03	**2.6%**	-0.02	0.06	-78.0	6.5
3109622	142.65	Siltstone	***	Far.	2	0.07	111.6	9	**-0.05**	0.06	**-44.0**	6.5	**2.88**	0.02	**2.4%**	-0.06	0.06	-65.4	6.5
3109628	143.11	Siltstone	***	Far.	2	0.07	108.6	9	**-0.17**	0.06	**-15.1**	6.5	**3.06**	0.02	**2.4%**	-0.19	0.06	-38.6	6.5
3109638	145.53	Limest-Sand.	***	Far.	2	0.07	300.2	9	**-0.07**	0.06	**-18.2**	6.5	**1.15**	0.01	**2.3%**	-0.09	0.06	-44.7	6.5
3109658	146.14	Siltstone	***	Far.	2	0.07	71.3	9	**0.19**	0.06	**-82.9**	6.5	**3.97**	0.03	**2.8%**	0.16	0.06	-93.0	6.5
3109668	146.87	Carbonate-Silt	***	Far.	2	0.07	78.9	9	**0.23**	0.06	**-44.7**	6.5	**3.91**	0.03	**2.6%**	0.21	0.06	-62.1	6.5
3109674	149.91	Limest-Sand.	***	Far.	2	0.07	171.4	9	**0.07**	0.06	**431.1**	6.5	**1.30**	0.01	**3.6%**	0.01	0.06	440.3	6.5
3109676	150.84	Sand.-Siltstone	***	Far.	2	0.07	225.6	9	**0.07**	0.07	**-18.4**	5.9	**1.77**	0.01	**2.0%**	0.15	0.06	-54.8	5.9
3109688	153.71	Sand.-Siltstone	***	Far.	2	0.07	142.7	9	**-0.06**	0.07	**-34.6**	5.9	**2.26**	0.02	**2.5%**	-0.02	0.06	-55.4	5.9
3109748	157.83	Sand.-Siltstone	***	Far.	2	0.07	384.1	9	**-0.13**	0.07	**-15.2**	5.9	**0.77**	0.01	**2.7%**	-0.10	0.06	-29.1	5.9
3109706	158.43	Sand.-Siltstone	***	SEM	2	0.07	67.4	9	**0.06**	0.06	**11.7**	0.2	**4.81**	0.04	**2.5%**	0.04	0.06	-10.1	0.2
3109708	159.75	Sand.-Siltstone	***	Far.	2	0.07	77.5	9	**-0.02**	0.07	**-9.4**	5.9	**4.06**	0.03	**2.5%**	-0.02	0.06	-28.9	5.9
3109712	161.34	Limest-Sand.	***	Far.	2	0.07	634.9	9	**-0.36**	0.07	**-8.9**	7.4	**0.455**	0.003	**2.7%**	-0.33	0.06	-22.6	7.3
3109722	162.56	Limest-Sand.	***	Far.	2	0.07	494.3	9	**-0.35**	0.07	**-11.3**	7.4	**0.663**	0.005	**2.4%**	-0.28	0.06	-34.7	7.3
3109724	163.62	Sand.-Siltstone	***	SEM	2	0.07	221.3	9	**-0.36**	0.06	**-83.9**	0.2	**1.75**	0.01	**2.0%**	-0.33	0.06	-119.3	0.2
3109726	164.77	Sand.-Siltstone	***	Far.	2	0.07	113.7	9	**-0.01**	0.07	**-6.8**	7.4	**2.91**	0.02	**2.4%**	-0.01	0.06	-29.9	7.3
3109732	166.96	Siltstone	***	Far.	2	0.07	56.0	9	**0.09**	0.07	**-106.7**	7.4	**6.13**	0.05	**2.3%**	0.14	0.06	-131.5	7.3
3109736	167.74	Siltstone	***	Far.	2	0.07	128.6	9	**-0.05**	0.07	**-12.6**	7.4	**2.79**	0.02	**2.2%**	0.02	0.06	-42.3	7.3
3109738	168.52	Siltstone	***	Far.	2	0.07	102.2	9	**0.01**	0.07	**33.1**	9.7	**3.17**	0.02	**2.5%**	0.00	0.06	11.0	9.6
3109738 repl.	168.52	Siltstone	***	Far.	2	0.07	102.2	9	**-0.03**	0.07	**31.7**	9.7	**3.23**	0.02	**2.4%**	-0.01	0.06	7.6	9.6
3109740	169.02	Siltstone	***	Far.	2	0.07	106.5	9	**0.07**	0.07	**15.5**	9.7	**2.84**	0.02	**2.6%**	0.11	0.06	-1.3	9.6
3109744	169.93	Siltstone	***	Far.	2	0.07	58.3	9	**0.07**	0.07	**-80.3**	9.7	**5.64**	0.05	**2.4%**	0.10	0.06	-102.3	9.6
3109746	170.47	Siltstone	***	Far.	2	0.07	49.2	9	**0.11**	0.07	**-30.4**	9.7	**10.47**	0.04	**2.8%**	0.11	0.06	-38.1	9.6
3109752	171.07	Siltstone	***	Far.	2	0.07	39.6	9	**0.19**	0.07	**-4.7**	6.0	**8.31**	0.08	**2.4%**	0.23	0.06	-27.6	6.0
3109758	171.81	Siltstone	***	Far.	2	0.07	65.6	9	**0.21**	0.07	**8.6**	6.0	**5.00**	0.04	**2.4%**	0.22	0.06	-14.9	6.0
3109760	172.23	Siltstone	***	Far.	2	0.07	58.8	9	**0.13**	0.07	**63.8**	6.0	**4.87**	0.04	**2.8%**	0.16	0.06	52.0	6.0
3109764	173.35	Limest-Sand.	***	Far.	2	0.07	67.6	9	**0.22**	0.07	**-6.3**	6.0	**4.89**	0.04	**2.4%**	0.27	0.06	-30.6	6.0
3109778	175.30	Sand.-Siltstone	***	Far.	2	0.07	67.6	9	**-0.13**	0.07	**3.2**	6.0	**4.27**	0.03	**2.7%**	-0.11	0.06	-9.1	6.0
3109580-NA	135.56	Siltstone	***	Far.	2	0.07	44.00	9	**0.16**	0.08	**-46.6**	7.4	**6.50**	0.06	**2.7%**	-0.29	0.22	-60.2	7.3
3109612-NA	140.03	Siltstone	***	Far.	2	0.07	73.71	9	**-0.02**	0.06	**-153.6**	8.1	**4.40**	0.04	**2.4%**	-0.03	0.13	-176.9	8.0
3109674-NA	149.91	Limest-Sand.	***	Far.	2	0.07	168.90	9	**0.13**	0.07	**433.9**	5.9	**1.30**	0.01	**3.5%**	0.10	0.06	440.9	5.9
3109676-NA	150.84	Sand.-Siltstone	***	Far.	2	0.07	222.63	9	**0.09**	0.07	**-14.7**	5.9	**1.77**	0.01	**1.9%**	0.16	0.06	-53.4	5.9
3109712-NA	161.34	Limest-Sand.	***	Far.	2	0.07	633.23	9	**-0.27**	0.07	**-16.7**	7.4	**0.455**	0.003	**2.6%**	-0.27	0.06	-33.1	7.3

Table 3.8: Summary of isotopic compositions and concentrations of U in shales from the Zaonega Formation (Shunga Event, $\sim$ 2.0 Ga) measured in this study. Symbols and notations as in Table 3.2. Data published in [28].

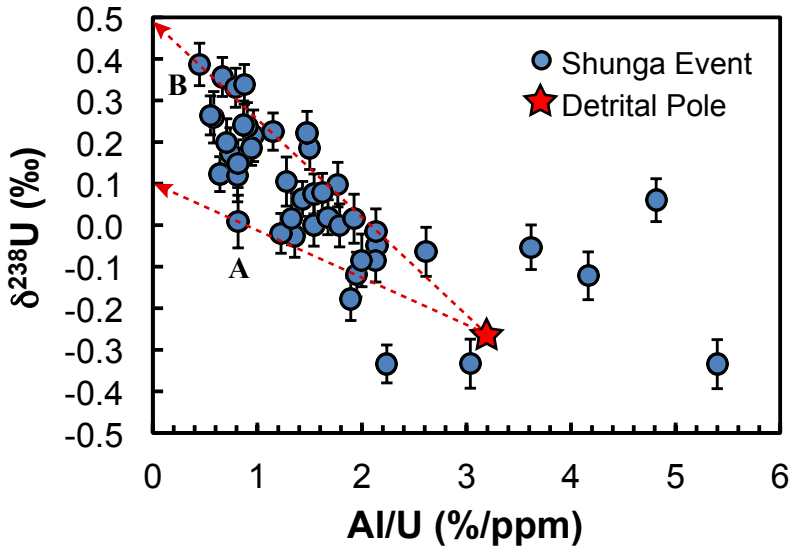

Figure 3.11: δ^{238}U *vs.* Al/U ratios. The data shows a mixing relationship between a detrital endmember (star symbol) and an authigenic endmember. The red arrows show the detrital corrections for arbitrary samples A and B, corresponding to Eq. (3.26). Figure modified from [28].

at Al/U= 0 (*i.e.*, no detrital influence, see Fig. 3.11) using the following equation:

$$\delta^{238}\mathrm{U}_{\mathrm{authigenic}} = \delta^{238}\mathrm{U} - \left(\frac{\mathrm{Al}}{\mathrm{U}}\right) \times \left(\frac{\delta^{238}\mathrm{U}_{\mathrm{det}} - \delta^{238}\mathrm{U}}{\left(\frac{\mathrm{Al}}{\mathrm{U}}\right)_{\mathrm{det}} - \left(\frac{\mathrm{Al}}{\mathrm{U}}\right)}\right) \tag{3.26}$$

where the "det" stands for detrital. The detrital endmember was obtained by averaging basalt and granite geostandards [430] and led to $\delta^{238}\mathrm{U}_{\mathrm{det}} = -0.267$ ‰ and $(\mathrm{Al/U})_{\mathrm{det}} = 3.19$ (geometric mean of the basalts and granites Al/U ratios). Similarly, the error in the $\delta^{238}\mathrm{U}_{\mathrm{authigenic}}$ value was calculated using the following equation (which propagates the error in the δ^{238}U value of the sample but not the error in Al/U ratio of the sample or the errors in elemental and isotopic composition of the detrital endmember):

$$\sigma_{\delta^{238}\mathrm{U}_{\mathrm{authigenic}}} = \sqrt{\left(1 + \frac{\left(\frac{\mathrm{Al}}{\mathrm{U}}\right)}{\left(\frac{\mathrm{Al}}{\mathrm{U}}\right)_{\mathrm{det}} - \left(\frac{\mathrm{Al}}{\mathrm{U}}\right)}\right)^2 \times \sigma^2_{\delta^{238}\mathrm{U}}} \tag{3.27}$$

Samples with Al/U ratios above 3 were not used, to avoid meaningless interpolations – when the measured data are very close to the detrital component, there is no leverage to properly extrapolate, and the error becomes excessively large. The corrected isotopic compositions are heavier than the uncorrected ones, showing an average $\delta^{238}U_{authigenic}$ value of $+0.35 \pm 0.22$ ‰, compared to the average measured $\delta^{238}U$ of $+0.07 \pm 0.18$ ‰. The corrected $\delta^{238}U$ values show no clear correlation with proxies such as Mo concentrations or Fe speciation, and the average U isotopic composition after correction is the same whether the entire sample set is considered or only the euxinic samples are considered. Samples deposited under euxinic conditions were identified from the standard test of evaluating the ratio of highly reactive iron to total iron [$Fe_{HR}/Fe_T > 0.38$ for anoxic environments] and the ratio of pyrite iron to highly reactive iron [$Fe_{PY}/Fe_{HR} > 0.8$ for euxinic environments], as in, for instance, [337]. This observation supports the conclusion reached from Fe and Mo isotopes that the entire section was deposited under euxinic conditions. Using the fractionation factor of $\Delta_{Anoxic/Euxinic\text{-}SW} = +0.6$ ‰ (see Section 3.4.3), the authigenic composition recorded corresponds to a seawater $\delta^{238}U$ value of -0.25 ± 0.22 ‰, which is indistinguishable from both the modern riverine input value (~ -0.24 ‰, see Section 3.4.3) and the average crustal value (-0.29 ± 0.03 ‰, see Section 3.3.2.3), and just within error of the modern seawater U isotopic composition (-0.392 ± 0.005 ‰, see Section 3.6.1).

3.5.5 U isotopic inferences about the redox state of the ocean 2.0 Gyr ago

Using the simple steady-state mass-balance model described in Section 3.4.1 with the fractionation factors summarized in Table 3.6, some first order inferences can be made about the redox state of the ocean using U isotopes.

The importance of the detrital correction cannot be overestimated. The average $\delta^{238}U$ values of the samples studied here, before the detrital correction is $+0.07 \pm 0.18$ ‰ and $+0.35 \pm 0.22$ ‰ after correction. This 0.28 ‰ difference corresponds to a five-fold difference in the size of the anoxic/euxinic U sink relative to the modern ocean (from the present

value of 14 % to $\sim$ 70 %, see Fig. 1.9, Section 1.3). Conclusions based on the U isotopic composition of the samples without detrital correction would thus be completely invalid.

The average isotopic composition of the authigenic U in the shale samples from the Sunga Event is inferred to be -0.25 ± 0.22 ‰. This result can be explained in two ways: (i) the process of U removal from the ocean did not involve significant fractionation, or (ii) the preferential removal of ^{238}U in anoxic/euxinic sediments was balanced by U removal into a sink preferentially incorporating ^{235}U (such as Fe-Mn nodules, and oxides). The first case could correspond to non-biologically mediated U reduction, which has been found not to fractionate U isotopes [418], while the second case corresponds to an ocean in which only biologically-mediated U reduction and U adsorption onto oxides are responsible for the removal of U from the oceanic system. In this second scenario, the U flux to anoxic/euxinic sediments could have represented anything from 0 % to $\sim$ 55 % of the total U flux out of the ocean (based on the inferred U isotopic composition of the seawater, see red line in Fig. 1.9). The upper limit would correspond to a four-fold increase of anoxia relative to the modern U oceanic budget (assuming that the U accumulation rate in anoxic/euxinic sediments was the same today and 2.0 Gyr ago). This is in agreement with the information gathered from Fe and Mo isotopes, from which it was found that the ocean was mostly euxinic at that time.

The conclusion that U was mostly partitioned between anoxic sediments and oxides would also makes sense in the framework proposed by Kendall et al. (2013) [236] where U is not mobilized by oxidative weathering on land but is instead oxidatively mobilized in subaerial settings (perhaps in oxygen oases). Such oases could also be the places where oxidation and precipitation of Fe and Mn oxides would preferentially occur, possibly allowing removal of dissolved U from the ocean through adsorption. Given the low amount of available dissolved U, Fe-Mn oxides could then represent a sink of U large enough to balance the fractionation imparted by U incorporation into anoxic/euxinic sediments, and thus keep the $\delta^{238}U_{SW}$ values close to the value of detrital/riverine input.

Clearly, U isotopes in black shales only provide an upper limit on the extent of anoxia in

the ocean at the time of sample formation (at least in the FAR-DEEP samples studied here). There are two main reasons for this: (i) the large uncertainty inherited from detrital corrections, and (ii) the fact that the fractionation factor associated with anoxic/euxinic sediment, $\Delta_{\text{Anoxic/Euxinic-SW}}$, can vary significantly as it is dependent on both the depositional settings and the reduction pathway (biotic *vs.* abiotic). Using a constant $\Delta_{\text{Anoxic/Euxinic-SW}}$ value is thus only valid to first order and finer scale reconstruction will not be possible using black shales as a rock record. The question is whether there is a better rock record to investigate.

3.6 Carbonate rocks as a better rock record?

3.6.1 The rationale for using carbonates and the boring billion

Carbonates could provide a better rock record than black shales for the U isotope systematics. Indeed, the fractionation factor associated with the carbonate sink is small, $\Delta_{\text{Carbonates-SW}} = +0.2 \pm 0.2$ ‰, and varies much less than the one associated with the anoxic/euxinic sink [68, 370]. This small and relatively regular offset between the isotopic composition of carbonates and the seawater can lead to enhanced reconstructions of paleo-redox conditions by decreasing the uncertainties on the inferred U isotopic composition of the seawater, in comparison to reconstructions using shales as the rock record.

Finer redox reconstruction power will be useful when investigating the so-called "boring billion": a one billion year period, in the middle of the Proterozoic era, of purported environmental oceanic stability [65] that starts with the disappearance of BIFs at $\sim$ 1.8 Ga. This last feature is widely interpreted to reflect a major change in the global redox state of the ocean. The question remains, however, as to whether the nature of this shift was towards oxic or euxinic (anoxic + sulfidic) conditions.

Presently, two models are competing to explain the evidence observed in the rock record of the "boring billion" (Fig. 3.12). In the traditional model of Holland (2006) [210], the disappearance of BIFs and Mn-oxide deposits, along with the absence of phosphorites, is

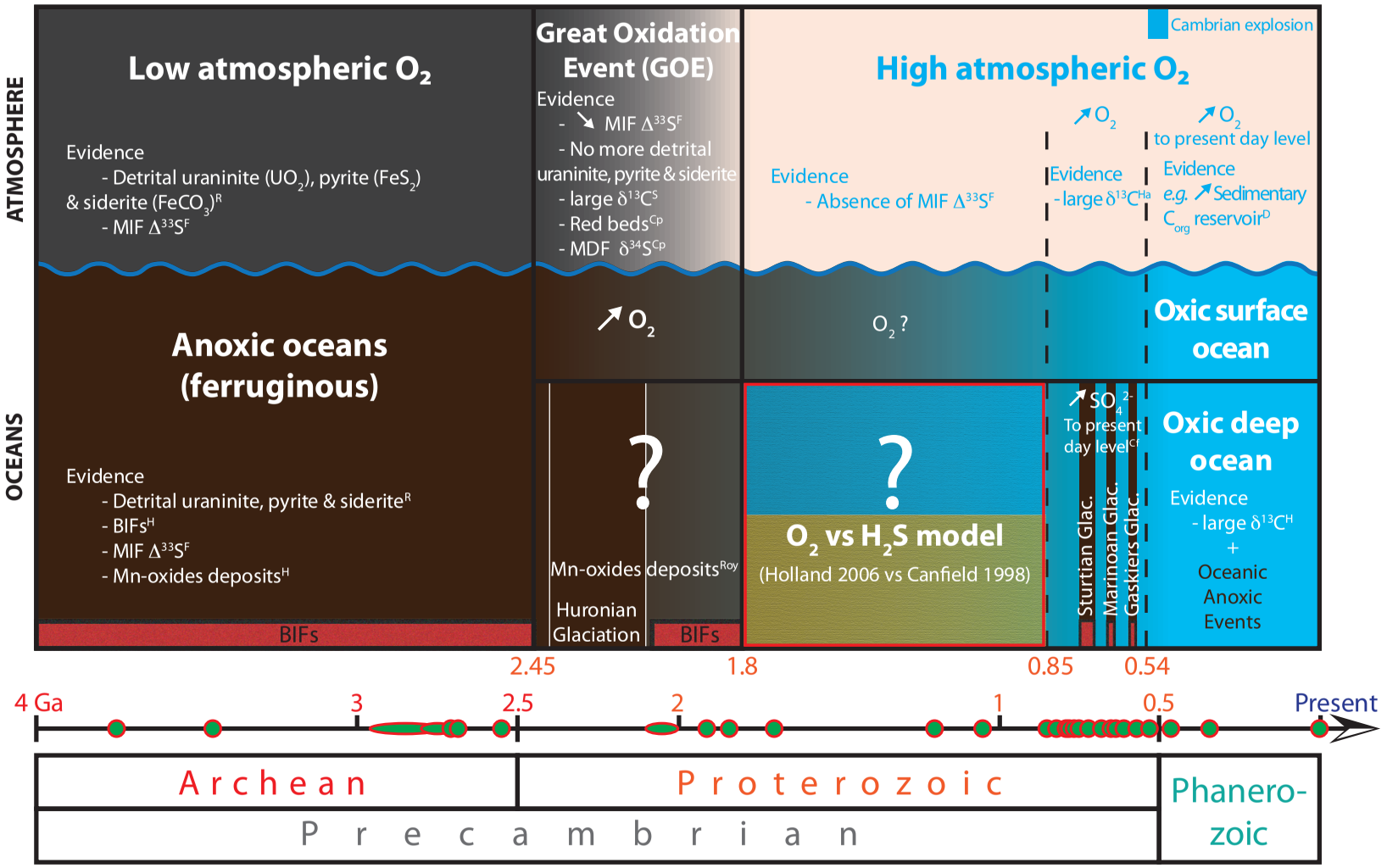

Figure 3.12: Main steps in the oxygenation of Earth's atmosphere and oceans. Question marks show places where significant work remains to be done. See main text for details of the Holland (2006) and Canfield (1998) models. Dots on the time arrow indicate carbonate samples available for analysis. The superscripts at the end of each bullet point refer to: Cf, [82]; Cp, [81]; D, [144]; F, [161]; H, [210]; Ha, [192]; R, [352]; Roy, [375]; S, [394]. With information from [322] as well.

taken as evidence of the oxygenation of the deep ocean, coupled with a small delivery rate of organic matter to the deep ocean. In contrast, Canfield (1998) [82] interpreted the increase in the net sulfur isotope fractionation between sulfate and sedimentary sulfides and the disappearance of BIFs at 1.8 Ga to reflect an increase of seawater sulfate and a transition to global euxinia in the ocean. Whereas this model seems to have been heavily supported by diverse geochemical data, the most recent data suggest that the global oceans were not uniformly euxinic during this time interval [265], and that anoxic, iron-rich and non-sulfidic conditions may have been widespread [333].

Provided carbonates can be shown to record faithfully the U isotopic composition of the seawater from which they form, much knowledge could be gained about the redox state of the ocean during the mid-Proterozoic. Two problems, however, could hamper the use of carbonates in paleoredox reconstructions: (i) the concentration of U in carbonate samples can be relatively low (below the ppm level), and (ii) the U isotopic composition recorded in carbonates might have been affected by secondary processes such as fluid circulation and re-crystallization (*i.e.*, diagenesis). The low concentration of U implies that large sample masses (0.05 to 2 g) need to be processed to obtain enough uranium to achieve high-precision U analysis, which increases the chances of tapping a part of the carbonate affected by secondary processes. To try and access the "original" δ^{238}U value recorded by the carbonate sample (even when this sample has been subjected to secondary processes likely to modify its bulk U isotopic composition), a step-leaching protocol was developed.

3.6.2 A step-leaching approach

The step-leaching protocol developed is based on the idea that easily mobilized U (*i.e.*, more likely to be of secondary origin) can be selectively removed from the sample by partial digestion with dilute acid. A similar protocol was originally developed by Bailey et al. (2000) [30] in order to study Sr isotopes in carbonates. Strontium concentrations are generally large enough in carbonates (tens to thousands of ppm) that only minute sample masses are needed

for analysis, allowing for the use of micro-dilling in "clean" sample regions to alleviate contamination concerns. In some cases though, bulk rock analysis might be required. Bailey et al. (2000) showed that progressive digestion of calcite samples ($74 \leq CaCO_3 \leq 98$ %) led to release of Sr fractions with significantly different isotopic composition depending on the amount of carbonate digested. When the amount of $CaCO_3$ digested was between 0 and 40 %, the Sr isotopic composition of the dissolved fraction showed clear deviation from the "expected" marine $^{87}Sr/^{86}Sr$ ratio at the time of deposition (obtained from comparison with samples at the same stratigraphic level in various locations, see [30]), indicating contamination from non-authigenic, water-soluble Sr adsorbed on the surface of the carbonate. Similarly, when the carbonate digestion reached 90 to 100 %, the isotopic composition was clearly different from the expected marine value, which is probably due to release of Sr from a non-carbonate residuum. The central cut (carbonate digestion between 40 and 90 %), however, seemed to record very closely the expected marine Sr isotopic composition.

The same progressive digestion experiment was conducted on carbonates to study the release pattern of U isotopes [434]. The tests were carried out on a modern (less than 10,000 yr old) stony coral from Florida ([U]$\sim$ 1.96 ppm), with dilute acetic acid (20 % vol), and aiming for 10 % increment digestion steps. The results are presented in Fig. (3.13).

The first few leachates are depleted in U while the intermediate and late leachates show concentrations oscillating around the bulk value. Similarly, the isotopic composition of the U fractions collected in each step is not constant and can differ from the isotopic composition of modern seawater by up to 0.2 ‰ (four times the 2SE of the measurements). The low concentration and heavy $\delta^{238}U$ values observed in the first few leachates suggest U loss in the most easily digested part of the carbonate. The plateau of isotopic composition observed between $\sim$ 30 % and $\sim$ 85 % digestion matches exactly the seawater composition, showing that corals do record the isotopic composition of the ambient seawater from which they formed. The deviation from seawater-like composition observed in the last few percent of carbonate digestion can be due to either (i) contamination from non-carbonate residuum, or

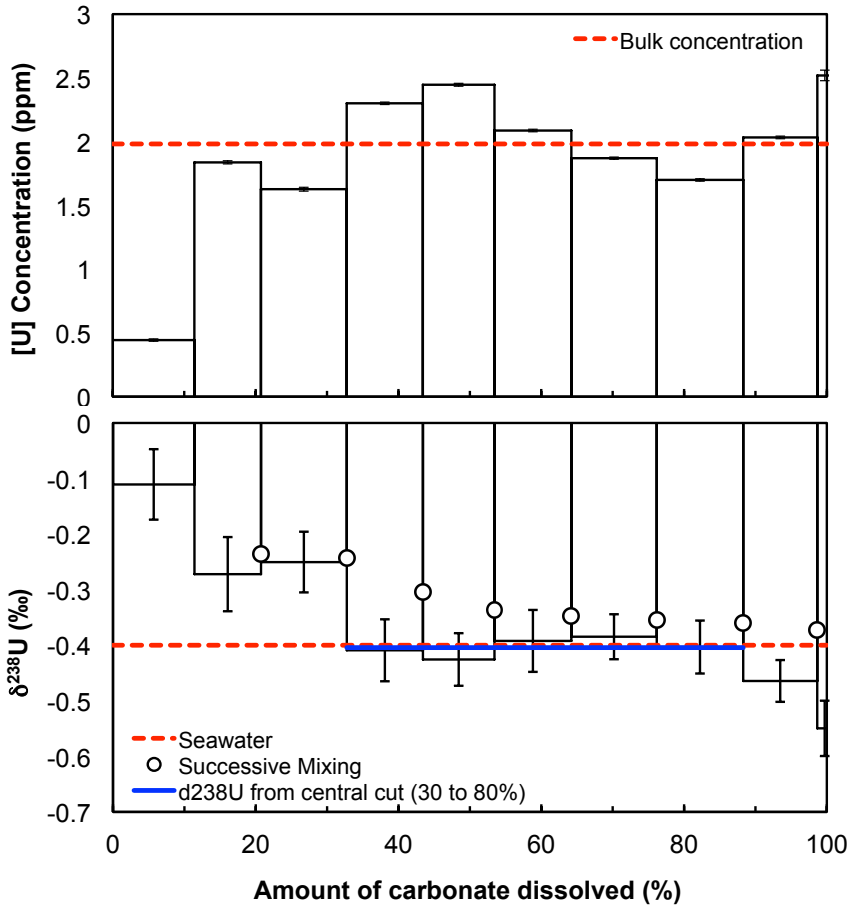

Figure 3.13: U concentration and isotopic composition of sequential leaches of modern coral plotted against the percentage of carbonate dissolved. "Successive mixing" (dots) show the δ^{238}U trend calculated using a two endmember mixing model (onto successive leaches). It can be seen that only leaches above $\sim 25-30$ % and below $\sim 85-90$ % digestion record the U isotopic composition of the seawater from which the sample formed.

(ii) preferential leaching of ^{238}U in the preceding steps, leaving a ^{235}U-enriched carbonate fraction to be digested last. As previously observed, the bulk coral has a composition indistinguishable from that of seawater [412, 460, 431], even though it is clear from Fig. (3.13) that only the "central leachate" of the carbonate (*i.e.*, the fraction of U released during digestion of $30-90$ % of the carbonate) records the composition of the seawater, and other U fractions are fractionated relative to this value.

From Fig. (3.13), a two step-leaching protocol was designed for application to carbonate samples. In the first leaching step only ~ 25 % of the sample is digested in order to remove

easily mobilized U (i.e., U contamination), then in a second step, the bulk of the carbonate ($\sim$ 70 % of the sample) is digested in order to access the original U isotopic composition of the carbonate sample. The reason for leaving 5 % of the sample undigested is to avoid leaching of U from phases other than carbonates (*e.g.*, detrital phases), whose isotopic composition will likely be different from that of the carbonate.

3.6.3 Assessing the effect of early diagenesis

Though corals seem to be faithful recorders of the U isotopic composition of the seawater from which they form, a recent study on surface and subsurface modern carbonates from the Bahamas [370] found that U precipitation from anoxic/euxinic porewater could affect the isotopic composition of carbonates. The study analyzed samples from 4 push cores (down to 40 cm below the water/sediment interface) and found an increased degree of isotopic variability with depth (δ^{238}U between -0.62 to $+0.14$ ‰ at 40 cm below the surface). These preliminary results suggests that the isotopic composition eventually recorded in carbonate rocks can be significantly different from that of seawater.

To assess the degree to which such early diagenesis impacts the carbonate record, a more systematic study was carried out on an array of modern carbonates taken along a $\sim$ 225 m long drill core in the Bahamas Bank. The drill core, Ocean Drilling Program (ODP) Leg 166 (The Bahamas transect) Site 1009 (see [150]), was selected for its high sedimentation rate (5 to 55 cm/kyr) and the time period it covers (from 0 to 1.5 Myr). The samples at Site 1009 consist of lithified to partially lithified peloidal and bioclastic mudstones, wackestones, packstones, and grainstones with interbedded foraminifer nannofossil ooze. The carbonate content of the samples is typically $\geq$ 90 wt%, while the aragonite content varies from 11 to 93 wt% and the total organic carbon is between 0 and 1.7 wt% [150].

Samples were taken every 5 m down the core, and the three-step leaching protocol outlined in the Section 3.6.2 was applied to all samples. Only the "central cut" ($30-90$ % carbonate digestion) was measured for U isotopes. Results are graphically presented in Fig. (3.14).

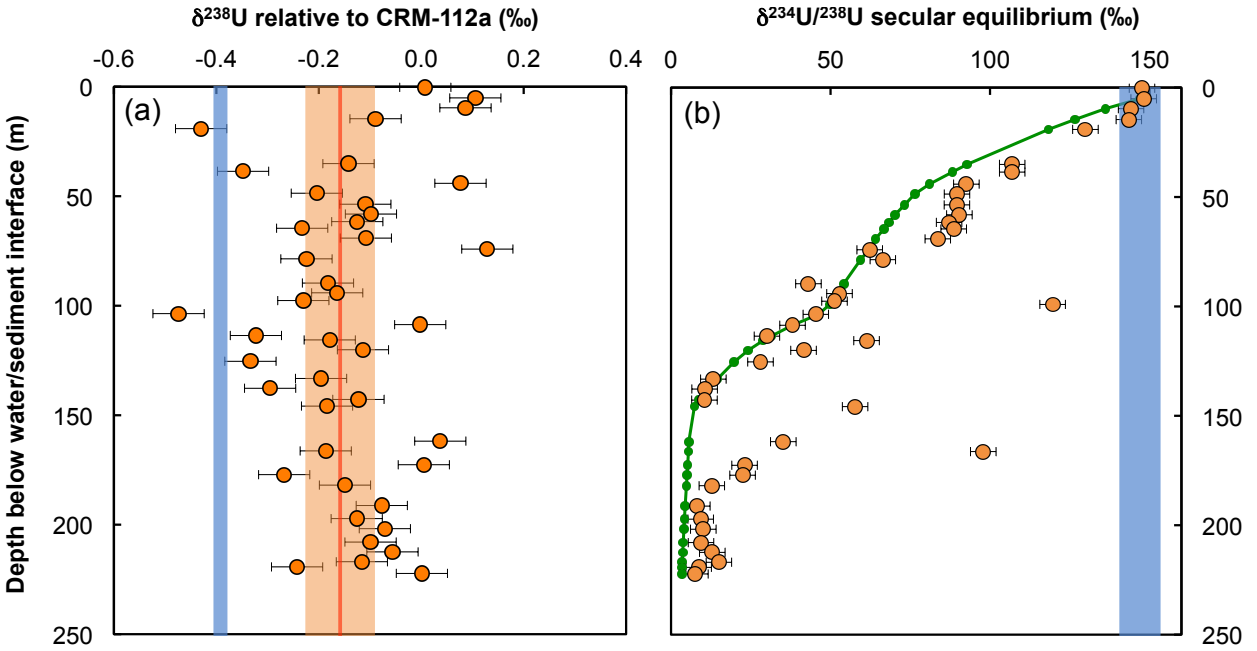

Figure 3.14: (a) δ^{238}U and (b) $\delta[^{234}\mathrm{U}/^{238}\mathrm{U}]$ plotted against depth below the water/sediment interface (m) for selected samples of the OPD Leg166 Site 1009 drill core [150]. The blue bands represent the typical composition of modern seawater, while the red line and orange band on the left panel show the average composition of the drill core samples and the 95 % confidence interval, respectively.

For all samples, both the δ^{238}U and $\delta[^{234}\mathrm{U}/^{238}\mathrm{U}]$ values are plotted. As explained in Section 1.1, the abundance of ^{234}U in a sample is a function of the decay constants of ^{234}U and ^{238}U (λ_{234} and λ_{238}) and the time since closure of the sample. At steady-state, the decay of ^{234}U is balanced by the creation of ^{234}U from ^{238}U decay, and the $^{234}\mathrm{U}/^{238}\mathrm{U}$ ratio in the sample is equal to the secular equilibrium ratio: $\lambda_{238}/\lambda_{234} = 5.497 \times 10^{-5}$. As seen in Fig. (3.14b), there is a strong decreasing trend in $\delta[^{234}\mathrm{U}/^{238}\mathrm{U}]$ values with depth, whereby the samples close to the water/sediment interface have seawater-like $\delta[^{234}\mathrm{U}/^{238}\mathrm{U}]$ values ($\sim +147$ ‰), and the samples close to the bottom of the core have $\delta[^{234}\mathrm{U}/^{238}\mathrm{U}]$ values close to secular equilibrium (~ 10 ‰).

To first order, this is in good agreement with closure of the samples a few meters below the water/sediment interface, and return to secular equilibrium in a closed system. The fit in Fig. (3.14b, green curve) is calculated using the age of the samples, t, as inferred from calcareous nanofossils and planktonic foraminiferal biostratigraphic datums (Eberli et al.,

1997) and the following equation:

$$\delta[^{234}\mathrm{U}/^{238}\mathrm{U}]_{\mathrm{fit}} = \delta[^{234}\mathrm{U}/^{238}\mathrm{U}] \times e^{-\lambda_{234}t} \tag{3.28}$$

Samples which do not fall on this curve are systematically enriched in ^{234}U, which indicates open-system behavior of U isotopes and exchange with a phase characterized by a high $\delta[^{234}\mathrm{U}/^{238}\mathrm{U}]$ value (most likely seawater). Nevertheless, the overall agreement between the measured and expected $\delta[^{234}\mathrm{U}/^{238}\mathrm{U}]$ values suggests that in most cases, the samples started behaving as closed systems with respect to U isotopes soon after they formed. Any diagenetic process affecting U isotopes must therefore have taken place while the system was still open, which means within the first $\sim$ 10 m below the water/sediment interface. Based on the ages of the samples, this corresponds to a duration of open-system behavior of $\sim$ 60 kyr.

Considering now the $^{238}\mathrm{U}/^{235}\mathrm{U}$ ratio (Fig. 3.14a), there doesn't seems to be any trend with depth. Instead, and despite some scatter in the data, the δ^{238}U values of the samples seem to be shifted relative to the seawater value by about $+0.25 \pm 0.06$ ‰. This value is in agreement with the observations of Romaniello et al. (2013) [370], and confirms that significant deviation from the seawater U isotopic composition can be recorded in carbonates (even after leaching of the easily mobilized U fraction). Given that the U system closed $\sim$ 60 kyr after carbonate formation, this offset must be the result of early diagenesis (probably due to precipitation of U from porewater within the sediment) rather than late secondary processes. The scatter in the data also implies that any reconstruction of past ocean redox conditions using U isotopes will have to rely on a large number of data points, in order to allow for the identification of statistically meaningful trends.

3.6.4 Exploring Earth's history: preliminary data

Despite the existence of a non-zero fractionation factor between the seawater and the carbonate U sink, $\Delta_{\text{Carbonates-SW}} = +0.25 \pm 0.06$ ‰, the smaller error associated with this

value (relative to the one associated with black shales) still warrants the use of carbonates as a potentially better rock record for paleoredox reconstructions using U "stable" isotopes. A large collection of carbonate samples was therefore assembled in order to track the evolution of the oxygenation of the ocean throughout Earth's history.

The sample selection was done so as to fulfill the following requirements:

1. The samples must be marine sediments, deposited in the open ocean, to ensure that the signal recorded in the samples corresponds to the global ocean redox conditions,

2. The samples must have experienced limited secondary alteration in order to minimize elemental and/or isotopic resetting of the U systematics,

3. The sample set must span most of Earths history, with a high time resolution.

Identification of the least altered and best-preserved samples was based on a combination of petrological evidence and an array of geochemical tracers that reveal the extent of post-depositional resetting of geochemical signatures. For example, as explained in Veizer et al. (1989) [446], alteration enriches the samples in Mn, and decreases their Sr/Ca ratios. In this context, alteration is understood as any secondary or primary (*e.g.*, mixing) phenomenon, which results in systematic displacement of some chemical parameter from some "pristine" values. Thus, samples with the highest Sr/Ca ratio and lowest Mn content were always selected in preference to other samples. Similarly, the isotopic compositions of oxygen and carbon were also considered, with preference given to samples characterized by higher δ^{18}O and δ^{13}C values, which are less likely to be affected by dissolution-reprecipitation or mantle contamination [445].

In total, more than 200 samples were selected, with ages ranging from the present to 3.4 Gyr ago. So far, only a handful of those 200 samples have gone through the entire U isotopic analysis protocol (*i.e.*, step-leaching, column chemistry and high-precision measurement on MC-ICPMS), and the data are graphically presented in Fig. (3.15).

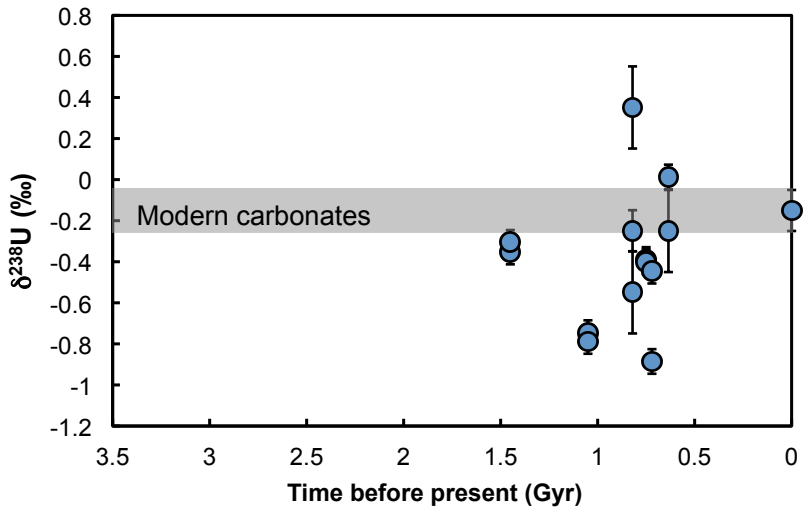

Figure 3.15: δ^{238}U value as a function of age (Gyr) in a small number of carefully selected carbonates. These samples are part of a much larger sample collection that is currently being processed for analysis. Interpretation will have to await these additional data.

Clearly, more data need to be analyzed before any conclusion can be drawn regarding the evolution of the redox conditions of the global ocean through time. If the variations shown in Fig. (3.15) prove to be statistically meaningful, they imply that the amount of anoxia in the ocean in the Ediacaran (635-541 Myr ago) was dramatically higher than in the modern ocean (in agreement with a very recent abstract [467]).

3.7 Conclusions

In this chapter, analytical equations were derived to allow for easy and rapid assessment of the impact of the natural variability of the $^{238}U/^{235}U$ ratio on Pb-Pb and U-Pb ages. Applying the high-precision U isotope analysis techniques developed throughout this dissertation, a systematic characterization of a large number of igneous rocks and geostandards was done. From this data set, the absence of Soret diffusion was demonstrated in the Lachlan Fold Belt granites, and the average U isotopic composition of the crust was calculated as -0.29 ± 0.03 ‰ (relative to CRM-112a), equivalent to an absolute $^{238}U/^{235}$ ratio of 137.797 ± 0.005. A large array of seawater samples was also measured, which showed that the open ocean has

a homogeneous isotopic composition at $\delta^{238}U_{SW} = -0.392 \pm 0.005$ ‰. Comparison of this value with predictions from several modern oceanic U budgets strengthened our confidence in the isotopic fractionation factors associated with each deposition environment and the fact that U is at steady-state in the modern ocean. From this analysis, the extent of modern anoxia in the ocean (*i.e.*, the percent of seafloor covered by anoxic/euxinic sediments) was constrained to be 0.21 ± 0.09 %, and the potential for U "stable" isotopes to track redox conditions on a global scale was demonstrated. The U proxy was then applied to black shales in the wake of the GOE, where the U signal, once corrected for detrital contribution, indicate that the extent of oceanic anoxia at that time could have been up to four times the present value. Finally, the development of a step-leaching protocol for carbonate samples and its application to modern samples from the Bahamas (0 to 1.5 Myr) showed that carbonates could be a better rock record for paleoredox reconstructions using U isotopes. Preliminary data on older carbonates were presented.

CHAPTER 4

U IN ANGRITES AND CAIS

"His answer to every problem, every setback, was 'I will work harder!'

– which he had adopted as his personal motto."

George Orwell – *The Animal Farm*

Part of this chapter is based on:

• [432]: Tissot F.L.H, Dauphas N., Grossman L. (Submitted to *Science Advances*) Origin of uranium isotope variations in early solar nebula condensates.

4.1 Introduction

At a large enough scale, the Solar System has a homogeneous U isotopic composition and, until recently, all SS materials where thought to be characterized by a unique $^{238}U/^{235}U$ ratio (within a small window of 4 ‰). With the appearance of the MC-ICPMS in the early 2000s, the analytical precision improved by two orders of magnitude (from ±5 ‰, to ±0.05 ‰). With the hope of finding evidence for live ^{247}Cm in the ESS, systematic characterization of meteoritic samples at high precision was undertaken by several research groups.

The first part of this chapter will present the current state of knowledge of the U isotopic composition of SS materials. Based on measurements done during this thesis, the specific case of angrite samples, some of which are used as anchors for relative dating methods (Al-Mg, Mn-Cr or Hf-W, [141]), will be discussed in the framework of ESS chronology. The second part of this chapter will focus on the work done on a series of Calcium, Aluminum-rich inclusions (CAIs), and how the discovery of a large ^{235}U excess brings definitive evidence that ^{247}Cm was alive in the ESS. The implications for models of nucleosynthesis and SS formation are discussed.

4.2 U isotope variations in SS materials and the ages of angrites

4.2.1 U isotopic composition of the Solar System

In order to assess the current state of knowledge about the U isotopic composition of SS materials, a compilation of high-precision literature data ($^{238}U/^{235}U$ ratios) in bulk meteorites, meteorite leachates, mineral separates, and meteoritic inclusions was made, and is shown in Fig. (4.1, top panel) [414, 415, 71, 14, 119, 69, 231, 221, 177, 18]. The compilation totals 216 measurements on 75 different meteorites (both chondrites and achondrites). A large fraction of these data (70 individual measurements) is only available as part of a Ph.D thesis (Kaltenbach (2013) [231]) and has not been through a peer-review process. This large data set would be valuable if it were reliable, which doesn't seem to be the case. This

conclusion arises from two main observations (i) the uncertainty on the measurements by [231] is typically large, and (ii) in some cases, the results obtained by [231] are extremely odd (non-reproducible anomalies between -18 to +33 ‰, in *bulk* chondrites). This last point in particular, which the author herself explains by potential contamination of the samples during handling at nuclear laboratories ([231], p. 116), challenges the quality of the whole data set, especially at the sub-permil level. In Fig. (4.1, bottom panel), the data of [231] are excluded from the compilation, and only this reduced data set is considered in the remaining of this discussion.

Considering only bulk meteorite measurements, the range of isotopic compositions is large, from -0.91 ‰ (Richardton, H5) to $+0.39$ ‰ (Elenovka, L5), but most samples appear to cluster at ~ -0.40 ‰ (Fig. 4.1, bottom panel). "Finds" (23 measurements on 16 different meteorites) define a Gaussian curve with δ^{238}U= -0.39 ± 0.20 ‰ (95 CI) while "falls" (45 measurements on 29 different meteorites) define an virtually identical Gaussian curve δ^{238}U= -0.38 ± 0.24 ‰ (95 CI) (Fig. 4.2). The highest (-0.91 ‰) and lowest ($+0.39$ ‰) δ^{238}U values occur in falls while the finds range extends from -0.65 to -0.12 ‰ only. U remobilization (by fluid alteration and/or metamorphism) in chondrites is evidenced by the highly variable U concentrations and U/Th ratios observed in carbonaceous chondrites [368]. The tighter distribution of U isotopic compositions observed in finds meteorites could then be due to terrestrial contamination, (the average isotopic composition of the crust is -0.29 ± 0.03 ‰, see Section 3.3.2.3, Chapter 3). In order to consider the full spread of composition measured so far, the discussion below only focuses on falls.

The average isotopic compositions for the various meteorite groups (falls only) are summarized in Table 4.1. The average values for carbonaceous, ordinary and enstatite chondrites are indistinguishable from one another, and calculated as, -0.38 ± 0.07 ‰ (n = 11; MSWD = 4.14), -0.30 ± 0.17 ‰ (n = 14; MSWD = 52.0) (95 CI of the mean) and -0.33 ± 0.20 ‰ (n = 1) (2SD), respectively. The average δ^{238}U value for chondrites is -0.33 ± 0.09 ‰ (95 CI of the mean; n = 26; MSWD = 26.8), while the average value for achondrites is -0.39 ± 0.06

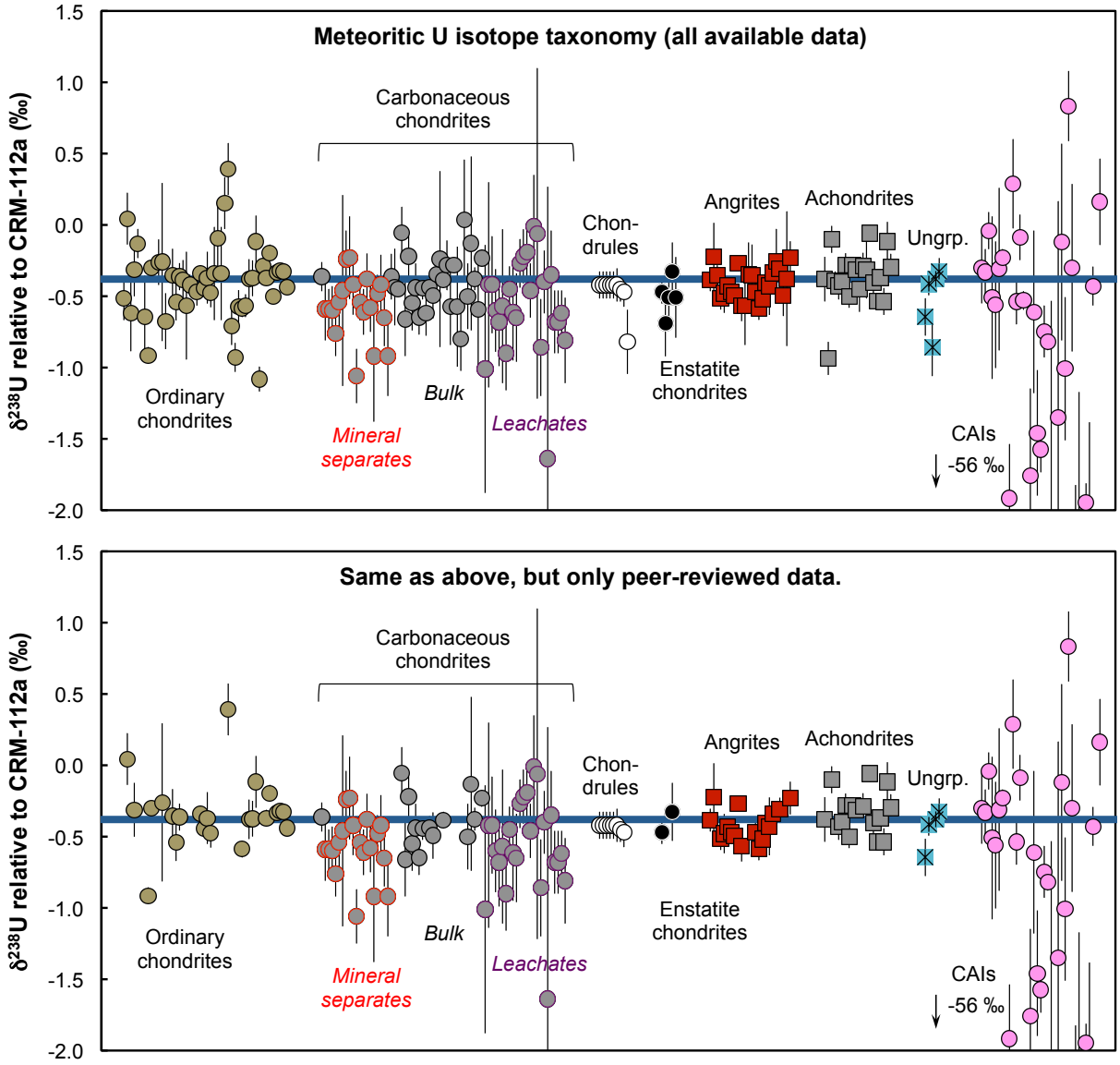

Figure 4.1: Compilation of the δ^{238}U values from literature data [414, 415, 71, 14, 57, 119, 69, 231, 221, 177, 18], and this work (some angrites and some CAIs, see Section 4.2.2 and 4.3). The bottom panel shows the same compilation minus the data from Kaltenbach (2013) [231], which is deemed unreliable (see main text). The isotopic composition of U in undifferentiated chondrites (ordinary, carbonaceous and enstatite) varies from -0.91 to $+0.39$ ‰, (average of ~ -0.33 ‰), while leachates of Allende and Murchison meteorites and mineral separates from Tafassasset show a larger spread from -1.64 to -0.02 ‰ [414, 415, 71, 14, 119, 177, 18]. The 8 chondrules measured so far are clustered at -0.43 ± 0.05 (2SD) ‰ [119]. Angrites, other achondrites (encompassing howardites, eucrites, aubrite, and acapulcoite samples) and ungrouped meteorites form another set of clusters at around -0.43 ± 0.25 (2SD) ‰ [414, 57, 119, 69, 430, 177]. Finally, CAIs show a large spread of values from -56 to $+0.83$ ‰, with the lighter isotopic composition being interpreted as evidence of live ^{247}Cm in the early Solar System [71, 14, 119, 432]. Modified from [431].

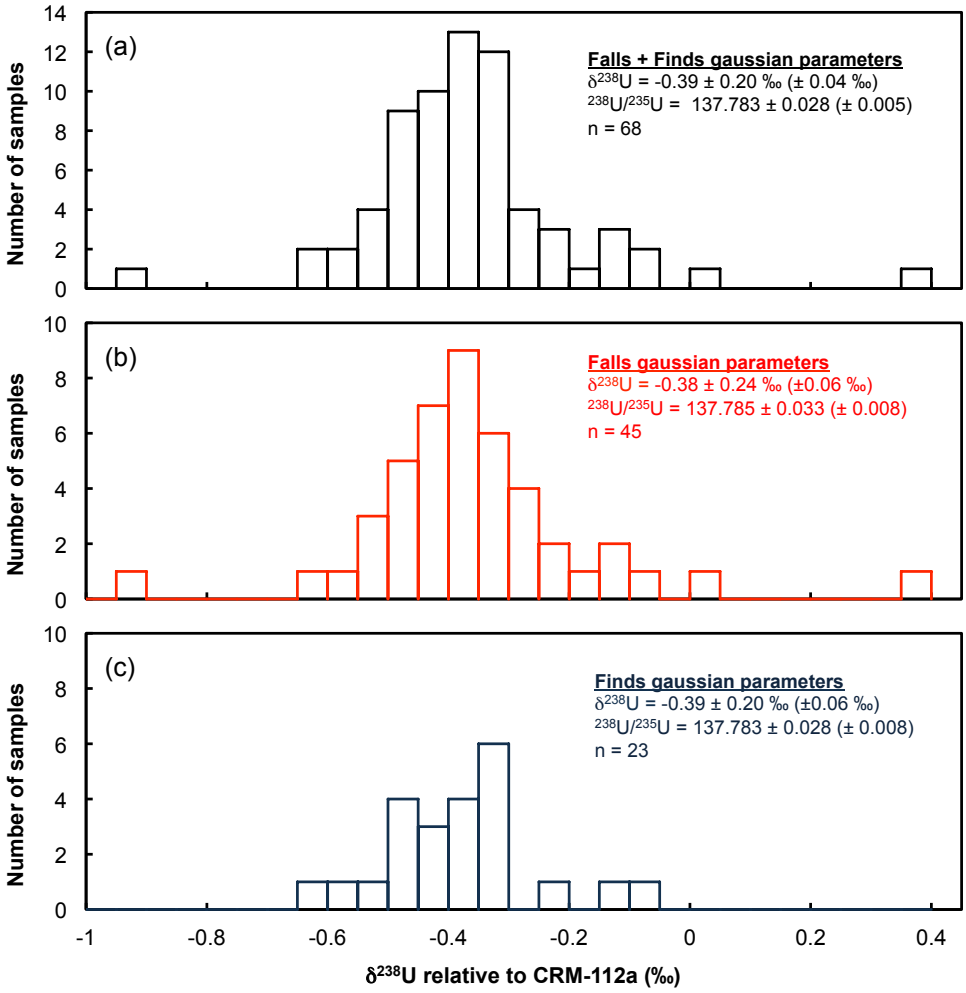

Figure 4.2: δ^{238}U values from literature data [119, 221, 177, 18], and this work (one angrite and Allende), shown in three histogram plots. Top panel shows all samples, the middle panel only the falls, and the bottom panel only the finds.

‰ (95 CI of the mean; n = 19; MSWD = 15.2). The global average δ^{238}U value of falls (including both chondrites and achondrites) is -0.36 ± 0.06 ‰ (95 CI of the mean; n = 45; MSWD = 20.0), and this last value is taken as representative of the Solar System composition. Using an absolute ^{238}U/^{235}U ratio for CRM-112a of 137.837 [367], the present best estimate of the ^{238}U/^{235}U ratio of the Solar System is thus 137.787 ± 0.009, similar to the recent estimates of 137.779 ± 0.013 (-0.42 ± 0.09 ‰) [119] and 137.793 ± 0.011 (-0.31 ± 0.04 ‰) [177]. Note that since all three studies used the same double spike (IRMM-3636), all measurements can be readily compared without considering the error on the double spike composition, and the above uncertainties do not include this error.

Compilation of the U isotopic compositions of falls

Sample	n	δ^{238}U (‰)	±	238U/235U	±	MSWD	Reference
CHONDRITES							
Abee	1	-0.33	0.20	137.792	0.028		Goldmann et al. 2015
H Chondrites	4	-0.38	0.63	137.784	0.087	118	Goldmann et al. 2015
H Chondrites	1	-0.30	0.05	137.796	0.007		Andersen et al. 2015
L chondrites	5	-0.20	0.46	137.809	0.064	60.9	Goldmann et al. 2015
L chondrites	1	-0.44	0.05	137.776	0.007		Andersen et al. 2015
LL chondrites	3	-0.30	0.23	137.796	0.031	10.0	Goldmann et al. 2015
Ordinary average	*14*	*-0.30*	*0.17*	*137.796*	*0.024*	*52.0*	
Carbonaceous chondrites	6	-0.42	0.04	137.779	0.006	0.85	Connelly et al. 2012
Carbonaceous chondrites	4	-0.29	0.22	137.797	0.030	6.30	Goldmann et al. 2015
Allende	1	-0.49	0.16	137.769	0.022		This work
Carbonaceous average	*11*	*-0.38*	*0.07*	*137.785*	*0.010*	*4.14*	
Chondrites average	***26***	***-0.33***	***0.09***	***137.791***	***0.013***	***26.2***	
ACHONDRITES							
AdoR	1	-0.51	0.08	137.766	0.011		This work
AdoR	1	-0.48	0.14	137.771	0.019		Goldmann et al. 2015
AdoR average	*2*	*-0.50*	*0.22*	*137.769*	*0.031*	*0.25*	
Eucrites	3	-0.39	0.15	137.783	0.020	2.02	Iizuka et al. 2014
Juvinas	1	-0.50	0.08	137.768	0.011		Connelly et al. 2012
Eucrites	8	-0.36	0.15	137.787	0.021	27.5	Goldmann et al. 2015
Eucrites	2	-0.34	0.36	137.790	0.050	7.22	Andersen et al. 2015
Eucrites average	*14*	*-0.38*	*0.08*	*137.785*	*0.011*	*18.0*	
Acapulco	1	-0.30	0.09	137.796	0.013		Goldmann et al. 2015
Petersburg	1	-0.54	0.09	137.763	0.013		Goldmann et al. 2015
Ungrouped Achondrite							
Bunburra Rockhole	1	-0.38	0.09	137.785	0.013		Goldmann et al. 2015
Achondrites average	***19***	***-0.39***	***0.06***	***137.783***	***0.009***	***15.2***	
AVERAGE METEORITES	**45**	***-0.36***	***0.06***	***137.787***	***0.008***	***20.0***	

All literature data have been renormalized to CRM-112a (also named SRM960, NBL112-a or CRM-145),
Absolute ratios are calculated using the 238U/235U ratio from Richter et al. (2010): 137.837

Table 4.1: Compilation of the U isotopic compositions of falls. Data from [119, 221, 177, 18] and two samples from this work.

The difference between the average Solar System value defined above (137.787 ± 0.009) and the consensus value (137.88, [409]) is important for Pb-Pb dating (see Section 3.2.1, Chapter 3). For samples where Pb-Pb ages were determined assuming the consensus value and for which no high-precision U data exists, a typical age adjustment of -0.98 ± 0.08 Myr can be applied (Fig. 3.1 and 3.2, Chapter 3). Of course, given the large range of variations observed in meteorites and the even larger spread observed in CAIs ([71, 432]), the ideal is

still to measure the U isotopic composition of each sample to obtain a proper Pb-Pb age.

It is important to realize that the δ^{238}U values of the SS derived above and in earlier studies, suffer from some two main shortcomings. First, most of the time, the mass of sample digested is small (*i.e.*, < 1 g). Uranium is, however, concentrated in minor phases such as apatite or oldhamite, and as a result, measurement can be affected by a nugget effect ([133]). Large sample masses thus need to be processed to get a representative average composition for each sample. The second problem is that secondary processes, such as aqueous alteration on Earth, can mobilize U and fractionate its isotopic composition (especially in meteorite finds). One way to identify recent mobilization of U is to measure the ^{234}U/^{238}U ratio. Any recent disturbance of the system (in the last 2.5 Myr), will result in addition/loss of ^{234}U (which, unlike ^{235}U and ^{238}U, is not lattice bound), thus shifting the ^{234}U/^{238}U ratio away from secular equilibrium. Because secondary processes may also affect the ^{238}U/^{235}U ratio, a conservative approach would be to consider only samples with ^{234}U/^{238}U ratios at secular equilibrium. At present, only 7 large-mass samples (> 10 g) have been characterized for both ^{238}U/^{235}U and ^{234}U/^{238}U isotopic ratios [18], and out of these, only two samples are falls at secular equilibrium (ordinary chondrite Zag and eucrite Juvinas). The average SS value obtained from these two samples is 137.795 ± 0.004 (-0.306 ± 0.026 ‰), in good agreement with the other estimates presented above, but obviously more work is needed to enlarge this minimal data set. Future studies should therefore use large sample masses and report both the ^{238}U/^{235}U ratio and the ^{234}U/^{238}U ratio of the samples, in order to consolidate our current estimate of the average Solar System U isotopic composition.

4.2.2 The ages of angrites

Angrites are differentiated meteorites, of basaltic (mafic) composition, of either volcanic or plutonic origin, and which display minimal post-crystallization alteration, metamorphism, shock or impact brecciation (*e.g.*, [233] and references therein). Their old U-Pb and Pb-Pb ages make angrites the recorders of some of the earliest volcanic activity in the SS, only ~ 4

Myr after CAI formation. Of all ESS materials, angrites are of particular importance in the context of chronology, as some of these rocks are used as "anchors" between the absolute dating techniques (*i.e.*, U-Pb, Pb-Pb) and the various relative dating methods (*e.g.*, ^{26}Al-^{26}Mg, ^{53}Mn-^{53}Cr, ^{182}Hf-^{182}W) [316, 242]. They also provide insights into the early stages of planetary melting and differentiation. The possibility that the U isotopic composition of angrites is not constant after all, implies that their U-Pb and Pb-Pb ages might have to be revised if these ages were determined assuming a constant U composition for all SS material (*e.g.*, [120, 10, 11]). Such modification of the ages of angrites can impact all short-lived chronometers which are anchored to these samples. Clearly, proper assessment of the ^{238}U/^{235}U ratio of angrites is a prerequisite to a reliable matching of relative and absolute ages.

4.2.2.1 Samples and methods

Given that U concentrations in angrites are relatively low (between 20 and 200 ppb), large sample masses are needed to obtain high-precision U isotopic data. In this work, the sample mass ranged from 140 mg for the most concentrated samples to 1.4 g for low concentration samples (see Table 4.2). When possible, a replicate measurement was performed on a newly processed sample aliquot (from fresh powder). The sample preparation (spiking, digestion) followed the general protocol detailed in Section 2.2.2 (Chapter 2). Digested samples were purified using either two or three column passes on U/Teva resin (Section 2.3.2). Some samples (denoted by a star in Table 4.2) were obtained as solution recovered from a previous chemistry meant to purify Fe. For these, spiking was only done after Fe chemistry and before U purification.

Based on sample availability, as broad a range of angrites as possible was selected for this work. The sample set includes two volcanic (quenched) angrites (D'Orbigny and Sahara 99555), and four plutonic angrites (NWA 4801, Angra dos Reis, NWA 4590 and NWA 6291). Angra dos Reis (hereafter AdoR) is the only observed fall.

4.2.2.2 U isotopic compositions of angrites

Results of the high-precision U isotopic analysis conducted on the samples are given in Table 4.2 and Fig. (4.3). The variable uncertainties are due to the low number of replicate measurements possible on some samples (*i.e.*, sample limited measurements). Taking the data at face value, quenched angrites tend to have heavier U isotopic composition than plutonic angrites, and even within plutonic angrites, there could be variations outside of analytical uncertainty (this last point is really at the limit of the current precision of the measurements).

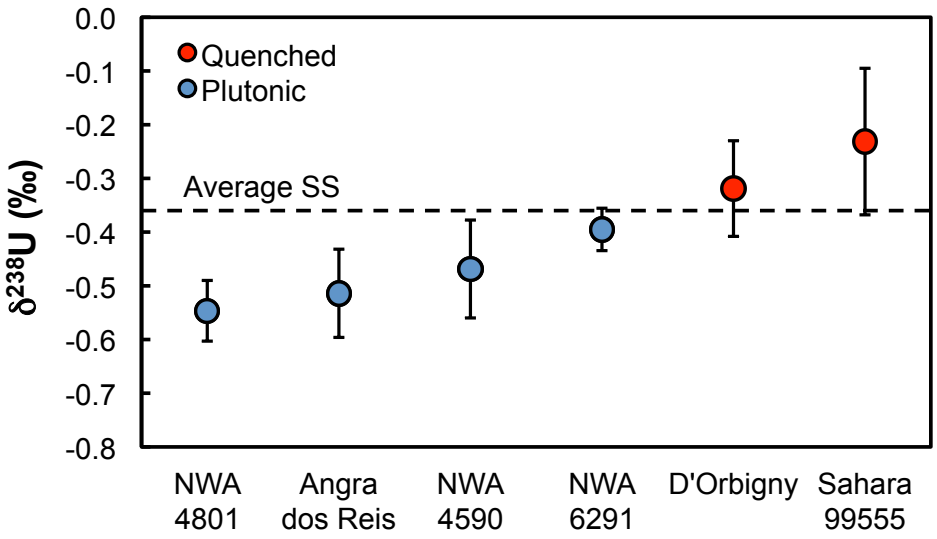

Figure 4.3: U isotopic composition of selected angrites. Values are expressed in δ^{238}U notation, relative to U standard CRM-112a. Quenched angrites tend to have heavier U isotopic composition than plutonic angrites. The total range of isotope variability in these samples has a bearing on their absolute ages as obtained from Pb-Pb dating.

An important question concerns the type of uncertainty to propagate onto the final revised ages of angrites. An earlier study [69] used the quadratic sum of the error coming from the U isotopic measurement and the error coming from the composition of the U double spike being used. The uncertainty on the spike composition is, however, a systematic uncertainty, which will affect all samples in a similar fashion. As long as the U isotopic composition of the samples whose ages are to be compared are determined with the same U double spike, it is not

Summary of U isotopic compositions and concentrations of selected angrites

Sample	Resin #	Mass (mg)	n	Blank contrib.	Double-spike data reduction							Sample-standard bracketing				Literature data		
					δ^{238}U (‰) blk corr.	±	δ [^{234}U/ ^{238}U]^{a}	±	Conc. (ng/g)	±	Usp/ Usmp	δ^{238}U (‰) blk corr.	±	δ [^{234}U/ ^{238}U]^{a}	±	Conc. (ng/g)	±^{b}	Ref.^{c}
PLUTONIC																		
* NWA 4590	2	389.3	5	0.24%	-0.47	0.09	241.6	0.9	68	3	5.3%	-0.44	0.33	308.2	1.3	96	4	(1)
* NWA 4801	2	258.8	4	0.28%	-0.65	0.10	73.8	1.0	81	8	2.7%	-0.52	0.37	57.5	1.5	94	1	(1)
NWA 4801 rep.	3	549.0	7	0.31%	-0.50	0.07	55.2	0.8	87	4	2.8%	-0.54	0.10	45.5	0.9	94	1	(1)
NWA 4801 average					*-0.55*	*0.06*						*-0.54*	*0.10*					
NWA 6291	2	189.4	3	0.33%	-0.30	0.12	472.3	1.1	98	6	4.7%	-0.24	0.42	513.8	1.7	156	*8*	(2)
NWA 6291 rep.	3	1390.3	14	0.09%	-0.41	0.04	511.7	0.6	128	1	3.9%	-0.48	0.06	532.3	1.0	156	*8*	(2)
NWA 6291 average					*-0.40*	*0.04*						*-0.47*	*0.06*					
* Angra dos Reis	2	141.0	6	0.17%	-0.51	0.08	0.0	0.8	238	17	2.3%	-0.69	0.30	-27.9	1.2	200	100	(1)
VOLCANIC (QUENCHED)																		
* D'Orbigny	2	213.8	3	0.32%	-0.33	0.12	41.1	1.1	84	6	4.3%	0.03	0.42	76.6	1.7	82	1	(1)
D'Orbigny	3	299.9	3	0.70%	-0.31	0.14	64.7	1.4	64	3	6.2%	-0.55	0.19	164.5	1.5	82	1	(1)
D'Orbigny average					*-0.32*	*0.09*						*-0.45*	*0.18*					
Sahara 99555	3	200.0	3	0.71%	-0.23	0.14	21.1	1.4	94	6	4.4%	-0.42	0.19	63.3	1.5	106	3	(1)

* Denotes samples that were elution cuts recovered from a previous chemistry meant to purify Fe.

[a] Activity ratio [234U/238U] of the sample relative to secular equilibrium (in ‰). δ [234U/238U] ={ (234U/238U)smp / (234U/238U)eq -1}*1000 where (234U/238U)eq is the atomic ratio at secular equilibrium and is equal to λ238U/λ234U= 5.497e-5 (Cheng et al. 2013).

[b] When no value is available for the uncertainty of the recommended concentration, a value of 5 % was assumed (noted in italic).

[c] References: (1) Riches et al. 2012, (2) Brennecka and Wadhwa 2012.

All measruements were made using: Aridus II + Spray Chamber + Jet Cones.

Cup configuration for 233/234/235/236/238U is L1/SEM/H1/H2/H3

Tailing from 238U on 236U, 235U and 234U was taken as, respectively, 0.6 ppm, 0.25 ppm and 0.1 ppm. Hydride formation was corrected using the value 238UH/238U = 7.3e-7.

Table 4.2: Summary of U isotopic compositions and concentrations of selected angrites.

necessary to propagate the uncertainty on the double-spike composition. If different double spikes are used on different samples (as was the case in [69]), then a proper age comparison requires propagation of the spike uncertainty onto the final ages. In the present work, all samples were spiked with the U double spike IRMM-3636. Except for three samples from [69] (D'Orbigny pyroxenes, AdoR phosphates and a replicate of D'Orbigny Bulk) all literature data published so far ([69, 119, 177]) also used the IRMM-3636 double spike. Therefore, only the errors coming from the isotopic measurements need to be considered when (i) comparing the various studies (Fig. 4.4), and (ii) propagating the uncertainties on the revised Pb-Pb ages (Table 4.5).

Considering only the error on the isotopic measurement leads to the conclusion that there is variability in the U isotopic composition of angrites (Fig. 4.3 and Table 4.2). This is in contrast to the conclusion of [69] that all angrites have a similar U isotopic composition. In Fig. (4.4a), the data from this work are compared to literature values (from [69, 119, 177]). The error bars show only the error on the isotopic measurement. There is overall a good agreement between the two sets of values, with some scatter around the 1 to 1 line. This scatter can be due, in part, to nugget effects: U is concentrated in minor phases, and the typical mass of sample digested for U isotopic work on angrites is small (below 1 g), allowing for the U concentration and isotopic composition of a small powder aliquot to be affected by a few "hot particles" of variable isotopic composition [133]. The variable U concentrations obtained in replicate analysis of freshly prepared powder aliquots (Table 4.2) supports this hypothesis.

The origin of the variability of the U isotopic composition of bulk angrites observed in Fig. (4.3) is uncertain. As on Earth, it could be due to secondary processes, such as aqueous alteration and/or redox processes, either on the angrite parent body or on Earth. The non-secular equilibrium values of the $\left[^{234}U/^{238}U\right]$ activity ratio of all finds is, in fact, evidence that some U mobilization occurred in the samples during their stay on Earth before discovery. Only AdoR (an observed fall) has a $\delta[^{234}U^{238}U]$ ratio of 0.0 ± 0.8 ‰ (*i.e.*, at secular

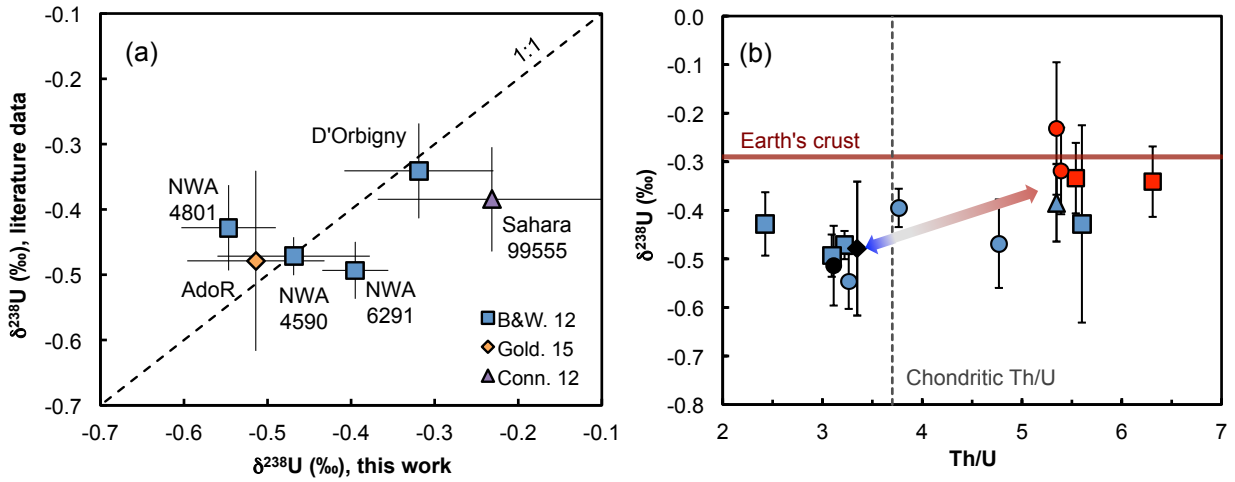

Figure 4.4: (a) Comparison of U isotopic composition of selected angrites measured in this study (x-axis) with literature values (y-axis, [69, 119, 177]). (b) δ^{238}U vs. Th/U ratios of selected angrites from this study (circles) and literature: [69], squares; [119], triangle; and [177], diamond. The U concentrations are the ones obtained from double-spike data reduction, and the Th concentrations are taken from Riches et al. (2012) [362] and G. Brennecka (personnal communication). Note that the Th/U ratio for Sahara 99555 from Connelly et al. (2012) (triangle shape, [119]) is assumed to be identical to the Th/U measured in this work. Blue and red symbols denote plutonic and quenched angrites, respectively. Black symbols denote AdoR (the only observed fall).

equilibrium), indicating no disturbance of U in this sample in the last 2.5 Myr.

Because Th is immobile during secondary processes, the Th/U ratio can provide insight into the extent of alteration of the samples. If terrestrial contamination were the main reason for the isotopic variability of angrites, one would expect the samples enriched in terrestrial U to have lower Th/U ratios, and isotopic compositions similar to the average crustal composition (-0.29 ± 0.03 ‰, see Section 3.3.2.3, Chapter 3). In Fig. (4.4b), the isotopic composition of the samples (this study and literature values, [69, 119, 177]) is plotted against their Th/U ratio (see figure caption and Table 4.3 for source of U/Th ratio data). It appears that samples with low Th/U ratios do not converge toward the crustal isotopic composition, as would be expected if terrestrial contamination were driving the correlation. There seems, actually, to be an opposite trend, whereby the δ^{238}U values of the samples increase with the Th/U ratio.

Two hypotheses can explain this observation. First, this trend could be the result of U loss

	This work				Connelly et al. (2012)				Brennecka & Wadhwa (2012)				Goldmann et al. (2015)			
Sample	Th (ppm)	Ref.	U (ppb)	Th/U	Th (ppm)	Ref.	U (ppb)	Th/U	Th (ppm)	Ref.	U (ppb)	Th/U	Th (ppm)	Ref.	U (ppb)	Th/U
NWA 2999	<0.2	B														
NWA 4590	0.325	A	68	4.8					0.364	C	113	3.2				
NWA 4801	0.283	A	87	3.3					0.182	C	75	2.4				
NWA 6291	0.483	C	128	3.8					0.483	C	156	3.1				
Angra dos Reis	0.74	A	238	3.1									0.740	A	194.6	3.35
AdoR phosphates									12.25	C	741	16.5				
D'Orbigny	0.454	A	84	5.4					0.454	C	72	6.3				
D'Orbigny									0.454	C	82	5.5				
D'Orbigny pyroxene										C	92	5.6				
Sahara 99555	0.500	A	94	5.3	0.500	A	94[a]	5.3								

[a] Assumed to be the same as measured in this work (for lack of any data in original publication).

Table 4.3: Th and U concentrations of angrites. U concentrations are from the four studies being compared (this work and [119, 69, 177]), while Th concentrations are from references: A, [362]; B, [175]; C, personal communication from G. Brennecka.

during aqueous alteration by oxidizing fluids. Equilibrium exchange between oxidized and reduced U can, indeed, lead to fractionation of U isotopes, in particular, enrichment of heavy U isotopes in the reduced phase (see NFS, Section 1.2.2, Chapter 1). Alteration by oxidizing fluids would therefore preferentially leach ^{235}U from the samples, leaving behind a heavier altered residual rock, as observed in mineralized ore deposits on Earth [51, 67, 305, 443]. The magnitude of the isotopic fractionation observed between angrites with low and high Th/U ratios (~ 0.15 ‰) is actually in line with the one experimental oxidation experiment conducted in non-acidic conditions [451].

A second possibility is that the trend in Fig. (4.4b) is the result of magmatic differentiation on the angrite parent body. Indeed, the distribution of U in angrites is controlled in part by minor phases such as phosphates (withlockite, for instance, in AdoR, [455]) which tend to form late in the crystallization sequence. If isotopic fractionation (either equilibrium, or kinetic) were taking place during the evolution of the magma, one would expect covariation of the Th/U ratio and the δ^{238}U values in the products of magmatic differentiation. Support for this hypothesis comes from the high Th/U ratio (16.5) and heavy U isotopic composition (-0.22 ± 0.24 ‰) measured in phosphates from AdorR, and the low Th/U ratio (5.6) and light U isotopic composition (-0.43 ± 0.20 ‰) measured in pyroxenes from D'Orbigny [69]. Additional evidence that pyroxenes and phosphates might not have the same U isotopic

composition comes from the 0.55 ± 0.29 Myr age difference (Pb-Pb ages, [15]) calculated between the two leachate fractions from NWA 4590 (each containing mostly pyroxene or phosphates) when the same U isotopic composition is assumed. This age difference would require a difference of 0.38 ± 0.20 ‰ between the δ^{238}U values of the two phases, a value in agreement with the ~ 0.20 ‰ lighter U isotopic composition of phosphate (from AdoR) relative to pyroxenes (from D'Orbigny) measured by [69].

It is possible that both processes are affecting the U isotopic composition of angrites. For instance, a leaching experiment conducted on NWA 6291 with dilute HNO_3 (0.5 M) found that the leachate (*i.e.*, containing the easily mobilized U, most likely to be of secondary origin) had a lighter U isotopic composition (δ^{238}U= -0.27 ± 0.05 ‰) than the residue δ^{238}U= -0.57 ± 0.11 ‰) [69]. The existence of two data clusters (one at Th/U of ~ 3.25 and the other at Th/U of ~ 5.6), however, suggests that another mechanism drives the first order correlation and that aqueous alteration might only be responsible for scatter in the data.

In this framework, the bulk U isotopic composition of the angrite parent body could be back-calculated assuming it has a chondritic Th/U ratio (3.8 ± 0.1, [105]) and using the first order correlation observed in Fig. (4.4b). This leads to a δ^{238}U of about -0.50 to -0.40 ‰, a value within uncertainty of the average SS value of -0.36 ± 0.07 ‰(see Section 4.2.1).

4.2.2.3 Corrected ages of angrites

Focusing now on ESS chronology, the main implication stemming from the variability of the U isotopic composition of angrites is that their Pb-Pb ages have to be revised. In Table 4.4, a summary of the ages of angrites before correction is presented. Using the data presented in this work, as well as literature data, the corrected ages of angrites are presented in Table 4.5. The age corrections were calculated using Eq. (3.3) and range from -0.17 to -1.20 Myr (ages younger than previously calculated using an assumed $^{238}U/^{235}U$ ratio).

The two quenched angrites (D'Orbigny and Sahara 99555) have essentially indistinguish-

Sample	Type	Age	± (2σ)	Method	Ref.	$^{238}U/^{235}U$ assumed/used	±
NWA 2999	Volcanic	4561.79	0.42	Pb-Pb isochron *	A	137.88	
NWA 4590	Volcanic	4557.93	0.28	Pb-Pb isochron *	B	137.789	0.021
NWA 4801	Volcanic	4558.06	0.15	Pb-Pb isochron *	A	137.88	
NWA 6291	Volcanic	4561.29	0.78	Pb-Pb isochron *	C	137.84	
Angra dos Reis	Volcanic	4557.65	0.13	Px fraction**	D	137.88	
D'Orbigny	Quenched	4564.42	0.12	Px + WR fraction***	D	137.88	
Sahara 99555	Quenched	4564.86	0.38	Pb-Pb isochron *	E	137.88	

* Used when common lead or redistribution of radiogenic Pb after crystallization is a concern.

** Weighted average of $^{207}Pb/^{206}Pb$ ages of acid washed pyroxene fractions, used when only radiogenic Pb is present in the fraction after washing and blank correction.

***Weighted average of $^{207}Pb/^{206}Pb$ ages of acid washed pyroxene and whole rock fractions, used when only radiogenic Pb is present in the fraction after washing and blank correction.

Table 4.4: Pb-Pb ages of angrites, method used for calculation and assumed U isotopic composition. References: A, [13]; B, [15]; C, [56]; D, [11]; E, [10].

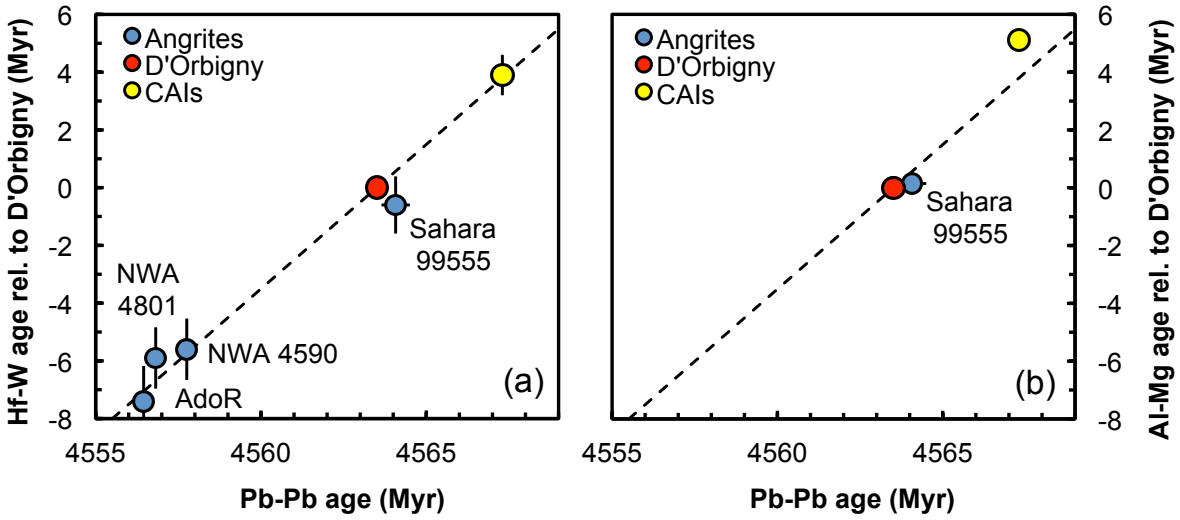

Figure 4.5: Comparison of absolute ages from the uranium-isotope-corrected Pb-Pb system (this work, Table 4.5) with relative ages calculated from the ^{182}Hf-^{182}W system (a), and the ^{26}Al-^{26}Mg system (b). D'Orbigny is used as the anchor between the absolute and relative ages. The ages based on short-lived radionuclides are expressed relative to the age of D'Orbigny. Hf-W and Pb-Pb ages are highly concordant. Al-Mg and Pb-Pb ages are not as concordant, and in particular, there is a discrepancy of $\sim$ 1.2 Myr in the age of CAIs calculated from both systematics. The uranium-isotope-corrected Pb-Pb ages of CAIs are from Allende SJ-101 [14] and three Efremovka CAIs [119]; all of which have the same age and are assumed to be characterized by the initial Solar System $^{26}Al/^{27}Al$ ratio of $(4.96 \pm 0.25) \times 10^{-5}$ [227] and $^{182}Hf/^{180}Hf$ ratio of $(9.72 \pm 0.44) \times 10^{-5}$ [74, 75]. The Al-Mg data for angrites are from [385] and the Hf-W data for angrites are from [242]. Figure modified after [141].

	This work								Previous work								
Sample	$\delta^{238}U$ (‰)[a] blk corr.	±	$^{238}U/^{235}U$[b]	±	Δt (Myr)	±	Corrected ages	±	$\delta^{238}U$[a] (‰)	±	$^{238}U/^{235}U$[b]	±	Δt (Myr)	±	Corrected ages	±	Ref.
NWA 2999																	
NWA 4590	-0.47	0.09	137.772	0.013	-0.17	0.13	4557.76	0.31	-0.47	0.03	137.772	0.004	-0.18	0.04	4557.75	0.28	A
NWA 4801	-0.55	0.06	137.762	0.008	-1.24	0.08	4556.82	0.17	-0.43	0.07	137.778	0.009	-1.07	0.09	4556.99	0.18	A
NWA 6291	-0.40	0.04	137.783	0.005	-0.60	0.06	4560.69	0.78	-0.49	0.04	137.769	0.006	-0.75	0.06	4560.54	0.78	A
NWA 6291 Leach									-0.27	0.05							
NWA 6291 Residue									-0.57	0.11	137.759	0.015	-0.85	0.16	4560.44	0.80	A
Angra dos Reis	-0.51	0.08	137.766	0.011	-1.20	0.12	4556.45	0.18	-0.48	0.14	137.771	0.019	-1.15	0.20	4556.50	0.24	B
AdoR phosphates									-0.22	0.24	137.806	0.033	-0.78	0.35	4556.87	0.37	A
D'Orbigny	-0.32	0.09	137.793	0.012	-0.91	0.13	4563.51	0.18	-0.34	0.07	137.790	0.010	-0.95	0.11	4563.47	0.16	A
D'Orbigny									-0.33	0.07	137.791	0.010	-0.94	0.11	4563.48	0.16	A
D'Orbigny pyroxene									-0.43	0.20							
Sahara 99555	-0.23	0.14	137.805	0.019	-0.79	0.20	4564.07	0.43	-0.38	0.08	137.784	0.011	-1.01	0.12	4563.85	0.40	C

[a] Values renormalized to CRM-112a.

[b] Absolute ratios are calculated using using the 238U/235U ratio of 137.837 for CRM-112a, from Richter et al. (2010).

Table 4.5: Corrected Pb-Pb ages of angrites. References: A, [69]; B, [177]; C, [119].

able ages, at about 4563.80 Myr, while the plutonic angrites have ages ranging from 4556.45 to 4560.89 Myr. These ages indicate that volcanic activity on the angrite parent body started no later than ~ 4 Myr after formation of the SS, and that it lasted for about 8 Myr.

A problem faced by ESS chronology was to reconcile the absolute and relative ages of some of the early-formed SS bodies (such as the angrites). To compare relative ages to absolute ages, a sample must be chosen in order to anchor the relative dating systematics to the absolute one. D'Orbigny, which quenched rapidly and has experienced no disturbances of any of the chronometric systems, has become a favored anchor in ESS chronology. In Fig. (4.5), the uranium-isotope-corrected Pb-Pb ages of angrites (this work) and four CAIs [14, 119], are compared to their relative ages obtained using the ^{182}Hf-^{182}W (Fig. 4.5a) and ^{26}Al-^{26}Mg (Fig. 4.5b) systematics.

As can be seen, after revision of the age of D'Orbigny (from 4564.42 ± 0.12 Myr [11], to 4563.51 ± 0.18 Myr, this work), the Hf-W ages and the Pb-Pb ages of both angrites and CAIs are in excellent agreement with each other. This is not the case, however, when the Al-Mg systematics is compared to the Pb-Pb systematics (Fig. 4.5b), and the age difference between CAIs and D'Orbigny calculated using each chronometric system is still discrepant by ~ 1.2 Myr. This value is smaller than before correction of the Pb-Pb age of D'Orbigny (the offset was then ~ 2.2 Myr), yet, the discrepancy remains. Several hypotheses have been put forward that could explain this disagreement between Al-Mg and Pb-Pb ages, such as (i) the possibility that the ^{26}Al/^{27}Al ratio in the CAI-forming region could have been higher than in other regions of the solar nebula [249], or (ii) the fact that the Pb-Pb and Hf-W systematics on the one hand, and the Al-Mg systematics on the other hand, do not date the same events in the CAI formation history [141].

The current conclusions on the discordant nature of the Al-Mg and Pb-Pb systematics are drawn from a very limited samples set (four CAIs of identical ages and two angrites), and determination of the Al-Mg ages for more angrites could shed some light on which of the two hypothesis outlined above is correct. At present, this issue remains unresolved.

4.3 Origin of U isotope variations in ESS condensates

Looking back at Fig. (4.1) it is clear that the isotopic variations observed in bulk meteorites and discussed in the above sections are small compared to the ones discovered in CAIs. The origin of the isotopic variability in CAIs is, however, highly debated, owing to the possibility that the ^{235}U excesses observed could be due to decay of now extinct ^{247}Cm in the ESS. If confirmed, the existence of this short-lived radionuclide (SLR) in the ESS would have profound implications for models of nucleosynthesis and SS formation. The following section focuses on the origin of the U isotopic variations in CAIs, and their implications.

4.3.1 The nature of the r-process: number and sites

All elements beyond the iron-peak (above $\sim$ 70 atomic mass units) are the products of three main processes of stellar nucleosynthesis: the *s*- (*slow* neutron capture), *r*- (*rapid* neutron capture) and *p*- (*proton*) process [72, 79]. Unlike the *s*- and *p*-processes, which are relatively well understood (neutron capture in AGB-stars for the *s*-process and photodisintegration of seed nuclei in supernovae for the *p*-process) [45, 355], little is known regarding the astrophysical conditions under which *r*-process nuclides are produced [453, 294, 224, 129, 220]. The *r*-process label may comprise some diversity as it was suggested that up to three *r*-processes were responsible for producing light *r*-nuclides (A $\lesssim 135-140$, up to $\sim$ Ba), heavy *r*-nuclides (A $\gtrsim 135-140$) and actinides (U, Th). The rationale for the existence of multiple *r*-processes comes from (i) spectroscopic observations in Low Metallicity Halo Stars (LMHS, *i.e.*, stars with low metal content, which formed early in the history of the Galaxy, before the onset of the *s*-process in AGB stars), and (ii) the relative abundance of short-lived radionuclides in meteorites.

The apparently decoupled behaviors of light *r*-nuclides, heavy *r*-nuclides and actinides (relative to the solar *r*-pattern) in some LMHS points to multiple types and sites of *r*-processes operating early in the history of the Galaxy. For instance, while metal-rich stars

have solar or supersolar Ba/Fe ratios and Sr/Ba ratios clustering around the pure r-process ratio, metal-poor stars have Ba/Fe ratios $\sim 10\times$ lower than solar, and Sr/Ba ratios $10-100\times$ higher than solar. Because metal-poor stars formed early in the Galaxy, before the onset of the s-process, the presence of Sr and Ba in those stars is the results of r-process nucleosynthesis. The difference in the abundances of the r- component of these two elements (Sr: A=88, Z=38; and Ba: A=137, Z=56) in metal-poror stars indicates that the nucleosynthetic production of lighter r-nuclides is favored over heavier r-nuclides in the progenitors of some metal-poor stars, early in the history of the Galaxy ([439] and references therein). The decoupling between r-nuclides of lower and higher atomic masses is readily seen in, for example, the composition of star CS 22892-052 [404, 122]. The existence of an actinide-specific r-process is suggested by the overabundance of Th and U relative to lighter r-nuclides (*e.g.*, Eu) in one LMHS (CS 31082-001, see [92, 203]). The age of CS 31082-001 as inferred from its U/Th ratio is consistent with formation early in the history of the Galaxy (14.0 ± 2.4 Gyr, [203, 450]; and 15.5 ± 3.2 Gyr, [382]). On the other hand, the age of this star as inferred from its Th/Eu ratio is negative [203, 382, 450], (*e.g.*, -5.1 ± 9.3 Gyr, equivalent to saying that this star *will form* in 5.1 Gyr), which means that CS 31082-001 must have formed with a Th/Eu ratio that was higher than that relevant to the Solar System, a feature that requires an actinide specific r- process. A hint that an incomplete r-process existed early in the Galaxy was even found in star HD 122563 in the form of a gradual decrease in the abundance pattern of r-nuclides as a function of atomic number, from Sr to Yb [405, 458, 403, 212].

The second line of evidence pointing to a multiplicity of r-processes comes from the relative abundance of short-lived radionuclides (SLR) in meteorites. In particular, the abundance of ^{182}Hf ($t_{1/2} = 8.90$ Myr) in the ESS is too high relative to that of another short-lived r-nuclide, ^{129}I ($t_{1/2} = 15.7$ Myr). This led Wasserburg et al. (1996) [453] to propose that different r-processes were responsible for the light r-nuclides ($A \lesssim 140$) and the heavy r-nuclides ($A \gtrsim 140$), respectively. The existence of an actinide-specific site was also hypothesized based on the low meteoritic abundance of ^{244}Pu ($t_{1/2} = 79.3$ Myr) compared to ^{182}Hf [129].

The fact that there is a general broad agreement between the number of different r-processes inferred from elemental abundances in LMHS and from SLR abundances in meteorites does not necessarily mean that the processes at play in the early Galaxy are relevant to long-term galactic chemical evolution (GCE). In fact, the variability of r-patterns observed in LMHS might only be the expression of exotic processes occurring early in the history of the Galaxy, when low metallicity conditions prevailed. The steady-state r-process of the Galaxy is therefore better explored by focusing on the meteoritic evidence.

As pointed out above, three r-processes have been suggested based on SLR abundances in meteorites. The suggestion of an actinide-specific site [129] is, however, not necessarily warranted because ^{244}Pu has a long half-life and its stellar yield is uncertain [312], which makes it poorly sensitive to the history of nucleosynthesis prior to SS formation and whether or not multiple r-process sites contributed to the synthesis of this nuclide. In contrast, Curium-247, which decays into ^{235}U, has a much shorter half-life ($t_{1/2}$ = 15.6 Myr) and would be very well suited to address this question, provided its abundance in the ESS can be accurately and precisely determined.

4.3.2 The elusive ^{247}Cm

By definition, an extinct radionuclide is a nuclide that was alive when the SS formed, but has, by now, completely decayed. Today, 4.5 billion years after SS formation, the only way to prove that something was "alive" in the ESS and "died", is to find the "dead body". In this regard, the isotope cosmochemist is like a detective investigating a cosmic crime scene, in search of extinct radionuclides. The end product of live ^{247}Cm decay (*i.e.*, the "dead body" in the detective analogy) is ^{235}U (see Fig. 1.7). A very minor alternative decay path exists, in which neutron-induced fission of ^{247}Cm results in possibly isotopically anomalous or excess fission Xe, noted Xe$_{fiss}$. This is, however, of little help in searching for ^{247}Cm, as the composition of this Xe$_{fiss}$ is unknown and cannot be predicted by systematic considerations [77]. Given that the n-induced fission of ^{235}U has a ^{136}Xe$_{fiss}$ yield of $\sim$ 6 %, a third

indicator of live ^{247}Cm would be the excess fissiogenic Xe due to curium decay into "excess" ^{235}U. This last option is also of little use, since the ESS abundance of ^{247}Cm expected from GCE models is low [312] and the excess $^{136}Xe_{fiss}$ will be essentially unresolvable in ESS materials [77]. The only way to chase the now extinct ^{247}Cm is therefore to search for ^{235}U excesses in ESS materials.

Unlike ^{247}Cm itself, the search for ^{247}Cm is rather long-lived. Since Blake and Schramm [46] first discussed the potential of ^{247}Cm as a short-lived chronometer in 1973, the question of whether or not live ^{247}Cm was present in the ESS has remained unanswered. Early studies, "yoyo-ed" between finding ^{235}U excesses of a few percent (in Allende inclusions, [427]), and up to 200 % (in meteorite leaches, [26]), and finding no detectable excess, within $\pm$ 4 ‰, in any type of samples (bulk meteorites, acid leaches, coarse- and fine-grained CAIs from Allende, phosphates from meteorites with abundant ^{244}Pu decay products, [100, 101, 102, 103]). By the mid 1980s, it appeared that the early excesses were non-reproducible and that no U isotope variations outside of uncertainties were resolvable in any ESS material, leading G. J. Wasserburg to summarize the situation by the famous saying: "^{247}*Cm occurred abundantly in a journal called Nature, but did not occur in nature*" [452]. An upper limit for $(^{247}\mathrm{Cm}/^{235}\mathrm{U})_{\mathrm{ESS}}$ was estimated to be $< 4 \times 10^{-3}$ [103].

Having reached the limits of modern instrumentation, researchers had to stop and wait for the mass spectrometry to catch up with the level of precision needed to detect smaller isotopic variations. The appearance of the MC-ICPMS at the turn of the century led to a renewed interest in the hunt for ^{247}Cm. Again, no resolvable excesses where found in bulk meteorites or meteorite leaches, even at the sub-permil level [414, 415], and a new lower limit was derived, as $(^{247}\mathrm{Cm}/^{235}\mathrm{U})_{\mathrm{ESS}} < 7.7 \times 10^{-5}$. In 2010, however, Brennecka et al. [71] found ^{235}U excesses of up to 3.5 ‰ in four fine-grained CAIs. Those excesses correlate with Nd/U ratios (Nd is taken as a proxy for Cm because Cm has no long-lived isotope [64]), so the authors interpreted these results as evidence of live ^{247}Cm in the ESS at a level of $(^{247}\mathrm{Cm}/^{235}\mathrm{U})_{\mathrm{ESS}} \sim (1.1 - 2.4) \times 10^{-4}$.

Far from bringing the search for ^{247}Cm to an end, these findings were soon challenged by others workers [14, 119] who pointed out that such ^{235}U enrichments could also reflect mass-dependent fractionation during evaporation/condensation of solid CAIs from nebular gas. As explained in Section 1.2.3, the kinetic theory of gases predicts that the lighter isotope (^{235}U) should condense faster than the heavier isotope (^{238}U), resulting in fractionations that scale as the square-root of the masses of the condensing isotopes and can reach $\sqrt{238/235} = 1.0063$‰ (see Fig. 1.6 and Section 1.2.3). If only a fraction of the U initially present in the gas condensed, as inferred for fine-grained CAIs that are depleted in U, then kinetic isotopic fractionation could be expressed. In both cases (^{247}Cm-decay and fractionation during evaporation/condensation), U isotopic variations are expected to correlate with the degree of U depletion. The question at the heart of the hunt for ^{247}Cm therefore changed from "*Are there any ^{235}U excesses in ESS materials?*" to "*Which is responsible for the observed excesses: ^{247}Cm decay or isotopic fractionation during evaporation/condensation?*"

The answer to this question awaits the discovery of a meteoritic material that is highly depleted in uranium and displays a ^{235}U excess outside of the ± 6 ‰ window allowed by fractionation during evaporation/condensation. Because the abundance of ^{247}Cm in the ESS is expected to be low [312], such large excesses of ^{235}U from ^{247}Cm decay will only be resolvable in ESS phases with ^{144}Nd/^{238}U ratios exceeding $\sim$ 1300.

4.3.3 Samples and methods

4.3.3.1 Sample selection

The oldest phases known in the SS are the CAIs whose Pb-Pb ages in fact define the cosmochemical time zero of the SS (4.567 Gyr ago, [59, 14]). Among the CAIs, fine-grained CAIs tend to (i) be depleted in U relative to coarse-grained CAIs ($\sim$ 20 ppb *vs.* $\sim$ 100 ppb), and (ii) display large Nd/U ratios [274]. The challenge is therefore to find a fine-grained CAI with a ^{144}Nd/^{238}U ratio $\gtrsim$ 1300, yet massive enough for its U isotopic composition to

be properly measured.

After visual inspection of numerous (> 200) slabs of Allende, the largest fine-grained CAIs (12 in total) were selected for this study along with three coarse-grained CAIs. Fine-grained CAIs are readily identifiable from their texture (μm-sized grains), color (from white/grey to purple, with most being pink due to FeO in spinel) and irregular shapes. By comparison, coarse-grained CAIs are mostly white, with much coarser crystals (mm-sized) than fine-grained CAIs (Fig. 4.6). Coarse-grained CAIs are thought to have originated as molten droplets, while the chemical compositions of fine-grained CAIs are those expected from partial condensation of refractory elements from solar composition gas [185, 268]. Since group II REE patterns [424, 274] and significant U depletions are characteristic of fine-grained CAIs, the hope was that among the 12 fine-grained CAIs selected, ^{235}U excesses from ^{247}Cm decay would be detectable in some of them.

The coarse-grained CAIs were taken to serve as reference samples because the effect of ^{247}Cm decay in coarse-grained CAIs is expected to be much smaller than in fine-grained CAIs. Indeed, the Nd/U ratios (a proxy for the Cm/U ratio) in fine-grained and coarse-grained CAIs are typically around 752 and 97, respectively (average values from [186, 187, 188, 274, 71]), which is equivalent to ^{144}Nd/^{238}U ratios of 180 and 23, respectively (when normalized to CI chondrites the ratios are 12.4 and 1.6, respectively). This one order of magnitude difference in the Cm/U ratio of coarse- and fine-grained CAIs translates directly into a one order of magnitude difference in the size of the expected isotopic anomalies in these objects. In a δ^{235}U *vs.* Cm/U plot (isochron plot), fine-grained CAIs will define the slope of the isochron and coarse-grained CAIs, the intercept at the origin.

4.3.3.2 Sample characterization

A small chip of each CAI was extracted using cleaned stainless steel dental tools (Hu-Friedy), under a stereoscopic zoom microscope, and mounted in epoxy for characterization. All samples were mapped using a JEOL JSM-5800LV SEM, and the major elemental compo-

sition of the CAIs are shown as oxide weight percents in Table 4.6. For each CAI, Secondary Electron (SE), Backscattered Electron (BSE) images, and false color RGB (Mg/Ca/Al) maps of a selected field of view are also shown in Fig. (4.7) to (4.20) (note the changes of scale on the various images). The red numbered circles show the location of Laser Ablation spots, while the yellow areas show zones mapped at higher magnification. Each yellow area is composed of 1 to 4 subzones, labeled by a letter (a to d) starting on the top left corner and moving clockwise. Typical grain size was about 10 μm for the fine-grained CAIs, which were mostly composed of spinel, pyroxene, sodalite and nepheline, with small and varying amounts of grossular and melilite, and some rare olivine, in good agreement with [187]. The coarse-grained CAIs were mostly made of melilite, pyroxene, anorthite, and spinel, with a small amount of grossular and perovskite, in agreement with [188].

Following SEM characterization, all samples were then analyzed by LA-ICPMS using a Varian quadrupole ICP-MS connected to a New Wave UP213 laser ablation system at the Field Museum (Chicago). All twelve fine-grained CAIs were found to have a group II REE pattern (Fig. 4.21), while coarse-grained CAI AL8S8 showed an essentially flat pattern at about 18× CI (group V REE pattern), and coarse-grained CAI ME-3364-4.2 showed a flat pattern for the light REEs (9× CI) with a positive anomaly in Eu (15× CI) (group I REE pattern, [274]).

In addition to providing REE patterns, the LA-ICPMS study also indicated that many of the CAIs surveyed were depleted in uranium relative to light REEs (LREEs) and Th (Fig. 4.21). Based on their near-identical valence state, ionic radii and volatilities, the LREEs are believed to be good proxies for some of the actinides during nebular processes ([262, 64, 229] and references therein). For instance, the expected coherency of Pu and Nd [64] has been confirmed in both partitioning experiments [230] and in analyses of differentiated meteorites [262, 229], which provides evidence that Pu and all of the LREEs are likely good proxies for Cm during nebular processes. Though Th has sometimes been used as a proxy for Cm [427, 71] no coherent behavior is expected for the Th-Cm and Th-Pu pairs based on the ionic

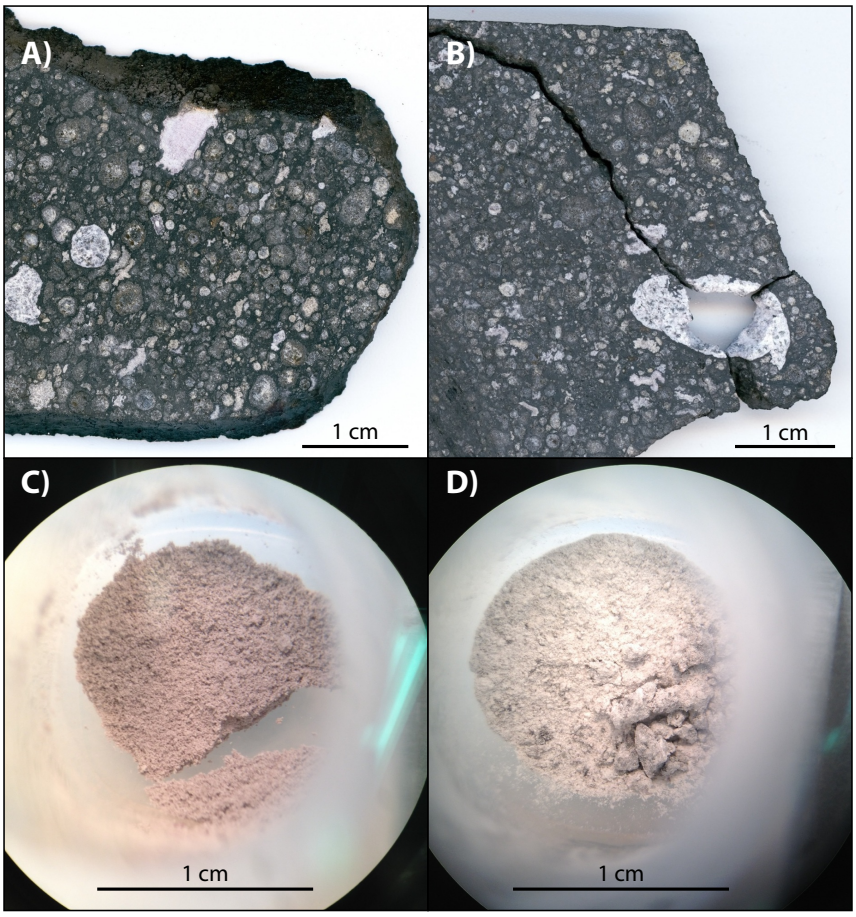

Figure 4.6: Pictures of typical fine-grained (left) and coarse-grained (right) CAIs. The top panels (a and b) show the CAIs still within the meteorite (Allende), and the bottom panels (c and d) show the powders in Teflon beakers after extraction (using cleaned stainless steel dental tools). See text for details about the texture and mineralogy of fine- and coarse-grained CAIs. Figure submitted in [432].

Results of SEM analysis on small chips of CAIs mounted in epoxy (in wt %, normalized to 100 %).

	Na2O	MgO	Al2O3	SiO2	CaO	TiO2	Fe2O3
ME-3364-2.2	0.5 ± 0.7	2.9 ± 0.4	25.1 ± 3.1	34.6 ± 5.1	35.1 ± 2.7	0.4 ± 0.8	1.4 ± 1.1
ME-3364-3.2	14.8 ± 2.4	0.7 ± 0.2	44.0 ± 3.0	32.1 ± 1.6	3.4 ± 1.0	0.7 ± 0.3	4.2 ± 1.6
ME-3364-4.2	0.6 ± 0.5	2.5 ± 2.8	34.8 ± 6.7	25.6 ± 5.4	34.9 ± 6.8	1.2 ± 2.2	0.4 ± 0.4
ME-3364-22.2	3.5 ± 1.0	11.8 ± 3.8	19.8 ± 9.5	42.6 ± 8.0	17.5 ± 4.2	0.5 ± 0.8	4.3 ± 0.5
ME-3364-25.2	4.0 ± 1.2	5.8 ± 3.0	26.7 ± 3.3	34.8 ± 1.6	21.4 ± 1.3	0.7 ± 0.2	6.6 ± 4.1
ME-2639-16.2	5.2 ± 3.7	13.2 ± 2.4	37.6 ± 1.4	29.1 ± 1.6	8.6 ± 3.2	1.5 ± 0.4	4.9 ± 2.0
ME-2639-33.9	3.2 ± 0.9	11.6 ± 1.4	34.1 ± 1.2	29.9 ± 0.7	13.7 ± 1.9	1.3 ± 0.3	6.1 ± 0.6
ME-2639-49.7	4.0 ± 0.3	11.5 ± 0.6	26.7 ± 1.2	34.8 ± 0.7	15.1 ± 1.1	0.7 ± 0.4	7.1 ± 1.9
ME-2639-51.1	4.5 ± 2.3	5.6 ± 2.1	30.9 ± 2.2	34.8 ± 1.5	19.6 ± 3.5	0.6 ± 0.4	3.9 ± 1.8
AL3S5	3.4 ± 0.4	12.9 ± 0.5	37.9 ± 0.7	27.5 ± 1.2	14.2 ± 0.9	0.5 ± 0.3	3.6 ± 0.5
AL4S6	4.7 ± 0.3	9.1 ± 2.1	24.8 ± 3.5	37.8 ± 2.4	15.1 ± 0.7	1.1 ± 0.4	7.6 ± 0.3
AL8S2	3.5 ± 1.2	6.9 ± 1.9	22.8 ± 3.0	39.9 ± 1.2	19.6 ± 2.3	0.5 ± 0.2	6.9 ± 2.3
AL8S8	0.2 ± 0.3	7.1 ± 1.5	26.4 ± 5.1	30.6 ± 3.6	34.2 ± 2.5	1.1 ± 1.5	0.3 ± 0.4
AL10S1	6.7 ± 1.8	14.4 ± 2.0	44.1 ± 1.8	22.3 ± 2.3	4.7 ± 0.9	0.4 ± 0.2	7.5 ± 1.4

Table 4.6: Results of major elemental composition analysis of the CAIs studied in this work, obtained by energy-dispersive x-ray microanalysis done with a scanning electron microscope (SEM-EDX). Table submitted in [432].

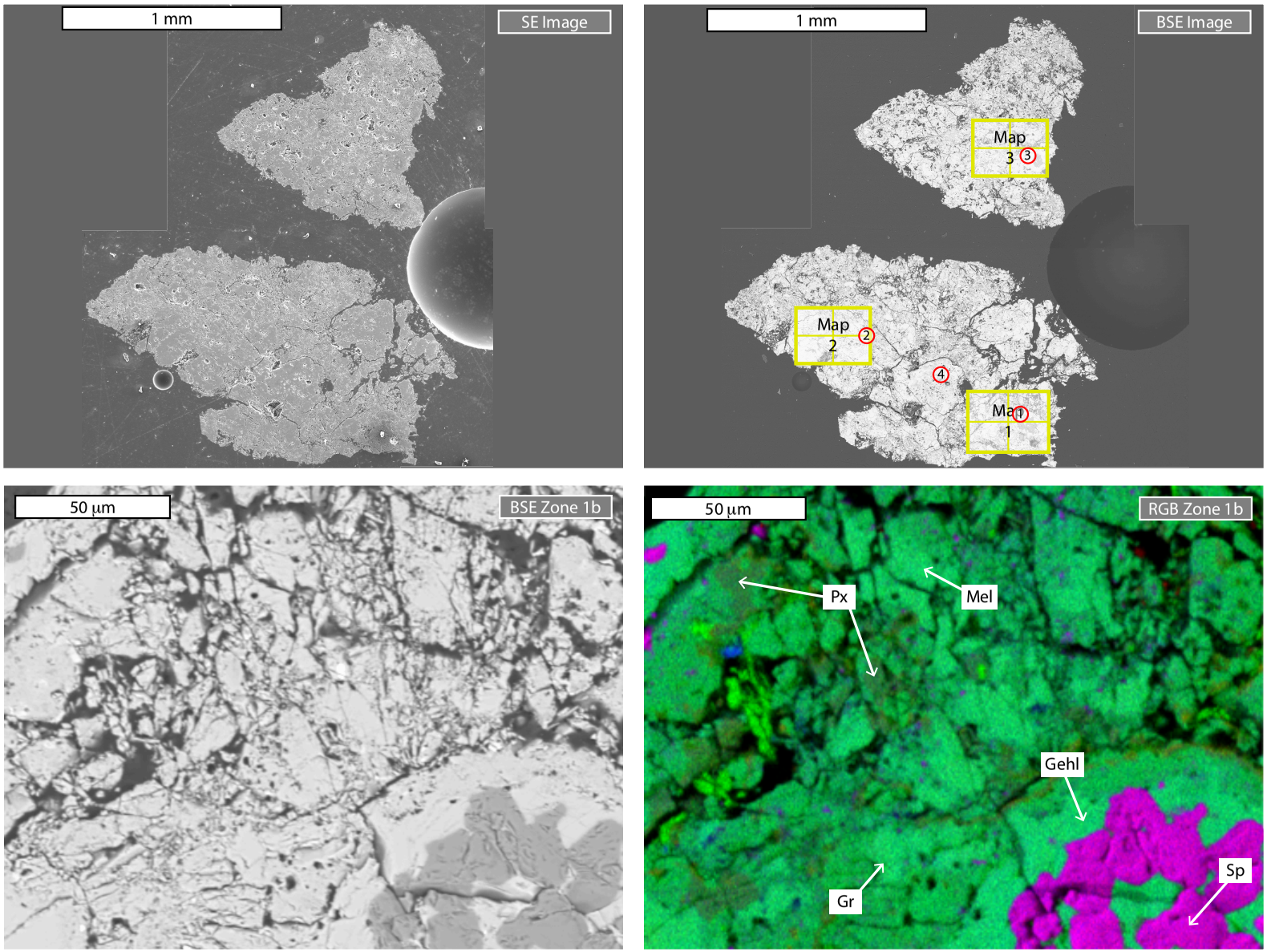

Figure 4.7: SE, BSE and RGB (Mg/Ca/Al) images of fine-grained CAI ME-3364-2.2. See text for details.

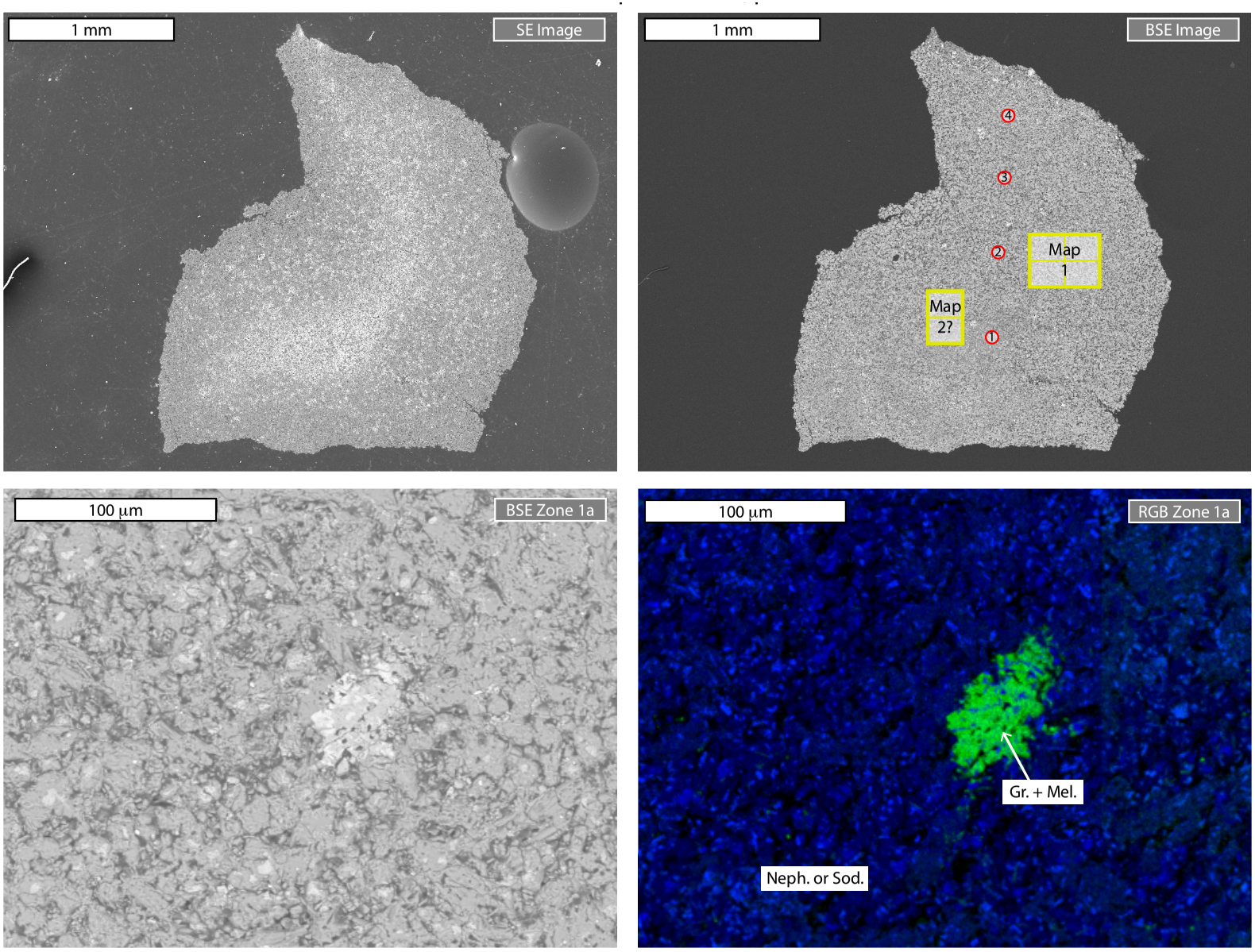

Figure 4.8: SE, BSE and RGB (Mg/Ca/Al) images of fine-grained CAI ME-3364-3.2. See text for details.

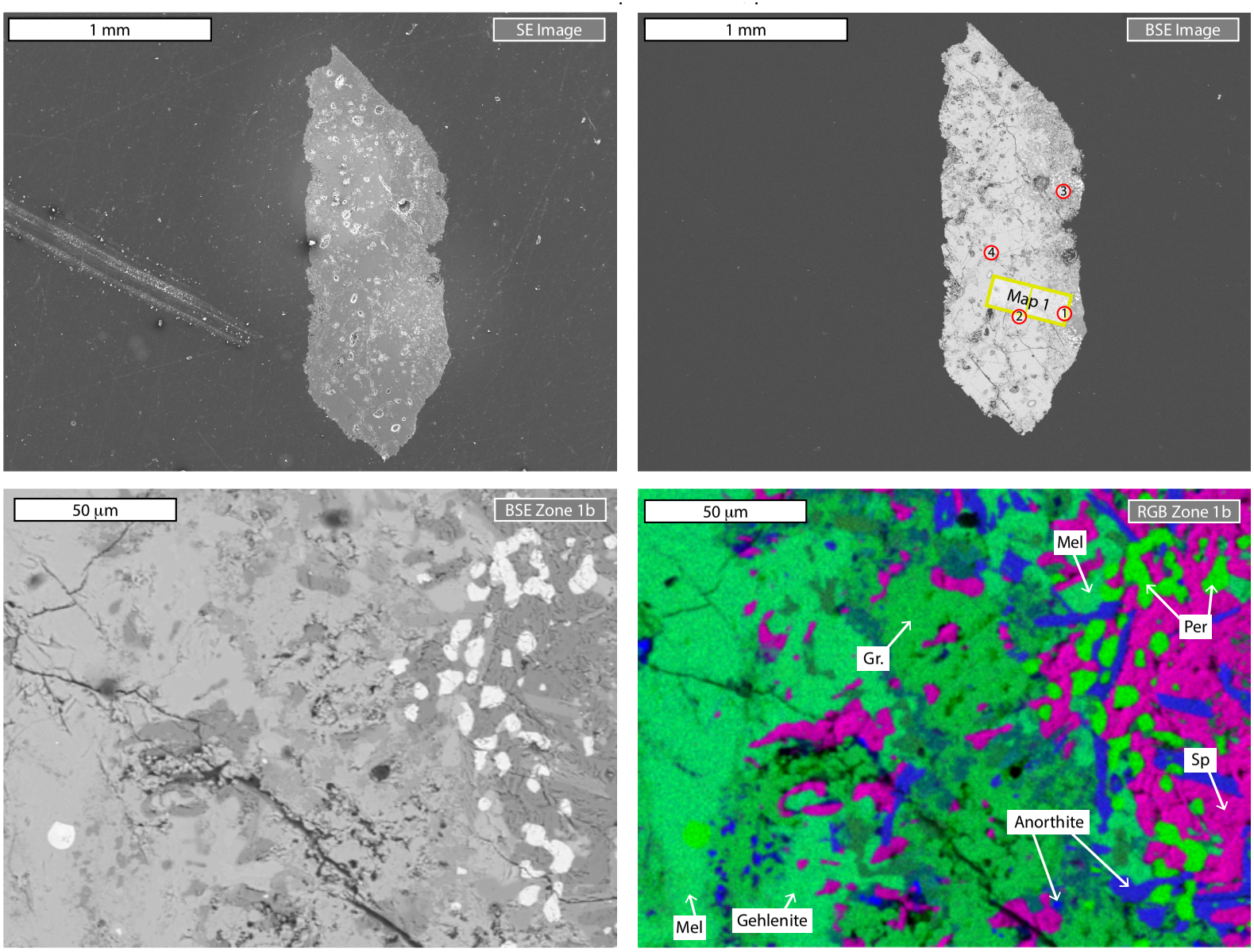

Figure 4.9: SE, BSE and RGB (Mg/Ca/Al) images of coarse-grained CAI ME-3364-4.2. See text for details.

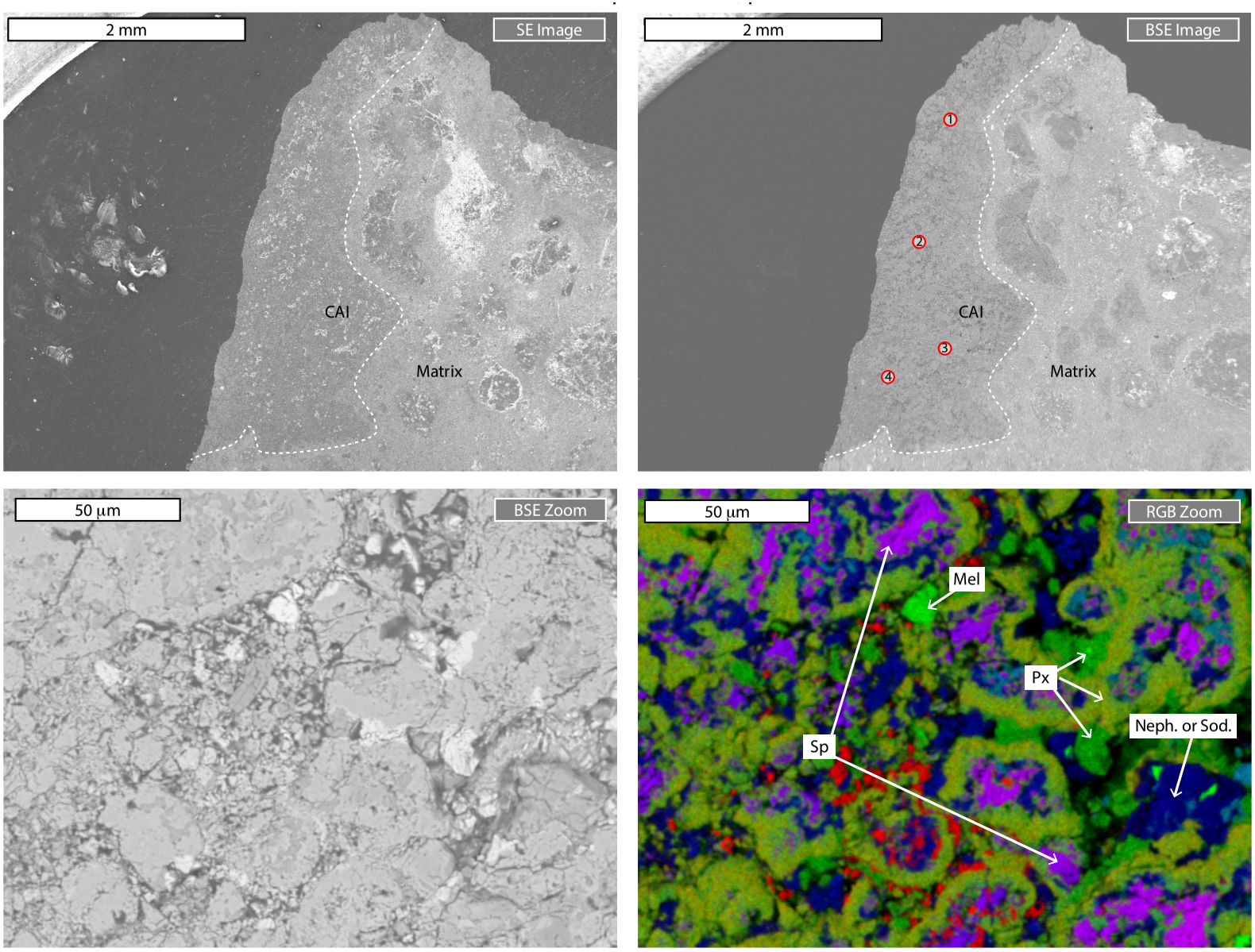

Figure 4.10: SE, BSE and RGB (Mg/Ca/Al) images of fine-grained CAI ME-3364-22.2. See text for details.

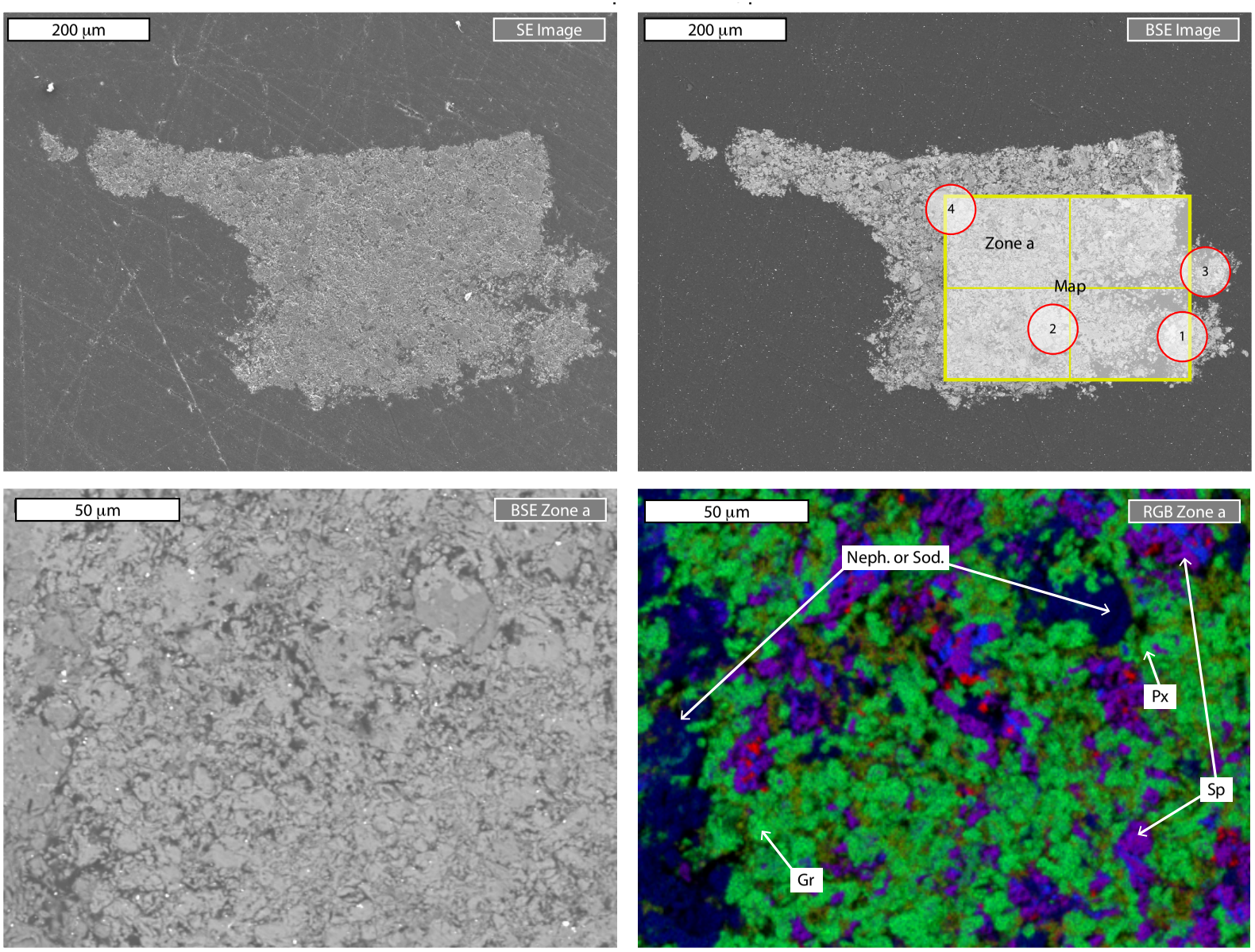

Figure 4.11: SE, BSE and RGB (Mg/Ca/Al) images of fine-grained CAI ME-3364-25.2. See text for details.

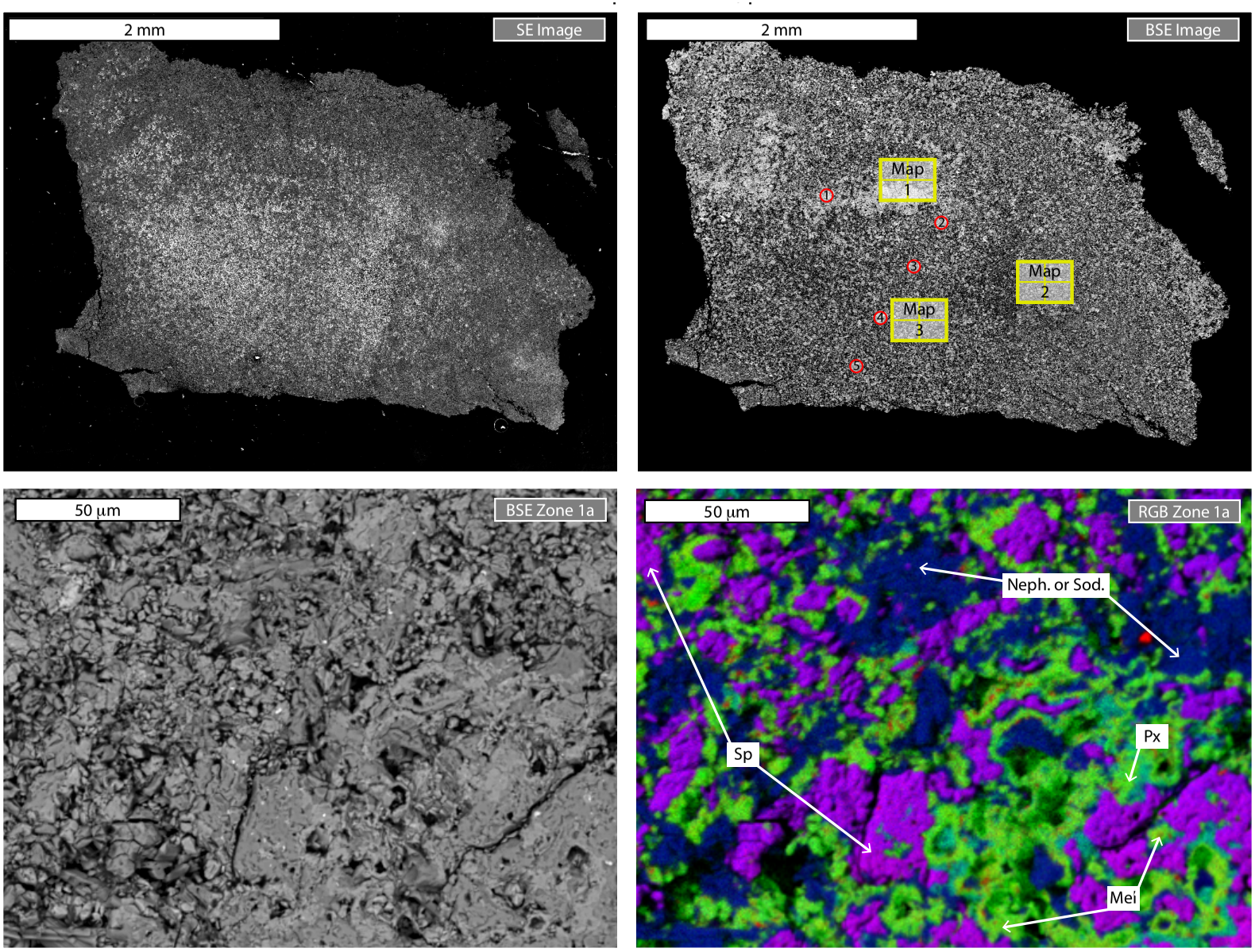

Figure 4.12: SE, BSE and RGB (Mg/Ca/Al) images of fine-grained CAI ME-2639-16.2. See text for details.

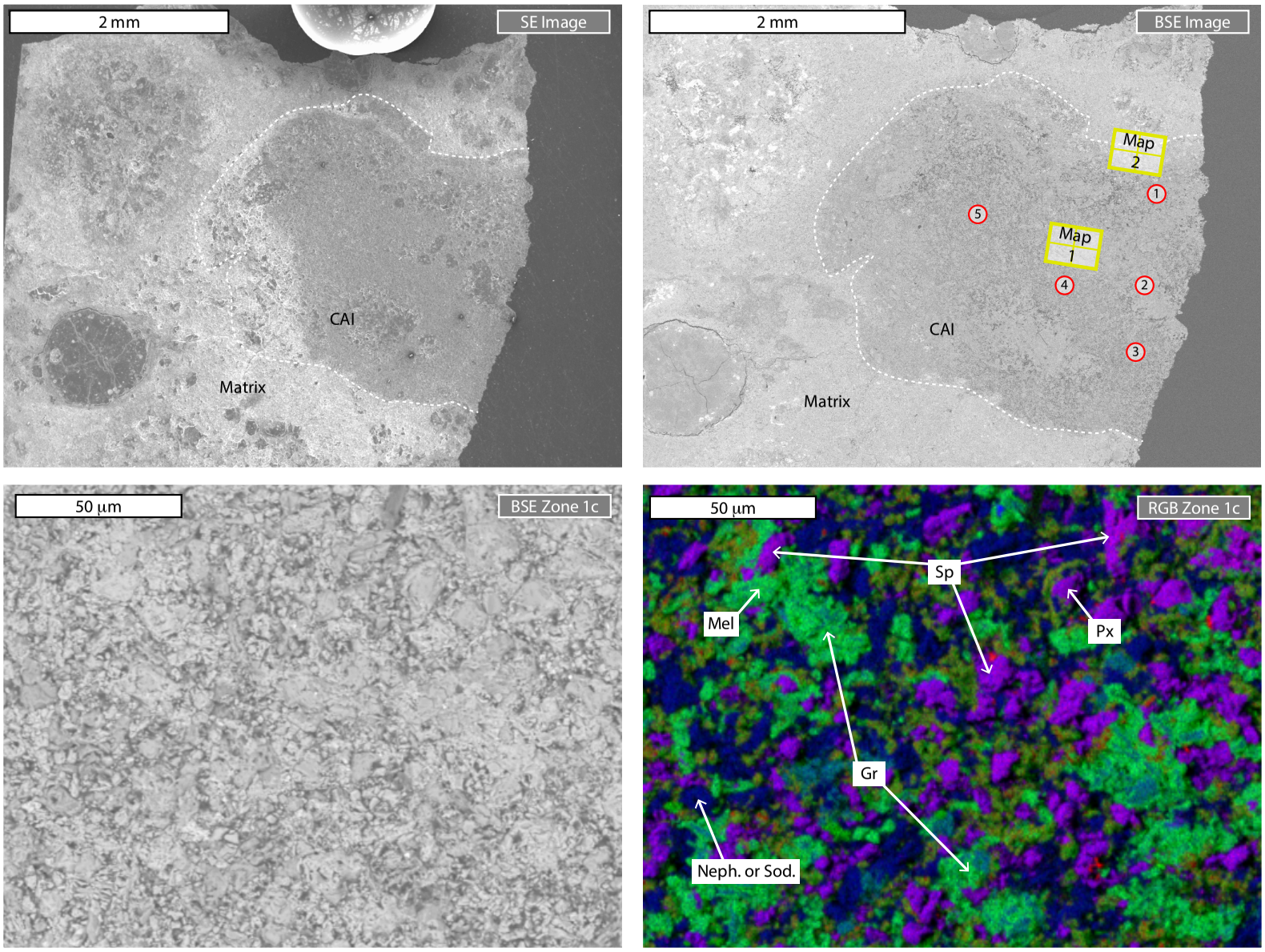

Figure 4.13: SE, BSE and RGB (Mg/Ca/Al) images of fine-grained CAI ME-2639-33.9. See text for details.

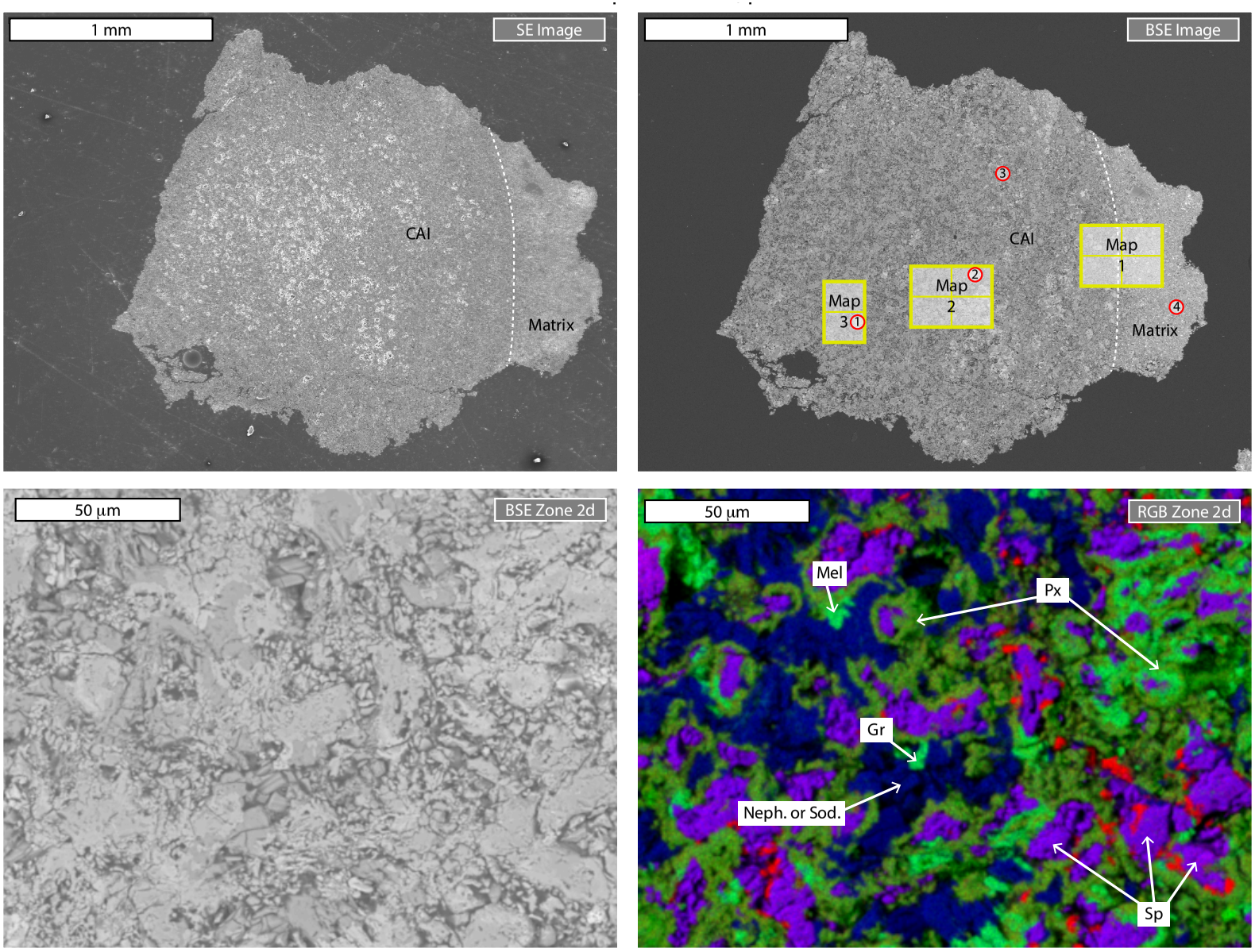

Figure 4.14: SE, BSE and RGB (Mg/Ca/Al) images of fine-grained CAI ME-2639-49.7. See text for details.

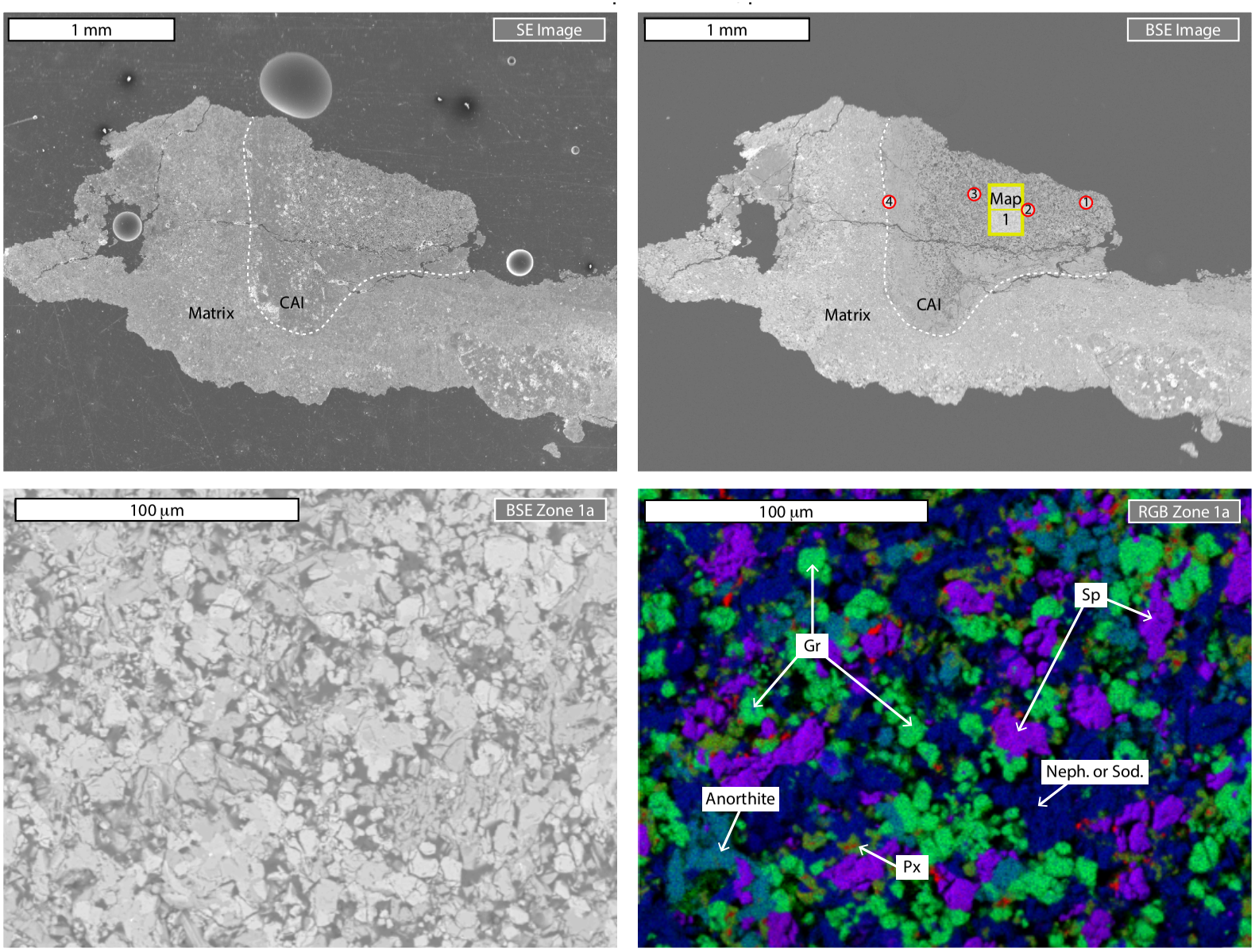

Figure 4.15: SE, BSE and RGB (Mg/Ca/Al) images of fine-grained CAI ME-2639-51.1. See text for details.

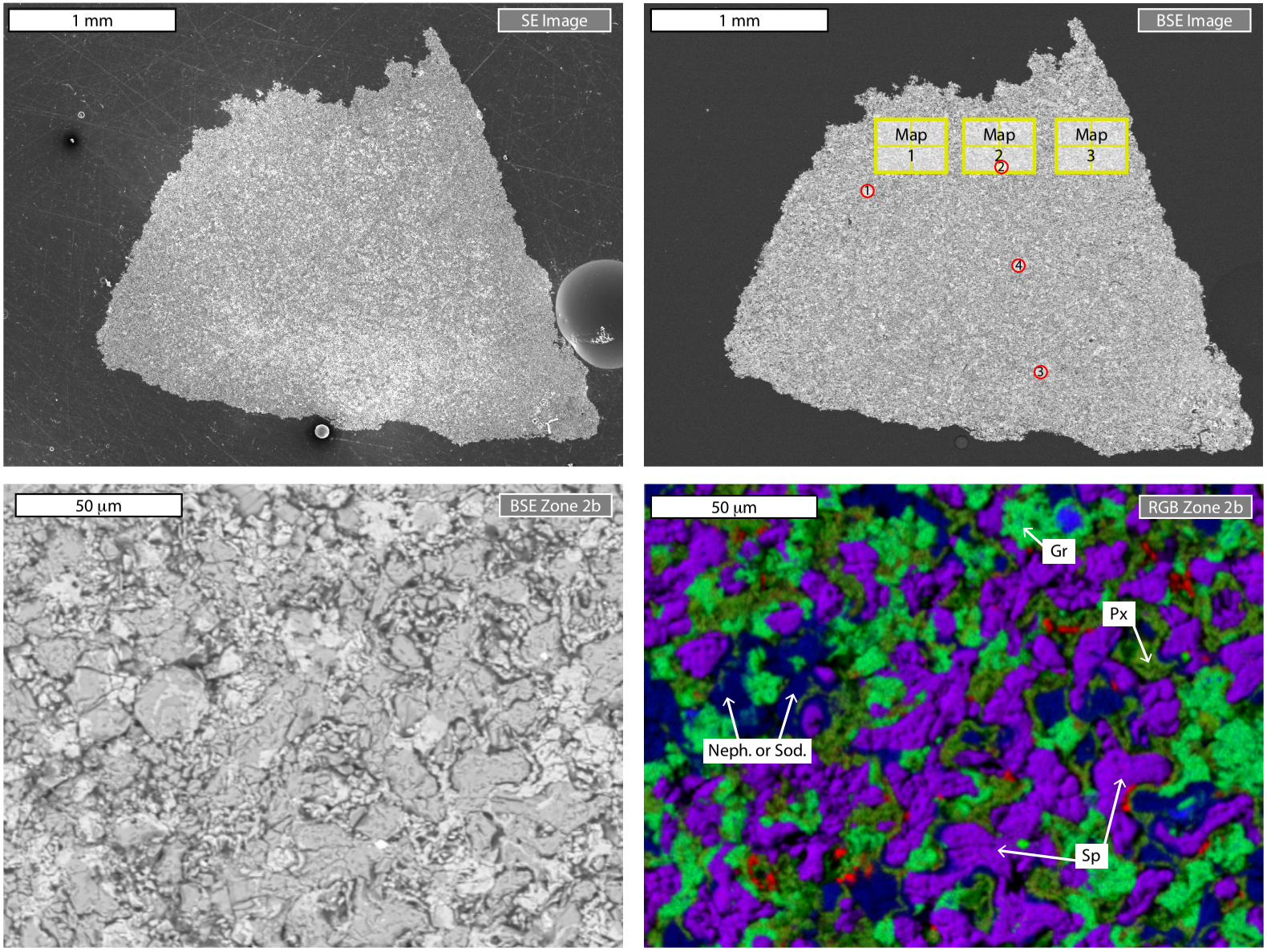

Figure 4.16: SE, BSE and RGB (Mg/Ca/Al) images of fine-grained CAI AL3S5. See text for details.

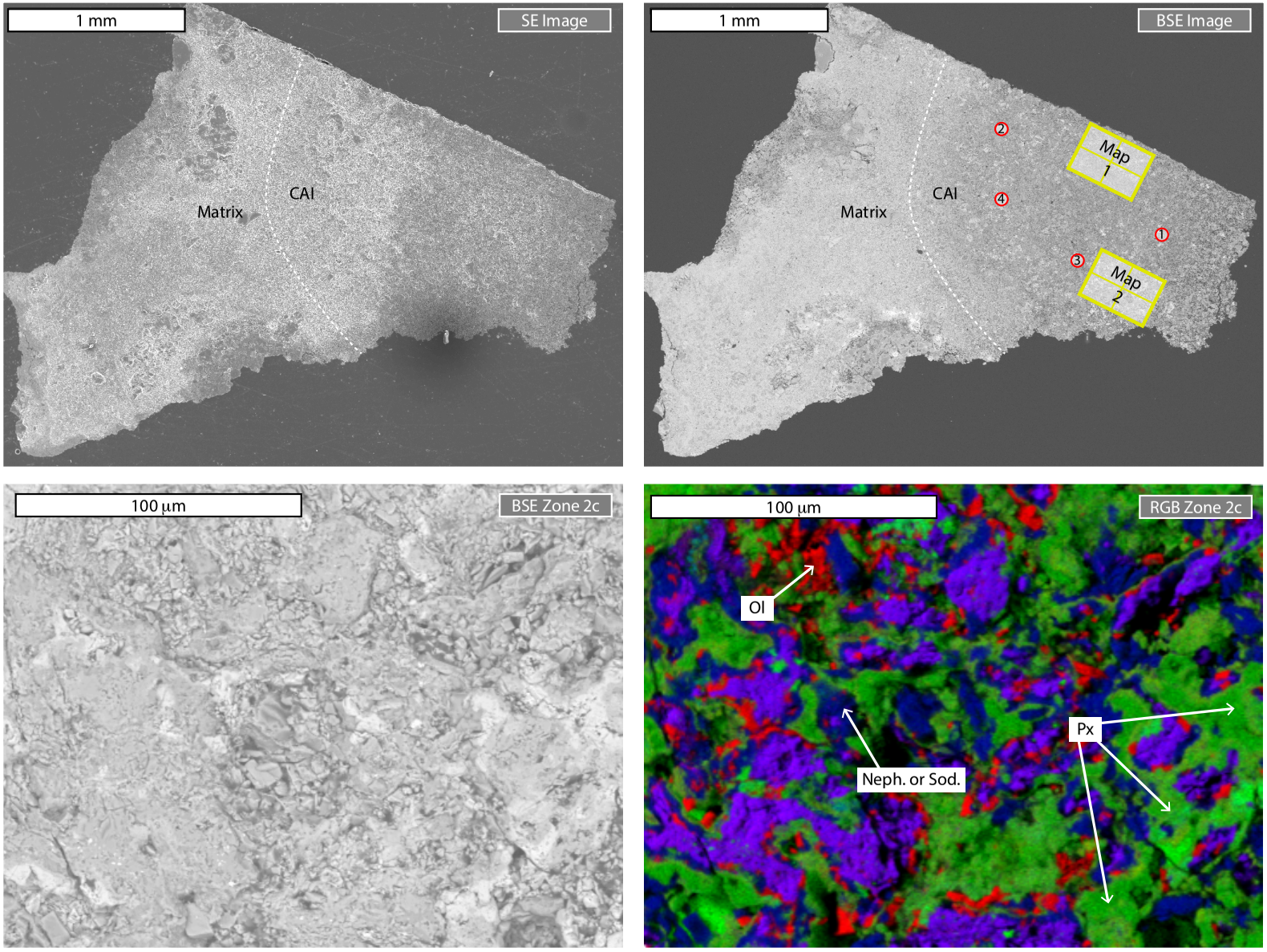

Figure 4.17: SE, BSE and RGB (Mg/Ca/Al) images of fine-grained CAI AL4S6. See text for details.

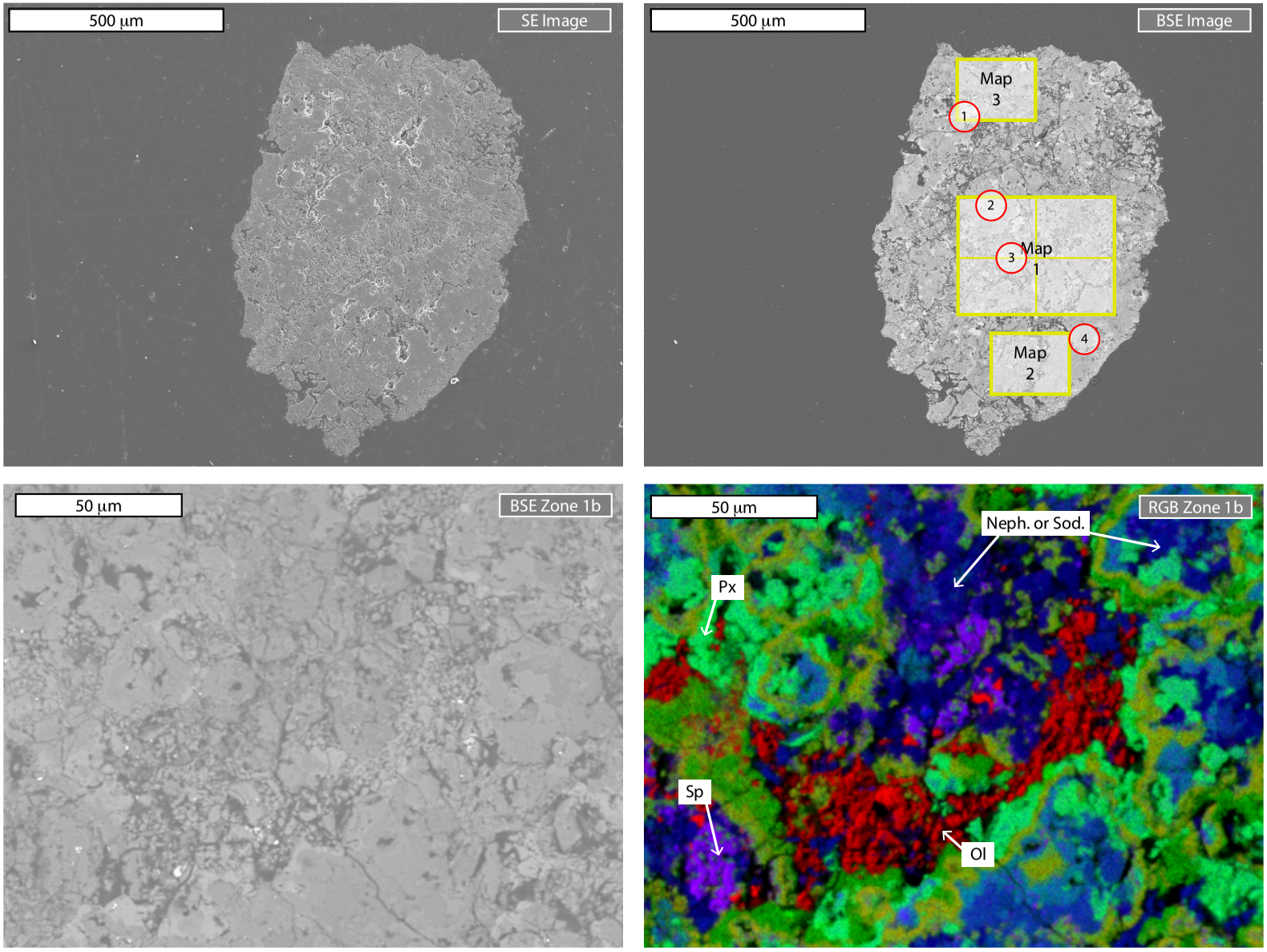

Figure 4.18: SE, BSE and RGB (Mg/Ca/Al) images of fine-grained CAI AL8S2. See text for details.

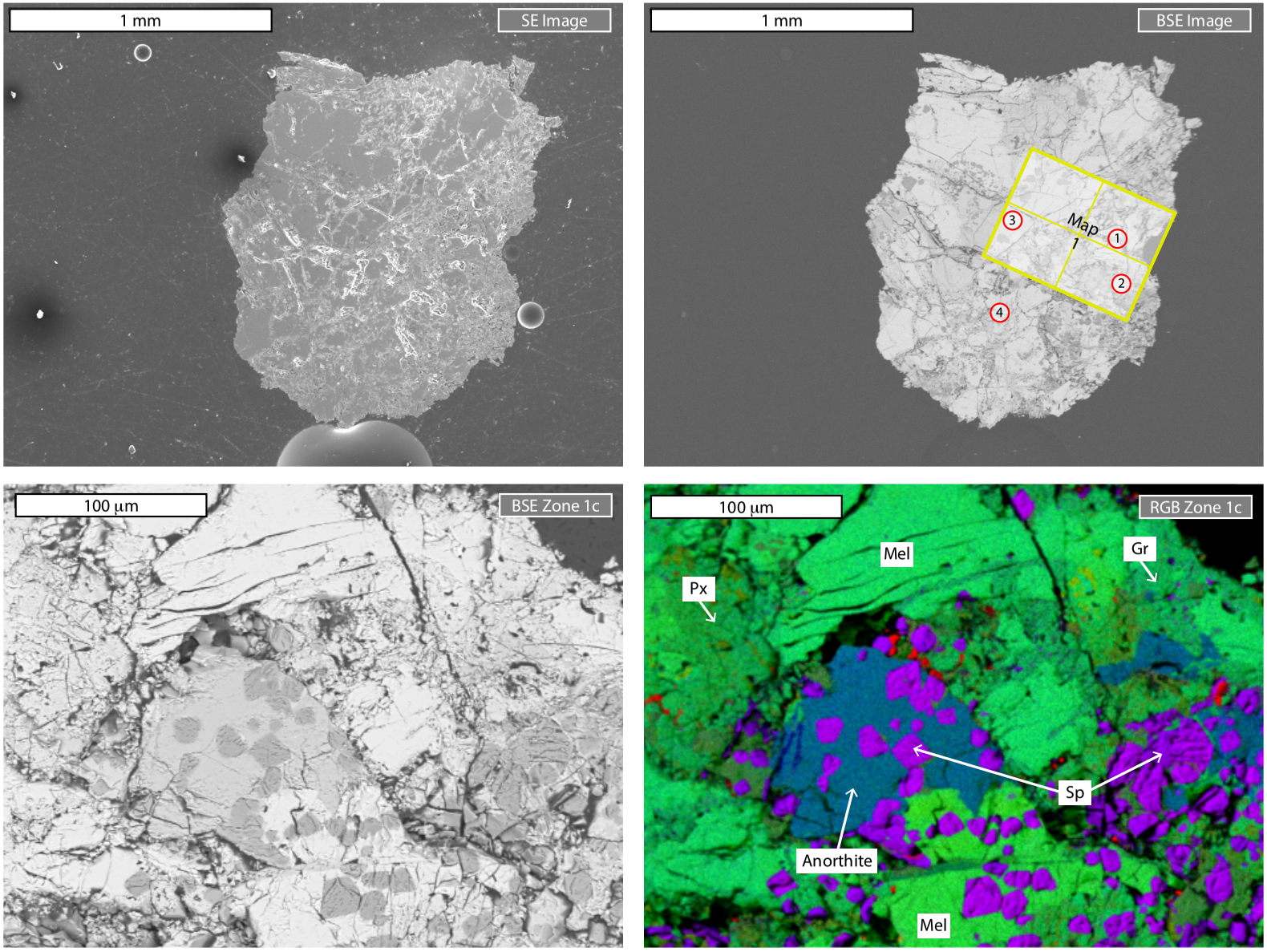

Figure 4.19: SE, BSE and RGB (Mg/Ca/Al) images of coarse-grained CAI AL8S8. See text for details.

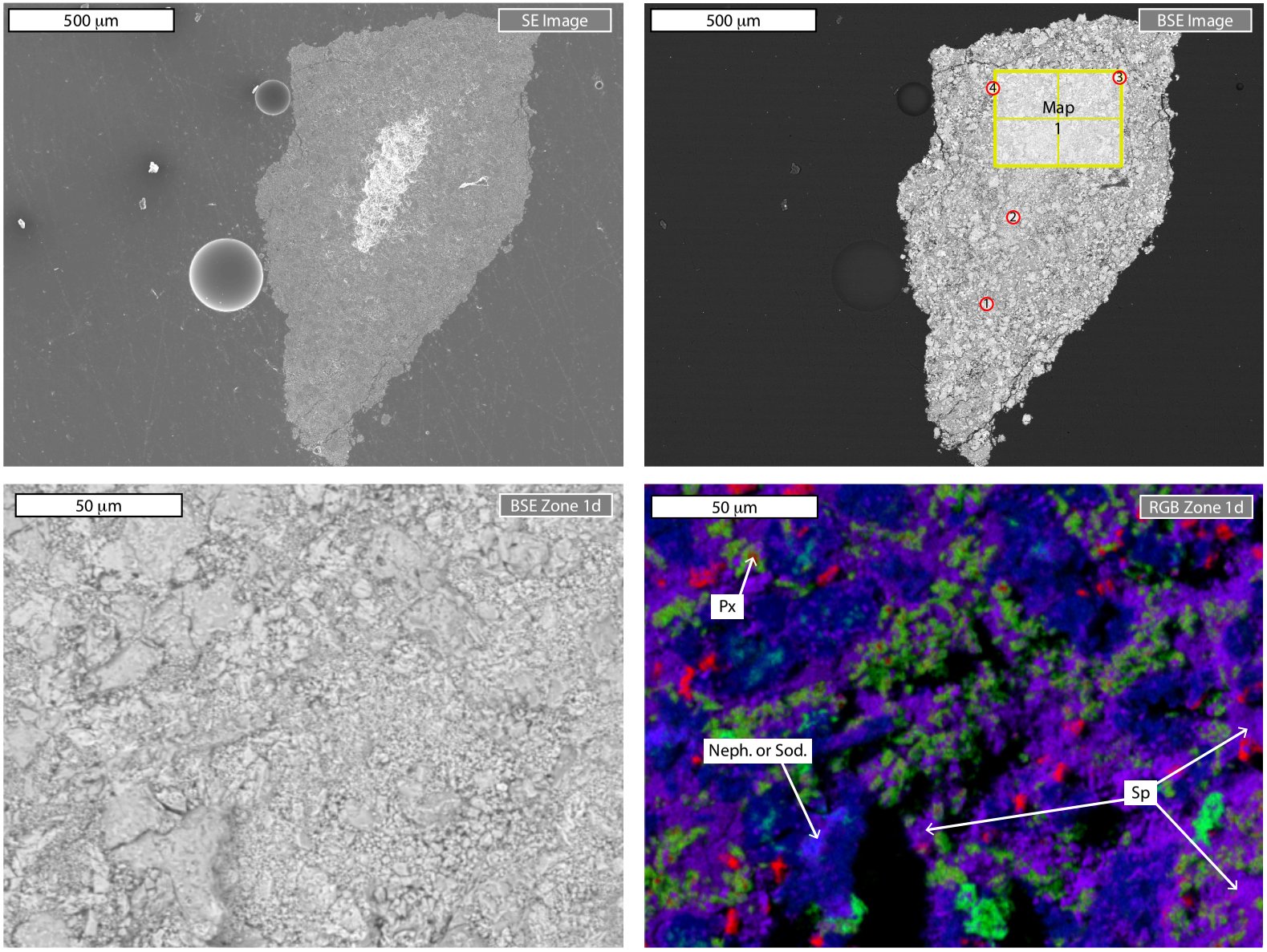

Figure 4.20: SE, BSE and RGB (Mg/Ca/Al) images of fine-grained CAI AL10S1. See text for details.

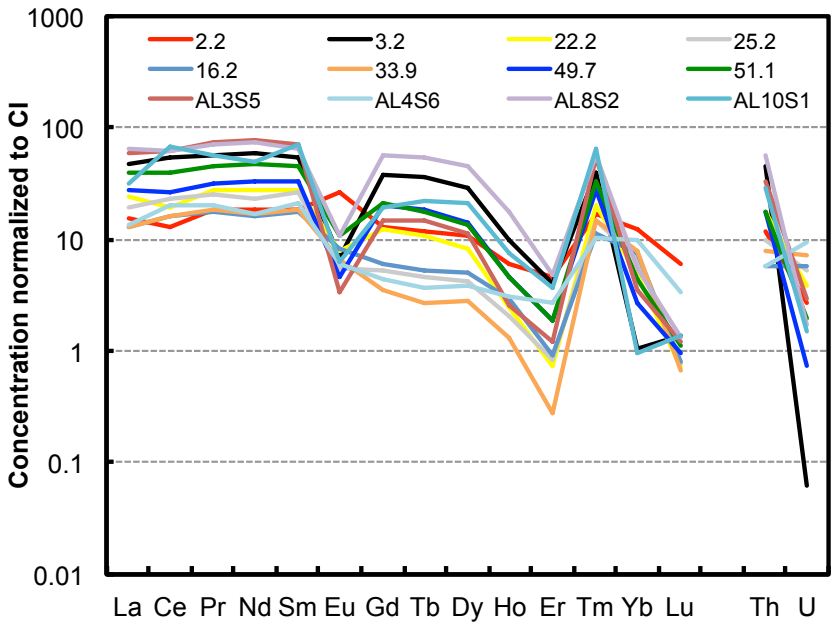

Figure 4.21: REE, Th and U abundance patterns of all twelve fine-grained CAIs analyzed in this study. All CAIs show a group II pattern, in which the most refractory (heavy REEs except Tm and Yb) and most volatile elements (Eu and Yb) are depleted relative to the moderately refractory light REEs. This pattern is thought to represent a snapshot in the condensation sequence as it corresponds to the composition of nebular dust condensates after depletion of the gas in ultra-refractory elements that condensed in hibonite [267] or perovskite [140], and before condensation of the more volatile ones that stayed behind in the gas [63, 140]. These samples are particularly well suited to search for ^{235}U excesses resulting from ^{247}Cm decay, owing to their high Nd/U ratios (*i.e.*, a proxy for the Cm/U ratio). Figure submitted in [432].

radii of these elements [64]. In fact, the lack of coherency of the Pu-Th and Pu-U pairs in the same samples showing coherent behavior of Pu and Nd [262] is a strong indication that neither Th nor U are proper proxies for Cm during nebular processes. This conclusion is supported by the elemental patterns presented in Fig. (4.21), where it can be seen that Th, though enriched relative to U, is not enriched to the same level as either Nd or Sm. Based on the expected coherency of Pu, Cm, and the LREEs and the demonstrated coherent behavior of Pu, Sm and Nd during nebular processes, it is clear that Nd (or Sm) are the most reliable proxies for Cm. In this work, Nd is used, but note that the results presented hereafter would be unchanged if Sm were used instead, because both elements display near-identical enrichment levels in the CAIs studied here.

The depletion of U relative to the LREEs (*i.e.*, to Cm) in the samples investigated, and in particular, the extreme depletion observed in CAI ME-3364-3.2 (black curve on Fig. 4.21), confirmed that some of the CAIs in the sample set were good candidates in which to search for the past presence of ^{247}Cm (*i.e.*, they have large Nd/U ratios).

4.3.3.3 Sample extraction and digestion

Powders of each sample were extracted using cleaned dental tools under a stereoscopic zoom microscope, and collected on weighing paper before being transferred into triple cleaned Teflon beakers. Great care was brought into collecting only the CAI, and any meteoritic matrix accidentally extracted was removed from the collected fraction using cleaned tweezers. Sample masses ranged from 15 to 760 mg (Table 4.7). Note that one of the coarse-grained CAIs (TS32) used in this study was characterized in an earlier paper [399] and was obtained directly in powder form for this work. The REE pattern of TS32 is essentially flat at enrichment of 21× CI (group V REE pattern).

All samples were fully digested using Optima quality acids with two one-week attacks in HF/HNO_3 3:1 (+ drops of $HClO_4$) followed by two one-week attacks in HCl/HNO_3 2:1 on a hot plate at 160°C. During each acid attack, the beakers were placed in a sonicator for $\sim$ 1 h. After the fourth acid attack, each sample was taken back in concentrated HNO_3 and put back on a hot plate for 4 days, before dilution to 3 M HNO_3. All samples were transferred into cleaned centrifuge tubes and centrifuged for 5 min at $\sim$ 1500 rpm. No residue was visible.

At this stage, one fifth of the solution was saved for future work, leaving 80 % of the sample available for characterization of the U isotopic composition. A small aliquot (between 0.5 and 4 %) of the solution was sampled for concentration analyses on the Q-ICPMS at the Field Museum.

Sample	Type	REE pattern	$^{144}Nd/^{238}U$	±	Mass CAI used (mg)	Sample used (%)	ng U	Resin #	^{235}U Setup	Double Spike	n	Cycles	Data reduction	$\delta^{235}U$ meas. (‰)	±	$\delta[^{234}U/^{238}U]$ (‰)	±	U_{sp}/U_{smp}	$\delta^{235}U$ blk[a]. (‰)	±	Blank contrib.	±	[U] blk corr. (ppb)	±	$\delta^{235}U$ (‰) blk corr.	±
GEOSTANDARDS																										
BCR-2	Basalt		4.3	0.4	11.39	100%	18.34	1	10e12 Ω	✓	1	90	MCS	0.34	0.19	195.0	1.0	3.2%	0	10	0.16%	0.04%	1609	159	0.34	0.19
								2	10e11 Ω	✓	1	42	MCS	0.15	0.28	0.6	0.8	3.2%	0	10	0.11%	0.03%	1611	154	0.15	0.28
								3	10e11 Ω	✓	1	38	MCS	0.23	0.28	3.0	0.8	3.2%	0	10	0.12%	0.03%	1613	152	0.23	0.28
																									BCR-2 weighted average	***0.27***	***0.14***
BHVO-2	Basalt		16.0	2.0	48.55	100%	18.25	1	10e12 Ω	✓	1	90	MCS	0.67	0.19	51.9	1.0	3.1%	0	10	0.17%	0.04%	376	37	0.68	0.19
								1	10e11 Ω	✓	1	80	MCS	0.24	0.30	45.1	0.4	3.1%	0	10	0.11%	0.03%	376	38	0.24	0.30
																									BHVO-2 weighted average	***0.55***	***0.16***
Faedra	Seawater				160710		0.767	1	10e12 Ω	✓	1	25	MCS	0.15	2.01	154.7	5.5	2.8%							0.15	2.01
Allende	CV3		12.2	1.5	1016.08	100%	21.89	1	10e12 Ω	✓	1	90	MCS	0.61	0.19	71.3	1.0	2.1%	0	10	0.08%	0.02%	21.5	2.6	0.61	0.19
								1	10e11 Ω	✓	1	88	MCS	0.21	0.30	46.7	0.4	2.1%	0	10	0.05%	0.01%	21.5	2.6	0.21	0.30
																									Allende weighted average	***0.49***	***0.16***
CAIs																										
ME-3364-2.2a	fg-CAI	gr. II	97.6	9.9	29	79.9%	0.62	1	10e12 Ω	✓	1	26	MCS	1.93	1.55	66.7	5.5	7.2%	0	10	0.98%	0.24%	21.1	0.4	1.95	1.57
ME-3364-2.2b			92.3	9.9	6.0	16.5%	0.15	3	10e12 Ω	✓	1	23	MCS	5.27	7.64	1545.5	7.4	4.6%	0	10	8.21%	0.63%	22.3	0.9	5.74	8.38
	Weighted average		*95.0*	*7.0*																					***ME-3364-2.2 weighted average***	***2.08***	***1.54***
ME-3364-3.2a	fg-CAI	gr. II	13724	488	594	77.4%	0.29	1	10e12 Ω	✓	1	29	MCS	52.12	14.72	1213.1	18.4	0.6%	0	10	1.27%	0.38%	0.482	0.008	52.79	14.91
ME-3364-3.2b			12996	2211	80	10.4%	0.048	2	SEM		1	41	Excel	51.59	1.26				0	10	12.73%	2.82%	0.51	0.09	59.12	2.80
ME-3364-3.2c			15612	3811	44	5.8%	0.032	3	SEM		1	31	Excel	42.09	1.46				1.61	3.58	29.43%	1.16%	0.42	0.10	58.97	2.72
	Weighted average		*13720*	*472*																					***ME-3364-3.2 weighted average***	***58.94***	***1.93***
ME-3364-4.2a	cg-CAI		74.2	7.5	40	79.7%	0.61	1	10e12 Ω	✓	1	29	MCS	1.35	1.52	122.6	5.4	7.3%	0	10	0.94%	0.24%	15.2	0.2	1.36	1.54
ME-3364-4.2b			72.1	7.5	8.4	16.7%	0.14	3	10e12 Ω	✓	1	32	MCS	0.89	7.64	110.0	7.4	4.6%	0	10	7.50%	1.09%	15.6	0.5	0.96	8.30
	Weighted average		*73.2*	*5.3*																					***ME-3364-4.2 weighted average***	***1.35***	***1.52***
ME-3364-22.2a	fg-CAI	gr. II	108.3	5.4	42	79.7%	1.24	1	10e12 Ω	✓	1	18	MCS	0.23	0.73	27.4	2.6	7.2%	0	10	0.39%	0.10%	29.7	0.3	0.23	0.73
ME-3364-22.2b			102.2	5.7	8.9	17.1%	0.29	3	10e12 Ω	✓	1	21	MCS	-0.75	2.01	76.6	5.5	4.8%	0	10	3.68%	0.28%	31.5	0.8	-0.78	2.12
	Weighted average		*105.4*	*3.9*																					***ME-3364-22.2 weighted average***	***0.12***	***0.69***
ME-3364-25.2a	fg-CAI	gr. II	65.7	4.0	81	79.8%	3.29	1	10e12 Ω	✓	1	77	MCS	1.67	0.60	21.3	1.2	6.1%	0	10	0.33%	0.08%	40.5	0.2	1.68	0.60
ME-3364-25.2b			61.6	3.8	17	17.1%	0.76	3	10e12 Ω	✓	1	24	MCS	-0.48	0.88	55.8	2.3	4.9%	0	10	1.52%	0.12%	43.2	0.6	-0.49	0.90
	Weighted average		*63.5*	*2.7*																					***ME-3364-25.2 weighted average***	***1.01***	***0.50***
ME-2639-16.2	fg-CAI	gr. II	40.5	4.1	350	79.8%	15.74	1	10e12 Ω	✓	1	84	MCS	-0.89	0.35	10.4	1.3	5.3%	0	10	0.10%	0.03%	45.01	0.06	-0.89	0.35
			40.5	4.0				2	10e12 Ω	✓	1	90	MCS	-0.77	0.35	25.2	1.3	5.3%							-0.77	0.35
	Weighted average		*40.5*	*2.9*																					***ME-2639-16.2 weighted average***	***-0.83***	***0.25***
ME-2639-33.9a	fg-CAI	gr. II	33.9	3.4	40	79.7%	2.29	1	10e12 Ω	✓	1	41	MCS	0.59	0.64	30.1	1.7	7.3%	0	10	0.32%	0.08%	56.9	0.5	0.60	0.64
ME-2639-33.9b			31.9	3.3	8.6	17.2%	0.53	3	10e12 Ω	✓	1	22	MCS	-1.28	1.44	54.2	3.9	4.9%	0	10	1.98%	0.15%	60.5	1.6	-1.30	1.49
	Weighted average		*32.9*	*2.4*																					***ME-2639-33.9 weighted average***	***0.30***	***0.59***
ME-2639-49.7a	fg-CAI	gr. II	642	44	45	79.7%	0.27	1	10e12 Ω	✓	1	27	MCS	0.37	2.19	-5.0	3.0	6.7%	0	10	1.78%	0.44%	5.8	0.06	0.38	2.23
ME-2639-49.7b			502	83	9.7	17.1%	0.085	3	SEM		1	31	Excel	3.58	1.03				1.61	3.58	14.02%	0.51%	7.4	1.1	3.90	1.33
	Weighted average		*612*	*39*																					***ME-2639-49.7 weighted average***	***2.98***	***1.14***
ME-2639-51.1a	fg-CAI	gr. II	344	13	51	79.7%	0.79	1	10e12 Ω	✓	1	30	MCS	2.13	0.96	26.7	3.1	6.7%	0	10	0.66%	0.17%	15.5	0.2	2.15	0.96
ME-2639-51.1b			327	14	11	16.6%	0.18	3	10e12 Ω	✓	1	26	MCS	1.03	7.64	414.1	7.4	4.6%	0	10	7.74%	0.61%	16.3	0.4	1.11	8.33
	Weighted average		*336*	*10*																					***ME-2639-51.1 weighted average***	***2.13***	***0.96***
AL3S5	fg-CAI	gr. II	396	9	377	79.8%	8.50	1	10e12 Ω	✓	1	90	MCS	3.39	0.35	277.3	1.3	4.4%	0	10	0.11%	0.03%	22.53	0.04	3.40	0.35
			395	9				2	10e12 Ω	✓	1	22	MCS	3.28	0.26	102.7	2.0	4.4%							3.28	0.26
	Weighted average		*395*	*6*																					***AL3S5 weighted average***	***3.32***	***0.21***
AL4S6	fg-CAI	gr. II	26.8	2.7	331	79.8%	23.93	1	10e12 Ω	✓	1	78	MCS	1.90	0.19	17.4	1.0	5.5%	0	10	0.07%	0.02%	72.35	0.10	1.90	0.19
			26.8	2.7				2	10e12 Ω	✓	1	89	MCS	2.00	0.19	34.2	1.0	5.5%							2.00	0.19
	Weighted average		*26.8*	*1.9*																					***AL4S6 weighted average***	***1.95***	***0.14***
AL8S2a	fg-CAI	gr. II	640	39	13	79.7%	0.18	1	10e12 Ω	✓	1	23	MCS	0.46	2.19	900.2	3.0	5.8%	0.00	10	2.84%	0.71%	13.3	0.4	0.48	2.27
AL8S2b			505	95	2.6	16.1%	0.058	3	SEM		1	29	Excel	2.84	1.21				1.61	3.58	19.75%	0.85%	16.9	3.0	3.14	1.75
																									AL8S2	***3.14***	***1.75***
AL8S8	cg-CAI		19.1	1.9	200	79.8%	22.99	1	10e12 Ω	✓	1	86	MCS	0.43	0.19	20.5	1.0	6.5%	0	10	0.07%	0.02%	114.7	0.2	0.43	0.19
			19.1	1.9				2	10e12 Ω	✓	1	90	MCS	0.43	0.19	13.2	1.0	6.5%							0.43	0.19
	Weighted average		*19.1*	*1.4*																					***AL8S8 weighted average***	***0.43***	***0.14***
AL10S1a	fg-CAI	gr. II	477	13	57	79.7%	0.67	1	10e12 Ω	✓	1	20	MCS	5.98	1.02	62.8	5.0	6.8%	0	10	0.73%	0.18%	11.8	0.2	6.03	1.03
AL10S1b			451	15	12	17.1%	0.16	3	10e12 Ω	✓	1	19	MCS	6.06	7.64	210.5	7.4	4.7%	0	10	7.91%	0.61%	12.4	0.3	6.58	8.35
	Weighted average		*465*	*10*																					***AL10S1 weighted average***	***6.03***	***1.02***
TS32a	cg-CAI		20.6	2.1	34	79.6%	3.96	1	10e12 Ω	✓	1	46	MCS	0.00	0.32	-59.2	1.7	7.2%	0	10	0.28%	0.07%	115.0	1.1	0.00	0.32
TS32b			18.9	2.0	7.4	17.2%	0.93	3	10e12 Ω	✓	1	21	MCS	-1.41	0.88	-39.1	2.3	4.8%	0	10	1.20%	0.09%	123.7	3.9	-1.43	0.89
	Weighted average		*19.7*	*1.4*																					***TS32 weighted average***	***-0.16***	***0.30***

[a] In most cases, the signal on 235U was too low to determine the d235U of the chemistry blank reliably. An arbitrary value of 0 ± 10 ‰ was used. This approach is conservative as the 10 ‰ uncertainty is propagated into the final estimate of the blank corrected d235U of the samples.

[b] The double spike data reduction was done using a Mathematica code and error propagation by MonteCarlo Simluations (MCS) as detailed in Tissot and Dauphas (2015). Data for unspiked samples were reduced using excel (*i.e.*, On Peak Zero, sample-standard bracketing and blank correction).

Table 4.7: Summary of U isotopic compositions and concentrations of CAIs and geostandards. Table submitted in [432].

4.3.3.4 Nd and U concentrations

Given that the values of the $^{144}Nd/^{238}U$ ratios are of major importance in defining the slope of the isochron ($\delta^{235}U$ *vs.* $^{144}Nd/^{238}U$, see Figs. 1.10, and 4.25), the Nd and U concentrations in the CAIs were determined with high precision and accuracy.

For Nd, the concentrations were measured by Q-ICPMS for all CAIs, and by standard addition using an Alfa Aesar Nd single element solution (1000 μg/g, Lot# 801149A) for some selected samples (CAI ME-3364-3.2, ME-3364-22.2, ME-3364-25.2, ME-2639-49.7, ME-2639-51.1, AL3S5, AL8S2 and AL10S1). Both sets of values agree with each other within 7 %. For Q-ICPMS measurements, the typical uncertainty is $\pm$ 10 %. The stated uncertainties on the standard addition measurement are the 95 % confidence intervals (typically $\sim$ 2 to 6 %) and were calculated using the R statistical software. For instance, Fig. (4.22) shows the results of the standard addition carried out on sample ME-3364-3.2, with the 95 % CI envelope.

For U, the concentrations were obtained from (i) the double-spike data reduction [431] when samples were spiked, and (ii) sample-standard bracketing when samples were not spiked. Each sample was measured twice (see Table 4.7) and the U concentrations obtained in the two analyses typically agree within 5 to 20 %. The double-spike values are more precise and accurate than the bracketing values. For each U isotopic measurement, a value of the $^{144}Nd/^{238}U$ ratio of the sample can be calculated (with its corresponding 95 % confidence interval value). The final $^{144}Nd/^{238}U$ ratio used for a given sample is the weighted average of the individual $^{144}Nd/^{238}U$ ratios obtained for each sample (see Table 4.7 and 4.9).

4.3.3.5 Double spike and uranium purification

Samples were spiked using the commercially available IRMM-3636 double spike (50.45 % ^{233}U and 49.51 % ^{236}U, [447]). Since the two spike isotopes (^{233}U, ^{236}U) do not occur naturally and the spike is very pure (low ^{235}U and ^{238}U content), optimization of the spike

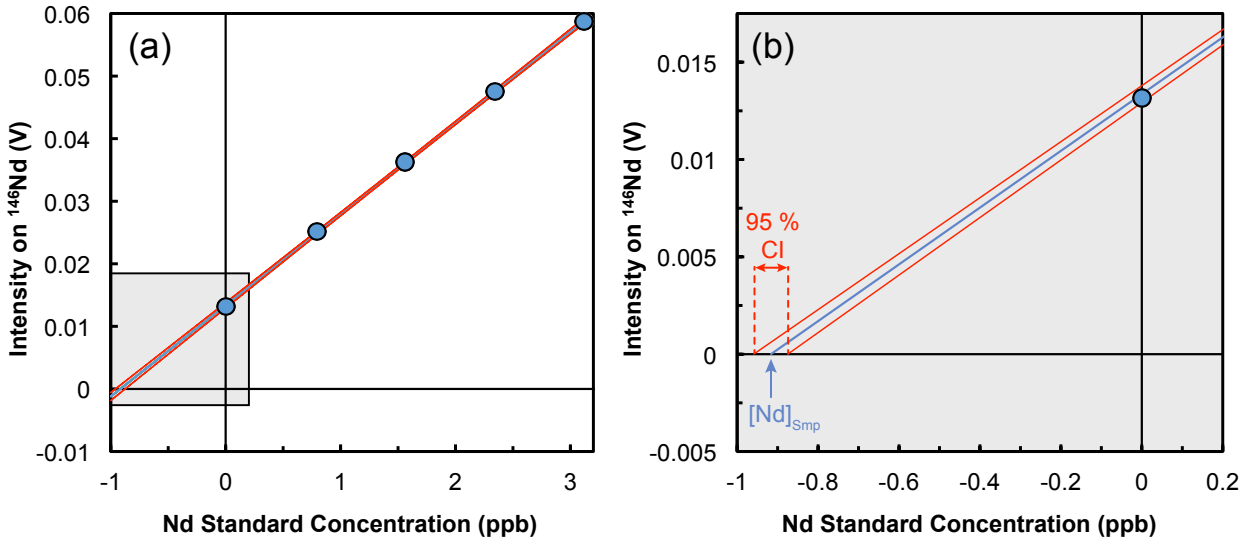

Figure 4.22: (a) Standard addition measurements on CAI ME-3364-3.2 and (b) close-up near the x intercept. In standard addition, an array of solutions are prepared, containing the same amount of sample solution (whose concentration, C, is to be determined) and the same final volume, but varying amount of standard solution (of known concentration). Here, the relative proportion of sample/standard/MQ water are (points from left to right in panel (a): (1:0:4), (1:1:3), (1:2:2), (1:3:1) and (1:4:0). The signal intensity is linearly related to x, the standard concentration in the solution by $\mathrm{I}(x) = a(C + x)$. The sample concentration is thus the absolute value of the intercept of the regression (blue line) with the x-axis (when $\mathrm{I}(x) = 0$, $x = -C$). The red curves show the 95 % CI of the fit. Figure submitted in [432].

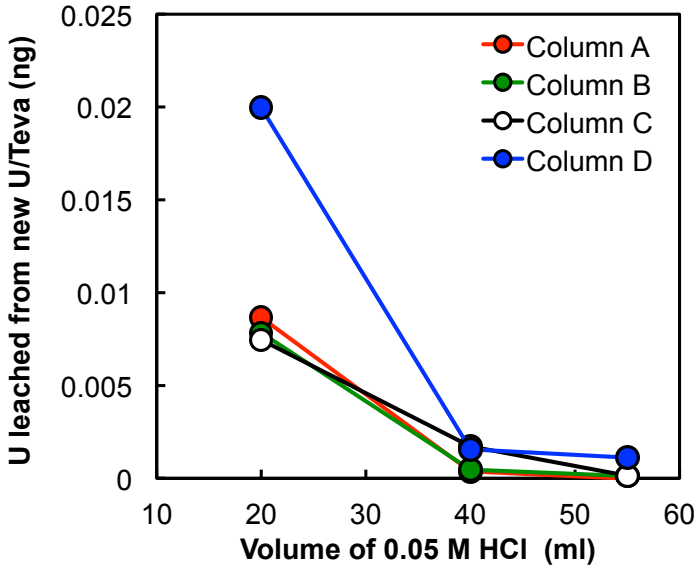

Figure 4.23: U blank from new U/Teva resin plotted against the volume of 0.05 M HCl passed through the column (test done with 2 mL prepacked cartridges). Essentially all U initially bound to the resin is removed (down to the ppt level) with 40 mL of 0.05 M HCl. Proper cleaning on the resin is crucial for work on low U content samples (*e.g.*, replicate 2 and 3 of ME-3364-3.2 contained less than 0.050 ng of U each). Figure submitted in [432].

to sample ratio is not critical. A minimum amount of spike, however, needs to be used to achieve high precision measurement of the spike isotopes while minimizing amplifier noise, as well as limiting the abundance sensitivity effect of ^{238}U on ^{236}U. To fulfill these requirements, previous studies used a U_{Spike}/U_{Sample} ratio of ~ 3 % (e.g., [460]). As underspiking would be more detrimental than overspiking, all samples were spiked, aiming for a U_{Spike}/U_{Sample} ratio of 6 %. The measured U_{Spike}/U_{Sample} ratio was ~ 6 % for all but one sample (CAI ME-3364-3.2, whose spiking level was only 0.5 %, Table 4.7). This sample is the one with the largest digested mass (740 mg) and the underestimation in the U content is likely due to matrix effects during concentration measurements.

To ensure full equilibration of the spike with the sample [286], the samples were dried completely after spike addition, taken back into concentrated HNO_3 and diluted to 3 M HNO_3. No residues were visible after this new digestion step.

U separation and purification were done using U/Teva resin, following the method described in [431] and Section 2.3. Due to the low U content of some of the samples, extensive column cleaning was done using 40 mL of 0.05 M HCl, removing essentially all U initially bound to the resin (down to the ppt level, Fig. 4.23). This extensive cleaning is important as the amount of U bound to new U/Teva resin cartridges was typically 0.02 ng, which represents up to 70 % of the total U content of some of the samples measured in this study (see CAI ME-3364-3.2 replicate 2 and 3 in Table 4.7). The rest of the chemistry went as follows: (1) conditioning with 10 mL of 3 M HNO_3, (2) sample loading in 3 M HNO_3, (3) matrix elution with 30 mL of 3 M HNO_3, (4) resin conversion to HCl with 5 mL of 10 M HCl, (5) Th elution in 12 mL of 5 M HCl and (6) U elution with 32 mL of 0.05 M HCl.

The U cut was then dried completely, and taken back into 200 μL of 1:1 HNO_3/H_2O_2. This step oxidizes the organics leached from the resin into the U cut. The samples were then dried again completely and taken back into 0.1 mL of concentrated HNO_3, before being evaporated to near-dryness and being finally taken back in 0.3 M HNO_3. At this stage, the samples were ready for mass spectrometric analysis. Some samples showed either particles

or the solution did not wet the Teflon beakers like pure 0.3 M HNO_3 (*i.e.*, asymmetrical shape of the liquid droplet and/or variable contact angle of the droplet with the Teflon). In those rare instances, the last drying sequence (hydrogen peroxide / concentrated nitric / dilute nitric) was repeated until particles were dissolved and the solution behaved like pure 0.3 M HNO_3.

4.3.3.6 Mass spectrometry

Though the sensitivity of the MC-ICPMS is excellent for U isotopes (1.4 to 1.6 V/ppb), the total amount of U contained in fine-grained CAIs is small (typically 1 to 5 ng). Sensitivity tests were done to determine the precision of the measurements of the $^{235}U/^{238}U$ ratio as a function of the measured ^{238}U intensity, using a standard solution spiked with IRMM-3636 double spike (Fig. 4.24, left panel). To resolve $\delta^{235}U$ anomalies on the order of 3 ‰, the ^{238}U signal must be at least 2 V (which translates into a minimum sample concentration of $\sim$ 1.25 ppb). Therefore, after U purification, a 5 μL aliquot was taken from each sample to determine the quantity of U recovered. The sample volume (and thus its U concentration) was adjusted in order to optimize the precision achievable for each CAI. The samples with the least U (0.3 to 3.7 ng) were measured in 0.25 to 0.50 mL, allowing for only a single measurement and no opportunity for its verification.

Details of the cup configuration used for the measurements are given in Table 4.8. To avoid wasting any data, the take-up time was set to zero and the cycles leading to the intensity plateau were manually removed during data reduction. When it was found that CAI ME-3364-3.2 had an $\sim$ +50 ‰ anomaly in $\delta^{235}U$ (see Section 4.3.4), a new measurement setup was designed in which sufficient precision would be achieved to remeasure this unique sample while using only 10 % of the original sample solution (*i.e.*, half of the aliquot saved before sample spiking, containing about 0.04 ng of U). This was realized by measuring ^{235}U on the SEM and ^{238}U on a Faraday cup with a 10^{11} Ω resistor. In this setup, the sample was not spiked, as the signal of the spiked isotopes would have been too low ($<$ 6 mV) for

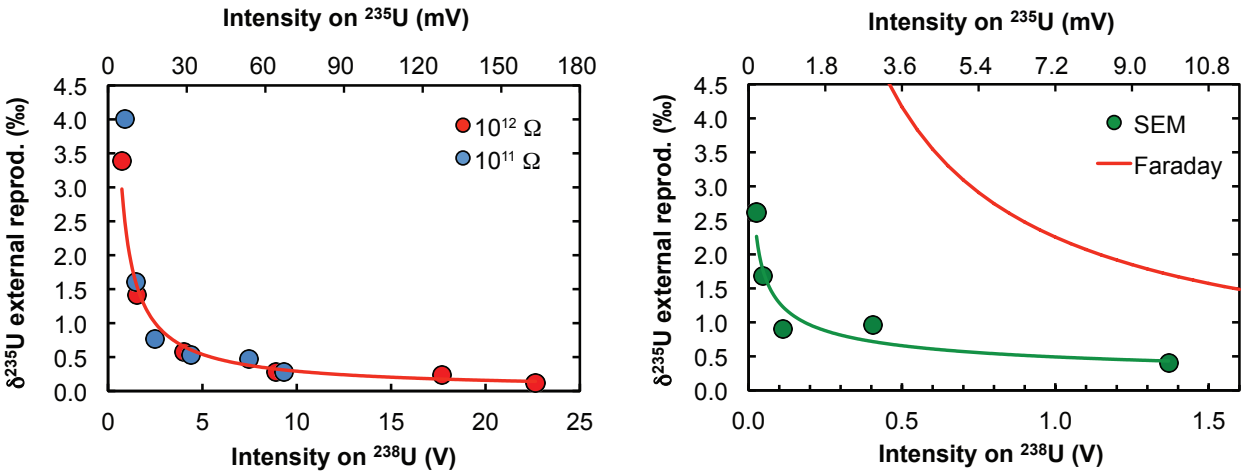

Figure 4.24: Results of precision tests done using two configurations: the *Faraday* setup, where ^{235}U is measured on a Faraday cup (with either a 10^{12} Ω resistor or a 10^{11} Ω resistor) (left) and the *SEM* setup where ^{235}U is measured on the SEM (right). In both cases ^{238}U is being measured using a 10^{12} Ω resistor (see Table 4.8 for detail of each setup). Each point represents 210 s of analyses: 50 cycles of 4.194 s for *Faraday* setup and 100 cycles of 2.097 s for the *SEM* setup). For very low U concentrations, higher precision can be obtained by measuring ^{235}U on the SEM rather than on a 10^{12} Ω or 10^{11} Ω resistor. Figure submitted in [432].

Specifics of U isotopic measurements for low U samples by MC-ICPMS

	L2	L1	Axial	H1	H2	H3	Integration	Cycles	Rinse time
Faraday setup[a]									
Isotope	-	^{233}U	^{234}U	^{235}U	^{236}U	^{238}U	2.097 sec	100	> 500 sec
Resistor (Ω)	-	10^{11}	SEM	10^{12}	10^{11}	10^{11}			
SEM setup[a]									
Isotope	^{233}U	^{234}U	^{235}U	^{236}U	^{238}U	-	2.097 sec	100	> 500 sec
Resistor (Ω)	10^{11}	10^{11}	SEM	10^{11}	10^{11}	-			

[a] For extremely small U amounts (0.01 to 0.05 ng of U) the *SEM* setup was used instead of the *Faraday* setup. See comparison of achievable precision with each setup in Fig. (4.11).

Table 4.8: Details of the two cup configurations used to measure the U isotopic composition of the CAIs in this work. Table submitted in [432].

the double spike technique to be useful. Instead, the measurements were done by sample-standard bracketing. Results of precision tests using this configuration, with 2.097 seconds integration time and 100 cycles, are shown in Fig. (4.24) (right panel). From this figure, it is easily seen that higher precision can be obtained for very low U concentrations by measuring ^{235}U on the SEM rather than on a 10^{12} Ω resistor.

4.3.4 Results

As in previous studies, most samples display low ^{144}Nd/^{238}U ratios and their δ^{235}U values are within 6 ‰ of the bulk Solar System value at δ^{235}U = +0.36 ‰ (relative to CRM-112a) (see Section 4.2.1). One sample (ME-3364-3.2), however, has an extremely high ^{144}Nd/^{238}U ratio ($\sim$ 13720) and a δ^{235}U excess of $+58.9 \pm 1.9$ ‰ (Table 4.9 and Fig. 4.25). For comparison, the highest ^{144}Nd/^{238}U ratio and ^{235}U excess measured in CAIs prior to this work were 481 and 3.43 ‰, respectively [71].

Given the very low amount of U contained in CAI ME-3364-3.2 and the unprecedented magnitude of the ^{235}U excess found in this sample, considerable effort was expended to make sure that no analytical bias could account for any of the anomalies found in this sample and others. The full series of tests performed is presented below. In short, confirmation of the result involved triplicating the measurement using different sample purification schemes and various measurement setups ($+52.79 \pm 14.91$ ‰ after one purification step with ^{235}U measured on a Faraday cup, $+59.12 \pm 2.80$ ‰ after two purifications with ^{235}U on an electron multiplier, and $+58.97 \pm 2.72$ ‰ after three purifications with ^{235}U on an electron multiplier). Extensive testing was also done to ensure that no interferences or matrix effects were affecting the measurement by combining the matrix cut from CAI ME-3364-3.2 with CRM-112a U standard, and finding that after purification, the measured U isotopic composition is correct.

Sample	Type[a]	REE pattern[b]	Mass (mg)	ng U	n	^{144}Nd/ ^{238}U	±	δ^{235}U (‰) blk corr.	±
Allende	CV3		1016	21.9	2	12.2	1.5	0.49	0.16
ME-3364-2.2	fg-CAI	gr. II	35.2	0.77	2	95.0	7.0	2.08	1.54
ME-3364-3.2	fg-CAI	gr. II	717.9	0.37	3	13720	472	58.94	1.93
ME-3364-4.2	cg-CAI	gr. I	48.4	0.76	2	73.2	5.3	1.35	1.52
ME-3364-22.2	fg-CAI	gr. II	50.4	1.53	2	105.4	3.9	0.12	0.69
ME-3364-25.2	fg-CAI	gr. II	98.3	4.05	2	63.5	2.7	1.01	0.50
ME-2639-16.2	fg-CAI	gr. II	349.7	15.7	2	40.5	2.9	-0.83	0.25
ME-2639-33.9	fg-CAI	gr. II	48.7	2.82	2	32.9	2.4	0.30	0.59
ME-2639-49.7	fg-CAI	gr. II	54.9	0.35	2	612	39	2.98	1.14
ME-2639-51.1	fg-CAI	gr. II	61.4	0.98	2	336	10	2.13	0.96
AL3S5	fg-CAI	gr. II	377.3	8.50	2	395	6	3.32	0.21
AL4S6	fg-CAI	gr. II	330.7	23.9	2	26.8	1.9	1.95	0.14
AL8S2	fg-CAI	gr. II	15.61	0.24	2	505	95	3.14	1.75
AL8S8	cg-CAI	gr. V	200.4	23.0	2	19.1	1.4	0.43	0.14
AL10S1	fg-CAI	gr. II	68.6	0.83	2	465	10	6.03	1.02
TS32	cg-CAI	gr. V	41.8	4.89	2	19.7	1.4	-0.16	0.30

[a] "fg" and 'cg" stand for "fine-grained" and "coarse-grained", respectively.
[b] "gr. X" stands for "group X REE pattern".

Table 4.9: Type, REE pattern, mass, U content, ^{144}Nd/^{238}U ratio, and U isotopic composition of the samples analyzed in this study. n is the number of replicate analyses for each sample (starting from solutions). The Nd/U ratios and isotopic compositions are corrected for blank contributions (see Table 4.7). $\delta^{235}\mathrm{U} = [(^{235}\mathrm{U}/^{238}\mathrm{U})_{\mathrm{Sample}}/(^{235}\mathrm{U}/^{238}\mathrm{U})_{\mathrm{CRM\text{-}112a}} - 1] \times 10^3$. Error bars are 95 % confidence intervals. The Nd/U ratio was calculated using the U concentration from the double spike technique and Nd concentration from the standard addition technique. Table submitted in [432].

4.3.4.1 General tests

Abundance sensitivity (the fact that the tail of the ^{238}U peak is still present at mass 236, 235 and 234) can potentially affect the measurement of the ^{235}U/^{238}U ratio. The typical contribution of the ^{238}U tail on ^{236}U, ^{235}U and ^{234}U, is 0.6 ppm, 0.25 ppm and 0.1 ppm of the ^{238}U signal, respectively [431]. Not correcting for this effect only affects the ^{235}U/^{238}U ratio by 0.1 ‰. Furthermore, the samples and bracketing standards are spiked to similar levels and their concentrations are matched within at least 10 %. Thus, the actual effect of the abundance sensitivity correction is smaller than 0.1 ‰. Therefore, the abundance

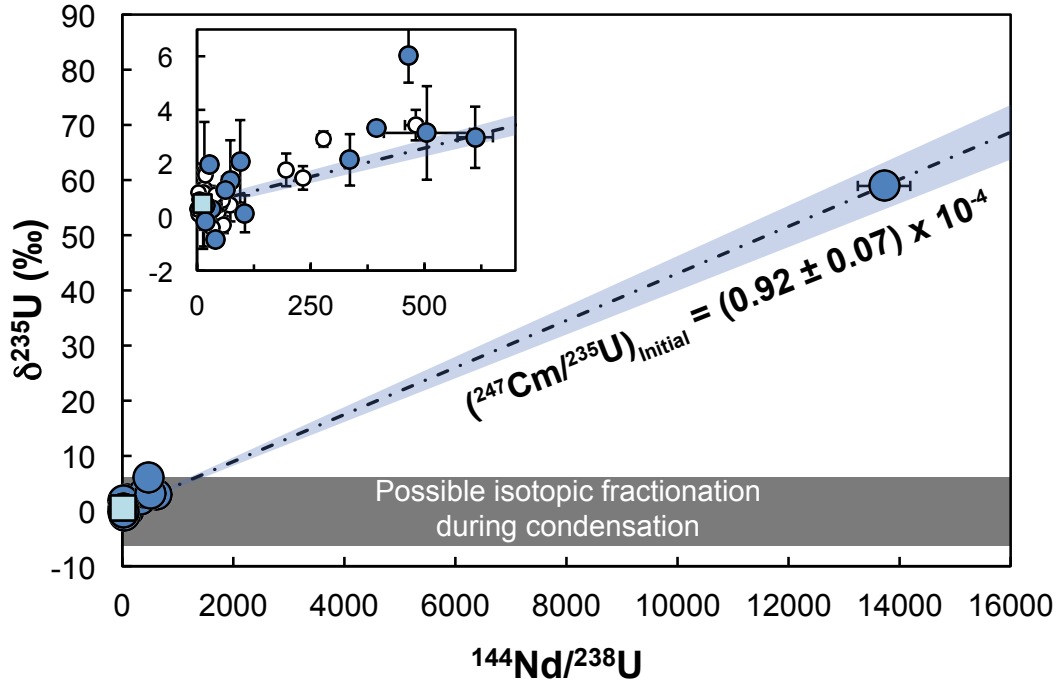

Figure 4.25: δ^{235}U plotted as a function of the ^{144}Nd/^{238}U ratio in meteoritic samples (open circles: previous studies [414, 415, 71, 14, 119, 177]; blue filled circles: Allende CAIs in this work; light blue square: bulk Allende from this work). The +59 ‰ δ^{235}U value observed in CAI ME-3364-3.2 is well outside the range of variations expected from fractionation during condensation (grey rectangle), and is thus interpreted as definitive evidence for live ^{247}Cm in the ESS. The scatter in the data (*e.g.*, at very low Nd/U ratios) suggests that stable isotopic fractionation during condensation also influenced the U isotopic composition of CAIs. The slope of the two-point isochron between CAI ME-3364-3.2 and the rest of the samples translates into a (^{247}Cm/^{235}U) of $(0.9 \pm 0.07) \times 10^{-4}$ at the time of Nd/U fractionation in CAI ME-3364-3.2.

sensitivity cannot explain the U isotopic variations documented here.

Hydride formation could also be an issue. The ratio $^{238}UH^+/^{238}U$ was regularly monitored and found to be on the order of 5×10^{-7}, in agreement with literature data [460, 428, 431]. At this level, hydrides have no influence on the measurements. The hydride ratio would need to be on the order of 10^{-3} to produce an anomaly of 2 ‰. Since the hydride formation ratio is so low, the possibility that $^{232}ThH^+$ interferences on ^{233}U could affect the double spike correction is also effectively ruled out. Again, the samples and bracketing standards are spiked at the same level, which would mitigate the influence of uranium hydrides on isotopic analyses in any event.

To test if mismatch in acid molarity between the sample and standard could affect the measurements [134, 425], a 1 ppb CRM-112a solution (*i.e.*, the minimum concentration at which the measurements were performed with ^{235}U on a Faraday cup) was spiked with IRMM-3636 ($U_{Spike}/U_{Sample} = 6$ %) and several aliquots were dried and taken back in 0.3 M, 0.5 M, 1 M, 1.5 M, 2 M, and 3 M HNO_3. All these solutions were measured against a 0.3 M solution and the analyses yielded normal results within the 2 ‰ reproducibility of the measurements at this concentration.

The effect of the chemistry blank was also investigated. The $^{235}U/^{238}U$ ratios of six chemistry blanks measured over a four-month period were compiled and their effect on a sample measured at 1 ppb (*i.e.*, 1 to 1.5 V on ^{238}U depending on the sensitivity of the instrument) was calculated (Table 4.10). The effect was found to be between -0.9 and 2.8 ‰ at most. Since the samples are dried with H_2O_2 right before analysis, a series of tests were done in which 17 to 54 mg of H_2O_2 was added to 0.25 mL of a 1 ppb standard solution (spiked at 6 %) before analysis. No effect on the $^{235}U/^{238}U$ ratio was found.

4.3.4.2 Assessment of data accuracy

Small amounts of matrix elements can still be present after chemical purification and may affect the accuracy of the measurement [134, 425]. Two tests were performed to make sure that no interference or matrix effect influenced the results.

1. The four samples with the most U (8 to 20 ng) were analyzed twice. Half the sample was analyzed after one purification step, while the other half was subjected to a second step of column chemistry before analysis. For all samples, both results are identical within error bars (0.1 ‰) (Table 4.7).

2. For all samples (but the above four), the matrix cuts retrieved from the column chromatography were recombined and doped with a quantity of U standard CRM-112a similar to the amount of U initially present in the sample. These doped samples were

#	H_2O_2	Session	Resins #	Cycle #	^{235}U (V or cps)	± (2SD)	^{238}U (V)	± (2SD)	$^{238}U/^{235}U$ blk	$\delta^{238}U$ blk (‰)	± (2SD)	Sensitivity (V/ppb)	Blk contribution (%)[a]	Effect on $\delta^{238}U$ meas. (‰)[a]
1	Yes	CAI Dec2014 a	1	38	2.0E-04	6.1E-05	0.029	0.007	144.449	33	199	1.05	2.78%	0.9
2	Yes	CAI Dec2014 b	1	90	1.1E-04	4.2E-05	0.015	0.004	138.208	-12	315	1.05	1.41%	-0.2
3	Yes	SEM Dec2014[b]	2	39	*4437.9*	*6417.8*	0.010	0.015	133.409	-46	83	1.44	0.66%	-0.3
4	Yes	Far Jan 2015	1	33	2.2E-04	4.9E-05	0.035	0.005	157.504	126	136	1.58	2.24%	2.8
5	Yes	Far Mar 2015	3	24	6.2E-04	7.0E-05	0.086	0.006	137.740	-15	98	1.42	6.07%	-0.9
6	Yes	SEM Mar 2015[b]	3	31	*31877.0*	*2093.3*	0.071	0.004	139.997	0.8	9.2	1.27	5.59%	0.0

[a] The blank contribution and effect on the $\delta^{238}U$ measured are calculated assuming a sample solution at 1 ppb is measured (*i.e.*, about 1 to 1.5 V on ^{238}U)
[b] The cps to volts conversion factor used in these sessions was estimated to be ~ 62e6 ± 0.3e6.

Table 4.10: Compilation of chemistry blanks and effect on the U "stable" isotope ratio. Table submitted in [432].

Sample	Type	ng U	Resin #	^{235}U Setup	Double Spike	n	Cycles	Data reduction	$\delta^{235}U$ meas. (‰)	±	$\delta[^{234}U/^{238}U]$ (‰)	±	U_{sp}/U_{smp}	$\delta^{235}U$ blk[a]. (‰)	±	Blank contrib.	±	**$\delta^{235}U$ (‰) blk corr.**	±
DOPING TESTS																			
Sample matrix	Doping standard																		
ME-3364-2.2	CRM-112a	0.49	1	10e12 Ω	✓	1	23	MCS	-0.74	1.18	-22.3	2.5	6.2%	0	10	0.97%	0.14%	-0.75	1.20
ME-3364-3.2	CRM-112a	0.34	1	10e12 Ω	✓	1	32	MCS	2.10	16.77	65.3	22.7	0.5%					2.10	16.77
ME-3364-4.2	CRM-112a	0.59	1	10e12 Ω	✓	1	25	MCS	1.02	1.18	147.3	2.5	6.3%	0	10	0.94%	0.13%	1.03	1.20
ME-3364-22.2	CRM-112a	1.17	1	10e12 Ω	✓	1	25	MCS	-0.18	1.18	74.5	2.5	6.3%	0	10	0.70%	0.10%	-0.18	1.19
ME-3364-25.2	CRM-112a	3.14	1	10e12 Ω	✓	1	23	MCS	0.03	0.53	153.4	2.8	6.3%	0	10	0.45%	0.06%	0.03	0.54
ME-2639-33.9	CRM-112a	2.21	1	10e12 Ω	✓	1	41	MCS	-0.06	0.53	4.0	2.8	6.3%	0	10	0.44%	0.06%	-0.06	0.54
ME-2639-49.7	CRM-112a	0.26	1	10e12 Ω	✓	1	30	MCS	-0.33	2.72	1.1	3.9	6.2%					-0.33	2.72
ME-2639-51.1	CRM-112a	0.84	1	10e12 Ω	✓	1	24	MCS	0.38	1.18	-37.2	2.5	6.3%	0	10	0.71%	0.10%	0.38	1.19
AL8S2a	CRM-112a	0.18	1	10e12 Ω	✓	1	26	MCS	-41.20	2.72	-63.9	3.9	5.5%					-41.20	2.72
AL8S2b	CRM-112a	0.18	1	10e12 Ω	✓	1	32	MCS	-17.89	3.19	-39.5	5.2	5.9%	0	10	2.29%	0.32%	-18.31	3.28
AL10S1a	CRM-112a	0.69	1	10e12 Ω	✓	1	23	MCS	1.59	2.72	90.8	3.9	6.3%					1.59	2.72
AL10S1b	CRM-112a	0.69	1	10e12 Ω	✓	1	24	MCS	0.03	1.18	-34.7	2.5	6.3%	0	10	0.84%	0.12%	0.03	1.19
TS32	CRM-112a	3.77	1	10e12 Ω	✓	1	34	MCS	0.46	0.53	92.3	2.8	6.3%	0	10	0.36%	0.06%	0.46	0.53

[a] In most cases, the signal on 235U was too low to determine the d235U of the chemistry blank reliably. An arbitrary value of 0 ± 10 ‰ was used. This approach is conservative as the 10 ‰ uncertainty is propagated into the final estimate of the blank-corrected d235U of the samples.
[b] The double spike data reduction was done using a Mathematica code and error propagation by MonteCarlo Simluations (MCS) as detailed in Tissot and Dauphas (2015). Data for unspiked samples were reduced using excel (*i.e.*, On Peak Zero, sample-standard bracketing and blank correction).

Table 4.11: Summary of doping tests conducted on the CAIs. In these tests, the matrix of the CAI (*i.e.*, the matrix cuts retrieved from the column chemistry) were recombined and doped with a quantity of U standard CRM-112a similar to the amount of U initially present in the sample. These "doped" samples were subjected to column chemistry once before U isotopic analysis. Only one sample (AL8S2) showed an interference/matrix effect, and the value obtained for this sample after a single chemistry pass is not considered further in the discussion. Table submitted in [432].

passed through chemistry once before analysis, and for all but one, the δ^{235}U measured was indistinguishable from the CRM-112a value ($\delta^{235}U_{\text{CRM-112a}} = 0$ ‰, by definition), indicating a lack of interference/matrix effect for these samples.

One "doped" sample presented a large ^{235}U deficit (−42 ‰): CAI AL8S2 (Table 4.11. The same test was repeated for this sample, and once again, a ^{235}U deficit was found (−18 ‰). These values are in complete disagreement with each other, as well as with the measurement of the actual sample done using 80 % of the sample solution, which was measured at $+0.48 \pm 2.27$ ‰. Since the U added to the sample for the doping test is the CRM-112a standard, and because the sample was double spiked and the yield was above 90 %, the only plausible explanation is that some interference/matrix effects are responsible for the ^{235}U deficit observed in the "doped" sample. The δ^{235}U value of AL8S2 obtained using 80 % of the sample solution after one pass through column chemistry is thus non-reliable and neither considered in the discussion nor plotted in the figures.

Two geostandards (BCR-2, BHVO-2) and a sample of Allende were prepared along with the CAIs to ensure that no systematic biases were introduced by the sample preparation. The mass of sample used was calculated to give $\sim$ 20 ng of U for each geostandard, corresponding to the highest level of U contained in the CAIs used in this study. The ^{235}U/^{238}U ratios determined for the three geostandards are in excellent agreement with literature data ([431] and references therein).

Before spiking and chemistry, the samples were split 80/20, with the first aliquot being used for U analysis and the second being saved for future work. Some samples with large U content were replicated by splitting the 80 % aliquot into two (see above). For the others, it was decided to use the 20 % aliquot for a duplicate measurement. The 20 % aliquot was used and passed through the chemistry three times to make sure that no matrix elements remained after purification. The samples were measured within error of each other (Fig. 4.26), except for ME-3364-25.2 and TS32, for which the two replicates (with ^{235}U measured on a Faraday cup in both replicate measurements) are just outside of uncertainties of each

other. Because, these two samples have low $^{144}Nd/^{238}U$ (49 and 16, respectively) they are not heavily weighted in the determination of the slope of the isochron, and thus do not influence the main result of this study, *i.e.*, the initial abundance of ^{247}Cm in the ESS.

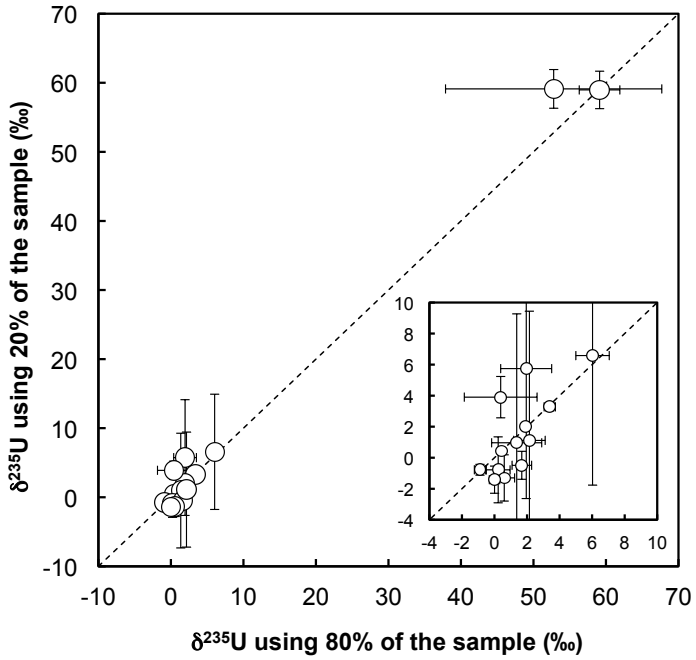

Figure 4.26: Comparison of the $\delta^{235}U$ determined using 80 % (x-axis) and 20 % (y-axis) of the sample. CAI ME-3364-3.2 was measured three times (see Section 4.3.4.3 and Fig. 4.27). All data are given relative to CRM-112a. Figure submitted in [432].

4.3.4.3 The special case of CAI ME-3364-3.2

Figure (4.27) summarizes the tests done on CAI ME-3364-3.2. In addition to the "doping" test described above, the $^{235}U/^{238}U$ ratio of this sample was measured three times:

- first using 80 % of the original sample solution spiked with IRMM-3636 and passed through the column chemistry once. All isotopes were measured using Faraday cups (Faraday setup in Table 4.8)
- then using $\sim$ 10 % of the original sample solution, non-spiked, and passed through column chemistry twice. The low abundance isotope ^{235}U was measured using the Secondary Electron Multiplier (SEM) collector (SEM setup in Table 4.8)

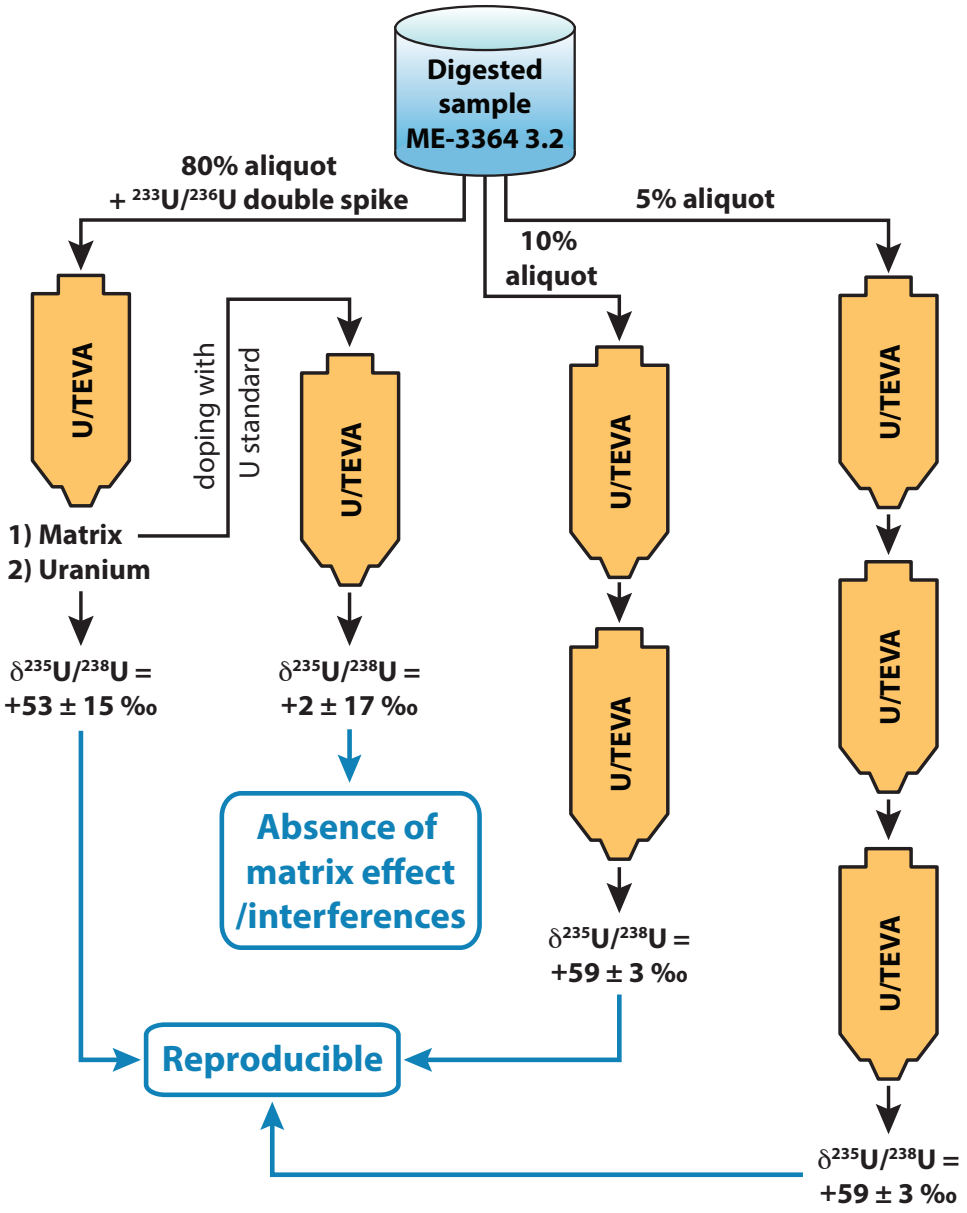

Figure 4.27: Flow chart of the tests conducted on CAI ME-3364-3.2. An 80 % aliquot of the sample was spiked with IRMM-3636a (^{233}U/^{236}U double spike) and purified by column chemistry once. Analysis was done on a Neptune MC-ICPMS with ^{238}U (10^{11} Ω) and ^{235}U (10^{12} Ω) on Faraday cups. The matrix of the sample (all elements but U) was doped with U standard CRM-112a, then subjected to one step of purification and analyzed to quantify potential matrix effects. The remaining 20 % of the sample was split in two halves, purified two and three times, respectively. Analysis was done with ^{238}U (10^{11} Ω) on a Faraday cup and ^{235}U on the SEM. All measurements yielded identical values (within uncertainties). Figure submitted in [432].

- and finally using ~ 5 % of the original sample solution, non-spiked, and passed through column chemistry three times. The low abundance isotope ^{235}U was measured using the SEM setup.

Despite important differences in the protocols of chemical purification and isotopic analysis, all three measurements yielded identical results (within uncertainties). This demonstrates that the large ^{235}U excess measured in CAI ME-3364-3.2 is real. This conclusion is strengthened by the fact that after three column passes, the acid chemistry blank was high enough (~ 0.01 ng of U) for its ^{235}U/^{238}U ratio to be measured using the SEM setup. The blank composition was found to be indistinguishable from that of natural U ($+0.8 \pm 9.2$ ‰).

4.3.5 The initial abundance of ^{247}Cm in the ESS

4.3.5.1 Evidence for ^{247}Cm in the ESS

The finding of such a large excess of ^{235}U in a normal (non-FUN) CAI can only be explained by decay of ^{247}Cm into ^{235}U. Below we examine other processes that could potentially lead to U isotope variations in ESS materials and show that they all suffer from serious shortcomings:

1. Isotopic fractionation during secondary processes (*e.g.*, aqueous alteration and/or redox processes) either on the meteorite parent body or on Earth, can impart large isotopic fractionation to light elements (such as Li). The degree of fractionation, however, generally decreases as the mass of the element increases, and for U on Earth, the largest variations are limited to $\sim 1.5 - 2$ ‰ [431]. Though this process could lead to some scatter in the data around the isochron, it cannot explain a 59 ‰ anomaly.

2. Large isotopic variations of nucleosynthetic origin have been documented for refractory elements in CAIs, and are usually readily identified as departures from mass-dependent fractionation. For U, which possesses only two stable isotopes, it is impossible to distinguish between ^{247}Cm decay and nucleosynthetic anomalies. Nevertheless, considering

that anomalies on the order of tens of ‰ in neutron rich isotopes (*e.g.*, ^{50}Ti, ^{54}Cr) are only found in FUN CAIs, and given that CAI ME-3364-3.2 (δ^{238}U $\sim$ 59 ‰) is not a FUN CAI as shown by the small ^{50}Ti anomaly ($\sim$ +0.9 ‰), the large ^{235}U-excess found here cannot be reasonably ascribed to the presence of nucleosynthetic anomalies.

3. Lastly, U isotopic fractionation could be the result of fractionation during evaporation/condensation processes. During condensation, the light isotope of U condenses faster, leading to a large ^{235}U depletion in the condensing gas and the instantaneous solid, but ^{235}U excesses limited to +6 ‰ (Fig. 1.6). Similarly, during evaporation, the highest ^{235}U excess predicted by the kinetic theory of gases is limited to $\sim$ 6 ‰. Consequently, evaporation/condensation processes cannot explain the 59 ‰ ^{235}U-excess observed in CAI ME-3364-3.2, which leaves ^{247}Cm-decay as the only possible explanation.

4.3.5.2 The ^{247}Cm/^{235}U chronometer

The 59 ‰ ^{235}U excess discovered in CAI ME-3364-3.2 is definitive evidence that ^{247}Cm was alive in the ESS. From this excess, knowledge of the initial abundance of ^{247}Cm at the time of formation of CAI ME-3364-3.2 can be gained, as is shown below.

The Cm/U chronometer is based on the decay of ^{247}Cm into ^{235}U, which decays ultimately into ^{207}Pb [46, 103, 414]. Calculation of the abundance of ^{235}U at any given time can be obtained by solution of a differential equation of the kind commonly used in U-series studies [54]:

$$\frac{d^{235}\mathrm{U}}{dt} = -\lambda_{235}\ {}^{235}\mathrm{U} + \lambda_{247}\ {}^{247}\mathrm{Cm} \tag{4.1}$$

Solving this equation gives the present day cosmic abundance of ^{235}U, denoted ^{235}U$_\mathrm{P}$, as:

$$^{235}\mathrm{U_P} = {}^{247}\ \mathrm{Cm}_0 \left(\frac{\lambda_{247}}{\lambda_{235} - \lambda_{247}}\right)\left(e^{-\lambda_{247}t} - e^{-\lambda_{235}t}\right) + {}^{235}\ \mathrm{U}_0 e^{-\lambda_{235}t} \tag{4.2}$$

where the subscript P stands for present, the subscript 0 denotes the initial number of atoms at the time t of closure of the system, and λ_i the decay constant of the isotope i. The first term on the RHS of Eq. (4.2) represents the contribution of ^{247}Cm to the total ^{235}U content, while the second term on the RHS represents the contribution of the initial amount of ^{235}U in the sample at the start of the Solar System. Equation (4.2) can be divided by the present cosmic abundance of ^{238}U, equal to $^{238}\mathrm{U_P} = {}^{238}\mathrm{U}_0 e^{-\lambda_{238} t}$, to obtain:

$$\left(\frac{^{235}\mathrm{U}}{^{238}\mathrm{U}}\right)_{\mathrm{smp,P}} = \frac{^{247}\mathrm{Cm}_{\mathrm{smp,0}}}{^{238}\mathrm{U}_{\mathrm{smp,P}}} \left(\frac{\lambda_{247}}{\lambda_{235} - \lambda_{247}}\right) \left(e^{-\lambda_{247} t} - e^{-\lambda_{235} t}\right) + \left(\frac{^{235}\mathrm{U}}{^{238}\mathrm{U}}\right)_{\mathrm{smp,0}} \frac{e^{-\lambda_{235} t}}{e^{-\lambda_{238} t}} \quad (4.3)$$

where the subscript "smp" stands for "sample". Cm having no stable isotopes, a stable isotope proxy needs to be used in order to build an isochron. As discussed in Section (4.3.3.2) Nd or Sm are two elements that are thought to behave like Cm during nebular processes [64]. In the following, we use ^{144}Nd as in most previous studies. Eq. (4.3) thus becomes:

$$\left(\frac{^{235}\mathrm{U}}{^{238}\mathrm{U}}\right)_{\mathrm{smp,P}} = \left(\frac{^{247}\mathrm{Cm}}{^{144}\mathrm{Nd}}\right)_{\mathrm{smp,0}} \left(\frac{\lambda_{247}}{\lambda_{235} - \lambda_{247}}\right) \left(e^{-\lambda_{247} t} - e^{-\lambda_{235} t}\right) \left(\frac{^{144}\mathrm{Nd}}{^{238}\mathrm{U}}\right)_{\mathrm{smp,P}} + \left(\frac{^{235}\mathrm{U}}{^{238}\mathrm{U}}\right)_{\mathrm{smp,0}} \frac{e^{-\lambda_{235} t}}{e^{-\lambda_{238} t}} \quad (4.4)$$

Assuming that Cm is not chemically fractionated from Nd (*i.e.*, Nd is a valid proxy for Cm, and therefore $(\mathrm{Cm/Nd})_{\mathrm{smp}} = (\mathrm{Cm/Nd})_{\mathrm{solar}}$) and that all samples form with the same initial U isotopic composition, Eq. (4.4) can be rewritten:

$$\left(\frac{^{235}\mathrm{U}}{^{238}\mathrm{U}}\right)_{\mathrm{smp,P}} = \left(\frac{^{247}\mathrm{Cm}}{^{144}\mathrm{Nd}}\right)_{\mathrm{solar,0}} \left(\frac{\lambda_{247}}{\lambda_{235} - \lambda_{247}}\right) \left(e^{-\lambda_{247} t} - e^{-\lambda_{235} t}\right) \left(\frac{^{144}\mathrm{Nd}}{^{238}\mathrm{U}}\right)_{\mathrm{smp,P}} + \left(\frac{^{235}\mathrm{U}}{^{238}\mathrm{U}}\right)_{\mathrm{solar,0}} \frac{e^{-\lambda_{235} t}}{e^{-\lambda_{238} t}} \quad (4.5)$$

Introducing an arbitrary reference nuclide X (^{235}U in Fig. 4.25 and 4.29), one gets:

$$\left(\frac{^{235}\mathrm{U}}{^{238}\mathrm{U}}\right)_{\mathrm{smp,P}} = \left(\frac{^{247}\mathrm{Cm}}{\mathrm{X}}\right)_{\mathrm{solar},0} \left(\frac{\mathrm{X}}{^{144}\mathrm{Nd}}\right)_{\mathrm{solar},0} \left(\frac{\lambda_{247}}{\lambda_{235}-\lambda_{247}}\right) \times \left(e^{-\lambda_{247}t} - e^{-\lambda_{235}t}\right) \left(\frac{^{144}\mathrm{Nd}}{^{238}\mathrm{U}}\right)_{\mathrm{smp,P}} + \left(\frac{^{235}\mathrm{U}}{^{238}\mathrm{U}}\right)_{\mathrm{solar},0} \frac{e^{-\lambda_{235}t}}{e^{-\lambda_{238}t}} \quad (4.6)$$

Given that ^{247}Cm has a short half-life compared to ^{235}U (*i.e.*, $\lambda_{247} >> \lambda_{235}$), Eq. (4.6) can be simplified to:

$$\left(\frac{^{235}\mathrm{U}}{^{238}\mathrm{U}}\right)_{\mathrm{smp,P}} = \left(\frac{^{247}\mathrm{Cm}}{\mathrm{X}}\right)_{\mathrm{solar},0} \left(\frac{\mathrm{X}}{^{144}\mathrm{Nd}}\right)_{\mathrm{solar},0} e^{-\lambda_{235}t} \left(\frac{^{144}\mathrm{Nd}}{^{238}\mathrm{U}}\right)_{\mathrm{smp,P}} + \left(\frac{^{235}\mathrm{U}}{^{238}\mathrm{U}}\right)_{\mathrm{solar},0} \frac{e^{-\lambda_{235}t}}{e^{-\lambda_{238}t}} \quad (4.7)$$

This last formula was used by earlier studies [414, 415, 71]; however, it leads to a systematic error of 2.2 % on the initial $\left(^{247}\mathrm{Cm}/\mathrm{X}\right)_{\mathrm{solar},0}$, so Eq. (4.6) was retained for all calculations in this work.

Equation (4.6) describes the isochron that ESS samples should follow, had ^{247}Cm been alive at the start of the SS. From the slope of the isochron (Eq. 4.8),

$$\mathrm{Slope} = \left(\frac{^{247}\mathrm{Cm}}{\mathrm{X}}\right)_{\mathrm{solar},0} \left(\frac{\mathrm{X}}{^{144}\mathrm{Nd}}\right)_{\mathrm{solar},0} \left(\frac{\lambda_{247}}{\lambda_{235}-\lambda_{247}}\right) \left(e^{-\lambda_{247}t} - e^{-\lambda_{235}t}\right), \quad (4.8)$$

the initial abundance of ^{247}Cm at the time of closure of the samples can be calculated, while the intercept (Eq. 4.9),

$$\mathrm{Intercept} = \left(\frac{^{235}\mathrm{U}}{^{238}\mathrm{U}}\right)_0 e^{(\lambda_{238}-\lambda_{235})t}, \quad (4.9)$$

provides the initial $^{235}\mathrm{U}/^{238}\mathrm{U}$ ratio in the ESS.

Using the data from this work (Table 4.9) the initial ratio at the time of U depletion in CAI ME-3364-3.2 is calculated as $(^{247}\mathrm{Cm}/^{235}\mathrm{U}) = (0.92 \pm 0.07) \times 10^{-4}$.

The error on the slope was calculated as follows. The slope of the isochron is mostly

constrained by the coordinate (x_2, y_2) of CAI ME-3364-3.2, and the cluster of CAIs at low $^{144}Nd/^{238}U$ ratio. Using the coordinate of the bulk Allende measurement, (x_1, y_1), as the anchoring point in the cluster ($^{144}Nd/^{238}U = 12.24 \pm 1.49$ and $\delta^{235}U = 0.49 \pm 0.16$ ‰), the slope, a, can be calculated as:

$$a = \frac{y_2 - y_1}{x_2 - x_1} \tag{4.10}$$

Under the assumption that only the error on the coordinates of CAI ME-3364-3.2, $(\sigma_{x_2}, \sigma_{y_2})$, are influencing the error on the slope (a valid assumption given that the uncertainties associated with the Allende coordinates, $(\sigma_{x_1}, \sigma_{y_1})$, are small in comparison), the error on the slope, σ_a, is simply calculated as:

$$\sigma_a = a \times \sqrt{\left(\frac{\sigma_{y_2}}{y_2 - y_1}\right)^2 + \left(\frac{\sigma_{x_2}}{x_2 - x_1}\right)^2} \tag{4.11}$$

An identical slope, and associated uncertainty, is obtained if the scatter in the data is assumed to come, not from the measurement, but from another source of error (*e.g.*, the samples did not form exactly at the same time, and therefore do not define a perfect isochron). In this case, a constant error, σ_c, can be added to the uncertainty on the $\delta^{238}U$ value, and adjusted until the MSWD of the isochron is brought back to 1 (*i.e.*, the samples are part of the same population, statistically speaking).

4.3.5.3 Initial *vs.* Early Solar System $^{247}Cm/^{235}U$: closure age

Even though the samples with low $^{144}Nd/^{238}U$ ratios define a trend with $\delta^{235}U$, the slope of the isochron in Fig. (4.25) is mainly leveraged by CAI ME-3364-3.2 ($^{144}Nd/^{238}U$ ratio $\sim$ 13720). The initial $^{247}Cm/^{235}U$ ratio of $(0.92 \pm 0.07) \times 10^{-4}$ thus corresponds to the time when this CAI acquired its high $^{144}Nd/^{238}U$ ratio. Terrestrial alteration is ruled out because the Allende meteorite is an observed fall that did not experience much terrestrial weathering. The extreme uranium depletion in CAI ME-3364-3.2 is thus most likely due to solar nebula condensation and/or nebular/parent body alteration.

All fine-grained CAIs in this study display a typical group II REE pattern (Fig. 4.21), thought to represent a snapshot in time and space of the condensation sequence [63, 140]. The most refractory REEs (heavy REEs except Tm and Yb) are depleted in these CAIs because they were sequestered in ultrarefractory dust such as perovskite [140] or hibonite [267], while the more volatile REEs (Eu, Yb) and uranium are also depleted, as they stayed in the gas phase when those CAIs formed. In most samples, U and Yb present similar levels of depletion relative to solar composition and the abundance of other refractory lithophile elements (Fig. 4.28), indicating that those two elements have similar behavior during evaporation/condensation processes under solar nebula conditions. This is in good agreement with the microscale distribution of U and Th in Allende CAIs, which indicates that loss or gain of U in CAIs are unimportant, and that the abundance of U in CAIs is instead mostly controlled by the volatility of U [306]. In CAI ME-3364-3.2, however, the U/Nd ratio is 1000 times lower than solar composition, while the Yb/Nd ratio is only depleted by a factor of 50. If U and Yb have similar behavior during condensation, one would expect the U/Nd ratio to be 50 times lower than solar, not 1000 times as is observed. Compared to other fine-grained CAIs analyzed, ME-3364-3.2 is peculiar in that it is extremely altered, which is manifested by the extensive replacement of high-T phases by low-T alteration products such as nepheline and sodalite (its Na_2O is 15 wt% when other CAIs are all lower than 6.7 wt%; Table 4.6). Such alteration may have mobilized U, producing a twentyfold U depletion on top of the fiftyfold depletion associated with condensation.

Some of these alteration products could have formed (i) in the nebula, (ii) on an earlier generation of water-rich asteroid, (iii) or during aqueous alteration on Allende itself (*e.g.*, [373, 380, 421] and references therein). Regardless of the location, dating of aqueous alteration products on meteorite parent bodies with extinct radionuclides ^{36}Cl ($t_{1/2}$ = 0.301 Myr), ^{26}Al ($t_{1/2}$ = 0.717 Myr), ^{53}Mn ($t_{1/2}$ = 3.74 Myr) or ^{129}I ($t_{1/2}$ = 15.7 Myr) suggests it took place no later than 10 Myr after SS formation. This is a conservative upper limit as secondary alteration phases in fine-grained inclusions may have formed very early in the

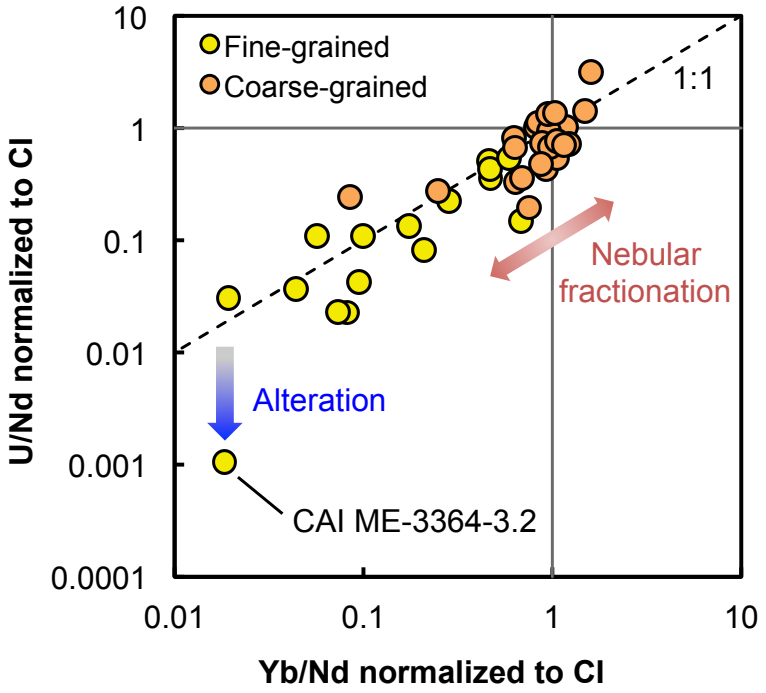

Figure 4.28: Correlation between U and Yb abundances relative to solar composition and the abundance of Nd (a refractory lithophile element) (data from [186, 187, 274] and this study). This correlation indicates that those two elements have similar behavior during evaporation/condensation processes under solar nebula conditions. CAI ME-3364-3.2 plots off the 1:1 line, with a CI-normalized U/Nd ratio 20 times lower than that of Yb/Nd. This CAI is extremely altered, (see Table 4.6), and such alteration may have mobilized U, producing a twentyfold U depletion on top of the fiftyfold depletion associated with condensation. Figure submitted in [432].

nebula. The half-life of ^{247}Cm is 15.6 Myr, meaning that a time-span of $\sim 5 \pm 5$ Myr between SS formation and CAI alteration (and possible U depletion) translates into a correction for the initial ^{247}Cm/^{235}U ratio of 25 ± 25 % (the uncertainty on this factor takes into account the uncertainty on the closure age). The present best estimate of the initial Solar System ^{247}Cm/^{235}U is thus (Fig. 4.29)

$$\left(\frac{^{247}\mathrm{Cm}}{^{235}\mathrm{U}}\right)_{\mathrm{ESS}} = (1.1 \pm 0.3) \times 10^{-4}, \tag{4.12}$$

equivalent to $(^{247}\mathrm{Cm}/^{238}\mathrm{U})_{\mathrm{ESS}} = (3.7 \pm 0.9) \times 10^{-5}$ and $(^{247}\mathrm{Cm}/^{232}\mathrm{Th})_{\mathrm{ESS}} = (1.6 \pm 0.4) \times 10^{-5}$. This value is in agreement with the $(^{247}\mathrm{Cm}/^{235}\mathrm{U})_{\mathrm{ESS}}$ value of $(1.1 - 2.4) \times 10^{-4}$

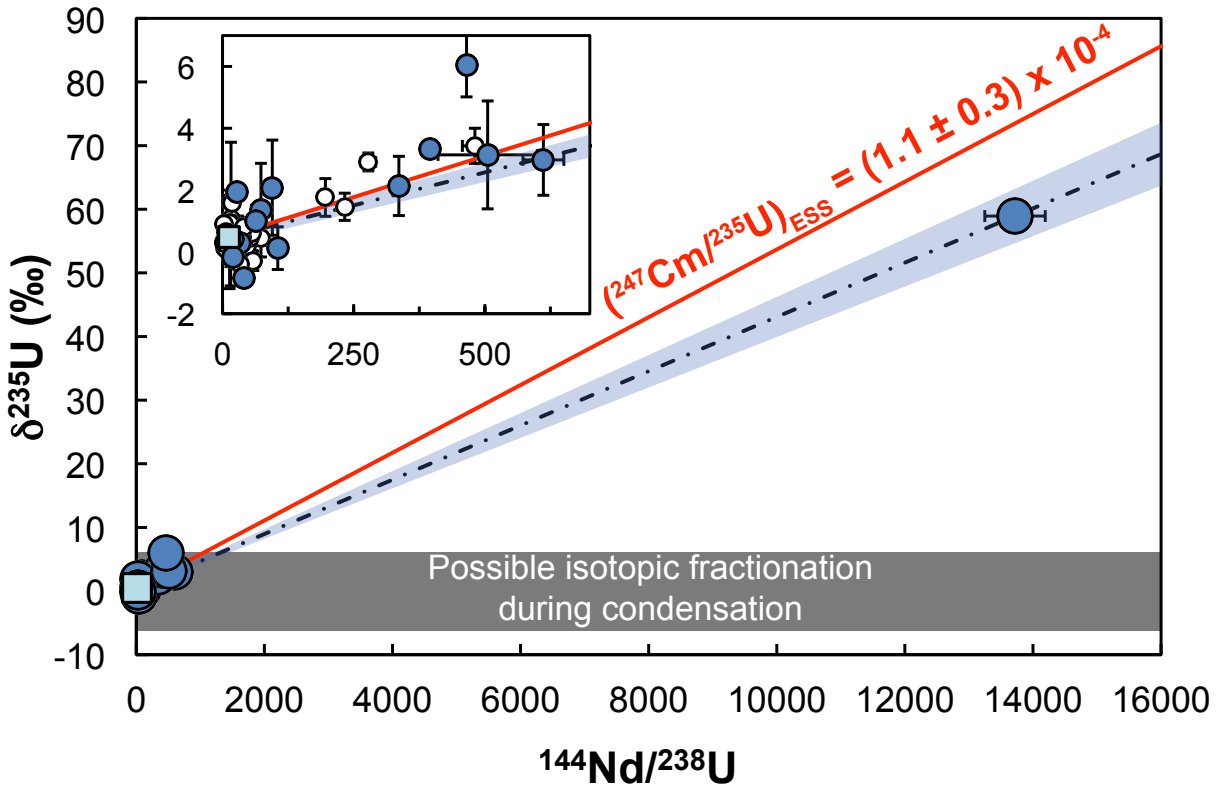

Figure 4.29: Same as Fig. (4.25). Accounting for a possible $\sim 5 \pm 5$ Myr delay between SS formation and Nd/U fractionation in CAI ME-3364-3.2 (possibly related to extensive alteration of this CAI), the inferred $(^{247}\mathrm{Cm}/^{235}\mathrm{U})$ ratio in the ESS is $(1.1 \pm 0.3) \times 10^{-4}$. The corresponding isochron is plotted (red line). Figure submitted in [432].

obtained by [71] based on CAI measurements and an upper limit of $\sim 4 \times 10^{-3}$ inferred from earlier meteoritic measurements [103]. It is also in line with what is predicted from modeling of Galactic Chemical Evolution (GCE) [312]: $(5.0 \pm 2.6) \times 10^{-5}$.

The initial estimate derived in this study is slightly higher than the upper limit of $(^{247}\mathrm{Cm}/^{235}\mathrm{U})_{\mathrm{ESS}} \leq 7.7 \times 10^{-5}$ derived from meteorite leachates [414, 415]. Chemical leachate studies, however, can incongruently digest some minerals and the Nd/U ratio measured in those leachates can be fractionated. This has been documented before with Mn-Cr and Re-Os systematics of leachates, which give disturbed isochrons with little age significance.

4.3.5.4 Evidence for fractionation of U "stable" isotopes during evaporation/condensation

Some of the samples with low $^{144}Nd/^{238}U$ ratios show significant scatter around the isochron (see inset Fig. 4.29) outside of analytical uncertainties. In particular, samples with $^{144}Nd/^{238}U$ ratio as low as ~ 20 span a range of $\delta^{235}U$ values of 3.5 ‰, a feature that led previous workers [14, 119] to question the conclusion of Brennecka et al. [71] that ^{247}Cm was responsible for U isotope variations. Such isotopic variations can be due to several processes that are examined here.

1. As discussed in Section 4.3.5.1, U isotopic fractionation during aqueous alteration and/or redox processes result in fractionations of only $\sim 1.5 - 2$ ‰ [431], and is therefore unlikely to explain a 3.5 ‰ spread in the $^{235}U/^{238}U$ ratio of samples with chondritic Nd/U ratio (*i.e.*, where no U gain/loss occurred).

2. Nd and/or U remobilization during secondary processes could affect the CAIs so that the closure age of fine-grained CAIs is not uniquely defined. This is unlikely to be the cause of the observed scatter because the fine-grained CAIs in this study are characterized by typical group II REE patterns and, except for CAI ME-3364-3.2, U follows Yb quite well (Fig. 4.28). Therefore, the Nd/U fractionation must be primarily controlled by the difference in volatility of Nd and U rather than by secondary elemental mobilization. This hypothesis would also not explain why some CAIs have $\delta^{235}U$ values that are lower than the average SS composition.

3. Heterogeneous distribution of ^{247}Cm could result in U isotopic variations in ESS materials. Extinct radionuclides with short half-lives are more likely to display heterogeneity in SS materials because their abundances in the interstellar medium are low and easily dominated by the contribution of one or several massive stars. Yet, it is highly unlikely that CAIs would display sample-to-sample heterogeneity in their ^{247}Cm abundance, given that the half-life of ^{247}Cm (15.6 Myr) is three times larger than the threshold

($\sim$ 5 Myr) below which heterogeneity is thought to become a concern [294]. For comparison, ^{182}Hf has a half-life of 8.90 Myr and all available evidence suggests that it was uniformly distributed in the ESS [211].

4. Nucleosynthetic anomalies are also unlikely to result in large U isotope variations in non-FUN CAIs, especially in samples with higher-than-chondritic U abundances.

5. U isotopic fractionation can finally be the product of evaporation/condensation processes. As shown in Fig. (1.6), such processes would naturally create fractionation of up to +6.3 ‰ in the condensate, and negative anomalies in the residual gas and instantaneous solid, as condensation proceeds.

Given (i) the fact that CAIs with chondritic Nd/U ratios show ^{235}U anomalies both positive and negative relative to the average SS value, (ii) the low likelihood for most of the above processes to result in significant isotopic fractionation, and (iii) the scale of the variations expected from fractionation during condensation, it is most likely that the scatter around the isochron observed in the data (especially at low Nd/U ratios, Fig. 4.29), is due to fractionation during evaporation/condensation processes. This suggests that better isochronous behavior could be obtained if such fractionation could be corrected for.

4.3.6 Implications for the r-process

In addition to the dating implications that large ^{235}U/^{238}U variations have on the Pb-Pb ages of the CAIs (see Section 3.2, Chapter 3), the existence of ^{247}Cm in the ESS has implications for the nucleosynthesis of r-process elements.

4.3.6.1 Galactic Chemical Evolution and Short-Lived Radionuclides

Galactic Chemical Evolution (GCE) models describe the spatial and temporal evolution of the chemical composition of a galaxy, as successive generations of stars enrich the interstellar medium (ISM) with the products of nucleosynthesis (*e.g.*, [110, 321, 312]). Models of

GCE take as input a relatively small number of parameters: (i) the initial composition of the Galaxy, (ii) the abundances of the isotopes produced during nucleosynthetic reactions (the so-called *stellar yields*), (iii) the star formation rate, which is often taken as being a function of the gas surface density of the disk, (iv) the number distribution of stars forming in a given mass range per unit of time (the so-called *initial mass function*), which is often assumed to be constant in both space and time, and (v) whether infall of gas from the halo onto the galactic disk and outflows from the galactic winds occur (*i.e.*, open- or closed-system behavior).

The outputs of GCE models of the Milky Way have to match a certain number of observables. Namely, (i) the abundance of elements in the ESS, which represent a snapshot of the composition of the ISM, 4.567 Gyr ago, (ii) the evolution of stellar metallicity with time (the so-called *age-metallicity relationship*), (iii) the time evolution of abundance ratios of elements produced by different nucleosynthetic processes, which places constraints on the stellar environment of these processes, (iv) the abundance gradients observed in the Milky Way, and (v) the metallicity distribution of G-dwarfs, which are low mass stars, (*i.e.*, $\sim 0.9 - 1.1\times$ the mass of the Sun) with lifetimes greater than the age of the galactic disk, and whose envelope compositions represent the composition of the ISM at the time of their formation. The metallicity distribution of G-dwarfs represents the evolution of the star formation rate since the Galaxy formed, and any realistic GCE model must fit this key parameter.

Numerous analytical and numerical GCE models have been developed. The simplest GCE model that successfully reproduces the metallicity distribution of G-dwarfs in the Galaxy requires an infall of gas onto the galactic disk (*i.e.*, open-system, [312, 110, 135]). In such a model, the abundance ratio of an SLR normalized to a stable nuclide is:

$$\left(\frac{\mathrm{N_{SLR}}}{\mathrm{N_{Stable}}}\right)_{\mathrm{ISM}} = \left(\frac{\mathrm{P_{SLR}}}{\mathrm{P_{Stable}}}\right)\frac{(\mathrm{k}+1)\tau}{\mathrm{T}} \tag{4.13}$$

where N is the abundance, P is the production rate, τ is the mean life of the SLR ($\tau = 1/\lambda$),

T is the age of the galaxy at the time when the ratio N_{SLR}/N_{Stable} is to be calculated, and k is a constant that distinguishes closed-box (k=0) from infall models (typically, $k = 2 \pm 1$) (8, 23-25). If T is taken as the presolar age of the galaxy, T* (= $T_G - T_{SS}$ = 8.7 Gyr), then the ratio N_{SLR}/N_{Stable} in the ISM at the time of isolation of the protosolar molecular cloud from fresh nucleosynthetic input can be calculated. This value can be compared to the N_{SLR}/N_{Stable} ratio in the ESS as obtained from meteoritic measurements. The difference between the two values is often interpreted as a "free-decay interval", Δ, between the last nucleosynthetic event that produced the SLR and the formation of the SS:

$$\left(\frac{N_{SLR}}{N_{Stable}}\right)_{ESS} = \left(\frac{N_{SLR}}{N_{Stable}}\right)_{ISM} e^{\left(-\frac{\Delta}{\tau}\right)} \tag{4.14}$$

At present, the meteoritic abundances of only three short-lived *r*-nuclides (^{129}I, ^{182}Hf, ^{244}Pu) have been estimated, yielding three different Δ values (100 ± 7 Myr, ~ 35 Myr, and 158 ± 85 Myr, respectively) [129]. The limit of our understanding of the *r*-process is well illustrated by the fact that there have been as many *r*-processes proposed as short-lived *r*-nuclides investigated.

Incorporating the new information brought by the ESS abundance of ^{247}Cm in this picture can help constrain the number of *r*-processes. The open, non-linear model of Clayton (1988) [111] and Dauphas et al. (2003) [135], is used with k= 1.7 ± 0.4 and a presolar age of the galaxy of 8.7 Gyr. These parameters were chosen in order to reproduce the G-dwarf metallicity distribution. The only missing input parameters to predict the steady-state abundance of the elements in the ISM are the production ratios.

4.3.6.2 Production ratios

The estimation of production ratios is difficult, especially for elements that are produced by the *r*-process, as their predicted abundances depend on the nuclear mass function and anchoring of the model results to SS stable isotope abundances, which are missing for actinides

(the closest stable isotope to the actinides is ^{209}Bi).

To assess the robustness of the production ratios to be used in this study, compilation and comparison of data from several recent studies was done (Table 4.12). There is typically a factor of 2-3 difference between the various models. When the production ratios from the various studies agreed within an order of magnitude, the mid-range value was used as the production ratio value (*i.e.*, [Max + Min]/2) with the error reaching to the min and max values. Otherwise, a best estimate was taken, and an arbitrary uncertainty of 50 % was assigned to this production ratio (see caption of Table 4.12 for details). In the case of ^{182}Hf, the protocol designed by Meyer and Clayton (2000) [294] was followed: the best estimate production ratio (^{182}Hf/^{177}Hf = 0.55) was calculated using the decomposition into *s*- and *r*-process components of its daughter isotope ^{182}W and the model of Bisterzo et al. (2014) [45].

Nuclide	τ = 1/λ (Myr)	Norm.	Meyer & Clayton 2000	Jacobsen 2005	Nittler and Dauphas 2006	Huss et al., 2009	Lugaro et al. 2014	**Best estimate**	Refs.[a]
Beryllium-10	2.16	9Be							
Aluminum-26	1.07	27Al	0.004	5.4E-03		0.02		**1.1E-02 ± 7E-03**	*
Chlorine-36	0.434	35Cl	0.0065			0.03		**1.8E-02 ± 1.1E-02**	*
Calcium-41	0.144	40Ca	0.003	1.0E-03		0.003		**2E-03 ± 1E-03**	*
Manganes-53	5.34	55Mn	0.13	0.19	0.13	0.85		**0.15 ± 0.08**	**,[b]
Iron-60	2.16	56Fe	0.00003	1.2E-04		0.0001		**7.5E-05 ± 4.5E-05**	*
Niobium-92	50.1	92Mo			0.0015 ± 0.0006			**1.5E-03 ± 6E-04**	
Palladium-107	9.38	108Pd	0.65	1.50		1.29	2.09	**1.37 ± 0.72**	*
Palladium-107	9.38	110Pd^{r}			1.36			**1.36 ± 0.68**	***
Iodine-129	23.1	127I	1.40	2.00		1.84		**1.70 ± 0.30**	*
Iodine-129	23.1	127I^{r}			1.45		1.35	**1.40 ± 0.70**	**
Samarium-146	149	144Sm	0.1	0.95	0.18 ± 0.06	3.05		**0.14 ± 0.07**	**,b,c
Hafnium-182	13	177Hf^{r}			0.81			**0.55 ± 0.27**	A ***
Hafnium-182	13	180Hf	0.21	0.37		0.43	0.91	**0.56 ± 0.35**	*
Plutonium-244	117	238U			0.53 ± 0.36			**0.53 ± 0.36**	B
Plutonium-244	117	232Th	0.7	0.67	0.32 ± 0.27	1.33		**0.32 ± 0.27**	B
Curium-247	22.5	235U			0.281 ± 0.165		0.40	**0.341 ± 0.170**	**
Curium-247	22.5	238U			0.159 ± 0.075			**0.159 ± 0.075**	B
Curium-247	22.5	232Th			0.098 ± 0.052			**0.098 ± 0.052**	B

The superscript r refers to the r-process component of the cosmic abundance, obtained after subtracting the s-process contribution from the solar abundances, from Bisterzo et al. (2014). Note that Nittler and Dauphas (2006) used the decomposition of Arlandini et al. (1999). The esitmatation of the r component of 182W is significantly different in the two studies.

[b] The value from Huss et al. (2009) is not used.

[c] The value from Jacobsen (2005) is not used.

*The best estimate is taken as the mid-range value from the four studies compiled in this table, with the errors reaching to the min. and max. values.

**The best estimate is taken as the average value from the four studies compiled in this table, with 50% relative uncertainty.

Table 4.12: Production ratios of SLRs present in the ESS normalized to a stable isotope produced in the same or similar nucleosynthetic process. Data from [294, 224, 312, 220, 259]. Note: (A) the best estimate of the ^{182}Hf/^{177}Hf^{r} production ratio is calculated as the ratio of the *r*-component of ^{182}W to ^{177}Hf using the values from [45]; (B) Only the models giving a ^{232}Th/^{238}U production ratio consistent with the production ratio inferred from meteoritic measurements (1.75 +1.10/-1.01, [130]) are considered, (*i.e.*, cases 1, 3-4, 7-9, 13, 20 ,22 and 30 in Table 1 and 2 of [178]). Table submitted in [432].

The normalizing isotopes shown in Table 4.12 are the ones used in the studies being compared. Since what is being considered is the *production ratio* of two nuclides produced in a single nucleosynthetic process, it is preferable that the normalizing nuclide be one produced by the same process as the SLR being investigated. For instance, ^{110}Pd, ~ 96 % of whose abundance in the SS is due to the r-process, is to be preferred to ^{108}Pd, only 35 % of which is made in the r-process.

To be consistent, only the r-component of the normalizing isotope should be used when calculating the ESS abundance ratio. This will allow proper comparison of the abundance ratio N_{SLR}/N_{Stable} in the ESS to the production ratio P_{SLR}/P_{Stable}. Continuing with the example of palladium, the relationship between the $^{107}Pd/^{110}Pd^{r}$ ratio and the $^{107}Pd/^{110}Pd$ ratio is simply:

$$\left(\frac{^{107}\mathrm{Pd}}{^{110}\mathrm{Pd}^{r}}\right)_{\mathrm{ESS}} = \left(\frac{^{107}\mathrm{Pd}}{^{110}\mathrm{Pd}}\right)_{\mathrm{ESS}} \times \frac{\mathrm{N}^{110}\mathrm{Pd}}{\mathrm{N}^{110}\mathrm{Pd}^{r}} \tag{4.15}$$

where N is the solar abundance of the isotope considered, and the superscript r denotes the r-process component (see, for instance, the models of Arlandini et al. (1999) and Bisterzo et al. (2014) [27, 45]).

4.3.6.3 Free-decay interval

In the simplest approach, the difference between the ratio N_{SLR}/N_{Stable} in the ISM and ESS is due to a "free-decay" interval, Δ, during which the protosolar molecular cloud is isolated from further nucleosynthetic input and the various SLRs freely decay.

Using the ratio of $(^{247}Cm/^{232}Th)_{ESS} = (1.6 \pm 0.4) \times 10^{-5}$ obtained in this work leads to a "free-decay interval", $\Delta = 87 \pm 14$ Myr. In Table 4.13, this value is compared to earlier experimental and theoretical estimates from [414, 415, 71, 312].

There is a general agreement between all studies on the initial abundance of ^{247}Cm in the ESS, and thus, on the free-decay interval obtained using this SLR. The chronometric information obtained from curium can now be compared to the information obtained using

Compilation of Cm/U isochron data and free decay interval data from experimental and theoretical studies.

	Stirling et al. 2005	Stirling et al. 2006	Brennecka et al. 2010	This work	Theoretical lower limit
δ^{238}U vs ^{144}Nd/^{238}U intercept	0.0072512 ± 1.9E-06	0.0072512 ± 1.2E-06	0.0072541 ± 7E-07	0.0072517 ± 1.2E-06	
$(^{235}U/^{238}U)_{ESS}$	0.32111 ± 8.3E-05	0.32111 ± 5.5E-05	0.32124 ± 3.2E-05	0.32113 ± 5.2E-05	
δ^{238}U vs ^{144}Nd/^{238}U slope	< 3.3E-08	< 2.6E-08	3.7E-08 ± 7E-09	3.1E-08 ± 2E-09	> 1.7E-08 ± 9E-09
$(^{247}Cm/^{144}Nd)_{INITIAL}$				2.7E-06 ± 1.9E-07	
$(^{247}Cm/^{235}U)_{INITIAL}$				9.2E-05 ± 6.5E-06	
$(^{247}Cm/^{238}U)_{INITIAL}$				3.0E-05 ± 2.1E-06	
$(^{247}Cm/^{232}Th)_{INITIAL}$				1.3E-05 ± 9.0E-07	
Assuming alteration occurred at t (Myr)				5 ± 5	
$(^{247}Cm/^{144}Nd)_{ESS}$	< 2.9E-06	< 2.3E-06	3.3E-06 ± 6E-07	3.4E-06 ± 8E-07	> 1.5E-06 ± 8E-07
$(^{247}Cm/^{235}U)_{ESS}$	< 9.8E-05	< 7.7E-05	1.1E-04 ± 2E-05	1.1E-04 ± 3E-05	> 5.0E-05 ± 2.6E-05
$(^{247}Cm/^{238}U)_{ESS}$	< 3.2E-05	< 2.5E-05	3.5E-05 ± 6E-06	3.7E-05 ± 9E-06	> 1.6E-05 ± 8E-06
$(^{247}Cm/^{232}Th)_{ESS}$	< 1.4E-05	< 1.1E-05	1.5E-05 ± 3E-06	1.6E-05 ± 4E-06	6.9E-06 ± 4E-06
Using ^{238}U as the normalizing isotope					
R/P $(^{247}Cm/^{238}U_{stable})$ ESS[a]	< 1.4E-04	< 1.1E-04	1.6E-04 ± 8.0E-05	1.7E-04 ± 8.7E-05	7.2E-05 ± 5.0E-05
R/P $(^{247}Cm/^{238}U_{stable})$ ISM[b]	7.0E-03 ± 1.6E-03				
Free decay interval, Δ (Myr)	**> 88**	**> 93**	**85 ± 13**	**84 ± 13**	**103 ± 17**
Using ^{232}Th as the normalizing isotope					
R/P $(^{247}Cm/^{232}Th_{stable})$ ESS[a]	< 1.2E-04	< 9.8E-05	1.4E-04 ± 7.8E-05	1.5E-04 ± 8.4E-05	6.3E-05 ± 4.7E-05
R/P $(^{247}Cm/^{232}Th_{stable})$ ISM[b]	7.0E-03 ± 1.6E-03				
Free decay interval, Δ (Myr)	**> 91**	**> 96**	**88 ± 14**	**87 ± 14**	**< 106 ± 17**
δ^{238}U vs ^{232}Th/^{238}U intercept			0.007255 ± 8.7E-07		
$(^{235}U/^{238}U)_{ESS}$			0.32126 ± 3.9E-05		
δ^{238}U vs ^{232}Th/^{238}U slope			4.7E-07 ± 1.2E-07		
$(^{247}Cm/^{232}Th)_{ESS}$			3.3E-05 ± 8E-06		
$(^{247}Cm/^{235}U)_{ESS}$			2.4E-04 ± 6E-05		
$(^{247}Cm/^{238}U)_{ESS}$			7.7E-05 ± 1.9E-05		
Using ^{238}U as the normalizing isotope					
R/P $(^{247}Cm/^{238}U_{stable})$ ESS[a]			3.5E-04 ± 1.8E-04		
R/P $(^{247}Cm/^{238}U_{stable})$ ISM[b]			7.0E-03 ± 1.6E-03		
Free decay interval, Δ (Myr)			**68 ± 13**		
Using ^{232}Th as the normalizing isotope					
R/P $(^{247}Cm/^{232}Th_{stable})$ ESS[a]			3.0E-04 ± 1.8E-04		
R/P $(^{247}Cm/^{232}Th_{stable})$ ISM[b]			7.0E-03 ± 1.6E-03		
Free decay interval, Δ (Myr)			**71 ± 14**		

The age of the solar system is taken as 4.567 Gyr, and the mean life (1/λ) of ^{247}Cm = 22.5 Myr.
The present abundances of 144Nd (0.197), 232Th (0.0335), 235U (6.48e-5), and 238U (0.0089) are taken from Anders and Grevesse (1989).
The ESS abundances of 232Th (0.04197), 235U (0.00582), and 238U (0.0181) are calculated using λ232=4.93e-11, λ235=9.85e-10 and λ238=1.55e-10 yr^{-1}, respectively.
The production ratios of 247Cm/238U=0.159 ± 0.075 and 247Cm/232Th=0.098 ± 0.052 are taken from Goriely and Arnould (2001). Only the models giving a 232Th/238U production ratio consistent with the production ratio inferred from meteoritic measurements (1.75 +1.10/-1.01, Dauphas, 2005) are considered, (i.e., cases 1, 3-4, 7-9, 13, 20 ,22 and 30 in Table 1 and 2 of Goriely and Arnould (2001)).
[a] Because the isotopes used for nomarlization are not stable (only long-lived), the R/P ratio has to be corrected for the decay of the long-lived isotope. This is done by multiplying the R/P (247Cm/238U) ratio by the N/P ratio of 238U in the ESS (0.71) and the N/P (247Cm/232Th) ratio by the N/P ratio of 232Th in the ESS (0.89). Both values are taken from Nittler and Dauphas (2006).
[b] The N/P ratios in the ISM are calculated using Eq. (2) of the main text (open nonlinear GCE model of Dauphas et al. (2003)), with a k=1.7±0.4 (2σ), and a presolar age of the galaxy Tg=8.7±1.5 Gyr (2σ).

Table 4.13: Compilation of Cm/U isochron data and free-decay interval data from experimental and theoretical studies. Table submitted in [432].

other short-lived r-nuclides. In Table 4.14, a summary of the abundances and production ratios of all SLRs that have been found to be alive in the ESS is presented. For isotopes synthesized by the p-, s-, and r-proceeses, the data are graphically presented in Fig. (4.30).

As can be seen on Fig. (4.30), the value of $\Delta = 87 \pm 14$ Myr obtained from ^{247}Cm is in good agreement with the Δ value of ~ 100 Myr derived from ^{129}I and ^{244}Pu but is much longer then the value of ~ 35 Myr obtained from ^{107}Pd and ^{182}Hf. If ^{107}Pd and ^{182}Hf are indeed pure r-process isotopes then a multiplicity of r-process environments is needed to explain the inconsistent Δ values [453, 129]. This is evident when looking at Fig. (4.30):

Extinct radionuclides in the ESS.

Nuclide		τ = 1/λ (Myr)	Norm.	R	Refs	P	R/P[a]
Aluminum-26	Stars, Irradiation	1.07	27Al	(5.2 ± 0.1) x 10^-5	A	(1.1 ± 0.7) x 10^-2	(4.6 ± 3.0) x 10^-3
Chlorine-36	Irradiation, Stars	0.434	35Cl	(1.8 ± 0.1) x 10^-5	B	(1.8 ± 1.1) x 10^-2	(1.0 ± 0.6) x 10^-3
Calcium-41	Stars, Irradiation	0.144	40Ca	~ 4 x 10^-9	C	(2.0 ± 1.0) x 10^-3	(2.0 ± 1.0) x 10^-6
Manganes-53	Stars, Gal. Bkgd	5.34	55Mn	(6.7 ± 0.6) x 10^-6	D	(1.5 ± 0.8) x 10^-1	(4.5 ± 2.3) x 10^-5
Iron-60	Stars, Gal. Bkgd	2.16	56Fe	(7.1 ± 2.3) x 10^-9	E	(7.5 ± 4.5) x 10^-5	(9.5 ± 6.5) x 10^-5
Niobium-92	p-process	50.1	92Mo	(2.8 ± 0.5) x 10^-6	F	(1.5 ± 0.6) x 10^-3	(1.9 ± 0.8) x 10^-2
Palladium-107	s+r process	9.38	108Pd	(5.9 ± 2.2) x 10^-5	G	1.4 ± 0.7	(4.3 ± 2.8) x 10^-5
			110Pd^{r}	(1.4 ± 0.5) x 10^-4	G	1.4 ± 0.7	(1.0 ± 0.6) x 10^-4
Iodine-129	r-process	23.1	127I	(1.2 ± 0.2) x 10^-4	H	1.7 ± 0.3	(7.0 ± 1.7) x 10^-5
			127I^{r}	(1.3 ± 0.2) x 10^-4	H	1.4 ± 0.7	(8.9 ± 4.7) x 10^-5
Samarium-146	p-process	149	144Sm	(8.4 ± 0.5) x 10^-3	I	(1.4 ± 0.7) x 10^-1	(6.0 ± 3.0) x 10^-2
Hafnium-182	s+r-process	13	177Hf^{r}	(2.2 ± 0.1) x 10^-4	J	(5.5 ± 2.8) x 10^-1	(4.1 ± 2.1) x 10^-4
			180Hf	(9.7 ± 0.4) x 10^-5	J	(5.6 ± 3.5) x 10^-1	(1.7 ± 1.1) x 10^-4
Plutonium-244	r-process	117	232Th	(2.9 ± 0.4) x 10^-3	K	(3.2 ± 2.7) x 10^-1	(8.1 ± 7.1) x 10^-3
Curium-247	r-process	22.5	232Th	(1.6 ± 0.4) x 10^-5	L	(9.8 ± 5.2) x 10^-2	(1.5 ± 0.8) x 10^-4

The superscript r refers to the r-process component of the cosmic abundance (obtained after subtracting the s-process contribution from solar abundances, from Arlandini et al. (1999); Bisterzo et al. (2014)). R is the initial abundance ratio in the ESS, P is the production ratio (see best estimate values in Table 4.12).

[a] When the isotope used for normalization is not stable (e.g., X/238U or X/232Th), the R/P ratio has to be corrected for the decay of the long-lived isotope. This is done by multiplying the R/P ratio by the N/P ratio of the normalizing isotope in the ESS (0.71 for 238U and 0.89 for 232Th, both values are taken from Nittler and Dauphas (2006)).

Table 4.14: Extinct radionuclides in the ESS. References: A, [227, 252]; B, [225, 255]; C, [223, 256]; D, [141, 43, 396, 437]; E, [425, 350, 395]; F, [193, 389]; G, [104, 388]; H, [360, 66]; I, [62, 260, 343]; J, [74, 243, 465]; K, [219]; L, This work, [71]. Table submitted in [432].

^{107}Pd and ^{129}I have similar $(N_{SLR}/N_{Stable})/(P_{SLR}/P_{Stable})$ ratios but different half-lives, making it impossible for both isotopes to be produced in a single event/process.

4.3.6.4 Three-phase ISM

A second model, probably more physically meaningful, is the three-phase mixing model of Clayton 1983 [109]. In this model, the product of supernovae explosions is injected into the warm ISM, which exchanges matter with large H1 clouds on a timescale τ_{12}, which in turn, exchanges matter with the protosolar molecular cloud on a timescale τ_{23}. In this model, the abundance of a SLR in the ESS is not controlled by the time since the last nucleosynthetic event, but by the exchange timescales between the ISM and the molecular clouds. As the mixing timescale increases, the abundance of the SLR in the molecular cloud decreases, but not as rapidly as in the free decay interval model (for a given value of $\Delta = \tau_{12} = \tau_{23}$).

Despite being more realistic, this model also fails to explain the abundances of all SLRs with a single mixing timescale (Fig. 4.31). Instead, the abundances of the *p*-, *s*-, and *r*-

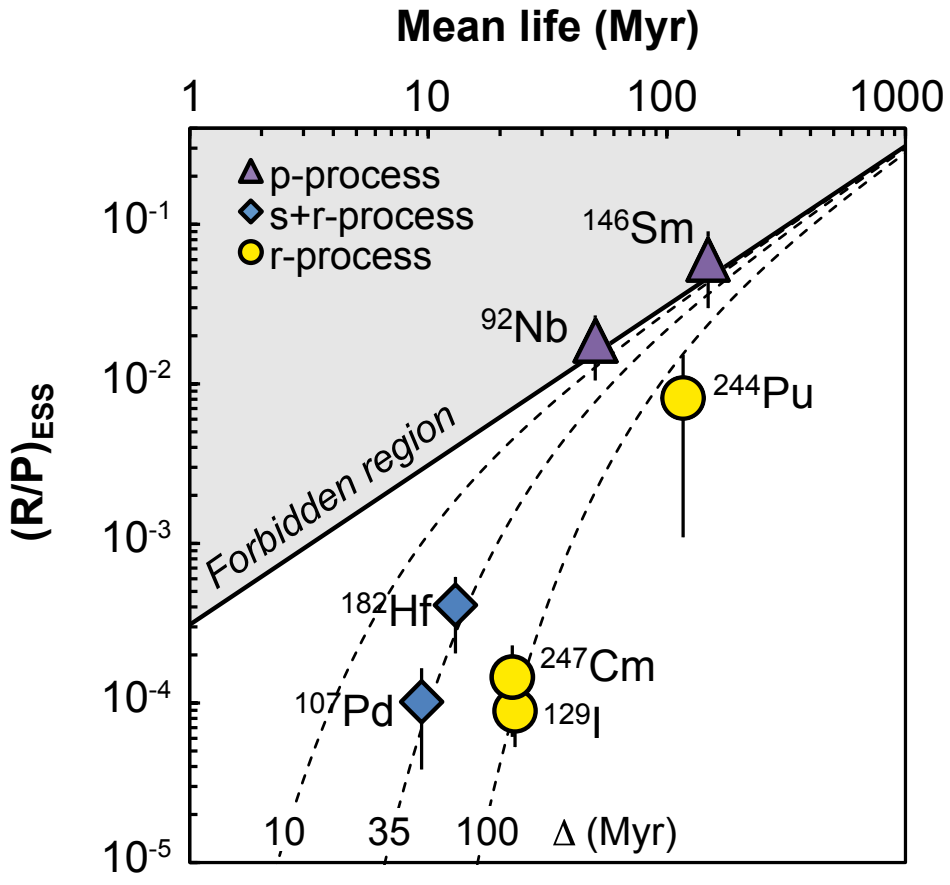

Figure 4.30: Meteoritic abundance ratios of extinct radionuclides to stable nuclides produced by the same process (*e.g.*, $^{129}I/^{127}I^{r}$), normalized to stellar production ratios *vs.* mean-lives ($\tau = t_{1/2}/ln(2)$). The superscript "r" refers to the *r*-process component of the cosmic abundance [obtained after subtracting the *s*-process contribution from solar abundances, [45]]. When the normalizing isotope is not stable (*e.g.*, X/^{238}U or X/^{232}Th), the R/P ratio, $(N_{SLR}/N_{Stable})/(P_{SLR}/P_{Stable})$, is corrected for the decay of the long-lived isotope by multiplication by the N/P ratio of the normalizing isotope in the ESS (0.71 for ^{238}U and 0.89 for ^{232}Th, values from [312]). Triangles denote *p*-process isotopes, diamonds denote *r*-process nuclides with possible large *s*-process contributions, and circles denote *r*-process isotopes. The data are compared to model steady-state abundances in the ISM, using the model of [135] with k= 1.7 ± 0.4 and a presolar age of the galaxy of 8.7 Gyr. Dotted curves show model abundances assuming free-decay intervals of 10, 35 and 100 Myr, respectively. The abundances of all *r*-process nuclides can be explained by a single *r*-process event about 100 Myr before SS formation provided that ^{182}Hf and ^{107}Pd in meteorites originate from the *s*-process [294, 259]. See Table 4.14 for source data. Figure submitted in [432].

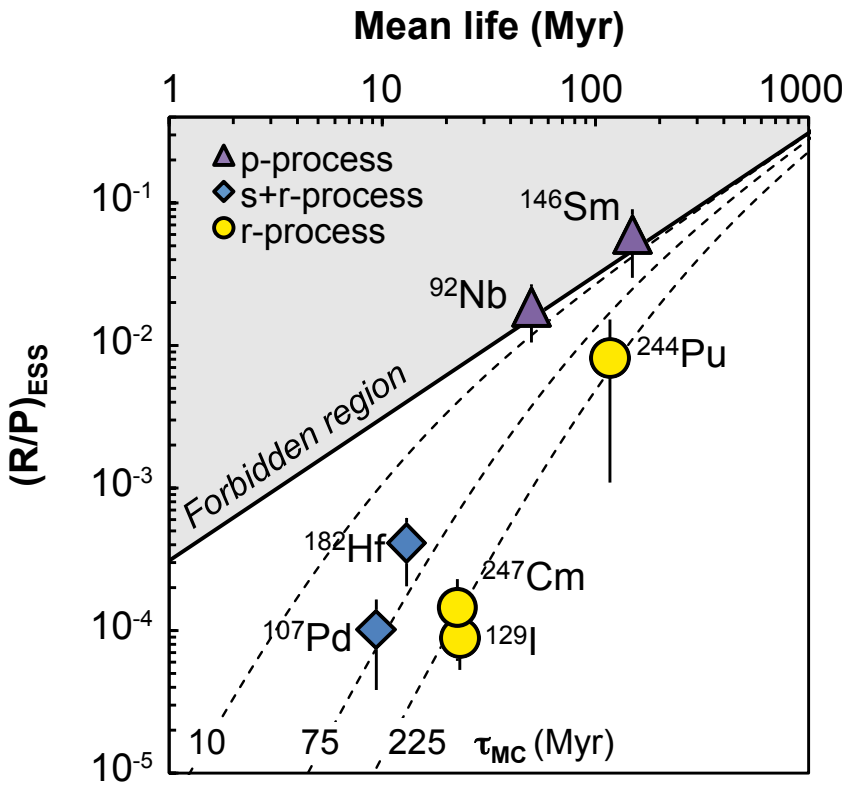

Figure 4.31: Same as Fig. (4.30), but the dotted curves now show model abundances assuming a 3-phase mixing model [109] with mixing timescales ($\tau_{12} = \tau_{23}$) of 10, 75, and 225 Myr, respectively. In this model, the abundances of the *p*-, *s*-, and *r*-process nuclides fit different mixing timescales, which is hard to understand physically, if all nuclides started in the ISM and traveled along the same path to reach the protosolar molecular cloud. A far-fetched explanation would be that the *p*-, *s*-, and *r*-nuclides do not follow the same path to reach the protosolar cloud, as they are synthesized in different stellar environments.

process nuclides fit different mixing timescales, which is hard to understand physically, if all nuclides started in the ISM and traveled along the same path to reach the protosolar molecular cloud.

4.3.6.5 Two *s*-process nuclides and a single *r*-process

From the above analysis, it appears that no single *r*-process (or event) can produce both ^{107}Pd (or ^{182}Hf) and ^{129}I, no matter what model is used for the evolution of the SLR abundances in the giant molecular cloud parental to the Solar System (*e.g.*, free decay

interval *vs.* 3-phase mixing ISM [220, 109]). This is true, however, only if ^{107}Pd and ^{182}Hf are indeed pure r-process nuclides.

Recent nucleosynthetic models have, however, reconsidered the origin of ^{107}Pd and ^{182}Hf and find a significant s-process contribution (70 to 80 %) for both isotopes [294, 259]. In such a framework, the initial abundance of all r-process SLRs in the ESS can be explained by a single r-process event, which last injected material into the protosolar molecular cloud ~ 100 Myr before SS formation. Short-lived radionuclides produced by the s- and p-processes seem to indicate a last injection for s- and p-nuclides ~ 35 and ~ 10 Myr before SS formation, respectively.

In the event that the nucleosynthesis of ^{182}Hf is once again reassessed and found to be of definite r-process origin, a multiplicity of r-processes would have to be invoked to make sense of the SLR meteoritic abundances. Note that the above discussion assumes that the actual production ratios of the nuclides shown in Figs. (4.30) and (4.31) are not outside of their respective uncertainty range (see Table 4.12).

The uniqueness of the r-process as evidenced by the SLR abundances in meteorites is at odds with the variable r-nuclide abundance patterns in some low metallicity halo stars, which point to the existence of at least 3 distinct r-processes. These stars, however, formed from gas that had been enriched in r-process nuclides by synthesis in very low metallicity stars formed early in the history of the Galaxy. The meteorite evidence presented here suggests that such r-processes may only be relevant to exotic conditions that prevailed in the earliest generation of stars in the history of the Galaxy, and that a single r-process may still be relevant to long-term models of the chemical evolution of the Galaxy.

4.3.6.6 Anchoring production ratio models

GCE models rely on production ratios to predict the steady-state abundances of the elements in the ISM. The estimation of production ratios is, however, not a trivial task, and several sources of uncertainty can affect the modeling results, such as (i) the parametric

model and its relevance to describing the r-process, (ii) the nuclear physics parameters used (*e.g.*, rates of β-decay, neutron separation energy), and (iii) the composition to which the model is fitted (decomposition of the solar composition into s- and r-process components). An additional difficulty exists for the actinides, as the closest anchor to which the model can be fitted is ^{209}Bi, an isotope 35 atomic mass units lower than the actinides [178].

For this reason, nucleosynthesis models have long struggled with the difficulty of predicting the abundances of actinides. The initial abundance of ^{247}Cm obtained in this study therefore provides a new reliable reference point through which production ratio models can be fitted, and it will be interesting to see what improvement this new input parameter can bring to modeling endeavors.

4.4 Conclusions

In this chapter, the high-precision U isotope analysis techniques developed throughout this thesis have been applied to a selected body of meteoritic samples: angrites and CAIs from the Allende meteorite. The characterization of the U isotopic composition of angrites allowed the revision of their Pb-Pb ages. This led, most importantly, to the modification of the age of the D'Orbigny specimen, resulting in a high concordance of the Pb-Pb and Hf-W ages between angrites and CAIs, and a reduction of the discrepancy between Pb-Pb and Al-Mg ages from ~ 2.25 Myr, to only ~ 1.2 Myr. The reason for this remaining discrepancy is still an open question at this time, yet, the concordance of Pb-Pb and Hf-W ages suggests that D'Orbigny could be a proper anchor for absolute and relative chronometers. High-precision measurements on a set of fine-grained CAIs from the Allende meteorite led to the discovery of a 59 ‰ ^{235}U excess in CAI ME-3364-3.2, which is definitive evidence that ^{247}Cm was alive in the ESS, and puts to rest a four-decade long controversy. Live ^{247}Cm in the ESS argues against the existence of an actinide-specific r-process site, and instead suggests that a single r-process nucleosynthetic environment is relevant to the long-term evolution of the Galaxy. The ESS abundance of ^{247}Cm derived herein provides the first anchor in the

actinide region for nucleosynthetic models.

CHAPTER 5

CONCLUSIONS AND PERSPECTIVES

"Je sers la science et c'est ma joie !"

Basile – *Léonard est un génie*

In 1939, Alfred O. Nier measured the ratio of U "stable" isotopes ($^{238}U/^{235}U$) as 139.0 ± 1.4 [311], thereby defining the U isotopic composition of the Solar System and its every component. Little did he know that in this one percent uncertainty an entire field of isotope chemistry was hiding, and that it would take nearly three-quarters of a century to start to uncover it. Today, the variations in the $^{238}U/^{235}U$ ratio of natural samples have become a powerful tool in isotope geo- and cosmochemistry, allowing the study of past redox conditions in Earth's atmosphere/ocean, as well as the refinement of models of stellar nucleosynthesis and Solar System formation.

This dissertation is part of the scientific expedition venturing in the realm of this one percent uncertainty.

In **Chapter 1**, I reviewed some of the basic concepts about mass-dependent and mass-independent isotopic fractionation, which led to the introduction of the concept of Nuclear Field Shift: a volume-dependent isotopic fractionation that is the main mechanism responsible for the isotopic variations of U isotopes in low-temperature environments (Fig. 1.3). The rest of Chapter 1 was dedicated to introducing the first order problems that the "stable" isotopes of U could help address in both geo- and cosmochemistry.

Chapter 2 started by explaining the general methods of sample preparation and purification using extraction chromatography. The "theory of plates" (1947) was introduced as a means of predicting and optimizing separation schemes (Fig. 2.11). This was followed by a description of the first Pneumatic-Fluoropolymer HPLC system, covering in detail both the development of this new instrument (Fig. 2.5) and its performance relative to traditional isotope chemistry setups. The enhanced separation efficiency of the system was demonstrated on two notoriously difficult separation schemes: Ni-Mg column chemistry (Fig. 2.6) and REE column chemistry (Fig. 2.13). The remainder of Chapter 2 delved into the specifics of the

high-precision (±0.05 ‰) analytical routine for U "stable" isotopes, from column chemistry to MC-ICPMS measurements with a static cup configuration (Table 2.11). The partition coefficients (K_d; Fig. 2.15 and Table 2.8) and elution behavior (Fig. 2.16 and Table 2.9) of 16 elements on the uranium specific resin U/Teva were reported and the height equivalent to a theoretical plate (HETP) of the U/Teva resin was quantified (HETP= 0.5 mm). Details of the data reduction procedure to propagate uncertainties properly on the $^{238}U/^{235}U$ ratios, corrected for laboratory and mass spectrometry-induced mass fractionation (using the IRMM-3636 double spike), were presented. The architecture of the data reduction software (written in Mathematica language) was also adapted to U-Th age calculations (Table 2.12), as part of an effort to properly estimate the uncertainties on those ages. At the end of Chapter 2, a general quality control test for double spike measurements was introduced that takes advantage of the fact that at least two naturally occurring isotopes have small contribution from the spike (Fig. 2.24).

The focus of **Chapter 3** was the geochemical applications of U isotope systematics. Starting with the impact of the variability of the $^{238}U/^{235}U$ ratio on Pb-Pb and U-Pb ages, three analytical equations (Eqs. 3.3, 3.12, and 3.17) were derived which allow for easy and rapid assessment of the age correction to apply to a sample of any age and any U isotopic composition (Figs. 3.1 and 3.2). The uranium isotopic compositions of 20 granitoids from the Lachlan Fold Belt (Table 3.1) and 41 geostandards were measured (Table 3.2), along with an array of seawater samples and selected river water, lake water, oyster, evaporite and coral samples (Table 3.5). These measurements were augmented with a thorough compilation of published data from 32 studies (Fig. 3.4 and Supplementary Material Tables S2 in [431]). From the Lachlan Fold Belt granite data, the absence of Soret diffusion was demonstrated (Fig. 3.3), a result that adds to a growing list of arguments that fluid exsolution and fractional crystallization are the primary mechanisms for the $\delta^{56}Fe$ variations of felsic rocks [428]. Using abundances of different rock types in the crust and estimates

of their U isotopic compositions (Table 3.3), the continental crust was estimated to have $\delta^{238}U_{Crust} = -0.29 \pm 0.03$ ‰ (95 CI). Combining this with U isotopic analyses of oceanic basalts, taken as proxies for the composition of the mantle, a bulk Earth U isotopic composition was calculated ($\delta^{238}U = -0.29 \pm 0.02$ ‰), which is within error of the best estimate of the average meteoritic $\delta^{238}U$ of -0.36 ± 0.07 ‰ (Section 4.2.1). The analysis of a series of seawater samples showed that the open ocean has a homogeneous $\delta^{238}U_{SW}$ value of -0.392 ± 0.005 ‰. By comparing this value with predictions from recent U budgets of the modern ocean, this result was used to (i) constrain the extent of modern anoxia in the ocean (*i.e.*, the percent of seafloor covered by anoxic/euxinic sediments) to be 0.21 ± 0.09 % (Table 3.7), (ii) validate the assumption that the U oceanic budget is in steady-state, and (iii) validate the assumption that the ratio of U "stable" isotopes tracks the global redox conditions of the ocean (Fig. 3.7). The U proxy was then applied to black shales in the wake of the GOE (Shunga Event, 2.05 Ga). A method for detrital contribution correction was introduced (Eq. 3.26 and Fig. 3.11), which was used to show that the authigenic U signal recorded in the black shale samples indicate that the extent of oceanic anoxia during the Sunga Event could have been up to four times the present value. As a conclusion to Chapter 3, a step-leaching protocol for carbonate samples was developed (Fig. 3.13) and its application to modern samples from the Bahamas (ODP Leg 166, Site 1009, ages from 0 to 1.5 Myr) showed that carbonates could be a better rock record for paleoredox reconstructions using U isotopes (Fig. 3.14). Some very preliminary data on older carbonates were presented (Fig. 3.15).

Chapter 4 opened with an estimate of the mean $\delta^{238}U_{SS}$ value of the Solar System as -0.36 ± 0.07 ‰, using a compilation of literature data. This was followed by the characterization of selected angrite samples, which allowed the revision of their Pb-Pb ages (Table 4.5). The modification of the age of the D'Orbigny meteorite (from 4564.42 ± 0.12 Myr to 4563.51 ± 0.18 Myr), resulted in a high concordance of Pb-Pb and Hf-W ages between

angrites and CAIs, and a reduction of the discrepancy between Pb-Pb and Al-Mg ages from $\sim$ 2.25 Myr, to only $\sim$ 1.2 Myr (Fig. 4.5). The reason for this remaining discrepancy is still an open question at this time, yet, the concordance of Pb-Pb and Hf-W ages suggests that D'Orbigny could be a proper anchor for absolute and relative chronometers in Early Solar System objects. The main part of Chapter 4 was dedicated to the work performed on a set of fine-grained, group II CAIs from the Allende meteorite (Figs. 4.7 to 4.20), in an effort to find definitive evidence for or against the existence of live ^{247}Cm in the ESS. The discovery of a 59 ‰ ^{235}U excess in CAI ME-3364-3.2 is proof that ^{247}Cm was alive in the ESS, and its initial abundance was estimated to be $(^{247}\mathrm{Cm}/^{235}\mathrm{U})_{\mathrm{ESS}} = (1.1 \pm 0.3) \times 10^{-4}$ (this value takes into account the uncertainties associated with the timing of alteration of CAI ME-3364-3.2, Fig. 4.29). This value is consistent with the ESS abundance of ^{244}Pu and ^{129}I (two *r*-process nuclides), and an origin for ^{182}Hf mainly by the *s*-process. This result is incompatible with the existence of an actinide-specific *r*-process site, and instead suggests that a single *r*-process nucleosynthetic environment is relevant to the long-term evolution of the Galaxy, with the last *r*-process production event occurring $\sim$ 100 Myr before SS formation (Fig. 4.30). The ESS abundance of ^{247}Cm derived in this work provides the first anchor in the actinide region for nucleosynthetic models, for which the prediction of the abundances of actinides is a long-standing difficulty.

Though considerable progress has been made in the hunt for ^{247}Cm, the "stable" U isotopes will keep playing an important role in ESS chronology in the decades to come. As more fine-grained CAIs will be measured, the initial abundance of ^{247}Cm will be further refined. Moreover, high-precision characterization of the U isotopic composition of ESS materials will be needed to obtain proper Pb-Pb ages for these samples. Undoubtedly, more and more research effort is going to be spent on the paleoredox reconstruction capabilities of the U systematics (not to mention the implications for environmental remediation). The

preliminary results shown on carbonate rocks (Chapter 3) are a promising trail to follow with large potential implications regarding the evolution of the oxygenation of the ocean. At a finer time-resolution scale, study of individual events (such as Neoproterozoic glaciations) will also shed light on the global response of the oceanic system to rapid climate shifts.

Some basic studies are also still missing, and would be obvious follow-up investigations, such as: (i) a systematic characterization of the U isotopic composition of large rivers around the world (only 3 measurements are available so far), (ii) a verification that the isotopic fractionation associated with U removal in coastal retention zones is similar to the one observed in Fe-Mn deposits and oxides, and (iii) a proper assessment of the magnitude and isotopic composition of the groundwater U flux to the ocean. These three questions are the main unknowns remaining in our understanding of the modern oceanic U budget.

REFERENCES

[1] Abe, M. and Suzuki, T. and Fujii, Y. and Hada, M. and Hirao, K. An ab initio molecular orbital study of the nuclear volume effects in uranium isotope fractionations. *The Journal of Chemical Physics*, 129(16):1–7, 2008.

[2] Ackermann, R. J. and Chandrasekharaiah, M. S. Systematic thermodynamic properties of actinide metal-oxygen systems at high temperatures: Emphasis on lower valence states. In *Symposium on thermodynamics of nuclear materials*, pages 3–24. International Atomic Energy Agency, Vienna, Jan 1974.

[3] Albalat, E. and Telouk, P. and Albarède, F. Er and Yb isotope fractionation in planetary materials. *Earth and Planetary Science Letters*, 355-356:39–50, 2012.

[4] Albarède, F. and Albalat, E. and Telouk, P. Instrumental isotope fractionation in multiple-collector ICP-MS. *Journal of Analytical Atomic Spectrometry*, pages 1736–1742, 2015.

[5] Albarède, F. and Télouk, P. and Blichert-Toft, J. and Boyet, M. and Agranier, A. and Nelson, B. Precise and accurate isotopic measurements using multiple-collector ICPMS. *Geochimica et Cosmochimica Acta*, 68(12):2725–2744, 2004.

[6] Ali, A. and Srinivasan, G. Precise thermal ionization mass spectrometric measurements of $^{142}Nd/^{144}Nd$ and $^{143}Nd/^{144}Nd$ isotopic ratios of Nd separated from geological standards by chromatographic methods. *International Journal of Mass Spectrometry*, 299(1):27–34, 2011.

[7] Allègre, C. J. and Poirier, J.-P. and Humler, E. and Hofmann, A. W. The chemical composition of the Earth. *Earth and Planetary Science Letters*, 134(3-4):515–526, 1995.

[8] Alt, J. C. and Teagle, D. A. H. Hydrothermal alteration of upper oceanic crust formed at a fast-spreading ridge: Mineral, chemical, and isotopic evidence from ODP Site 801. *Chemical Geology*, 201(3-4):191–211, 2003.

[9] Amelin, Y. The prospect of high-precision Pb isotopic dating of meteorites. *Meteoritics & Planetary Science*, 41(1):7–17, 2006.

[10] Amelin, Y. The U-Pb systematics of angrite Sahara 99555. *Geochimica et Cosmochimica Acta*, 72(19):4874–4885, 2008.

[11] Amelin, Y. U-Pb ages of angrites. *Geochimica et Cosmochimica Acta*, 72(1):221–232, 2008.

[12] Amelin, Y. and Connelly, J. and Zartman, R. E. and Chen, J. H. and Gopel, C. and Neymark, L. A. Modern U-Pb chronometry of meteorites: Advancing to higher time resolution reveals new problems. *Geochimica et Cosmochimica Acta*, 73(17):5212–5223, 2009.

[13] Amelin, Y. and Irving, A. J. Seven million years of evolution on the angrite parent body from Pb-isotopic data. In *Chronology of Meteorites and the Early Solar System*, pages 20–21, 2007.

[14] Amelin, Y. and Kaltenbach, A. and Iizuka, T. and Stirling, C. H. and Ireland, T. R. and Petaev, M. and Jacobsen, S. B. U-Pb chronology of the Solar System's oldest solids with variable $^{238}U/^{235}U$. *Earth and Planetary Science Letters*, 300(3-4):343–350, 2010.

[15] Amelin, Y. and Kaltenbach, A. and Stirling, C. H. The U-Pb systematics and cooling rate of plutonic angrite NWA 4590. In *Lunar and Planetary Science Conference*, volume 42, 2011. # 1682.

[16] Anbar, A. D. and Rouxel, O. Metal stable isotopes in paleoceanography. *Annual Review of Earth and Planetary Sciences*, 35:717–746, 2007.

[17] Anders, E. and Grevesse, N. Abundances of the elements: Meteoritic and solar. *Geochimica et Cosmochimica Acta*, 53(1):197–214, 1989.

[18] Andersen, M. B. and Elliott, T. and Freymuth, H. and Sims, K. W. W. and Niu, Y. and Kelley, K. A. The terrestrial uranium isotope cycle. *Nature*, 517(7534):356–359, 2015.

[19] Andersen, M. B. and Romaniello, S. and Vance, D. and Little, S. H. and Herdman, R. and Lyons, T. W. A modern framework for the interpretation of $^{238}U/^{235}U$ in studies of ancient ocean redox. *Earth and Planetary Science Letters*, 400:184–194, 2014.

[20] Anderson, G. M. Error propagation by Monte-Carlo method in geochemical calculations. *Geochimica et Cosmochimica Acta*, 40(12):1533–1538, 1976.

[21] Anderson, J. L. Proterozoic anorogenic granite plutonism of north america. *Proterozoic Geology*, 161:133–154, 1983.

[22] Anderson, R. F. and Fleisher, M. Q. and LeHuray, A. P. Concentration, oxidation state, and particulate flux of uranium in the Black Sea. *Geochimica et Cosmochimica Acta*, 53(9):2215–2224, 1989.

[23] Andersson, P. S. and Porcelli, D. and Gustafsson, O. and Ingri, J. and Wasserburg, G. J. The importance of colloids for the behavior of uranium isotopes in the low-salinity zone of a stable estuary. *Geochimica et Cosmochimica Acta*, 65(1):13–25, 2001.

[24] Andreasen, R. and Sharma, M. Solar nebula heterogeneity in p-process samarium and neodymium isotopes. *Science*, 314(5800):806–809, 2006.

[25] Andreasen, R. and Sharma, M. Mixing and homogenization in the early solar system: Clues from Sr, Ba, Nd, and Sm isotopes in meteorites. *Astrophysical Journal*, 665:874–883, 2007.

[26] Arden, J. W. Isotopic composition of uranium in chondritic meteorites. *Nature*, 269:788, 1977.

[27] Arlandini, C. and Käppeler, F. and Wisshak, K. and Gallino, R. and Lugaro, M. and Busso, M. and Straniero, O. Neutron capture in low-mass asymptotic giant branch stars: Cross sections and abundance signatures. *Astrophysical Journal*, 525(2):886–900, 1999.

[28] Asael, D. and Tissot, F. L. H. and Reinhard, C. T. and Rouxel, O. and Dauphas, N. and Lyons, T. W. and Ponzevera, E. and Liorzou, C. and Chéron, S. Coupled molybdenum, iron and uranium stable isotopes as oceanic paleoredox proxies during the Paleoproterozoic Shunga Event. *Chemical Geology*, 362(0):193–210, 2013.

[29] Axelsson, M. D. and Rodushkin, I. and Ingri, J. and Öhlander, B. Multielemental analysis of Mn-Fe nodules by ICP-MS: Optimisation of analytical method. *Analyst*, 127(1):76–82, 2002.

[30] Bailey, T. R. and McArthur, J. M. and Prince, H. and Thirlwall, M. F. Dissolution methods for strontium isotope stratigraphy: Whole rock analysis. *Chemical Geology*, 167(3-4):313–319, 2000.

[31] Baker, J. and Waight, T. and Ulfbeck, D. Rapid and highly reproducible analysis of rare earth elements by multiple collector inductively coupled plasma mass spectrometry. *Geochimica et Cosmochimica Acta*, 66(20):3635–3646, 2002.

[32] Balaram, V. Recent trends in the instrumental analysis of rare earth elements in geological and industrial materials. *TrAC Trends in Analytical Chemistry*, 15(9):475–486, 1996.

[33] Barnes, C. E. and Cochran, J. K. Uranium removal in oceanic sediments and the oceanic-U balance. *Earth and Planetary Science Letters*, 97(1-2):94–101, 1990.

[34] Barnes, C. E. and Cochran, J. K. Uranium geochemistry in estuarine sediments: Controls on removal and release processes. *Geochimica et Cosmochimica Acta*, 57(3):555–569, 1993.

[35] Basu, A. and Sanford, R. A. and Johnson, T. M. and Lundstrom, C. C. and Loffler, F. E. Uranium isotopic fractionation factors during U(VI) reduction by bacterial isolates. *Geochimica et Cosmochimica Acta*, 136:100–113, 2014.

[36] Bekker, A. and Holland, H. D. and Wang, P.-L. and Rumble III, D. and Stein, H.J. and Hannah, J. L. and Coetzee, L. L. and Beukes, N. J. Dating the rise of atmospheric oxygen. *Nature*, 427(6970):117–120, 2004.

[37] Bekker, A. and Holmden, C. and Beukes, N. J. and Kenig, F. and Eglingtone, B. and Patterson, W. P. Fractionation between inorganic and organic carbon during the Lomagundi ($2.22 - 2.1$ Ga) carbon isotope excursion. *Earth and Planetary Science Letters*, 271(1-4):278–291, 2008.

[38] Bennett, V. C. and Brandon, A. D. and Nutman, A. P. Coupled ^{142}Nd-^{143}Nd isotopic evidence for hadean mantle dynamics. *Science*, 318(5858):1907–1910, 2007.

[39] Berner, R. A. A new geochemical classification of sedimentary environments. *Journal of Sedimentary Petrology*, 51(2):359–366, 1981.

[40] Bertine, K. K. and Turekian, K. K. Molybdenum in marine deposits. *Geochimica et Cosmochimica Acta*, 37(6):1415–1434, 1973.

[41] Bigeleisen, J. Nuclear size and shape effects in chemical reactions. Isotope chemistry of the heavy elements. *Journal of the American Chemical Society*, 118(15):3676–3680, 1996.

[42] Bigeleisen, J. and Mayer, M. G. Calculation of equilibrium constants for isotopic exchange reactions. *The Journal of Chemical Physics*, 15(5):261–267, 1947.

[43] Birck, J.-L. and Allègre, C. J. Evidence for the presence of ^{53}Mn in the early solar system. *Geophysical Research Letters*, 12(11):745–748, 1985.

[44] Birck, J. L. and Lugmair, G. W. Nickel and chromium isotopes in Allende inclusions. *Earth and Planetary Science Letters*, 90(2):131–143, 1988.

[45] Bisterzo, S. and Travaglio, C. and Gallino, R. and Wiescher, M. and Käppeler, F. Galactic chemical evolution and solar *s*-process abundances: Dependence on the ^{13}C-pocket structure. *Astrophysical Journal*, 787(10):14pp, 2014.

[46] Blake, J. B. and Schramm, D. N. ^{247}Cm as a short-lived *r*-process chronometer. *Nature Physical Science*, 243:138–140, jun 1973.

[47] Blanchard, M. and Dauphas, N. and Hu, M. Y. and Roskosz, M. and Alp, E. E. and Golden, D. C. and Sio, C. K. and Tissot, F. L. H. and Zhao, J. and Gao, L. and Morris, R. V. and Fornace, M. and Floris, A. and Lazzeri, M. and Balan, E. Reduced partition function ratios of iron and oxygen in goethite. *Geochimica et Cosmochimica Acta*, 151:19–33, 2015.

[48] Bogard, D.D. Neutron-capture ^{36}Cl, ^{41}Ca, ^{36}Ar, and ^{150}Sm in large chondrites: Evidence for high fluences of thermalized neutrons. *Journal of Geophysical Research*, 100(E5):9401–9416, 1995.

[49] Boltwood, B. B. On the ultimate disintegration products of the radio-active elements. Part II. The disintregation products of uranium. *American Journal of Science*, 23(134):77–88, 1907.

[50] Bonin, B. A-type granites and related rocks: Evolution of a concept, problems and prospects. *Lithos*, 97(1-2):1–29, 2007.

[51] Bopp, C. J. and Lundstrom, C. C. and Johnson, T. M. and Glessner, J. J. G. Variations in ^{238}U/^{235}U in uranium ore deposits: Isotopic signatures of the U reduction process? *Geology*, 37(7):611–614, 2009.

[52] Bopp, C. J. and Lundstrom, C. C. and Johnson, T. M. and Sanford, R. A. and Long, P. E. and Williams, K. H. Uranium $^{238}U/^{235}U$ isotope ratios as indicators of reduction: Results from an in situ biostimulation experiment at Rifle, Colorado, USA. *Environmental Science & Technology*, 44(15):5927–5933, 2010.

[53] Bouchet, J. M. Étude océanographique des chenaux du bassin d'Arcachon. *Etude Océanographique des Chenaux du Bassin d'Arcachon*, page 306, 1968. Thèse Doct. Sci. Nat.

[54] Bourdon, B. and Turner, S. and Henderson, G. M. and Lundstrom, C. C. Introduction to U-series geochemistry. *Reviews in Mineralogy and Geochemistry*, 52(1):1–21, 2003.

[55] Bourdon, B. and Turner, S. and Henderson, G. M. and Lundstrom, C. C. *Uranium-series geochemistry*. Reviews in mineralogy and geochemistry. Mineralogical Society of America, Washington, D.C., 2003.

[56] Bouvier, A. and Brennecka, G. A. and Sanborn, M. E. and Wadhwa, M. U-Pb Chronology of a newly recovered angrite. In *Lunar and Planetary Science Conference*, volume 42, March 2011. # 2747.

[57] Bouvier, A. and Spivak-Birndorf, L. J. and Brennecka, G. A. and Wadhwa, M. New constraints on early Solar System chronology from Al-Mg and U-Pb isotope systematics in the unique basaltic achondrite Northwest Africa 2976. *Geochimica et Cosmochimica Acta*, 75(18):5310–5323, 2011.

[58] Bouvier, A. and Vervoort, J.D. and Patchett, P. J. The Lu-Hf and Sm-Nd isotopic composition of CHUR: Constraints from unequilibrated chondrites and implications for the bulk composition of terrestrial planets. *Earth and Planetary Science Letters*, 273(1-2):48–57, 2008.

[59] Bouvier, A. and Wadhwa, M. The age of the solar system redefined by the oldest Pb-Pb age of a meteoritic inclusion. *Nature Geoscience*, 3(9):637–641, 2010.

[60] N. L. Bowen. Diffusion in silicate melts. *The Journal of Geology*, 29(4):pp. 295–317, 1921.

[61] Boyet, M. and Carlson, R. W. Geochemistry: ^{142}Nd evidence for early (>4.53 Ga) global differentiation of the silicate earth. *Science*, 309(5734):576–581, 2005.

[62] Boyet, M. and Carlson, R. W. and Horan, M. Old Sm-Nd ages for cumulate eucrites and redetermination of the solar system initial $^{146}Sm/^{144}Sm$ ratio. *Earth and Planetary Science Letters*, 291(1-4):172–181, 2010.

[63] Boynton, W. V. Fractionation in the solar nebula: Condensation of yttrium and the rare earth elements . *Geochimica et Cosmochimica Acta*, 39(5):569–584, 1975.

[64] Boynton, W. V. Fractionation in the solar nebula, II. Condensation of Th, U, Pu, and Cm. *Earth and Planetary Science Letters*, 40(1):63–70, 1978.

[65] Brasier, M. D. and Lindsay, J. F. A billion years of environmental stability and the emergence of eukaryotes: New data from northern Australia. *Geology*, 26(6):555–558, 1998.

[66] Brazzle, R. H. and Pravdivtseva, O. V. and Meshik, A. P. and Hohenberg, C. M. Verification and interpretation of the I-Xe chronometer . *Geochimica et Cosmochimica Acta*, 63(5):739–760, 1999.

[67] Brennecka, G. A. and Borg, L. E. and Hutcheon, I. D. and Sharp, M. A. and Anbar, A. D. Natural variations in uranium isotope ratios of uranium ore concentrates: Understanding the $^{238}U/^{235}U$ fractionation mechanism. *Earth and Planetary Science Letters*, 291(1-4):228–233, 2010.

[68] Brennecka, G. A. and Herrmann, A. D. and Algeo, T. J. and Anbar, A. D. Rapid expansion of oceanic anoxia immediately before the end-Permian mass extinction. *Proceedings of the National Academy of Sciences*, 108(43):17631–17634, 2011.

[69] Brennecka, G. A. and Wadhwa, M. Uranium isotope compositions of the basaltic angrite meteorites and the chronological implications for the early Solar System. *Proceedings of the National Academy of Sciences*, 109(24):9299–9303, 2012.

[70] Brennecka, G. A. and Wasylenki, L. E. and Bargar, J. R. and Weyer, S. and Anbar, A. D. Uranium isotope fractionation during adsorption to Mn-oxyhydroxides. *Environmental Science and Technology*, 45(4):1370–1375, 2011.

[71] Brennecka, G. A. and Weyer, S. and Wadhwa, M. and Janney, P. E. and Zipfel, J. and Anbar, A. D. $^{238}U/^{235}U$ variations in meteorites: Extant ^{247}Cm and implications for Pb-Pb dating. *Science*, 327(5964):449–451, 2010.

[72] Burbidge, E. Margaret and Burbidge, G. R. and Fowler, William A. and Hoyle, F. Synthesis of the elements in stars. *Rev. Mod. Phys.*, 29:547–650, Oct 1957.

[73] Burger, M. and Krähenbühl, U. Critical evaluation of the determination of zirconium and hafnium in meteorites by instrumental and radiochemical neutron activation analysis. *Analytica Chimica Acta*, 254(1-2):119–126, 1991.

[74] Burkhardt, C. and Kleine, T. and Bourdon, B. and Palme, H. and Zipfel, J. and Friedrich, J. M. and Ebel, D. S. Hf-W mineral isochron for Ca, Al-rich inclusions: Age of the solar system and the timing of core formation in planetesimals. *Geochimica et Cosmochimica Acta*, 72(24):6177–6197, 2008.

[75] Burkhardt, C. and Kleine, T. and Dauphas, N. and Wieler, R. Nucleosynthetic tungsten isotope anomalies in acid leachates of the Murchison chondrite: Implications for hafnium-tungsten chronometry. *The Astrophysical Journal Letters*, 753(1):L6, 2012.

[76] Burnett, D. and Huneke, J. and Podosek, F. and Price Russ, G., III and Wasserburg, G. The irradiation history of lunar samples. *Proc. Second Lunar Sci. Conf.*, 2:1671–1679, 1971.

[77] Busemann, H. and Lorenzetti, S. and Eugster, O. Noble gases in D'Orbigny, Sahara 99555 and D'Orbigny glass – Evidence for early planetary processing on the angrite parent body. *Geochimica et Cosmochimica Acta*, 70(21):5403–5425, 2006.

[78] Calvert, S. E. and Pedersen, T. F. Geochemistry of recent oxic and anoxic marine sediments: Implications for the geological record. *Marine Geology*, 113(1-2):67–88, 1993.

[79] Cameron, A. G. W. *Stellar evolution, nuclear astrophysics, and nucleogenesis. Second edition.* 1957.

[80] Campbell, D. O. Rapid rare earth separation by pressurized ion exchange chromatography. *Journal of Inorganic and Nuclear Chemistry*, 35(11):3911–3919, 1973.

[81] Campbell, I. H. and Allen, C. M. Formation of supercontinents linked to increases in atmospheric oxygen. *Nature Geoscience*, 1(8):554–558, 2008.

[82] Canfield, D. E. A new model for Proterozoic ocean chemistry. *Nature*, 396(6710):450–453, 1998.

[83] Canfield, D. E. The early history of atmospheric oxygen: Homage to Robert M. Garrels. *Annual Review of Earth and Planetary Sciences*, 33:1–36, 2005.

[84] Carignan, J. and Hild, P. and Mevelle, G. and Morel, J. and Yeghicheyan, D. Routine analyses of trace elements in geological samples using flow injection and low pressure on-line liquid chromatography coupled to ICP-MS: A study of geochemical reference materials BR, DR-N, UB-N, AN-G and GH. *Geostandards Newsletter*, 25(2-3):187–198, 2001.

[85] Carlson, R. W. and Boyet, M. and Horan, M. Chondrite barium, neodymium, and samarium isotopic heterogeneity and early earth differentiation. *Science*, 316(5828):1175–1178, 2007.

[86] Caro, G. and Bourdon, B. and Birck, J.-L. and Moorbath, S. ^{146}Sm-^{142}Nd evidence from Isua metamorphosed sediments for early differentiation of the Earth's mantle. *Nature*, 423(6938):428–432, 2003.

[87] Caro, G. and Bourdon, B. and Birck, J.-L. and Moorbath, S. High-precision ^{142}Nd/^{144}Nd measurements in terrestrial rocks: Constraints on the early differentiation of the Earth's mantle. *Geochimica et Cosmochimica Acta*, 70(1):164–191, 2006.

[88] Caro, G. and Bourdon, B. and Halliday, A. N. and Quitté, G. Super-chondritic Sm/Nd ratios in Mars, the Earth and the Moon. *Nature*, 452(7185):336–339, 2008.

[89] Carroll, J. and Moore, W. S. Uranium removal during low discharge in the Ganges-Brahmaputra mixing zone. *Geochimica et Cosmochimica Acta*, 57(21-22):4987–4995, 1993.

[90] Cassidy, R.M. and Chauvel, C. Modern liquid chromatographic techniques for the separation of Nd and Sr for isotopic analyses. *Chemical Geology*, 74(3):189–200, 1989.

[91] Catling, D. C. and Claire, M. W. How earth's atmosphere evolved to an oxic state: A status report. *Earth and Planetary Science Letters*, 237(1-2):1–20, 2005.

[92] Cayrel, R. and Hill, V. and Beers, T. C. and Barbuy, B. and Spite, M. and Spite, F. and Plez, B. and Andersen, J. and Bonifacio, P. and Francois, P. and Molaro, P. and Nordstrom, B. and Primas, F. Measurement of stellar age from uranium decay. *Nature*, 409(6821):691–692, 2001.

[93] Cerrai, E. and Testa, C. Separation of rare earths by means of small columns of Kel-F supporting di(2-ethylhexyl)orthophosphoric acid. *Journal of Inorganic and Nuclear Chemistry*, 25(8):1045–1050, 1963.

[94] Chappell, B. W. Source rocks of I- and S-type granites in the Lachlan Fold Belt, southeastern Australia. *Philosophical Transactions of the Royal Society A: Mathematical, Physical and Engineering Sciences*, 310:693–707, 1984.

[95] Chappell, B. W. and White, A. J. R. Two contrasting granite types. *Pacific Geology*, 8:173–174, 1974.

[96] Chappell, B. W. and White, A. J. R. I- and S-type granites in the Lachlan Fold Belt. *Transactions - Royal Society of Edinburgh: Earth Sciences*, 83(1-2):1–26, 1992.

[97] Chappell, B. W. and White, A. J. R. Two contrasting granite types: 25 years later. *Australian Journal of Earth Sciences*, 48(4):489–500, 2001.

[98] Chappell, B. W. and White, A. J. R. and Wyborn, D. The cowra granodiorite and its enclaves. page 67, 1993.

[99] Chen, J. H. and Edwards, R. L. and Wasserburg, G. J. ^{238}U, ^{234}U and ^{232}Th in Seawater. *Earth and Planetary Science Letters*, 80(3-4):241–251, 1986.

[100] Chen, J. H. and Wasserburg, G. J. A search for isotopic anomalies in uranium. *Geophysical Research Letters*, 7(4):275–278, 1980.

[101] Chen, J. H. and Wasserburg, G. J. Cm/U, Th/U, and ^{235}U/^{238}U in Meteorites. *Meteoritics*, 16:301, December 1981.

[102] Chen, J. H. and Wasserburg, G. J. Precise isotopic analysis of uranium in picomole and subpicomole quantities. *Analytical Chemistry*, 53(13):2060–2067, 1981.

[103] Chen, J. H. and Wasserburg, G. J. The isotopic composition of uranium and lead in Allende inclusions and meteoritic phosphates. *Earth and Planetary Science Letters*, 52(1):1–15, 1981.

[104] Chen, J. H. and Wasserburg, G. J. Live ^{107}Pd in the Early Solar System and Implications for Planetary Evolution. In *Earth Processes: Reading the Isotopic Code*, pages 1–20. American Geophysical Union, 1996.

[105] Chen, J. H. and Wasserburg, G. J. and Papanastassiou, D. A. The Th and U abundances in chondritic meteorites. In *Lunar and Planetary Science Conference*, volume 24, pages 277–278, March 1993.

[106] Chen, J. H. and Wasserburg, G. J. and Vondamm, K. L. and Edmond, J. M. The U-Th-Pb systematics in hot-springs on the East Pacific rise at 21-degrees-N and Guaymas-Basin. *Geochimica et Cosmochimica Acta*, 50(11):2467–2479, 1986.

[107] Cheng, H. and Edwards, R. L. and Shen, C. C. and Polyak, V. J. and Asmerom, Y. and Woodhead, J. and Hellstrom, J. and Wang, Y. J. and Kong, X. G. and Spotl, C. and Wang, X. F. and Alexander, E. C. Improvements in ^{230}Th dating, ^{230}Th and ^{234}U half-life values, and U-Th isotopic measurements by multi-collector inductively coupled plasma mass spectrometry. *Earth and Planetary Science Letters*, 371:82–91, 2013.

[108] Church, T. M. and Sarin, M. M. and Fleisher, M. Q. and Ferdelman, T. G. Salt marshes: An important coastal sink for dissolved uranium. *Geochimica et Cosmochimica Acta*, 60(20):3879–3887, 1996.

[109] Clayton, D. D. Extinct radioactivities - A three-phase mixing model. *Astrophysical Journal*, 268:381–384, May 1983.

[110] Clayton, D. D. Galactic chemical evolution and nucleocosmochronology - Standard model with terminated infall. *Astrophysical Journal*, 285:411–425, October 1984.

[111] Clayton, D. D. Nuclear cosmochronology within analytic models of the chemical evolution of the solar neighbourhood. *Monthly Notices of the Royal Astronomical Society*, 234(1):1–36, 1988.

[112] Clemens, J. D. and Holloway, J. R. and White, A. J. R. Origin of an A-type granite: Experimental constraints. *American Mineralogist*, 71(3-4):317–324, 1986.

[113] Cloud, P. Beginnings of biospheric evolution and their biogeochemical consequences. *Paleobiology*, 2(3):351–387, 1976.

[114] Cochran, J. K. The oceanic chemistry of the U and Th series nuclides. In Ivanovich, M. and Harmon, R.S., editor, *Uranium-Series Disequilibrium: Applications to Earth, Marine and Environmental Sciences*, pages 334–395. Clarendon Press, Oxford, 1992.

[115] Collins, W. J. and Beams, S. D. and White, A. J. R. and Chappell, B. W. Nature and origin of A-type granites with particular reference to southeastern Australia. *Contributions to Mineralogy and Petrology*, 80(2):189–200, 1982.

[116] Compston, W. and Oversby, V. M. Lead isotopic analysis using a double spike. *Journal of Geophysical Research*, 74(17):4338–4348, 1969.

[117] Condie, K. C. and Des Marais, D. J. and Abbott, D. Precambrian superplumes and supercontinents: A record in black shales, carbon isotopes, and paleoclimates? *Precambrian Research*, 106(3-4):239–260, 2001.

[118] Condon, D. J. and McLean, N. and Noble, S. R. and Bowring, S. A. Isotopic composition $^{238}U/^{235}U$ of some commonly used uranium reference materials. *Geochimica et Cosmochimica Acta*, 74(24):7127–7143, 2010.

[119] Connelly, J. N. and Bizzarro, M. and Krot, A. N. and Nordlund, A. and Wielandt, D. and Ivanova, M. A. The absolute chronology and thermal processing of solids in the solar protoplanetary disk. *Science*, 338(6107):651–655, 2012.

[120] Connelly, J. N. and Bizzarro, M. and Thrane, K. and Baker, J. A. The Pb-Pb age of angrite SAH99555 revisited. *Geochimica et Cosmochimica Acta*, 72(19):4813–4824, 2008.

[121] Cotta, A. J. B. and Enzweiler, J. Classical and new procedures of whole rock dissolution for trace element determination by ICP-MS. *Geostandards & Geoanalytical Research*, 36(1):27–50, 2012.

[122] Cowan, J. J and Sneden, C. Advances in *r*-process nucleosynthesis. *Origin and Evolution of the Elements*, 1:27, 2004.

[123] Creaser, R. A. and Price, R. C. and Wormald, R. J. A-type granites revisited: Assessment of a residual-source model. *Geology*, 19(2):163–166, 1991.

[124] Criss, R. E. *Principles of stable isotope distribution*. Oxford University Press, USA, 1999.

[125] Crock, J. G. and Lichte, F. E. and Wildeman, T. R. The group separation of the rare-earth elements and yttrium from geologic materials by cation-exchange chromatography. *Chemical Geology*, 45(1-2):149–163, 1984.

[126] Crusius, J. and Calvert, S. and Pedersen, T. and Sage, D. Rhenium and molybdenum enrichments in sediments as indicators of oxic, suboxic and sulfidic conditions of deposition. *Earth and Planetary Science Letters*, 145(1-4):65–78, 1996.

[127] Dahl, T. W. and Boyle, R. A. and Canfield, D. E. and Connelly, J. N. and Gill, B. C. and Lenton, T. M. and Bizzarro, M. Uranium isotopes distinguish two geochemically distinct stages during the later Cambrian SPICE event. *Earth and Planetary Science Letters*, 401:313–326, 2014.

[128] Dang, C. and Sauriau, P. G. and Savoye, N. and Caill-Milly, N. and Martinez, P. and Millaret, C. and Haure, J. and De Montaudouin, X. Determination of diet in manila clams by spatial analysis of stable isotopes. *Marine Ecology Progress Series*, 387:167–177, 2009.

[129] Dauphas, N. Multiple sources or late injection of short-lived *r*-nuclides in the early solar system? *Nuclear Physics A*, 758:757C–760C, 2005.

[130] Dauphas, N. The U/Th production ratio and the age of the Milky Way from meteorites and Galactic halo stars. *Nature*, 435:1203–1205, June 2005.

[131] Dauphas, N. and Cook, D. L. and Sacarabany, A. and Fröhlich, C. and Davis, A. M. and Wadhwa, M. and Pourmand, A. and Rauscher, T. and Gallino, R. Iron 60 evidence for early injection and efficient mixing of stellar debris in the protosolar nebula. *Astrophysical Journal*, 686(1):560, 2008.

[132] Dauphas, N. and Marty, B. and Reisberg, L. Molybdenum evidence for inherited planetary scale isotope heterogeneity of the protosolar nebula. *Astrophysical Journal*, 565(1):640, 2002.

[133] Dauphas, N. and Pourmand, A. Thulium anomalies and rare earth element patterns in meteorites and Earth: Nebular fractionation and the nugget effect. *Geochimica et Cosmochimica Acta*, 163:234–261, 2015.

[134] Dauphas, N. and Pourmand, A. and Teng, F.-Z. Routine isotopic analysis of iron by HR-MC-ICPMS: How precise and how accurate? *Chemical Geology*, 267(3-4):175–184, 2009. Advances in experimental and theoretical isotope geochemistry.

[135] Dauphas, N. and Rauscher, T. and Marty, B. and Reisberg, L. Short-lived p-nuclides in the early solar system and implications on the nucleosynthetic role of X-ray binaries. *Nuclear Physics A*, 719:C287–C295, 2003.

[136] Dauphas, N. and Remusat, L. and Chen, J. H. and Roskosz, M. and Papanastassiou, D. A. and Stodolna, J. and Guan, Y. and Ma, C. and Eiler, J. M. Neutron-rich chromium isotope anomalies in supernova nanoparticles. *Astrophysical Journal*, 720(2):1577, 2010.

[137] Dauphas, N. and Roskosz, M. and Alp, E. E. and Golden, D. C. and Sio, C. K. and Tissot, F. L. H. and Hu, M. Y. and Zhao, J. and Gao, L. and Morris, R. V. A general moment NRIXS approach to the determination of equilibrium Fe isotopic fractionation factors: Application to goethite and jarosite. *Geochimica et Cosmochimica Acta*, 94(0):254–275, 2012.

[138] Dauphas, N. and Roskosz, M. and Alp, E. E. and Neuville, D. R. and Hu, M. Y. and Sio, C. K. and Tissot, F. L. H. and Zhao, J. and Tissandier, L. and Médard, E. and Cordier, C. Magma redox and structural controls on iron isotope variations in Earth's mantle and crust. *Earth and Planetary Science Letters*, 398(0):127–140, 2014.

[139] Dauphas, N. and Teng, F.-Z. and Arndt, N. T. Magnesium and iron isotopes in 2.7 Ga Alexo komatiites: Mantle signatures, no evidence for Soret diffusion, and identification of diffusive transport in zoned olivine. *Geochimica et Cosmochimica Acta*, 74(11):3274–3291, 2010.

[140] Davis, A. M. and Grossman, L. Condensation and fractionation of rare earths in the solar nebula . *Geochimica et Cosmochimica Acta*, 43(10):1611–1632, 1979.

[141] Davis, A. M. and McKeegan, K. D. 1.11 - Short-lived radionuclides and early Solar System chronology. In Turekian, H. D. and Holland, K. K., editor, *Treatise on Geochemistry*, pages 361–395. Elsevier, Oxford, second edition, 2014.

[142] Debaille, V. and Brandon, A. D. and Yin, Q. Z. and Jacobsen, B. Coupled ^{142}Nd-^{143}Nd evidence for a protracted magma ocean in Mars. *Nature*, 450(7169):525–528, 2007.

[143] DePaolo, D. J. and Wasserburg, G. J. Nd isotopic variations and petrogenetic models. *Geophysical Research Letters*, 3:249–252, 1976.

[144] Derry, L. A. and France-Lanord, C. Neogene growth of the sedimentary organic carbon reservoir. *Paleoceanography*, 11(3):267–275, 1996.

[145] Dietz, L. A. and Land, G. A. and Pachucki, C. F. Internal standard technique for precise isotopic abundance measurements in thermal ionization mass spectrometry. *Analytical Chemistry*, 34(6):709–710, 1962.

[146] M. H. Dodson. Closure temperature in cooling geochronological and petrological systems. *Contributions to Mineralogy and Petrology*, 40(3):259–274, 1973.

[147] Dodson, M. H. A theoretical study of use of internal standards for precise isotopic analysis by surface ionization technique. 1. General first-order algebraic solutions. *Journal of Scientific Instruments*, 40(6):289–295, 1963.

[148] Dujardin, T. and Lonchampt. G. In Fujii, Y. and Nomura, M. and Okamoto, M. and Onitsuka, H. and Nakanishi, T., editor, *Bulletin of Research Laboratory for Nuclear Reactors*, page 214. Tokyo, special issue edition, 1992.

[149] Dunk, R. M. and Mills, R. A. and Jenkins, W. J. A reevaluation of the oceanic uranium budget for the holocene. *Chemical Geology*, 190(1-4):45–67, 2002.

[150] Eberli, G. P. and Swart, P. K. and Malone, M. J. and et al. Proceedings of the ocean drilling program, initial reports, volume 166. page 850. College Station, TX (Ocean Drilling Program).

[151] Eby, G. N. The A-type granitoids: A review of their occurrence and chemical characteristics and speculations on their petrogenesis. *LITHOS*, 26(1-2):115–134, 1990.

[152] Edwards, R. L. and Gallup, C.D. and Cheng, H. Uranium-series dating of marine and lacustrine carbonates. *Reviews in Mineralogy & Geochemistry*, 52(1):363–405, 2003.

[153] Emerson, S. R. and Huested, S. S. Ocean anoxia and the concentrations of molybdenum and vanadium in seawater. *Marine Chemistry*, 34(3-4):177–196, 1991.

[154] Epstein, S. The variations of the $^{18}O/^{16}O$ ratio in nature and some geologic implications. In, P.H. Abelson (Ed.). In *Researches in Geochemistry*, pages 217–240. Wiley, New York, 1959.

[155] Eugster, O. and Tera, F. and Burnett, D. S. and Wasserburg, G. J. Isotopic composition of gadolinium and neutron-capture effects in some meteorites. *J Geophys Res*, 75(14):2753–2768, 1970.

[156] Eugster, O. and Tera, F. and Burnett, D. S. and Wasserburg, G. J. The isotopic composition of Gd and the neutron capture effects in samples from Apollo 11. *Earth and Planetary Science Letters*, 8(1):20–30, 1970.

[157] Eugster, O. and Tera, F. and Wasserburg, G. J. Isotopic analyses of barium in meteorites and in terrestrial samples. *Journal of Geophysical Research*, 74(15):3897–3908, 1969.

[158] Farquhar, J. and Bao, H. and Thiemens, M. Atmospheric influence of Earth's earliest sulfur cycle. *Science*, 289(5480):756–758, 2000.

[159] Farquhar, J. and Johnston, D. T. The oxygen cycle of the terrestrial planets: Insights into the processing and history of oxygen in surface environments. *Reviews in Mineralogy and Geochemistry*, 68:463–492, 2008.

[160] Farquhar, J. and Peters, M. and Johnston, D. T. and Strauss, H. and Masterson, A. and Wiechert, U. and Kaufman, A. J. Isotopic evidence for mesoarchaean anoxia and changing atmospheric sulphur chemistry. *Nature*, 449(7163):706–709, 2007.

[161] Farquhar, J. and Wing, B. A. Multiple sulfur isotopes and the evolution of the atmosphere. *Earth and Planetary Science Letters*, 213(1-2):1–13, 2003.

[162] Flood, R. H. and Shaw, S. E. A cordierite-bearing granite suite from the New England Batholith, N.S.W., Australia. *Contributions to Mineralogy and Petrology*, 52(3):157–164, 1975.

[163] Florence, T. M. and Batley, G. E. and Ekstrom, A. and Fardy, J. J. and Farrar, Y. J. Separation of uranium isotopes by uranium(IV)-uranium(VI) chemical exchange. *Journal of Inorganic and Nuclear Chemistry*, 37(9):1961–1966, 1975.

[164] Fouillac, A. M. and Javoy, M. Composition isotopique de l'oxygène, de l'hydrogène et du carbone dans la croute atlantique du Leg 51 (IPOD). *Sixth réunion annuelle des sciences de la terre*, page 167, 1978.

[165] French, B. M. and Eugster, H. P. Experimental control of oxygen fugacities by graphite-gas equilibriums. *Journal of Geophysical Research*, 70(6):1529–1539, 1965.

[166] Frimmel, H. E. Archaean atmospheric evolution: Evidence from the witwatersrand gold fields, south africa. *Earth-Science Reviews*, 70(1-2):1–46, 2005.

[167] Fujii, Y. and Ishida, T. and Takeuchi, K. In Fujii, Y. and Nomura, M. and Okamoto, M. and Onitsuka, H. and Nakanishi, T., editor, *Bulletin of Research Laboratory for Nuclear Reactors*, page 214. Tokyo, special issue edition, 1992.

[168] Fujii, Y. and Nomura, M. and Okamoto, M. and Onitsuka, H. and Kawakami, F. and Takeda, K. An anomalous isotope effect of ^{235}U in U(IV)-U(VI) chemical-exchange. *Zeitschrift Fur Naturforschung Section a-a Journal of Physical Sciences*, 44(5):395–398, 1989.

[169] Fujii, Y. and Nomura, M. and Okamoto, M. and Takeda, K. Anomalous isotope fractionation in uranium enrichment process. *Journal of Nuclear Science and Technology*, 26(11):1061–1064, 1989.

[170] Gagné, J. M. and Nguyen Van, S. and Saint-Dizier, J. P. and Pianarosa, P. Isotope shift of ^{234}U, ^{236}U, ^{238}U in UI. *J. Opt. Soc. Am.*, 66(12):1415–1416, Dec 1976.

[171] Gagné, J.-M. and Saint-Dizier, J.-P. and Pianarosa, P. Odd-even staggering of ^{235}U from the 5027 Å line in U I. *Optics Communications*, 20(2):269–270, 1977.

[172] Gagné, J.-M. and Saint-Dizier, J.-P. and Pianarosa, P. Isotope shift ^{238}U-^{233}U from some lines in the UI spectrum . *Optics Communications*, 26(3):348–350, 1978.

[173] Gannoun, A. and Boyet, M. and Rizo, H. and El Goresy, A. ^{146}Sm-^{142}Nd systematics measured in enstatite chondrites reveals a heterogeneous distribution of ^{142}Nd in the solar nebula. *Proceedings of the National Academy of Sciences*, 108(19):7693–7697, 2011.

[174] Gast, P. W. and Hubbard, N. J. and Wiesmann, H. Chemical composition and petrogenesis of basalts from Tranquillity Base. *Geochimica et Cosmochimica Acta Supplement*, 1:1143, 1970.

[175] Gellissen, M. and Palme, H. and Korotev, R. L. and Irving, A. J. NWA 2999, a unique angrite with a large chondritic component. In *Lunar and Planetary Science Conference*, volume 38 of *Lunar and Planetary Science Conference*, March 2007. # 1612.

[176] German, C. R. and Seyfried Jr., W. E. 8.7 - Hydrothermal processes. In Turekian, H. D. and Holland, K. K., editor, *Treatise on Geochemistry*, pages 191–233. Elsevier, Oxford, second edition, 2014.

[177] Goldmann, A. and Brennecka, G. and Noordmann, J. and Weyer, S. and Wadhwa, M. The uranium isotopic composition of the Earth and the Solar System. *Geochimica et Cosmochimica Acta*, 148:145–158, 2015.

[178] Goriely, S. and Arnould, M. Actinides: How well do we know their stellar production? *Astronomy & Astrophysics*, 379(3):1113–1122, 2001.

[179] Goto, K. T. and Anbar, A. D. and Gordon, G. W. and Romaniello, S. J. and Shimoda, G. and Takaya, Y. and Tokumaru, A. and Nozaki, T. and Suzuki, K. and Machida, S. and Hanyu, T. and Usui, A. Uranium isotope systematics of ferromanganese crusts in the Pacific Ocean: Implications for the marine ^{238}U/^{235}U isotope system. *Geochimica et Cosmochimica Acta*, 146:43–58, 2014.

[180] Gouveia, M. A. and Prudêncio, M. I. New data on sixteen reference materials obtained by INAA. *Journal of Radioanalytical and Nuclear Chemistry*, 245(1):105–108, 2000.

[181] Govindaraju, K. 1994 compilation of working values and sample description for 383 geostandards. *Geostandards Newsletter*, 18(SPEC. ISSUE):1–158, 1994.

[182] Govindaraju, K. 1995 working values with confidence limits for twenty-six CRPG, ANRT and IWG-GIT geostandards. *Geostandards Newsletter*, 19(SPEC. ISSUE):1–32, 1995.

[183] Grandstaff, D. E. Origin of uraniferous conglomerates at Elliot Lake, Canada and Witwatersrand, South Africa: Implications for oxygen in the Precambrian atmosphere. *Precambrian Research*, 13(1):1–26, 1980.

[184] Grossman, L. Condensation in the primitive solar nebula. *Geochimica et Cosmochimica Acta*, 36(5):597–619, 1972.

[185] Grossman, L. Petrography and mineral chemistry of Ca-rich inclusions in the Allende meteorite. *Geochimica et Cosmochimica Acta*, 39(4):433–454, 1975.

[186] Grossman, L. and Ganapathy, R. Trace elements in the Allende meteorite - I. Coarse-grained, Ca-rich inclusions. *Geochimica et Cosmochimica Acta*, 40(3):331–344, 1976.

[187] Grossman, L. and Ganapathy, R. Trace elements in the Allende meteorite - II. Fine-grained. Ca-rich inclusions. *Geochimica et Cosmochimica Acta*, 40(8):967–977, 1976.

[188] Grossman, L. and Ganapathy, R. and Davis, A. M. Trace elements in the Allende meteorite - III. Coarse-grained inclusions revisited. *Geochimica et Cosmochimica Acta*, 41(11):1647–1664, 1977.

[189] Grossman, L. and Larimer, J. W. Early chemical history of the solar system. *Reviews of Geophysics*, 12(1):71–101, 1974.

[190] Guan, Y. and Huss, G. R. and Leshin, L. A. ^{60}Fe-^{60}Ni and ^{53}Mn-^{53}Cr isotopic systems in sulfides from unequilibrated enstatite chondrites. *Geochimica et Cosmochimica Acta*, 71(16):4082–4091, 2007.

[191] Haley, B. A. and Klinkhammer, G. P. Complete separation of rare earth elements from small volume seawater samples by automated ion chromatography: Method development and application to benthic flux. *Marine Chemistry*, 82(3-4):197–220, 2003.

[192] Halverson, G. P. and Hoffman, P. F. and Schrag, D. P. and Maloof, A. C. and Rice, A. H. N. Toward a neoproterozoic composite carbon-isotope record. *Geological Society of America Bulletin*, 117(9-10):1181–1207, 2005.

[193] Harper, Jr., C. L. Evidence for ^{92}Nb in the early Solar System and evaluation of a new p-process cosmochronometer from ^{92}Nb/^{92}Mo. *Astrophysical Journal*, 466:437, July 1996.

[194] Hart, S. R. and Staudigel, H. The control of alkalies and uranium in seawater by ocean crust alteration. *Earth and Planetary Science Letters*, 58(2):202–212, 1982.

[195] Henderson, G. M. and Anderson, R. F. The U-series toolbox for paleoceanography. *Uranium-Series Geochemistry*, 52:493–531, 2003.

[196] Henderson, P. and Pankhurst, R. J. Chapter 13 - Analytical chemistry. In Henderson, P., editor, *Rare Earth Element Geochemistry*, volume 2 of *Developments in Geochemistry*, pages 467–499. Elsevier, 1984.

[197] Hidaka, H. and Ebihara, M. and Shima, M. Determination of the isotopic compositions of samarium and gadolinium by thermal ionization mass spectrometry. *Analytical Chemistry*, 67(8):1437–1441, 1995.

[198] Hidaka, H. and Ebihara, M. and Yoneda, S. Isotopic study of neutron capture effects on Sm and Gd in chondrites. *Earth and Planetary Science Letters*, 180(1-2):29–37, 2000.

[199] Hidaka, H. and Ebihara, M. and Yoneda, S. Neutron capture effects on samarium, europium, and gadolinium in Apollo 15 deep drill-core samples. *Meteoritics & Planetary Science*, 35(3):581–589, 2000.

[200] Hidaka, H. and Yoneda, S. Sm and Gd isotopic shifts of Apollo 16 and 17 drill stem samples and their implications for regolith history. *Geochimica et Cosmochimica Acta*, 71(4):1074–1086, 2007.

[201] Hidaka, H. and Yoneda, S. and Nishiizumi, K. Cosmic-ray exposure histories of Martian meteorites studied from neutron capture reactions of Sm and Gd isotopes. *Earth and Planetary Science Letters*, 288(3-4):564–571, 2009.

[202] Hiess, J. and Condon, D. J. and McLean, N. and Noble, S. R. $^{238}U/^{235}U$ systematics in terrestrial uranium-bearing minerals. *Science*, 335(6076):1610–1614, 2012.

[203] Hill, V. and Plez, B. and Cayrel, R. and Beers, T. C. and Nordström, B. and Andersen, J. and Spite, M. and Spite, F. and Barbuy, B. and Bonifacio, P. and Depagne, E. and François, P. and Primas, F. First stars. I. The extreme r-element rich, iron-poor halo giant CS 31082-001. *Astronomy & Astrophysics*, 387(2):560–579, 2002.

[204] Hine, R. and Williams, I. S. and Chappell, B. W. and White, A. J. R. Contrasts between I- and S-type granitoids of the Kosciusko Batholith. *Journal of the Geological Society of Australia*, 25(4):219–234, 1978.

[205] Hirahara, Y. and Chang, Q. and Miyazaki, T. and Takahasi, T. and Kimura, J.-I. Improved Nd chemical separation technique for $^{143}Nd/^{144}Nd$ analysis in geological samples using packed Ln resin columns. *JAMSTEC Rep. Res. Dev.*, 15:27–33, 2012.

[206] Hirt, B. and Epstein, S. A search for isotopic variations in some terrestrial and meteoritic calcium. *Transactions American Geophysical Union*, 45, 1964.

[207] Hofmann, A. W. Chemical differentiation of the earth: The relationship between mantle, continental crust, and oceanic crust. *Earth and Planetary Science Letters*, 90(3):297–314, 1988.

[208] Holland, H. D. *The Chemical Evolution of the Atmosphere and Oceans*, 1984.

[209] Holland, H. D. Early proterozoic atmospheric change. *Early Life on Earth*, pages 237–244, 1994.

[210] Holland, H. D. The oxygenation of the atmosphere and oceans. *Philosophical Transactions of the Royal Society B: Biological Sciences*, 361(1470):903–915, 2006.

[211] Holst, J. C. and Olsen, M. B. and Paton, C. and Nagashima, K. and Schiller, M. and Wielandt, D. and Larsen, K. K. and Connelly, J. N. and Jøorgensen, J. K. and Krot, A. N. and Nordlund, Å. and Bizzarro, M. ^{182}Hf-^{182}W age dating of a ^{26}Al-poor inclusion and implications for the origin of short-lived radioisotopes in the early Solar System. *Proceedings of the National Academy of Sciences*, 110(22):8819–8823, 2013.

[212] Honda, S. and Aoki, W. and Ishimaru, Y. and Wanajo, S. and Ryan, S. G. Neutron-capture elements in the very metal poor star HD 122563. *Astrophysical Journal*, 643(2):1180, 2006.

[213] Hooker, P. J. and O'Nions, R. K. and Pankhurst, R. J. Determination of rare-earth elements in USGS standard rocks by mixed-solvent ion exchange and mass-spectrometric isotope dilution. *Chemical Geology*, 16(3):189–196, 1975.

[214] Horwitz, E. P. and Bloomquist, C. A. A. Chemical separations for super-heavy element searches in irradiated uranium targets. *Journal of Inorganic and Nuclear Chemistry*, 37(2):425–434, 1975.

[215] Horwitz, E. P. and Dietz, M. L. and Chiarizia, R. and Diamond, H. and Essling, A. M. and Graczyk, D. Separation and preconcentration of uranium from acidic media by extraction chromatography. *Analytica Chimica Acta*, 266(1):25–37, 1992.

[216] Horwitz, E. P. and McAlister, D. R. and Dietz, M. L. Extraction chromatography versus solvent extraction: How similar are they? *Separation Science and Technology*, 41(10):2163–2182, 2006.

[217] Huang, F. and Chakraborty, P. and Lundstrom, C. C. and Holmden, C. and Glessner, J. J. G. and Kieffer, S. W. and Lesher, C. E. Isotope fractionation in silicate melts by thermal diffusion. *Nature*, 464(7287):396–400, 2010.

[218] Huang, S. and Farkaš, J. and Yu, G. and Petaev, M. I. and Jacobsen, S. B. Calcium isotopic ratios and rare earth element abundances in refractory inclusions from the Allende CV3 chondrite. *Geochimica et Cosmochimica Acta*, 77:252–265, 2012.

[219] Hudson, G. B. and Kennedy, B. M. and Podosek, F. A. and Hohenberg, C. M. The early solar system abundance of ^{244}Pu as inferred from the St. Severin chondrite. In Ryder, G. and Sharpton, V. L., editor, *Lunar and Planetary Science Conference*, volume 19, pages 547–557, 1989.

[220] Huss, G. R. and Meyer, B. S. and Srinivasan, G. and Goswami, J. N. and Sahijpal, S. Stellar sources of the short-lived radionuclides in the early solar system. *Geochimica et Cosmochimica Acta*, 73(17):4922–4945, 2009.

[221] Iizuka, T. and Amelin, Y. and Kaltenbach, A. and Koefoed, P. and Stirling, C. H. U-Pb systematics of the unique achondrite Ibitira: Precise age determination and petrogenetic implications. *Geochimica et Cosmochimica Acta*, 132:259–273, 2014.

[222] Ireland, T. J. and Tissot, F. L. H. and Yokochi, R. and Dauphas, N. Teflon-HPLC: A novel chromatographic system for application to isotope geochemistry and other industries. *Chemical Geology*, 357(0):203–214, 2013.

[223] Ito, M. and Nagasawa, H. and Yurimoto, H. A study of Mg and K isotopes in Allende CAIs: Implications to the time scale for the multiple heating processes. *Meteoritics & Planetary Science*, 41(12):1871–1881, 2006.

[224] Jacobsen, S. B. The birth of the solar system in a molecular cloud: Evidence from the isotopic pattern of short-lived nuclides in the early solar system. In Krot, A. N. and Scott, E. R. D. and Reipurth, B., editor, *Chondrites and the Protoplanetary Disk*, volume 341 of *Astronomical Society of the Pacific Conference Series*, pages 548–557, December 2005.

[225] Jacobsen, S. B. and Matzel, J. and Hutcheon, I. D. and Krot, A. N. and Yin, Q.-Z. and Nagashima, K. and Ramon, E. C. and Weber, P. K. and Ishii, H. A. and Ciesla, F. J. Formation of the Short-lived Radionuclide ^{36}Cl in the Protoplanetary Disk During Late-stage Irradiation of a Volatile-rich Reservoir. *The Astrophysical Journal Letters*, 731(2):L28, 2011.

[226] Jacobsen, S. B. and Wasserburg, G. J. Sm-Nd isotopic evolution of chondrites and achondrites, II. *Earth and Planetary Science Letters*, 67(2):137–150, 1984.

[227] Jacobsen, S. B. and Yin, Q.-Z. and Moynier, F. and Amelin, Y. and Krot, A. N. and Nagashima, K. and Hutcheon, I. D. and Palme, H. ^{26}Al-^{26}Mg and ^{207}Pb-^{206}Pb systematics of Allende CAIs: Canonical solar initial ^{26}Al/^{27}Al ratio reinstated. *Earth and Planetary Science Letters*, 272(1-2):353–364, 2008.

[228] Johnson, C. M. and Beard, B. L. Correction of instrumentally produced mass fractionation during isotopic analysis of Fe by thermal ionization mass spectrometry. *International Journal of Mass Spectrometry*, 193(1):87–99, 1999.

[229] Jones, J. H. The geochemical coherence of Pu and Nd and the ^{244}Pu/^{238}U ratio of the early solar system. *Geochimica et Cosmochimica Acta*, 46(10):1793–1804, 1982.

[230] Jones, J. H. and Burnett, D. S. Experimental geochemistry of Pu and Sm and the thermodynamics of trace element partitioning. *Geochimica et Cosmochimica Acta*, 51(4):769–782, 1987.

[231] Kaltenbach, A. *Uranium isotopic analysis of terrestrial and extraterrestrial samples*. PhD thesis, University of Otago, 2013.

[232] Kaufman, A. J. and Johnston, D. T. and Farquhar, J. and Masterson, A. L. and Lyons, T. W. and Bates, S. and Anbar, A. D. and Arnold, G. L. and Garvin, J. and

Buick, R. Late archean biospheric oxygenation and atmospheric evolution. *Science*, 317(5846):1900–1903, 2007.

[233] Keil, K. Angrites, a small but diverse suite of ancient, silica-undersaturated volcanic-plutonic mafic meteorites, and the history of their parent asteroid. *Chemie der Erde - Geochemistry*, 72(3):191–218, 2012.

[234] Kelley, K. A. and Plank, T. and Farr, L. and Ludden, J. and Staudigel, H. Subduction cycling of U, Th, and Pb. *Earth and Planetary Science Letters*, 234(3-4):369–383, 2005.

[235] Kelley, K. A. and Plank, T. and Ludden, J. and Staudigel, H. Composition of altered oceanic crust at ODP Sites 801 and 1149. *Geochemistry, Geophysics, Geosystems*, 4(6), 2003.

[236] Kendall, B. and Brennecka, G. A. and Weyer, S. and Anbar, A. D. Uranium isotope fractionation suggests oxidative uranium mobilization at 2.50 Ga. *Chemical Geology*, 362:105–114, 2013.

[237] Kendall, B. and Brennecka, G. and Weyer, S. and Anbar, A. D. Onset of oxidative uranium mobilization on the late Archean earth? *Astrobiology Science Conference*, page 5445, 2010.

[238] Kendall, B. and Komiya, T. and Lyons, T.W. and Bates, S. M. and Gordon, G. W. and Romaniello, S. J. and Jiang, G. and Creaser, R. A. and Xiao, S. and McFadden, K. and Sawaki, Y. and Tahata, M. and Shu, D. and Han, J. and Li, Y. and Chu, X. and Anbar, A. D. Uranium and molybdenum isotope evidence for an episode of widespread ocean oxygenation during the late ediacaran period. *Geochimica et Cosmochimica Acta*, 156:173–193, 2015.

[239] Kennedy, C. W. and Bartelt, G. E. and Orlandini, K. A. Uranium in water and suspended sediments of the great miami river ohio. *Radiological and Environmental Research Division Annual Report, Ecology 77*, 1977.

[240] King, P. L. and White, A. J. R. and Chappell, B. W. and Allen, C. M. Characterization and origin of aluminous A-type granites from the Lachlan Fold Belt, Southeastern Australia. *Journal of Petrology*, 38(3):371–391, 1997.

[241] Kirschvink, J. L. and Raub, T. D. and Fischer, W. Archean "whiffs of oxygen" go poof! *Goldschmidt Conference*, 76, 2012.

[242] Kleine, T. and Hans, U. and Irving, A. J. and Bourdon, B. Chronology of the angrite parent body and implications for core formation in protoplanets. *Geochimica et Cosmochimica Acta*, 84:186–203, 2012.

[243] Klelne, T. and Münker, C. and Mezger, K. and Palme, H. Rapid accretion and early core formation on asteroids and the terrestrial planets from Hf-W chronometry. *Nature*, 418(6901):952–955, 2002.

[244] Klinkhammer, G.P. and Palmer, M.R. Uranium in the oceans: Where it goes and why. *Geochimica et Cosmochimica Acta*, 55(7):1799–1806, 1991.

[245] Ku, T. L. and Knauss, K. G. and Mathieu, G. G. Uranium in open ocean - concentration and isotopic composition. *Deep-Sea Research*, 24(11):1005–1017, 1977.

[246] Kump, L. R. and Junium, C. and Arthur, M. A. and Brasier, A. and Fallick, A. and Melezhik, V. and Lepland, A. and Črne, A.E. and Luo, G. Isotopic evidence for massive oxidation of organic matter following the great oxidation event. *Science*, 334(6063):1694–1696, 2011.

[247] Lacks, D. J. and Goel, G. and Bopp, C. J. and Van Orman, J. A. and Lesher, C. E. and Lundstrom, C. C. Isotope fractionation by thermal diffusion in silicate melts. *Physical Review Letters*, 108(6), 2012.

[248] Langmuir, D. Uranium solution-mineral equilibria at low-temperatures with applications to sedimentary ore-deposits. *Geochimica et Cosmochimica Acta*, 42(6):547–569, 1978.

[249] Larsen, K. K. and Trinquier, A. and Paton, C. and Schiller, M. and Wielandt, D. and Ivanova, M. A. and Connelly, J. N. and Nordlund, A. and Krot, A. N. and Bizzarro, M. Evidence for magnesium isotope heterogeneity in the solar protoplanetary disk. *Astrophysical Journal Letters*, 735(2), 2011.

[250] Le Fevre, B. and Pin, C. An extraction chromatography method for Hf separation prior to isotopic analysis using multiple collection ICP-mass spectrometry. *Analytical Chemistry*, 73(11):2453–2460, 2001.

[251] Lee., S.-G. and Tissot, F. and Dauphas, N. Distribution coefficient (Kd) between HIBA (Hydroxy Isobutyric Acid) and Resin (AG50W-X8). In *Annual meeting of the Geological Society of Korea Conference Abstracts*, page 148, 2013.

[252] Lee, T. and Papanastassiou, D. A. and Wasserburg, G. J. Demonstration of ^{26}Mg excess in Allende and evidence for ^{26}Al. *Geophysical Research Letters*, 3(1):41–44, 1976.

[253] Lehn, G. O. and Jacobson, A. D. and Holmden, C. Precise analysis of Ca isotope ratios ($\delta^{44/40}$Ca) using an optimized ^{43}Ca-^{42}Ca double-spike MC-TIMS method. *International Journal of Mass Spectrometry*, 351:69–75, 2013.

[254] Lichte, F. E. Determination of elemental content off rocks by laser ablation inductively coupled plasma mass spectrometry. *Analytical Chemistry*, 67(14):2479–2485, 1995.

[255] Lin, Y. and Guan, Y. and Leshin, L. A. and Ouyang, Z. and Wang, D. Short-lived chlorine-36 in a Ca- and Al-rich inclusion from the Ningqiang carbonaceous chondrite. *Proceedings of the National Academy of Sciences*, 102(5):1306–1311, 2005.

[256] Liu, M.-C. and Chaussidon, M. and Srinivasan., G and McKeegan, K. D. A lower initial abundance of short-lived ^{41}Ca in the Early Solar System and its implications for Solar System formation. *Astrophysical Journal*, 761(2):137, 2012.

[257] Loiselle, M. C. and Wones, D. R. Characteristics and origin of anorogenic granites. *Geological Society of America Abstracts with Programs*, 11(7):468, 1979.

[258] Lovley, D. R. and Phillips, E. J. P. and Gorby, Y. A. and Landa, E. R. Microbial reduction of uranium. *Nature*, 350(6317):413–416, 1991.

[259] Lugaro, M. and Heger, A. and Osrin, D. and Goriely, S. and Zuber, K. and Karakas, A. I. and Gibson, B. K. and Doherty, C. L. and Lattanzio, J. C. and Ott, U. Stellar origin of the ^{182}Hf cosmochronometer and the presolar history of solar system matter. *Science*, 345(6197):650–653, 2014.

[260] Lugmair, G. W. and Galer, S. J. G. Age and isotopic relationships among the angrites Lewis Cliff 86010 and Angra dos Reis. *Geochimica et Cosmochimica Acta*, 56(4):1673–1694, 1992.

[261] Lugmair, G. W. and Marti, K. Neutron capture effects in lunar gadolinium and the irradiation histories of some lunar rocks. *Earth and Planetary Science Letters*, 13(1):32–42, 1971.

[262] Lugmair, G. W. and Marti, K. Sm-Nd-Pu timepieces in the Angra dos Reis meteorite. *Earth and Planetary Science Letters*, 35(2):273–284, 1977.

[263] Lugmair, G.W. and Scheinin, N.B. and Marti, K. Sm-nd age and history of apollo 17 basalt 75075: Evidence for early differentiation of the lunar exterior. *Proc. 6th Lunar Sci. Conf.*, pages 1419–1429, 1975.

[264] Lundstrom, C. Hypothesis for the origin of convergent margin granitoids and Earth's continental crust by thermal migration zone refining. *Geochimica et Cosmochimica Acta*, 73(19):5709–5729, 2009.

[265] Lyons, T. W. and Anbar, A. D. and Severmann, S. and Scott, C. and Gill, B. C. Tracking euxinia in the ancient ocean: A multiproxy perspective and Proterozoic case study. *Annual Review of Earth and Planetary Sciences*, 37(1):507–534, 2009.

[266] Lyons, T. W. and Reinhard, C. T. and Planavsky, N. J. The rise of oxygen in Earth's early ocean and atmosphere. *Nature*, 506(7488):307–315, 2014.

[267] MacPherson, G. J. and Davis, A. M. Refractory inclusions in the prototypical CM chondrite, Mighei. *Geochimica et Cosmochimica Acta*, 58(24):5599–5625, 1994.

[268] MacPherson, G. J. and Simon, S. B. and Davis, A. M. and Grossman, L. and Krot, A. N. Calcium-Aluminum-rich inclusions: Major unanswered questions. In Krot, A. N. and Scott, E. R. D. and Reipurth, B., editor, *Chondrites and the Protoplanetary Disk*, volume 341 of *Astronomical Society of the Pacific Conference Series*, page 225, December 2005.

[269] Makishima, A. and Nath, B. N. and Nakamura, E. New sequential separation procedure for Sr, Nd and Pb isotope ratio measurement in geological material using MC-ICP-MS and TIMS. *Geochemical Journal*, 42(3):237–246, 2008.

[270] Mane, P. and Brennecka, G. A. and Romaniello, S. J. and Wadhwa, M. Mg and U isotopic systematics in Allende CAIs implications for the origin of U isotopic variation in refractory inclusions. *LPI Contributions*, page 1685, 2014.

[271] Marechal, C. N. and Telouk, P. and Albarède, F. Precise analysis of copper and zinc isotopic compositions by plasma-source mass spectrometry. *Chemical Geology*, 156(1-4):251–273, 1999.

[272] Martin, A. J. P. and Synge, R. L. M. A new form of chromatogram employing two liquid phases I. A theory of chromatography 2. Application to the micro-determination of the higher monoamino-acids in proteins. *Biochemical Journal*, 35:1358–1368, 1941.

[273] Martin, R. F. A-type granites of crustal origin ultimately result from open-system fenitization-type reactions in an extensional environment. *Lithos*, 91(1-4):125–136, 2006.

[274] Mason, S. R. and Taylor, B. Inclusions in the Allende Meteorite. *Smithsonian Contributions to the Earth Sciences, No. 25, Smithsonian Institution, Washington, DC*, 1982.

[275] Mathew, K. and Mason, P. and Voeks, A. and Narayanan, U. Uranium isotope abundance ratios in natural uranium metal certified reference material 112-A. *International Journal of Mass Spectrometry*, 315:8–14, 2012.

[276] Matsui, M. and Aoki, T. and Kumagai, T. Forced-flow chromatography of rare earths using sensitive spectrophotometry. *Bulletin of the Institute for Chemical Research, Kyoto University*, 59(3), 9 1981. (Commemoration issue dedicated to professor Megumi Tashiro on the occasion of his retirement).

[277] Matthews, K. A. and Murrell, M. T. and Goldstein, S. J. and Nunn, A. J. and Norman, D. E. Uranium and Thorium concentration and isotopic composition in five glass (BHVO-2G, BCR-2G, NKT-1G, T1-G, ATHO-G) and two powder (BHVO-2, BCR-2) reference materials. *Geostandards & Geoanalytical Research*, 35(2):227–234, 2011.

[278] McCulloch, M. T. and Wasserburg, G. J. Barium and neodymium isotopic anomalies in the allende meteorite. *Astrophys. J.*, 220:L15–L19, 1978.

[279] McCulloch, M.T. and Wasserburg, G.J. More anomalies from the allende meteorite samarium. *Geophysical Research Letters*, 5:599–602, 1978.

[280] McDonough, W. F. 3.16 - Compositional model for the Earth's core. In Turekian, H. D. and Holland, K. K., editor, *Treatise on Geochemistry*, volume 3, pages 559–577. Elsevier, Oxford, second edition, 2014.

[281] McDonough, W. F. and Sun, S.-S. The composition of the Earth. *Chemical Geology*, 120(3-4):223–253, 1995.

[282] McKee, B. A. and DeMaster, D. J. and Nittrouer, C. A. Uranium geochemistry on the Amazon shelf: Evidence for uranium release from bottom sediments. *Geochimica et Cosmochimica Acta*, 51(10):2779–2786, 1987.

[283] McLean, N. M. and Bowring, J. F. and Bowring, S. A. An algorithm for U-Pb isotope dilution data reduction and uncertainty propagation. *Geochemistry Geophysics Geosystems*, 12, 2011.

[284] McQuarrie, D. A. and Simon, J. D. *Physical chemistry: A molecular approach*. University Science Books, 1997.

[285] Medvedev, P. V. and Melezhik, V. A. and Filippov, M. M. Palaeoproterozoic petrified oil field (Shunga Event). *Paleontological Journal*, 43(8):972–979, 2009.

[286] Meisel, T. and Moser, J. and Fellner, N. and Wegscheider, W. and Schoenberg, R. Simplified method for the determination of Ru, Pd, Re, Os, Ir and Pt in chromitites and other geological materials by isotope dilution ICP-MS and acid digestion. *Analyst*, 126:322–328, 2001.

[287] Meisel, T. and Schöner, N. and Paliulionyte, V. and Kahr, E. Determination of rare earth elements, Y, Th, Zr, Hf, Nb and Ta in geological reference materials G-2, G-3, SCo-1 and WGB-1 by sodium peroxide sintering and inductively coupled plasma-mass spectrometry. *Geostandards Newsletter*, 26(1):53–61, 2002.

[288] Melezhik, V. A. and Fallick, A. E. and Filippov, M. M. and Larsen, O. Karelian shungite - an indication of 2.0-Ga-old metamorphosed oil-shale and generation of petroleum: Geology, lithology and geochemistry. *Earth Science Reviews*, 47(1-2):1–40, 1999.

[289] Melezhik, V. A. and Fallick, A. E. and Hanski, E. J. and Kump, L. R. and Lepland, A. and Prave, A. R. and Strauss, H. Emergence of the aerobic biosphere during the Archean-Proterozoic transition: Challenges of future research. *GSA Today*, 15(11):4–11, 2005.

[290] Melezhik, V. A. and Fallick, A. E. and Medvedev, P. V. and Makarikhin, V. V. Extreme $^{13}C_{carb}$ enrichment in ca. 2.0 Ga magnesite-stromatolite-dolomite-'red beds' association in a global context: A case for the world-wide signal enhanced by a local environment, journal=Earth-Science Reviews. 48(1-2):71–120, 1999.

[291] Melezhik, V. A. and Filippov, M. M. and Romashkin, A. E. A giant Palaeoproterozoic deposit of shungite in NW Russia: Genesis and practical applications. *Ore Geology Reviews*, 24(1-2):135–154, 2004.

[292] Melezhik, V. A. and Lepland, A. and Romashkin, A. E. and Rychanchik, D. V. and Mesli, M. and Finne, T. E. and Conze, R. The great oxidation event recorded in paleoproterozoic rocks from Fennoscandia. *Scientific Drilling*, (9):23–29, 2010.

[293] Melezhik, V. A. and Prave, A. R. and Hanski, E. J. and Fallick, A. E. and Lepland, A. and Kump, L. R. and Strauss, H. *Reading the Archive of Earth's Oxygenation*, 2013.

[294] Meyer, B. S. and Clayton, D. D. Short-lived radioactivities and the birth of the sun. *Space Science Reviews*, 92(1-2):133–152, 2000.

[295] Michard, A. and Albarède, F. Hydrothermal uranium uptake at ridge crests. *Nature*, 317(6034):244–246, 1985.

[296] Millet, M. A. and Dauphas, N. Ultra-precise titanium stable isotope measurements by double-spike high resolution MC-ICP-MS. *Journal of Analytical Atomic Spectrometry*, 29(8):1444–1458, 2014.

[297] Mishra, R. K. and Chaussidon, M. Fossil records of high level of ^{60}Fe in chondrules from unequilibrated chondrites. *Earth and Planetary Science Letters*, 398:90–100, 2014.

[298] Mishra, R. K. and Goswami, J. N. Fe-Ni and Al-Mg isotope records in UOC chondrules: Plausible stellar source of ^{60}Fe and other short-lived nuclides in the early Solar System. *Geochimica et Cosmochimica Acta*, 132:440–457, 2014.

[299] Mojzsis, S. J. and Coath, C. D. and Greenwood, J. P. and McKeegan, K. D. and Harrison, T. M. Mass-independent isotope effects in Archean (2.5 to 3.8 Ga) sedimentary sulfides determined by ion microprobe analysis. *Geochimica et Cosmochimica Acta*, 67(9):1635–1658, 2003.

[300] Montoya-Pino, C. and Weyer, S. and Anbar, A. D. and Pross, J. and Oschmann, W. and van de Schootbrugge, B. and Arz, H. W. Global enhancement of ocean anoxia during oceanic anoxic event 2: A quantitative approach using u isotopes. *Geology*, 38(4):315–318, 2010.

[301] Morford, J. L. and Emerson, S. The geochemistry of redox sensitive trace metals in sediments. *Geochimica et Cosmochimica Acta*, 63(11-12):1735–1750, 1999.

[302] Mostefaoui, S. and Lugmair, G. W. and Hoppe, P. and El Goresy, A. Evidence for live ^{60}Fe in meteorites. *New Astronomy Reviews*, 48(1-4):155–159, 2004. Astronomy with Radioactivities {IV} and Filling the Sensitivity Gap in MeV Astronomy.

[303] Mottl, M. J. and Wheat, G. and Baker, E. and Becker, N. and Davis, E. and Feely, R. and Grehan, A. and Kadko, D. and Lilley, M. and Massoth, G. and Moyer, C. and Sansone, F. Warm springs discovered on 3.5 Ma oceanic crust, eastern flank of the Juan de Fuca Ridge. *Geology*, 26(1):51–54, 1998.

[304] Murakami, T. and Sreenivas, B. and Sharma, S. D. and Sugimori, H. Quantification of atmospheric oxygen levels during the Paleoproterozoic using paleosol compositions and iron oxidation kinetics. *Geochimica et Cosmochimica Acta*, 75(14):3982–4004, 2011.

[305] Murphy, M. J. and Stirling, C. H. and Kaltenbach, A. and Turner, S. P. and Schaefer, B. F. Fractionation of ^{238}U/^{235}U by reduction during low temperature uranium mineralisation processes. *Earth and Planetary Science Letters*, 388:306–317, 2014.

[306] Murrell, M. T. and Burnett, D. S. Actinide chemistry in Allende Ca-Al-rich inclusions. *Geochimica et Cosmochimica Acta*, 51(4):985–999, 1987.

[307] Nabelek, P.I. and Russ-Nabelek, C. and Denison, J. R. The generation and crystallization conditions of the Proterozoic Harney Peak Leucogranite, Black Hills, South Dakota, USA: Petrologic and geochemical constraints. *Contributions to Mineralogy and Petrology*, 110(2-3):173–191, 1992.

[308] Nash, K. L. and Jensen, M. P. Analytical-scale separations of the lanthanides: A review of techniques and fundamentals. *Separation Science and Technology*, 36(5-6):1257–1282, 2001.

[309] Neue, U. D. *HPLC columns: theory, technology, and practice*. Wiley-VCH, New York, 1997.

[310] Niederer, F. R. and Papanastassiou, D. A. and Wasserburg, G. J. Absolute isotopic abundances of Ti in meteorites. *Geochimica et Cosmochimica Acta*, 49(3):835–851, 1985.

[311] Nier, A. O. The isotopic constitution of uranium and the half-lives of the uranium isotopes. I. *Phys. Rev.*, 55:150–153, Jan 1939.

[312] Nittler, L. R. and Dauphas, N. *Meteorites and the chemical evolution of the Milky Way*, pages 127–146. 2006.

[313] Nomura, M. and Higuchi, N. and Fujii, Y. Mass dependence of uranium isotope effects in the U(IV)-U(VI) exchange reaction. *Journal of the American Chemical Society*, 118(38):9127–9130, 1996.

[314] Noordmann, J. and Weyer, S. and Montoya-Pino, C. and Dellwig, O. and Neubert, N. and Eckert, S. and Paetzel, M. and Böttcher, M. E. Uranium and molybdenum isotope systematics in modern euxinic basins: Case studies from the central Baltic Sea and the Kyllaren fjord (Norway). *Chemical Geology*, 396:182–195, 2015.

[315] Noordmann, J. and Weyer, S. and Sharma, M. and Georg, R. B. and Rausch, S. and Bach, W. Fractionation of $^{238}U/^{235}U$ during weathering and hydrothermal alteration. *Mineral. Mag.*, 75, 2011.

[316] Nyquist, L. E. and Kleine, T. and Shih, C.-Y. and Reese, Y. D. The distribution of short-lived radioisotopes in the early solar system and the chronology of asteroid accretion, differentiation, and secondary mineralization. *Geochimica et Cosmochimica Acta*, 73(17):5115–5136, 2009. The Chronology of Meteorites and the Early Solar System.

[317] O'Neil, J. and Carlson, R. W. and Francis, D. and Stevenson, R. K. Neodymium-142 evidence for hadean mafic crust. *Science*, 321(5897):1828–1831, 2008.

[318] Ono, S. and Eigenbrode, J. L. and Pavlov, A. A. and Kharecha, P. and Rumble III., D. and Kasting, J. F. and Freeman, K. H. New insights into archean sulfur cycle from mass-independent sulfur isotope records from the hamersley basin, australia. *Earth and Planetary Science Letters*, 213(1-2):15–30, 2003.

[319] Ovchinnikova, G. V. and Kuznetsov, A. B. and Melezhik, V. A. and Gorokhov, I. M. and Vasil'eva, I.M. and Gorokhovskii, B. M. Pb-Pb age of Jatulian carbonate rocks: The Tulomozero formation of southeast Karelia. *Stratigraphy and Geological Correlation*, 15(4):359–372, 2007.

[320] Owens, S. A. and Buesseler, K. O. and Sims, K. W. W. Re-evaluating the ^{238}U-salinity relationship in seawater: Implications for the ^{238}U-^{234}Th disequilibrium method. *Marine Chemistry*, 127(1-4):31–39, 2011.

[321] Pagel, B. E. J. *Nucleosynthesis and chemical evolution of galaxies*. Cambridge University Press, 2 edition, 2009.

[322] Papineau, D. and Mojzsis, S. J. and Schmitt, A. K. Multiple sulfur isotopes from Paleoproterozoic Huronian interglacial sediments and the rise of atmospheric oxygen. *Earth and Planetary Science Letters*, 255(1-2):188–212, 2007.

[323] Partin, C. A. and Bekker, A. and Planavsky, N. J. and Scott, C. T. and Gill, B. C. and Li, C. and Podkovyrov, V. and Maslov, A. and Konhauser, K. O. and Lalonde, S. V. and Love, G. D. and Poulton, S. W. and Lyons, T. W. Large-scale fluctuations in Precambrian atmospheric and oceanic oxygen levels from the record of U in shales. *Earth and Planetary Science Letters*, 369-370:284–293, 2013.

[324] Partin, C. A. and Lalonde, S. V. and Planavsky, N. J. and Bekker, A. and Rouxel, O. J. and Lyons, T. W. and Konhauser, K. O. Uranium in iron formations and the rise of atmospheric oxygen. *Chemical Geology*, 362:82–90, 2013. Special Issue dedicated to H.D. Holland: Evolution of the atmosphere and ocean through time.

[325] Patchett, P. J. Sr isotopic fractionation in Ca-Al inclusions from the Allende meteorite. *Nature*, 283(5746):438–441, 1980.

[326] Patterson, C. Age of meteorites and the Earth. *Geochimica et Cosmochimica Acta*, 10(4):230–237, 1956.

[327] Patterson, C. and Tilton, G. and Inghram, M. Age of the Earth. *Science*, 121(3134):69–75, 1955.

[328] Pavlov, A. A. and Kasting, J. F. Mass-independent fractionation of sulfur isotopes in archean sediments: Strong evidence for an anoxic archean atmosphere. *Astrobiology*, 2(1):27–41, 2002.

[329] Pierce, T. B. and Peck, P. F. Use of di-(2-ethylhexyl) orthophosphoric acid for the separation of the rare earths by reverse phase partition chromatography. *Nature*, 195:597, 1962.

[330] Pierce, T. B. and Peck, P. F. and Hobbs, R. S. The separation of the rare earths by partition chromatography with reversed phases - Part II behavior of individual elements on HDEHP-Corvic columns. *Journal of chromatography*, 12:81–88, 1963.

[331] Pin, C. and Santos Zalduegui, J.F. Sequential separation of light rare-earth elements, thorium and uranium by miniaturized extraction chromatography: Application to isotopic analyses of silicate rocks. *Analytica Chimica Acta*, 339(1-2):79–89, 1997.

[332] Planavsky, N. J. and Bekker, A. and Hofmann, A. and Owens, J. D. and Lyons, T. W. Sulfur record of rising and falling marine oxygen and sulfate levels during the Lomagundi event. *Proceedings of the National Academy of Sciences*, 109(45):18300–18305, 2012.

[333] Planavsky, N. J. and McGoldrick, P. and Scott, C. T. and Li, C. and Reinhard, C. T. and Kelly, A. E. and Chu, X. and Bekker, A. and Love, G. D. and Lyons, T. W. Widespread iron-rich conditions in the mid-Proterozoic ocean. *Nature*, 477(7365):448–451, 2011.

[334] Pogge von Strandmann, P. A. E. and James, R. H. and van Calsteren, P. and Gíslason, S. R. and Burton, K. W. Lithium, magnesium and uranium isotope behaviour in the estuarine environment of basaltic islands. *Earth and Planetary Science Letters*, 274(3-4):462–471, 2008.

[335] Poldervaart, A. Chemistry of the Earth's crust. In *Crust of the earth - a symposium (ed. A. Poldervaart)*, pages 110–144, 1955.

[336] Porcelli, D. and Andersson, P. S. and Wasserburg, G. J. and Ingri, J. and Baskaran, M. The importance of colloids and mires for the transport of uranium isotopes through the Kalix River watershed and Baltic Sea. *Geochimica et Cosmochimica Acta*, 61(19):4095–4113, 1997.

[337] Poulton, S. W. and Canfeld, D. E. Ferruginous conditions: A dominant feature of the ocean through earth's history. *Elements*, 7(2):107–112, 2011.

[338] Poulton, S. W. and Fralick, P. W. and Canfield, D. E. Spatial variability in oceanic redox structure 1.8 billion years ago. *Nature Geoscience*, 3(7):486–490, 2010.

[339] Pourmand, A. and Dauphas, N. Distribution coefficients of 60 elements on TODGA resin: Application to Ca, Lu, Hf, U and Th isotope geochemistry. *Talanta*, 81(3):741–753, 2010.

[340] Pourmand, A. and Dauphas, N. and Ireland, T. J. A novel extraction chromatography and MC-ICP-MS technique for rapid analysis of REE, Sc and Y: Revising CI-chondrite and Post-Archean Australian Shale (PAAS) abundances. *Chemical Geology*, 291:38–54, 2012.

[341] Pourmand, A. and Tissot, F. L. H. and Arienzo, M. and Sharifi, A. Introducing a comprehensive data reduction and uncertainty propagation algorithm for U-Th

geochronometry with extraction chromatography and isotope dilution MC-ICP-MS. *Geostandards & Geoanalytical Research*, 38(2):129–148, 2014.

[342] Press, W. H. and Teukolsky, S. A. and Vetterling, W. T. and Flannery, B. P. *Numerical recipes 3rd edition: The art of scientific computing*. Cambridge University Press, New York, NY, USA, 3 edition, 2007.

[343] Prinzhofer, A. and Papanastassiou, D. A. and Wasserburg, G. J. Samarium-neodymium evolution of meteorites. *Geochimica et Cosmochimica Acta*, 56(2):797–815, 1992.

[344] Puchtel, I. S. and Arndt, N. T. and Hofmann, A. W. and Haase, K.M. and Kröner, A. and Kulikov, V. S. and Kulikova, V. V. and Garbe-Schönberg, C. D. and Nemchin, A. A. Petrology of mafic lavas within the Onega plateau, central Karelia: Evidence for 2.0 Ga plume-related continental crustal growth in the Baltic Shield. *Contributions to Mineralogy and Petrology*, 130(2):134–153, 1998.

[345] Puchtel, I. S. and Brügmann, G. E. and Hofmann, A. W. Precise Re-Os mineral isochron and Pb-Nd-Os isotope systematics of a mafic-ultramafic sill in the 2.0 Ga Onega plateau (Baltic Shield). *Earth and Planetary Science Letters*, 170(4):447–461, 1999.

[346] Pukhtel, I. S. and Zhuravlev, D. Z. and Ashikhmina, N. A. and Kulikov, V. S. and Kulikova, V. V. Sm-Nd age of the Suisarian suite on the Baltic Shield. *Trans Russ Acad Sci*, 326(4):706–711, 1992.

[347] Qin, L. and Carlson, R. W. and Alexander, C. M. Correlated nucleosynthetic isotopic variability in Cr, Sr, Ba, Sm, Nd and Hf in Murchison and QUE 97008. *Geochimica et Cosmochimica Acta*, 75(24):7806–7828, 2011.

[348] Quitté, G. and Halliday, A. N. and Meyer, B. S. and Markowski, A. and Latkoczy, C. and Günther, D. Correlated iron-60, nickel-62, and zirconium-96 in refractory inclusions and the origin of the Solar System. *Astrophysical Journal*, 655(1):678, 2007.

[349] Quitté, G. and Latkoczy, C. and Schönbächler, M. and Halliday, A. N. and Günther, D. ^{60}Fe-^{60}Ni systematics in the eucrite parent body: A case study of Bouvante and Juvinas. *Geochimica et Cosmochimica Acta*, 75(23):7698–7706, 2011.

[350] Quitté, G. and Markowski, A. and Latkoczy, C. and Gabriel, A. and Pack, A. Iron-60 heterogeneity and incomplete isotope mixing in the early Solar System. *Astrophysical Journal*, 720(2):1215, 2010.

[351] Rademacher, L. K. and Lundstrom, C. C. and Johnson, T. M. and Sanford, R. A. and Zhao, J. and Zhang, Z. Experimentally determined uranium isotope fractionation during reduction of hexavalent U by bacteria and zero valent iron. *Environmental Science and Technology*, 40(22):6943–6948, 2006.

[352] Ramdohr, P. *New observations on the ores of the Witwatersrand in South Africa and their genetic significance*. Geological Society of South Africa, 1958.

[353] Rasmussen, B. and Buick, R. Redox state of the Archean atmosphere: Evidence from detrital heavy minerals in ca. 3250-2750 Ma sandstones from the Pilbara Craton, Australia. *Geology*, 27(2):115–118, 1999.

[354] Rasmussen, B. and Fletcher, I. R. and Bekker, A. and Muhling, J. R. and Gregory, C. J. and Thorne, A. M. Deposition of 1.88-billion-year-old iron formations as a consequence of rapid crustal growth. *Nature*, 484(7395):498–501, 2012.

[355] Rauscher, T. and Dauphas, N. and Dillmann, I. and Fröhlich, C. and Fülöp, Zs. and Gyürky, Gy. Constraining the astrophysical origin of the p-nuclei through nuclear physics and meteoritic data. *Reports on Progress in Physics*, 76(6):066201, 2013.

[356] Regelous, M. and Elliott, T. and Coath, C. D. Nickel isotope heterogeneity in the early solar system. *Earth and Planetary Science Letters*, 272(1-2):330–338, 2008.

[357] Rehkämper, M. and Gärtner, M. and Galer, S. J. G. and Goldstein, S. L. Separation of Ce from other rare-earth elements with application to Sm-Nd and La-Ce chronometry. *Chemical Geology*, 129(3-4):201–208, 1996.

[358] Reinhard, C. T. and Planavsky, N. J. and Robbins, L. J. and Partin, C. A. and Gill, B. C. and Lalonde, S. V. and Bekker, A. and Konhauser, K. O. and Lyons, T. W. Proterozoic ocean redox and biogeochemical stasis. *Proceedings of the National Academy of Sciences*, 110(14):5357–5362, 2013.

[359] Reinhard, C. T. and Raiswell, R. and Scott, C. and An Bar, A. D. and Lyons, T. W. A late archean sulfidic sea stimulated by early oxidative weathering of the continents. *Science*, 326(5953):713–716, 2009.

[360] Reynolds, J. H. Determination of the age of the elements. *Phys. Rev. Lett.*, 4:8–10, Jan 1960.

[361] Reynolds, M. R. Physical oceanography of the Gulf, Strait of Hormuz, and the Gulf of Oman-Results from the Mt Mitchell expedition. *Marine Pollution Bulletin*, 27(C):35–59, 1993.

[362] Riches, A. J.V. and Day, J. M. D. and Walker, R. J. and Simonetti, A. and Liu, Y. and Neal, C. R. and Taylor, L. A. Rhenium-osmium isotope and highly-siderophile-element abundance systematics of angrite meteorites. *Earth and Planetary Science Letters*, 353-354:208 – 218, 2012.

[363] Richter, F. M. Timescales determining the degree of kinetic isotope fractionation by evaporation and condensation. *Geochimica et Cosmochimica Acta*, 68(23):4971–4992, 2004.

[364] Richter, F. M. and Dauphas, N. and Teng, F.-Z. Non-traditional fractionation of non-traditional isotopes: Evaporation, chemical diffusion and soret diffusion. *Chemical Geology*, 258(1-2):92–103, 2009.

[365] Richter, F. M. and Davis, A. M. and Ebel, D. S. and Hashimoto, A. Elemental and isotopic fractionation of Type B calcium-, aluminum-rich inclusions: Experiments, theoretical considerations, and constraints on their thermal evolution. *Geochimica et Cosmochimica Acta*, 66(3):521–540, 2002.

[366] Richter, F. M. and Watson, E. B. and Mendybaev, R. A. and Teng, F.-Z. and Janney, P. E. Magnesium isotope fractionation in silicate melts by chemical and thermal diffusion. *Geochimica et Cosmochimica Acta*, 72(1):206–220, 2008.

[367] Richter, S. and Eykens, R. and Kuhn, H. and Aregbe, Y. and Verbruggen, A. and Weyer, S. New average values for the n(^{238}U)/n(^{235}U) isotope ratios of natural uranium standards. *International Journal of Mass Spectrometry*, 295(1-2):94–97, 2010.

[368] Rocholl, A. and Jochum, K. P. Th, U and other trace elements in carbonaceous chondrites: Implications for the terrestrial and solar-system Th/U ratios. *Earth and Planetary Science Letters*, 117(1-2):265–278, 1993.

[369] Rogers, J. J. W. and Adams, J. A. S. Uranium. *Handbook of Geochemistry*, 92, 1969.

[370] Romaniello, S. J. and Herrmann, A. D. and Anbar, A. D. Uranium concentrations and ^{238}U/^{235}U isotope ratios in modern carbonates from the Bahamas: Assessing a novel paleoredox proxy. *Chemical Geology*, 362:305–316, 2013.

[371] Ronov, A. B. and Yaroshevsky, A. A. Chemical composition of the Earth's crust. *The Earth's Crust and Upper Mantle*, 13:37–57, 1969.

[372] Roskosz, M. and Sio, C.K. and Dauphas, N. and Bi, W. and Tissot, F. L. H. and Hu, M. Y. and Zhao, J. and Alp, E. E. Spinel-olivine-pyroxene equilibrium iron isotopic fractionation and applications to natural peridotites. *Geochimica et Cosmochimica Acta*, 169:184–199, 2015.

[373] Ross, D. K. and Simon, J. I. and Simon, S. B. and Grossman, L. Two generations of sodic metasomatism in an Allende Type B CAI. In *Lunar and Planetary Science Conference*, volume 46, March 2015. # 2552.

[374] Rouxel, O. J. and Bekker, A. and Edwards, K. J. Iron isotope constraints on the Archean and Paleoproterozoic ocean redox state. *Science*, 307(5712):1088–1091, 2005.

[375] Roy, S. Genetic diversity of manganese deposition in the terrestrial geological record. *Geological Society, London, Special Publications*, 119(1):5–27, 1997.

[376] Rudge, J. F. and Reynolds, B. C. and Bourdon, B. The double spike toolbox. *Chemical Geology*, 265(3-4):420–431, 2009.

[377] Rudnick, R. L. and Gao, S. 4.1 - Composition of the continental crust. In Turekian, H. D. and Holland, K. K., editor, *Treatise on Geochemistry*, pages 1–51. Elsevier, Oxford, second edition, 2014.

[378] Rugel, G. and Faestermann, T. and Knie, K. and Korschinek, G. and Poutivtsev, M. and Schumann, D. and Kivel, N. and Günther-Leopold, I. and Weinreich, R. and Wohlmuther, M. New measurement of the ^{60}Fe half-life. *Phys. Rev. Lett.*, 103:072502, Aug 2009.

[379] Russ III, G. P. and Burnett, D. S. and Lingenfelter, R. E. and Wasserburg, G. J. Neutron capture on ^{149}Sm in lunar samples. *Earth and Planetary Science Letters*, 13(1):53–60, 1971.

[380] Russell, S. S. and MacPherson, G. J. Alteration of CAIs: Times and places. In *Workshop on parent-body and nebular modification of chondritic materials*, page 4054, 1997.

[381] Saari, H.-K. and Schmidt, S. and Huguet, S. and Lanoux, A. Spatiotemporal variation of dissolved ^{238}U in the Gironde fluvial-estuarine system (France). *Journal of Environmental Radioactivity*, 99(2):426–435, 2008.

[382] Schatz, H. and Toenjes, R. and Pfeiffer, B. and Beers, T. C. and Cowan, J. J. and Hill, V. and Kratz, K.-L. Thorium and uranium chronometers applied to CS 31082-001. *Astrophysical Journal*, 579(2):626, 2002.

[383] Schauble, E. A. Applying stable isotope fractionation theory to new systems. *Reviews in Mineralogy and Geochemistry*, 55(1):65–111, 2004.

[384] Schauble, E. A. Role of nuclear volume in driving equilibrium stable isotope fractionation of mercury, thallium, and other very heavy elements. *Geochimica et Cosmochimica Acta*, 71(9):2170–2189, 2007.

[385] Schiller, M. and Baker, J. A. and Bizzarro, M. ^{26}Al-^{26}Mg dating of asteroidal magmatism in the young Solar System . *Geochimica et Cosmochimica Acta*, 74(16):4844–4864, 2010.

[386] Schmitz, M. D. and Schoene, B. Derivation of isotope ratios, errors, and error correlations for U-Pb geochronology using ^{205}Pb-^{235}U-(^{233}U)-spiked isotope dilution thermal ionization mass spectrometric data. *Geochemistry Geophysics Geosystems*, 8, 2007.

[387] Schoene, B. 4.10 - U-Th-Pb geochronology. In Turekian, H. D. and Holland, K. K., editor, *Treatise on Geochemistry*, pages 341–378. Elsevier, Oxford, second edition, 2014.

[388] Schönbächler, M. and Carlson, R. W. and Horan, M. F. and Mock, T. D. and Hauri, E. H. Silver isotope variations in chondrites: Volatile depletion and the initial ^{107}Pd abundance of the solar system. *Geochimica et Cosmochimica Acta*, 72(21):5330–5341, 2008.

[389] Schönbächler, M. and Rehkämper, M. and Halliday, A. N. and Lee, D.-C. and Bourot-Denise, M. and Zanda, B. and Hattendorf, B. and Günther, D. Niobium-zirconium chronometry and early Solar System development. *Science*, 295(5560):1705–1708, 2002.

[390] Schörder, S. and Bekker, A. and Beukes, N. J. and Strauss, H. and Van Niekerk, H. S. Rise in seawater sulphate concentration associated with the Paleoproterozoic positive carbon isotope excursion: Evidence from sulphate evaporites in the $\sim 2.2 - 2.1$ Gyr shallow-marine Lucknow Formation, South Africa. *Terra Nova*, 20(2):108–117, 2008.

[391] Sha, L.-K. and Chappell, B. W. Apatite chemical composition, determined by electron microprobe and laser-ablation inductively coupled plasma mass spectrometry, as a probe into granite petrogenesis. *Geochimica et Cosmochimica Acta*, 63(22):3861–3881, 1999.

[392] Sharp, Z. *Principles of stable isotope geochemistry*. Pearson/Prentice Hall, 2007.

[393] Shiel, A. E. and Laubach, P. G. and Johnson, T. M. and Lundstrom, C. C. and Long, P. E. and Williams, K. H. No measurable changes in $^{238}U/^{235}U$ due to desorption-adsorption of U(VI) from groundwater at the Rifle, Colorado, integrated field research challenge site. *Environmental Science and Technology*, 47(6):2535–2541, 2013.

[394] Shields, G. and Veizer, J. Precambrian marine carbonate isotope database: Version 1.1. *Geochemistry, Geophysics, Geosystems*, 3(6):1 of 12–12 of 12, 2002.

[395] Shukolyukov, A. and Lugmair, G. W. Live iron-60 in the early solar system. *Science*, 259(5098):1138–1142, 1993.

[396] Shukolyukov, A. and Lugmair, G. W. Manganese-chromium isotope systematics of carbonaceous chondrites. *Earth and Planetary Science Letters*, 250(1-2):200–213, 2006.

[397] Shukolyukov, A. and Lugmair, G.W. ^{60}Fe in eucrites. *Earth and Planetary Science Letters*, 119(1-2):159–166, 1993.

[398] Siebert, C. and Nagler, T. F. and Kramers, J. D. Determination of molybdenum isotope fractionation by double-spike multicollector inductively coupled plasma mass spectrometry. *Geochemistry Geophysics Geosystems*, 2:art. no.–2000GC000124, 2001.

[399] Simon, S. B. and Davis, A. M. and Grossman, L. Origin of compact type A refractory inclusions from CV3 carbonaceous chondrites. *Geochimica et Cosmochimica Acta*, 63(7/8):1233–1248, 1999.

[400] Sisson, D. H. and Alan Mode, V. and Campbell, D. O. High-speed separation of the rare earths by ion exchange part II. *Journal of Chromatography A*, 66(1):129–135, 1972.

[401] Sivaraman, N. and Kumar, R. and Subramaniam, S. and Vasudeva Rao, P.R. Separation of lanthanides using ion-interaction chromatography with HDEHP coated columns. *Journal of Radioanalytical and Nuclear Chemistry*, 252(3):491–495, 2002.

[402] Slack, J. F. and Grenne, T. and Bekker, A. and Rouxel, O. J. and Lindberg, P. A. Suboxic deep seawater in the late Paleoproterozoic: Evidence from hematitic chert and iron formation related to seafloor-hydrothermal sulfide deposits, central Arizona, USA. *Earth and Planetary Science Letters*, 255(1-2):243–256, 2007.

[403] Sneden, C. and Cowan, J. J. Genesis of the heaviest elements in the milky way galaxy. *Science*, 299(5603):70–75, 2003.

[404] Sneden, C. and Cowan, J. J. and Lawler, J. E. and Ivans, I. I. and Burles, S. and Beers, T. C. and Primas, F. and Hill, V. and Truran, J. W. and Fuller G. M. and Pfeiffer, B. and Kratz, K.-L. The extremely metal-poor, neutron capture-rich star CS 22892-052: A comprehensive abundance analysis. *Astrophysical Journal*, 591(2):936, 2003.

[405] Sneden, C. and Parthasarathy, M. The *r*- and *s*-process nuclei in the early history of the galaxy - HD 122563. *Astrophysical Journal*, 267:757–778, April 1983.

[406] Sochacka, R. J. and Siekierski, S. Reversed-phase partition chromatography with di-(2-ethylhexyl) orthophosphoric acid as the stationary phase. Part I. Separation of rare earths. *Journal of Chromatography A*, 16(C):376–384, 1964.

[407] Staudigel, H. 4.16 - Chemical fluxes from hydrothermal alteration of the oceanic crust. In Turekian, H. D. and Holland, K. K., editor, *Treatise on Geochemistry*, volume 4, pages 583–606. Elsevier, Oxford, second edition, 2014.

[408] Steele, R. C. J. and Elliott, T. and Coath, C. D. and Regelous, M. Confirmation of mass-independent Ni isotopic variability in iron meteorites. *Geochimica et Cosmochimica Acta*, 75(24):7906–7925, 2011.

[409] Steiger, R. H. and Jäger, E. Subcommission on geochronology: Convention on the use of decay constants in geo- and cosmochronology . *Earth and Planetary Science Letters*, 36(3):359–362, 1977.

[410] Stewart, F. H. Chapter Y. Marine evaporites. In *Data of Geochemistry*, pages Y1–Y52. United States Government Printing Office, sixth edition, 1963.

[411] Stewart, K. and Kassakian, S. and Krynytzky, M. and DiJulio, D. and Murray, J. W. Oxic, suboxic, and anoxic conditions in the black sea. In Yanko-Hombach, V. and Gilbert, A. S. and Panin, N. and Dolukhanov, P. M., editor, *The Black Sea Flood Question: Changes in Coastline, Climate, and Human Settlement*, pages 1–21. Springer Netherlands, 2007.

[412] Stirling, C. H. and Andersen, M. B. and Potter, E. K. and Halliday, A. N. Low-temperature isotopic fractionation of uranium. *Earth and Planetary Science Letters*, 264(1-2):208–225, 2007.

[413] Stirling, C. H. and Andersen, M. B. and Warthmann, R. and Halliday, A. N. Isotope fractionation of ^{238}U and ^{235}U during biologically-mediated uranium reduction. *Geochimica et Cosmochimica Acta*, 163(0):200–218, 2015.

[414] Stirling, C. H. and Halliday, A. N. and Porcell, D. In search of live Cm-247 in the early solar system. *Geochimica et Cosmochimica Acta*, 69(4):1059–1071, 2005.

[415] Stirling, C. H. and Halliday, A. N. and Potter, E. K. and Andersen, M. B. and Zanda, B. A low initial abundance of Cm-247 in the early solar system and implications for r-process nucleosynthesis. *Earth and Planetary Science Letters*, 251(3-4):386–397, 2006.

[416] Storzer, D. and Selo, M. Fission track age of magnetic anomaly M-zero and some aspects of sea-floor weathering. *Initial Reports of the Deep Sea Drilling Project*, pages 1129–1133, 1979.

[417] Strelow, F. W. E. and Jackson, P. F. S. Determination of trace and ultratrace quantities of rare earth elements by ion exchange chromatography-mass spectrography. *Analytical Chemistry*, 46(11):1481–1486, 1974.

[418] Stylo, M. and Neubert, N. and Wang, Y. and Monga, N. and Romaniello, S. J. and Weyer, S. and Bernier-Latmani, R. Uranium isotopes fingerprint biotic reduction. *Proceedings of the National Academy of Sciences*, 112(18):5619–5624, 2015.

[419] Swarzenski, P. and Campbell, P. and Porcelli, D. and McKee, B. The estuarine chemistry and isotope systematics of ^{234},^{238}U in the Amazon and Fly Rivers. *Continental Shelf Research*, 24(19):2357–2372, 2004.

[420] Swarzenski, P. W. and McKee, B. A. Seasonal uranium distributions in the coastal waters off the Amazon and Mississippi Rivers. *Estuaries*, 21(3):379–390, 1998.

[421] Swindle, T. D. and Caffee, M.W. and Hohenberg, C.M. Iodine-xenon studies of Allende inclusions: Eggs and the Pink Angel. *Geochimica et Cosmochimica Acta*, 52(9):2215–2227, 1988.

[422] Tachibana, S. and Huss, G. R. The initial abundance of ^{60}Fe in the Solar System. *The Astrophysical Journal Letters*, 588(1):L41, 2003.

[423] Takeda, K. and Obanawa, H. and Kawakami, F. In Fujii, Y. and Nomura, M. and Okamoto, M. and Onitsuka, H. and Nakanishi, T., editor, *Bulletin of Research Laboratory for Nuclear Reactors*, page 192. Tokyo, special issue edition, 1992.

[424] Tanaka, T. and Masuda, A. Rare-earth elements in matrix, inclusions, and chondrules of the allende meteorite. *Icarus*, 19(4):523–530, 1973.

[425] Tang, H. and Dauphas, N. Abundance, distribution, and origin of Fe-60 in the solar protoplanetary disk. *Earth and Planetary Science Letters*, 359:248–263, 2012.

[426] Tang, H. and Dauphas, N. Low ^{60}Fe abundance in semarkona and Sahara 99555. *Astrophysical Journal*, 802(1), 2015.

[427] Tatsumoto, M. and Shimamura, T. Evidence for live Cm-247 in the early solar system. *Nature*, 286:118–122, jul 1980.

[428] Telus, M. and Dauphas, N. and Moynier, F. and Tissot, F. L. H. and Teng, F.-Z. and Nabelek, P. I. and Craddock, P. R. and Groat, L. A. Iron, zinc, magnesium and uranium isotopic fractionation during continental crust differentiation: The tale from migmatites, granitoids, and pegmatites . *Geochimica et Cosmochimica Acta*, 97(0):247–265, 2012.

[429] Thrane, K. and Connelly, J.N. and Bizzarro, M. and Meyer, B.S. and The, L.-S. Origin of excess ^{176}Hf in meteorites. *Astrophysical Journal*, 717(2):861–867, 2010.

[430] Tissot, F. L. H. and Dauphas, N. ^{238}U/^{235}U ratios of anagrams: Angrites and granites. In *Lunar and Planetary Institute Science*, volume 43, 2012. # 1981.

[431] Tissot, F. L. H. and Dauphas, N. Uranium isotopic compositions of the crust and ocean: Age corrections, U budget and global extent of modern anoxia. *Geochimica et Cosmochimica Acta*, 167:113–143, 2015.

[432] Tissot, F. L. H. and Dauphas, N. and Grossman, L. Origin of uranium isotope variations in early solar nebula condensates. *Submitted to Science Advances*.

[433] Tissot, F. L. H. and Dauphas, N. and Reinhard, C. T. and Lyons, T. W. and Asael, D. and Rouxel, O. 7.10.6 Mo and U Geochemistry and Isotopes. In Melezhik, V. A. and Prave, A. R. and Hanski, E. J. and Fallick, A. E. and Lepland, A. and Kump, L. R. and Strauss, H., editor, *Reading the Archive of Earth's Oxygenation*, Frontiers in Earth Sciences, pages 1500–1506. Springer Berlin Heidelberg, 2013.

[434] Tissot, F. L. H. and Go, B. M. and Dauphas, N. and Asael, D. and Reinhard, C. T. and Rouxel, O. and Lyons, T. W. and Ponzevera, E. and Liorzou, C. and Chéron, S. On the ^{238}U/^{235}U paleoredox proxy: A word of caution with black shales and the need for sequential leaching of carbonates. In *Lunar and Planetary Institute Science*, volume 45, 2014. # 2590.

[435] Tribovillard, N. and Algeo, T. J. and Baudin, F. and Riboulleau, A. Analysis of marine environmental conditions based on molybdenum-uranium covariation -Applications to Mesozoic paleoceanography. *Chemical Geology*, 324-325:46–58, 2012.

[436] Tribovillard, N. and Algeo, T. J. and Lyons, T. and Riboulleau, A. Trace metals as paleoredox and paleoproductivity proxies: An update. *Chemical Geology*, 232(1-2):12–32, 2006.

[437] Trinquier, A. and Birck, J.-L. and Allègre, C. J. and Göpel, C. and Ulfbeck, D. ^{53}Mn-^{53}Cr systematics of the early Solar System revisited. *Geochimica et Cosmochimica Acta*, 72(20):5146–5163, 2008.

[438] Trinquier, A. and Elliott, T and Ulfbeck, D. and Coath, C. and Krot, A. N. and Bizzarro, M. Origin of nucleosynthetic isotope heterogeneity in the solar protoplanetary disk. *Science*, 324(5925):374–376, 2009.

[439] Truran, J. W. and Cowan, J. J. and Pilachowski, C. A. and Sneden, C. Probing the neutron-capture nucleosynthesis history of galactic matter. *Publications of the Astronomical Society of the Pacific*, 114(802):1293–1308, 2002.

[440] Turekian, K. The oceans, streams and atmosphere. *Handbook of Geochemistry*, 1:297–323, 1969.

[441] Turner, S. P. and Foden, J. D. and Morrison, R. S. Derivation of some A-type magmas by fractionation of basaltic magma: An example from the Padthaway Ridge, South Australia. *Lithos*, 28(2):151–179, 1992.

[442] Urey, H. C. The thermodynamic properties of isotopic substances. *J. Chem. Soc.*, pages 562–581, 1947.

[443] Uvarova, Y. A. and Kyser, T. K. and Geagea, M. L. and Chipley, D. Variations in the uranium isotopic compositions of uranium ores from different types of uranium deposits. *Geochimica et Cosmochimica Acta*, 146:1–17, 2014.

[444] Veeh, H. H. Deposition of uranium from ocean. *Earth and Planetary Science Letters*, 3(2):145–150, 1967.

[445] Veizer, J. and Hoefs, J. and Lowe, D. R. and Thurston, P. C. Geochemistry of Precambrian carbonates: II. Archean greenstone belts and Archean sea water. *Geochimica et Cosmochimica Acta*, 53(4):859–871, 1989.

[446] Veizer, J. and Hoefs, J. and Ridler, R.H. and Jensen, L.S. and Lowe, D.R. Geochemistry of Precambrian carbonates: I. Archean hydrothermal systems. *Geochimica et Cosmochimica Acta*, 53(4):845–857, 1989.

[447] Verbruggen, A. and Alonso, A. and Eykens, R. and Kehoe, F. and Kuhn, H. and Richter, S. and Aregbe, Y. Preparation and certification of IRMM-3636, IRMM-3636a and IRMM-3636b. *JRC Scientific and Technical Reports*, 2008.

[448] Verma, S. P. and Santoyo, E. High-performance liquid and ion chromatography: Separation and quantification analytical techniques for rare earth elements. *Geostandards & Geoanalytical Research*, 31(3):161–184, 2007.

[449] Walsh, J. N. and Buckley, F. and Barker, J. The simultaneous determination of the rare-earth elements in rocks using inductively coupled plasma source spectrometry. *Chemical Geology*, 33(1-4):141–153, 1981.

[450] Wanajo, S. and Itoh, N. and Ishimaru, Y. and Nozawa, S. and Beers, T. C. The r-process in the neutrino winds of core-collapse supernovae and U-Th cosmochronology. *Astrophysical Journal*, 577(2):853, 2002.

[451] Wang, X. and Johnson, T. M. and Lundstrom, C. C. Isotope fractionation during oxidation of tetravalent uranium by dissolved oxygen. *Geochimica et Cosmochimica Acta*, 150:160–170, 2015.

[452] Wasserburg, G. J. Isotopic adventures - geological, planetological, and cosmic. *Annual Review of Earth and Planetary Sciences*, 31(1):1–74, 2003.

[453] Wasserburg, G. J. and Busso, M. and Gallino, R. Abundances of actinides and short-lived nonactinides in the interstellar medium: Diverse supernova sources for the *r*-processes. *Astrophysical Journal*, 466(2):L109–L113, 1996.

[454] Wasserburg, G. J. and Jacobsen, S. B. and DePaolo, D. J. and McCulloch, M. T. and Wen, T. Precise determination of Sm/Nd ratios, Sm and Nd isotopic abundances in standard solutions. *Geochimica et Cosmochimica Acta*, 45(12):2311–2323, 1981.

[455] Wasserburg, G. J. and Tera, F. and Papanastassiou, D. A. and Huneke, J. C. Isotopic and chemical investigations on Angra dos Reis. *Earth and Planetary Science Letters*, 35(2):294–316, 1977.

[456] Webb, P. C. and Thompson, M. and Potts, P. J. and Stephen, A. and Wilson, S. A. GeoPT28 - an international proficiency test for analytical geochemistry laboratories - report on round 28 (Shale, SBC-1)/January 2011. *GeoPT28 Report*, 2011.

[457] Wedepohl, K. H. The composition of the continental crust. *Geochimica et Cosmochimica Acta*, 59(7):1217–1232, 1995.

[458] Westin, J. and Sneden, C. and Gustafsson, B. and Cowan, J. J. The *r*-process-enriched low-metallicity giant HD 115444. *Astrophysical Journal*, 530(2):783, 2000.

[459] Wetherill, G. W. Isotopic composition + concentration of molybdenum in iron meteorites. *Journal of Geophysical Research*, 69(20):4403–4408, 1964.

[460] Weyer, S. and Anbar, A.D. and Gerdes, A. and Gordon, G. W. and Algeo, T. J. and Boyle, E. A. Natural fractionation of $^{238}U/^{235}U$. *Geochimica et Cosmochimica Acta*, 72(2):345–359, 2008.

[461] Whalen, J. B. and Chappell, B. W. Opaque mineralogy and mafic mineral chemistry of I-and S-type granites of the Lachlan fold belt, Southeast Australia. *American Mineralogist*, 73(3-4):281–296, 1988.

[462] Whalen, J. B. and Currie, K. L. and Chappell, B. W. A-type granites: Geochemical characteristics, discrimination and petrogenesis. *Contributions to Mineralogy and Petrology*, 95(4):407–419, 1987.

[463] White, W. M. *Geochemistry*. Wiley, 2013.

[464] Wohlers, A. and Wood, B. J. A Mercury-like component of early Earth yields uranium in the core and high mantle ^{142}Nd. *Nature*, 520(7547):337–340, 2015.

[465] Yin, Q.-Z. and Jacobsen, S. B. and Yamashita, K. and Blichert-Toft, J. and Télouk, P. and Albarède, F. A short timescale for terrestrial planet formation from Hf-W chronometry of meteorites. *Nature*, 418(6901):949–952, 2002.

[466] Yoshida, K. and Haraguchi, H. Determination of rare earth elements by liquid chromatography/inductively coupled plasma atomic emission. *Analytical Chemistry*, 56(13):2580–2585, 1984.

[467] Zhang, F. An episode of widespread ocean anoxia during the latest Ediacaran Period revealed by light U isotope compositions in carbonates. In *American Geophysical Union Conference Abstracts*, 2015.

APPENDIX

Publication list:

A: [137], Dauphas N., Roskosz M., Alp E.E., Golden D.C., Sio C.K., Tissot F.L.H., Hu M., Zhao J., Gao L., Morris R.V. (2012). A general moment NRIXS approach to the determination of equilibrium Fe isotopic fractionation factors: Application to goethite and jarosite. *Geochim. Cosmochim. Acta* **94**, 254-275.

DOI address: http://dx.doi.org/10.1016/j.gca.2012.06.013

B: [433], Tissot F.L.H., Dauphas N., Reinhard C., Lyons T., Asael D., Rouxel O. (2012) Mo and U Geochemistry and Isotopes. Chapter 7.10.6 In *Reading the Archive of Earth's Oxygenation* (Melezhik, V.A. et al., Eds.), *Volume 3: Global Events in the Fennoscandian Arctic Russia - Drilling Early Earth Project*, 1500-1506.

DOI number: 10.1007/978-3-642-29670-3_10

C: [428], Telus M., Dauphas N., Moynier F., Tissot F.L.H., Teng F.-Z., Nabelek P.I., Craddock P.R., Groat L.A. (2012) Iron, magnesium, zinc and uranium isotopic fractionation during continental crust differentiation: The tale from migmatites, granites, and pegmatites. *Geochim. Cosmochim. Acta* **97**, 247-265.

DOI address: http://dx.doi.org/10.1016/j.gca.2012.08.024

D: [222], Ireland T.J., Tissot F.L.H., Yokochi R., Dauphas N. (2013) Teflon-HPCL: A novel chromatographic system for application to isotope geochemistry and other industries. *Chem. Geol.* **357**, 203-214.

DOI address: http://dx.doi.org/10.1016/j.chemgeo.2013.08.001

E: [28], Asael D., Tissot F.L.H., Reinhard C.T., Rouxel O., Dauphas N., Lyons T.W., Ponzevera E., Liorzou C., Chéron S. (2013) Coupled molybdenum, iron and uranium stable isotopes as oceanic paleoredox proxies during the Paleoproterozoic Shunga Event. *Chem. Geol.* **362**, 193-210.

DOI address: http://dx.doi.org/10.1016/j.chemgeo.2013.08.003

F: [341], Pourmand A., Tissot F.L.H., Arienzo M., Sharifi A. (2014) Introducing a comprehensive data reduction and uncertainty propagation algorithm for U-Th geochronometry with extraction chromatography and isotope dilution MC-ICP-MS, *Geostand. Geoanal. Res.* **38-2**, 129-148.

DOI number: 10.1111/j.1751-908X.2013.00266.x

G: [138], Dauphas N., Roskosz M., Alp E.E., Neuville D., Hu M., Sio C.K., Tissot F.L.H., Zhao J., Tissandier L., Médard E., Cordier C. (2014) Magma redox and structural controls on iron isotope variations in Earth's mantle and crust, *Earth Planet. Sci. Lett.* **398** 127-140.

DOI address: http://dx.doi.org/10.1016/j.epsl.2014.04.033

H: [47], Blanchard M., Dauphas N., Hu M.Y., Roskosz M., Alp E.E., Golden D.C., Sio C.K., Tissot F.L.H., Zhao J., Gao L., Morris R.V., Fornace M., Floris A., Lazzeri M., Etienne Balan E. (2015) Reduced partition function ratios of iron and oxygen in goethite, *Geochim. Cosmochim. Acta* **151**, 19-33.

DOI address: http://dx.doi.org/10.1016/j.gca.2014.12.006

I: [431], Tissot F.L.H., Dauphas N. (2015) Uranium isotopic compositions of the crust and ocean: Constraints on the U budget and global extent of modern anoxia, *Geochim. Cosmochim. Acta*, **167**, 113-143.

DOI address: http://dx.doi.org/10.1016/j.gca.2015.06.034

J: [372], Roskosz M., Sio C.K., Dauphas N., Bi W., Tissot F. L. H., Hu M. Y., Zhao J., Alp E. E. (2015) Spinel-olivine-pyroxene equilibrium iron isotopic fractionation and applications to natural peridotites, *Geochim. Cosmochim. Acta*, **169**, 184-199.

DOI address: http://dx.doi.org/10.1016/j.gca.2015.07.035